UNIVERSITAT POLITÈCNICA DE VALÈNCIA

ELECTRONIC ENGINEERING DEPARTMENT

Electronic devices for the combination of electrically controlled drug release, electrostimulation, and optogenetic stimulation for nerve tissue regeneration

Doctoral Dissertation in Electronic Engineering

Author: Javier Monreal Trigo

Supervisors: Miguel Alcañiz Fillol
Ramón Martínez Máñez

València, Spain
March 2023

Instituto Interuniversitario de Reconocimiento Molecular y Desarrollo Tecnológico

UNIVERSITAT POLITÈCNICA DE VALÈNCIA

Miguel Alcañiz Fillol, PhD in Electronic Engineering and Associate Professor (*Profesor Titular*) at the Universitat Politècnica de València, and **Ramón Martínez Máñez**, PhD in Chemistry and Full Professor (*Catedrático de Universidad*) at the Universitat Politècnica de València.

Hereafter, **CERTIFY**:

That the work *"Electronic devices for the combination of electrically controlled drug release, electrostimulation, and optogenetic stimulation for nerve tissue regeneration"* has been developed by **Javier Monreal Trigo** under their supervision in the Instituto Interuniversitario de Investigación de Reconocimiento Molecular y Desarrollo Tecnológico (IDM), in the Universitat Politècnica de València section, as a **Thesis Project** in order to obtain the degree of **PhD in Electronic Engineering** at the Universitat Politècnica de València.

València, February 21st, 2023.

Prof. Miguel Alcañiz Fillol

Prof. Ramón Martínez Máñez

Dedicado a mis padres y a mi hermana, mis gigantes.

«El arte de la vida es más parecido a luchar que a bailar».
Marco Aurelio

«Si quieres ir rápido, camina solo. Si quieres llegar lejos, ve acompañado».
Proverbio

«Si he logrado ver más lejos ha sido porque he subido a hombros de gigantes».
Isaac Newton

Agradecimientos

Es difícil de expresar con palabras el profundo agradecimiento que quisiera transmitir a todas las personas que me han servido de inspiración, guía, y apoyo durante estos cuatro años y medio de estudios de doctorado.

En primer lugar, quiero agradecer a mis directores, Prof. Miguel Alcañiz y Prof. Ramón Martínez, por ofrecerme la oportunidad de desarrollar este trabajo doctoral, y su guía y orientación en el proceso, en el que el resultado no sólo es el presente documento, si no mi formación como investigador.

Gracias a mis colegas del Grupo en Desarrollo Electrónico y Sensores Impresos (ged+ps IDM): a Rafael Masot, Cristian Olguín, Eduardo García, Javier Ibáñez, Luis Gil, Laura Contat, Nicolás Laguarda, José Vicente Lidón, y Clara Pérez. Gracias a mi colega de grupo y compañero de laboratorio José Manuel Terrés por todo el apoyo técnico y moral durante estos años, en los que hemos forjado una bonita amistad. También agradecer a mi compañero de laboratorio Javier Carrascosa, por su perenne alegría y por siempre tener un momento para ayudarme en el laboratorio cuando lo he necesitado.

Esta tesis no hubiera sido posible sin la colaboración con el grupo NanoSens del IDM. Gracias a todos los que la habéis sido parte: Alba Fernández, Paula Díez, Angy Morella, Cris de la Torre, Bea de Luis, Toni Llopis, Juanfran Blandez y Bea Lozano. Tampoco hubiera sido posible sin la colaboración del grupo en Regeneración Tisular y Neural del CIPF, gracias, Victoria Moreno, Esther Giraldo, María Pedraza, María del Mar Sánchez, Beatriz Martínez, y Neus Torres. También agradecer a Mario Soriano su ayuda en la aplicación de la activación con plasma en los sustratos poliméricos.

Una parte muy relevante de mi tesis ha sido mi estancia en el Serotonin Group de la Universidad de California, Los Ángeles. Gracias Prof. Anne Andrews por acogerme en su equipo, así como a Martin Hartel, Liv Heidenreich, Merel Dagher, Katie Perrota, Sara Erwin, Cameron Movassaghi, Olena Lukayonova, Noelle Mitchell, y Keionna Newton, porque me hicisteis sentir como en casa aun estando a miles de kilómetros de aquí. Gracias a Belén Aranda, Irene Mendoza, y Rubén Manuel por ser mi familia californiana el tiempo de la estancia.

En memoria de Samantha Mensah, una luz brillante en un mundo que a veces resulta demasiado desolador.

Agradecer profundamente a mi familia por su apoyo incondicional: a mis padres y a mi hermana. Siempre habéis estado ahí, vosotros habéis sido mis gigantes.

A Raquel, mi compañera, con mucho por agradecer: por arrojar claridad y perspectiva cuando me vencía el desánimo, por velar porque no me *quemara* cuando me dejaba llevar por la impaciencia y quería terminar la tesis en una jornada maratoniana, por todo el apoyo físico y moral estos últimos meses de escritura, y la lista podría seguir. Somos un gran equipo.

Casi cinco años dan para mucho, y sois muchas las personas a las que me gustaría mencionar: A David Ebrí y Juanan Oliver, mis antiguos compañeros de piso y grandes amigos, que siempre creyeron en mí. A Ivan Balaguer, Anna Beltran, Nacho Díaz, David Chulià, Antonio Martínez, y Nuria Pastor, por todo vuestro calor, me alegra teneros cerca aún terminada nuestra etapa como estudiantes. A Patricio Hidalga, gran amigo y mentor en afrontar los retos de la tesis, del karate, y de la vida. A José Prieto, Sofía Benítez, Juandi Coronel, Alex Martínez, Julián Miguel, y Antonio Parejo, por vuestro apoyo en distintos momentos y formas durante este período.

Los estudios anteriores, desde la primaria hasta la maestría, siguen un camino definido: sus opciones están claramente delimitadas. Sin embargo, esta última etapa de estudios ya no consiste en seguir un camino trazado. Consiste en abrir un nuevo sendero, con la aspiración a que nuestros pasos puedan ser seguidos por otros en el futuro. Con la intención de contribuir al conocimiento científico global. En esta titánica tarea no he estado solo, os he tenido a mi lado. Pero también me ha enseñado que nadie puede dar mis pasos, me ha enseñado a asumir la responsabilidad de aquello que depende de mí. Ha requerido de iniciativa, creatividad, y persistencia; cualidades que estoy contento de haber desarrollado. Pero sin duda, esta tesis no hubiera culminado, o sería claramente inferior en alcance y profundidad, si no fuese por el calor de todos los que me habéis acompañado en este camino. Gracias.

Abstract

Neural precursor cells, a type of *stem cell*, have revolutionized medicine. Their ability to proliferate to form different specialized cells gives them the potential to serve as the basis for effective therapies for pathologies whose treatment was unimaginable until just two decades ago. However, this capacity is mediated by specific and complex physiological, chemical, and electrical stimuli that complicate their translation to clinical routine. For this reason, stem cells represent a field of study in which the scientific community is investing a great deal of effort.

In the field of nerve regeneration, using bio-potentiating substrates and cell membrane matrices makes it possible to provide neural precursor cells with the mechanical and physiological support necessary for their proliferation. To modulate their development and differentiation, pharmacological treatment, electrostimulation, and optogenetic stimulation are techniques that are achieving promising results. For this reason, we have developed a set of electronic systems to allow the combined application of these techniques *in vitro*, with a view to their application *in vivo*.

We have designed a novel technology for the electrically controlled release of drugs. This technology is based on mesoporous silica nanoparticles and bipyridine-heparin molecular gates. The molecular gates are electrochemically reactive and entrap the drugs inside the nanoparticles, releasing them upon electrical stimulus. We have characterized this technology and validated it by controlled release of rhodamine in HeLa cell cultures. For combining electrostimulation and controlled drug release we have developed devices that allow applying the different electrical stimuli in a configurable way from a graphical user interface. In addition, we have designed an expansion module that allows multiplexing electrical signals to different cell cultures. For combining both techniques, we have worked with platforms based on PEDOT conductive polymer derivatives, performing the first successful releases and electrostimulations.

In addition, we have designed an optogenetic stimulation device. This type of stimulation consists of genetically modifying cells to make them sensitive to light radiation of a specific wavelength. In tissue regeneration using neural precursor cells, it is interesting to be able to induce calcium waves, favoring the cell differentiation into neurons and the formation of synaptic circuits. The designed device is compatible with P-24 *in vitro* cell culture matrices and presents reduced dimensions for its incorporation in a confocal microscope. In this way, we can obtain real-time images of the transient responses of cells upon irradiation. The device has been validated by irradiating fetal neurons modified with a photoactivable adenyl cyclase (bPAC)

and measuring the consequent calcium waves propagation upon 100 ms pulsed light stimulation. We have also designed a complementary electronic irradiance measurement device to allow calibration of the irradiator equipment and measuring irradiance in real time during *in vitro* experiments.

The results of using bioactuators in complex and dynamic processes, such as nerve tissue regeneration, are limited in an open loop. One of the main aspects analyzed, which could represent a leap forward in these treatments, is the development of biosensors that would allow quantifying of specific biomolecules to adjust the stimulation provided in real time. Serotonin secretion is an early biochemical response indicator of elongation and neuronal differentiation in precursor cells. Along with serotonin, there are several other biomolecules of interest. Developing biosensors that can selectively measure biomolecules in real time would enable the implementation of closed-loop control. Among the state-of-the-art technologies, biosensors based on field effect transistors (FETs) functionalized with aptamers are promising for this application. However, this technology did not allow the simultaneous measurement of more than one target biomolecule in a small volume due to interferences between the different FETs, whose terminals are immersed in the solution. This is why we have developed electronic instrumentation capable of simultaneously measuring several of these biosensors. We validated the instrumentation with the simultaneous pH measurement by FET biosensors and the preliminary detection of serotonin and glutamate with aptamer-functionalized FETs. Overall, these are significant steps forward in developing closed-loop control of modulation techniques for neural precursor cell development.

Resumen

Las células precursoras neurales, un tipo de *células madre*, han revolucionado la medicina. Su capacidad para proliferar formando distintas células especializadas les otorga la potencialidad de servir de base para terapias efectivas para patologías cuyo tratamiento era inimaginable hasta hace apenas dos décadas. Sin embargo, esta capacidad se encuentra mediada por estímulos fisiológicos, químicos, y eléctricos, específicos y complejos, que dificultan su traslación a la rutina clínica. Por ello, las células madre representan un campo de estudio en el que se invierten amplios esfuerzos por parte de la comunidad científica.

En el ámbito de la regeneración nerviosa, el uso de sustratos bio-potenciadores y matrices de membrana celular permite dotar a las células precursoras neurales del soporte mecánico y fisiológico necesario para su proliferación. Para modular su desarrollo y diferenciación el tratamiento farmacológico, la electroestimulación, y la estimulación optogenética son técnicas que están consiguiendo prometedores resultados. Es por ello por lo que en la presente tesis se ha desarrollado un conjunto de sistemas electrónicos para permitir la aplicación combinada de estas técnicas *in vitro*, con perspectiva a su aplicación *in vivo*.

Hemos diseñado una novedosa tecnología para la liberación eléctricamente controlada de fármacos. Esta tecnología está basada en nanopartículas de sílice mesoporosa y puertas moleculares de bipiridina-heparina. Las puertas moleculares son electroquímicamente reactivas, y encierran los fármacos en el interior de las nanopartículas, liberándolos ante un estímulo eléctrico. Hemos caracterizado esta tecnología, y la hemos validado mediante la liberación controlada de rodamina en cultivos celulares de HeLa. Para la combinación de liberación controlada de fármacos y electroestimulación hemos desarrollado dispositivos que permiten aplicar los estímulos eléctricos de forma configurable desde una interfaz gráfica de usuario. Además, hemos diseñado un módulo de expansión que permite multiplexar las señales eléctricas a diferentes cultivos celulares. Para la combinación de ambas técnicas, hemos trabajado con plataformas basadas en derivados del polímero conductivo PEDOT, realizando las primeras liberaciones y electroestimulaciones satisfactorias.

Además, hemos diseñado un dispositivo de estimulación optogenética. Este tipo de estimulación consiste en la modificación genética de las células para que sean sensibles a la radiación lumínica de determinada longitud de onda. En el ámbito de la regeneración de tejido mediante células precursoras neurales, es de interés poder inducir ondas de calcio, favoreciendo su diferenciación en neuronas y la formación de circuitos sinápticos. El dispositivo diseñado es compatible con matrices de cultivo celular *in vitro* P-24, y presenta dimensiones reducidas para su incorporación en un microscopio confocal. De esta forma, somos

capaces de obtener imágenes en tiempo real de las respuestas transitorias de las células al ser irradiadas. El dispositivo se ha validado irradiando neuronas fetales modificadas con una adenil ciclasa fotoactivable (bPAC) y midiendo la consecuente propagación de ondas de calcio tras la estimulación con luz pulsada de 100 ms. También hemos diseñado un dispositivo electrónico complementario de medida de irradiancia con el doble fin de permitir la calibración del equipo de irradiancia y medir la irradiancia en tiempo real durante los experimentos *in vitro*.

Los resultados del uso de los bioactuadores en procesos complejos y dinámicos, como la regeneración de tejido nervioso, son limitados en lazo abierto. Uno de los principales aspectos analizados, que podrían suponer un salto adelante en estos tratamientos, es el desarrollo de biosensores que permitiesen la cuantización de ciertas biomoléculas para ajustar la estimulación suministrada en tiempo real. La segregación de serotonina es una respuesta bioquímica indicadora temprana de elongación y diferenciación neuronal en células precursoras. Además de la serotonina, hay otras biomoléculas de interés. El desarrollo de biosensores con capacidad de medir de forma selectiva biomoléculas en tiempo real permitiría la implementación del control en lazo cerrado. Entre las tecnologías en el estado del arte, los biosensores basados en transistores de efecto de campo (FET) funcionalizados con aptámeros son realmente prometedores para esta aplicación. Sin embargo, esta tecnología no permitía la medición simultánea de más de una biomolécula objetivo en un volumen reducido debido a las interferencias entre los distintos FETs, cuyos terminales se encuentran inmersos en la solución. Por ello, hemos desarrollado instrumentación electrónica capaz de medir simultáneamente varios de estos biosensores. Hemos validado la instrumentación con la medición simultánea de pH mediante biosensores FET y la detección preliminar de serotonina y glutamato con FETs funcionalizados con aptámeros. En términos generales, se trata de avances significativos en el desarrollo de un control en lazo cerrado para las técnicas de modulación del desarrollo de células precursoras neurales.

Resum

Les cèl·lules precursores neurals, un tipus de *cèl·lules mare*, han revolucionat la medicina. La seua capacitat per a proliferar formant diferents cèl·lules especialitzades els atorga la potencialitat de servir de base per a teràpies efectives per a patologies el tractament de les quals era inimaginable fins fa a penes dues dècades. No obstant això, aquesta capacitat es troba mediada per estímuls fisiològics, químics, i elèctrics, específics i complexos, que dificulten la seua translació a la rutina clínica. Per això, les cèl·lules mare representen un camp d'estudi en el qual s'inverteixen amplis esforços per part de la comunitat científica.

En l'àmbit de la regeneració nerviosa, l'ús de substrats bio-potenciadors i matrius de membrana cel·lular permet dotar a les cèl·lules precursores neurals del suport mecànic i fisiològic necessari per a la seua proliferació. Per a modular el seu desenvolupament i diferenciació el tractament farmacològic, l'electroestimulació, i l'estimulació optogenética són tècniques que estan aconseguint prometedors resultats. És per això que en la present tesi s'ha desenvolupat un conjunt de sistemes electrònics per a permetre l'aplicació combinada d'aquestes tècniques *in vitro*, amb perspectiva a la seua aplicació *in vivo*.

Hem dissenyat una nova tecnologia per a l'alliberament elèctricament controlat de fàrmacs. Aquesta tecnologia està basada en nanopartícules de sílice mesoporosa i portes moleculars de bipiridina-heparina. Les portes moleculars són electroquímicament reactives, i tanquen els fàrmacs a l'interior de les nanopartícules, alliberant-los davant un estímul elèctric. Hem caracteritzat aquesta tecnologia, i l'hem validada mitjançant l'alliberament controlat de rodamina en cultius cel·lulars de HeLa. Per a la combinació d'alliberament controlat de fàrmacs i electroestimulació hem desenvolupat dispositius que permeten aplicar els estímuls elèctrics de manera configurable des d'una interfície gràfica d'usuari. A més, hem dissenyat un mòdul d'expansió que permet multiplexar els senyals elèctrics a diferents cultius cel·lulars. Per a la combinació de totes dues tècniques, hem treballat amb plataformes basades en derivats del polímer conductiu PEDOT, realitzant els primers alliberaments i electroestimulacions satisfactòries.

A més, hem dissenyat un dispositiu d'estimulació optogenètica. Aquest tipus d'estimulació consisteix en la modificació genètica de les cèl·lules perquè siguen sensibles a la radiació lumínica de determinada longitud d'ona. En l'àmbit de la regeneració de teixit mitjançant cèl·lules precursores neurals, és d'interés poder induir ones de calci, afavorint la seua diferenciació en neurones i la formació de circuits sinàptics. El dispositiu dissenyat és compatible amb matrius de cultiu cel·lular *in vitro* P-24, i presenta dimensions reduïdes per a la seua incorporació en un microscopi confocal. D'aquesta manera, tenim la capacitat d'obtindre

imatges en temps real de les respostes transitòries de les cèl·lules en ser irradiades. El dispositiu s'ha validat irradiant neurones fetals modificades amb una adenil ciclasa fotoactivable (bPAC) i mesurant la conseqüent propagació d'ones de calci després de l'estimulació amb llum polsada de 100 ms. També hem dissenyat un dispositiu electrònic complementari de mesura d'irradiància amb el doble fi de permetre el calibratge de l'equip d'irradiància i mesurar la irradiància en temps real durant els experiments *in vitro*.

Els resultats de l'ús dels bioactuadors en processos complexos i dinàmics, com la regeneració de teixit nerviós, són limitats en llaç obert. Un dels principals aspectes analitzats, que podrien suposar un salt avant en aquests tractaments, és el desenvolupament de biosensors que permeteren la quantització de certes biomolècules per a ajustar l'estimulació subministrada en temps real. La segregació de serotonina és una resposta bioquímica indicadora primerenca d'elongació i diferenciació neuronal en cèl·lules precursores. A més de la serotonina, hi ha altres biomolècules d'interés. El desenvolupament de biosensors amb capacitat de mesurar de manera selectiva biomolècules en temps real permetria la implementació del control en llaç tancat. Entre les tecnologies en l'estat de l'art, els biosensors basats en transistors d'efecte de camp (FET) funcionalitzats amb aptàmers són realment prometedors per a aquesta aplicació. No obstant això, aquesta tecnologia no permetia el mesurament simultani de més d'una biomolècula objectiu en un volum reduït a causa de les interferències entre els diferents FETs, els terminals dels quals es troben immersos en la solució. Per això, hem desenvolupat instrumentació electrònica capaç de mesurar simultàniament diversos d'aquests biosensors. Hem validat la instrumentació amb el mesurament simultani del pH mitjançant biosensors FET i la detecció preliminar de serotonina i glutamat amb FETs funcionalitzats amb aptàmers. En termes generals, es tracta d'avanços significatius en el desenvolupament d'un control en llaç tancat per a les tècniques de modulació del desenvolupament de cèl·lules precursores neurals.

Preface

Since the dawn of medicine, the regeneration of central nervous system injuries has inspired myths and legends. People without the ability to walk due to spinal cord injury could walk again by a miracle. With scientific and technical progress, what was once just a wish (or even unimaginable) has progressively become part of our current reality, thanks to the meritorious efforts of many men and women. The discovery of stem cells, cells with the capacity to generate any specialized cell in the human body, represented the first realistic aspiration to find an effective treatment for lesions in the central nervous system, among many other applications. However, the complexity of the mechanisms that allow this capacity is still under study.

Nowadays, the study of these mechanisms and the application of stimuli to modulate stem cell development for specific applications are two sides of the same coin. The triad of stimulation techniques with the greatest potential comprises pharmacological administration, electrostimulation, and optogenetics (based on the genetic cell modification to make them responsive to optical stimuli). Every technique induces biochemical responses from the stem cells. Thus, real-time monitoring of the biochemical responses will allow us to modulate the stimuli, engineering closed-loop systems.

The development of electronic devices for the application and real-time measurement of the response of these stimuli is advancing at the same pace as the discipline itself.

In the present doctoral thesis in electronic engineering, we designed electronic devices for this purpose, actively participating in the conceptualization, development, and validation of their *in vitro* application. The structure of the document is as follows:

- **Chapter 1**: we describe the design, development, and validation of equipment for the *in vitro* combination of electrostimulation and controlled drug release.
- **Chapter 2**: focused on designing and characterizing a new technology for voltage-controlled drug release.
- **Chapter 3**: we explain the advances in the application of electrostimulation for the modulation of stem cell development *in vitro*.
- **Chapter 4**: we debate the design, development, and validation of optogenetic stimulation equipment with real-time visualization by confocal microscopy.
- **Chapter 5**: we discuss the design, development, and validation of equipment for real-time measurement of biomolecules related to stem cell modulation processes.

A transdisciplinary line of research such as this requires combining knowledge and techniques from electronic engineering, organic and inorganic chemistry, cell biology, and genetics. Some thematic units may be unfamiliar to the reader with an electronic engineering background but without experience in stem cell therapy or gated materials. This may be particularly noticeable in the Introduction and Chapters 2 and 3. For this reason, a section summary is included at the end of some sections of these parts of the thesis that delve into the biological or chemical details of this research line. These paragraphs are preceded by the bold indicator "**section summary**" or "**subsection summary**".

On the other hand, the uninitiated in electronics can avoid reading the core part *Chapter 1* by going directly to the conclusion, which summarizes the importance of the devices developed for *Chapter 2* and *Chapter 3*.

Chapter 4 (optogenetics) and *Chapter 5* (biosensing), however, are thematic units in which the specifications of the electronic design, its details, and its experimental validation are intimately related. It has not been possible to disaggregate the electronic design from its application, as in the case of electrostimulation and controlled drug release.

Scientific production

The scientific production during the development of this doctoral thesis up to the date of publication has been as follows.

Directly related to the doctoral thesis

Journal articles

- García-Fernández, Alba; Lozano-Torres, Beatriz; Blandez, Juan F.; Monreal-Trigo, Javier; Soto Camino, Juan; Collazos-Castro, Jorge E.; Alcañiz, Miguel; Marcos, María D.; Sancenón, Félix; Martínez-Máñez, Ramón (2020). **Electro-responsive films containing voltage responsive gated mesoporous silica nanoparticles grafted onto PEDOT-based conducting polymer**. Journal of Controlled Release (323) 421 - 430. https://doi.org/10.1016/j.jconrel.2020.04.048
- Monreal-Trigo, Javier; Terrés-Haro, José Manuel; Martínez-Rojas, Beatriz; Sánchez-Martín, María del Mar; Giraldo, Esther; Moreno Manzano, Victoria; Alcañiz Fillol, Miguel (2023) **Optogenetic stimulation array for confocal microscopy fast transient monitoring**. IEEE Transactions on Biomedical Circuits and Systems 16 (6), 1397-1405. https://doi.org/10.1109/TBCAS.2022.3226558
- Monreal-Trigo, Javier; Heidenreich, Liv; Hartel, Martin C.; Mitchell, Noelle; Lukoyanova, Olena; Alcañiz Fillol, Miguel; Andrews, Anne M. (2023). **Fully integrated measurement platform for real-time multiplexed field-effect transistor biosensors**. Sensors & Actuators B: Chemical. Submitted.

International congress participations

- Monreal-Trigo, Javier; Alcañiz Fillol, Miguel (2019). **Electronic system for combined techniques: electrostimulation and controlled electrochemical drug release**. XIII International Workshop on Sensors and Molecular Recognition (IWOSMOR 2019). (76 - 79). València, Spain.
- Monreal-Trigo, Javier; Bastida-Molina, Cristina; Vengut-Tro, Roberto; Alcañiz Fillol, Miguel (2021). **Remote electronic system for long-duration in-vitro combination of electrostimulation and electrically controlled drug release**. XIV International Workshop on Sensors and Molecular Recognition (IWOSMOR 2021). (198 - 201). València, Spain.
- Luís Alamán-Escolano; Monreal-Trigo, Javier; Blandez, Juan F.; Garcia-Breijo, Eduardo; Giraldo-Reboloso, Esther; Sánchez-Martin, María del Mar; Moreno-Manzano, Victoria (2021). **In-vitro culture well for the combined application of electrostimulation and**

electrically-controlled drug release. XIV International Workshop on Sensors and Molecular Recognition (IWOSMOR 2021). (152 - 155). València, Spain.

- Terrés-Haro, José Manuel; Monreal-Trigo, Javier; Martínez-Rojas, Beatriz; Giraldo-Reboloso, Esther; Moreno-Manzano, Victoria (2021). **OSIVE prototype for optogenetic stimulation.** XIV International Workshop on Sensors and Molecular Recognition (IWOSMOR 2021). (140 - 143). València, Spain.
- Beltrán Morte, Vicente; Monreal-Trigo, Javier; Terrés-Haro, José Manuel; Giraldo-Reboloso, Esther; Martínez-Rojas, Beatriz; Moreno-Manzano, Victoria (2021). **High-irradiance real-time measurement system for in-vitro optogenetic stimulation.** XIV International Workshop on Sensors and Molecular Recognition (IWOSMOR 2021). (206 - 209). València, Spain.
- Monreal-Trigo, Javier; Terrés-Haro, José Manuel; Giraldo-Reboloso, Esther; Moreno-Manzano, Victoria (2021). **Development and perspectives of optochemogenetic devices at IDM**. XIV International Workshop on Sensors and Molecular Recognition (IWOSMOR 2021). (24 - 27). València, Spain.
- Klaas Meersman; Bert Pyck; Alejandro López-Rodríguez; Monreal-Trigo, Javier; Alcañiz Fillol, Miguel (2022). **Evaluation of the potential distribution in a two-electrode electrochemical cell**. XV International Workshop on Sensors and Molecular Recognition (IWOSMOR 2022). (80 - 82). València, Spain.
- Beltrán Morte, Vicente; Monreal-Trigo, Javier; Jakob Sabbe; Flor Boydens; Alcañiz Fillol, Miguel; Heidenreich, Liv K. (2021). **Low cost measurement system for biosensors based on Organic Electrochemical Transistors (OECTs) and Field Effect Transistors (FETs).** XIV International Workshop on Sensors and Molecular Recognition (IWOSMOR 2021). (28 - 31). València, Spain.
- Heidenreich, Liv; Monreal-Trigo, Javier; Hartel, Martin C.; Lukoyanova, Olena; Alcañiz Fillol, Miguel; Andrews, Anne M. (2021). **Custom measurement platform for aptamer Field Effect Transistor arrays**. Brain Research Institute 31st Annual Neuroscience Poster Session. Los Angeles, California, United States.
- Jorge Benedicto Centeno; Klaas Meersman; Monreal-Trigo, Javier; Alejandro López-Rodríguez; Alcañiz Fillol, Miguel (2022). **Design and implementation of an electronic measurement system based on electrochemical organic transistors (OECTs) functionalized with aptamers**. XV International Workshop on Sensors and Molecular Recognition (IWOSMOR 2022). (73 - 75). València, Spain.
- Monreal-Trigo, Javier; Heidenreich, Liv K.; Hartel, Martin C.; Terrés-Haro, José Manuel; Lukayonova, Olena; Alcañiz Fillol, Miguel (2022). **Data analysis graphic user interface for transistor-based biosensors**. XV International Workshop on Sensors and Molecular Recognition (IWOSMOR 2022). (83 - 86). Valencia, Spain.

Other scientific production during the period of the doctoral thesis

Journal articles

- Terrés-Haro, José Manuel; Hernández-Montoto, Andy; María Pardo-Huguet; De La Torre-Paredes, Cristina; Monreal-Trigo, Javier; Ibáñez Civera, Francisco Javier; Masot-Peris, Rafael; Martínez-Máñez, Ramón; García-Breijo, Eduardo (2022). **Validation of an automated system for the experimentation of photothermal therapies on cell cultures**. Sensors and Actuators A: Physical, 113426 (337). https://doi.org/10.1016/j.sna.2022.113426
- Monreal-Trigo, Javier; Alcañiz, Miguel; Martínez-Bisbal, M. Carmen; Loras, Alba; Pascual, Lluís; Ruiz-Cerdá, José Luis; Ferrer, Alberto; Martínez-Máñez, Ramón (2022). **New bladder cancer non-invasive surveillance method based on voltammetric electronic tongue measurement of urine**. iScience 25(9), 104829. https://doi.org/10.1016/j.isci.2022.104829
- Terrés-Haro, José Manuel; Monreal-Trigo, Javier; Hernández-Montoto, Andy; Ibáñez-Civera, Francisco Javier; Masot-Peris, Rafael; Martínez-Máñez, Ramón (2023). **Finite Element Models of gold nanoparticles and their suspensions for photothermal effect calculation**. MDPI Bioengineering, 10(2), 232. https://doi.org/10.3390/bioengineering10020232
- Terrés-Haro, José Manuel; Monreal-Trigo, Javier; Sánchez-Martín, María del Mar; Martínez-Rojas, Beatriz; Giraldo, Esther; Moreno Manzano, Victoria; Alcañiz Fillol, Miguel (2023). **High-irradiance optogenetic stimulation device for in-vitro real-time rapid transitory response observation**. IEEE Transactions on Biomedical Circuits and Systems. Submitted.
- Ramón, José Enrique; Gandia-Romero, José Manuel; Monreal-Trigo, Javier; Bataller, Román; Soto, Juan; Alcañiz, Miguel (2023). **Integrated Network of Sensors for Smart Corrosion Monitoring in Reinforced Concrete Structures**. Sensors & Actuators B: Chemical. Submitted.

International congress participations

- Victoria Pacherres; Bert Pyck; Alejandro López-Rodríguez; Monreal-Trigo, Javier; Alcañiz Fillol, Miguel (2022). **Design and implementation of an electronic system for the measurement of impedimetric sensors functionalised with aptamers**. XV International Workshop on Sensors and Molecular Recognition (IWOSMOR 2022). (91 - 94). València, Spain.
- Monreal-Trigo, Javier; Jakob Sabbe; Terrés-Haro, José Manuel; Alcañiz Fillol, Miguel (2022). **Encoded light powered and commanded system for drug controlled release for**

skin biomedical applications. XV International Workshop on Sensors and Molecular Recognition (IWOSMOR 2022). (87 - 90). València, Spain.

- Alejandro López-Rodríguez; Alcañiz Fillol, Miguel; Monreal-Trigo, Javier; Rodríguez-Ballester, Francisco (2022). **Design and development of a wearable EIT system for real-time hand gesture recognition using Machine Learning**. XV International Workshop on Sensors and Molecular Recognition (IWOSMOR 2022). (76 - 79). València, Spain.
- Terrés-Haro, José Manuel; Monreal-Trigo, Javier; Ibáñez Civera, Francisco Javier; Garcia-Breijo, Eduardo (2022). **Thermopile for laser power measurement in optical hyperthermia**. XV International Workshop on Sensors and Molecular Recognition (IWOSMOR 2022). (95 - 98). Valencia, España.

Index

Introduction

The nervous tissue regeneration research presents well-founded hopes since the discovery of *stem cells*. Their pluripotentiality made them the spark of a revolution in several applications in the medical field. However, no revolution triumphs in one single act. Instead, the initial enthusiastic optimism often encounters the obstacles of harsh reality. The lessons learned from these encounters forged the knowledge that truly makes such a revolution. Soon after their discovery, we became increasingly aware of the complexity of the underlying mechanisms involved in stem cells' proliferation into specialized cells. This complexity made the study of stem cells a vast research field, delaying but preparing the breakthrough of the already announced revolution of their application. Nowadays, we can affirm that the application of stem cells in several medical applications is a reality, and the radical paradigm shift has begun. Nevertheless, one of the most promising applications is yet to be developed: the induction of functional nervous tissue regeneration in the severely injured spinal cord.

Hence, in this introduction, we are going to address the following:

1. **Neural precursor cells**, as a particular kind of stem cells.
2. Application potentialities of neural precursor cell-based therapy for **spinal cord injury** treatment.
3. **Techniques for modulating neural precursor cell development** regarding biochemical, electric, and optogenetic stimulation.
4. **Electrochemical techniques**, given the need to apply electric stimulation to the neural precursor cells or to trigger a controlled drug release.
5. **Controlled drug release**, a discipline with the capability to deliver pharmacological treatment by applying a stimulus, *e.g.*, electrical.
6. **Real-time** feedback needs on biochemical systems through next-generation **biosensors**, specifically via aptamer-FET technology.

1. Neural Precursor Cells (NPC)

The definition of *stem cells* has been a scientific debate for the last decades. A definition with the general agreement can be cited from van der Kooy & Weiss [1] "stem cells are the multipotential, self-renewing cells that sit at the top of the lineage hierarchy and proliferate to make differentiated cell types of a given tissue *in vivo"*.

From this consensus, different questions arise: How many cell divisions are required to be considered a stem cell (Gao *et al.* [2])? How many different cell types need to be generated by a stem cell (Götz [3])? Or are induced multipotent cells stem cells or not (Götz *al.* [4])? Rather than considering stem cells as undifferentiated cells, it may be more productive to consider them appropriately differentiated for their specific tissue niches (Watt & Hogan [5]). Two different classifications are worth mentioning:

- According to their **cell fate**, stem cells can present four potential outcomes: quiescence, symmetric self-renewal, asymmetric self-renewal, or symmetric division without self-renewal (see Kolios & Moodley [6]).
- According to their **potentiality**, stem cells can be classified as totipotent (capable of forming an entire organism), pluripotent (able to differentiate into ectoderm, endoderm, and mesoderm cells, *i.e.*, from all germ layers), multipotent (able to differentiate into cells from a single germ layer), oligopotent (into lineages within a specific tissue), or unipotent (forming only one lineage) (see Biehl & Russell [7]).

The progenitor cells of the central nervous system (CNS) that give rise to the majority of the glial and neuronal cell types are called *neural progenitor cells* (or *neural precursor cells*) (NPCs). Regarding their potentiality, NPCs do not create all the cells found in the CNS, *e.g.*, non-neural cells found in the CNS, such as the immune system cells.

Even if NPCs can be found in the CNS of developing embryos, they can also be found in the mature adult brain. Hence, not all NPCs can be labeled as embryonic stem cells. The current evidence indicates that embryonic NPCs may lead to adult NPCs, as found in the cerebral cortex. This differentiation also manifests in their potentiality and cell fate, given that embryonic NPCs have more potential than NPCs in the adult brain. NPCs are characterized based on their location in the CNS, morphology, gene expression profile, temporal distribution, and function (Martínez-Cerdeño & Noctor [8]). NPCs can be outsourced from *induced pluripotent stem cells* (iPSC) or embryonic stem cells differentiated *in vitro*. iPSCs are adult cells genetically engineered to have a state of pluripotency resembling an embryo, typically from fibroblasts or blood cells.

Section summary: *Stem cells* are a broad category of cells that can proliferate into specialized cells. Their definition and classification are still under debate. Among stem cells, *neural precursor cells* (NPCs) can proliferate into specialized neural cells, such as neurons, glia, and oligodendrocytes. NPCs can be obtained from engineered cells (iPSCs) or embryonic stem cells. NPCs form a heterogeneous category: each lineage can be characterized according to genetic, functional, and morphological parameters, among others. Therefore, cell therapies based on NPCs need to consider these characteristics appropriately.

2. NPC application potentialities in the Spinal Cord Injury

Spinal Cord Injury (SCI) is a devastating traumatic event disconnecting the brain from the peripheral nervous system (PNS). Patients may suffer from urinary and bowel incontinence, sexual dysfunction, and sensorimotor paralysis (Furlan *et al.* [9], Simpson *et al.* [10]). It is a pathology that affects 930,000 people every year (James *et al.* [11]). Conventional approaches for SCI treatment involve therapeutic agents (*e.g.* riluzole, with neuroprotective properties), Rho[1] antagonists, and surgical decompression. However, they present limited effectiveness. The use of stem cell therapy and optogenetics are the two main approaches to overcome their limitation (Ahmad *et al.* [12]).

The severity of an SCI is not homogeneous. According to Shinozaki *et al.* [13] there are three kinds of SCI: incomplete, pseudo-complete, and complete (see **Figure 1**).

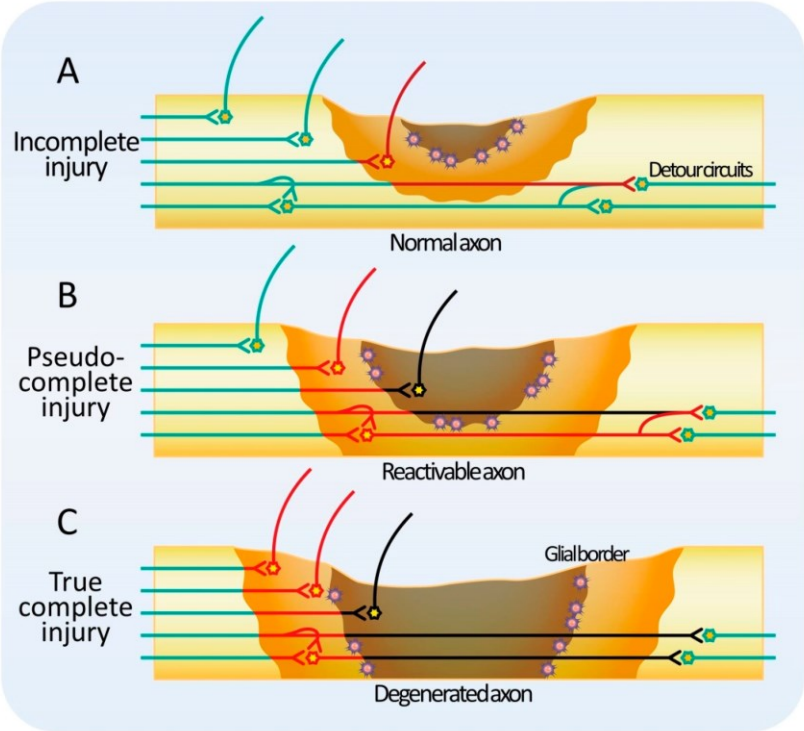

Figure 1. Classification of Spinal Cord Injuries. (**A**) Incomplete injury with residual functional tissue. Recovery is expected with conventional treatment. (**B**) Pseudo-complete injury. Non-functional but reactivable tissue (light brown) extends through the spinal cord, breaking the craniocaudal functional continuity. Recovery is difficult with conventional treatment. Functional recovery is expected by promoting axonal elongation and promoting neural activity in reactivable tissue. (**C**) True complete injury. Aneural tissue (also known as *gray*)

[1] Rho (*Ras homologous*) are monomeric proteins that function in signal transduction pathways in response to chemical or mechanical stimuli, regulating critical biological processes such as cell growth, transformation, metastasis, apoptosis, response to stress, and certain aspects of development. In SCI they are associated with neural circuit reorganization inhibition.

spans the entire spinal cord, and treatment of surrounding reactivable tissue at the rostral or caudal location does not provide a functional cranial connection. Reproduced from [13]. Cells (CC BY 4.0) 2021 MDPI.

In all of them, providing combinations of permissive substrates, chemoattractive growth factors, and activating intrinsic growth (mechanically, electrically, or via other methods) can result in substantial growth through non-neural lesion cores (see the works of Blesch *et al.* [14] and Anderson *et al.* [15]), guiding the otherwise aberrant synaptogenesis (Kaplan *et al.* [16]).

Nevertheless, **in the pseudo-complete and complete SCI, more is needed**. Three compartments can be identified in these kinds of SCI, with different mechanisms underlying regeneration failure: the non-neural (stromal) lesion core, astrocyte scar borders, and spared reactive neural tissue (Sofroniew [17]). These compartments are composed of various cell types with highly distinct functions in regeneration and repair. Each compartment's unique cell biology and molecular pathways have a particular impact on axon growth and regeneration.

After the removal of debris, stromal and remaining inflammatory cells constitute the non-neural lesion core. Astrocyte scars create limiting borders around non-neural lesion cores to contain inflammation. All the elements of functional neural tissue are present in damaged but reactive neural tissue. As a result, this tissue experiences circuit reconfiguration in areas right next to the limiting boundaries around lesion cores. The existence of growth inhibitory mechanisms restricts axon sprouting and synaptic remodeling in spared and reorganizing tissue. The main factor contributing to regeneration failure is the lack of adequate levels of numerous growth facilitators in the non-neural lesion core and its surroundings.

At least some neuronal connection across the lesion level is preserved in anatomically incomplete SCI, even if the injury is initially functionally complete. This connectivity, preserved after the injury or sparse, may reconnect through two primary paths: directly, from supraspinal sources, or indirectly, via relay circuits in the propriospinal region. As circuits restructure, this may or may not result in different degrees of spontaneous functional recovery. Anatomically incomplete SCI outcomes are improved by treatments that improve the restructuring and function of spared connections. In comparison, anatomically complete SCI requires innovative therapies to reconnect neuronal networks across the lesion because there is no neural connectivity at all at the lesion level (Sofroniew [17]).

The anatomically complete SCI **lacks spontaneous regeneration capabilities** due to a series of factors that hinder axon regeneration. The most important ones are related to the chondroitin sulfate proteoglycans (CSPG) secretion from astrocytes creating an extracellular matrix, leading to fibrotic scar formation which lacks regeneration support (see Klapka & Müller [18]). The characteristics of this scar have a natural role in the limitation of neurite outgrowth (see the works of Schachtrup *et al.* [19], Lang *et al.* [20], and Filous & Silver [21]).

Nevertheless, it is not an unequivocal constraint to be removed, as pointed out by Göritz *et al.* [22], rather it can be regeneration-supportive with laminin, anti-fibrotic, and axon-specific growth factors (conclusions from Anderson *et al.* [15], Filous & Silver [21], Adams & Gallo [23], and Zhu *et al.* [24] works), also CSPG modulates synapses plasticity (Mironova & Giger [25]). Other major circumstances are the decreased intracellular cAMP[2] concentration (Lu *et al.* [26]), and myelin-related growth factors (Schwab & Strittmatter [27]), among other variables related to the macro- and microglia and inflammatory response (see the works of Göritz *et al.* [22], Zhu *et al.* [24], and Burda & Sofroniew [28]).

According to Sofroniew [17], complete and pseudo-complete SCI are promising targets for neural precursor cells (NPC) and supportive stem cell (SSC) therapy. The works of Kadoya *et al.* [29], Rosenzweig *et al.* [30], and Kumamaru *et al.* [31] demonstrated the capabilities of **NPC grafts** for the implementation of a **relay mechanism**, bridging the lesion connecting the spared but reactive neural tissue at both sides. This relay needs to be followed by a relative reinforcement of functional connections, as shown in the works of Hilto *et al.* [32] and Wahl *et al.* [33]. Furthermore, the reestablishment of neural connections and circuit reorganization modulation shall be combined with neuroprotection and inflammation control strategies (O'Shea *et al.* [34]).

NPC therapy has demonstrated inflammatory modulation capabilities (see Cusimano *et al.* [35]), cAMP upregulation, resulting in ramified microglia and controlled scar (as reported by Martínez-Rojas *et al.* [36], from our collaborators at Victoria Moreno Manzano's group at CIPF) in SCI.; Supportive stem cell (SSC) therapy showed differentiation (Kumar *et al.* [37]), neuroprotective and axon-regeneration support (Gu *et al.* [38] and Sharp *et al.* [39]), and anti-inflammatory, anti-apoptotic and immunomodulatory effects (Mukhamedshina *et al.* [40]) in these severe lesions. Also, re-myelinization seems to facilitate regeneration through the transplantation of oligodendrocyte progenitor cells (OPC) (Kamata *et al.* [41]) and NPCs (Hunt *et al.* [42]), even if it is shown to not be an indispensable factor (Duncan *et al.* [43]). Both, supportive stem cell (SSC), and neural precursor cells (NPC), are useful for tissue reactivation and regeneration.

Biomaterial characteristics for tissue regeneration are reviewed in depth by Kharbikar *et al.* [44]. For relay bridging, an **adequate substrate implant** becomes a necessity in semi-complete and complete SCI. Its biodegradation should pace the formation of functional tissue.

[2] Cyclic adenosine monophosphate (cAMP, cyclic AMP, or 3',5'-cyclic adenosine monophosphate) is a second messenger important in many biological processes. cAMP is a derivative of adenosine triphosphate (ATP) and used for intracellular signal transduction in many organisms, conveying the cAMP-dependent pathway.

Section summary: Spinal Cord Injury (SCI) presents low or no intrinsic regeneration capabilities. The main reason is that the natural scar formation lacks adequate levels of growth facilitators. The strategies for administrating these growth factors include pharmacological injections, supportive scaffolds, and cell therapy. Among them, NPCs and other supportive-cell therapies have shown promising results. Furthermore, the core of the SCI lacks neural connectivity. Both edges of the lesion need to be reconnected to recover function. With this purpose, NPC grafts in appropriate substrates can be implanted to bridge the lesion.

3. Techniques for modulating neural precursor cell development

At this point, it is evident that tissue engineering is composed of three key factors: stem cells, scaffold, and stimulating factors, as stated by Bhardwaj *et al.* [45]. The selection of the scaffold and the stimulating factors are interrelated. There are, mainly, three techniques for the modulation of the neural precursor cell fate:

1. **Biochemical modulation**, applying pharmacologic treatment, or guiding the axonal regeneration via engineered scaffolds and surfaces.
2. **Electrostimulation**, through the application of electric and magnetic fields, or electrical currents through the injured nervous tissue to induce a relay bridge.
3. **Optogenetic stimulation**, based on optically-evoked neuronal activity, that induces the formation of new circuits or the release of neurotrophic factors. Genetic targeting restricts manipulating only the cell population of interest (Janovjak & Kleinlogel [46]).

3.1 Techniques based on biochemical modulation

Four types of environmental axon guidance molecules have been identified by developmental neurobiology (Tessier-Lavigne & Goodman [47], and Dodd & Jessell [48]):

1. Diffusible chemoattractive.
2. Diffusible chemorepulsive.
3. Contact-attractive.
4. Contact-repulsive.

The existence of both chemoattractive and chemorepulsive molecules has been corroborated in research. The lack of spontaneous regeneration in SCI raised two opposed hypotheses: it was mainly due to the presence of chemorepulsive molecules or principally due to the absence of chemoattractive factors. The latter has been corroborated in the regular

accumulation of evidence: the lack of growth facilitators in the injured adult CNS is the determining factor for its regeneration failure. Therefore, **chemoattractive growth factors and permissive substratum** are critical for axon growth in SCI (Sofroniew [17]).

After the revision of state of the art, the following rationale is developed (and explained, point by point): Given the limitations in spontaneous regeneration (1), supportive stem cells (SSC) (2), and drug delivery (3), with NPCs relaying the non-neural lesion core on adequate substrates (4) is the most promising strategy for SCI treatment. However, the precise growth factors equilibrium for every stage of the treatment must be met (5):

1. Adult CNS neurons downregulate axon growth capacity after maturity (Goldberg *et al.* [49]) and **exhibit poor reactivation** of intrinsic growth programs after injury (He & Jin [50]).
2. Grafts of genetically modified cells can have a **supporting** role, providing a permissive substrate, and chemoattractive growth factors attract injured axon regrowth across SCI lesions and beyond (Deng *et al.* [51] and Alto *et al.* [52]).
3. Genetic and biochemical **reactivation** of neuron-intrinsic growth can reproducibly stimulate long-distance axon regrowth through adult neural tissue (as shown in the works of Sun *et al.* [53], Benowitz *et al.* [54], Bei *et al.* [55], and Liu *et al.* [56])
4. Nevertheless, this is not enough in the adult **non-neural lesion core** tissue (Zukor *et al.* [57]), where **grafted NPCs** are needed (Kadoya *et al.* [29], Rosenzweig *et al.* [30], and Kumamaru *et al.* [31]).
5. Combining the activation of neuron-intrinsic growth with the delivery of chemoattractive factors synergistically augments axon regrowth through SCI lesions. The absence or inadequate presence of multiple required facilitators contributes critically to regeneration failure across non-neural lesion cores and their astrocyte limitans borders (Anderson *et al.* [15]).

Growth factors are polypeptide molecules secreted by cells to regulate a multitude of cellular functions essential for healing, such as migration, proliferation, and differentiation (Boyce & Mendell [58]). Several chemoattractive growth factors have shown positive results separately, such as brain-derived neurotrophic factor (BDNF) and neurotrophin-3 (NT3) for sensory axons (Anderson *et al.* [59], and Alto *et al.* [60]), glia-derived neurotrophic factor (GDNF) for propriospinal axons (Deng *et al.* [61]), insulin-like growth factor-1 (IGF1) for corticospinal axons (Özdinler *et al.* [62]), among others such as transforming growth factor-alpha (TGFα) (White *et al.* [63]) and fibroblast growth factor (FGF) (Rabchevsky *et al.* [64]). The use of bioactive compounds for glia fate guiding, differentiation, neurogenesis boosting, gliogenesis boosting, and maturation are also of great interest (Janowska *et al.* [65]). But, as commented, for further results, **precise temporal administration** and an **adequate combination**

of the correct growth factors are essential. Otherwise, a severe nociceptive state can be developed (see Lin *et al.* [66]).

The biomaterial delivery technologies for tissue repair and regeneration in the central nervous system is extensive (see Donaghue *et al.* [67]). Among them, gated materials for **controlled drug release** (CDR) (Aznar *et al.* [68]), especially **mesoporous silica nanoparticles** (MSN), pose great potential for this purpose (Kumar *et al.* [69]). They can release in a sustained manner (*e.g.*, Wang *et al.* [70]) or upon the presence of a stimulus, as it will be detailed in the following section *5. Controlled drug release* of the present Introduction. The work of Cheah *et al.* [71] is worth to mention, being the most extensive growth factor externally triggerable CDR for tissue regeneration review up to date (see **Figure 2**). Additionally, the potentialities of MSN represent a continuously growing list, *e.g.*, their *decoration* with Ceria nanocrystals made them a highly efficient regenerative wound healing tool (Wu *et al.* [72]).

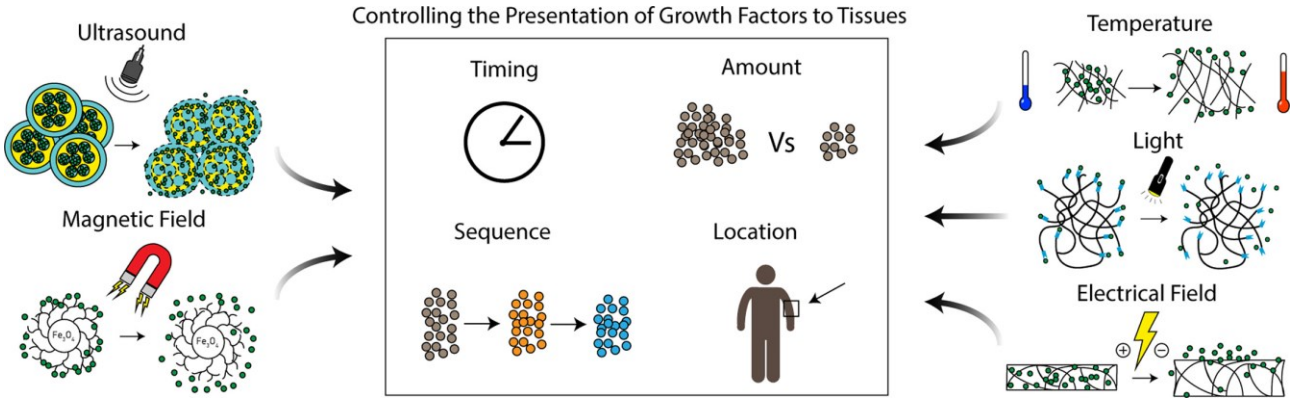

Figure 2. Graphical Abstract of Externally triggered release of growth factors - A tissue regeneration approach. Reproduced with permission from [71]. Journal of Controlled Release © 2021 Elsevier.

Control over the timing, sequence, amount, and location of growth factor presentation is essential to achieve the optimum therapeutic outcomes from growth factor therapy (Cheah *et al.* [71]). Site-specific administrations and topical applications frequently prove futile and inefficient due to the problem of quick deterioration at the delivery site (Tria *et al.* [73]). At the same time, intravenous delivery struggles with short plasma half-lives but also poor spatial specificity, which might result in ineffectiveness or off-target effects (Tria *et al.* [73], Roberts *et al.* [74], Kontos & Hubbell [75]). To address some of these problems, controlled drug release technologies have been developed (Vo *et al.* [76], Tayalia *et al.* [77], Caballero Aguilar *et al.* [78], Ladewig [79], Tabata [80]). In these systems, the pharmaceutical is often enclosed in a polymeric matrix intended to release at a set rate. However, for growth factors to reach their full potential, a controllable and pulsatile delivery is frequently desired over prolonged release (Siegel & Pitt [81], Kikuchi & Okano [82], Youan [83]). Materials with qualities that internal or external stimuli can alter can be used to control growth factor release better (Wei *et al.* [84]).

Biosensors, advanced coatings, and artificial muscles are just a few examples of biomedical uses for these so-called *smart* materials (Wei *et al.* [84], Raza *et al.* [85]). Researchers and physicians can adjust the timing, sequence, amount, and placement of growth factor presentation by taking advantage of a material's ability to actuate upon applying an external trigger signal.

Among substrates, **conductive polymers** present the advantage of allowing the **indirect electrostimulation** of NPCs seeded on them by applying an electric field beside the cells. **PEDOT:PSS** has been widely explored as a tool for controlling cell growth for tissue regeneration, *e.g.*, Karagkiozaki *et al.* [86] and Marzocchi *et al.* [87] works. It has been discovered that biofunctionalized conducting polymers with peptides derived from the extracellular matrix promote cell attachment. Examples of these peptides are arginine-glycine-aspartic acid (RGD), collagen, fibronectin, laminin, and vitronectin. The underlying reason is that these peptides feature intrinsic biological recognition sites for cells via specific integrin receptors (de Mel *et al.* [88]). Tethering RGD peptide sequences onto PEDOT:PSS has been found to induce a cascade of biological processes that eventually regenerates or replaces the functional tissue in SCI (Karagkiozaki *et al.* [86]).

Subsection summary: Adult neurons exhibit poor reactivation and regeneration. Hence, supportive cell therapy and growth factors administration can induce neuron regrowth, elongation, and reactivation. The growth factors administration needs adequate combinations, levels, and timings, a purpose for which the controlled drug release technologies are an adequate tool. At the same time, the SCI core needs to be bridged with grafted NPCs. Conductive polymers, such as PEDOT:PSS, are one of the most promising substrates, allowing indirect electrostimulation and surface biofunctionalization.

Let us then address the second group of techniques for neural precursor cell development modulation: electrostimulation.

3.2. Techniques based on electrostimulation

There are three traditional ways to deliver **electrical stimulation** (ES): **direct** coupling, **capacitive** coupling, or **inductive coupling** (see **Figure 3**, Ballint *et al.* [89]). According to Chen *et al.* [90], capacitive coupling is the most biologically safe. However, a higher voltage and longer treatment time are needed. In contrast, even if it mimics the natural potential transfer in the human body, inductive coupling presents an important disadvantage that generates tumorigenesis in unexpected areas. Therefore, direct coupling is the most used electrical stimulation delivery approach. Nevertheless, **electrodes biocompatibility** and electrochemical

generation of harmful byproducts are two concerns to keep in mind in the use of the direct ES delivery option.

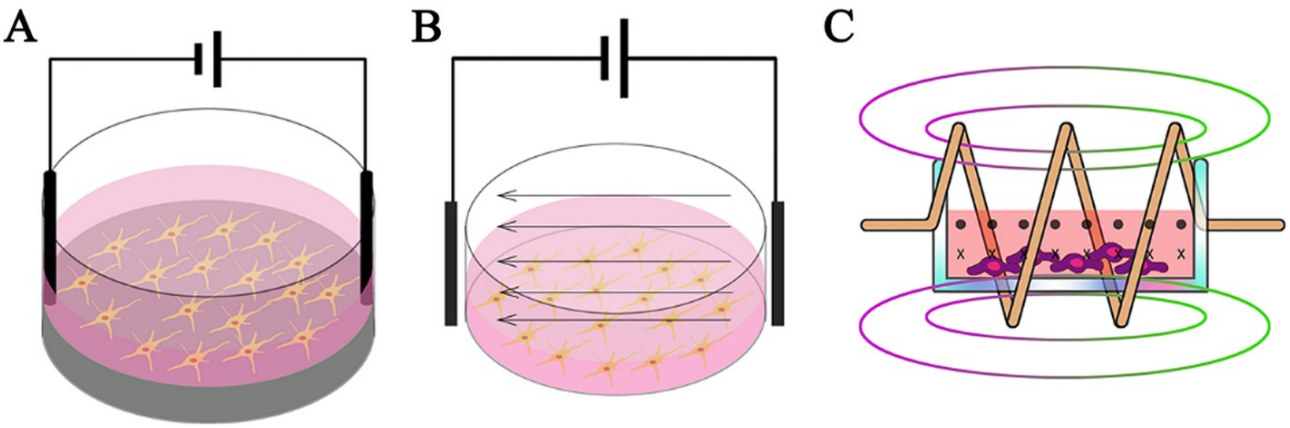

Figure 3. Three ways to deliver electrical stimulation: (**a**) direct coupling, (**b**) capacitive coupling, and (**c**) inductive. Reproduced with permission from [89]. Tissue Engineering Part B: Reviews © 2013 Mary Ann Liebert.

Using a **conductive scaffold** provides a different kind of **non-invasive directly-coupled electrostimulation** (ES). The ES indirectly affects the cells seeded on the conductive scaffold. This method places the scaffold between the chamber (containing the medium) and an insulator material to prevent liquid leakage from the cell culture medium *in vitro*. Scaffold tip ends (left outside the culture media) are connected to a power source to perform the electrostimulation. In this configuration, the scaffold becomes the main pathway for the electrical current to reach the cells instead of the culture medium. Scaffold biomechanical design allows tuning its mechanical and physicochemical characteristics and specific surface geometries. This versatility permits **overcoming the typical limitations** associated with electrode-based systems (Kanaan & Piedade [91]).

Electrostimulation showed promising **reactivation** and **reorganization** of neural circuits, as shown in the inspiring works of Angeli *et al.* [92] and Wagner *et al.* [93], and in regenerative tissue engineering, *e.g.*, the work of Jara *et al.* [94], all of them examples of direct coupling ES. Differentiation, migration, and proliferation are biological responses to electrostimulation due to several pathways (Liu *et al.* [95]). Other responses, such as apoptosis, attachment/adhesion, or alignment, are also achieved through various metabolic activities influenced by exogenous ES. They are the results of internal processes at the cellular level: redistribution of integral membrane proteins, ROS production, electrophoretic import of morphogenes through gap junction, lipid rafts, reorganization of microfilament/cytoskeletal structures, modulation of Ca^{2+} entry, modulation of integrin signals by voltage-dependent conformational change, or plasma membrane depolarization (**Figure 4**, Leppik *et al.* [96]).

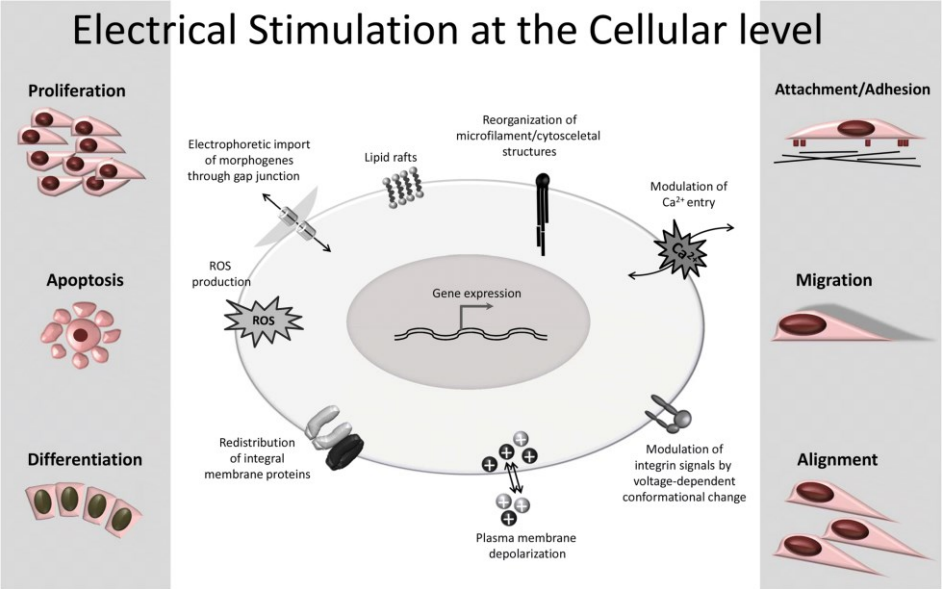

Figure 4. Cellular mechanisms and functions activated by electrostimulation. Reproduced from [96]. European Journal of Trauma and Emergency Surgery (CC BY 4.0) 2020 Springer Nature Switzerland.

Among electroactive biomaterials, **conductive polymers** (CP) are one of the most encouraging materials (see Guo & Ma [97], Kaur *et al.* [98], and Kanaan & Piedade [91]). Specially PEDOT:PSS is one of the most promising CPs for SCI, due to its higher porosity, physical flexibility, and cellular attachment and growth enhancement, as shown in the works of Park *et al.* [99], Šafaříková *et al.* [100], and Talikowska *et al.* [101]. They permit the controlled indirect electric flow below the NPCs and sparse but reactive neural tissue.

Electrostimulation on conductive polymers allows **precise control** with **no chemical residuals** left (Feng *et al.* [102]), boosts migration (Li *et al.* [103]), proliferation (Du *et al.* [104]), differentiation (Du *et al.* [104], Thrivikraman *et al.* [105], and Sordini *et al.* [106]), elongation, and alignment (Kaur *et al.* [98]). Among other ways, ES mainly affects NPCs through Ca^{2+} signal pathways (Zhu *et al.* [107]), in which the stimulus, which can be mimicked with ES (de Mernoval *et al.* [108]), has a demonstrated key role in NPC differentiation and axon regeneration (Tonelli *et al.* [109], de Groot [110]). Electrostimulation shall be synergistic and comprehensive with the axon regeneration intrinsic mechanisms (Mahar & Cavalli [111]). ES can adopt many forms *in vivo* depending on the tissue being stimulated. As seen in the first lines of this subsection, the ES application accomplished astonishing progress in spare neural tissue elongation and reorganization (Krucoff *et al.* [112]).

The therapeutic capabilities of electrical fields for both ES and controlled drug release (CDR) are under the scope, as shown in the work of Kolosnjaj-Tabi *et al.* [113], and they presented significant advances in brain injury treatment (Cheng *et al.* [114]). Recently, Li *et al.*

[115] have published a microfluidic CDR with ES microelectrodes, highlighting the necessity of exploring these combinations.

Subsection summary: Using a conductive scaffold, such as a conductive polymer (CP), allows the non-invasive directly-coupled electrostimulation. It employs low-power signals, there is no harmful byproducts, and allows a precise control of the stimulation. It has showed promising results in the reactivation and reorganization of neural circuits. Furthermore, these platforms allow the combination of electrostimulation and controlled drug release.

3.3. Techniques based on optogenetic stimulation

Optogenetics has demonstrated great potential in the fields of tissue engineering and regenerative medicine (Hu *et al.* [116], Spagnuolo *et al.* [117]). Optogenetics is a set of strategies that includes a way to excite or inhibit neural cells modified to express light-gated ion channels artificially and to activate other light-sensitive proteins developed over the last two decades. This set of tools follows the emergence of protein-coding **opsin** genes that **respond to illumination** at specific optical wavelengths. From this point, optogenetic techniques have seen increasing development and interest, being chosen in 2010 as *Method of the Year* by *Science.* This **neuromodulation** method makes it possible, among other things, to control the behavior of particular cells present in a system with a level of precision never seen and event triggering in a non-invasive way and with a high temporal resolution (Park *et al.* [118], Joshi *et al.* [119], and Rein & Deussing [120]). A representation of the optogenetic principle, with four different opsins as an example, is shown in **Figure 5**.

The response of these biosystems is mainly characterized by triggering events and hyperpolarizing and depolarizing currents. Mattis *et al.* [121] show a profound study of the current response vs. wavelength, irradiance, and exposure time for a set of opsins.

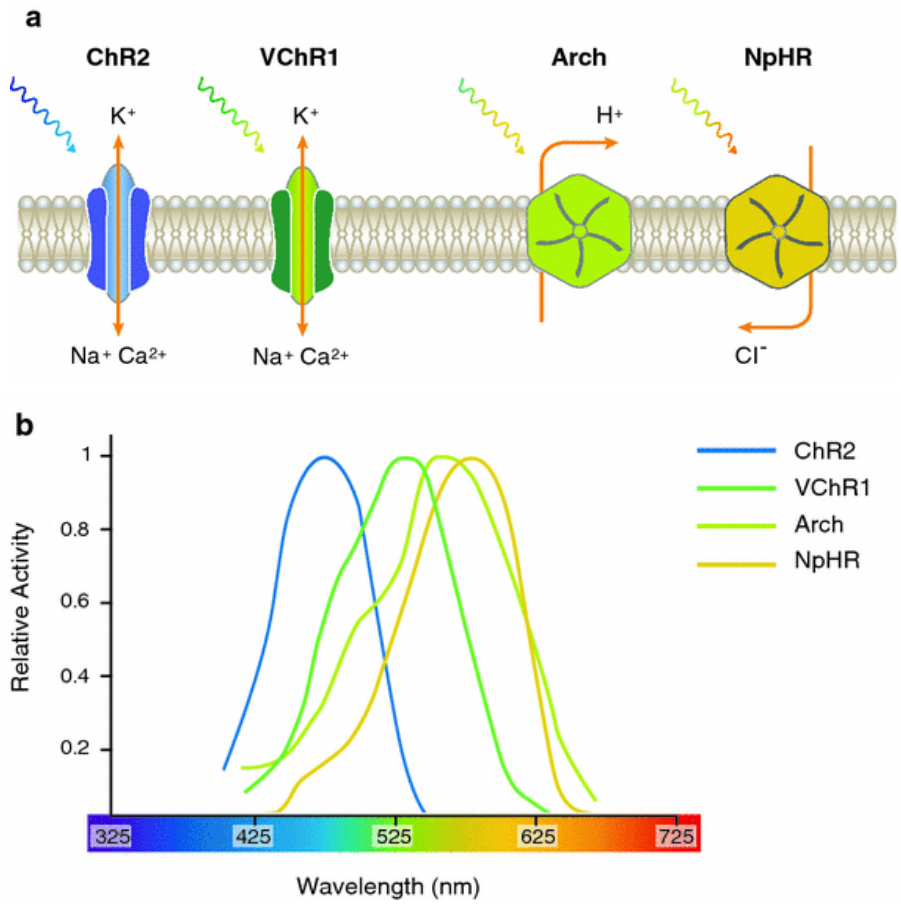

Figure 5. The optogenetic principle: changing the membrane voltage potential of excitable cells. **a** Activating tools—channelrhodopsins: channelrhodopsin-2 from *Chlamydomoas reinhardtii* (ChR2) and channelrhodopsin-1 *Volvox carteri* (VChR1) from nonselective cation channels leading to depolarization of target cells. Silencing tools—ion pumps: archaerhodopsin-3 (Arch) from *Halorubrum sodomense* works as a proton pump and leads to hyperpolarization of the target cell such as the chloride pump NpHR (NpHR) from *Natronomonas pharaonis*. **b** Spectral working properties of light-sensitive membrane proteins. Reproduced from [120]. Molecular Genetics and Genomics (CC BY NC 2.0) 2012 Springer Nature Switzerland.

In the nervous lesion location, specialized cells, such as neurons, astrocytes, and oligodendrocytes, must be provided to form **functional tissue**. As mentioned, NPCs can be transplanted or grafted into the lesion with this purpose, and their differentiation and configuration need to assemble functional structures. Hence, the therapeutic tools need **selective cell targeting capabilities** to induce each to proportion a specific and needed role in the whole tissue (Jayaprakash *et al.* [122]). Viral tools can be used to transfer and express the genetic sequences of optogenetic tools in a cell-type-specific way (Deubner *et al.* [123], Loong Teh *et al.* [124], Kappler *et al.* [125]). As a result, it is possible to monitor neural stem cells that express optogenetic actuators after transplantation and to activate just the neurons that do so without harming the host neurons (Weitz & Lee [126], Habibey *et al.* [127]) (see **Figure 6**).

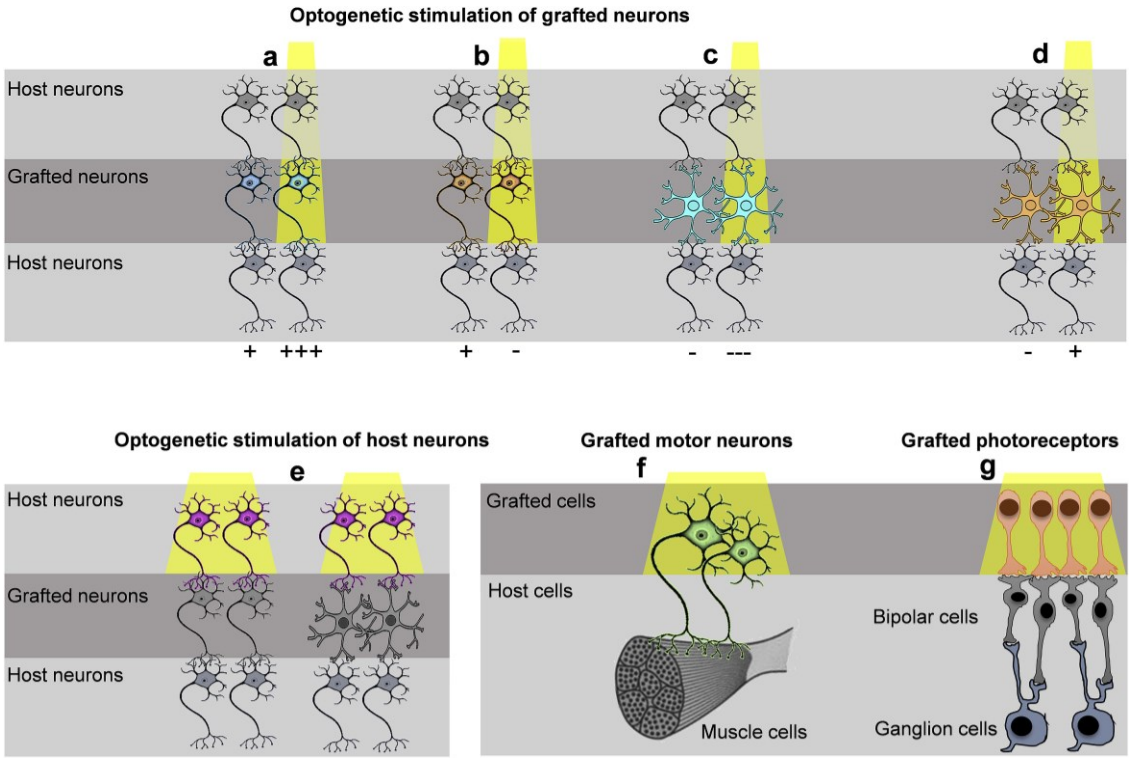

Figure 6. Optogenetic stimulation targeting transplanted or host neurons in brain, spinal cord and retina. a) Glutamatergic neurons expressing ChR2 grafted into peri-ischemic regions after stroke. Optical stimulation indirectly increased firing rate of host neurons through synaptic communication (Daadi *et al.* [128]). b) eNpHR-expressing dopaminergic neurons transplanted to Parkinsonian brain and optical stimulation exploited to inhibit motor deficits (Steinbeck *et al.* [129]). c) ChR2-expressing GABAergic neurons grafted into epileptic hippocampus to optically silence its hyperexcitability (Cunningham *et al.* [130], Avaliani *et al.* [131], and Ryu *et al.* [132]). d) eNpHR-expressing GABAergic neurons have not been studied in neural transplantation studies, however it has been tried *in vivo* to decipher circuit functions (Sharpe *et al.* [133]). e) Optogenetic stimulation of ChR2 expressing host neurons to promote differentiation and survival of the grafted excitatory or inhibitory neurons (Avaliani *et al.* [131]). f) ChR2-expressing motor neurons implanted in spinal cord are optically stimulated to control muscle function (Bryson *et al.* [134]). g) Engineered eNpHR or Jaws expressing photoreceptors implanted into a blind retina. By illuminating these photoreceptors transfer eNpHR and Jaws-related signals into bipolar and retinal ganglion cells (Garita-Hernandez *et al.* [135]). Reproduced from [127]. Biochemical and Biophysical Research Communications (CC BY 4.0) 2020 Elsevier.

Wang *et al.* [136] modulated neural stem cell proliferation through optogenetic stimulation. Paschon *et al.* [137] provided new perspectives for SCI treatment based on recently developed technologies, including clustered regularly interspaced short palindromic repeats (CRISPR)-based methods (including prime editing), optogenetics, and designer receptor exclusively activated by designer drugs (DREADDs). The possibilities are countless, and the optogenetics application in the SCI for functional recovery (as shows the work of Deng *et al.* [138]), and more broadly, Central Nervous System (CNS) injuries, are really promising. Yu *et al.* pioneered this path in brain injury [139], where the application of optogenetics is of great interest (Delaney *et al.* [140]).

Calcium imaging of neural precursor cell (NPC) grafts revealed that they formed localized synaptic networks that are spontaneously active. For this, host corticospinal tract axons were induced to grow into the grafts. Their optogenetic stimulation caused multiple and segregated neural network responses throughout the graft. Additionally, graft-derived axons that extended into the denervated spinal cord were optogenetically activated. This optogenetic stimulation elicited neural network responses from the local host. It was discovered through *in vivo* imaging that behavioral activation also caused focused synaptic responses in the grafts. Thus, **functional synaptic subnetworks can be created via NPC grafts** whose activity patterns match a complete spinal cord (Ceto *et al.* [141]).

Our collaborators in RTN-CIPF engineered neural precursor cells (NPC) to express the excitatory light-sensitive protein channelrhodopsin-2 (ChR2) artificially. Blue-light stimulation prompted an influx of cations and a subsequent increase in proliferation and differentiation into oligodendrocytes and neurons (Giraldo *et al.* [142]). It also provoked the polarization of astrocytes from a pro-inflammatory phenotype to a pro-regenerative/anti-inflammatory phenotype. Therefore, prompting a more pro-regenerative profile for further NPC therapeutic applications such as spinal cord injury or stroke.

The application of optogenetics not only to CNS but to Peripheral Nervous System (PNS) injuries is also emerging (Xu *et al.* [143]). Other approaches, yet in the conceptualization stage, aim to restore motor function using optogenetics and neural engraftment. One example is the use of intraneural grafts of optogenetically-engineered stem cell-derived motor neurons that could be placed close to the motor-entry point of the target muscle. This reinnervation could be addressed through a brain–machine interface embedded in the primary motor cortex (Bryson *et al.* [144]). Another example is optogenetic spinal stimulation (OSS). OSS has been explored as a less invasive and cell-type-specific alternative to electrical intraspinal microstimulation (ISMS) by Mondello *et al.* [145].

Subsection summary: Modifying neural precursor cells with opsin genes make them able to respond to illumination. The discipline of neuromodulation from a controlled light source is called *optogenetics*. Using different opsins and localized irradiation, we can selectively target portions of the cell population to respond in specific ways to form functional tissue. Using modified NPC with opsins grafts implanted in the SCI lesion, functional synaptic networks can be created with the host tissue, making it indirectly responsive to the optogenetic stimulation.

4. Electrochemical techniques

For the application of electrical stimuli in the context of a solution, it is necessary to define the concept of electrochemical cell, and the different methods that can be applied. One subset of techniques is of particular interest: the voltammetric techniques. For them, it is necessary to explain the operation of the electronic circuit for simultaneous application and measurement of electrical variables: the **potentiostat**, that will be addressed in *Chapter 1. Electronic instrumentation for in vitro electrostimulation and controlled drug release*, section *1.3. Potentiostat*.

4.1. Electrochemical processes in an electrode

As commented in the former sections, a **conductive polymeric scaffold** is proposed to relay the lesion core in SCI. In this scaffold or substrate, neural precursor cells will be grafted. This substrate has three primary functions:

1. The **physical support** for intercellular adhesion and intercellular connection.
2. The **electrical conductor** to perform the indirect electrostimulation.
3. The **carrier** of the electrically controlled **drug** release.

In biomedical applications, this substrate will be found in a solution, in a liquid medium suitable for cell survival, whether artificial in an *in vitro* culture or natural for *in vivo* application. To apply or measure electrical signals in this context, an electrical circuit composed of two or more electrodes immersed in a solution must be present. This arrangement is called an **electrochemical cell**, as shown in **Figure 7**.

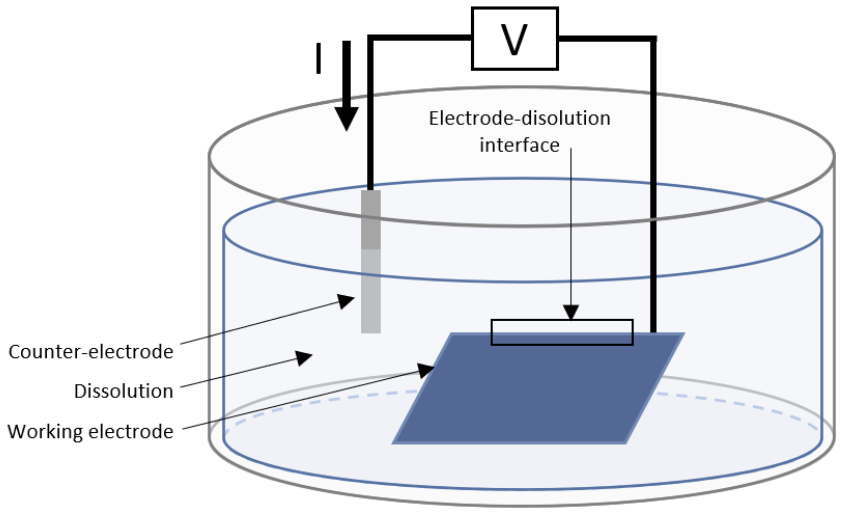

Figure 7. Electrochemical cell representation.

If we apply an external voltage V between the two electrodes, it will produce the flow of an electric current, I. This electric current originates due to the electrochemical processes occurring at the electrode-solution interface of each of them. In most applications, the current can be decomposed in two: **charge transfer** due to chemical reactions (**faradic processes**) or **charge reorganization** at each electrode-solution interface (**non-faradic processes**).

For drug release, we are interested in inducing chemical reactions (faradic processes) in compounds fixed on the surface of one of the electrodes, called the **working electrode** (WE). For this purpose, we will have to control the applied voltage at the WE-solution interface.

4.1.1. Faradic processes

Normally in electrochemistry studies focus on one of the electrodes, the working electrode (WE). Suppose that a generic reaction of the type shown in **Equation 1** occurs at this electrode.

$$O + n \cdot e^{-} \leftrightarrows R \qquad \textbf{Equation 1}$$

Depending on the applied potential, the reaction may be enhanced in one or the other direction, resulting in the circulation of current in one or the other direction. The relationship between the potential at the electrode-solution interface and the current derived from the charge transfer during the reaction is given by the electroanalytical Butler-Volmer equation (see Dickinson & Wain [146]) (see **Equation 2**).

$$i = n \cdot F \cdot A \cdot k^{0} \cdot \left[C_O \cdot e^{\frac{\alpha \cdot n \cdot F}{R \cdot T} \cdot \left(E - E^{0\prime}\right)} - C_R \cdot e^{\frac{(1-\alpha) \cdot n \cdot F}{R \cdot T} \cdot \left(E - E^{0\prime}\right)} \right] \qquad \textbf{Equation 2}$$

Where:

- i: electrical current through the electrode-solution interface.
- F: Faraday constant (96485.34 C mol^{-1}).
- A: contact surface between the electrode and the solution.
- k^0: standard reaction speed constant.
- C_O: O specie concentration at the interface.
- α: transference coefficient.
- n: number of electrodes involved in the reaction (see **Equation 1**).
- R: universal constant for ideal gases (8.314472 J K^{-1} mol^{-1}).
- E: electric potential at the electrode-solution interface.
- $E^{0\prime}$: redox pair normal potential.

- C_R: R specie concentration at the interface.

A particular stress in the *electroanalytical* adjective shall be given since the standard Butler-Volmer equation cannot be applied to multielectron transfer processes (see Guidelli *et al.* [147]). Hence, n refers to the total number of electrodes. Otherwise, a multistep process shall be taken into account, therefore being $n = 1$. No problem arises in the application of the conventional formula regarding the multielectron transfer processes as multistep one-electron transfer processes (see Compton *et al.* [148]).

As can be seen, this relationship is conditioned by the intrinsic characteristics of the reaction (which in turn depend on the nature of the electrode and the reacting species), the contact surface between the electrode and the solution, the concentration of the species involved in the reaction, and the temperature. This equation explains the behavior related to charge transfer right at the electrode-solution interface. To understand the process at the level of the electrochemical cell it is necessary to consider other phenomena such as:

1. **The transport of species from within the solution to the interface so that they can react**. This movement of matter is called mass transport and in the case of electrochemical systems may be due to hydrodynamic phenomena (produced by the agitation of the solution, the rotation of the electrode, or the forced flow of the solution across the electrode), migration (due to the interaction with an electric field) or diffusion (due to concentration gradients). In **Equation 2** the values of C_R and C_O correspond to the concentration values at the interface. These values evolve with time. On the one hand, as the reaction proceeds the concentration of the species being consumed will decrease. On the other hand, this decrease will be compensated by mass transport processes. The evolution of the current generated will be marked by the rate at which new quantities of the species being consumed arrive at the interface from within the solution.
2. **Adsorption or desorption processes**. In the adsorption process the ions or molecules present in the solution adhere to the electrode, reducing the effective surface area on which the reactions can take place. In the desorption process the adhered substances are separated from the electrode.
3. Other reactions that may occur before or after the reaction giving rise to the charge transfer.

An interesting particular case of the Butler-Volmer equation is to consider the situation in which there is no current circulation, *i.e.*, when there is equilibrium in the reaction of **Equation 1** and no net charge transfer in either direction. In this case the value of the potential at the electrode-solution interface can be expressed as a function of the concentrations of the

reacting species as shown in **Equation 3**. This expression is called the Nernst equation (see Chibuzor *et al.* [149]).

$$E = E^{0'} + \frac{R \cdot T}{n \cdot F} \ln\left(\frac{C_O}{C_R}\right) \qquad \textbf{Equation 3}$$

Butler-Volmer empirical nature made this equation a useful and practical approximation for a wide pool of applications. Further studies are showing the relationship between asymmetric Marcus-Hush model reorganization energy (λ) parameter, which enables to rationalize the electrode kinetics in terms of the microscopic nature of the electrochemical system, and the k^0 in Butler-Volmer (see Batchelor-McAuley *et al.* [150]). The application of stochastic statistics in random walk models of diffusion (see Singh & Lemay [151]) is also a significant contemporary consideration which is out of the scope of the present work.

4.1.2. Non-faradic processes

The Butler-Volmer equation explains the faradic phenomena occurring at the electrode-solution interface, *i.e.*, those related to charge transfer. However, in the vicinity of the interface, in addition to the reacting species, ions of other species for which the reaction potential is not reached can be found. These ions, although they do not produce charge transfer, are attracted or repelled by the electrode surface depending on the applied potential. This movement of charge when the potential changes give rise to a current like that produced when the terminal voltage of a capacitor changes (see Kissinger & Heinemann [152], and Bard *et al.* [153]). In fact, the structure formed at the electrode-solution interface, called electrical double layer (see **Figure 8**), has some similarity with a capacitor.

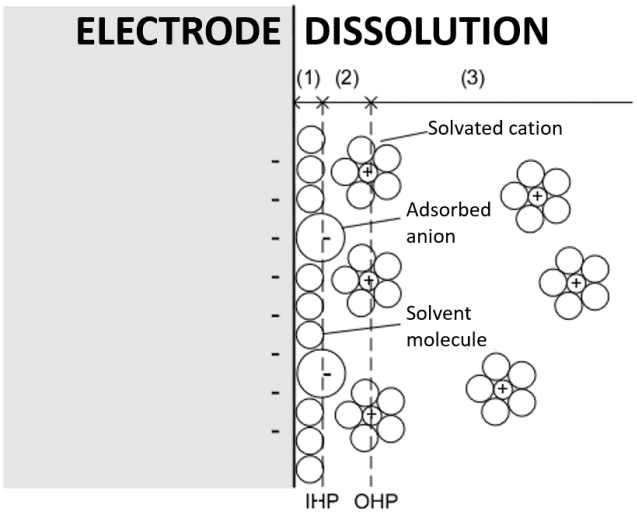

Figure 8. Double electric layer structure representation. Adapted with author's permission from [154].

This structure integrates several layers. The first layer (1), the one closest to the electrode, is composed of solvent molecules and sometimes of other molecules or ions that are specifically adsorbed. This layer is called the inner, compact, Helmholtz or Stern layer. The plane formed by the centers of these specifically adsorbed ions is called the Internal Helmholtz Plane (IHP). Behind this layer are the solvated ions; the plane formed by the centers of these ions is called the Outer Helmholtz Plane (OHP) and marks the minimum distance at which these ions can approach the electrode surface. The interactions between these ions and the electrode are limited to electrostatic forces. Beyond the OHP is the diffuse layer. In this zone the distribution of ions is established based on thermal random motion and attraction/repulsion forces between the ions and the electrode surface. The diffuse layer has a very small thickness and depends on the total ion concentration (for concentrations greater than 10^{-2} M, the thickness is less than 100 Å). Beyond the diffuse layer the ions do not perceive the electrostatic attraction forces produced by the electrode. In fact, in the absence of current, the potential drop between two electrodes occurs at the interfaces and not within the solution. When there is current circulation, a small potential drop is generated in the solution due to its finite conductivity.

If changes occur in the potential applied to the electrode, the structure of the electrical double layer must reorganize itself based on the new potential, which generates a transient current (charging current). This current must be considered in electrochemical experiments since in some cases it can be higher than the faradic current.

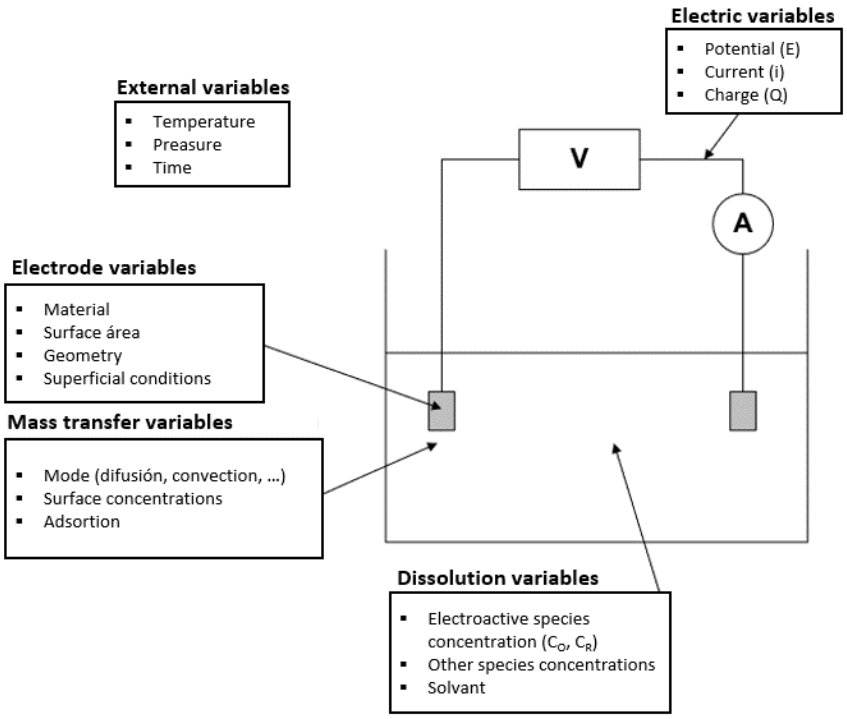

Figure 9. Variables involved in electrochemical processes. Adapted with author's permission from [154].

An electrochemical cell is therefore a complex system in which several processes occur simultaneously and in which different variables are interrelated. **Figure 9** details the most important variables involved in electrochemical processes (see Bard *et al.* [153]).

Electrochemical techniques aim to fix some of these variables from the control instrumentation and measure others. For example, in voltammetry, a specific potential is applied to the working electrode, and the current flowing through it is measured. The current measurement carries information to determine the concentration variation of one of the electroactive species present in the solution. In electrically controlled drug release, the sampled current is potentially an early indicator of the released content with the voltammetry application.

4.2. Classification of electrochemical methods of measurement

The classification varies depending on the bibliography consulted, such as in Zoski [155], Kissinger & Heinemann [152], Bard *et al.* [153], Mei *et al.* [156], and Harvey [157]. A general overview based on the mentioned references is summarized in the following diagram in **Figure 10**:

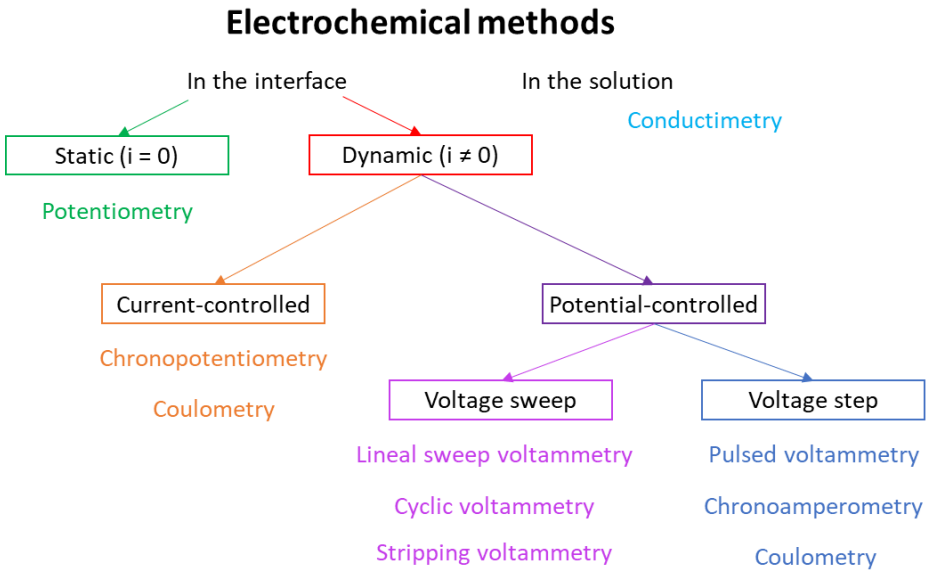

Figure 10. Fundamental electrochemical methods.

First, a distinction must be made between those techniques that are applied within the solution and those that focus on the study of the processes that occur at the interface between the solution and the electrode. Within the first group, the most important technique is conductimetry, which consists of measuring the conductivity of the solution by applying an

alternating square signal and measuring the current flowing. For each half-period of the square signal, the quotient between the applied voltage and the measured current corresponds to the resistance of the solution between the two electrodes. Knowing the geometrical characteristics of the electrodes, the conductivity can be deduced from the measured resistance.

Within the interfacial electrochemical methods, two groups can be distinguished: static and dynamic. Static electroanalytical techniques work with the system in equilibrium, *i.e.*, there is no current flow. The best known of these is potentiometry. Within the dynamic techniques, a new separation should be made between those for which the controlled electrical parameter is the current and those for which the controlled parameter is the voltage. Of the first group, the most significant are current-controlled coulometry and chronopotentiometry. But the most widely used dynamic interfacial electrochemical techniques are the voltage-controlled ones, in which the control can be by potential sweeps (linear sweep voltammetry, cyclic voltammetry and stripping voltammetry) or by potential steps (pulse voltammetry, chronoamperometry and voltage-controlled coulometry). This broad classification is in constant evolution, given the evolution and design of new kinds of voltammetric techniques.

Dynamic interfacial potential sweep techniques can also be classified into hydrodynamic and stationary techniques. In the stationary ones, the solution remains at rest while in the hydrodynamic ones, the movement of the species in the vicinity of the electrode is provoked to facilitate the reaction. It is necessary to consider the existence of elements that make it difficult for the species to reach the electrode surface, such as physiosorbed molecules and ions or reaction residues. The aim of the movement is to dislodge these elements to facilitate the diffusion towards the electrode surface of the species to be reacted. This movement can be triggered in three ways:

- By rotating the electrode: Rotating Disk Electrode (RDE).
- Stirring the solution.
- By circulating a flow of solution across the electrode Surface

Finally, although it appears in only one of the classifications found in the literature (see Zoski [155]), impedance spectroscopy is a very powerful analytical technique (see Bard *et al.* [153], Macdonald & Barsoukov [158], and Masot [159]). This technique can be applied both at the electrode-solution interface and to measure properties within the solution.

4.3. Potentiometry

Potentiometry is based on the measurement of the potential established between two electrodes when they are immersed in a solution and there is no current flow. The measured potential is the difference between the potentials established at each of the electrodes, as shown in **Figure 11**.

Under zero current conditions the potential of each electrode is given by the Nernst equation (see **Equation 3**). Therefore, the measured external potential will depend, among other things, on the material of the electrodes, the nature and concentration of the species present in the solution and the temperature. It is also interesting to note that in this case there is no direct dependence on the contact surface between the electrode and the solution.

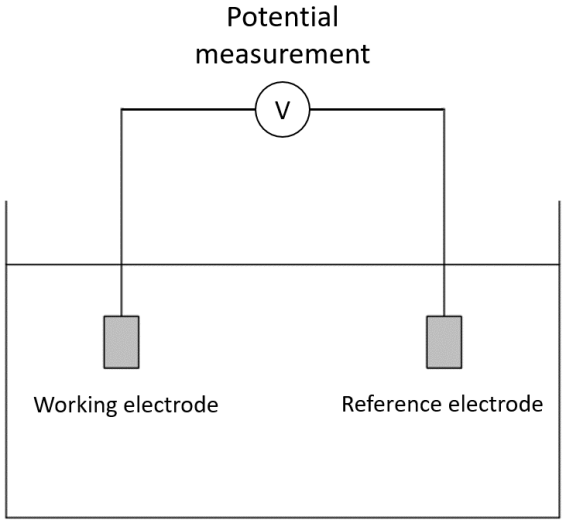

Figure 11. Block diagram of a potentiometry setup. Adapted with author's permission from [154].

In potentiometry, it is only of interest to obtain information on one of the electrodes (working or indicator electrode). The other electrode serves only as a reference (counter electrode or reference electrode) and, therefore, must have a stable potential so that it does not affect the measurements of the working electrode. Basically, the reference electrode must ensure that its potential is stable in the face of changes in the concentration of the solute in the solution. There are several types of reference electrodes; the best known are the standard hydrogen electrode, the calomel electrode, and the silver-silver chloride electrode (see section *4.5. Reference electrode*).

With a stable reference electrode, variations in the measured potential will be due to changes in the interface potential of the working electrode which, in turn, depends on the solute concentration. Therefore, by choosing the right material for the working electrode, a relationship can be established between the solute concentration and the voltage measured

between the two electrodes. In potentiometry there are several types of working electrodes: metal electrodes, ion-selective electrodes, and others.

Equation 3 is valid for the case of simple solutions. Still, when there are several species in the solution, the potential generated no longer depends on the concentration of a single species. It depends on the interactions that occur between all of them (see Vlasov *et al.* [160]). Therefore, it is not possible to establish a relationship between the measured voltage and the concentration of one of the species. A possible solution to this problem is using ion-selective electrodes (ISE). Another is using a matrix of cross-sensitive electrodes, the base of the potentiometric electronic tongues (see Gil [161]).

Further developments in the biosensor field gave birth to new technologies for the analyte quantization in complex media, as will be addressed in the last section of this Introduction, *6. Real-time feedback on biochemical systems*. Nevertheless, in this work, potentiometry is employed only to set the equilibrium point of any given electrochemical cell: the WE vs. CE voltage that gives zero current flow, also known as zero-current potential (OCP).

4.4. Voltammetric techniques

4.4.1. Measurement methodology. 3-electrode configuration.

The objective of voltammetry is to apply a controlled voltage to the electrode-solution interface of the working electrode and to measure the current flowing through it. To carry out this process, it is necessary to use at least two electrodes: the working electrode (which is the one where the electrochemical processes to be analyzed will take place) and a **counter-electrode** (CE) that allows the circuit to be closed so that the current can flow. However, performing a voltammetry test in a two-electrode configuration poses a series of problems derived from the fact that electrochemical processes also occur at the counter-electrode that will affect the measurement of those occurring at the working electrode. **Figure 12** shows a 2-electrode electrochemical cell to which a WE potential is applied. In the lower part of the figure the simplified electrical model of such a cell has been added (see Kissinger & Heineman [152]).

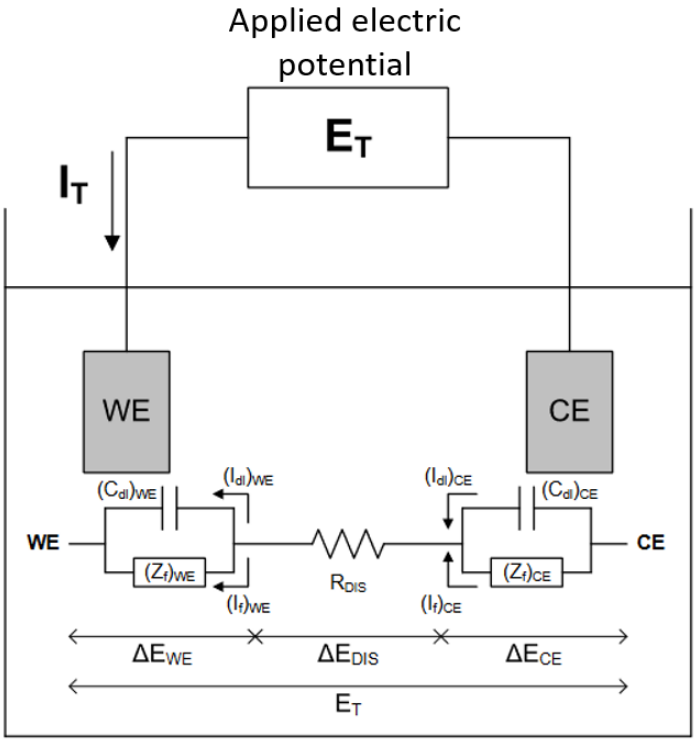

Figure 12. Voltammetry setup with 2-electrode configuration. Adapted with author's permission from [154].

As seen in section *4.1. Electrochemical processes in an electrode* of this subsection, the total current flowing through the electrode-solution interface is the sum of the current due to charge transfer (faradic current I_f) and the current due to charge reorganization in the electrical double layer (non-faradic current I_{dl}). The relationship between the faradic current and the voltage applied to the electrode-solution interface is represented by the potential-dependent impedance Z_f. This model is a simplification since this current depends not only on the applied potential but also on other variables such as concentration. Furthermore, Z_f presents a non-linear behavior, as its impedance will be one in the application of positive voltages vs. RE (inducing the oxidation in the reactive species), and other in the application of negative ones (inducing reduction) (see Martínez-Ibernón *et al.* [162]). As for the non-faradic current, its relation to the voltage is established by a capacitor C_{dl}. This representation is again a simplification because, in turn, the value of this capacitor depends on the applied voltage. However, for practical purposes this model allows us to understand the relationship between the potential applied to the electrode and the current flowing through it. This relationship would be given by the capacitor C_{dl} and the impedance Z_f, which, in turn, depend on the different variables involved in the process. The electrical model of the solution section from the working electrode to the counter-electrode is established by a resistance R_{DIS} (which depends on the conductivity of the solution). Therefore, when we apply a certain voltage between the working electrode and the counter-electrode inside the electrochemical cell, this voltage is spread over 3 potential drops: the potential drop at the working electrode interface (ΔE_{WE}), the potential

drop in the solution (ΔE_{DIS}), the potential drop at the counter-electrode interface (ΔE_{CE}). The potential drop in the solution is generally small and moreover, depending only on the conductivity of the solution, it could be compensated. However, the drop in the counter-electrode is a problem since its value depends on many variables that will evolve during the test. For this reason, in a 2-electrode configuration, even if we apply a controlled potential between the working electrode and the counter-electrode, it is not possible to control the potential that will actually be applied to the electrode-solution interface at the working electrode.

To solve this problem it is necessary to work in a 3-electrode configuration (see Bard *et al.* [153], Kissinger & Heineman [152], and Harvey [163]) and use a potentiostat to control the voltage applied to the interface of the working electrode as shown in **Figure 13**.

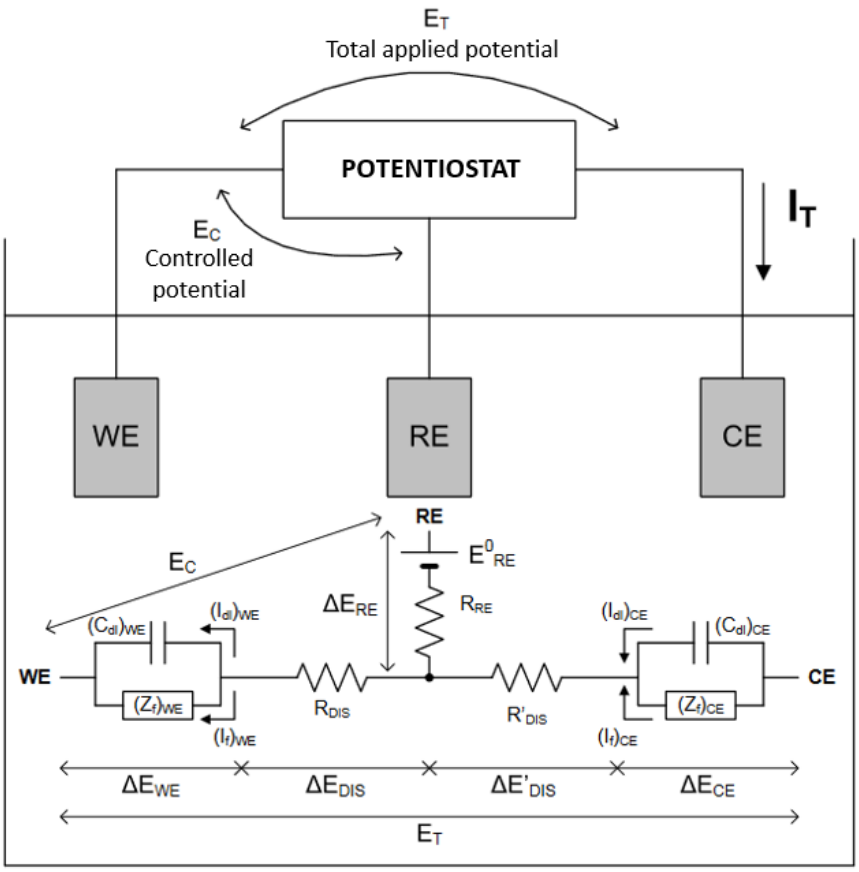

Figure 13. Voltammetry setup with 3-electrode configuration. Adapted with author's permission from [154].

In the 3-electrode configuration:

- **A counter electrode (CE):** its mission is only to allow the current to flow towards the working electrode. The potential drop occurring at the counter electrode is not

important for the operation of the system (unless it could cause a saturation of the total applied potential WE).

- **A reference electrode (RE):** this electrode must meet two conditions. First, the reference electrode must be connected to a high impedance input of the potentiostat so that no current flows through it. When the current through it is zero an electrode can be represented by a battery connected to the solution through a resistor. The battery corresponds to the voltage generated at its interface as indicated by the Nernst equation (see **Equation 3**). The second condition that the reference electrode must fulfill is that its Nernst potential must be very stable in the presence of concentration changes in the solution so that the battery voltage can be considered constant.
- **A working electrode (WE)**: this is the electrode on which measurements are to be made. The objective is to be able to apply a controlled voltage to it and measure the current flowing through it.

The potentiostat, whose internal structure and operation will be described in section **1.3. Potentiostat** of **Chapter 1**, must ensure the proper functioning of the system. To this end, two conditions must be met:

- The connection to the reference electrode must be a high impedance input to prevent current flow through it.
- The potentiostat must apply between the reference electrode and the working electrode a controlled potential (E_C) that should not be affected by what happens at the counter electrode. On the other hand, the value of the total voltage applied between the working electrode and the counter electrode (E_T) can vary depending on the processes occurring at the counter electrode and in the section of the solution from the counter electrode to the reference electrode ($\Delta E'_{DIS}$).

Under these conditions, the potential applied to the electrode-solution interface of the working electrode (ΔE_{WE}) will be given by the expression of **Equation 4**.

$$\Delta E_{WE} = E_C - E^0_{RE} - \Delta E_{DIS} \qquad \textbf{Equation 4}$$

As we have just explained, by choosing the appropriate reference electrode, the potential E^0_{RE} can be considered constant; moreover, the potential drop in the solution is usually small. Therefore, by setting the value of the E_C potential it is possible to control the voltage applied to the electrode-solution interface of the working electrode. For the case of low conductivity solutions, a system for the compensation of the ΔE_{DIS} drop should be implemented. One possibility to make this voltage drop negligible is to bring the reference electrode as close as possible to the working electrode. Another possibility is to measure the conductivity of the

solution during the test, calculate the potential drop ΔE_{DIS} and modify the E_C value to take this drop into account.

4.4.2. Voltammetric techniques of interest

There is a wide variety of voltammetric techniques, as shown in *4.2. Classification of electrochemical methods of measurement*, and there is no one-fits-all classification. The features of the recently available technology, the way of performing the tests, and the way of analyzing the data have changed substantially, leading to the current situation of new multiple classifications. One of the classic ones states that voltammetric techniques can be classified in two groups depending on the stimulus applied: a voltage sweep or a potential pulse. One technique of each group is of particular interest in the present group: cyclic voltammetry and chronoamperometry.

In the **sweep voltammetric techniques**, the voltage applied to the electrode varies slowly. In the **cyclic voltammetry (CV).** a potential is applied to the working electrode which increases linearly at a rate usually varying between 10mV/s and 10V/s and the resulting current is measured. Once the maximum potential is reached, a new sweep is carried out in the opposite direction until the initial potential is reached (see **Figure 14**). The evolution of the current as a function of the applied potential is then plotted. This type of graphical representation is called a voltagram or voltammogram. When the reaction potential of one of the species present in the solution is reached, there is a significant increase in the current. However, as the reaction proceeds the concentration of the reacting species decreases and, if there is no hydrodynamic process, the current will begin to fall. This process will produce a current peak in the voltagram that will allow the identification of the reaction potential.

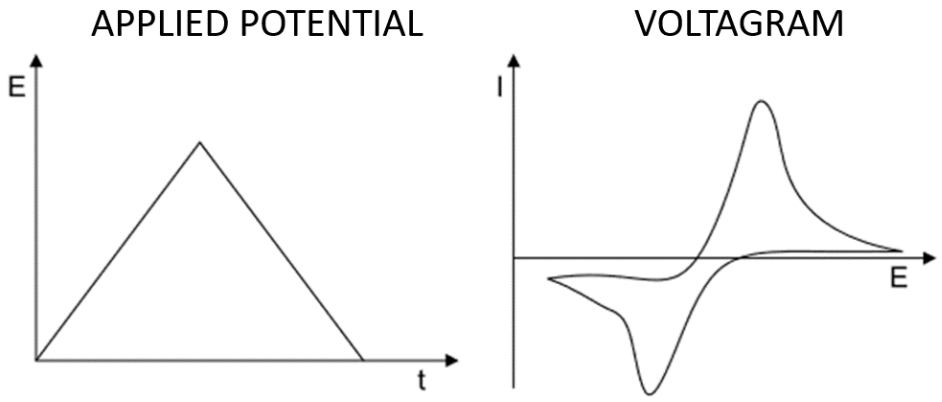

Figure 14. Cyclic Voltammetry representation. Adapted with author's permission from [154].

In the **pulse voltammetry techniques**, the variety of techniques can be classified according to the pulse amplitude or the ratio between the pulse application and electrical current sampling. In the **chronoamperometry**, the current is sampled at a much lower periodicity than the pulse duration, as shown in **Figure 15**. In the last two decades, pulse voltammetry techniques are being used in which the pulse design is tailored to the application and the current signal is sampled in the style of chronoamperometry (see Winquist [164]).

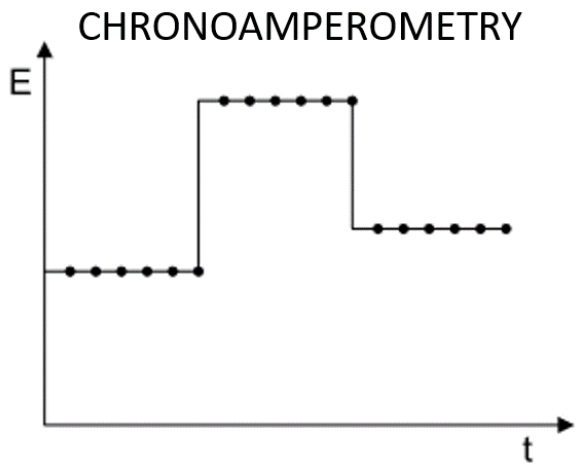

Figure 15. Chronoamperometry techniques representation. Adapted with author's permission from [154].

If each of the pulses is analyzed individually, it is observed that the current signal has an exponential behavior. This behavior is determined by the contribution of the non-faradic current (due to the reorganization of the charges in the electrical double layer) and the faradic current (corresponding to the oxidation-reduction reactions occurring at the electrode-solution interface). If the amplitude of the applied potential is not sufficient to cause oxidation-reduction reactions the current will have only a non-faradic component, as shown in **Figure 16a**. However, if the applied potential produces an oxidation-reduction reaction the current obtained will be the sum of the non-faradic current and the faradic current resulting from the reaction (see **Figure 16b**). Both the faradic and non-faradic currents are related to the nature of the electrode and the nature and concentration of the species present in the solution. Therefore, the study of the time evolution of the total current provides information on the chemical composition of the sample.

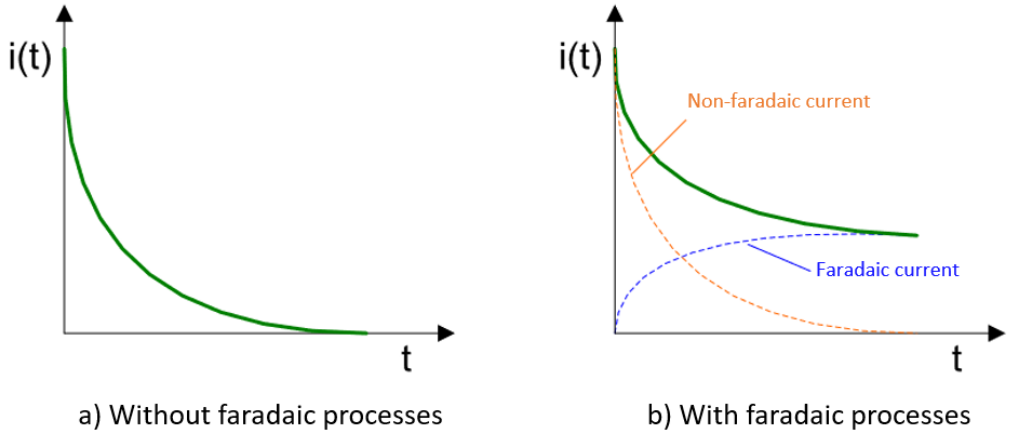

Figure 16. Current response to potential step representation. Adapted with author's permission from [154].

The choice of the most appropriate voltammetric technique for each experiment will depend on the objective of the experiment, *i.e.*, the electrochemical process variable to be controlled (working electrode vs. reference electrode potential, faradic current, or others) or measured (analyte concentration, diffusion coefficient, characteristics of the electrical double layer, oxidation-reduction potential or others). For example, in chronoamperometry (and similar techniques), if the current measurement is made at the beginning of the pulse or if the pulses are of very short duration, the results obtained will be closely related to the electric double layer; however, if the pulses are long and the measurement is made at the end, the measured values will be related to faradic and mass transport effects.

4.5. Reference electrode

A reference electrode (RE) must provide a stable potential so that the variations detected in the electrochemical cell potential correspond to the working electrode (see Harvey [163]). There are several types of reference electrodes, the three most important of which are listed below:

The **standard hydrogen electrode** (SHE) is not usually used in practical assemblies due to the complexity of its implementation. Its importance lies in the fact that it is the reference electrode used to establish the standard potential of the other electrodes; its potential is 0 V at any temperature. It consists of a platinized electrode immersed in a solution in which the activity of the hydrogen proton H+ is 1.00 and in which H_2 gas bubbles at a pressure of 1 atm (see **Figure 17a**).

The **saturated calomel electrode** (SCE) (see **Figure 17b**) consists of an inner tube containing a paste with Hg, Hg_2Cl_2 and saturated KCl. This tube is inside another tube containing

a saturated KCl solution. A small hole connects the two tubes. At the tip of the outer tube is the salt bridge implemented by means of porous glass or asbestos fiber. The potential of this electrode at 25°C is +0.2444 V and remains stable at that temperature as long as the solution in the outer tube is saturated. The problem with this type of electrode is that the solubility of KCl is temperature sensitive, so it cannot be used at high temperatures.

The **silver/silver chloride** (Ag/AgCl) electrode consists of a silver wire whose end is coated with a thin layer of AgCl (see **Figure 17c**). For ambient temperature operation, the wire is usually immersed in a KCl solution andthe whole is introduced into a tube at the end of which a salt bridge is implemented by means of porous glass. Its potential when the KCl solution is saturated is +0.197 V. For high temperature or size-constrained applications, the AgCl layer is implemented through a polymer composite and exposed directly to the solution (without porous glass nor KCl saturated solution), offering degradation endurance and miniaturizing the electrode. However, this electrode is more prone to reactions with the sample that give rise to insoluble silver complexes, compared with the SCE.

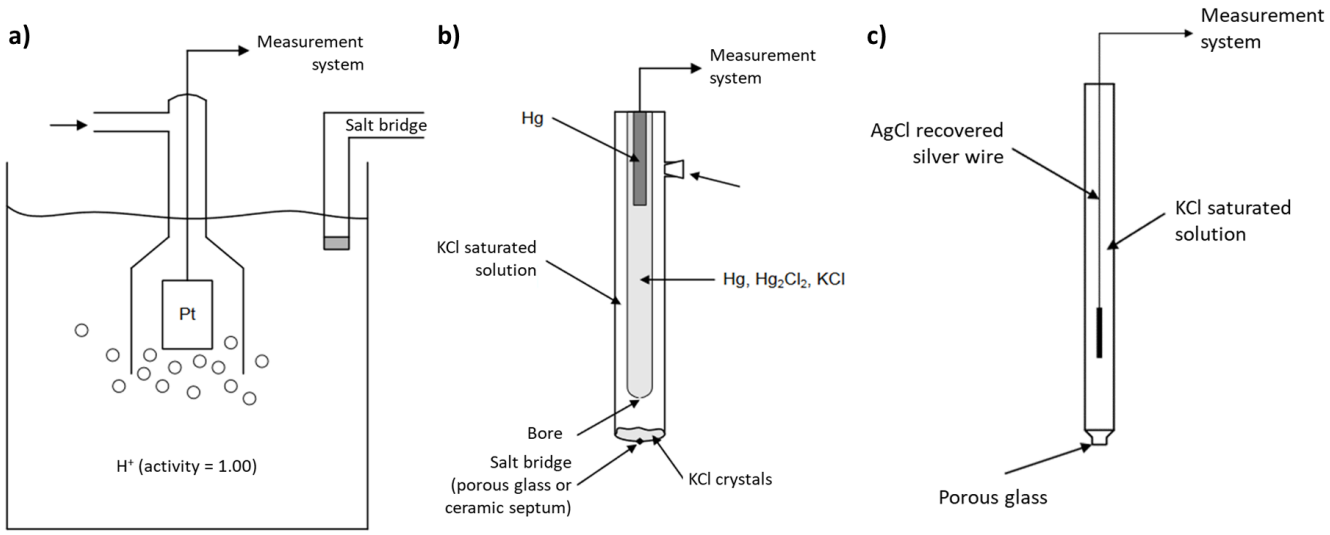

Figure 17. a) Standard Hydrogen Electrode representation. **b)** Saturated Calomel Electrode representation. **c)** Ag/AgCl Electrode representation. Adapted with author's permission from [154].

5. Controlled drug release

In this section, we will provide a brief introduction to the discipline of controlled drug release in the following subsections:

- Definition of the broad discipline, which is application-oriented.
- Applications and potential in clinical and research routines.
- Classification in terms of the carrier, escape mechanism, and trigger.
- We will delve into gated materials, particularly mesoporous silica nanoparticles.
- We will address the mechanisms available to trigger a controlled drug release.
- Finally, addressing electrically triggered controlled drug release for spinal cord injury.

5.1. Definition

The controlled drug release discipline designs, characterizes, and develops biomaterial and engineered biochemical solutions to develop systems capable of releasing in a pulsed or regulated way loaded and retained specific molecules in a material upon the presence of a target or condition, the application of a stimulus, or a combination of them. A controlled drug release is composed of four elements:

1. The **cargo** or **payload**, *i.e.*, the drug to be released upon suitable conditions.
2. The **carrier** or **container** in which inner space will be filled with the cargo.
3. The **barrier** or **gate** impedes the cargo from leaving the container.
4. The **trigger**, or **condition**, is an **event** or **circumstance** that modulates the barrier.

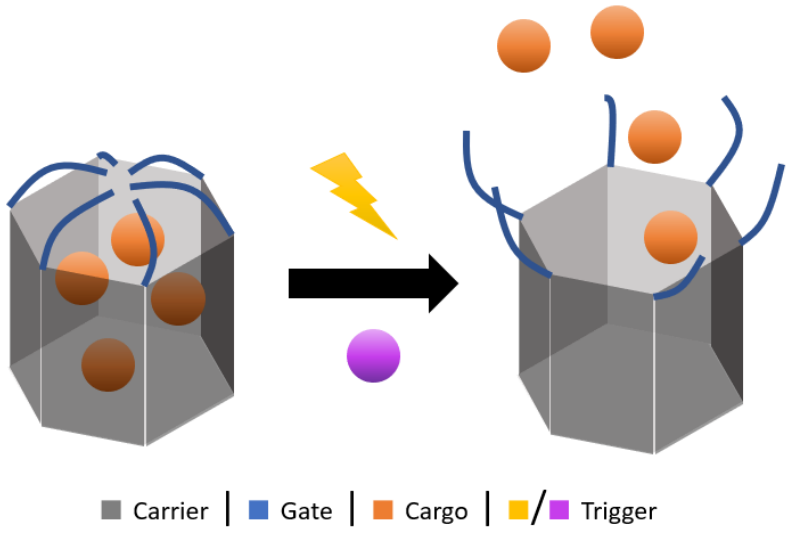

Figure 18. General scheme of a controlled drug release systems on a porous support.

The barrier may be an independent physical element or a property of the container. It is mainly related to the **drug escape mechanism** of the technique. A general diagram is shown in **Figure 18** for a porous system containing a drug in the pore voids.

Dalcanale & Pinalli, in the *Encyclopedia of Polymeric Nanomaterials* [165] offer a precise definition of the current state of the discipline: "Controlled release is the tailorable delivery of compounds (*e.g.*, drugs, proteins, fertilizers, nutrients, and other biologically active agents) at an effective level in response to time and stimuli (*e.g.*, pH, temperature, enzymes, UV light, magnetic fields, osmosis)".

5.2. Applications and potential

Conventional release systems such as tablets, capsules, and injections, among others, result in an abrupt increase in the drug concentration in the bloodstream once administered. These methods present certain inconveniences when frequent administrations are necessary because every pharmacologic compound has a minimum effective concentration and a maximum safe concentration for a given subject, depending on their characteristics. Treatment effects are absent when the bloodstream's drug concentration is below its minimum. On the other hand, surpassing the maximum desired level may imply acute symptoms or other kinds of short and long-term damage because of the toxicity effects of such concentration. The conventional administration, with the before mentioned abrupt increases, has an exponential decay in concentration because of the absence of a continuous drug administration source. Therefore, after every intake or injection, it is common to surpass the maximum desired level and, soon after, perceive a concentration decrease below the minimum effective level.

In the 1950s, the development of polymeric systems allowed the implementation of drug release systems with gradual drug diffusion, called extended drug release systems. They allowed overcoming this first limitation with comprehensive development until the 1980s (see Lee & Li [166]).

The current drug administration methods in the research routines and clinical therapies, with the widespread use of extended-release technologies, rely on the following:

- Research or sanitary personnel drug administration.
- Subject or patient drug auto-administration.

More than a decade ago, the knowledge gathered from the chronotherapy of specific diseases and the most recent developments in chronobiology clearly implied that the one-size-

fits-all, all-the-time approach to drug administration was no longer valid (Youan [167]). Therefore, new fields in the Pharmaceutics discipline emerged, such as chronopharmocology and chronopharmacokinetics: Choudhary *et al.* [168] define them as:

- **Chronopharmacology**: "science that carries out the study of the biological rhythm's dependencies of the medicaments".
- **Chronopharmacokinetics**: "used to treat different diseases based on circadian rhythm by developing different drug delivery systems that can release the drug at the peak time of the disease".

They rely on the development of new technologies able to surpass the extended-release systems. The drug concentration can be kept within the therapeutic range for a long time with the help of extended-release devices. Nonetheless, this is not necessarily the optimal treatment at any given disease state. Chronotherapeutic drug delivery systems can provide fast drug release with a designed lag time (Gowthami *et al.* [169]). This fast response is the opposite of keeping a constant drug level for an extended period of time: optimal delivery of drugs and treatments should be efficiently regulated to reach the appropriate therapeutic plasma levels and pharmacologic reactions at the specified time (Lin [170]).

Therefore, the new drug carriers can provide accurate control over the delivery time and the amount of drug injected into the patient's body, in contrast to old drug carriers, which could only manage the release of the compounds in a monotonous manner. With this purpose, the state of the art has been nourished with structured and demand-driven methods. The on-demand techniques include systems directly controlled by an operator/practitioner, possibly with a remote device triggering/affecting the implanted or injected drug carrier. In contrast, the structured or programmed methods offer dosage forms with an advanced architecture to accurately adjust the release rate for a specific time. The ultimate goal of such devices is to provide a customizable release pattern and increase the effectiveness of therapy by precisely regulating dosage, time, and location of drug release (Davoodi *et al.* [171]).

The development of controlled drug release techniques has been extensive, giving a massive pool of available technology in the field. Nevertheless, they have been shown to be effective in the laboratory or with small animals. Hence, there is a gap between the current state of the art and the clinical and research routines. Being aware that there is a significant gap between clinically superior treatments and therapies currently available in clinical routine, there is an evident opportunity for developing and applying multifunctional controlled drug delivery systems from external stimuli. There is even research on externally controlled drug release systems with reversibility so that they can be "turned on", causing a gradual release, and "turned off", stopping it.

In a nutshell, traditional procedures, including extended-time drug release, present the following limitations:

- Local diseases, such as chronic arthritic pain or tumors, require constant invasive or non-local administrations, reporting discomfort, pain, collateral administration to non-targeted areas, and even tissue damage.
- Personnel constant involvement, or patient effort and discipline, is required.
- When extended-release is employed, there is no chance of release modulation or rectification. Dose amplification to deal with drug tolerance is not always gradual (mainly through intakes).

Controlled drug release techniques aim to relieve the current drug administration methods in the research and clinical therapies in these cases, allowing:

- Minimal or zero invasive drug administration for local diseases.
- Dose and timing modulation of the drug administration through automation.
- A battery of substances can be set to be available in case the situation demands them.

Even a new generation of controlled drug release is emerging from the micro-electro-mechanical systems (MEMS) disruptive technology. They are out of the scope of the present work. However, they are worth mentioning, given that they may challenge and transform the current discipline following the methods used in the fabrication of integrated circuits but with biocompatible materials, as commented by Villarruel Mendoza *et al.* [172]. Other release technologies, such as the engineered microneedle patches, also mix external electronic devices with drug release technologies to offer unique solutions to the current drawbacks and limitations of today's drug administration protocols, as reviewed by Jamaledin *et al.* [173].

Subsection summary: For all drug applications, there is a minimum threshold concentration to start to take effect and a maximum limit concentration that involves harmful consequences for the subject. Nevertheless, these limits are not static, and the need and tolerance of different pharmacological levels vary according to internal and external factors within the patient or biological system. Pulsatile controlled drug release technologies are overcoming the traditional approaches of periodic or extended-release administrations. They are minimally invasive and allow for dose and timing modulation externally or upon the presence of internal triggers.

5.3. Classification

Controlled drug release systems can be broadly classified mainly in three different ways: depending on the carrier used, according to the cargo escape mechanism, or according to the trigger condition for the release.

Regarding the carrier, many platforms have been developed, such as:

- solid-lipid nanoparticles, *e.g.,* Mühlen *et al.* [174],
- polymer microspheres, *e.g.,* Freiberg *et al.* [175],
- gold nanostars, *e.g.*, Hernández-Montoto *et al.* [176],
- hydrogel-nanoparticle-networks, *e.g.*, Huang *et al.* [177],
- coated conducting polymers, *e.g.*, Alves-Sampaio *et al.* [178],
- mesoporous silica nanoparticles (MSN), *e.g.*, García-Fernández *et al.* [179],

In the second classification scheme, we can establish five categories according to the cargo escape mechanism as stated by Lee *et al.* [180] (**Figure 19**):

- Diffusion-controlled release.
- Carrier degradation.
- Hydrolytic cleavage of the carrier-drug linker.
- Solvent-controlled release.
- Stimuli-sensitive destruction of the diffusion barrier.

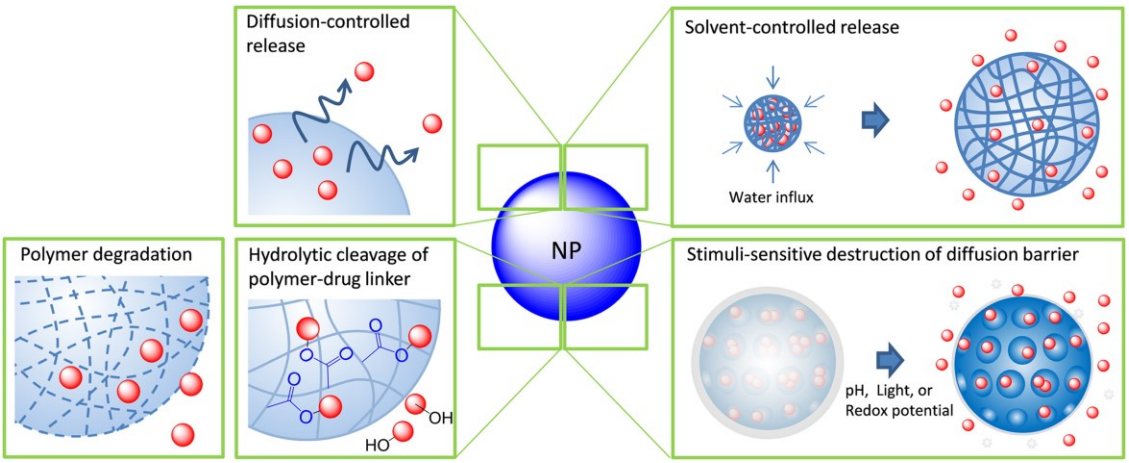

Figure 19. Drug release mechanisms from a nanoparticle (NP). Reproduced with permissions from [180]. Chemical Engineering Science © 2014 Elsevier.

The external stimulus or triggerable controlled drug release is the one in which the escape mechanism is the stimuli-sensitive destruction of the diffusion barrier. This diffusion barrier

can be **molecular gate**, and in combination with the carrier materials (usually mesoporous silica) study and research, they compose the **gated materials** discipline of study.

We will address the third classification approach (triggers) soon, in *5.5. Drug release stimuli.*

5.4. Gated mesoporous silica nanoparticles

There are excellent recent reviews regarding gated materials and mesoporous silica nanoparticles that have been used as direct support for this subsection:

- Aznar *et al.* [68] and Sancenón *et al.* [181] offer in-depth reviews in the gated materials field and applications, both from Martínez-Máñez group from our research institute.
- Tarn *et al.* [182], Zhou *et al.* [183], Li *et al.* [184], Argyo *et al.* [185], and Kumar *et al.* [69] give a deep comprehension of mesoporous silica nanoparticles fabrication, characterization, gating options, functionalization, degradation, biocompatibility, and applications.

According to Aznar *et al.* [68], these gated materials are hybrid materials due to the presence of two subunits:

- An inorganic porous scaffold that is the carrier of the cargo.
- A capping molecular or supramolecular element as a diffusion barrier (molecular gate, also known as gatekeeper or nanovalve).

The second element, the molecular gate, is designed to allow the diffusion of the cargo upon the presence of a particular stimulus (physical, chemical. or biochemical).

Among gated materials scaffolds, **mesoporous silica nanoparticles (MSN)** stand out. Candela Noguera's thesis dissertation offers a close and profound view of their capabilities, fabrication, and functionalization [186], whereas Llopis Lorente's presents frontier applications of this technology [187], both from Prof. Martínez-Máñez group.

According to Tarn *et al.* [182], MSNs present the following advantages:

- They can be manufactured with a high degree of uniformity in terms of size, pore size, and degree of dispersion by colloidal chemistry and evaporation.
- An exceptionally high ratio of surface area per gram, easily exceeding 1000 m^2/g.

- Pore size and surface chemistry can be modified independently, and different charges can be loaded, offering higher capacity levels in comparison with other carriers such as liposomes or polymers.
- Engineered biofunctionality and biocompatibility are possible thanks to the ability to independently modify MSN's surface and interior (**Figure 20**).

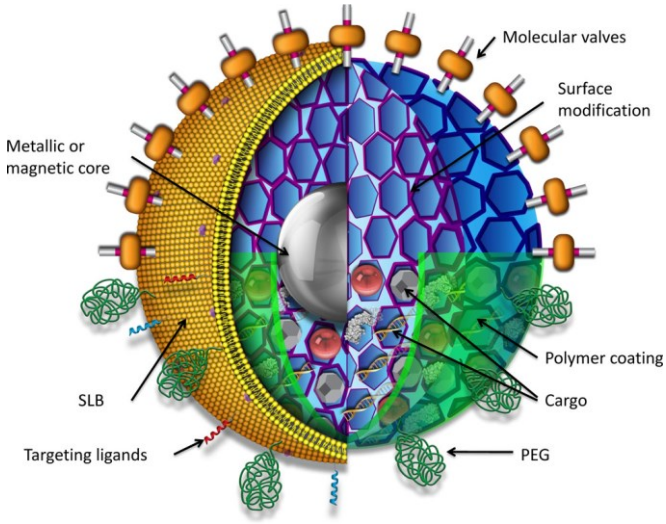

Figure 20. Schematic of a multifunctional mesoporous silica nanoparticle showing possible core/shell design, surface modifications, and multiple types of cargos. Reproduced with permission from [182]. Accounts of Chemical Research © 2013 American Chemical Society.

This last characteristic is regarded by Zhou *et al.* [183] as *two functional surfaces*: "[…] namely cylindrical pore surface and exterior particle surface. These silanol-contained surfaces can be selectively functionalized to control drug loading and release better. Moreover, the external surface can be conjugated with targeting ligands for efficient cell-specific drug delivery."

Finally, its good biocompatibility [183], *i.e.*, inertness and thermal stability, as well as its transparency (see Yamamoto *et al.* [188]), makes of the MSN technology one of the most promising emerging tools in nanomedicine and related areas.

Summarizing, their main functionalities, listed by Tarn *et al.* [182], are:

1. High visibility or contrast in multiple imaging modalities.
2. Dispersibility.
3. Binding specificity to a particular target.
4. Ability to load and deliver large concentrations of diverse cargos.
5. Triggered or controlled release of cargo.

Therefore, the applications of gated materials technologies are not constrained to drug delivery: diagnostics, sensing, and bioimaging are other of their vast fields of application [68]. The application field of gated materials is still expanding, as shown by the recent works of Llopis-Lorente *et al.* from Prof. Martínez-Máñez group: developing nanosystems capable of *reading* environmental information and respond accordingly [189] and even to talk to one another [190].

Mesoporous silica nanoparticles have great potential for such biomedical applications. According to Li *et al.* [184], MSN "offers a broad palette of opportunities (…) ranging from sol–gel science, the fabrication of nanomaterials, supramolecular chemistry, controllable drug delivery and targeted theranostics in biology and medicine". According to Argyo *et al.* [185], MSN are a universal platform for drug delivery thanks to their multiple functionalities targeting or entering different kinds of cells or biomaterials.

Their wide applications and capabilities explain the wide variety of molecular gates in this field of study, offering different capabilities in terms of sensibility. Sancenón *et al.* [181] offer a systematic review, which is out of the scope of the present work.

In contrast with passive delivery, where cargo is usually released by simple diffusion or after degradation of the carrier, these smart release functionalities are upscaling to revolutionize medicine. Depending on the application, they can be tailored to co-deliver drugs, can be used in diagnosis imaging, be chemically modified for heavy metals removal, and launch a drug release upon a stimulus (see Kumar *et al.* [69]). Among stimuli studied to induce cargo release in gated materials, the use of redox processes has been widely explored, *e.g.*, Lai *et al.* [191], Liu *et al.* [192], and Qu *et al.* [193], but it is not the only one.

Subsection summary: *gated materials* are composed by an inorganic porous carrier, and an gate closing the pores. They represent one of the main controlled drug release technologies, as they allow loading the pores with cargo and entrapping it with the gates in a reliable and flexible way. Among carriers, *mesoporous silica nanoparticles* (MSN) stand out: they offer high visibility for imaging, dispersibility, binding capabilities, large payload, and present high versatility in the engineering of the opening conditions of the gate.

5.5. Drug release stimuli

The **externally controlled drug release** was born with the first polymer composites with external stimulus control capability:

- Magnetic regulation of drug release (1985) by Edelman *et al.* [194].
- Thermal trigger and shutdown controlled drug release (1987) by Bae *et al.* [195].
- Ultrasound triggered controlled drug release (1988) by Miyazaki *et al.* [196].
- Ultrasound accelerated release (1989) by Kost *et al.* [197].

These advances represented an expansion of the controlled drug release discipline with the inclusion of the development of such technologies that allows **external control** of drug release and which this work will mainly address. From then on, the development of the discipline has been stellar. As sources for this subsection, we shall mention four recent reviews:

Mura *et al.* [198] classify the controlled drug release systems as exogenous (responsive to temperature, magnetic field, ultrasound intensity, light or electric pulses) or endogenous (changes in pH, enzyme concentration, or redox gradients), giving a framework classification between external and internal control of a controlled drug release system.

Timko & Kohane [199] and Said *et al.* [200] thoroughly explain the available NIR, UV, light, magnetic, electrochemical, ultrasound, thermal, and other methods, such as RF, for obtaining an externally controlled drug release system. Liu *et al.* [201] extensively review the various nanovehicles available for externally controlled NIR, ultrasound, and magnetic drug release.

Recalling that there were three classifications for controlled drug release technologies: depending on the carrier used, according to the cargo escape mechanism, or according to the trigger condition for the release; in this subsection, we will focus on the latter.

According to Alberti *et al.* [202], controlled drug release systems can be classified depending on the kind of stimulus to which they are sensitive in three categories: chemical, bioresponsive and physical. On the other hand, Mura *et al.* [198] establish a classification depending on the source of the stimuli to which the controlled drug release system is sensitive: exogenous, endogenous, and multistimuli. With this latter criterion, chemical and bioresponsive are subcategories inside the endogenous category. On the exogenous category, both Mura *et al.* and Said *et al.* [200] agree on five categories: light (including ultraviolet UV and near-infrared NIR), electric, magnetic, thermal, and ultrasound. A brief outlook is shown in the following list:

Endogenous controlled drug release technologies:

1. **Chemical** sensitivity:
    1. **pH**-responsive gates, as reported by Yang *et al.* [203] and Yang *et al.* [204].
    2. **Redox** reactive molecular gates, as reported by Giri *et al.* [205] and Liu *et al.* [206].

3. **Organo**-selective gates: sensitive to small organic molecules and ionic species, such as the ones developed by Zhao *et al.*, responsive to glucose [207] or Salinas *et al.* for explosives detection [208].

2. **Bioresponsive** sensitivity:
    1. Oligonucleotide-based (**DNA**), first reported by Climent *et al.* [209], from Prof. Martínez-Máñez group.
    2. **Enzyme**-responsive, *e.g.*, the one reported by Llopis-Lorente *et al.* [210], from Prof. Martínez-Máñez group.

Exogenous controlled drug release technologies, shown in **Figure 21**:

1. **Thermal**, origins beforementioned [195], with application among others in intratumoral drug release, *e.g.*, Tagami *et al.* [211] and from Prof. Martínez-Máñez group, Hernández-Montoto *et al.* [176].
2. **Magnetic**, pioneers already mentioned [194], which presents the possibility of performing magnetic resonance imaging for diagnosis with the same system which controls the drug release therapy (the theranostic approach, as reported by Yang *et al.* [212]).
3. **Ultrasound**, firstly reported by Miyazaki *et al.* [196], attains spatiotemporal control of the drug release, which application has resulted in significant suppression of metastatic dissemination, as shown by Rapoport *et al.* [213], among other applications.
4. **Light**, reported by Mal *et al.* [214], also achieves spatiotemporal control with even less invasiveness. Near-infrared radiation (NIR) higher penetration makes it the most interesting stimulus source for the light exogenous controlled drug release, *e.g.,* Mauriello Jimenez *et al.* [215], and from Prof. Martínez-Máñez group, Hernández-Montoto *et al.* [216,217].
5. **Electrical**, sensitive to weak electric fields (~1V). The principle of operation depends on the technology. The electric field may induce a redox reaction, *e.g.*, Ge *et al.* [218], or the electrically induced solution of a barrier, for instance, a polymeric one, in the work of Im *et al.* [219]. Within the present thesis, we reported a novel electrically controlled drug release responsive to weaker electric fields (García-Fernández *et al.* [220]).

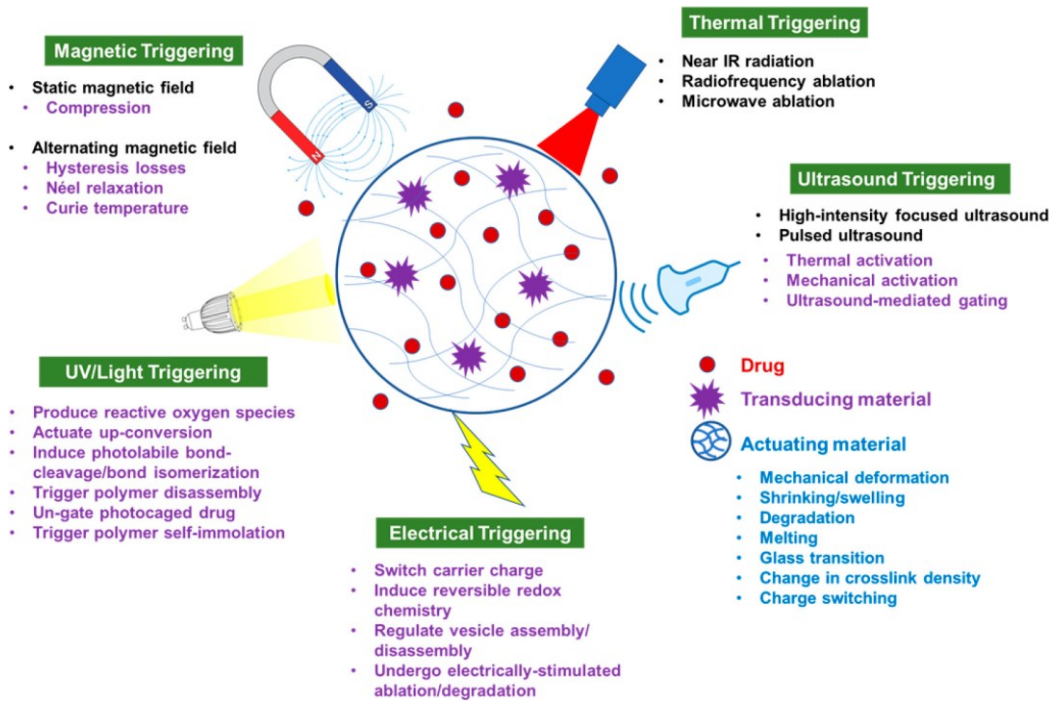

Figure 21. Modalities and mechanisms associated with externally triggered drug delivery. Reproduced with permission from [200]. Chemistry of Materials © 2019 American Chemical Society.

Subsection summary: controlled drug release (CDR) technologies can be classified as endogenous or exogeneous, depending on the nature of the trigger used to releasing the cargo. Among the exogenous triggers, electro-responsive CDR technologies are of particular interest to this work.

5.6. Electrically CDR (ECDR) for Spinal Cord Injury

As commented in *3. Techniques for modulating neural precursor cell development*, conducting polymers are a promising substrate for relaying SCI lesions with NPC grafts. This subsection will deepen their characteristics as drug carriers for controlled drug release (CDR), particularly from electrical triggers (namely ECDR). Furthermore, inspired by the nanoparticle-hydrogel approach, their ECDR capabilities could be enhanced by incorporating adequate engineered nanoparticles into the conductive polymer.

First, we shall consider that one of the key factors on the CDR for Spinal Cord Injury are the selection of the adequate **bio-compatible carriers**, as shown by the work of Donaghue *et al.* [67]. Hydrogels, as the one reported by Paradee *et al.* [221], and composites, as published by Mohapatra *et al.* [222] or the one reported by [223] Yun *et al.*, are recent examples of controlled drug release substrates for biomedical applications. **Conductive polymers** (CP) are one of the most promising candidates for this purpose, given their significant development in stimuli-

responsive drug release technologies (see Wells *et al.* [224]). They are organic materials with low electrical impedance and even semiconductor capabilities (see Guimard *et al.* work [225]). Among their multiple applications (see Tajik *et al.* [226]), such as the development of organic solar cells [227], printed electronics [228], and LEDs [229], they have multiple applications in the biomedical field, as Boehler *et al.* expose [230].

The characteristics and electromechanical properties of conductive polymers, and their biocompatibility, have boosted their application as a suitable tool in regenerative medicine and tissue engineering. According to Palza *et al.* [231], conductive polymers applications in the biomedical field mainly are:

- **Stimulate** overlaying, inserted, or in-between CP pads, **cells** in the context of **tissue engineering**, serving as a scaffold, as reported by Alves-Sampaia *et al.* [178] and by Guo *et al.* [97].
- **Deliver drugs** by changing their internal configuration under an electrical stimulus, as shown by Svirskis *et al.* [232] and Uppalapati *et al.* [233].
- Have **antimicrobial behavior** due to the conduction of electricity.
- Out of the scope of the present work, mimic muscles by converting electric energy into mechanical energy through an electromechanical response, as reported by Inal *et al.* [234].

They have also been used as biosensors, as shown by Naseri *et al.* [235], and neural interfaces, as shown by the works of Aqrawe *et al.* [236], Vara *et al.* [237], and Green *et al.* [238], among other applications. They are also of particular interest because of the fabrication strategies available to make them **biodegradable** (see Liu *et al.* work [239]).

Zhang *et al.* [240], and Brudno & Mooney [241] reviewed the current state of the art in stimuli-responsive polymeric depots to ultrasound, magnetic, electric, thermal, and light external stimulus, and to pharmacological stimulation based on nucleic acids and small molecules. Regarding hydrogels Campbell & Hoare [242], Nguyen *et al.* [243], Zhang *et al.* [244], and Merino *et al.* [245] explain both the chemical and physical cross-linking methods in hydrogels giving a spectrum of options such as ultrasound, thermal, electric, magnetic, or light responsive, and pH, and chemically reactive to different molecules. Externally addressable hydrogel composites obtain such properties mainly due to their **combination with nanoparticles**.

Regarding the conductive polymers' capabilities as drug delivery systems, they can be loaded with different molecules, which will be released with the presence of an electric field, usually provoking a redox reaction that will break the diffusion barrier retaining the cargo.

Illustrative examples of these capabilities are the works of Wadhwa *et al.* delivering dexamethasone from polypyrrole (Ppy) CP [246], Shamaeli *et al.*, releasing chlorpromazine from a biopolymer-doped Ppy [247], and Esrafilzadeh *et al.* delivering ciprofloxacin from poly(3,4-ethylene dioxythiophene) poly(styrene sulfonate) (PEDOT:PSS) with an outer shell layer of Ppy [248]. However, **conducting polymers as drug-release materials are far from ideal**, and several limitations have prevented their wide use in controlled-release applications. Conductive polymers present a **limited drug loading capacity**, the range of drugs that can be used is restricted due to charge and size requirements and show the inherent release of poorly adsorbed (bio)molecules even without the application of an electric stimulus. Moreover, although it has been reported that drugs delivered from conducting polymers could be suitable for a local delivery application, as shown by Richardson *et al.* [249] and Boehler *et al.* [250], the amount of drug delivered should still be increased for their applications in a majority range of diseases.

The **redox stimuli** have not only been used on conductive polymers as controlled drug release systems, but also on **gated materials**. For instance, the high presence of reducing agents in the intracellular media, such as glutathione, makes this kind of gate widely used when targeting the controlled release inside a cell. Examples are the works of Qiu *et al.* [251], Chen *et al.* [252], and Zhang *et al.* [253] on this application. There are also several redox-responsive molecular gates developed based on the same principle of action as the ones reported by Luo *et al.* [254], Du *et al.* [255], and Raza *et al.* [256].

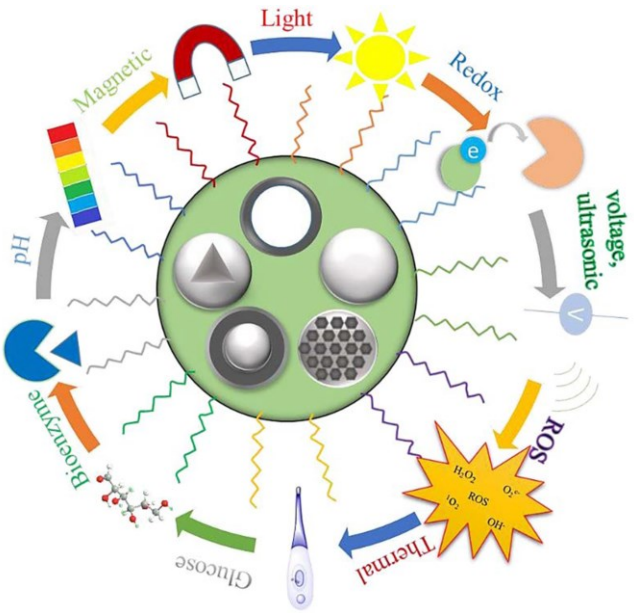

Figure 22. Types of silica nanoparticles and various stimuli attached to them to transform into stimuli-responsive drug delivery systems. Reproduced with permission from [257]. Polymer Advanced Technologies © 2022 John Wiley & Sons.

Grafting silica-based drug delivery systems in polymers, obtaining *smart polymers* which respond to the various external stimuli (pH, temperature, redox, reactive oxygen species (ROS), glucose concentration, enzymes, magnetic field, and so forth) is an emerging trend, as shows Shah *et al.* systematic review [257] (**Figure 22**).

However, examples of a drug released from **mesoporous silica nanoparticles** (MSNs) by applying an electric field are not abundant. Controlled drug release in MSNs under electrical stimulus is generally based on the functionalization of the MSN with ferrocene derivatives. The cargo is enclosed using a complex formed by grafted ferrocene derivative and β-cyclodextrin (β-CD), as done by Xiao *et al.* [258], Wang *et al.* [259], and Jiao *et al.* [260]. However, the use of these ferrocene-based systems in biological applications is limited due to the relatively high potential needed (ca. 1-1.5V) to induce ferrocene oxidation and cargo delivery.

Subsection summary: the controlled drug release (CDR) for Spinal Cord Injury (SCI) needs bio-compatible carriers. Conductive polymers allow electrical stimulation in tissue engineering applications and present biocompatibility and antimicrobial behavior, among other interesting characteristics. Nevertheless, their drug-loading capacity for CDR applications is limited. Inspired by the *smart composites*, based on the combination of hydrogels and nanoparticles responsive to different stimuli, *smart polymers* are based on conductive polymers bearing nanoparticles and can offer enhanced CDR capabilities. Electrical CDR nanoparticles can be triggered from the conductive polymer, given its electrical properties to carry electrical signals.

We will present our contribution to the field in the *Chapter 2. Electrically controlled drug release (ECDR)*.

6. Real-time feedback on biochemical systems

Real-time serotonin quantification is particularly relevance for spinal cord injury regeneration (see Perrin & Noristani [261]). The combination of serotonin receptor agonist release together with the application of electrostimulation has reported satisfactory results (see Ghosh & Pearse [262]). For this, serotonin levels must be between upper (see Oueghlani *et al.* [263]) and lower (Fickbohm & Katz [264]) limits. Serotonin synthesis by electrostimulation has also reported positive, albeit modest, results (Ghosh & Pearse [262]) in the absence of precise serotonin level monitoring. Current neurochemical techniques, such as microdialysis, voltammetry, and genetically encoded reporters, are limited in at least one crucial area requiring multiplexing or chemical, spatial, or temporal resolution.

Developing sensors for real-time quantification of serotonin is necessary for spinal cord injury regeneration. Furthermore, the measurement of other biomolecules is also of great importance. Combining effective treatments with sensory feedback would open the door to the application of control engineering. Among these treatments, we can mention pharmacological, electrostimulation, and optogenetic stimulation, as discussed in the previous sections. Modulating the stimuli according to the measured feedback would presumably increase the predictability of results and the efficiency of treatment protocols under development. Pioneering the area, the work of Polat *et al.* [265] shows the closed-loop control through fluorimetry feedback of voltage-gated molecule release.

6.1. Biosensor concept

Biosensors can be defined as analytical devices that use biomolecules as transducers and convert their responses into electrical signals (see Haleem *et al.* [266]). For the detection or quantization of biological analytes such as proteins, hormones, protozoa, bacteria, mycoplasma, or virus, an electrochemical process over a transducer is performed. Their capabilities may be increased by using different biorecognition elements, *e.g.,* antibodies, proteins, oligonucleotides, phages, or aptamers, bound to the transducers to which the electrochemical process or the signal readout will be performed. Transducer technologies in the state of the art include planar metals and ceramics, polymers, wires, fibers, nanoparticles, and arrays (see Cesewski & Johnson [267]). Combining biosensors with microfluidics and electrochemical techniques shows the most promising advances in point-of-care diagnostics amidst other applications (see Rackus *et al.* [268]).

6.2. Biosensors based on field-effect transistors (FETs)

Usually, biosensors based on FETs, namely bioFETs, utilize amperometry to read out their transimpedance variations, *i.e.*, via measured changes in source-drain channel conductivity that arise from the electric field of the sample environment (see Cesewski & Johnson [267]). The emergence of FET-based biosensors it's related to the fact that they overcome several problems. bioFETs offer label-free detection at lower cost and complexity, becoming competitive candidates for point-of-care testing applications versus optical-based in-vitro diagnosis. Both electrochemical biosensors and bioFETs offer miniaturization, low-cost fabrication, and portability making them direct competitors. The two biosensor technologies offer an excellent level of design flexibility, too. Even though, bioFETs' figures of merit, such as ultra-sensitive sensibility and specificity, and a higher degree of compatibility with conventional CMOS

circuits, make them the most suitable technology for a wide range of applications (see Wadhera *et al.* [269]). Furthermore, it is worth mentioning that FET-based biosensors' ultra-sensible detection of biomolecules capabilities is independent of their electrical charge [267]. This ultra-sensitivity may be enhanced by immobilizing biorecognition elements on the device's metal or polymer gate electrode [267,269].

6.3. Aptamers and aptamer-FET biosensors

There is a vast field in combining aptamers, nanoparticles, and other transducers to bioFETs to enhance their capabilities (see Peruzzi *et al.* [270]). Aptamers are a growing technology for the new generations of biosensors. They consist of single-stranded nucleic acids that bind to a target molecule with high selectivity. The response upon binding is a conformational change in the aptamer itself, which can be transduced into different signals through fluorescence, flow cytometry, upconverting nanoparticles, magnetic resonance, or transistor effect, amongst others (see Zhou *et al.* [271]). This selectivity makes them suitable for detecting or quantifying analytes in complex solutions, such as those in lab-on-a-chip and point-of-care biomedical applications (see Khan & Song [272]).

The methods that achieve the most extraordinary sensitivity are based on fluorescence, electrochemical interface, or field-effect transistors. It is worth mentioning works in state of the art, such as in the field of fluorescence aptamer-based sensors, with limit-of-detection (LOD) as lows as 10 pM for ATP (Liu *et al.* [273]), 1 pM for tyrosine kinase-7 (see Wang *et al.* [274]), or 20 aM for DNA (see Zuo *et al.* [275]). On the other hand, electrochemical biosensors based on aptamers showed 3.5 pM LOD for lysozyme (see Zhao *et al.* [276]), and 1 nM for cocaine and 5 nM for ATP (see Zhao *et al.* [277]). Biosensors based on FETs functionalized with aptamers (aptamer-FET) make selective electronic target detection possible. The stem-loop aptamers' reorientations near semiconductor channels modify its transconductance. This is due to the aptamer conformational change electrostatically affecting the depletion of the channel.

Based on In_2O_3 FET technology with specific aptamers, the 10 fM LOD of dopamine and serotonin, and 10 pM for lipid S1P and glucose were achieved (Nakatsuka *et al.* [278]), showing the astonishing capabilities of the bioFET technology combined with the aptamers ultra-selectivity and ultra-sensibility properties. Despite that, during this work, the measurements were performed using a high-cost and size silicon characterizer, being able to perform only one measure of one bioFET at a time, so these extraordinary performances must develop a path before they can be applied *in vivo*.

An aptamer can be described according to the rate of association (formation), k_{on}, and the rate of dissociation (rupture), k_{off}, of the aptamer-target complex. In the following subsection, we will address the electrical parameters in an aptamer-FET biosensor. In a nutshell, the I_{DS} current is the electrical signal transducing the target analyte concentration. This current will depend on two main controlled operation voltages: V_{DS} and V_{GS}. Hence, set V_{DS} and V_{GS}, the I_{DS} current over time can be analyzed as a function of the concentration variations. A representation of the biosensor displaying the beforementioned voltages and current is shown in **Figure 23**.

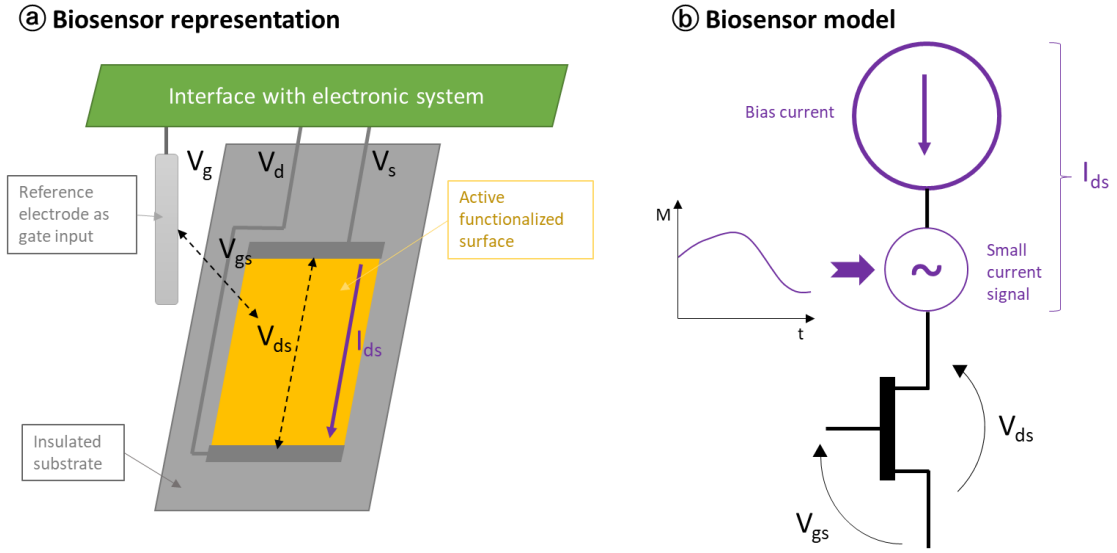

Figure 23. Biosensor ⓐ representation and ⓑ model, with most relevant voltages and current.

A baseline current, I_0, is present in the absence of the target. For each concentration of the target analyte in solution, a *plateau* current, $I_{plateau}(M)$, will be reached after a transitory time. These transitories are governed by **Equation 5** upon a concentration increase and **Equation 6** upon a decrease. Note that k_{on} units are $M^{-1}s^{-1}$, while k_{off} units are s^{-1} (concentration independent).

$$I_{DS}(t) = I_0 + \left(I_{plateau}(M) - I_0\right)\left(1 - e^{-k_{on}Mt}\right) \qquad \textbf{Equation 5}$$

$$I_{DS}(t) = I_0 + \left(I_0 - I_{plateau}(M)\right)\left(e^{-k_{off}t}\right) \qquad \textbf{Equation 6}$$

The relation between the former two is essential: $K_D = k_{off} / k_{on}$ (Wong & Melosh [279]), also known as the dissociation constant. Based on this relationship, high-affinity aptamers (which exhibit low K_D) are expected to dissociate slower. This results in a **trade-off between selectivity-sensibility and temporal resolution** for the aptamer-FET biosensors.

6.4. Calibrated response of aptamer-FET biosensors

The mechanical-to-electrical transduction on aptamer-FET biosensors is based on the conformational change that the aptamer suffers upon binding with the target molecule. Its assembly to the surface of the transistor's channel makes its reorientation a charge redistribution to the semiconductor surface electrons, as shown in **Figure 24** from Nakatsuka *et al.* [278]. The higher the target analyte concentration, the higher percentage of the aptamers anchored to the FET's channel will bind and reorient. Hence, the analyte concentration is transduced in transistor transimpedance variations.

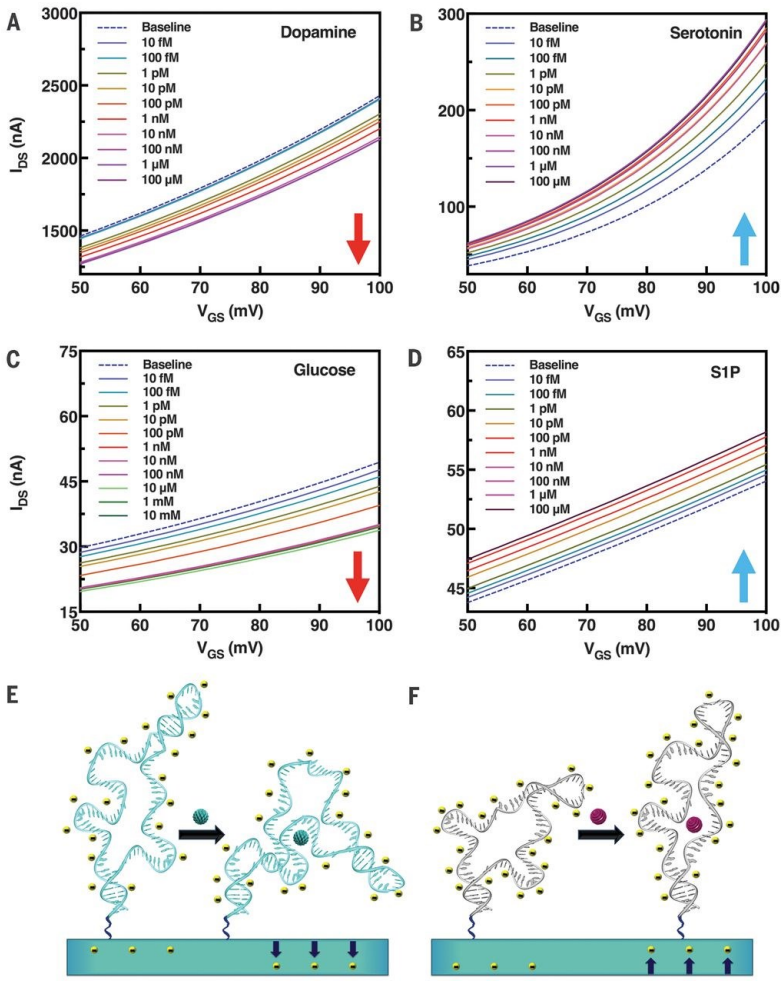

Figure 24. Aptamer-functionalized FET mechanisms. (**A**) Exposure of dopamine aptamer–FETs to dopamine (1× aCSF) led to concentration-dependent reductions in source-drain currents. (**B**) For serotonin aptamer–FETs, increasing concentrations of serotonin (1× aCSF) produced increases in source-drain currents. (**C**) Exposure of glucose aptamer–FETs to glucose (1× Ringer's) led to reductions in source-drain currents. (**D**) The S1P aptamer–FET transfer curves (1× HEPES) increased in response to target concentrations. Transfer curves shown are representative of $N = 6$ individual measurements. (**E** and **F**) Hypothesized mechanism of stem-loop aptamer target-induced reorientations in close proximity to semiconductor channels and within or near the Debye length. In (E), aptamers reorient closer to FETs to deplete channels electrostatically (e.g., dopamine, glucose). In (F), aptamer stem-loops reorient away from semiconductor channels, thereby increasing transconductance (e.g.,

serotonin, S1P). Schematics are idealized and do not reflect individual aptamer secondary structural motifs. Reproduced with permission from [278]. Science © 2022 American Association for the Advancement of Science.

An aptamer-FET biosensor is usually characterized as a standard transistor: for several drain-source voltages (V_{DS}), a gate-source sweep (V_{GS}) is applied, measuring the current flowing from drain to source (I_{DS}). Sometimes, the gate current (I_G) is also measured to ensure it is significantly smaller than I_{DS}. As FET, the transconductance is modulated through V_{GS}, and as a biosensor, it is also modulated by the aptamer-binding process. Then, a highest-sensibility (V_{GS}, V_{DS}) point can be found. This *optimal* operating point can be used to perform the measurements, tracking I_{DS} over time. This is the most basic operation mode, known as IT, standing from current (I) and time (T). Nevertheless, the reproducibility limitations of the aptamer-FET biosensors made of I_{DS} an electrical value that couldn't be universally related with to the analyte concentrations. Aptamer-FET suffers from severe device-to-device variations, even with normalization, requiring of device biosensor calibration before operation. This limits its application. More recently, the V_{GS} sweep characterization, namely IV sweep, with the main parameters shown in **Figure 25**, gave birth to a more robust methodology, suppressing this device-to-device variation: the calibrated response (CR) from Ishikawa *et al.* [280]

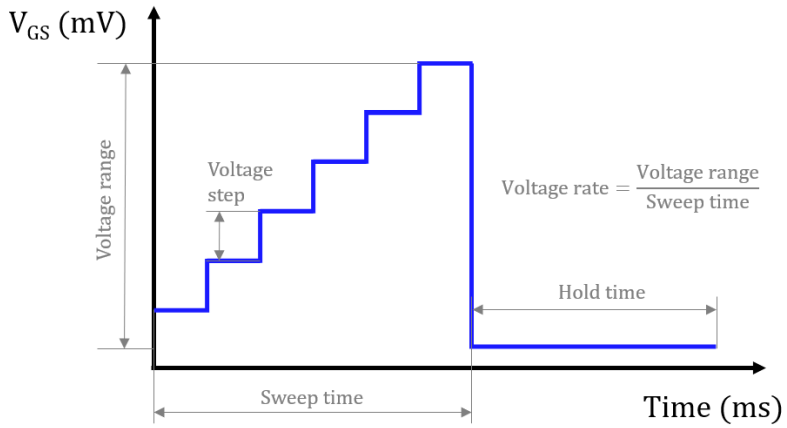

Figure 25. Voltage sweep representation in the gate of a bioFET, with the most relevant parameters labeled.

The CR method needs a sweep without analyte concentration and stores the electric current points for each V_{GS}. This first current curve is named the *baseline* curve. Every new sweep, acquiring a new set of current data points, will subtract the *baseline* curve, obtaining the absolute sensor response ΔI. The CR values can be obtained for a specific V_{GS} operating point. The device-to-device variation is suppressed through the application of **Equation 7**.

$$\mathrm{CR(mV)} = \frac{\Delta I}{dI_{DS}/dV_{GS}} \qquad \textbf{Equation 7}$$

Objectives of the doctoral thesis

The horizon of this work is developing an effective treatment for spinal cord injury. The current state of the art points out that using *stem cells* is the most promising approach. A biocompatible substrate is necessary to implant a stem cell graft into the lesion core. Material selection and biofunctionalization become critical factors of this substrate.

Furthermore, stem cell therapy needs such cells to be guided to form functional tissue. Several techniques are under the scope, showing positive results in the modulation of cell fate and function *in vitro* and *in vivo*. However, their combination has yet to be explored.

Therefore**, the main objective of this doctoral thesis is the development of platforms that allows the combination of the most promising techniques for *in vitro* nerve tissue regeneration**. The platforms must allow setting up stimulation patterns with total flexibility of the three following techniques:

- Electrostimulation
- Pharmacological treatment
- Optogenetic stimulation

Regarding pharmacological treatment, new controlled drug release technologies are emerging, inducing cargo delivery upon the presence of an external trigger. Regarding this technique, we aim to design and characterize a new electrically responsive technology, enhancing the graft substrate with controlled drug capabilities.

The control of the stimulation is as important as the stimulation itself. All the stimulation techniques for modulating stem cell development induce biochemical responses from the cells. Monitoring the concentration levels of the biomolecules of interest would allow for adjusting the stimulation intensity and duration. It would allow the stimulation to overcome the threshold to produce the desired response, remaining under the maximum overstimulation levels that would produce adverse effects.

Hence, **a secondary objective is developing the instrumentation for using biosensors that allow quantifying in real-time biomolecules of interest**, making possible the implementation of a closed loop in the stimulation protocols.

In vitro validation is necessary for the complete validation of the developed stimulation platforms. The validation of the biosensor instrumentation shall demonstrate the biosensor's operation in artificial solutions that simulate the cellular environment.

Chapter 1. Electronic instrumentation for *in vitro* electrostimulation and controlled drug release

Three stimulation techniques are proposed to modulate neural precursor cell development: pharmacologic stimulation, electrostimulation, and optogenetic stimulation. The pharmacologic stimulation can be controlled electrically using electro-responsive molecular gates. This opens the door to automating combined pharmacological and electric stimulation protocols from electrical stimuli. However, no such commercial equipment can currently operate in cell culture environments to explore this combination *in vitro*.

This chapter describes the electronic platforms designed to fulfill this purpose. These have measurement units to acquire, store and visualize the electrical response to an electrical stimulus (current response to a voltage stimulus, and vice versa, *i.e.*, voltage response to a current stimulus). Mainly two devices have been designed: the first, called FAEVIS, wireless; and the second, IVESDRIS, which overcomes the limitations of the previous one by being wired. Both are fully configurable, via a graphical user interface or high-level sequential instructions.

These devices have been published in international congress participations (Monreal-Trigo & Alcañiz [281], Monreal-Trigo *et al.* [282]). Furthermore, a Bachelor's Degree Final Project in Electronic Engineering was also developed in this part of the doctoral thesis (Alamán Escolano [283]), as an extension module for IVESDRIS.

1. Circuits for electrochemical techniques: potentiometric measurement and potentiostat

1.1. Electronic systems for potentiometric measurements

Nowadays, potentiometric systems are based on electronic voltmeters based on high input impedance operational amplifiers. In fact, the complete system consists of an input amplifier stage whose mission is to amplify the voltage and at the same time prevent current flow through the electrochemical cell. This is followed by a low-pass filter that removes the high, medium, and low frequency noise. Since what is to be measured is the voltage between the working electrode(s) (WE) and the reference electrode (RE), the latter is connected to the ground of the electronic circuit (which represents the zero potential).

Figure 26 shows the block diagram of an electronic system for potentiometric measurements. It consists of three stages: the amplification and filtering stage, the data acquisition system and the data processing system. The first stage has a high impedance input which prevents current flow in the cell. This stage also amplifies and filters the measured signal. The analog voltage obtained at the output of this block is digitized by a data acquisition system (consisting of an analog-to-digital converter). The data processing system (which can be a computer or a µP or µC system) collects the digital value corresponding to the captured sample and stores it in memory, displays it on the screen and/or processes it.

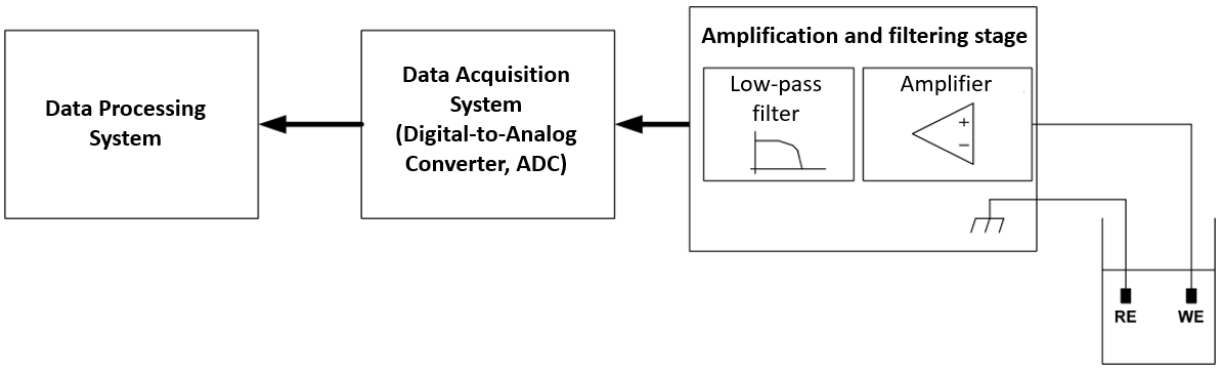

Figure 26. Potentiometric electronic measurement system block diagram. Adapted with author's permission from [154].

Some commercial systems are used to perform potentiometric measurement in biomedical applications, namely potentiometric electronic tongues, such as the TS-5000Z from Insent Inc. or the Astree2 from Alpha MOS (see Labańska *et al.* [284]), or LiquiLab from EcoSens (see Lvova *et al.* [285]). On the other hand, it is common to find systems purposely designed for specific applications. Sometimes the design is limited using a standard data acquisition board or smart digital multimeter to carry out the signal digitization and data processing from a personal computer (see Ghrissi *et al.* [286], Belugina *et al.* [287], Semenov *et al.* [288], and da Costa Arca *et al.* [289]); and in other cases, the complete system design is implemented (Kim *et al.* [290], and Ruch & Hu [291]).

1.2. Electronic systems for voltammetric measurements

Voltammetry tests require the use of electronic systems capable of generating voltage signals with low output impedance, applying the voltage to the electrochemical cell, collecting data on the current generated and storing the data for further processing.

Figure 27 shows a diagram with the different elements that are necessary to carry out voltammetry tests. The cell voltage control and current measurement is performed by the

potentiostat (see section *1.3. Potentiostat*). The signal generation and acquisition system establishes the analog voltage that the potentiostat must apply between the reference electrode and the working electrode ($V_{SETPOINT}$). The potentiostat measures the signals corresponding to the applied voltage (V_{VCE}) and convert the current flowing through the working electrode into a voltage (V_{IWE}) and transmits them to the signal generation and acquisition system for digitization. The operation of the system is coordinated by the data processing block which, on the one hand, establishes the type of signals to be applied to the electrochemical cell (constants, pulses, triangular, sinusoidal) and, on the other hand, receives the digitized voltage and current data and stores, displays and/or processes them.

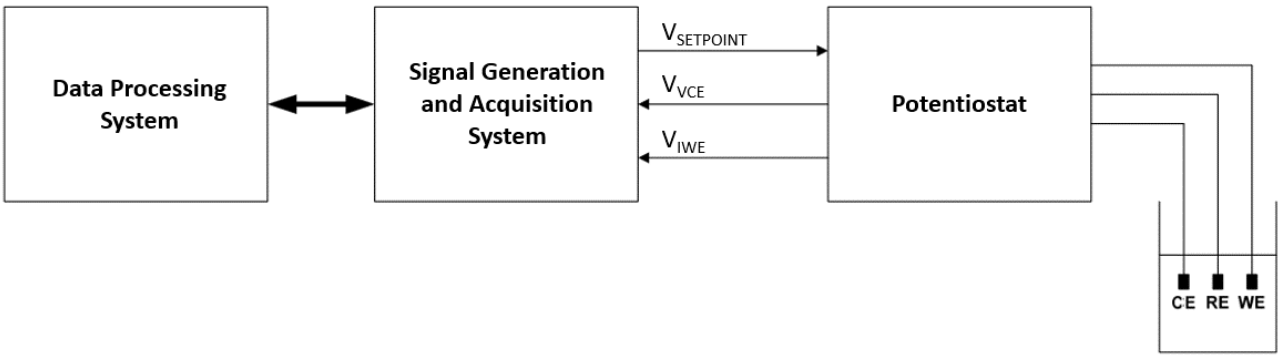

Figure 27. Voltammetric electronic measurement system block diagram. Adapted with author's permission from [154].

In most of the works consulted, commercial equipment is used to carry out voltammetry tests. The most frequently used equipment is the Autolab PGSTAT, as in Jarolímová *et al*. [292,293], Alatraktchi *et al.* [294], Juvêncio Silvo *et al.* [295], Pattananuwat & Aht-ong [296], and Lee *et al.* [297]; or other Metrohm Autolab solutions, such as the μ-Autolab Type III in Ashjari *et al.* [298]. EG&G Instruments commercial solutions is also a widespread option, as shown in Khaydukova *et al.* [299] using a PARSTAT, Bagheri & Marand [300] using a M273, Shatla *et al.* [301] employing a 273A, or Jee *et al.* [302] and Myung *et al.* [303] using a 263A model. Custom solutions in terms of data analysis are common between the examples mentioned before, but really scarce in terms of the whole setup, including the hardware. The development of high-density sensor arrays for cross-sensitivity voltametric electronic tongues report this kind of integral development (see Alcañiz Fillol [154] and Baldeón *et al*. [304]), but these solutions are found when miniaturization is needed, as shows the work of Segura & Osma [305] for remote biosensing, Pennazza *et al.* [306] for gas detection, Lin *et al.* [307] for noninvasive wearable electroactive pharmaceutical monitoring, Dieffenderfer *et al.* [308] in a sweat-based wireless wearable electrochemical sensor, or Poulladofonou *et al.* with an e-finger for submission drugs screening [309].

1.3. Potentiostat

Although there are several potentiostat configurations, the one most frequently found in the literature is the one shown in **Figure 28** (see Adams *et al.* [310], Lopin & Lopin [311], and Li *et al.* [312], Jenkins *et al.* [313]), or similar configurations (see Ainla *et al.* [314], and Hiolett *et al.* [315]).

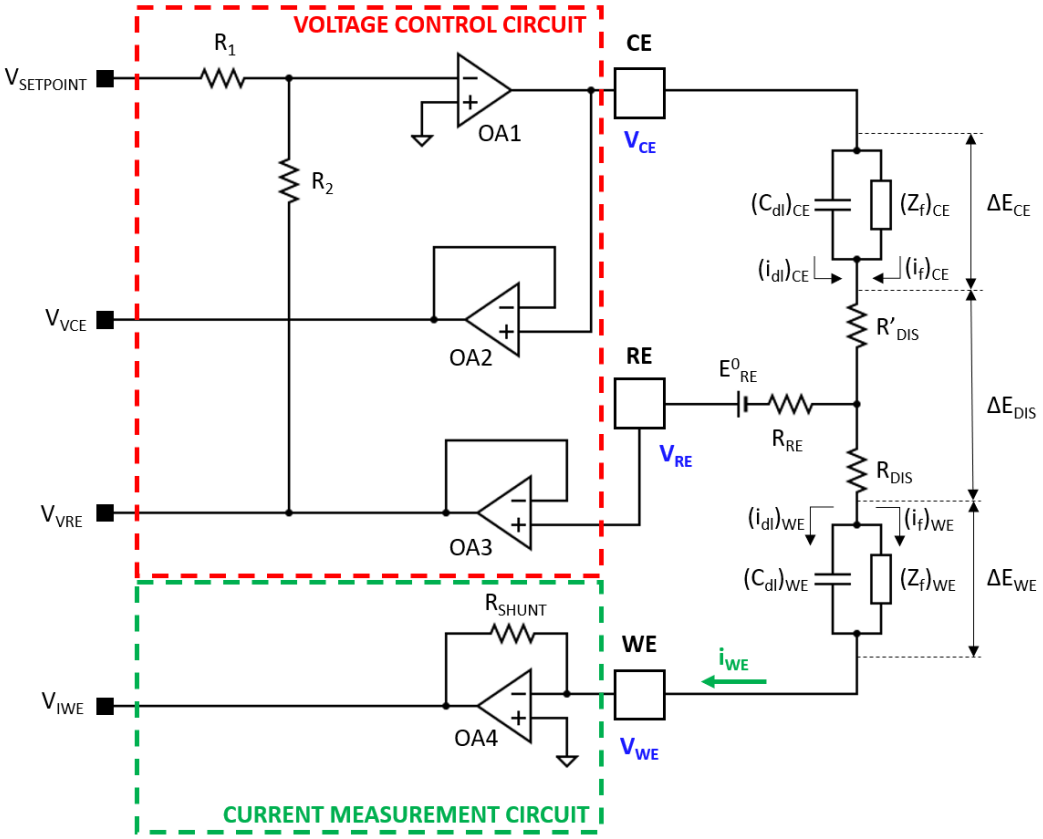

Figure 28. Potentiostat block diagram.

The potentiostat has two fundamental missions. On the one hand, it must apply between the reference electrode (RE) and the working electrode (WE) a controlled voltage that is independent of the processes occurring at the counter electrode (CE). On the other hand, the current flowing through the working electrode must be measured. In addition, it must be ensured that there is no current flowing through the reference electrode so that the conditions described in section *4.4. Voltammetric techniques* of the *Introduction* on the operation of the 3-electrode electrochemical cell can be fulfilled.

In addition to the three connection terminals to the electrochemical cell (CE, RE and WE), the potentiostat has three connections to the signal generation and acquisition system (see section *1.2. Electronic systems for voltammetric measurements*). Through one of these connections the signal generation and acquisition system establishes the voltage to be applied

between the terminals RE and WE ($V_{SETPOINT}$). On another of the connections the potentiostat provides the actual value of the voltage between terminals CE and WE (V_{VCE}). Normally $V_{SETPOINT}$ and V_{VRE} should have the same value but for some operating conditions of the potentiostat (instabilities) this may not be the case. For the third connection to the signal generation and acquisition system the potentiostat provides a voltage that corresponds to the current flowing through the working electrode (V_{IWE}).

The potentiostat is made up of two blocks, described in the following points:

- *1.3.1. Voltage control block*
- *1.3.2. Current control block*

Furthermore, potentiostats pose some problems arising from the following issues:

- The non-ideal characteristics of the operational amplifiers that compose it (finite input impedance and open-loop gain).
- The finite conductivity of the solution.
- The capacitive components of the electrochemical cell.
- The internal resistance of the reference electrode.

The most important difficulties to be faced when working with a potentiostat are instabilities, addressed in *1.3.3. Potentiostat instabilities*, which can lead to oscillations of the voltage and current signals, and the compensation of the solution resistance, commented on *1.3.4. Solution resistance compensation*.

1.3.1. Voltage control block

The voltage control block: this block has two missions. The first is to ensure that no current will flow through the reference electrode. This is achieved by placing a high impedance amplifier in follower configuration connected to the RE terminal. The second mission is to apply between the RE and WE terminals the setpoint voltage established at the $V_{SETPOINT}$ input. As we will see later, the WE terminal is connected to a "virtual ground", so for electrical purposes in the electronic system its potential can be considered to be 0 V. Therefore, to apply the $V_{SETPOINT}$ voltage between RE and WE it is sufficient to set a voltage equal to $V_{SETPOINT}$ on RE. To understand the operation of the control circuit, the elements $(C_{dl})_{CE}$, $(Z_f)_{CE}$, R'_{DIS} and R_{RE} are grouped into a single impedance called Z_{CE_RE} and the arrangement of the components is reorganized as shown in **Figure 29**.

If we consider the operational amplifier OA1 we see that it is configured as an inverting amplifier with a negative voltage feedback formed by Z_{CE_RE}, E^0_{RE}, the operational amplifier OA3 and R_2. Due to this negative feedback, it can be assumed that the "-" terminal of OA1 is connected to a virtual ground (considering that OA1 is an ideal operational amplifier). If we apply Kirchhoff's 1st law to the "-" terminal node of OA1 and assume an infinite input impedance for this operational amplifier, the equality of **Equation 8** is satisfied.

$$\frac{V_{SETPOINT}}{R_1} = \frac{V_{VRE}}{R_2} \qquad \textbf{Equation 8}$$

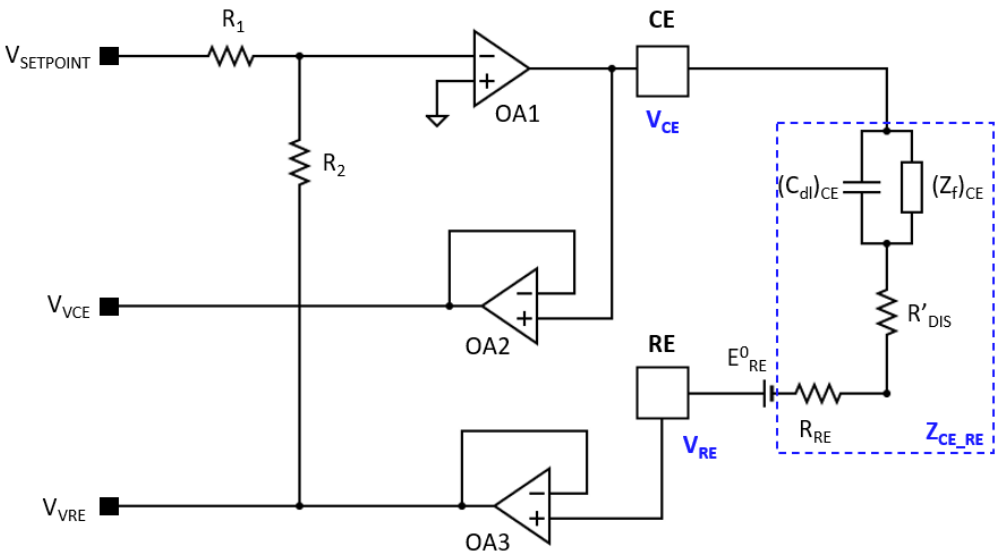

Figure 29. Potentiostat control circuit feedback loop.

If we choose R_1 and R_2 of the same value, V_{VRE} is equal to $-V_{SETPOINT}$; and since AO3 is configured as a follower, V_{RE} is also equal to $-V_{SETPOINT}$. As for V_{CE}, it should take the value that allows **Equation 8** to be fulfilled. Depending on the characteristics and location of the counter electrode and the nature of the solution, V_{CE} can be greater than V_{RE}. This is not a priori a problem as long as V_{CE} does not become higher than the saturation voltage of the operational amplifiers. This value is tracked through OA2, configured as a buffer, so V_{VCE} is equal to V_{CE}.

From the point of view of the electronic circuit the WE terminal is 0 V while the RE terminal has a voltage equal to $-V_{SETPOINT}$ applied. However, from the electrochemical point of view it can be considered that a potential is being applied to the electrode-solution interface of the working electrode whose expression would be given by **Equation 9**.

$$\Delta E_{WE} = -V_{SETPOINT} - E^0_{RE} - R_{DIS} \cdot i_{WE} \qquad \textbf{Equation 9}$$

Throughout this thesis we will consider that the potential is applied to the working electrode although from the electrical point of view the WE terminal is connected to the virtual

ground and the voltage is applied to the RE terminal. Since E^0_{RE} is a stable and known potential, it can be easily compensated. However, the value of the $R_{DIS} \cdot i_{WE}$ term can vary throughout the test, making its compensation more problematic.

1.3.2. Current control block

The current measurement block: this block must generate a voltage V_{IWE} that is proportional to the current flowing through the working electrode. In **Figure 28** we can see how the measurement circuit consists of an operational amplifier (OA4) configured in current-voltage converter mode with negative feedback through the R_{SHUNT} resistor. Under these conditions the "-" terminal of OA4 behaves as a virtual ground, so, applying again the 1st Kirchhoff's law and considering an infinite input impedance of the operational amplifier, the expression of Equation 7 will be fulfilled.

$$i_{WE} = -\frac{V_{IWE}}{R_{SHUNT}} \rightarrow V_{IWE} = -R_{SHUNT} \cdot i_{WE} \qquad \textbf{Equation 10}$$

1.3.3. Potentiostat instabilities

There are several publications that discuss the instability problems that can appear in potentiostat measurements under certain operating conditions (*e.g.,* Davis & Toren [316] or Bio-Logic Science Instruments' Application Note nº4 [317]). The instability problems can have their origin both in the voltage control circuit and in the current measurement circuit.

In [317] the transfer function of a simplified version of the voltage control circuit is established. In the obtained expression the quotient term can cancel out under certain conditions. These conditions depend on the open-loop gain of the operational amplifier, the characteristics of the electrochemical cell (highly capacitive electrochemical cells are more prone to instabilities) and the shunt resistance of the current measurement circuit. The zero value of the quotient would result in an infinite gain of the control circuit, which would cause the output voltage to saturate or go into oscillation. To avoid this problem, it is recommended to limit the bandwidth of the voltage control circuit, which can be achieved by placing a capacitor in the feedback loop of the voltage control circuit. Davis & Toren analyze in [316] the instabilities of the current measurement circuit in current-voltage converter configuration. For this purpose, they establish a model that considers a non-infinite open-loop gain of the operational. In the constructed model, an inductive component appears which, for certain frequencies and certain values of the shunt resistance, can enter resonance with the capacity of

the electrochemical cell, generating instabilities that cause oscillations at the output of the circuit. As a solution to this resonance problem, the use of low value shunt resistors (which is not feasible when low currents are to be measured) and the placement of a capacitor in parallel with the shunt resistor to compensate for this inductive component are proposed. In Doelling [318] and in the Gamry Instruments' guide [319] the instabilities of the potentiostat are related to the capacitive component of the electrochemical cell that introduces a phase shift that can cause the voltage control circuit to oscillate. To avoid this phase shift, solutions such as reducing the impedance of the reference electrode, reducing the bandwidth of the voltage control circuit, adding a resistor in series with the counter electrode or placing a capacitor in parallel with the shunt resistor of the current measurement circuit are proposed. In [320] two solutions are proposed to stabilize a potentiostat consisting of placing capacitors between the reference electrode and the counter electrode or in parallel with the shunt resistor. In SpectroInlets Technical Note #3 the effect of the series resistor to deal with the instability is explained [321].

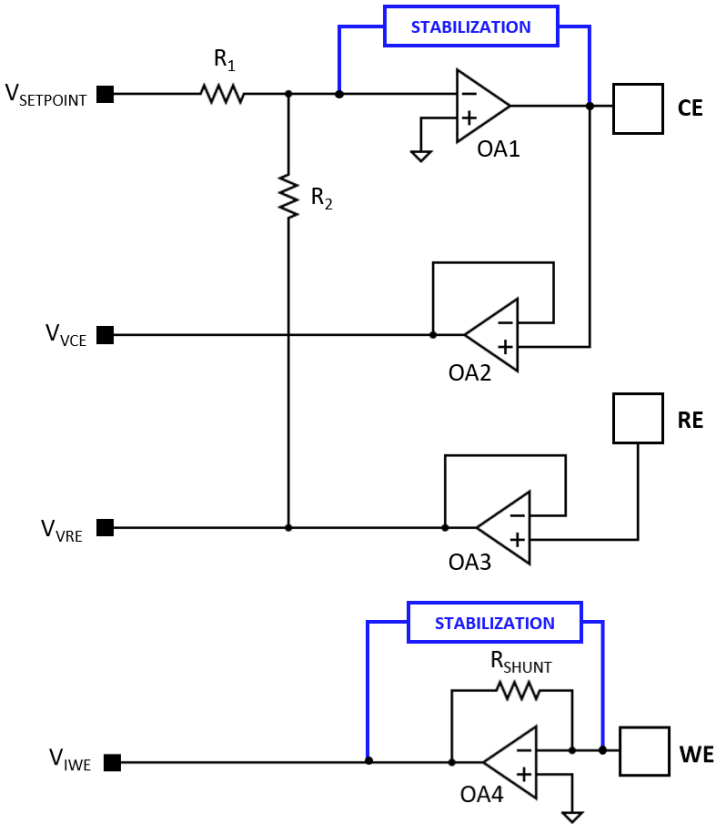

Figure 30. Potentiostat block diagram with stabilization circuits.

From the above, a series of considerations that must be taken into account when designing and working with a potentiostat can be deduced:

- The operational amplifiers used should have a behavior as close as possible to the ideal, especially with regard to open-loop gain and input impedance.

- The resistance of the reference electrode must be reduced by ensuring that the reference electrode used is in good working condition (see section *4.5. Reference electrode*).
- The capacitive component of the electrochemical cell must be minimized. Although it is not always possible to modify the internal structure of the cell, care can be taken with the wiring leading from the cell to the potentiostat.
- To stabilize the voltage control circuit, a capacitor can be placed in the feedback loop (see **Figure 30**). This capacitor will affect the generated signals, so it should be connected only when the potentiostat stability conditions require it.
- In order to stabilize the current measurement circuit, a capacitor can be placed in parallel with the shunt resistor as shown in **Figure 30**. The capacitor will modify the current measurement so the lowest value that stabilizes the system should be chosen.

1.3.4. Solution resistance compensation

From **Equation 9** it can be deduced that there is a difference between the setpoint voltage that is intended to be applied to the electrode-solution interface of the working electrode ($V_{SETPOINT}$) and that which is actually applied to it (ΔE_{WE}). This error is given by the potential of the reference electrode and by the potential drop in the solution in the section from the reference electrode to the working electrode. If working with a suitable reference electrode, the first term has a known and stable value; therefore, it does not represent a problem since it can be taken into account when setting the $V_{SETPOINT}$ value. However, the second term poses a problem since both the conductivity of the solution and the current may vary during the test and, therefore, the potential drop will not be constant or easily predictable [322].

There are methods to minimize this potential drop. For example, the conductivity of the solution can be increased by using a supporting electrolyte. Another option is to bring the working electrode very close to the reference electrode. But when it is needed to accurately control the voltage applied to the electrode-solution interface of the working electrode, the voltage drop in the solution must be compensated. The proposal made in [322] to carry out such compensation is to measure the R_{DIS} value during the test time at short time intervals in order to recalculate at each instant the $V_{SETPOINT}$ voltage value including the appropriate correction.

In none of the experiments carried out in the present thesis has it been necessary to rigorously establish a link between the experimental and theoretical values. Therefore, it has not been the objective of this thesis to fix the voltage at the electrode-solution interface of the

working electrode with total accuracy. On the other hand, in all the experiments developed, we have always worked with high conductivities of the samples. Consequently, it was not considered necessary to incorporate any compensation mechanism in the design of the measurement system.

2. Contextualization

As mentioned above, Neural Precursor Cells (NPC) have great potential for obtaining an effective protocol for the regeneration of nervous tissue. In the state of the art, pharmacological treatments and electrostimulation are two techniques that show the most promising results. By developing a technology that allows the electrically controlled release of drugs on the same substrate on which the seeding and electrostimulation of NPCs is performed, there is an opportunity to control both forms of stimulation by means of electronically controlled electrical stimuli.

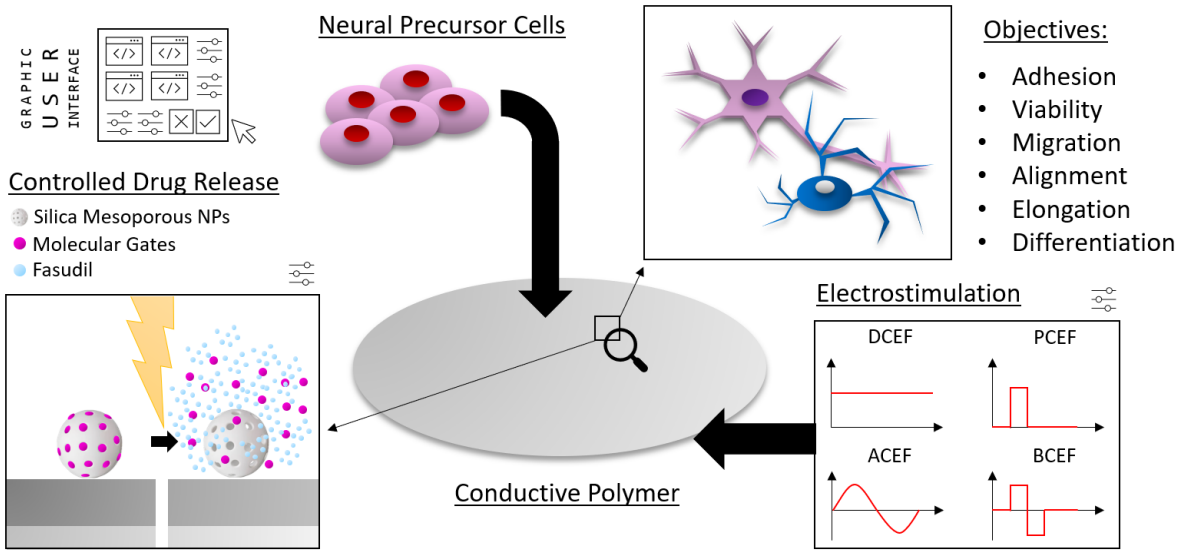

Figure 31. Conceptual representation of the *in vitro* combined therapy study platform. Neural precursor cells (NPC) are seeded onto a conductive polymer (CP) PEDOT:PSS. Voltage-gated silica mesoporous nanoparticles (vgMSN) are bonded to the CP, releasing the cargo on demand. Electrostimulation (ES) and electrical triggers for controlled drug release (CDR) are programmed from a graphic user interface (GUI). This platform will allow the thorough study of ES and CDR combinations.

In applying neurotrophic factors for SCI repair, choosing which ones to apply, how to apply them, at what time, and for how long is necessary. These parameters are under research (Hardy *et al.* [323], Yousefifard *et al.* [324]). Hence, an electronic platform controlling the CDR and the ES would be an excellent tool for this research. The equipment designed and described

below responds to the need for the configuration and application of the stimuli of both techniques, release and electrostimulation, in *in-vitro* cell culture. A conceptual representation is shown in **Figure 31**.

A total of two systems have been developed for this purpose, the next one overcoming the shortcomings of the previous one. In all of them, the last two letters stand for *Instrumentation System*:

- **FAEVIS**: Standing for Flexible and Autonomous Electrostimulation and Voltammetry IS.
- **IVESDRIS:** Standing for In-Vitro ElectroStimulation and Drug Release IS.

FAEVIS is an electronic device capable of applying electrostimulation and controlled drug release techniques in a cell culture environment in a flexible and sequenced way. It is a compact, battery-powered, portable equipment with a Bluetooth wireless connection that can run experiments inside fume hoods or cell culture incubators. The first version was developed during the author's MSc Final Project (Monreal Trigo [325]), it has been electrically characterized, and an electrochemical validation has been done by means of applying cyclic voltammetry in a ferrocyanide-ferricyanide solution.

FAEVIS has two hardware modifications regarding its first version: the incorporation of an additional electrostimulation mode, current injection, and the increase of the operating voltage range from ± 1.25 V to ± 2.5 V. But primarily, it is distinguished from the first version because of the high-end Graphic User Interface, with higher level control from the user side and additional functionalities, such as waveform design. FAEVIS software development did not end because of its identified limitations and the start of the IVESDRIS equipment development to overcome them. Given the declining priority of such development, there have also been no publications in journals or conferences of the work done in the development of FAEVIS.

IVESDRIS substitutes the wireless communication and the battery-powered approach with wired RS-485 differential pair communications and grid power. This allows IVESDRIS to achieve long-term experiments (weeks), overcoming the main limitation of FAEVIS: the battery's limited autonomy. Also, the electrical noise higher immunity of RS-485 offers higher transmission bandwidth for data communications, avoiding the recurrent problems observed with FAEVIS due to being operated inside an incubator acting as a Faraday cage. The initial specification applied for FAEVIS (the need for a wireless configuration and operation) was removed, and the specifications were modified. As natural, only by practice, we may identify what was wrong or irrelevant in our previous approach. Hence redefining our methods with this new light is the only way to achieve a higher level and get closer to our objectives.

3. Equipment requirements

As commented, FAEVIS requirements included that the device shall be wireless, suitable for the in-vitro culture environment, easily configured, and remotely controlled. A conceptual scheme of the system is shown in **Figure 32**.

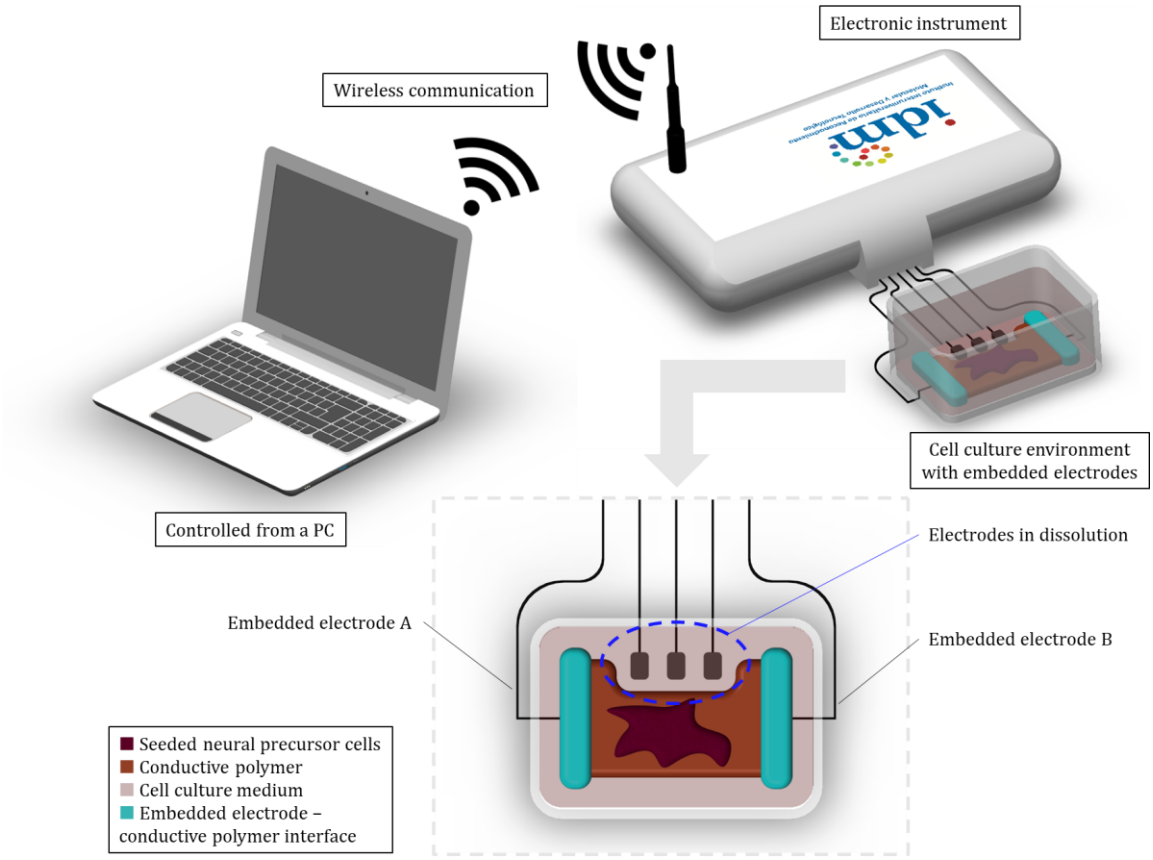

Figure 32. Conceptual representation of the equipment during an experiment. Designed with SolidWorks © 2021.

Cells are seeded on a conductive polymer, namely substrate, which is in the necessary solution for the cells' survival and development inside the *in vitro* cell culture. There are five electrodes controlled by the equipment: two of them are connected to opposite ends of the conductive polymer, and the other three of them are in solution, *i.e.*, they are not in contact with the substrate. The electrodes in solution are called working electrode (WE), reference electrode (RE), and counter electrode (CE), and the electrodes present on the substrate are called active electrode (A) and passive electrode (B), which can function as working electrode together (making the substrate behave as a single electrode), or in electrostimulation (a voltage is applied between A and B). Of the five electrodes present, two of them can generate potential with respect to different electrodes of the system: A with respect to B, and by means of a potentiostat, WE with respect to RE, or WE with respect to CE (this being the counter electrode in solution or the substrate functioning as such).

3.1. Electrochemical techniques list: equipment modes of operation

The different techniques that the electronic system must be able to apply through the electrode system are described below:

Solution potentiometry: Measurement of the resting potential of the WE with respect to the RE, obtaining the 0CP (zero-current potential), the potential for which the solution has stabilized in the presence of the electrodes or other variations. In three-electrode voltammetry, it is common to use the 0CP as the offset to apply the potentials.

Substrate potentiometry: Identical to the previous one, but using electrodes A and B, electrically connected to the substrate composed of a conductive polymer, as the working electrode during the measurement.

Two-electrode voltammetry from solution: A certain electrical potential, variable or not, is applied to the WE with respect to the CE, and the electrical current circulating through the WE is measured.

Two-electrode voltammetry from substrate: Identical to the previous one, but using electrodes A and B, electrically connected to the substrate composed of a conductive polymer, as working electrode.

Three-electrode voltammetry from solution: A certain electrical potential, variable or not, is applied to the WE with respect to the RE, and the electrical current that circulates through the WE is measured. In addition, the potential present in the CE with respect to the RE carries relevant information for some electrochemical reactions, and is also measured.

Three-electrode voltammetry from substrate: Identical to the previous one, but using electrodes A and B, electrically connected to the substrate composed of a conductive polymer, as working electrode in the experiment.

Potential gradient on the substrate: An electric potential, variable or not, is applied between A and B, measuring the current in B, revealing impedance parameters as a possible reflex of the phenomena present in the substrate and cell culture.

Current injection on the substrate: An electric current is injected between A and B, measuring the voltage in A versus B, revealing impedance parameters as a possible reflex of the phenomena present in the substrate and cell culture.

When the electronic system is not performing any experiments, all the electrodes must behave as high-impedance elements. This is because if they are not, the currents present in

them could cause a spontaneous release of the charge in the nanoparticles, affect the cell culture, damage the electrodes, or cause other inconveniences.

3.2. FAEVIS requirements

- The device must be able to apply the following techniques:
    - Potentiometry from the solution.
    - Potentiometry from the substrate.
    - Two-electrodes voltammetry from the solution.
    - Two-electrodes voltammetry from the substrate.
    - Three-electrodes voltammetry from the solution.
    - Three-electrodes voltammetry from the substrate.
    - Potential gradient between substrate ends.
    - Current injection between substrate ends.
- Capacity to apply ± 2.5 V voltages between required electrodes.
- Minimum accuracy of 20 mV in the application of voltages.
- Minimum accuracy of 2 µA in a $\pm$ 200 µA working range for current injection.
- Minimum accuracy of 10 mV in the measurement of voltages.
- Two current measurement scales:
    - Wide, with an accuracy of 20 µA in the range of ± 2.5 mA.
    - Accurate, with an accuracy of 200 nA in the range of $\pm$ 25 µA.
- High impedance when no experience is being performed.
- Suitable for operation in the cell culture environment (possibly disinfected and in extraction boxes with a thermoregulator system).
- Signal capture period less than 100 milliseconds.
- Signal application period less than 50 milliseconds.
- Application of waveforms of more than 200 points per period.
- Minimum capture capacity of 200 potentiometric points.
- Capacity of minimum capture of 1000 points of current in WE and voltage in CE, respectively.
- Operation based on battery with minimum autonomy of 24h.
- Wireless communication of configuration of experience and obtaining of obtained data.

3.3. IVESDRIS requirements

Regarding the requirements, IVESDRIS's minimum operating time was set to 30 days, vs. 24 h of FAEVIS. The minimum signal application width was reduced from 50 ms to 10 µs.

4. Relay multiplexing system

In order to have the ability to switch between all the different modes of operation, the following relay-based multiplexing system is designed, shown in **Figure 33**. In **Table 1**, every DPDT[3] position for every mode is shown.

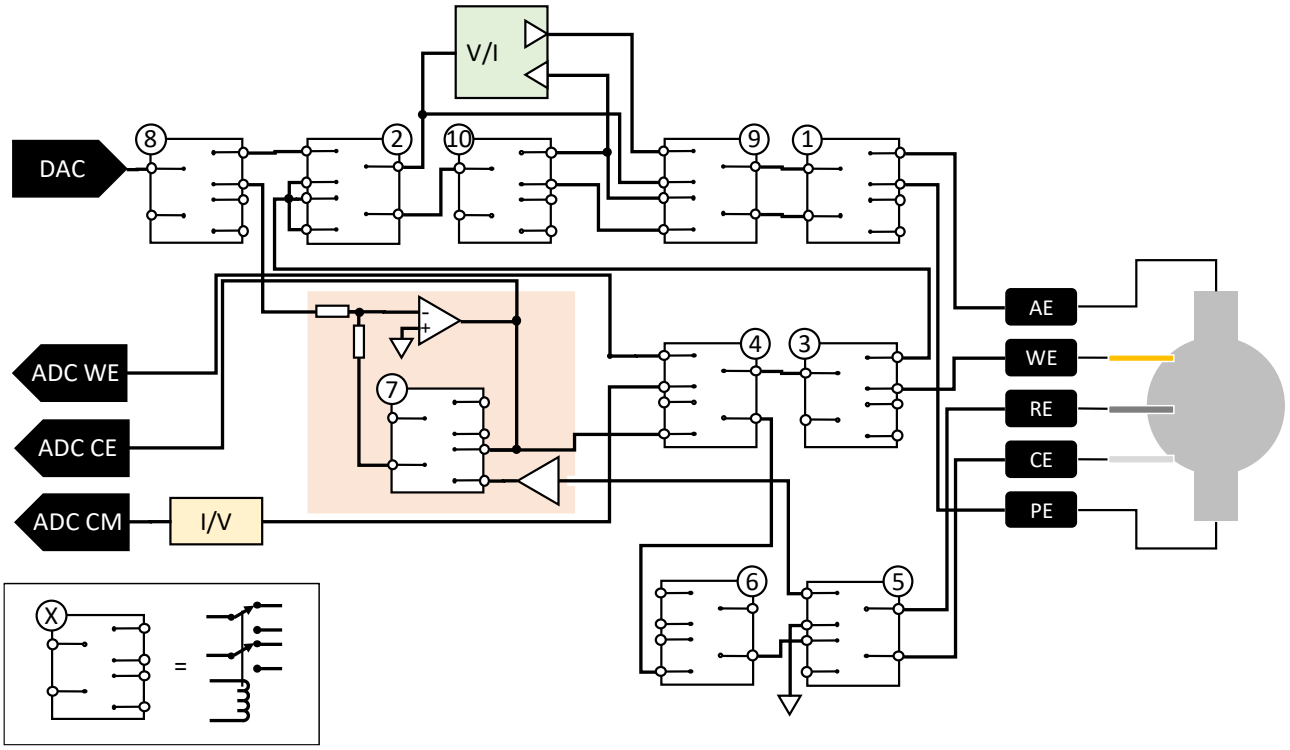

Figure 33. Relay-based multiplexing system for FAEVIS composed by a total of 10 DPDT latched relays. Three electronic subsystems are included: potentiostat (in orange), current injection (in green), and current measurement (in yellow).

Table 1. Relay array configuration for the different modes. DOWN (d, in orange), and UP (u, in green), represent the DPDT position regarding **Figure 33** as reference. White boxes represent an irrelevant DPDT position for the corresponding mode.

RELAY:	1	2	3	4	5	6	7	8	9	10
Idle	d		u	u	u	u			d	d
Solution potentiometry	d		d	u	d	d			d	d
2-e solution voltammetry	d		d	d	u	d	u	d	d	d
3-e solution voltammetry	d		d	d	u	d	d	d	d	d
Substrate potentiometry	u	d	u	u	d	d			d	d
2-e substrate voltammetry	u	d	u	d	u	d	u	d	d	d
3-e substrate voltammetry	u	d	u	d	u	d	d	d	d	d
Voltage gradient	u	u	u	d	u	u	u	u	d	d
Current Injection	u	u	u	u	u	u	u	u	u	u

[3] Double Pole Double Throw: kind of relay with a bipolar control input that sets up the position of two switches. Both will share the same position: *up* or *down*. Each switch connects a common terminal (pole) with one of two signal terminals.

5. FAEVIS: wireless ES & ECDR platform

FAEVIS general system diagram is shown in **Figure 34**: FAEVIS core is MKW41Z microcontroller, with internal ADC, DAC, and Bluetooth controller capabilities, selected to ease the migration to an *in vivo* implantable device in the future. For the *in vitro* application, the objective of this design, a cape to the evaluation board FRDM-KW41Z is designed, with the necessary electronic circuits to obtain the operating voltages from an external battery, generate the virtual ground of the system, multiplex the relay system in order to switch between techniques and analog circuits. FAEVIS is commanded and sends real-time data to a Graphic User Interface hosted in a Personal Computer through a Bluetooth link interface.

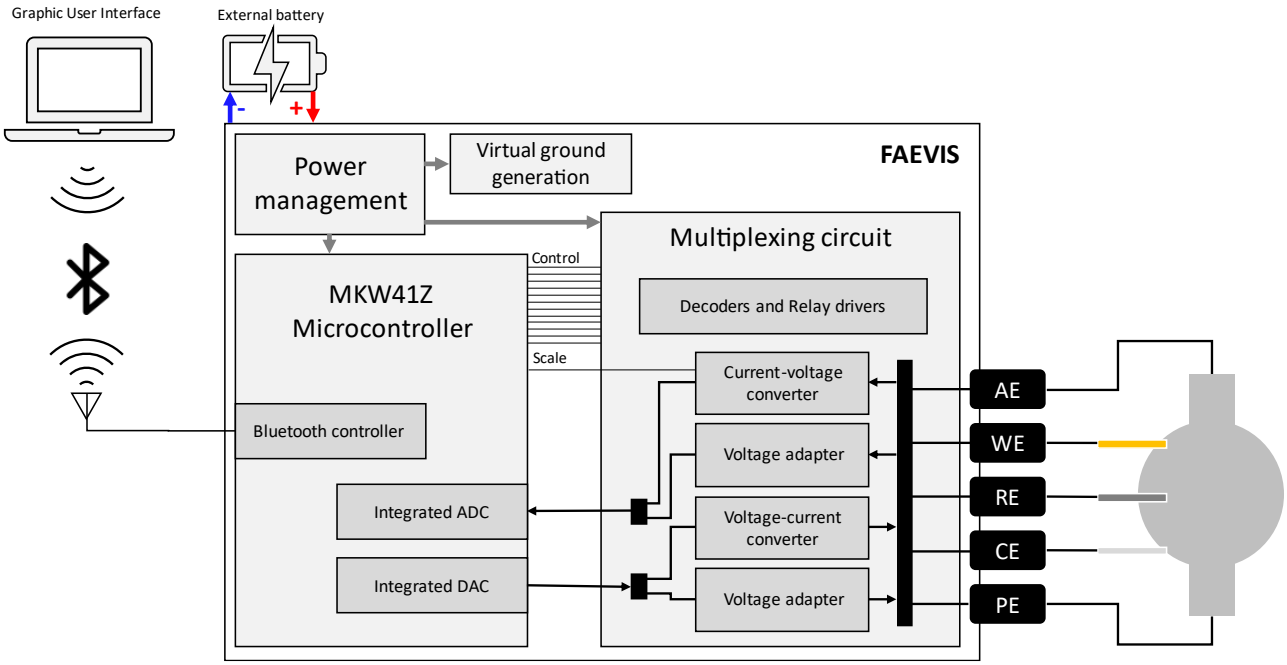

Figure 34. General diagram of the FAEVIS system.

This section describes, in the first three subsections, the hardware design, firmware implementation, and control application of FAEVIS. Finally, the last subsections show the final appearance of the device and a reproduction guide.

5.1. Hardware design

In this subsection, the system's general considerations for the hardware design will be exposed, then addressing sequentially each functional subsystem of FAEVIS, finally explaining the layout philosophy in the noise reduction subsection and finishing with the communications.

The complete schematics for FAEVIS can be found in *Annexes*:

- *Annex 01. FAEVIS Schematic 1/2.*
- *Annex 02. FAEVIS Schematic 2/2.*

5.1.1. Microcontroller unit

To ease the future migration of the *in vitro* system to an *in vivo* environment, the microcontroller chosen has an embedded Bluetooth controller, analog-to-digital (ADC) converters, and digital-to-analog (DAC) converters. Hence, with just the necessary operational amplifiers and passive components, at the expense of flexibility, an implantable device would be developed for this second step of the research line.

The NXP's MKW41Z microcontroller's main characteristics are:

- 48 MHz ARM® Cortex-M0+ core.
- Multi-Standard Radio (2.4 GHz Bluetooth Low Energy, 802.15.4, and Generic FSK).
- On-chip 512/256 KB Flash memory.
- On-chip 128/64 KB SRAM.
- 16-bit Analog-to-Digital Converter (ADC), with 500 kS/s with no averaging.
- 12-bit Digital-to-Analog Converter (DAC), with 1 µs conversion rate.
- 16-bit Low-Power Timer (LPTMR), 3 timer modules with 8 channels in total, a real-time clock (RTC), and a Programmable Interrupt Timer (PIT).
- Serial Wire Debug (SWD) interface and Micro Trace buffer.
- 9 MCU low-power modes, down to 182 nA consumption in idle mode, from 8.64 mA at maximum benchmark operation.

Hence, it is a reduced size, with an embedded wireless controller, DAC and ADC, low consumption microcontroller, and high versatility in supply input voltage. It allows internal debugging through SWD and Micro Trace. Cortex-M0+ uses between 1 to 4 cycles for each instruction, *i.e.*, between 21 and 84 ns, offering great capacities for digital processing.

The 48 pins of the microcontroller are used to satisfy the following functionalities:

- DC-DC operation: pins 8 to 15, to which the passive components to store the current or voltage in the internal power converter operation are connected. In this work, this functionality is bypassed.
- Supply lines: digital supply pins 20 and 44, radiofrequency supply pins 32, 35, and 36, and analog supply pins 26 (ground) and 28 (voltage) are used according to the

FRDM-KW41Z default in FAEVIS, and their filtering and adaptation are design for IVESDRIS (subsection *6.1.2. Supply considerations*).

- Antenna pins: 33 and 34.
- 32 MHz crystal pins: 29, 30, and 31, from which a crystal oscillator is supplied, obtaining a stable square signal of 32 MHz from which the communication frequencies (2.1 GHz for BLE) are obtained.
- 32 kHz crystal pins: 21 and 22, for the use of the Real-Time Clock.
- Digital-to-Analog Converter output: pin 23.
- Analog-to-Digital Converter inputs (multiplexed): pins 17, 18, 19, associated with the voltage measurement on the buffered counter-electrode, current-to-voltage converter output, and buffered working electrode, respectively.
- Current-to-voltage converter scale selector: pin 16, PTB0.
- Relay control for technique selection: pins 4-7, 37, 40, 42, 43, 45-48.

Since the microcontroller is powered, in its digital and analog domains, at +3.3 V, all pins, except for those related to DC-DC, have a functional operating range of 0 to +3.3 V.

The FRDM-KW41Z evaluation board[4] comes with functional circuits that may need to be disconnected, so it is possible assigning to the pins of the microcontroller another role given by the FAEVIS cape.

- The PTB1 pin is used by default for controlling the IR transceiver circuit. Hence, we will remove R55 to free the pin from the load composed by R55, R56, and the base current of transistor Q2.
- Pin PTB0 is used to control RED LED 3. It was observed that PTB0 at the LOW level presented a considerably high voltage value due to the sink current imposed by the ON LED3. This impeded the expected function of the ADG839 analog multiplexer. Hence R57 was removed.

Embedded analog-to-digital converter

The 16-bit ADC presents an effective number of bits (ENOB) between 11 and 12.5, averaging 32 samples per measurement. This means that for the data transmission, sending the

[4] FRDM-KW41Z evaluation board technical information available at official website (accessed February 2nd 2023): https://www.nxp.com/design/development-boards/freedom-development-boards/wireless-connectivy/freedom-development-kit-for-kinetis-kw41z-31z-21z-mcus:FRDM-KW41Z

12 most significant bits (MSBs) will carry the information, being the other four mostly digital noise.

The ADC low input level is the analog ground VSSA, electrically connected with the digital ground. The reference can be configured as the analog supply (VDDA. +3.3 V in our case) or an internally generated voltage reference (VREFH). In FAEVIS, we finally used the former because there is no other option in the FRDM-KW41Z evaluation board. The digital value acquired (DVA) will represent the voltage at the input of the ADC (V_{ADC}) as shown in **Equation 11**.

$$V_{ADC} = \frac{DVA}{2^{12}} \cdot (V_{DDA} - V_{SSA}) \qquad \textbf{Equation 11}$$

Embedded digital-to-analog converter

The 12-bit DAC reference options are identical to the ones shown for the ADC. The output voltage at the DAC_OUT pin will follow **Equation 12**, where V_{DAC} is the output analog voltage, and DVA is the Digital Value Applied:

$$V_{DAC} = \frac{DVA}{2^{12}} \cdot (V_{DDA} - V_{SSA}) \qquad \textbf{Equation 12}$$

5.1.2. Wireless communications

Bluetooth low-energy 4.0 (BLE) is deployed and controlled using *FreeRTOS* Real-Time Operative System (RTOS). A service for data transfer between the PC hosting the Graphic User Interface (GUI) and the microcontroller is implemented, consisting of a bidirectionally modifiable attribute with the maximum BLE extension: 20 bytes. A low-level handshake is, by default, implemented in the BLE protocol, making it a high-reliability transmission.

This functionality comes with a cost: the standard transmission period is increased up to 50 ms. In applying a voltage to the working electrode and measuring the voltage in the counter-electrode and the induced current, two packages (100 ms) would carry 15 datapoints. This means that data triage before sending is necessary for techniques with sampling frequencies higher than 150 Hz.

Regarding power considerations, data reception and transmission without internal DC-DC converter operation reaches 16.2 and 14.7 mA, respectively.

The FRDM-KW41Z connects the microcontroller pins: GANT to the digital ground and the ANT pin to a CLC filter. SMA and PCB antenna are both options for wireless communications in the evaluation board.

For the BLE communication with the PC application, a programable BLE USB dongle, with the same MKW41Z, the USB-KW41Z, is used, shown in **Figure 35**:

Figure 35. USB-KW41Z. NXP © 2016.

5.1.3. Supply subsystem

To obtain extended autonomy, 6 V 1.2 Ah sealed lead-acid battery is chosen from RS Pro. To obtain +3.3 V for the microcontroller, the FRDM-KW41Z LDO is used, and the internal DC-DC is set in bypass mode.

The system needs to be able to apply electrical stimuli in the range of ±2.5 V. Using a virtual ground (described in subsection *5.1.5. Virtual ground generation*), this objective can be achieved from a unipolar voltage supply of +5 V. Hence, +5V are obtained from the +6 V battery through a low-offset low-output-noise MCP1702 (Microchip) LDO. Analog voltage supply VA and digital voltage supply VD are obtained through different LDOs, with 1 µF input and output capacitors as recommended by the manufacturer. At the same time, analog and digital grounds are split, remaining physically connected through one point of the PCB.

5.1.4. Relay control and driving subsystem

For the technique selection and commutation, OMRON G6KU-2F-Y5DC relays were used, with 3 ms of maximum setting time and 100 mΩ contact resistance, implementing the multiplexing system described in *4. Relay multiplexing system*, driven by ULN2003LV Darlington transistor array (**Figure 36**).

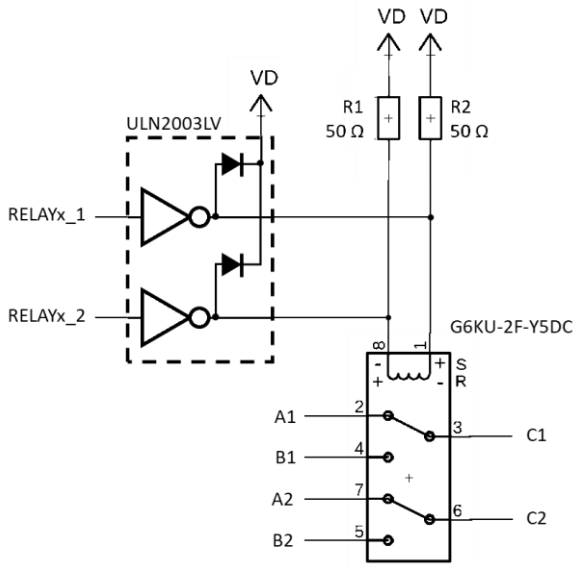

Figure 36. G6KU-2F-Y5DC relay for technique selection multiplexing, with driver circuit based on ULN2003LV Darlington transistor array and two current limiter resistors.

This circuit's functionality is controlling the relay's switch using two digital lines: `RELAYx_1` and `RELAYx_2`. The relay will switch to connect C1 and C2 to A1 and A2 respectively when `RELAYx_2` = `HIGH` and `RELAYx_1` = `LOW`; it will switch to connect C1 and C2 to B1 and B2 respectively when `RELAYx1` = `LOW`, and `RELAYx2` = `HIGH`; and will remain latched in the last position, with minimal quiescent consumption, when `RELAYx_1` = `LOW` and `RELAYx2` = `LOW`. This is represented in the following **Table 2**.

Table 2. Truth table for the relay control circuit.

	RELAYx_1	**RELAYx_2**
Latch	HIGH	HIGH
Connect Cx with Ax	LOW	HIGH
Connect Cx with Bx	HIGH	LOW
Latch (undesired)	LOW	LOW

From G6KU-2F-Y5DC's datasheet, the relays need the application of a voltage difference equivalent to 75% of the rated voltage, *i.e.*, 75% of 5V, 3.75 V, in between their commutation coil to produce the switching. Their coil resistance is 237 Ω. On the other hand, ULN2003LV can sink up to 140 mA per channel, with a low output typical voltage V_{OL} of 0.4 V. When setting a relay with this configuration, resistances R1 and R2 are needed to avoid short-circuiting VD

with V_{OL}. Furthermore, the higher their values, the smaller the power needed to switch the relays. These resistances are dimensioned according to **Equation 13** and **Equation 14**.

$$I_{min} = \frac{0.75 \cdot VD}{R_{COIL}} = 15.8\ mA \qquad \textbf{Equation 13}$$

$$R_{max} = \frac{VD - (0.75 \cdot VD + V_{OL})}{I_{min}} = 53.8\ \Omega \qquad \textbf{Equation 14}$$

The current consumption during switching is shown in **Equation 15**.

$$I_{SWITCH} = \frac{VD - V_{OL}}{R} + \frac{VD - V_{OL}}{R + R_{COIL}} = \frac{4.6\ V}{50\ \Omega} + \frac{4.6\ V}{287\ \Omega} = 108\ mA \qquad \textbf{Equation 15}$$

Given the insufficient GPIO outputs from the microcontroller, 74HCT238D decoders are employed. Their outputs are `RELAYx_1` and `RELAYx_2` signals for each ULN2003LV driver circuit.

5.1.5. Virtual ground generation

From a +5 V supply can be obtained a *virtual ground*: an intermediate voltage between the supply and the mass of the circuit, usually in the middle, with enough stability and sink and source capabilities for the application to be used as the ground in the subsequent circuits, commonly the analog front-end. Hence the virtual ground (VGND) in this application is +2.5 V in the [0, +5] V range. From this VGND, we define our virtual range as [-2.5, +2.5] V. The ±2.5 V will be employed in the analog front end, *i.e.*, in the voltage applied to the electrochemical cell.

To satisfy the first criterion to obtain a virtual ground, the voltage stability, a reference IC is used, *i.e.*, an integrated circuit that, once supplied with a voltage with non-demanding stability, offers at its output a high-precision, low-noise, temperature-compensated output. The LM4040DEM3 +2.5 V reference is employed. To satisfy the second criteria, the output of the reference is buffered with high-current operational amplifiers TLV24621DG, with an output drive capability of ±80 mA at a high slew rate and low output noise. With two in parallel, a total of ±160 mA sink-source capability virtual ground is obtained. Regarding the maximum application current of ±2.5 mA, a virtual ground with two orders of magnitude in its sink-source capabilities will not differ from a physical ground. The circuit is shown in **Figure 37**.

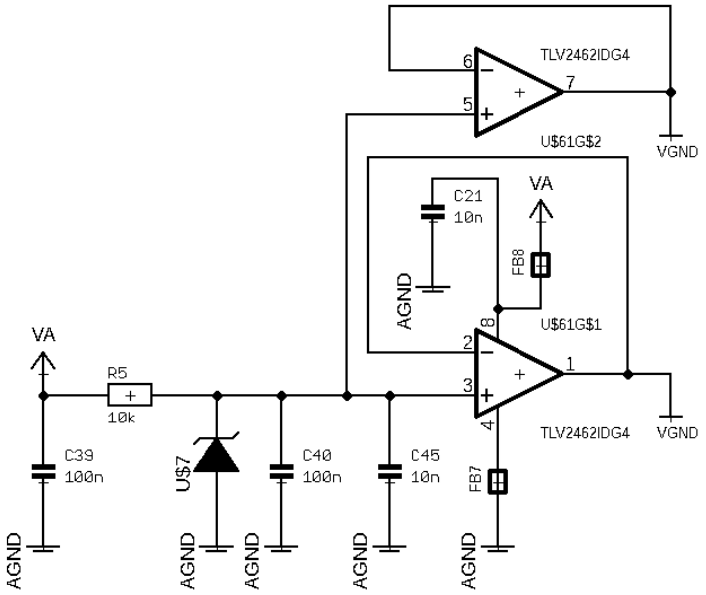

Figure 37. +2.5 V in [0, +5] V virtual ground generation with LM4040DEM3 reference and two TLV24621DG operational amplifiers as buffers.

5.1.6. Signal adaptation subsystems

Whereas the microcontroller's ADC and DAC operating range is [0, +3.3] V, electrical signal measurements and applications need to be in the range of virtually [-2.5, +2.5] V, physically [0, +5] V. Low-noise and low-polarization-current operational amplifiers OPAx376-Q1 are used for this and the following subcircuits.

Initially, the analog reference voltage for ADC and DAC was intended to be set to +3 V. Nevertheless, the internal reference generation of the MKW41Z microcontroller is set to +1.2 V, and the FAEVIS shield does not host an external +3 V reference IC. If an external reference is chosen, it shall be considered that the 8th pin of J2 (connected to the µC's VREF pin) is connected to the +3.3 V in the evaluation board, and the SH3 tin connection should be opened/desoldered. Hence, the resistors dimensioned in this section specifically translate the voltages to or from the [0, +3] V range, and keeping these values in a [0, +3.3] V range means certain resolution loss.

The ADC range adaptation circuit is shown in **Figure 38** for the working electrode voltage, and it is identical for the counter-electrode and the current measurement output voltages. **Equation 16** relates the voltage in the range [0, +5] V, $V_{[0,+5]}$, to the voltage range of the ADC, namely V_{ADC}.

$$V_{ADC} = \frac{R7}{R6 + R7} V_{[0,+5]} = 0.6 \cdot V_{[0,+5]}$$ **Equation 16**

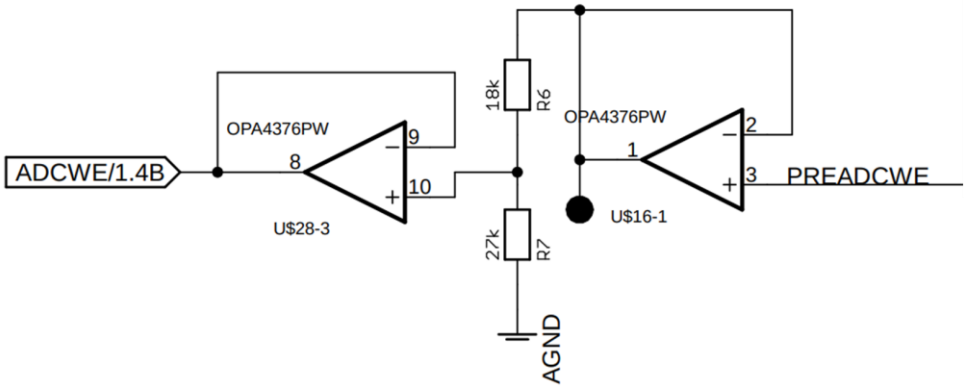

Figure 38. Signal adaptation subcircuit for the ADC. It adapts the [0, +5] V range to the ADC [0, +3] V range.

The DAC adaptation from [0, +3] V to the output range [0, +5] V is obtained through a non-inverter amplifier configuration, as shown in **Figure 39**. **Equation 17** governs the converter, where $V_{[0,+5]}$ is the amplified signal from the V_{DAC} in the range of [0, +3] V.

$$V_{[0,+5]} = \left(1 + \frac{R2}{R1}\right) \cdot V_{DAC} = \frac{5}{3} \cdot V_{DAC}$$ **Equation 17**

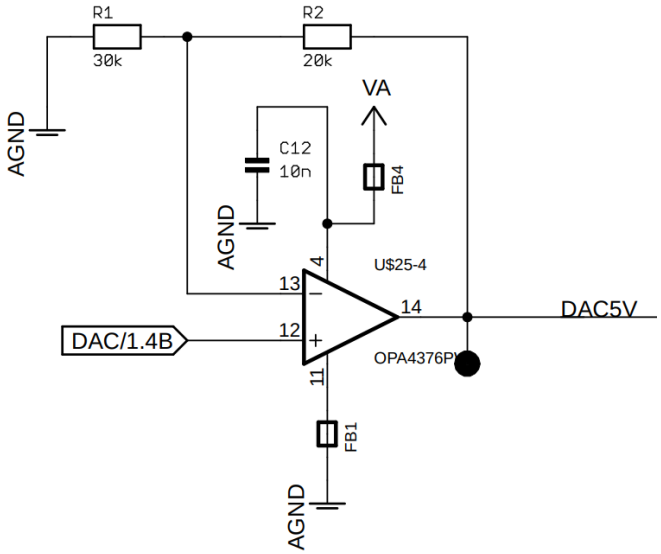

Figure 39. Signal adaptation subcircuit for the DAC. It adapts the [0, +3] V range to the operating range.

Ideal conversion with ADC and DAC working at [0, +3] V and the actual conversion with the [0, +3.3] V range, are shown in **Table 3**. Resolution decreased by 9.1%, from 1.22 mV/LSB to 1.34 mV/LSB.

Table 3. Digital and analog [-2.5, +2.5] V values correspondence for +3 V and +3.3 V µC's VREF.

Digital value [0, +3] V:	0000	2048	4095
Theoretical analog value:	-2500.00 mV	0.00 mV	+2498.78 mV
Digital value [0, +3.3] V:	0000	1862	3724

5.1.7. Potentiostat

The potentiostat circuit has been explained in *1.3. Potentiostat*. Through RELAY 7, in the circuit shown in **Figure 40**, it can be switched between 2-electrode and 3-electrode voltammetry techniques.

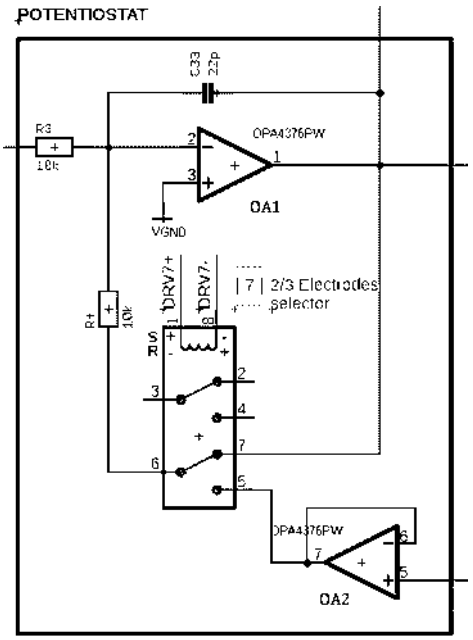

Figure 40. Potentiostat circuit of FAEVIS, with amplification gain = 1. RELAY 7 allows switching directly from 2-electrodes voltammetric techniques to 3-electrodes one, by closing the negative feedback of the superior operational amplifier, or from the buffered RE voltage.

If RELAY 8 is set to allow applying a voltammetry technique, the block input (through R3) will be connected to the adapted DAC output. OA1 output is the output of the potentiostat, namely POTOUT, and will be connected to the counter-electrode (CE) in the application of these techniques. OA2, if used, buffers the reference electrode (RE) voltage to guarantee its operation condition of zero-current flow.

5.1.8. Current measurement circuit

The current measurement circuit is composed of an operational amplifier (OA) with a resistor, R_{IV}, in its negative feedback. Its inverting input is connected to the current input terminal of the circuit, the working electrode (WE) or the passive electrostimulation electrode (EB), and the non-inverting terminal is connected to VGND. Due to the negative feedback condition, in a non-saturation situation, V-=V+, *i.e.*, V_{WE} or V_{EB} = VGND.

R_{IV} can be modified through ADG389 analog switch. Digital signal `SEL_SCA` allows the current scale selection directly from a GPIO output of the microcontroller. Being ±2.5 V, the dynamic voltage range, namely DVR, we can obtain the current measurement range depending on R_{IV}, CMR(R_{IV}), with **Equation 18**. Hence, for R_{IV} = 1 kΩ, CMR = ±2.5 mA; and for R_{IV} = 100 kΩ, CMR = ±25 µA. The circuit is shown in **Figure 41**.

$$\mathrm{CMR}(R_{IV}) = -\frac{\mathrm{DVR}}{R_{IV}} \qquad \textbf{Equation 18}$$

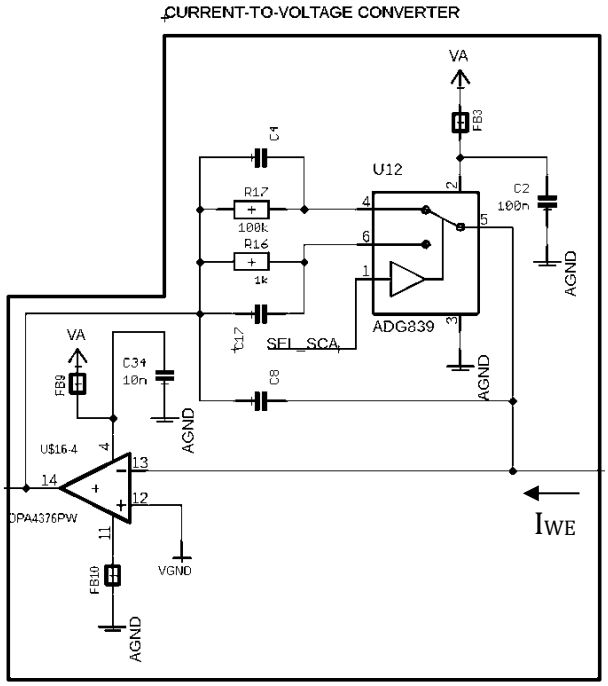

Figure 41. Current-to-voltage converter circuit of FAEVIS, with two current scales: ±2.5 mA and ±25 µA. They are eligible through an analog multiplexer, commanded by the microcontroller's GPIO output SEL_SCA.

Capacitors C4, C17, and C8 are left unplaced if they are needed to satisfy specific stability conditions. The ±2.5 V is afterwards converted to the ADC range as described in *5.1.6. Signal adaptation subsystems*.

5.1.9. Current injection circuit

The current injection circuit is designed to offer the application of ±200 µA in between electrostimulation electrodes. With this purpose, ±2.5 V adapted DAC output is the control input of the circuit, as signal CII. A resistor, namely R_{VI}, is connected between CII and the inverting input of the OA. The non-inverting input of the OA is connected to the VGND. As can be seen in **Figure 42**, the negative feedback of the OA is obtained through the electrostimulation substrate.

In this configuration, in no saturation condition of the operational amplifier, the inverting input of the OA will be at the VGND because of the virtual short-circuit condition. The voltage at CII, V_{CII} in the ±2.5 V range, will produce a current flow through R_{VI}. Because of the high-impedance condition of the OA inputs, the current shall flow through CI1 until CI2. The control function is shown in **Equation 19**.

$$I_{injected} = \frac{V_{CII}}{R_{VI}} \qquad \textbf{Equation 19}$$

The saturation condition will not be reached if the product of $I_{injected}$ and the resistance of the electrostimulation substrate is not higher than 2.5 V. This means that the full-scale can only be applied if the load resistance is inferior to 12.5 kΩ.

The current injection circuit is shown in **Figure 42**.

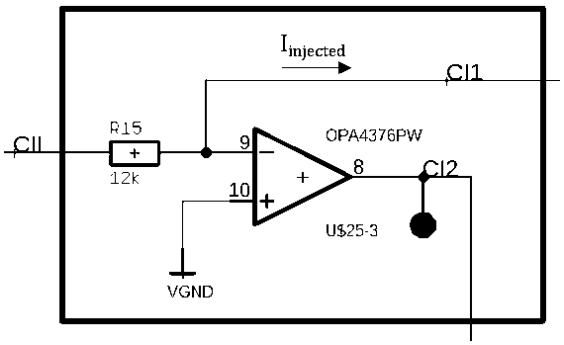

Figure 42. Current injection circuit of FAEVIS, with ±200 µA range controlled from the microcontroller's DAC.

5.1.10. PCB design

Regarding the physical design, as commented at the beginning of this section, due to the selection of an evaluation board as THE carrier of the MCU, a custom printed circuit board (PCB) is designed to be connected on the top of the evaluation board, namely *cape* or *shield*,

giving additional functionalities to the system based on the evaluation board. Taking into consideration where are disposed the BLE antenna and the analog inputs and outputs in the evaluation board, a total of four areas are delimited, as shown in **Figure 43**:

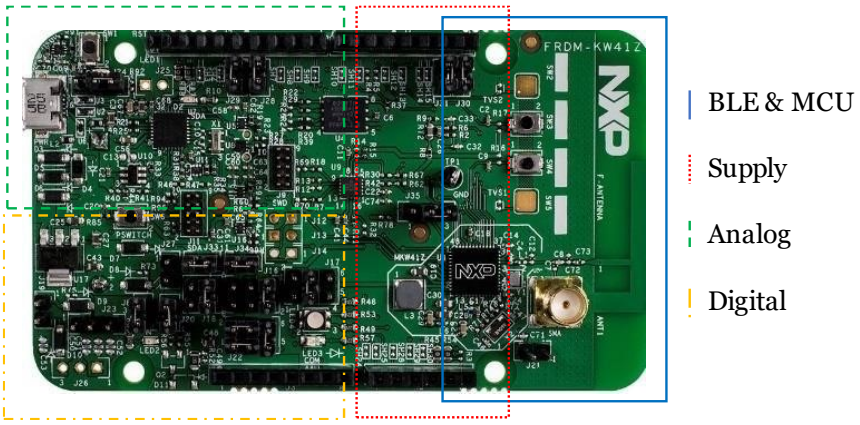

Figure 43. Regions of the FRDM-KW41Z evaluation board: digital (yellow), analog (green), supply (red), BLE & MCU (blue). FRDM-K441Z image obtained from NXP © 2016.

With these criteria, the layout of a two-layer PCB (standard fabrication technologies, Eurocircuits © 6C class) shield, both top and bottom, is designed, as shown in **Figure 44** for FAEVIS.

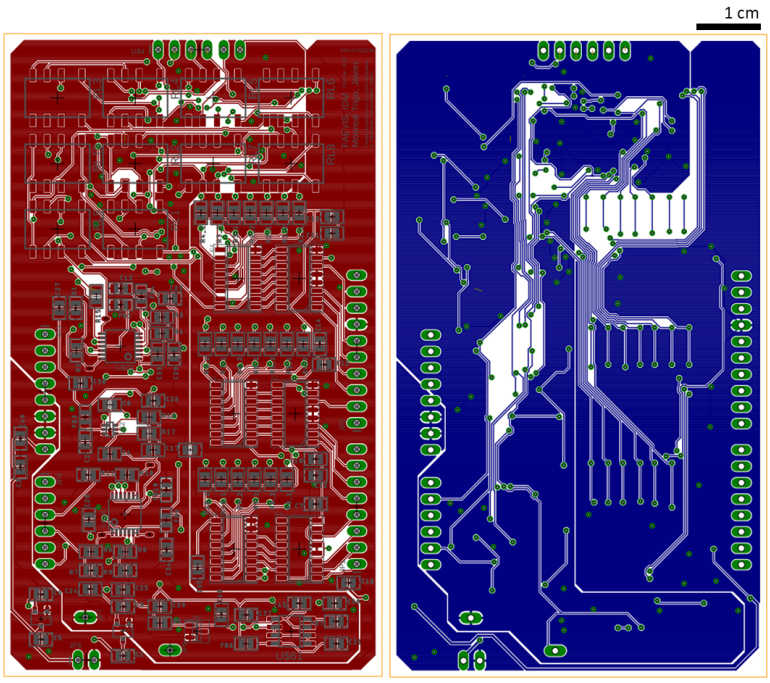

Figure 44. FAEVIS shield top layers (left) and bottom layers (right). Obtained with EAGLE © 2022 Autodesk.

Ferrite beads shown in the schematic in the supply and ground connections of the operational amplifiers had no effect or negative effect and were removed.

5.2. Firmware description

In this subsection, the microcontroller instruction code, namely firmware, is described. A general description of the firmware is addressed. Then, the main characteristics and modules are explained: memory, communications, configuration, finite state machine, experience runtime, and calibration.

For the firmware development, NXP's MCUXpresso tools[5] were used, licensed software free to use in non-commercial applications:

- **MCUXpresso IDE**: An easy-to-use integrated development environment (IDE) for creating, building, debugging, and optimizing your application.
- **MCUXpresso Config Tools**: A comprehensive suite of system configuration tools, including pins, clocks, SDK builder and more.

NXP's software development kits (SDK) for FRDM-KW41Z and USB-KW41Z offered basic example projects using the different functionalities of the microcontroller boards for a quick kick-off development. All code was implemented in C++ and compiled with GCC.

SEGGER J-link EDU Mini JTAG & SWD debug probe[6] was used for step-by-step execution, trace-back and variable monitoring on runtime.

5.2.1. General description of the microcontroller code

Once the FAEVIS microcontroller is turned on, the system configures each GPIO with its specific functionality (input or output), clock signals, and ADC and DAC internal peripherals. The system works essentially with two constant and two temporal periodic interrupts:

Constant periodic interrupts:

- ZOIS timer executes the Finite State Machine (FSM) with a periodicity of 100 ms.
- B LE communications are handled through the Hermes service application based on *FreeRTOS* as OSAL, in which a new message reception flag is checked every 1 ms.

[5] See more at: https://mcuxpresso.nxp.com/en/welcome
[6] See more at: https://www.segger.com/products/debug-probes/j-link/models/j-link-edu-mini/

Temporal periodic interrupts:

- Electrical signal application and acquisition, with a configurable period higher than 10 µs, with the highest priority.
- The relay switch is a 50 ms one-shot timer set 10 times in a row, one for each relay when a new configuration for the relay is set.
- BLE scanning timer, with 3 seconds period.

A general and simplified flow diagram for FAEVIS firmware is shown in **Figure 45**.

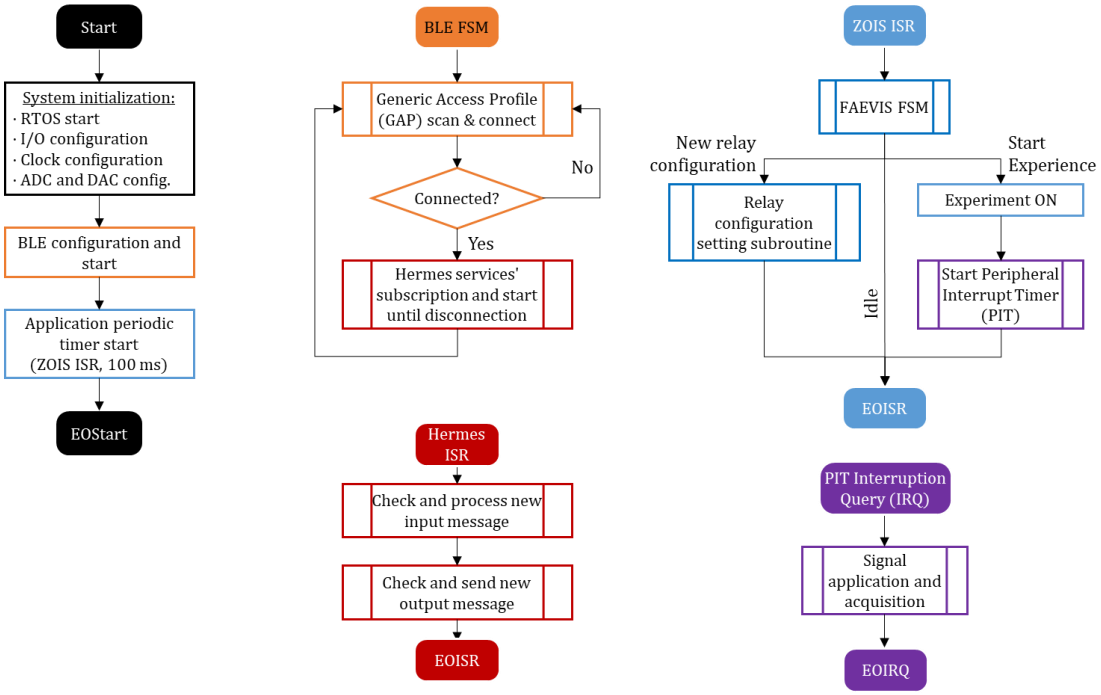

Figure 45. General and simplified flow diagram for FAEVIS firmware.

Once the USB dongle and FAEVIS are online, the USB dongle will access the FAEVIS Hermes service, a custom BLE application for bidirectional message communication with acknowledgment. The first task in the normal use of the application would be the calibration data and configuration parameters reception that will be stored. The information would vary depending on the nature of the electrical experience nature, passive (potentiometry) or active (voltammetry or electrostimulation). This will be addressed in *5.2.3. Experience setup transmission*. In the active experiences, the waveform datapoints to be applied shall also be transferred from the PC's GUI to FAEVIS.

Once all the configuration information has been transferred, upon the reception of the *start experience* command, FAEVIS will establish adequate relay configuration, connecting the internal ADC and DAC modules to the external electrodes through the necessary analog

circuits. Then, the microcontroller's Peripheral Interrupt Timer (PIT) is configured to execute an electrical signal application and measurement at the established pace. If a new value is applied and measured faster than 250 Sps, after sample 10,000 (vector size), only some cycles will be received by the GUI because it surpasses the maximum BLE throughput (see ***¡Error! No se encuentra el origen de la referencia.***).

5.2.2. Memory considerations

The DAC resolution and ADC effective resolution of 12 bits impose the use of long unsigned integer variables (uint16_t) to store such values. Four vectors are therefore declared, trying to use almost all RAM available:

- 1000 points for the electrical signal application.
- 1000 points for potentiometry acquisition.
- 10000 points for voltage measurement during voltammetry or electrostimulation.
- 10000 points for current measurement during voltammetry or electrostimulation.

Additionally, the following vectors are also declared:

- 20 elements 8-bit buffers, for input and output messages, the maximum payload for a BLE attribute.
- 9 elements 16-bit variables for DAC, WE ADC, CE ADC, large scale current measurement (CM) ADC, and precision scale CM ADC calibration.
- 15 elements 8-bit vector and 10 elements 16-bit vector, for data conversion upon reception from byte to word and before sending from word to byte.

Finally, multiple configuration structures and application variables are also declared, using 69.3% of the 96 KB SRAM available in total. FLASH memory is used in 44.0% (225 KB of 512).

5.2.3. Experience setup transmission

For further details on the Bluetooth Low Energy (BLE) operation, consult ***¡Error! No se encuentra el origen de la referencia.***. There are, mainly, three configuration commands:

- `0xC1`: potentiometry configuration.
- `0xC2`: voltammetry/electrostimulation configuration.

- `0x58`: waveform to be applied transmission.

The potentiometry configuration (CMD = `0xC1`) dataframe is shown in **Figure 46**:

- MSG[2], EXP, selects the Experience: Substratum or Solution Potentiometry.
- MSG[3,4], TOUT, establishes the **potentiometry timeout** (PT) (in ms). PT can be set off if TOUT = 0.
- MSG[5,6], TBS, establishes the Time Between Samples (in ms).
- MSG[7], ΔVM, sets the maximum voltage variation between two consecutive samples to keep the potentiometry experience.
- MSG[8], AVG, established the number of former samples to average with the new value. **potentiometry averaging** (PA) can be set off if AVG = 0 and ΔVM = 0.

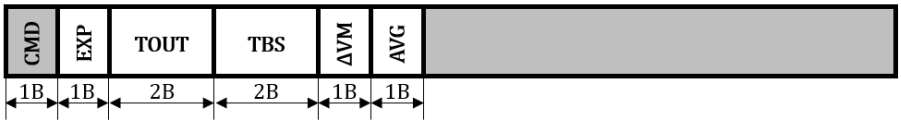

Figure 46. Potentiometry configuration dataframe. HEAD, CHKS and END are omitted.

We can distinguish four operation modes:

1. Potentiometry until manual stop (PT & PA off).
2. Potentiometry until voltage variation is below a thereshold (PA on, PT off).
3. Potentiometry during certain time (PT on, PA off).
4. Smart potentiometry measurement (PT & PA on).

An ACK message will be sent (CMD = `0xC1`). If the command is not coherent an error message with CMD = `0xEE`, MSG[2] = `0xC1` will be sent. Incoherence criteria are:

- The EXP selected differs from `0xDD` (solution) or `0x55` (substratum).
- TOUT > 0 and TBS > TOUT, what would imply just acquiring one sample.

On the other hand, the voltammetry/electrostimulation configuration (CMD = `0xC2`) dataframe is shown in **Figure 47**:

- MSG[2], EXP, selects the Experience, allows the selection between:
  - Solution 2-electrodes voltammetry (`0x21`).
  - Solution 3-electrodes voltammetry (`0x31`).
  - Substratum 2-electrodes voltammetry (`0x22`).
  - Substratum 3-electrodes voltammetry (`0x32`).

    - Electrostimulation voltage gradient (`0x66`).
    - Electrostimulation current injection (`0x11`).
- MSG[3], CS, for Current Selection, large (`0x11`) or precision (`0x22`).
- MSG[4], COMP, for Compensate OCP, *i.e.*, apply the voltage waveform using the last potentiometry value as offset. Interpreted as `FALSE` only if `0x00`, and as `TRUE` if `0x01`.
- MSG[5,6], NWC, for the establishment of the Number of Waveform Cycles, calculated with **Equation 20**.

$$\text{No. of waveform cyles} = \text{NUMB} \cdot 10^{\text{MULT}} \qquad \textbf{Equation 20}$$

- MSG[7-10], ST, for establishing the Sample Time, in microseconds.
- MSG[11,12], WNP, for establishing the waveform number of points.

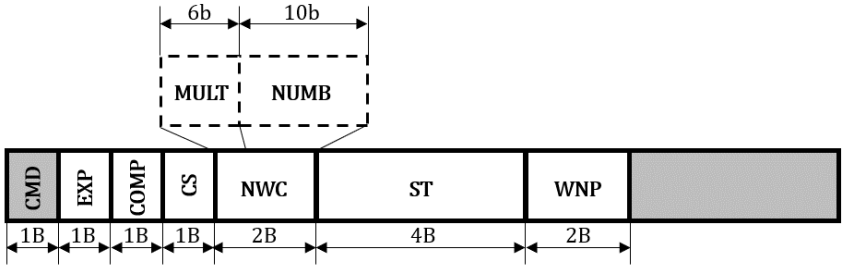

Figure 47. Voltammetry/Electrostimulation configuration dataframe. HEAD, CHKS and END are omitted.

An ACK message will be sent (CMD = `0xC2`). If incoherence is detected, and an error message with CMD = `0xEE`, MSG[2] = `0xC2` will be sent. The following criteria is used to detect incoherence:

- EXP does not match with any of the available options.
- CS does not match with any of the available options.
- COMP does not match with any of the available options.
- WNP = 0.
- NWC = 0.
- ST < 10 μs.

Finally, FAEVIS needs to have previously received a coherent `0xC2`, storing the WNP value to set up the waveform to be applied. The dataframe for each message from the GUI to FAEVIS, transmitting the waveform datapoints, is shown in **Figure 48**. Each dataframe contains an NSEQ nibble, an NP nibble, and up to 10 data points of 12 bits each.

- NSEQ (at the GUI) and internal NSEQ (iNSEQ) (at FAEVIS) are two variables that begin with a value 0 at the start of the transmission. NSEQ can be conceptualized as a temporal message indexer, used by FAEVIS to indicate the GUI which message is expected next.
    - Upon reception, NSEQ will be compared with iNSEQ, and the message will only be processed if they match.
    - After storing the received data, iNSEQ will be incremented and sent back to the GUI in the ACK message.
- NP is the number of points that carries the message.
- P1 to P10 are the 12-bit data points. Their arrangement in the byte structure makes the necessary conversion to store the values.

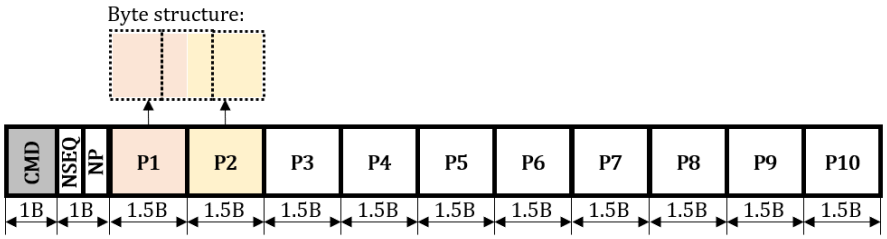

Figure 48. Waveform transmission dataframe from the GUI to FAEVIS. HEAD, CHKS, and END bytes omitted.

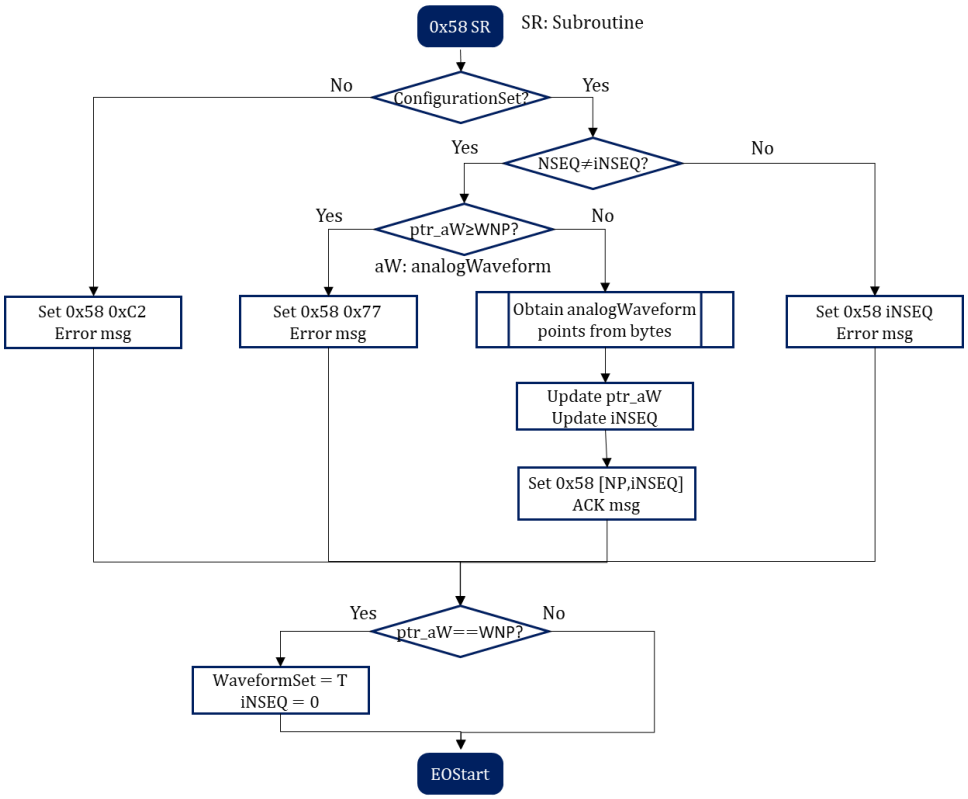

Figure 49. Flow diagram for waveform reception.

The simplified flow diagram for the waveform reception is shown in **Figure 49**. Only if the configuration (`0xC2`) has been set a valid WNP would be stored. Then, the received NSEQ is compared with the internal NSEQ (iNSEQ). If they match, the GUI sends the expected waveform values, and an ACK with the updated iNSEQ will be sent. Otherwise, a specific error message will be FAEVIS' reply.

5.2.4. FAEVIS Finite State Machine

The ZOIS Timer is executed every 100 ms, executing the `FAEVIS_FSM` function (**¡Error! No se encuentra el origen de la referencia.**), stating in the **IDLE** state.

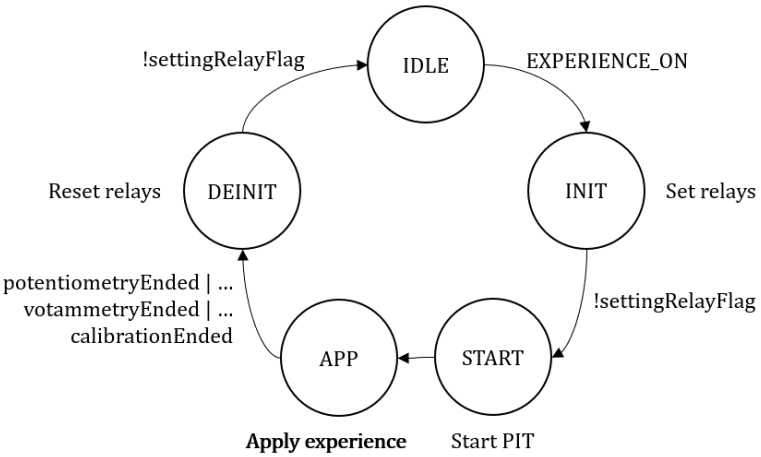

Figure 50. FAEVIS FSM diagram.

Upon the reception of a start command, it is checked if a valid configuration has been received: a potentiometry configuration, a voltammetry/electrostimulation, or a valid waveform to apply have been set. The *START Condition* is shown in **Equation 21**.

$$\begin{aligned}&\text{START Condition} = \\ &= \text{Calibration} \mid \left((\text{Voltammetry} \mid \text{Potentiometry}) \,\&\, \overline{\text{ExperienceStarted}}\right)\end{aligned} \qquad \textbf{Equation 21}$$

All pointers are initialized to zero in this case, and the `EXPERIMENT_ON` flag is set `TRUE`. This is the transition from the **IDLE** state to the **INIT** (initialization) state when the relays switch to their required positions and the involved variables are initialized. Once the `settingRelayFlag` is turned `FALSE`, the state will move to **START**, starting the PIT to perform the periodic signal application and sampling measurement, and entering the state of operation: **APP**, from the experience application.

The flags `calibrationEnded`, `voltammetryEnded` (flag common for electrostimulation), or `potentiometryEnded`, depending on the case, will indicate the end of the experience, reestablishing the variables to the default values and returning to **IDLE** state through a **DEINIT** previous state, switching the relays to the idle position.

If the FAEVIS FSM function output is `TRUE`, the variables for the **APP** process are populated, and the necessary pointers are reset. Then, the `setRelayConfiguration` function is called, which will turn `TRUE` the `settingRelayFlag` if the relay setting process is not over. It will turn it `FALSE` in its last iteration, triggering the state transition from **INIT** to **START**.

5.2.5. Signal application and sample measurement module

The PIT interrupt query (IRQ) is executed at a constant period. The first task is to clear the status flag to enable the interrupt routine to be accessed in the following period. If the experiment and calibration flags are `FALSE`, and the PIT will be stopped, disabled, and deinitialized. Different routines are executed depending on the application under execution, potentiometry, voltammetry/electrostimulation, or calibration.

a) Potentiometry

The PIT recurrent interrupt is set to 100 µs. The variable `ptr_100us` is used to keep track of the time and measure every TBS established. An overflow control of the potentiometry measurements vector is performed before acquiring the next voltage value. It is obtained with AVG sequential ADC measurements. Then, ΔVM and TOUT control is executed (if any of these features is online).

b) Voltammetry / Electrostimulation

The PIT period is set to the new value application and sample acquisition specified time. The applied DAC value will consider the last OCP if the `CompensateOCP` flag is ON. After updating the DAC output, `ptr_analogWaveform` is updated.

Two variables will be acquired and sent: CE voltage and WE current (namely CM, current measurement). They are stored in `countervoltageWaveform` and currentWaveform vectors. Each new value is stored to the element indicated by a pointer variable, with the prefix "`ptr_`" before the name of the waveform. Additionally, two additional pointers for the data transmission, which purpose will be addressed in *5.2.6. Real time data transmission*, will be

used, with the prefix “ptr_send” before the name of the waveform. If a *restart measurement* command has been received (`0x8D`), all four pointers will be reset.

Then, CE and CM values are acquired through the ADC, stored in the abovementioned variable, and their pointers are updated. Finally, it is checked if a cycle has reached an end, and the number of cycles elapsed is compared with the number of cycles configured for the experience, setting the appropriate flags `FALSE` and stopping, disabling, and deiniting the PIT if it has been reached.

c) Calibration

Three modes of calibration can be distinguished:

- Potentiometry autocalibration
- CE and CM calibration with large current scale.
- CE and CM calibration with precision current scale.

In the three modes, nine iterations are performed. A DAC value is applied in each of them, and the electric signal(s) are acquired: WE voltage in potentiometry, CE voltage and CM in the large current scale calibration, and CM in precision scale calibration. They are stored in their corresponding vectors, and the routine ends by setting the appropriate flags `FALSE` and stopping, disabling, and deiniting the PIT, sending a message to the GUI with the acquired values. In the case of large-scale calibration, a second command must be sent from the GUI (0xB2) to receive the calibration CE measurements.

5.2.6. Real time data transmission

In the potentiometry, voltammetry, or electrostimulation application, real-time data transmission is performed during the experience. For simplicity, the GUI is always the master of communications. Hence it has the entire initiative, and FAEVIS simply replies:

- GUI request `0x1D` to start sending potentiometry data.
  - `0x17` reply, with the available data, or `0x1E` if not.
- GUI can request new data with the `0x17` request.
  - `0x17` will be replied with new data, or `0x1E` if not.

In voltammetry and electrostimulation experiences, CM and CE requests from the GUI are alternating, hence:

- GUI request `0x2D` is replied with `0x27` and CE data.
- Then GUI requests `0x3D`, being replied by `0x37` and CM data.
- Next, GUI will enter in the mentioned alternation:
    - GUI request `0x27`, replied with `0x27` and CE data.
    - GUI request `0x37`, replied with `0x37` and CM data.
- Until GUI request `0xX7` is replied with `0xXE` acknowledgment, this is the last X data to be sent, and the experiment has finished.
- If GUI requested `0x27`, it would request then `0x37`, or vice versa, to receive the last datapoints, from CM (`0x3E`) or CE (`0x2E`), accordingly.

5.3. Application description

The Graphic User Interface (GUI) has been developed in this subsection. The GUI allows setting up and controlling FAEVIS. Also, it will enable visualizing the results in real time. The application is divided into modules that will be described separately.

They are implemented using MATLAB, a programming language and software environment for numerical computing, visualization, and data analysis. For the GUI implementation, the "Graphic User Interface Development Environment" (GUIDE) toolbox has been used, except for the Merge Calibration Files submodule in the Calibration module, which has been implemented using AppDesigner, MATLAB's next-generation GUI development environment.

5.3.1. Calibration module

The calibration module is a GUI window consisting of sub-modules, as shown in **Figure 51**: communications, subsystem selection (DAC or others), real-time representation, and merge calibration files button.

The *Serial Communications* submodule is a panel that will be shared across several submodules. The panel locks the COM port list drop-down once a successful connection has been made and a response has been received from FAEVIS, displaying the CONNECT button in green. Pressing it again performs a disconnection. The first steps to be taken are shown in a pop-up window (**Figure 52**) by pressing the HELP button in the upper left corner.

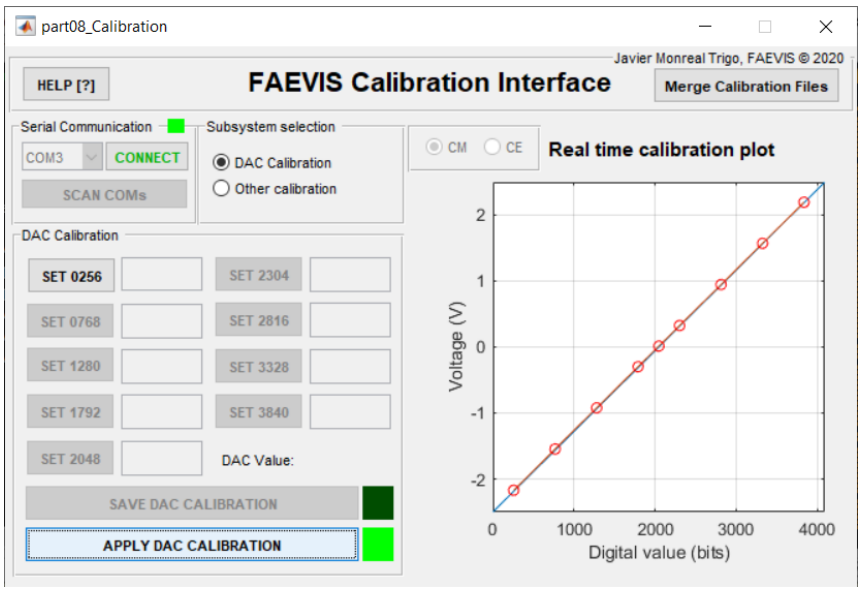

Figure 51. DAC calibration plot in FAEVIS Calibration module. Obtained with MATLAB 2018 © Mathworks.

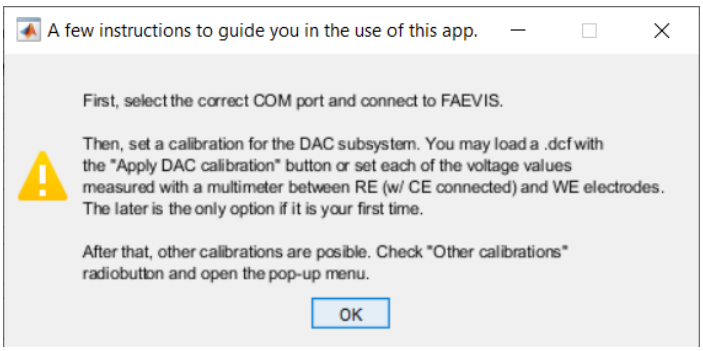

Figure 52. Pop-up message when HELP button is pressed in the FAEVIS Calibration module. Obtained with MATLAB 2018 © Mathworks.

Each calibrated subsystem generates its calibration file. These can be merged later using the Merge Calibration Files button in the upper right corner. Initially, it is necessary to calibrate the DAC since it is the active element to apply the potentials needed to calibrate the other subsystems. For this purpose, each digital value must be set as an output of the DAC by pressing the SET [VALUE] buttons and noting the recorded voltage value in the adjacent box. Alternatively, if previously performed, a previous DAC calibration can be loaded. The result is displayed in real-time in the plot on the right (**Figure 51**), obtaining a calibration curve (**Equation 22**, with the units in between straight brackets, V for volts and b indicating unitless binary), where the output voltage V_{out} is function of the binary word set BW.

$$V_{out}[b] = \text{slope}\left[\frac{b}{V}\right] \cdot BW[b] + \text{offset}\,[V] \qquad \textbf{Equation 22}$$

So the application will apply the calibration curve of the DAC as follows (**Equation 23**) before sending the binary value to apply. $BW_{to\ send}$ is the binary word sent by the GUI to FAEVIS, and $V_{objective}$ is the output voltage we desire to have at the output of the DAC:

$$BW_{to\ send}[b] = (V_{objective} - offset)[V] \cdot slope^{-1}\left[\frac{b}{V}\right] \qquad \textbf{Equation 23}$$

Once the DAC calibration is loaded or established, it is possible to access the calibration submodule of other calibrations (**Figure 53**). We can calibrate the potentiometry, CE voltage, and current (CM) measurements on large and precise scales. Current injection calibration is not implemented in the current version.

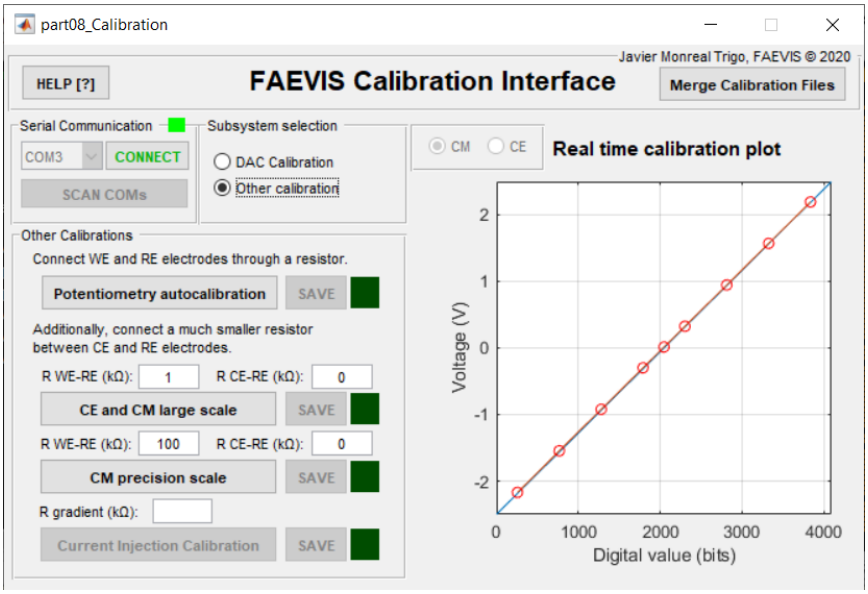

Figure 53. Potentiometry, CE ADC, large scale and precision scale CM ADC calibrations in FAEVIS Calibration module. Obtained with MATLAB 2018 © Mathworks.

The calibration files generated are:

- DAC calibration file (.dcf).
- Potentiometry calibration file (.pcf).
- Precision scale calibration file (.pscf), with current measurement data.
- Large scale calibration file (.lscf), including CE and CM calibration.

The contents of each are shown in **Figure 54**.

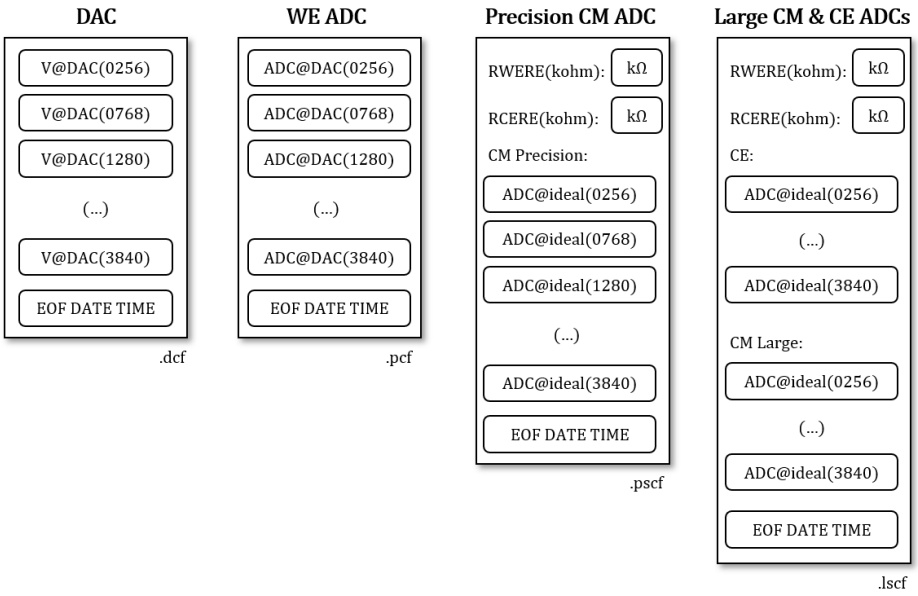

Figure 54. Calibration data files' structure.

The calibration curves regard the binary values acquired (ADCs) and applied (DAC):

- For potentiometry, the ADC measurement of WE on the ordinates and the applied DAC value on abscissae.
- For the rest, the ADC measurement is also found on the ordinates, and its ideal value is on the abscissae.

In this case, the calibration will be performed in processing the binary data sent from FAEVIS on the GUI side. The potentiometry calibration curve follows **Equation 24**.

$$\mathrm{BW_{pot}[b]} = \mathrm{slope}\left[\frac{\mathrm{b}}{\mathrm{b}}\right] \cdot \mathrm{BW_{DAC}[b]} + \mathrm{offset\ [b]} \qquad \textbf{Equation 24}$$

Moreover, applying **Equation 23** to substitute $\mathrm{BW_{DAC}}$, regarding $\mathrm{V_{objective}}$ as $\mathrm{V_{pot}}$ (**Equation 25**), and clearing $\mathrm{V_{pot}}$ (**Equation 26**):

$$\mathrm{BW_{pot}[b]} = \frac{\mathrm{slope_{pot}}\left[\frac{\mathrm{b}}{\mathrm{b}}\right]}{\mathrm{slope_{DAC}}\left[\frac{\mathrm{V}}{\mathrm{b}}\right]} \cdot (\mathrm{V_{pot}} - \mathrm{offset_{DAC}})[\mathrm{V}] + \mathrm{offset_{pot}\ [b]} \qquad \textbf{Equation 25}$$

$$\mathrm{V_{pot}[V]} = \left(\mathrm{BW_{pot}} - \mathrm{offset_{pot}}\right)[\mathrm{b}] \cdot \frac{\mathrm{slope_{DAC}}\left[\frac{\mathrm{V}}{\mathrm{b}}\right]}{\mathrm{slope_{pot}}\left[\frac{\mathrm{b}}{\mathrm{b}}\right]} + \mathrm{offset_{DAC}[V]} \qquad \textbf{Equation 26}$$

For the other calibrations, we can apply the following expression (**Equation 27**):

$$\mathrm{BW}_{\mathrm{corrected}}[\mathrm{b}] = (\mathrm{BW}_{\mathrm{measured}} - \mathrm{offset})[\mathrm{b}] \cdot \mathrm{slope}^{-1}\left[\frac{\mathrm{b}}{\mathrm{b}}\right] \qquad \textbf{Equation 27}$$

To this $\mathrm{BW}_{\mathrm{corrected}}$ can be applied the regular conversion (**Equation 28**), where FS is the full-scale value: +2.5 V for CE voltage, +2500 µA for large scale CM, and +25 µA for precision scale CM:

$$\mathrm{Value}[\mathrm{V\ or\ \mu A}] = (\mathrm{BW} - 2^{11})[\mathrm{b}] \cdot \mathrm{FS}[\mathrm{V\ or\ \mu A}] \qquad \textbf{Equation 28}$$

The Calibration files merger button takes us to the sub-module with the same name (**Figure 55**), where we can load the calibration files of each subsystem and generate a single .mcf file to be used in the experience application modules. The file has the structure shown in **Figure 56**.

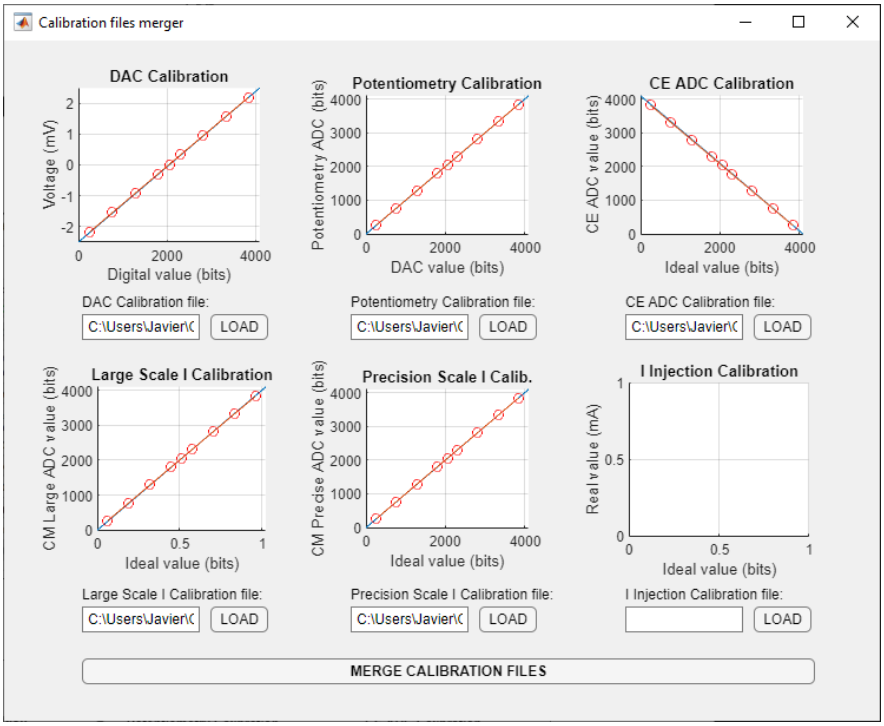

Figure 55. Merge calibration files submodule in FAEVIS Calibration module. Obtained with MATLAB 2018 © Mathworks.

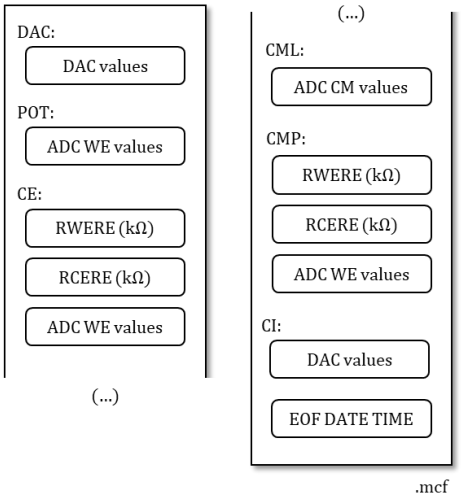

Figure 56. Merged calibration file.

5.3.2. Electrochemical experience designer module

The electrochemical experiments design module is used to configure complex signals with a number of points from 1 to 1000 and the desired number of repetitions.

A voltage value can be set for each time instant, obtaining an interpolation by one of the following three methods: piecewise, linear, or polynomial. An example of polynomial interpolation is shown in **Figure 57**.

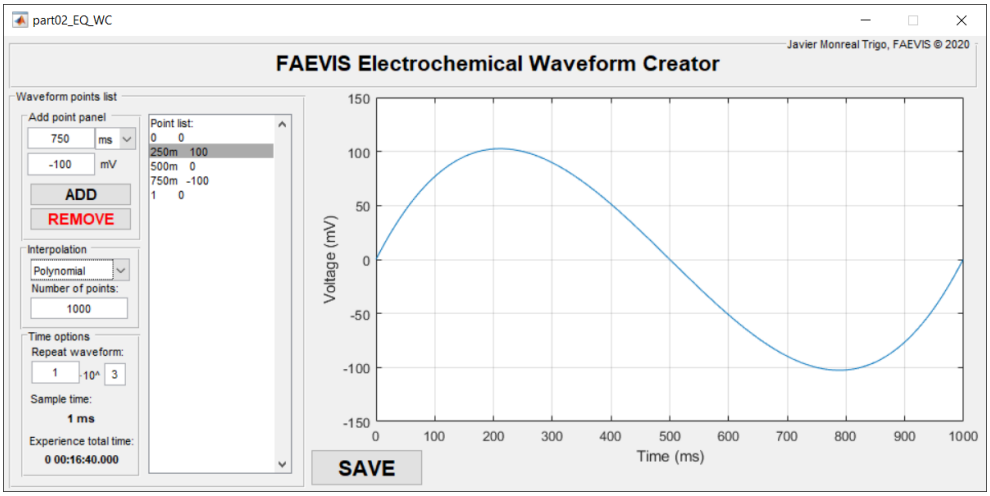

Figure 57. FAEVIS electrochemical waveform designer with polynomial interpolation. Obtained with MATLAB 2018 © Mathworks.

With the data entered, the sample time, as well as the total duration of the experience, is auto-calculated. The generated file has the structure shown in **Figure 58**.

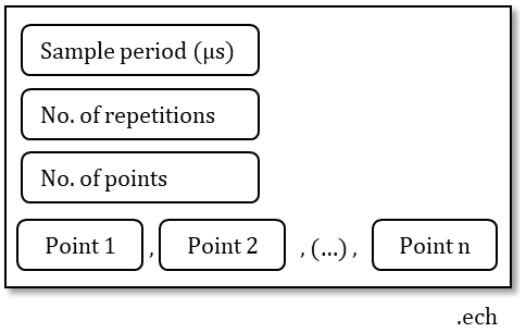

Figure 58. Electrochemical waveform file structure.

5.3.3. Electrochemical experience application module

The module for the application of electrochemical experiments has three main control buttons in the upper left corner and a side menu for control on the left side. Most of the interface is occupied with the graph to be populated in real-time. The side menu presents the same sub-module of communications as *5.3.1. Calibration module* in its upper part. Next, the user can perform a potentiometry or voltammetry experiment. The settings for each experiment are available in the side menu.

The .mcf file must be loaded using the "Load calibration" button. If there is no error, its indicator will light up.

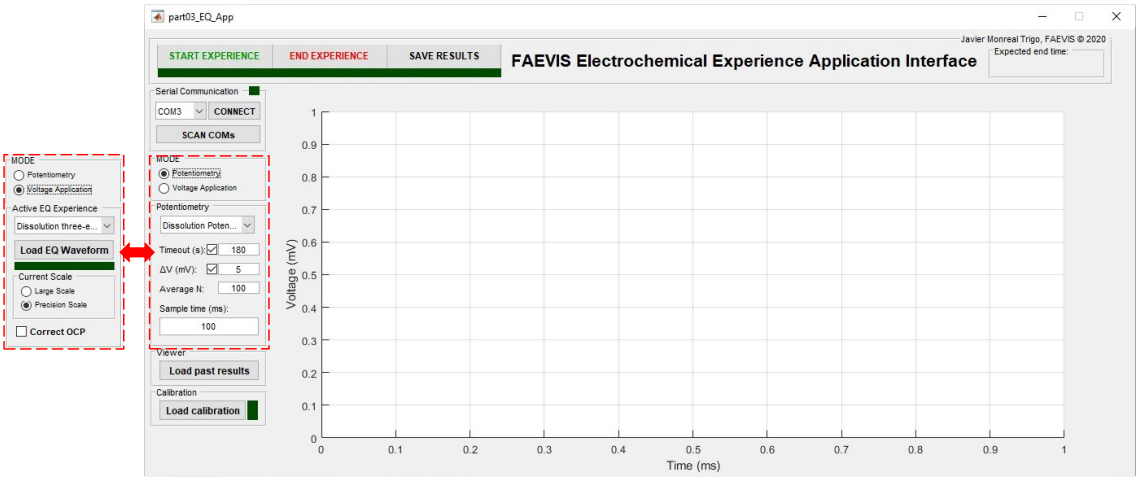

Figure 59. FAEVIS electrochemical experience application module. Obtained with MATLAB 2018 © Mathworks.

The generated files, .per for potentiometry experience results and .aer for active experience results, have the following structure (**Figure 60**):

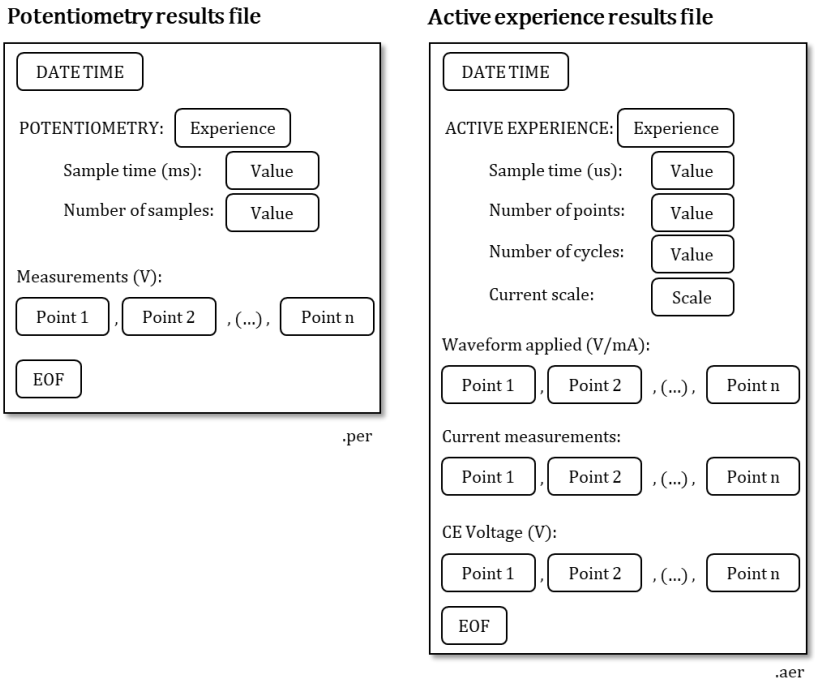

Figure 60. Potentiometry and active experience files' structure.

Finally, in the lower left corner, we find the "Load past results" button, where the results of a previous experience (*e.g.*, **Figure 61**) can be loaded and displayed in a pop-up window.

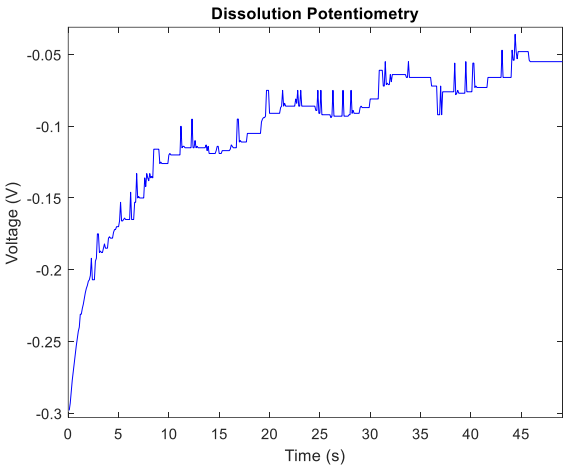

Figure 61. FAEVIS .per file ploted with *Load past results* button in FAEVIS electrochemical exp. app. module.

5.3.4. Electrostimulation experience designer module

For the configuration of an electrostimulation experiment, a .est file can be created using the Electrostimulation experience designer module (**Figure 62**) waveform generation with the structure shown in **Figure 63**.

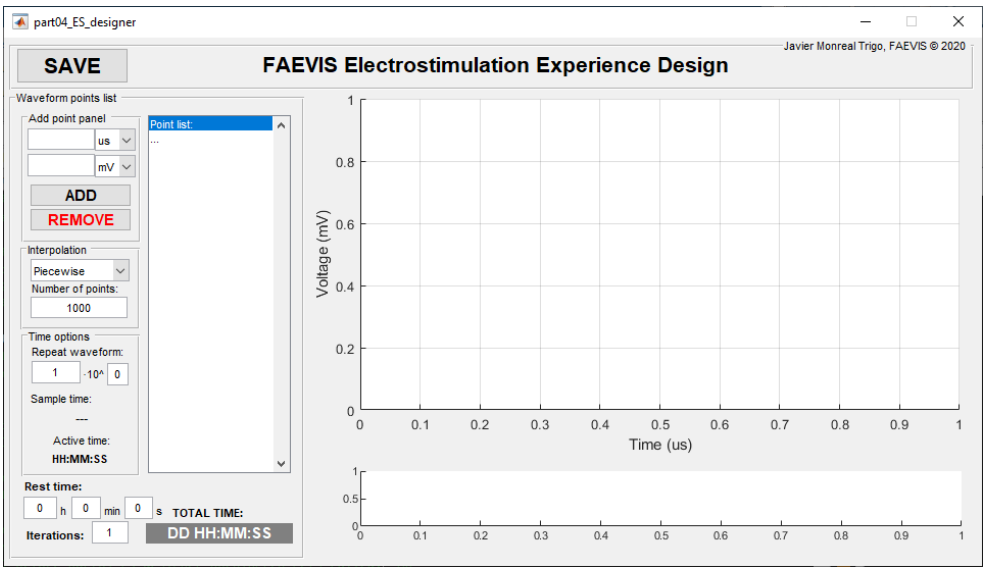

Figure 62. FAEVIS electrostimulation waveform designer. Obtained with MATLAB 2018 © Mathworks.

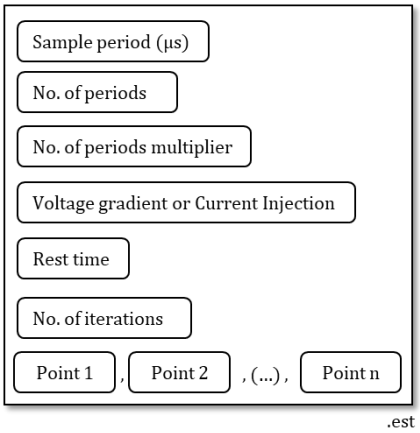

Figure 63. Electrostimulation experience configuration file structure.

As can be seen, the main difference with module *5.3.2. Electrochemical experience designer module* is that this one presents the option of setting a rest time between iterations.

5.3.5. Electrostimulation experience application module

This module is identical to the one described in subsection *5.3.3. Electrochemical experience application module*, except that the waveform to be loaded is electrostimulation (.est). The parameters stimulation type, active time, rest time, and total charging time are displayed in the left side menu after successful charging (see **Figure 64**). The data file saved is also a .aer file, already described.

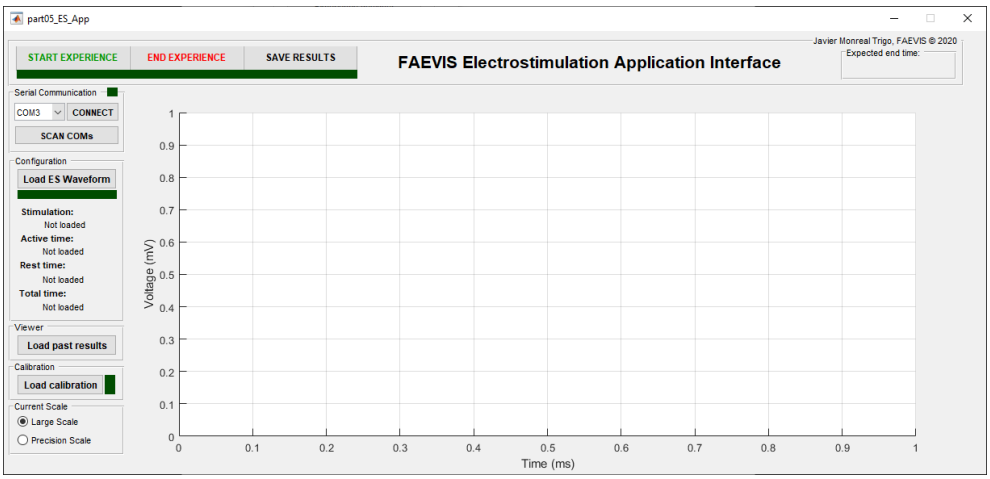

Figure 64. c

5.4. Final appearance

FAEVIS specific hardware design is an FRDM-KW41Z evaluation board shield that gives the latter technique multiplexing, signal application, and acquisition capabilities. A 3D-render of the resulting FAEVIS shield PCB is shown in the following **Figure 65**:

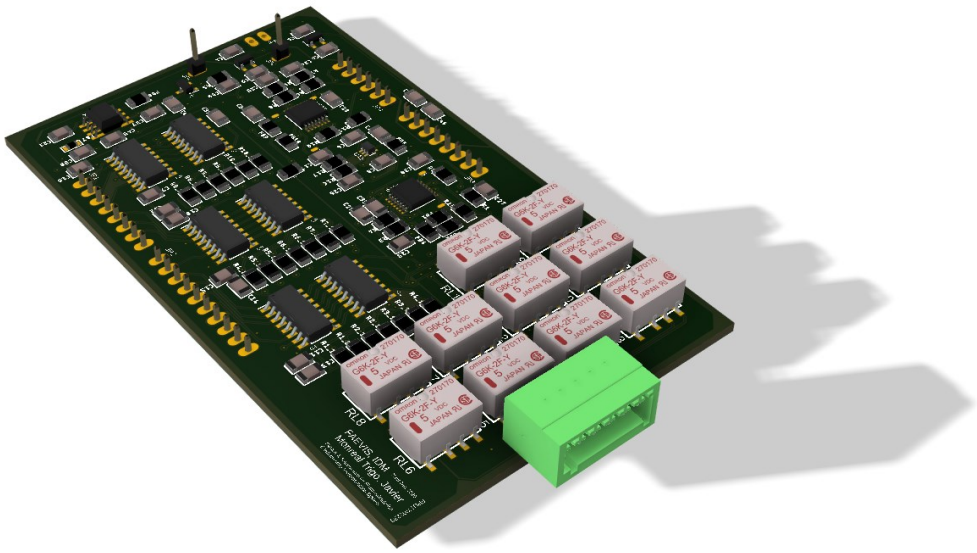

Figure 65. 3D-render of FAEVIS shield. Obtained with Fusion 360 © 2022 Autodesk.

A 12 cm x 10.5 cm x 6.8 cm 3-D printed box is designed, bearing in mind the objective of easing the assembly and housing the FRDM-KW41Z, its FAEVIS shield, and the battery. Furthermore, on the front cover are placed: a turn-on button, an on-indicator LED, a charging

2.1 mm ⌀ JACK plug, and a PHOENIX connector for connecting the electrodes. The system with the BLE USB is shown in **Figure 66**.

Figure 66. FAEVIS appearance, in PLA 3-D printed by parts box, with JACK battery charger socket, turn on button and signal PHOENIX connector.

5.5. Reproduction guide

In the following virtual space can be found:

- Gerber files and bill of materials for ordering a FAEVIS shield.
- Firmware files for flashing the FRDM-KW41Z evaluation board.
- Firmware files for flashing the USB-KW41Z.
- STL parts to 3-D print the box.
- Bill of materials for the FAEVIS system assembly.
- MATLAB software for the Graphic User Interface deployment.

Link to virtual space: https://github.com/JMonrealT/FAEVIS. Share, build, and modify FAEVIS, registered under BY-NC-SA Creative Commons 4.0 License.

6. IVESDRIS: improved ES & ECDR platform

The main limitations of FAEVIS, found after its use, are related to the limitation of autonomy for experiments longer than a few days found in the literature (up to 21 days). In addition, wireless communications from inside the incubator were often limited due to the Faraday cage-like behavior of the incubator. Therefore, an improved device, IVESDRIS, after *In Vitro Electrical Stimulation and Drug Release Instrumentation System*, has been designed to enhance the autonomy and capacity of real-time communications by wiring the power supply and communications.

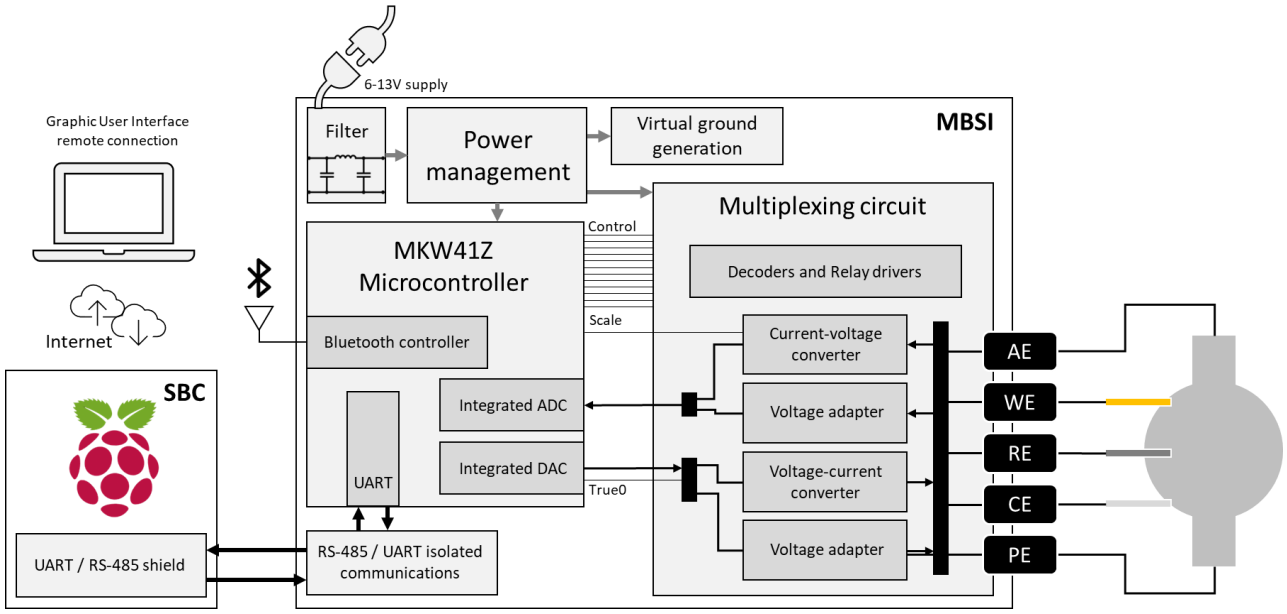

Figure 67. General diagram of the IVESDRIS system, composed by an SBC unit and a MBSI unit.

IVESDRIS comprises a single-board computer (SBC) and a microcontroller-based stimulation instrument (MBSI), as shown in **Figure 67**. The MBSI must remain inside the incubator to keep the cables to the electrodes the shortest possible and minimize coupled noise. The SBC will remain outside the incubator, connected through robust-to-interfaces differential pair RS-485 communications to the MBSI with 2 Mbps bandwidth. IVESDRIS, as FAEVIS, is intended to be able to apply eight different techniques: two potentiometry, two electrostimulation and four voltammetry techniques.

In the SBC, a Raspberry Pi 3B+, connected to the Internet through Wi-Fi, is used to host a Graphic User Interface (GUI) implemented in Python. The GUI is accessible from any PC connected to the Internet. The SBC has a custom PCB shield with Maxim Integrated's MAX3490 UART-RS485, replicating the one in the MBSI that will be further explained in *6.1.3. Serial communications*.

Regarding MBSI, it is composed of a single PCB, with the microcontroller NXP MKW41Z as its core. As commented for FAEVIS, the μC hosts a 12-bit DAC and four 12-bit ADC channels for signal generation and measurement.

This section describes, like for FAEVIS, the hardware design, the firmware implementation, and the software application development. Then, a brief description of an extension module will be addressed. Finally, the physical appearance of the platform and a reproduction guide are shown.

6.1. Hardware design

This subsection addresses the similarities and differences between FAEVIS and IVESDRIS systems. Then, each new subsystem of IVESDRIS is explained, finally describing the PCB designs.

IVESDRIS MBSI schematics can be found at *Annexes*:

- *Annex 04. IVESDRIS's MBSI Schematic 1/5*
- *Annex 05. IVESDRIS's MBSI Schematic 2/5*
- *Annex 06. IVESDRIS's MBSI Schematic 3/5*
- *Annex 07. IVESDRIS's MBSI Schematic 4/5*
- *Annex 08. IVESDRIS's MBSI Schematic 5/5*

6.1.1. Similarities and differences with FAEVIS

The main difference is the substitution of the PC for the SBC module, with a Raspberry Pi 3B+ in its core, hosting the user control connected to the Internet through a Wi-Fi link and accessible through a TCP/IP connection. The SBC has RS-485 via a custom shield.

As in FAEVIS, in the MBSI, a relay array for switching between modes is made using signal relays OMRON's G6KU-2F-Y5DC driven by Texas Instruments' ULN2003LV. They are latching relays with high impedance in the open state for the unused electrodes. Nexperia's 74HCT238D decoders handled all the necessary control lines from the MKW41Z GPIOs.

Also inherited from FAEVIS, Texas Instruments' LM4040 2.5 V reference is used to obtain a virtual ground, buffered via two-shunt low-noise low-offset high-drive Texas Instruments' TLV2462 operational amplifiers. The rest of the operational amplifier circuits are implemented

with ultralow-noise ultralow-offset Texas Instruments' OPAx376: buffers, potentiostat, inverting and non-inverting amplifiers, current-to-voltage, and voltage-to-current analog circuits. We use the Analog Device's ADG849 analog multiplexer in two subcircuits: for the current-scale in the current-to-voltage, allowing real-time current scale change, and for true zero volts setting without waiting for a relay commutation (which would take up to 50 ms).

As an improved feature, a true-zero-volts setter parallel to the DAC subcircuit output is implanted with the same analog multiplexer, which will be addressed in *6.1.5. True-zero-setter at the DAC output*.

Switching and electrical grid noise are thoroughly filtered: MBSI is supplied through an AC/DC low-noise converter. From the input 6-13V, after an embedded CLC filter, the input filtered voltage is used to obtain the different voltages. Digital 5V and analog 5V supplies are obtained through two Microchip's MCP1702 as in FAEVIS. Additionally, 3.3 V analog and digital supplies for the MKW41Z are obtained through ST's LD39015 LDOs, and the 3V reference is supplied by an Analog Device's high precision reference ADR5043.

The MKW41Z features embedded Bluetooth Low Energy communications, but they were substituted with RS485 because of the limitations of the wireless communication through the incubator.

6.1.2. Supply considerations

The power supply philosophy has been modified from FAEVIS: it will come from a switching power supply connected to the grid instead of a battery. Hence, it must be considered that a certain level of noise will be present, in the order of tens of mV, as multiples of the switching frequency, which varies between 1 kHz and 40 kHz in commercial devices. Filtering this noise is indispensable, for which a CLC filter will be placed at the power supply input before the 5V LDOs. The cutoff frequency is set to 400 Hz following **Equation 29**. The Bourns Inc. PM3308-151-RC inductor, with 1.2 Ω DCR (series parasitic resistance), and the United Chemi-Con's APSG190ELL102MH20S capacitor, with 12 mΩ (series parasitic resistance) are chosen, selecting components with a significant DCR and a despicable ESR. The schematic of the circuit and the frequency analysis by simulation are shown in **Figure 68** and **Figure 69**, respectively.

$$f_c = \frac{1}{2\pi\sqrt{LC}} \qquad \textbf{Equation 29}$$

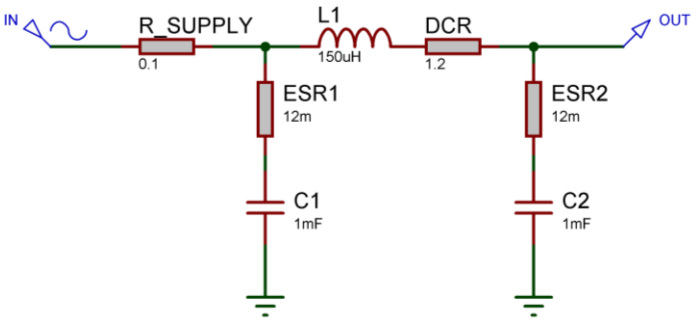

Figure 68. Circuit schematic for the CLC filter. Obtained with Proteus 8.1, Labcenter Electronics.

The ideal CLC filter response is shown in green in **Figure 69** (left). It has the characteristic resonation at f_c. The capacitor selection, with a small ESR, does not affect the filter response (in red). It can be compared with a hypothetical situation with EST = 12 Ω, in pink, displacing f_c to 10 kHz. The selection of a significant DCR in the inductor underdamps the response and shifts f_c towards 100 Hz at the expense of certain high-frequency attenuation. Finally, C_1 creates an RC filter previous to the LC response already analyzed, with the R_{supply}, the internal impedance of the power supply, increasing the attenuation for frequencies higher than 1 kHz, as shown in **Figure 69** (right). The CLC filter offers 20 dβ attenuation at 1 kHz and >70 dβ at 10 kHz.

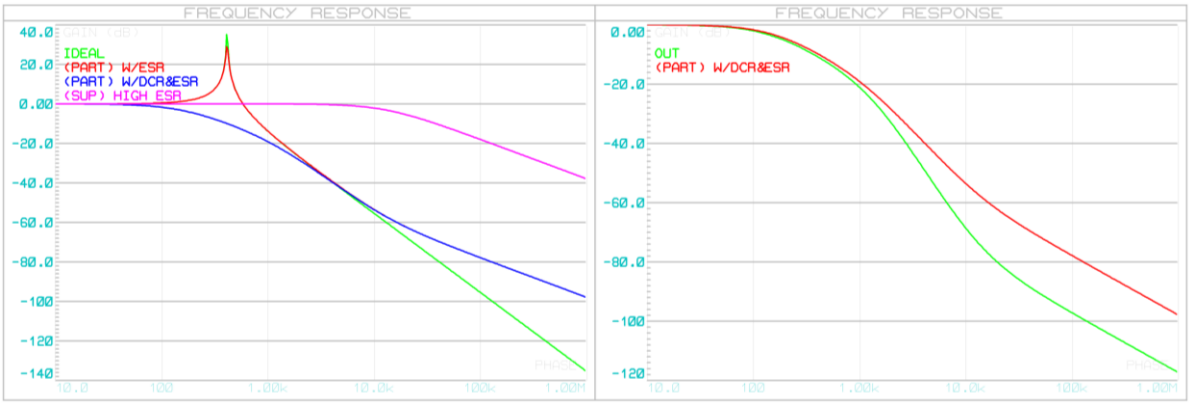

Figure 69. Frequency response of the CLC filter. Left: ideal (without parasistic resistances, green), with 12 mΩ ESR (red), with both DCR and ESR (blue), and with 12 Ω ESR (in pink). Right: complete output (green), and with both DCR and ESR (red). Obtained with Proteus 8.1 ©, Labcenter Electronics.

From the filtered supply voltage, digital and analog supply voltages are obtained through ST's LD39015 LDOs. Additional 10 µF output capacitors are placed on each of the LDOs. Virtual ground generation is inherited from FAEVIS and has been previously addressed in *5.1.5. Virtual ground generation*.

6.1.3. Serial communications

The RS-485 – UART interface is implemented with the MAX3490ECSA+ IC (**Figure 70**), offering full-duplex 10 Mbps communications between the MBSI and the SCB. Nevertheless, as we will address, the maximum MCU's UART operating frequency is 2 Mbps. Overall, the increase in the communication frequency increases the data transfer speed. Hence, the minimum application and sampling period becomes 10 µs for one variable, and 100 µs for four variables simultaneously. The reception side of each pair has a 120 Ω resistance as a termination to match the medium impedance and avoid reflections. Cables are chosen, and tracks are designed to keep 120 Ω.

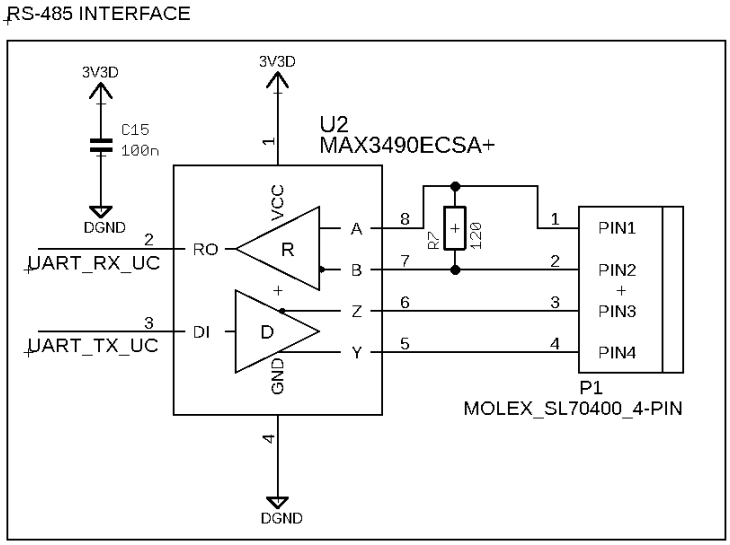

Figure 70. RS-485 – UART converter of IVESDRIS.

On the side of the SCB, the shield that interfaces the UART of the Raspberry Pi[7] with RS-485 is connected to pins 1 to 16:

- Pin 1 is used for supplying the shield.
- Pins 6, 9, and 14 are connected to the ground plane.
- Pins 8 and 10 are used as Tx and Rx pins for RPi's UART, respectively.

With the possibility of controlling from the same SBC a secondary device, two RS-485 interfaces are implemented. They are selected through pins 13 and 16 (channel 1, to MBSI), and

[7] Raspberry Pi's documentation: https://www.raspberrypi.com/documentation/computers/raspberry-pi.html. Accessed: December 24th, 2022.

11 and 15 (channel 2, to the secondary device, the Multiplexing System, described in *6.4. Extension module for stimulus multiplexing*).

6.1.4. MBSI microcontroller unit

The microcontroller unit pinout and directly related components schematic is shown in **Figure 71**. The necessary capacitors, and the antenna CLC filter, are reproduced from the FRDM-KW41Z design. A 32 MHz crystal oscillator (pins 30 & 31) and a 3V analog reference ADR5043 (pin 27), with the necessary biasing resistor and stabilization capacitors, are also implemented. A 10-pin JTAG connector (also known as Cortex) for SWD programming and debugging (pins 1 SDIO, 2 CLK, and 3 RESET) is implemented.

Additionally, the different signals are mapped to the pins of the microcontroller. It is worth mentioning:

- SET0V, mapped pin 48.
- UART_TX_UC and UART_RX_UC, mapped to pins 47 and 46, respectively.
- SEL_SCA, mapped to pin 41.
- ADC_CM12, ADC_CE, ADC_DAC, and ADC_WE, to pins 7, 17, 18, and 19, respectively.
- DAC, mapped to pin 23.

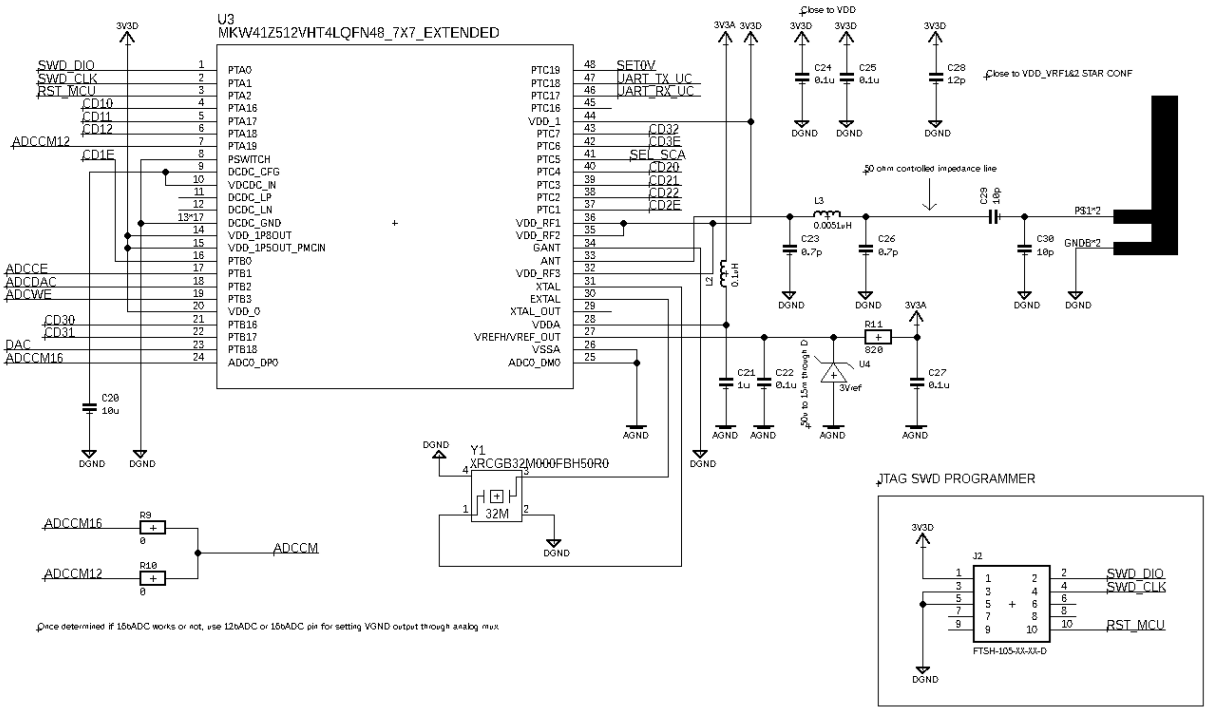

Figure 71. Microcontroller unit pinout, with antenna adaptation, analog voltage reference and JTAG programmer of IVESDRIS.

6.1.5. True-zero-setter at the DAC output

The adapted DAC output can apply 4096 values between -2.5 and +2.5 V. There will be a *step error* due to its resolution, within other phenomena, that will make the adapted DAC output significantly different from the desired output. According to *7.4. Signal application accuracy*, this error will be <10 mV. In the pulsed electrostimulation experiences, applying 10 mV during long amounts of accumulated time may mean a significantly different biological response versus the real non-application (*i.e.*, 0 mV).

The true-zero-setter allows the application of real 0 volts between the active terminal and the counter or passive terminal. This is performed through the analog multiplexing of the adapted DAC output to the active electrode. When real 0 volts are needed, SET0V signal HIGH will apply to the active terminal directly VGND, *i.e.*, 0 V (see **Figure 72**).

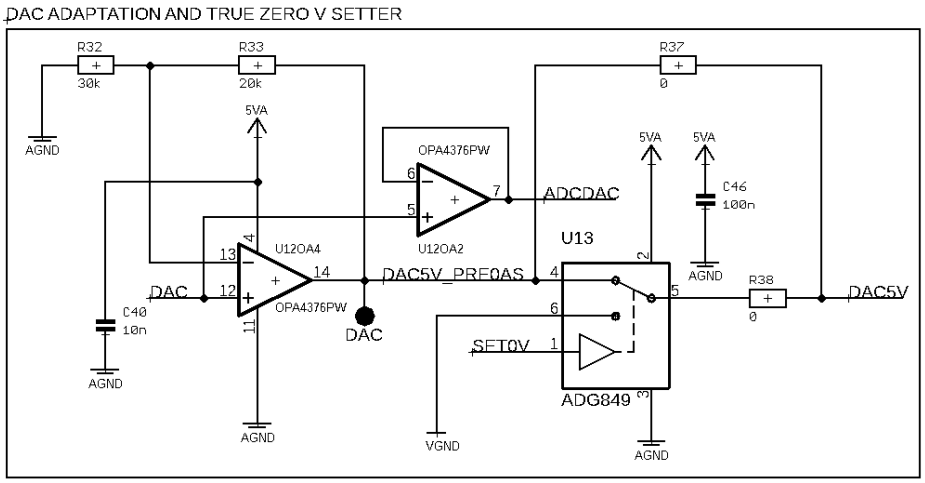

Figure 72. DAC voltage adaptation with true-zero-setter through analog multiplexer. The DAC adaptation subsystem incorporates a buffer to read out the µC's DAC output via an analog input pin to the internal ADC.

Additionally, the DAC output is buffered to the ADC DAC, an additional input of the internal ADC of the µC that is used to read the DAC output directly.

6.1.6. MBSI PCB design

To reduce noise induced on analog signals, the PCB is divided into two physically isolated ground planes electrically connected by a single point. The power supply is branched to feed the circuits located on each of the ground planes. Due to their noisy nature, the digital communication interfaces must be located at the far end of the connectors. There will necessarily be some connection between the two planes to control the relays, which carry

analog signals, but digital signals govern their switching. Even so, these will remain at rest during the application of an experiment so that they will not impact the noise of the signals of interest. The integrated ADC and DAC of the microcontroller will be located between the two planes. A diagram showing the physical layout of the main systems is shown in **Figure 73**.

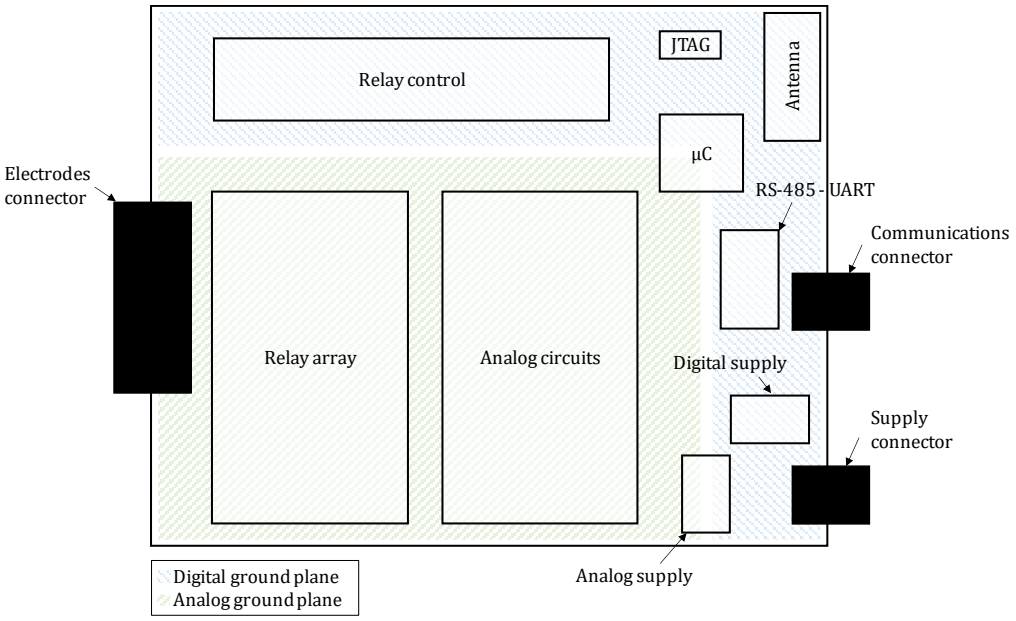

Figure 73. General layout diagram for IVESDRIS MBSI.

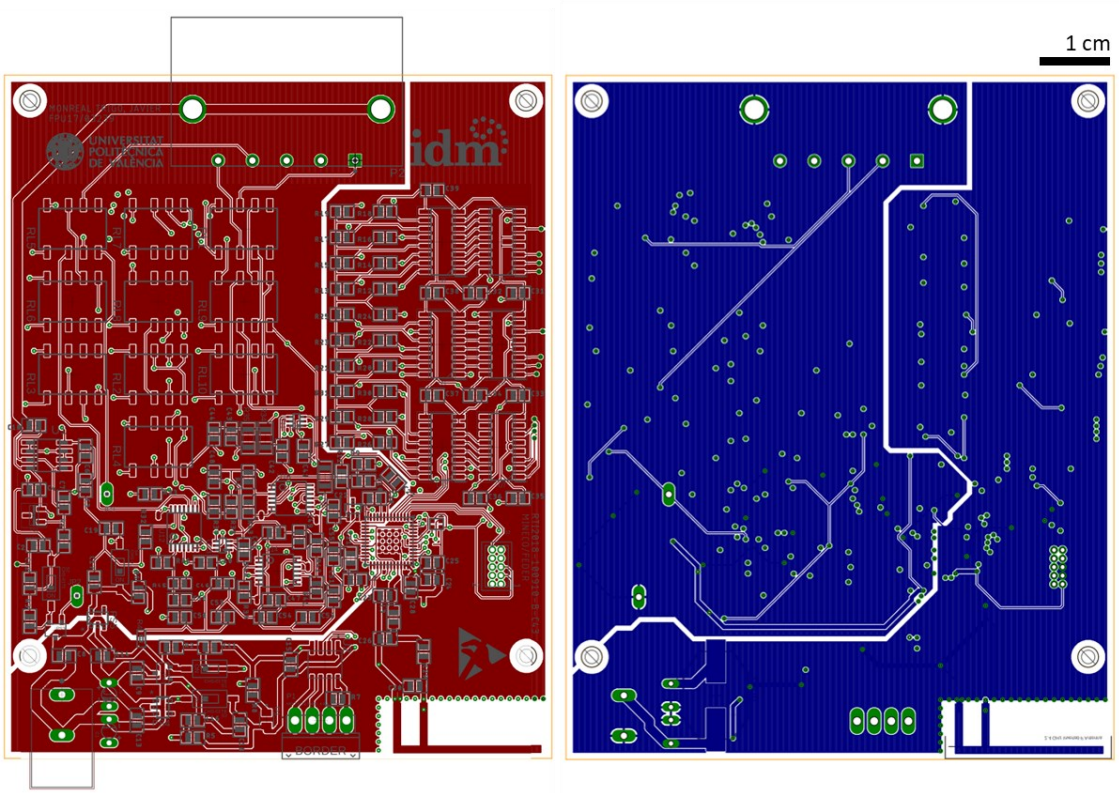

Figure 74. IVESDRIS MBSI top layer (left) and bottom layer (right). Obtained with EAGLE © 2022 Autodesk.

Internal layers are set as ground planes, and external layers as voltage planes, obtaining an additional in-built capacitance for decoupling purposes.

With these criteria, the layout of a four-layer PCB (standard fabrication technologies, Eurocircuits © 6C class). IVESDRIS MBSI top and bottom layers are shown in **Figure 74**.

6.1.7. SBC PCB design

A simple layout with the connection to the RPi pins at one side, and the RS-485 connectors on the other, placing the transceivers to keep the routing tracks as short as possible, is shown in **Figure 75**. Termination resistors and decoupling capacitors are also placed close to their corresponding terminals. The two-layers PCB is fabricated using standard fabrication technologies, Eurocircuits © 6C class.

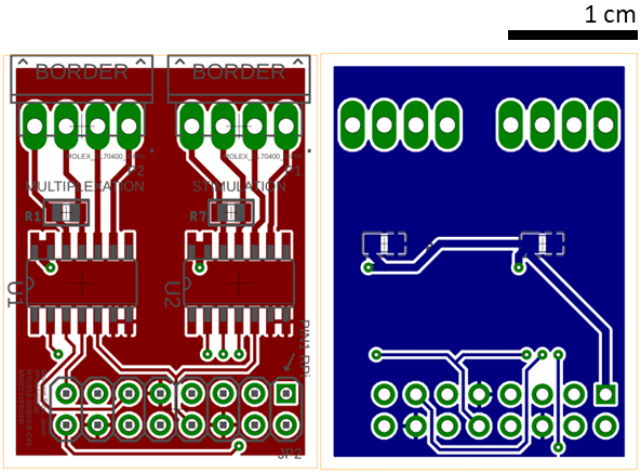

Figure 75. IVESDRIS SCB shield top layer (left) and bottom layer (right). Obtained with EAGLE © 2022 Autodesk.

6.2. Firmware description

The same development tools as FAEVIS have been used for firmware implementation. Although the PCB design has the capacity for BLE communication, this has not been implemented, and only RS-485 differential pair communications have been employed. In this way, the RTOS used in FAEVIS is not required, and all the code has been implemented in bare metal.

The IVESDRIS MBSI control philosophy has been simplified compared to its predecessor: the MBSI receives commands that generally require direct and simple action. Instead of

receiving a configuration command with all the necessary information to apply the desired technique, it will require several commands, one for each aspect, to be configured or modified. This provides superior flexibility on the SBC (and user) side.

6.2.1. General description of the MBSI code

Once the IVESDRIS' MBSI microcontroller is turned on, the system configures each GPIO with its specific functionality (input or output), clock signals, and ADC and DAC internal peripherals, as in FAEVIS. Additionally, it will do the same for the UART, DMA, and two timers (LPTMR and PIT).

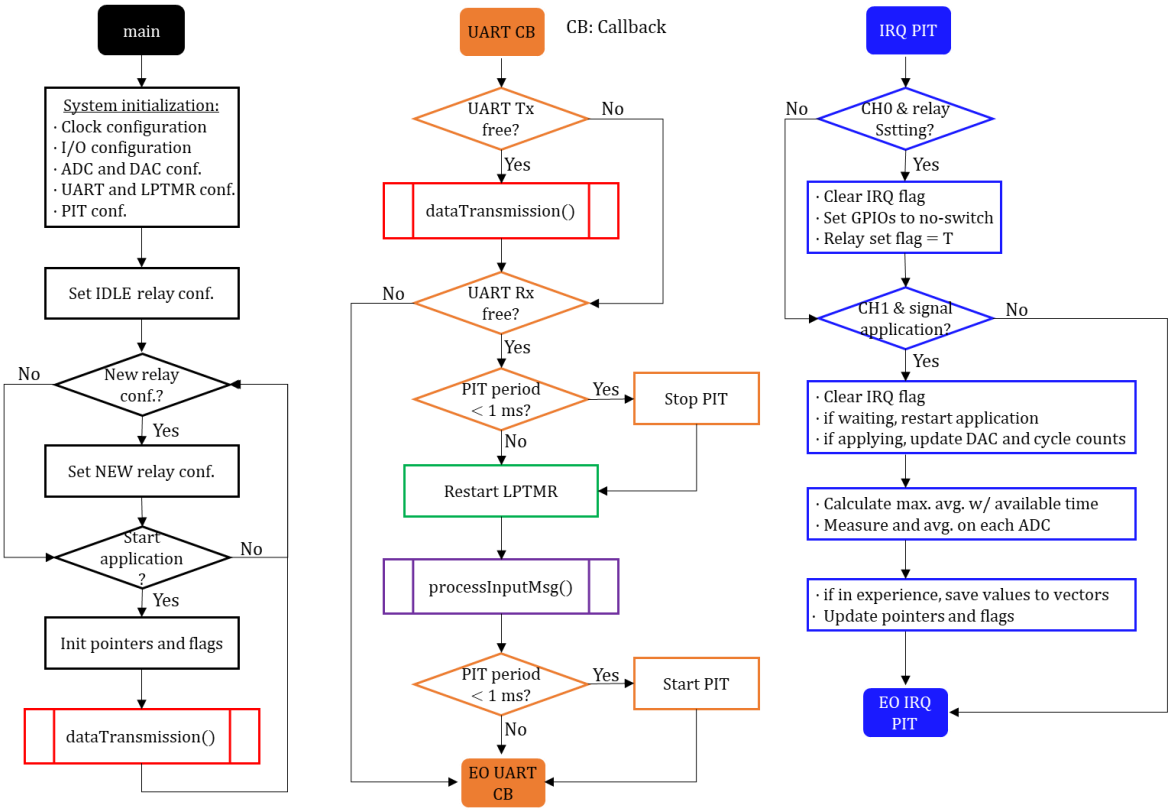

Figure 76. IVESDRIS' MBSI general flowchart.

The DMA (Direct Memory Access) is an internal module in the microcontroller that allows the direct memory to write from a peripheral in the assigned positions without the processor's involvement, freeing it for other tasks. In our case, it is used for the UART reception and transmission handling and will raise a flag to process the input message when all the expected bytes have been received. The LPTMR (Low-Power Timer) is another internal module that will evaluate periodically if partial writes have been performed in the UART reception space, *i.e.*, a timeout.

The PIT is used for high-frequency recurrent tasks, such as signal application, acquisition, and transmission during an experience application. Two of its channels are configured: channel 0 for relay setting and 50 ms period, and channel 1 for signal application-acquisition purposes, with a period specified by the SBC. A general flowchart of the microcontroller code is shown in **Figure 76**.

In the UART callback, the PIT period will be checked. If it is under 1 ms, the PIT interrupt is stopped before processing the input message and restarted afterward. It is because processing large messages (up to 1000 elements) may take more than this time, and the PIT interrupt query has the maximum priority to keep the desired application and acquisition priority under normal conditions. The reception of a large message during an experience would only occur due to unadvisable commands from the user side during the experience. This stop-restart avoids collisions and data loss.

6.2.2. Memory considerations

The DAC resolution and ADC effective resolution of 12 bits impose the use of long unsigned integer variables (`uint16_t`) to store such values:

- Four vectors to store until sending the ADC values are declared, which will be used as ring buffers, with a parametric size established in 256 elements.
- Five parametric vectors to store custom waveforms to be applied are also declared, namely *waveform slots*, established with 1000 elements each to store up to 1000 points to be applied repeatedly.

UART reception and transmission buffers are declared, with 4096 bytes size each.

Finally, multiple configuration structures and application variables are also declared, using 23.8% of the 128 KB SRAM available in total. FLASH memory is used in 5.9% (512 KB). This application's memory and FLASH requirements are further reduced compared with FAEVIS, allowing for future expansions if they are of interest.

6.2.3. RS-485 serial communications

The RS-485 communications are transparent on both sides of the communication thanks to the RS-485 – UART full-duplex converter at the SBC and the MBSI sides. The communication is established at 2 Mbps, the maximum speed at which the µC's UART can operate.

As already described, the UART is configured to operate through DMA, with two 4096-element buffers, one for reception and the other for transmission. The UART Callback is attended by the processor when a reception or writing event occurs, *i.e.*, a full message has been received or sent. A double-check at 50 ms timeout is implemented through the LPTMR module: if there are bytes at the input buffer twice and a reception event is not triggered, the buffer will be cleaned, and the UART DMA reception size will be set to default (4 bytes) and restarted.

6.2.4. Command list

In this subsection, the `processInputMsg()` function is addressed.

All messages start with a header byte, indicating the kind of message that has been sent, and the last byte of the message is a checksum byte for integrity control.

Upon reception, the checksum is calculated as the modulo 2^8 of the summatory of all the other bytes, which shall coincide with the received checksum byte.

Otherwise, an error reply, with the error header `OxAE` will be sent from the MBSI.

Four headers can be distinguished for the commands sent from the SBC to the MBSI:

- Regular header, `0xAC`.
- End of experience header, `0xEE`.
- Extension header, `0xA5`.
- Extended header, `0xA6`.

Regular header commands

All regular header commands are four-bytes messages, with the first and last bytes dedicated to the header and checksum. The two payload bytes, *i.e.*, 16 bits, are dedicated to the following:

- The three most significant bits to the command identification.
- The other thirteen bits of the data are related to the command.

Below each command is detailed:

- `0b000`: **configure relays**, with the 10 least significant bits to (LSBs) establish the new state for each relay.
- `0b001`: **set the current scale**, with the LSB indicating whether to use the precision scale (0) or the large scale (1).
- `0b010`: **set DAC output**, with the 12 LSBs carrying the new value.
- `0b011`: **request ADC value**, with the 2 LSBs selecting which ADC input.
- `0b100`: **stop experience**.
- `0b101`: **apply X waveform N times**, where X is carried by bits [12-10] and N by bits [9-0]. A higher N than 1023 can be established with extended commands that will be addressed afterward. In this case, N in this command shall be set to 0.
- `0b110`: **are you alive?**, expects an echo response.
- `0b111`: **set true 0V**, with the LSB indicating whether to set 0V at the output (1) or not (0) as described in **6.1.5. True-zero-setter at the DAC output**.

ADC inputs are numbered as follows:

- `0b00` (0): current measurement (CM).
- `0b01` (1): counter-electrode voltage (CE).
- `0b10` (2): working electrode voltage (WE).
- `0b11` (3): DAC output voltage.

How the acquisition is performed is addressed in the next subsection *6.2.5. Waveform application, signal measurement and transmission*.

For all regular header commands, the message to be sent from the MBSI to SCB is set to the DMA in the reception routine.

End of experience header

It is an acknowledgment from the SCB to the MBSI end-of-experience notification that will also be addressed in the following subsection.

Extension header

Regular messages from the SCB are compounded by four bytes, except for the extended header ones, with variable sizes. All extended messages shall be preceded by a four-bytes message indicating the length of the next extended message. The procedure is the following:

1. The SCB sends an extension header (`0xA5`) message that will indicate the size of the next incoming message.
2. The MBSI will configure the UART reception DMA if there is no error.
3. Then, the MBSI would reply with an acknowledgment, enabling the SCB extended message sending.

This is shown in the diagram of **Figure 77**.

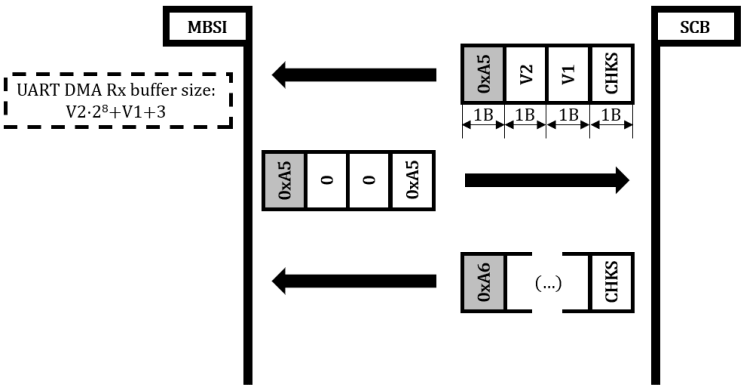

Figure 77. Protocol for enabling the reception of an extended message (larger than 4 B) in IVESDRIS.

The MBSI will reply with an acknowledgment or error message to the `0xA6` message.

Extended header

It is reserved for variable-size messages, which size is established with the preceding `0xA5` message. The structure of an incoming `0xA6` message is shown in **Figure 78**:

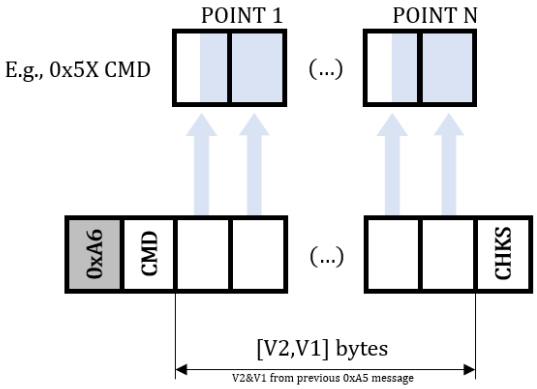

Figure 78. Extended message 0xA6 dataframe.

There are four kinds of commands carried in the second byte of the dataframe:

- `0x11`: **set the number of iterations** for an active experience application.
- `0x77`: **set time period** for an active experience application, in microseconds.
- `0x75`: **set wait time between iterations** for an active experience, in microseconds.
- `0x5X`: **set waveform for slot X**, carrying a 12-bit DAC value for every two bytes.

Upon the reception of an extended message, the UART DMA reception buffer is reset to the default value of 4 bytes.

6.2.5. Waveform application, signal measurement and transmission

By default, the PIT Channel 1 query will be operating at 1 ms period. This can be modified by the user using the `0x77` extended command. The flowchart has been shown in **Figure 76**. The steps in its execution are:

1. Clear the Channel 1 interrupt flag to enable the execution of the interrupt once the specified time has elapsed.
2. If the `waitOnFlag` is up, a wait between iterations has occurred and, the PIT period is established to the specified waveform application and signal acquisition period.
3. Otherwise, and if `ongoingApplicationFlag`, the code is in the application and acquisition operation, and the DAC output value is updated. Then, cycle counts are updated, establishing if `waitOnFlag` needs to be set and the PIT period established for a wait between iterations time.
4. Independently from steps 2 and 3, the maximum averaging samples with the remaining time is calculated, and all four ADC signals are obtained and stored.
5. If the `ongoingApplicationFlag` is up and the `waitOnFlag` is down, the acquired buffers are saved to the ring buffers, and the pointers updated.

Further details not included in **Figure 76** to fully describe the firmware behavior:

- Once an active experience ends, an *end of experience* header message is sent from the MBSI to the SCB every second until an acknowledgment message from the SBC is received.
- As the ADC is constantly acquiring, a *request ADC value* command is answered with the last value obtained for this ADC, stored in a temporal variable. The answer header will have the value `0xAX`, with X indicating the ADC ID, and 2nd, and 3rd bytes will carry the 12-bit measurement.

- `dataTransmission()` function configures the DMA to send a UART message during an active experience application. It is executed from the main infinite loop or upon the transmission end UART callback, both with lower priority than the PIT interrupt. The ADC values ring buffers have two pointers: save and send. A data transmission will be performed when the saving pointer is higher than the sending one. The dataframe of this message is shown in **Figure 79**.

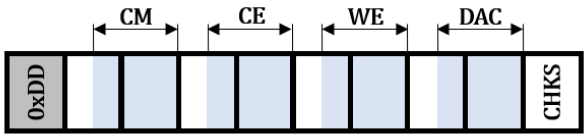

Figure 79. IVESDRIS 0xDD dataframe.

6.3. Application code in the single board computer

The application code, implemented in Python 3 to be executed in the Raspberry Pi 3B+, is composed of five .py files:

- `core.py`: library file where hardware initialization and higher-level functions are implemented.
- `com.py` has functions related to the periodic check and process of new input messages.
- `gui.py`: deploys a basic graphic user interface that allows users to order all the available commands.
- `script.py`: example to configure automatic experiences.
- `app.py`: allows users to program in Python a specific response to the different acknowledgments and errors that the MBSI may reply to.

6.3.1. IVESDRIS Graphic User Interface

The GUI allows the execution of all the available commands in the IVESDRIS through textboxes, buttons, and displays. The real-time communication between SCB (master, M) and MBSI (slave, S) can be printed in the left box (**Figure 80**).

Complex functions, such as loading an appliable waveform, establish the active period time or the wait time between iterations, can be set with just a single button, even if they involve more than one command.

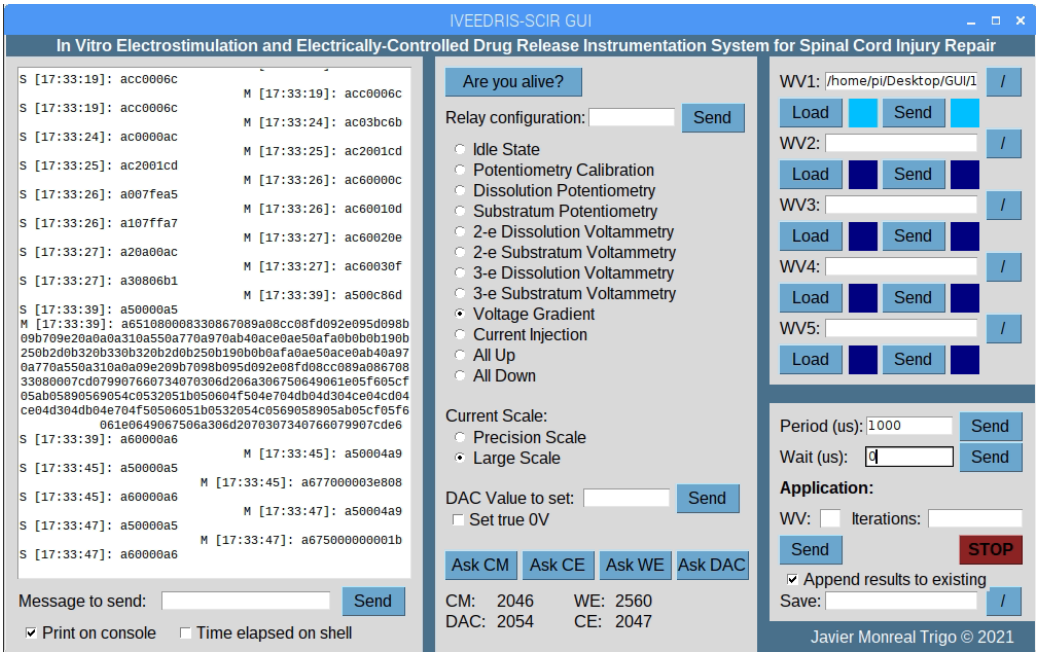

Figure 80. IVESDRIS Graphic User Interface.

Waveform files and saving directories can be obtained using the graphic interface for folder selection, represented with a button with the / symbol.

Primitive options, such as *message to send* and *relay configuration* textbox need to be written in hexadecimal and binary, respectively, using ASCII characters.

6.3.2. Waveform files

Waveform files are semicolon-separated files with up to 1000 elements, with .iwv extension. Each hosts a DAC value to be applied, from 0 to 4095. The 4096 is reserved for the true-zero-voltage application and will be interpreted as such.

6.3.3. Setup of active experiences

The `script.py` file allows the setup of experiences with simple modifications to the code. It imports the `core`, `com`, and `gui` libraries and allows the user to choose whether to launch the GUI or the programmed actions in the script by modifying the `GUIOn` flag.

Whether the GUI or the script execution is chosen, `hwInit()` and `updateMsgs()` will initialize the RPi hardware and start a continuous thread for the incoming RS-485 messages.

A modifiable script example is available in *6.6. Reproduction guide*. In the shell, it will be shown different messages indicating the situation of the execution.

6.3.4. Save files

The saved files follow the next structure (**Figure 81**):

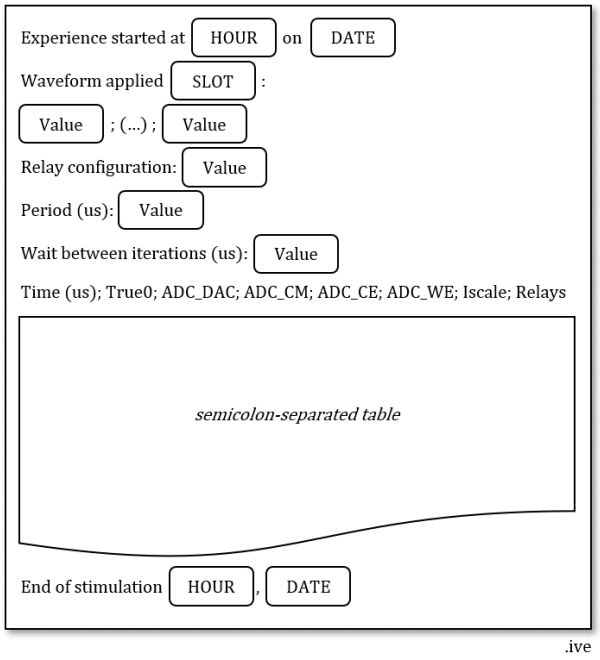

Figure 81. .ive save file format.

6.4. Extension module for stimulus multiplexing

An extension module for the IVESDRIS has been designed in the framework of this doctoral thesis as an Electronic Engineering BEng Final Project (Alamán Escolano [283]). Due to the length constraints of this document, only a brief description is addressed in this subsection. Nevertheless, the complete schematics, firmware, and software can be found in the link shown in *6.6. Reproduction guide.*

This expansion module allows one single IVESDRIS to apply electrical stimuli sequentially to different cell cultures without manually reconnecting the electrodes after each experiment. The extension module, namely *Multiplexing System* (MS), allows the multiplexing of the five analog signals from IVESDRIS' MBSI: working electrode, counter-electrode, reference electrode, and the electrostimulation pair of electrodes. The MS features 5 input terminals and 60 output

terminals. The input channel, with the 5 signals from the MBSI, can be switched between 12 different output channels.

The switching design employed is the same as in the MBSI: Omron's G6KU-2F-Y DC5 DPST signal relays driven by TI's ULN2003LVDR Darlington drivers. An Arduino Nano microcontroller board was employed to govern the MS. It is communicated with the IVESDRIS' SCB module through RS-485, using the same hardware design as the MBSI. The PCB dimensions are 17.8 cm x 28.8 cm. The layout of a four-layer PCB (standard fabrication technologies, Eurocircuits © 6C class). IVESDRIS MS top and bottom layers are shown in **Figure 82**.

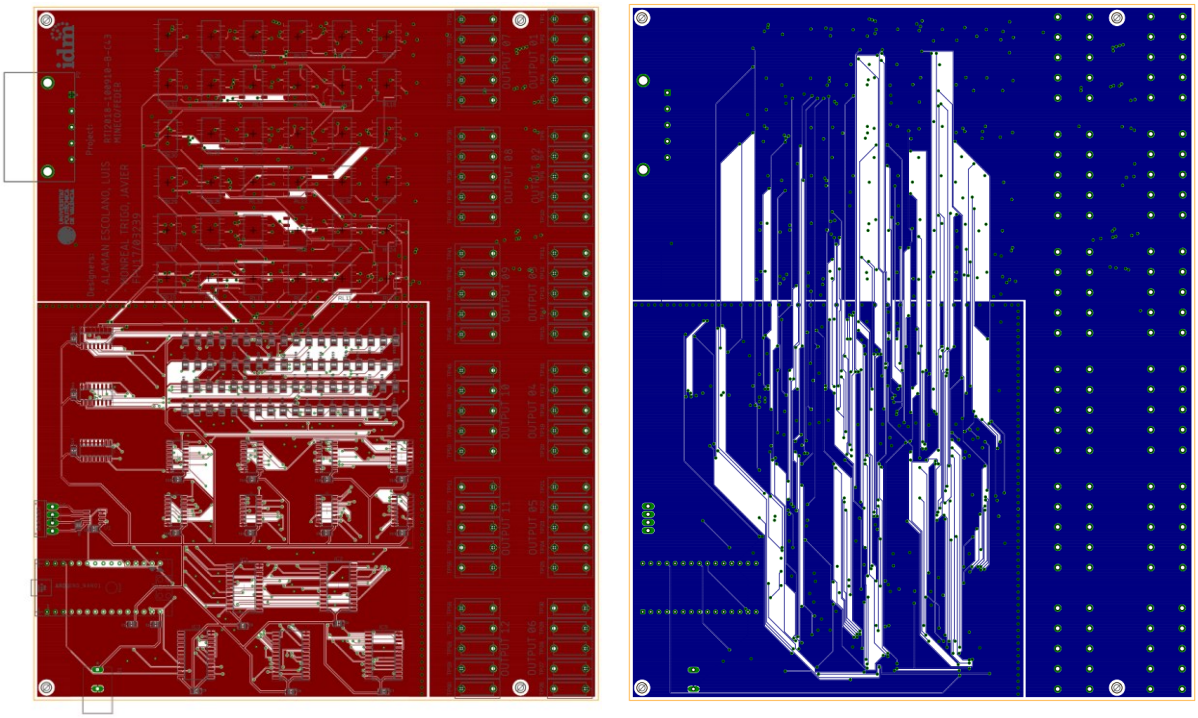

Figure 82. IVESDRIS MS board top layer (left) and bottom layer (right). Obtained with EAGLE © 2022 Autodesk.

The SCB shield was described in *6.1.7. SBC PCB design* already features two RS-485 outputs. A poka-yoke is implemented by assigning each RS-485 channel to different connectors.

6.5. Final appearance

IVESDRIS MBSI, based on MKW41Z microcontroller, is a platform with technique multiplexing capabilities. Each mode displays custom signal application and acquisition, with real-time transmission of this data. A 3D-render of the resulting IVESDRIS MBSI PCB is shown in the following **Figure 65**:

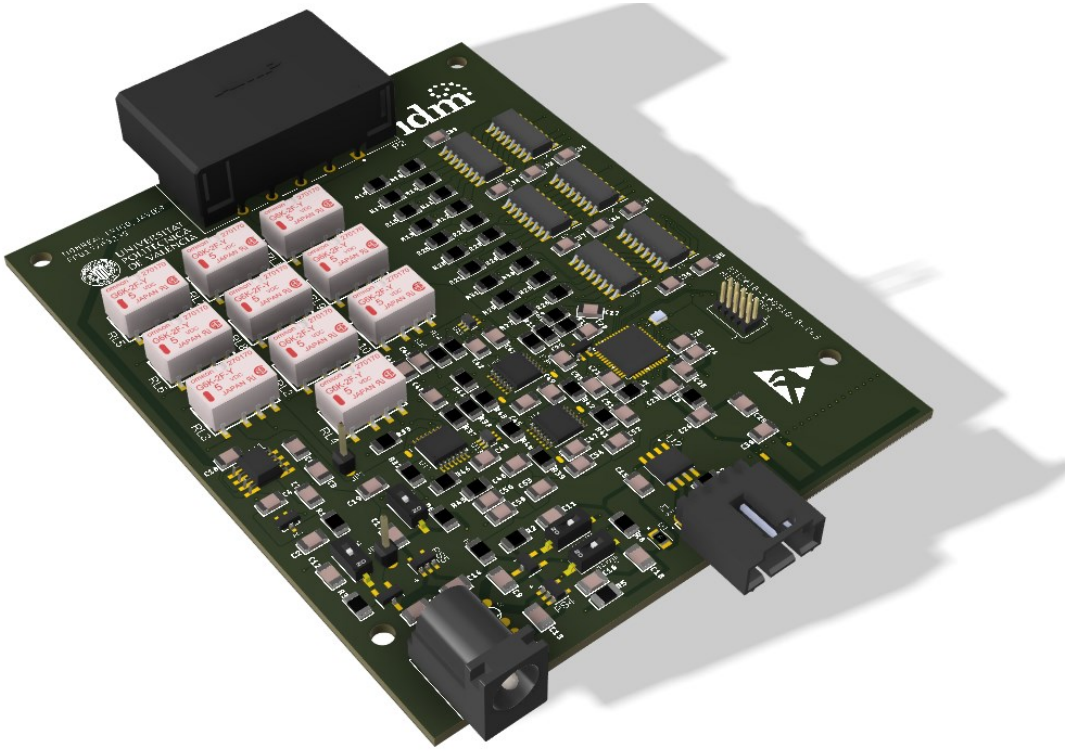

Figure 83. 3D-render of IVESDRIS MBSI. Obtained with Fusion 360 © 2022 Autodesk.

A printed box is designed for the MBSI board, and a custom lid for the Raspberry Pi commercial case embeds the RS-485 connectors. The MBSI and MS use TE Connectivity AMP Connectors 1-178128-5 and 1-316130-2 for the electrode connection. On the other hand, three use Molex's 0705530038 and 0050579404 for the RS-485 connectors. The communications between SCB and MBSI, and between SCB and MS are poka-yoked with different M12 connectors. The IVESDRIS (MBSI and SCB) is shown in **Figure 84**.

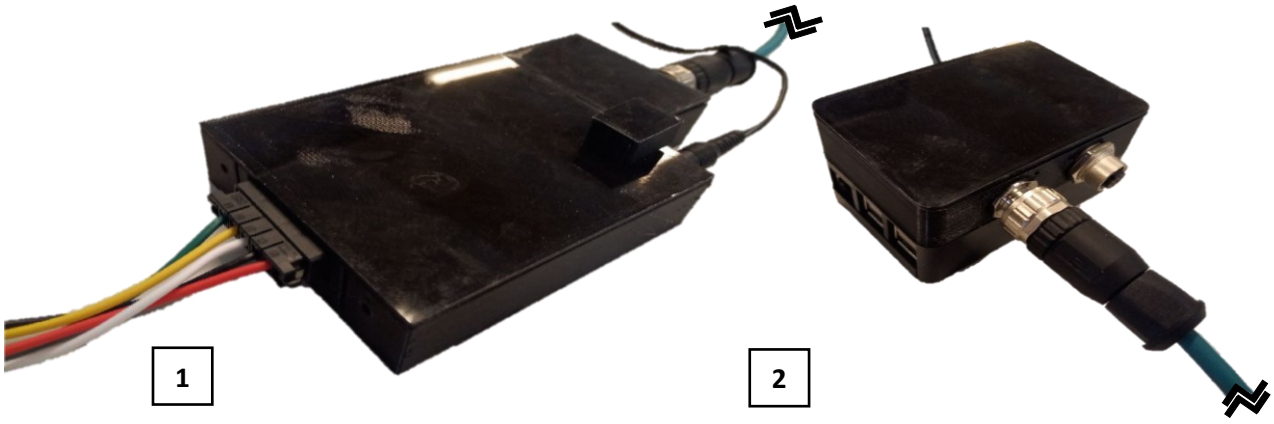

Figure 84. IVESDRIS appearance, in PLA 3-D printed by parts box. **1**) MBSI, supplied by a JACK connector; and **2**) SCB, supplied by the default micro-USB B connector from the Raspberry Pi 3B+. Both display the M12 connectors for RS-485 serial communications.

6.6. Reproduction guide

In the following virtual space can be found:

- Schematics for MBSI, SCB, and MS modules of IVESDRIS.
- Gerber files and bill of materials for ordering MBSI board.
- Gerber files and bill of materials for ordering SCB's shield.
- Gerber files and bill of materials for ordering MS' extension module.
- Firmware files for flashing the IVESDRIS's MBSI board.
- Firmware files for flashing the IVESDRIS's MS Arduino Nano microcontroller.
- STL parts to 3-D print the boxes.
- Bill of materials for the IVESDRIS system assembly.
- Guide for the Raspberry Pi 3B+ setup.
- Python software files for IVESDRIS control.

Link to virtual space: https://github.com/JMonrealT/IVESDRIS. Share, build, and modify IVESDRIS, registered under BY-NC-SA Creative Commons 4.0 License.

7. Electrical characterization

For the electrical validation of the device, the different techniques are applied in controlled resistive environments, comparing the theoretical value and the experimental value with the value obtained by FAEVIS. Experimental measurements are performed using the *Keithley 2000* multimeter. All measurements were recorded after FAEVIS calibration. Due to the similarities between the IVESDRIS and FAEVIS front ends, the electrical and electrochemical characterization are considered subsumed in those presented in FAEVIS.

7.1. Working electrode voltage measurement accuracy (potentiometry)

To measure the accuracy in potentiometry techniques, a resistive divider was implemented, and an external voltage source was employed to apply different voltages: +400, -400, +1200, -1200, +2000, -2000 mV.

In the *solution potentiometry* technique, the maximum measured error vs. the Keithley 2000 measurement was 3.92 mV, and the minimum error was 0.54 mV, with a mean accuracy of 1.28 mV and a standard deviation of 1.3 mV. The WE voltage measurement accuracy in

FAEVIS is <5.28 mV with a Confidence Interval of 99.7% (three standard deviation criteria), satisfying the requirement of minimum accuracy of 10 mV in the measurement of voltages.

7.2. Counter-electrode voltage measurement accuracy

As the former, it is required to reach a minimum accuracy of 10 mV. However, this voltage measurement system is employed in several techniques. We aim to test both the two- and three-electrodes configuration, from substrate and from solution, and the two current scales. We display the results involving two and three electrodes' configurations, and the two current scales:

1. *Two-electrodes voltammetry from solution* in the large current scale.
2. *Three-electrodes voltammetry from solution* in the precision current scale.
3. *Three-electrodes voltammetry from solution* in the large current scale.

Overall, setup 3 is included as the configuration featuring the worst accuracy from the 16 combinations.

The following voltages: +250 mV, -250 mV, 500 mV, -500 mV, 1000 mV, -1000 mV; are applied from FAEVIS to a resistive system. The experimental voltages measured with Keithley 2000 are compared with the ones obtained with FAEVIS.

In setup 1, minimum and maximum errors were 0.2 and 2.7 mV, respectively, with a mean error of 0.72 mV and a standard deviation of 0.80 mV. Accuracy is <3.12 mV (C. I. 99.7%).

In setup 2, minimum and maximum errors were 0.8 and 3.7 mV, respectively, with a mean error of 1.18 mV and a standard deviation of 1.13 mV. Accuracy is <4.57 mV (C. I. 99.7%).

In setup 3, minimum and maximum errors were 0.3 and 4.2 mV, respectively, with a mean error of 0.78 mV and a standard deviation of 1.42 mV. Accuracy is <5.04 mV (C. I. 99.7%).

Hence, counter-electrode voltage measurements satisfy the requirement of 10 mV accuracy.

7.3. Current measurement accuracy

In the former setup, the current was simultaneously tracked by FAEVIS. With the resistance measurement by Keithley 2000, currents are calculated through Ohm's Law. The specifications for each of the current scales are:

- On the wide or large scale, the accuracy of 20 μA in the range of $\pm$2.5 mA.
- On the accurate or precision scale, the accuracy of 200 nA in the range of $\pm$ 25 μA.

In setup 1, with the large current scale, minimum and maximum errors were 0.9 and 8.8 μA, respectively, with a mean error of 1.7 μA and a standard deviation of 3.2 μA. Accuracy is $<$11.3 μA (C. I. 99.7%).

In setup 3, with the large current scale, minimum and maximum errors were 1.5 and 12.4 μA, respectively, with a mean error of 3.7 μA and a standard deviation of 4 μA. Accuracy is $<$15.7 μA (C. I. 99.7%).

Hence, the large-scale current measurements satisfy the requirement of 20 μA accuracy.

In setup 2, with the precision current scale, minimum and maximum errors were 4 and 106 nA, respectively, with a mean error of 17 nA and a standard deviation of 40 nA. Accuracy is $<$137 nA (C. I. 99.7%).

It satisfies the current measurement accuracy in the precision mode of 200 nA.

7.4. Signal application accuracy

According to the specifications, it is required to be able to apply voltages in the range of $\pm$2.5 V with an accuracy of 20 mV and inject currents in the range of $\pm$200 μA with an accuracy of 2 μA.

From the former experiments, the voltage application resolution is obtained:

- In setup 1, minimum and maximum errors were 0.5 and 7.2 mV, respectively, with a mean error of 2.04 mV and a standard deviation of 2.40 mV. Accuracy is $<$9.24 mV (C. I. 99.7%).
- In setup 2, minimum and maximum errors were 1.1 and 8.1 mV, respectively, with a mean error of 3.03 mV and a standard deviation of 2.56 mV. Accuracy is $<$10.71 mV (C. I. 99.7%).

- In setup 3, minimum and maximum errors were 0.3 and 7.8 mV, respectively, with a mean error of 1.42 mV and a standard deviation of 2.70 mV. Accuracy is <9.53 mV (C. I. 99.7%).

Hence, the voltage application satisfies the requirement of 20 mV accuracy.

To evaluate the current injection accuracy, +50, -50, +100, -100, +150, and -150 µA were applied over a resistor. The current was measured through Keithley 2000. The minimum and maximum errors were 0.2 and 1.6 µA, respectively, with a mean error of 0.5 µA, and a standard deviation of 0.4 µA. Accuracy is <1.7 µA (C. I. 99.7%).

Hence, the current injection satisfies the requirement of 2 µA accuracy.

8. Electrochemical validation

In order to validate the designed electronic system in a real application environment, potentiometry and voltammetry have been applied to three electrodes in a controlled solution. The results obtained have been processed to obtain the cyclic voltagram, which provides information on the electrochemical system. To compare the results, the same techniques have been applied using commercial equipment and the electronic system developed. The commercial equipment used is Metrohm Autolab. The characteristics of the experience are detailed below, and finally, the results obtained are compared.

The electrochemical system consists of a solution of two compounds in a ratio of 50% and a concentration of 0.1 m (mol/g solvent). The two compounds are potassium ferrocyanide or Fe(II) [$K_4Fe(CN)_6$] and potassium ferricyanide or Fe(III) [$K_3Fe(CN)_6$].

Figure 85. $K_4Fe(CN)_6$ (left) and $K_3Fe(CN)_6$ (right).

This solution is of particular interest for the present validation purpose since, firstly, it presents a stable resting potential, allowing the application of potentiometry without

significant errors due to the electrochemical dynamics of the system. Secondly, by applying cyclic voltammetry is possible to oxidize and reduce this electrochemical system reversibly, obtaining the voltagram of the solution.

The cyclic voltagram is a graphical representation of the current variation with respect to the voltage when a linear potential sweep is applied to the electrochemical system. In this solution, two current peaks carry the most relevant information about the system: the anodic current peak and the cathodic current peak.

According to different parameters, such as the concentration of the solution, the surface area of the electrodes, and the waveforms applied in cyclic voltammetry, different amplitudes for the current peaks appear in the voltagram. These parameters are chosen so that the current peaks reach near the full scale of FAEVIS (±1.25 V operating range, first version).

Figure 86. Electrochemical cell and solution for electrochemical validation of FAEVIS compared to Metrohm Autolab.

The electrochemical cell comprises a 3 mm ⌀ gold working electrode (WE) and a gold counter electrode (CE). The equivalent surface area between the two is 0.066, obtained following **Equation 30**.

$$\text{Equivalent Surface Area} = \frac{\text{Area}_{\text{WE}}}{\text{Area}_{\text{WE}} + \text{Area}_{\text{CE}}} \qquad \textbf{Equation 30}$$

A Saturated Calomel Electrode (SCE) is used as a reference electrode (RE). The electrochemical cell in the solution is shown in **Figure 86**.

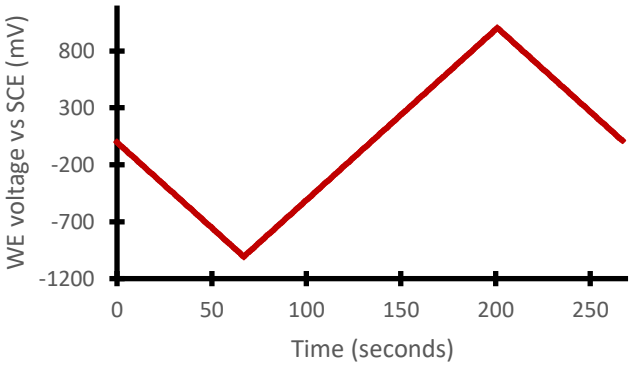

Figure 87. Voltage waveform applied in the cyclic voltammetry (one period).

Figure 87 shows the voltage waveform applied for two periods with a sweep speed of 15 mV/s. The cyclic voltagram is obtained for the second period.

First, 0CP (zero-current potential) potentiometry was measured using Metrohm Autolab, followed by cyclic voltammetry. FAEVIS was then installed in the experimental chamber. FAEVIS applied potentiometry and cyclic voltammetry. The 0CP value obtained by AUTOLAB is 189.341 mV, while the one obtained by FAVIS is 189.377 mV, experimentally validating the application of potentiometry in an electrochemical environment by the designed electronic system.

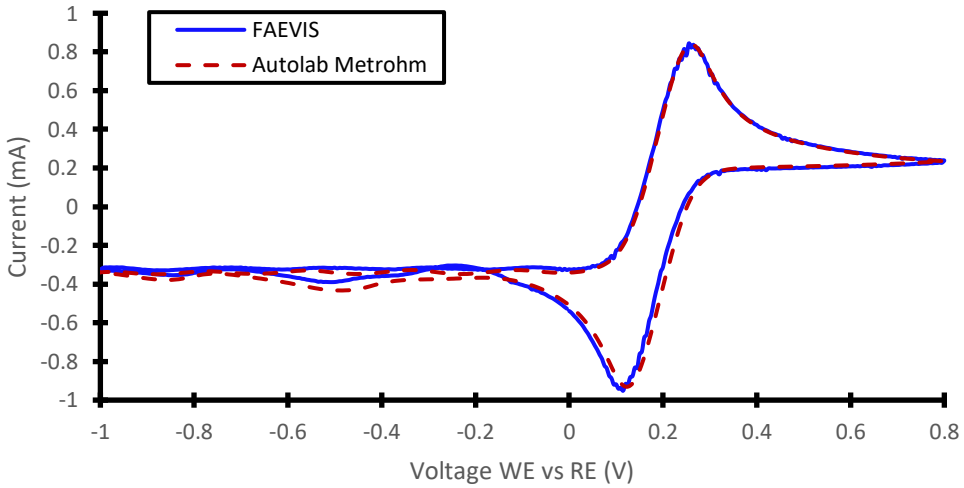

Figure 88. Cyclic voltammetry comparison between Autolab Metrohm and FAEVIS in a solution of potassium ferrocyanide and potassium ferricyanide.

The superimposed voltagrams obtained by ZOIS and Autolab are shown in **Figure 88**. As can be seen, the results are practically identical. The differences observed between both voltagrams do not represent an error in the measurement or application of the cyclic

voltammetry variables by the designed electronic equipment since even applying the technique using the commercial device, there are variations in the results of the experience when the test is repeated equal or superior to the one difference between the two devices shown in the figure. This variation between experiences is mainly due to the change in the distribution of the charges in the solution and the electrodes.

9. Conclusions

This first chapter addressed the electronic design for the *in vitro* combination of electrically controlled drug release (ECDR) and electrostimulation techniques.

Initially, we designed a wireless device, FAEVIS, powered by a battery and commanded from a personal computer (PC), communicating via Bluetooth. This device satisfied the initial requirements of 24h of autonomy and its operation inside the incubator.

However, after the first experiments, the need to increase the autonomy became apparent, communication problems related to the incubator acting as a Faraday cage were identified, and practical experience showed that it was possible to make connections to the inside of the incubator from the outside. Furthermore, keeping a PC in the surroundings of the incubator during the experiment involved problems related to spatial constraints in such a workplace.

Therefore, a second device, IVESDRIS, was designed. It was powered by a AC/DC converter from the grid and communicated with a small board computer (SBC) via RS-485 twisted pair communication, overcoming the limitations of its predecessor.

The devices, which share the analog front end, have been electrically characterized. An electrochemical validation has been performed by applying cyclic voltammetry to a solution with a standard redox response in the literature, comparing the results with those obtained with a commercial device.

With these devices, we have been able to perform the experiments described in *Chapter 2. Electrically controlled drug release (ECDR)* and *Chapter 3. Electrostimulation for nervous tissue regeneration in vitro*.

Chapter 2. Electrically controlled drug release (ECDR)

This chapter will explore the innovative development of electrically controlled drug release (ECDR) techniques on gated materials.

Given the strengths and drawbacks of gated mesoporous silica nanoparticles (MSNs) and conductive polymers, hereafter, we will present our original solution based on their combination. This innovative smart composite has been published in a Q1 journal, an original work part of the present doctoral thesis [220].

In our publication, MSNs are loaded with Rh B (as model molecule) and anchored to the PEDOT:PSS-*co*-MA conductive polymer (CP). The external surface of the nanoparticles is functionalized with a positively charged bipyridinium derivative. The pores capped upon the addition of the negatively charged polysaccharide heparin. The assembly, namely **P3**, can release Rh B by the application of a low voltage (<0.7 V), more suitable for biological applications than the state of the art, which require higher voltages (~1-1.5 V). **P3** films are used for the controlled release of Rh B in cell cultures of HeLa cells to corroborate the system's application and its biocompatibility.

The electrochemical characterization of the release mechanism upon electrical stimulus is covered as original work in this doctoral thesis in the section *2. Characterization of the electrochemical bipyridinium-heparin ECDR mechanism* of the present chapter.

The section *3. Voltage-responsive MSN on PEDOT:PSS-co-MA design and validation* describes the chemical design of the new electrically controlled drug release technique and the fabrication process of the CP-MSN assembly. It was performed by our collaborators from Prof. Martínez-Máñez group, and it is incorporated as technical design and validation results. The necessary electrical triggers were applied with FAEVIS, one of the devices described in *Chapter 1. Electronic instrumentation for in vitro electrostimulation and controlled drug release*.

After successfully validating the technology, we proposed to transfer it to a platform based on a polymeric substrate instead of ITO/glass slides, which is more suitable for the future *in vivo* transition that the application requires. Likewise, the electrodeposition of PEDOT:PSS-*co*-MA was replaced by commercial PEDOT:PSS screen printing in a flexible substrate. We will address the translation from a rigid to a flexible substrate in *Chapter 3. Electrostimulation for nervous tissue regeneration in vitro*. The flexible platform release experiments results and the explanation for their adverse outcomes are in subsection *4.1. Flexible substrate ECDR* of this chapter.

Finally, electrically controlled drug release from metallic and ceramic surfaces is studied through two approaches in subsection *4.2. ECDR from metallic and ceramic surfaces*: electrochemical and electrostatic. Gated mesoporous silica nanoparticles' electrochemical release in a gold surface is obtained; electrostatic release is only achieved through the direct gating of a porous surface without MSNs, and we hypothesize the reasons. Nevertheless, these results need further research, hence are not covered in detail in the present thesis dissertation.

1. Conceptualization of new ECDR: smart polymer with grafted MSN

Gated mesoporous silica nanoparticles (MSNs) are biocompatible, biodegradable, have high-encapsulation capacity, and can release different cargos on demand. The development of molecular gates that allow the electrically controlled release of drugs upon application of lower voltages (inferior to 0.7 V) would allow their wide and broad application in biological systems. Additionally, compared with conductive polymer drug delivery technology, they present an inherent higher load capacity and a more reduced passive diffusion without the presence of the trigger stimulus (*i.e.*, the electrical field).

We conceptualize the combination of conductive polymers (CPs) with MSNs gated with low-voltage electro-responsive molecular gates. This integration would enhance conductive polymer-based platforms' drug delivery capabilities in the applications where CPs are in the state of the art, such as in electrostimulation, bioactuators, and biosensors, among others. In this way, the biological applicability of conductive polymers could be enlarged in fields such as neural regeneration and others in which drug delivery can be finely tuned to provide selective control of glial and neuronal cell biology (Wang *et al.* [326]).

The electrically controlled drug release from MSNs on a conductive polymer has only been explored by Cho *et al.* [327]. In their study, the electric field application regulated the gradual release of the nerve growth factor (NGF) from the MSNs on Ppy CP, where PC12 cells were seeded. Specifically, in this study, the cargo from the MSNs was diffused considerably even without the electrical field application, the electrical stimulus regulated the drug release by accelerating this diffusion. MSNs were used principally as the carrier to improve the host capacity of the polymer and protection of the cargo molecule.

Without electrical stimulation, the non-planar surface generated due to the MSN-Ppy bilayer increased cellular adhesion. This parameter, and the neurite generation, were significantly increased with the NGF incorporation inside the MSNs. Studying the NGF influence in these results, Cho *et al.* compared the same parameters introducing the nerve growth factors (NGF) in the solution and loading it inside the MSNs:

- The NGF in solution option gave the unstimulated samples a better neurite development rate.

- The NGF loaded in MSNs gave the best overall results with electrical stimulation, explained due to the combination of the NGF release and the induced differentiation because of the electrical stimulation.

In the present thesis, the low-voltage electro-responsive molecular gates chosen for the design are composed of a bipyridinium derivative, electrostatically attaching a capping heparin moiety. The trigger mechanism is composed of the electrochemically induced reduction of the bipyridinium derivative, disrupting the electrostatic union. PEDOT:PSS-*co*-MA conductive polymer is chosen for the assembly, given the previous reports of good biocompatibility and multiple biofunctionalization capabilities, making it specifically suitable for lesion-bridging applications (Collazos *et al.* [328]).

2. Characterization of the electrochemical bipyridinium-heparin ECDR mechanism

The designed electro-responsive molecular gate will allow the release of the cargo upon applying an electrical voltage. In order to specify the voltage needed to induce the electrochemical release, a thorough study of the electrochemical reactions of the different components becomes compulsory. With this purpose, we will study the electrochemical reactions of the gated nanoparticles in solution. Then, we will study if there is a voltage shift when the gated nanoparticles are grafted onto the conductive polymer. We will perform the electrochemical studies through cyclic voltammetry: a triangular voltage waveform will be applied, acquiring the induced currents. Plotting the measured current vs. the applied voltage offers a *voltagram*. In short, current non-linearities, namely *current waves*, will be associated with electrochemical processes that can be identified, characterizing the electrochemical behavior of the assembly.

The gate assembly is slightly different if the voltage-responsive MSNs are in suspension or bonded to the conductive polymer.

For MSNs in suspension, they are composed by:

1. External surface functionalization with (3-iodopropyl)trimethoxysilane.
2. 1-methyl-4,4'-bypiridine iodide (**C1**).
3. Capping moiety: Heparin.

For MSNs grafted onto the conductive polymer, they are composed by:

1. External surface functionalization with (3-aminopropyl)trimethoxysilane.
2. 4,4'-bypiridinium-1-(carboxymethyl)-1'-methyl iodide bromide (**C2**).
3. Capping moiety: Heparin.

In both cases, a bipyridinium derivative acting as a gate will electrostatically interact with the negatively charged polysaccharide heparin, acting as a capping moiety or diffusion barrier. This positively charged bipyridine derivative will be electrochemically induced into a neutral form by applying an external voltage trigger. Hence, disrupting the former electrostatic interaction with the negatively charged heparin. The end of the electrostatic binding of the capping moiety puts an end to the diffusion barrier, therefore allowing cargo diffusion.

The external functionalization with (3-iodopropyl)trimethoxysilane is a wide-spread praxis, therefore chosen for the voltage-responsive MSNs in suspension, but it will not bind to the PEDOT:PSS-*co*-MA conductive polymer. In order to bind the MSNs to this CP, our collaborators in the Prof. Martínez-Máñez chemistry group analyzed the presence of carboxylic groups in the maleic acid copolymer, hence functionalizing the external surface of MSNs with (3-aminopropyl)trimethoxysilane instead. This decision involves the modification of the gate in order to bind it to the sides of the MSNs that are not bonded to the CP.

It is necessary to determine the voltage to be applied to guarantee electrically controlled release in the two conditions: in MSNs in suspension and MSNs bonded to the CP. Hence, in this section, the following four items are studied:

1. The electrochemical processes of compound **C1**, used in MSNs in suspension.
2. The electrochemical processes of compound **C2**, used in the MSNs bound to the CP.
3. The electrochemical characterization of the CP with and without MSNs.

2.1. Electrochemical characterization of compound C1

2.1.1. Literature review and analysis

Compound **C1**, 1-methyl-4,4'-bypiridine iodide (with the chemical structure shown in **Figure 89a**), is a derivative of 4,4'-bypiridine (see chemical structure in **Figure 89b**).

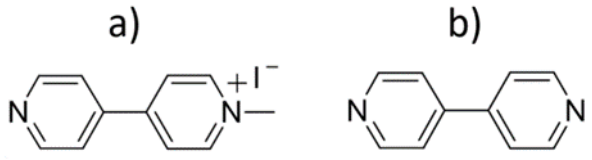

Figure 89. Chemical structure of a) 1-methyl-4,4'-bypiridine iodide, namely **C1**, and b) 4,4'-bypiridine.

4,4'-bypiridine molecular weight, M_r^0, is 156 g/mol, as shown in **Equation 31**. Compound **C1** molecular weight, M_r^1, is 283 g/mol, as shown in **Equation 32**.

$$M_r^0 = 2 \cdot N\left(14\frac{g}{mol}\right) + 10 \cdot C\left(12\frac{g}{mol}\right) + 8 \cdot H\left(1\frac{g}{mol}\right) \quad \textbf{Equation 31}$$

$$M_r^1 = M_r^0 + I\left(127\frac{g}{mol}\right) + C + 3 \cdot H \quad \textbf{Equation 32}$$

1,1-dimethyl-4,4'-bypiridine, also known as methyl viologen (MV) or paraquat, has been widely studied. Its chemical structure and redox states are shown in **Figure 90** by Wang *et al.* [329].

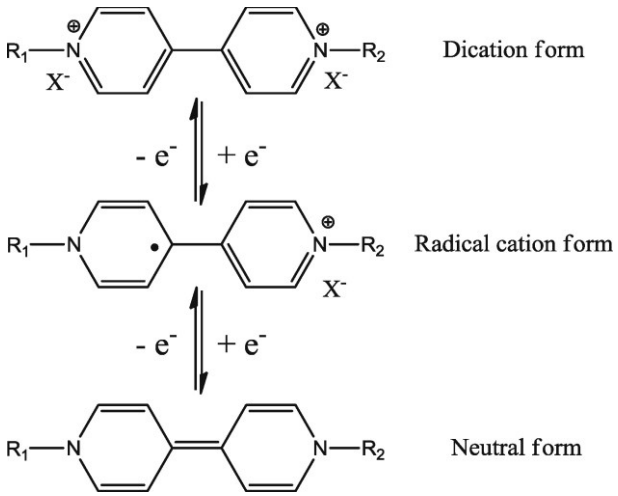

Figure 90. Three redox forms of viologens. Reproduced with permission from [329]. Electrochimia Acta © 2015 Elsevier.

This is formally expressed in **Equation 33** and **Equation 34**:

$$MV^{2+} + 1e^- \rightleftarrows MV^{\circ+} \quad \textbf{Equation 33}$$

$$MV^{\circ+} + 1e^- \rightleftarrows MV^0 \quad \textbf{Equation 34}$$

The electrochemical study of viologens was comprehensively addressed a long time ago (see Bird & Kuhn [330]): "Ito and Kuwana [331] quote the potential of the first reduction for

methyl viologen as -0.446 vs. NHE[8], citing the work of Elofsen and Edsberg, Osa and Kuwana, Michaelis and Hill, and Volke. They state that the value is Ph-independent in the range Ph 5-13 […]. The second reduction potential is given as -0.88 V".

Taking into account the potential of SCE[9] vs. NHE (see Jenck's guide [332]), SCE vs. NHE is +241 mV, the half-wave potentials vs. SCE for the two reduction processes of the methyl viologen are:

- Radical dication form to radical cation form: -687 mV vs. SCE.
- Radical cation form to neutral form: -1021 mV vs. SCE.

From Ito & Kuwana [331], we can estimate the potential threshold for the neutral form to radical cation form in -615 mV vs. SCE and its peak current potential for -715 mV vs. SCE.

Electrochemical studies of methyl viologen have been performed by Kim *et al.* [333] with a 100 mV/s cyclic voltammetry using a 0.071 cm^2 glass carbon electrode (GCE) as WE, an SCE as RE and a Pt CE under an inert Argon atmosphere in PBS 7 Ph 0.1 M solution as shown in **Figure 91** (dashed line). The WE was polished between experiments. Please note that the voltage in the X axis is inverted.

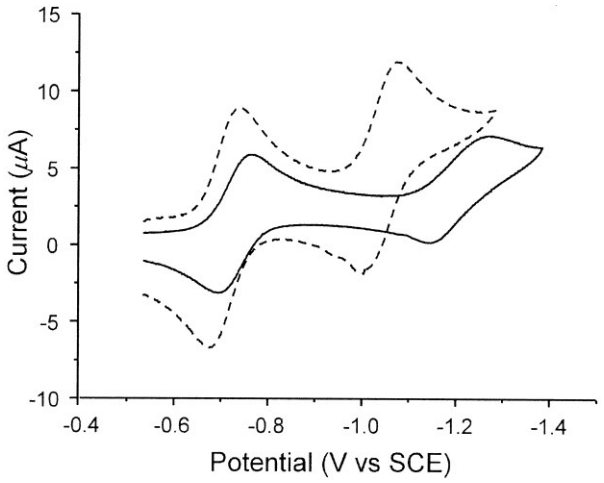

Figure 91. Cyclic voltammograms (0.1 $V \cdot s^{-1}$) of 0.5 Mm MV^{2+} in the presence of 3 equivalents of CB[7] (solid line) and absence of CB[7] (dashed line). SCE, saturated calomel electrode. Reproduced from [333]. PNAS © 2002 National Academy of Science.

Half-wave potentials, $E_{1/2}$, as the average between the oxidation and reduction peaks in mV vs. SCE, and the potential difference in mV between the cathodic and anodic peak potentials,

[8] Normal Hydrogen Electrode, described in *Introduction, 4.5. Reference electrode*.
[9] Saturated Calomel Electrode, described in *Introduction, 4.5. Reference electrode*.

ΔE_p, are obtained for process 1 (radical dication form – radical cation form), and process 2 (radical cation form – neutral form).

- $E_{1/2}^{1} = -704$ mV
- $\Delta E_p^1 = 64$ mV
- $E_{1/2}^{2} = -1014$ mV
- $\Delta E_p^2 = 64$ mV

Therefore, from the former values and **Figure 91**, peak potentials can be obtained, being the voltage for the cathodic peak of process X, E_{pc}^{X}; and the voltage for the anodic peak for the same process, E_{pa}^{X}.

- $E_{pc}^{1} = -736$ mV
- $E_{pc}^{2} = -1046$ mV
- $E_{pa}^{2} = -982$ mV
- $E_{pa}^{1} = -672$ mV

Iodide redox processes under cyclic voltammetry are well characterized in the literature under lithium perchlorate supporting electrolyte (see Popov & Geske [334]). More recently, Sun *et al.* [335] offer a clear voltagram of this process with different working electrodes.

Therefore, an additional redox process is expected in compound **C1**, with the expression of **Equation 35** and **Equation 36**.

$$I_3^- + 2e^- \rightleftarrows 3I^- \qquad \textbf{Equation 35}$$

$$3I_2 + 2e^- \rightleftarrows 2I_3^- \qquad \textbf{Equation 36}$$

Given that Sun *et al.* solution is not PBS; their current peak potentials cannot be taken as a reference. Nevertheless, it is relevant to point out the presence of a reduction potential <0 V vs. Ag/Ag^+, which may be present close to E_{pc}^{1} in our system.

Hence, we shall repeat to compound **C1** in the same conditions as the voltagram applied by Kim *et al.* to methyl viologen and study its reduction and oxidation voltages variation due to the iodide presence.

The electrostatic interactions of heparin with bipyridinium derivatives are studied through compound **C1** dication form: 1,1'-dimethyl-4,4'-bypiridine diiodide, namely (**C3**); allowing the heparin attachment on both sides of the bipyridinium derivative.

Compound **C3** only differences with compound **C1** is the presence of an additional methyl and iodide, as shown in **Figure 92**.

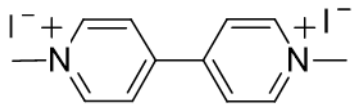

Figure 92. 1,1'-dimethyl-4,4'-bypiridine diiodide, namely **C3**.

Compound **C1** molecular weight, M_r^1, is 283 g/mol, as shown in **Equation 32**. Compound **C3** molecular weight, M_r^3, is 440 g/mol, as shown in **Equation 37**.

$$M_r^3 = M_r^0 + I\left(127\frac{g}{mol}\right) + 1 \cdot C\left(12\frac{g}{mol}\right) + 3 \cdot H\left(1\frac{g}{mol}\right) \qquad \textbf{Equation 37}$$

Compound **C3** presents higher solubility in PBS 0.1 M pH=7 than compound **C1** and is expected to present the same electrochemical behavior regarding the methyl viologen. Thus, compound **C3** is studied to characterize compound **C1**.

2.1.2. Experimental setup

PGSTAT100 from Autolab is used for the application of cyclic voltammetry. The electrochemical cell is composed by:

- A Saturated Calomel Electrode (SCE) from Crison as the reference electrode.
- A Ring Pt electrode from Crison as the counter-electrode.
- As the working electrodes, both 3 mm Ø, hence 0.071 cm^2:
    - Gold / Au (Metrohm 6.1204.320)
    - Glassed Carbon Electrode / GCE (Metrohm 6.1204.300)

Using different working electrodes allows us to estimate the threshold and peak current voltages' dependence on the working electrode employed.

All experiments are performed in 12 mL PBS 0.1 M pH=7 solution under an inert Argon atmosphere (5' gurgling, 5' atmosphere application). Used WE are polished before every experiment. All experiments are performed without stirring.

Compound **C3** concentration: 5 mM.

Cyclic voltammetry parameters:

- Range: from -1.2 to 0.95 V vs. SCE.
- Scan rate: 20 mV/s.

2.1.3. Results

The results reproducing [333] for compound **C3**, obtained using GCE and gold electrodes, are shown in **Figure 93** and **Figure 94**, respectively.

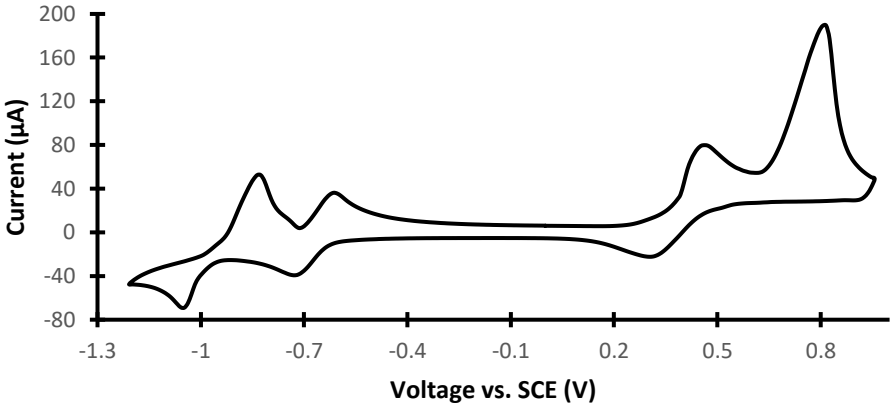

Figure 93. 20 mV/s cyclic voltammetry from -1.2 V to 0.95 V vs. SCE. WE: GCE. 5 mM of compound **C3**.

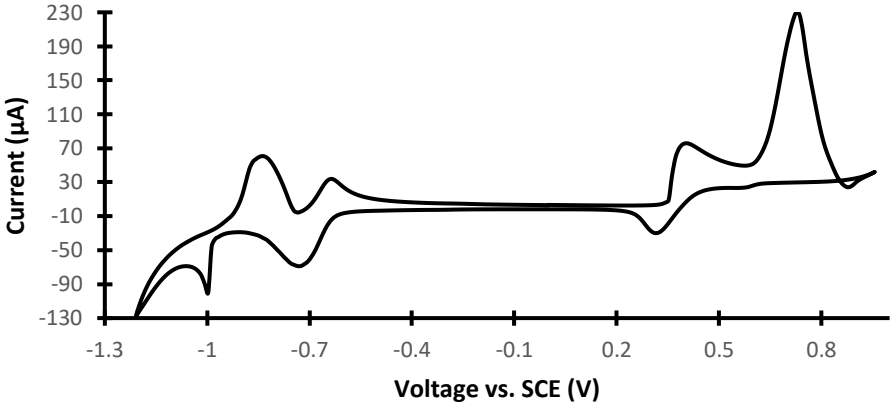

Figure 94. 20 mV/s cyclic voltammetry from -1.2 V to 0.95 V vs. SCE. WE: gold. 5 mM of compound **C3**.

Methyl viologen redox processes are present on the negative side of the voltagram. On the other hand, iodide oxidation processes, and one of its reduction processes, are present on the positive side of the voltagram. It is essential to highlight that the iodide/triiodide reduction (**Equation 35**) is not observed independently. Three options are feasible:

- It is present at a close voltage to other reduction processes.
- It is present at lower voltages than -1.2V vs. SCE.
- In these conditions, one of the iodide redox processes is irreversible.

Under non-rotating conditions, the threshold potential to start the reduction process (X), $E_{th}^{R}(X)$, can be identified by the increase of the current slope. Once the process reaches its peak potential $E_{p}^{R}(X)$, further voltages will not increment the reduction rate. Hence, the current slope

will flatten. Nominal $E_p^R(X)$ may be reached, or an effective $E_p^R(X)$ may appear before due to mass transport limitations. This is since the resultant species of the redox process at the vicinity of the WE may impede the arrival of new reagents, slowing down the reaction. The same phenomenon will be present to oxidation processes, hence obtaining $E_{th}^O(X)$ and $E_p^O(X)$. Regarding:

- $I_3^- + 2e^- \rightleftarrows 3I^-$ (**Equation 35**) as process (1).
- $3I_2 + 2e^- \rightleftarrows 2I_3^-$ (**Equation 36**) as process (2).
- $MV^{2+} + 1e^- \rightleftarrows MV^{\circ+}$ (**Equation 33**) as process (3).
- $MV^{\circ+} + 1e^- \rightleftarrows MV^0$ (**Equation 34**) as process (4).

Processes (3) and (4) can be studied regarding the negative side of the cyclic voltagram. **Figure 95a** shows the graphical obtention of the current peak and threshold potentials for the oxidation processes, in red. **Figure 95b** shows the graphical obtention of the current peak and threshold potentials for the reduction processes, in blue. GCE and gold WE CV present the same values excepting for $E_p^R(4)$, in which the gold WE CV presents an artifact. For this case, the GCE WE value is chosen.

We should notice that the oxidation and reduction wave areas are similar, thus, indicating that probably there is no third reduction process present.

Figure 95c and **Figure 95d** show the graphical obtention of the respective iodide cations' redox potentials. We should discard that any reduction process is present at a close voltage to other reduction processes. Redox process (2) is irreversible in the present conditions, or its reduction potential is in the far negative region $<$1.2 V vs. SCE:

- The first oxidation wave and the first reduction wave present area similarities, and their threshold potentials match their current peak potentials. Both are characteristics of reversible electrochemical processes. Hence, we should consider the reduction wave as of the process (1).
- The second oxidation wave, corresponding to the redox process (2), presents an area x2-3 times the first oxidation wave, but there is no area mismatch in any other redox process studied that may indicate that its reduction is taking place.

There is a significant difference between gold WE CV and GCE WE CV for oxidation potentials obtention. The projections are obtained for gold WE CV to compare its variations in the following subsection.

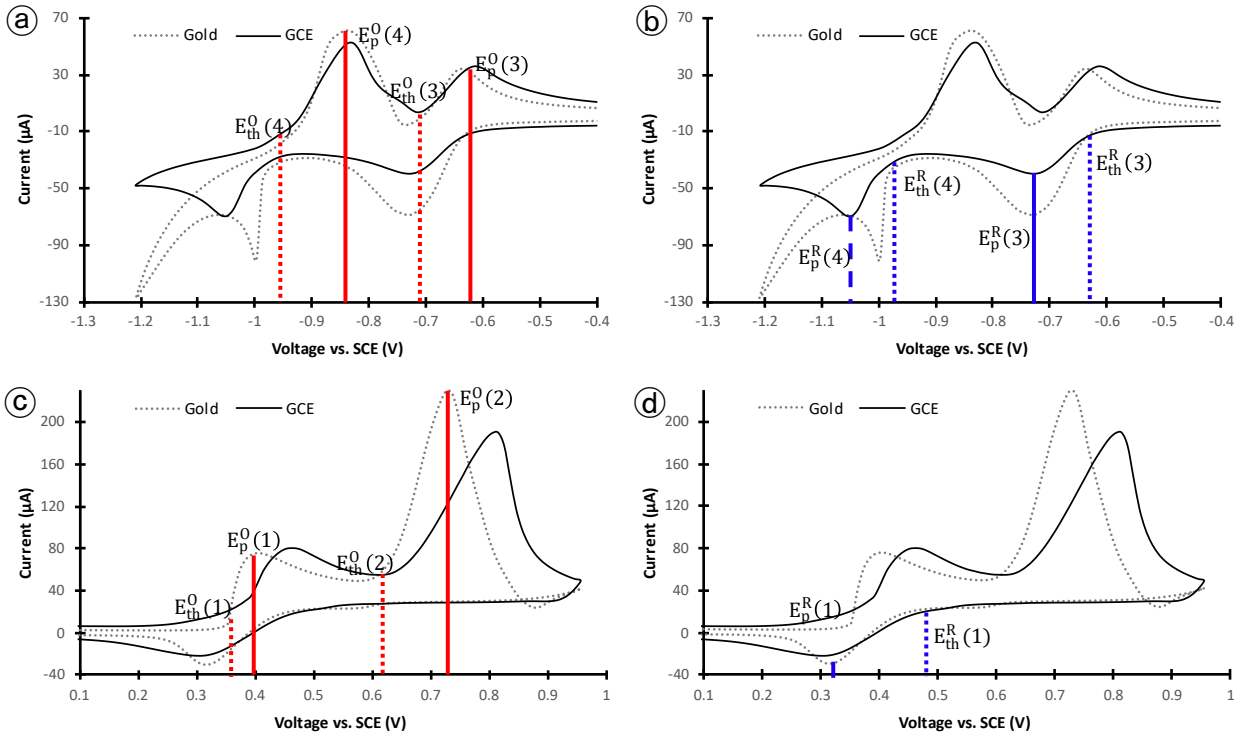

Figure 95. 20 mV/s cyclic voltammetry from -1.2 V to 0.95 V vs. SCE. WEs: Gold (solid black line) and GCE (doted gray line). 5 mM of compound **CC3**. ⓐ Detailed view on negative voltages vs. SCE: oxidation processes (3) and (4). Current peak potential projection (solid red line) and threshold potential (dotted red line) for both CVs. ⓑ Detailed view on negative voltages vs. SCE: reduction processes (3) and (4). Current peak potential projection (solid blue line) and threshold potential (dotted blue line) for both CVs. Current peak potential projection for process (4) is obtained only with GCE WE CV (dashed blue line). ⓒ Detailed view on positive voltages vs. SCE: oxidation processes (1) and (2). Current peak potential projection (solid red line) and threshold potential (dotted red line) for gold WE CV. ⓓ Detailed view on positive voltages vs. SCE: reduction process (1). Current peak potential projection (solid blue line) and threshold potential (dotted blue line) for both CVs.

The obtained threshold and current peak potentials are:

- $E_{th}^R(3) = -625$ mV
- $E_p^R(3) = -725$ mV
- $E_{th}^R(4) = -975$ mV
- $E_p^R(4) = -1050$ mV

- $E_{th}^O(4) = -960$ mV
- $E_p^O(4) = -840$ mV
- $E_{th}^O(3) = -710$ mV
- $E_p^O(3) = -625$ mV

- $E_{th}^O(1) = 360$ mV
- $E_p^O(1) = 395$ mV
- $E_{th}^O(2) = 620$ mV
- $E_p^O(2) = 730$ mV

- $E_{th}^R(1) = 525$ mV
- $E_p^R(1) = 325$ mV

Comparing our results with the ones obtained by Kim *et al.* [333]:

Kim *et al.* [333]:

- $E_{pc}^{1} = -736$ mV
- $E_{pc}^{2} = -1046$ mV
- $E_{pa}^{2} = -982$ mV
- $E_{pa}^{1} = -672$ mV

This work:

- $E_{p}^{R}(3) = -725$ mV
- $E_{p}^{R}(4) = -1050$ mV
- $E_{p}^{O}(4) = -840$ mV
- $E_{p}^{O}(3) = -625$ mV

Reduction potentials obtained are almost identical to the ones obtained by Kim *et al.*, and are the ones of most interest, in particular $E_{p}^{R}(3)$. The difference between E_{pa}^{2} and $E_{p}^{O}(4)$ is the most noticeable, with 142 mV.

Subsection summary: We characterized **C3** electrochemically. This compound is almost identical to **C1** but with enhanced solubility in PBS 0.1 M pH=7, easing the voltammetric responses for this characterization. **C1** is part of the gate component of the electro-responsive MSNs, which due to its positive charge, can close the loaded pore of the MSN by attracting a negatively charged molecule, which acts as a cap, entrapping the cargo. The reaction of interest related to the opening of the molecular gate is $MV^{2+} + 1e^{-} \rightarrow MV^{\circ +}$. The threshold and peak voltages for the reaction to occur are -625 and -725 mV vs. SCE, respectively, close to the values reported in the literature.

2.2. Electrochemical characterization of compound C2

2.2.1. Chemical structure

Compound **C2**, 4,4'-bypiridinium-1-(carboxymethyl)-1'-methyl iodide bromide (chemical structure shown in **Figure 97**).

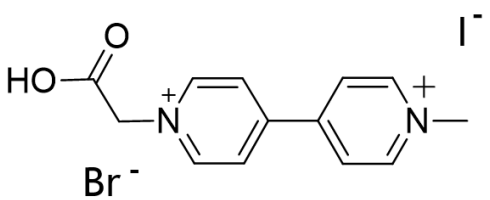

Figure 96. 4,4'-bypiridinium-1-(carboxymethyl)-1'-methyl iodide bromide, namely **C2.**

Compound **2** molecular weight, M_r^2, is 437 g/mol, as shown in **Equation 38**.

$$M_r^2 = M_r^0 + I\left(127\frac{g}{mol}\right) + Br\left(80\frac{g}{mol}\right) + 2\cdot O\left(16\frac{g}{mol}\right) + C\left(12\frac{g}{mol}\right) + H\left(1\frac{g}{mol}\right) \quad \textbf{Equation 38}$$

Due to the presence of the carboxyl acid group, a Kolbe electrolysis may be induced in the application of negative potentials at the WE (*i.e.*, a reduction process due to a cathodic current). The reduction is governed by **Equation 39** (see Sbei *et al.* [336]), and is irreversible.

$$2\cdot R-COOH + 4e^- \longrightarrow R-R + CO_2 + H_2 \quad \textbf{Equation 39}$$

On the other hand, according to Tariq [337], Br^-/Br_2 presents the following two reversible redox processes (see **Equation 40** and **Equation 41**) for the positive range of voltages:

$$3Br_2 + 2e^- \leftrightarrows 2Br_3^- \quad \textbf{Equation 40}$$

$$2Br_3^- + 4e^- \leftrightarrows 6Br^- \quad \textbf{Equation 41}$$

The specific threshold and current peak potentials from Tariq [337] cannot be taken as a reference because TBAS is used as the supporting electrolyte used instead of PBS.

As performed for compound **C3**, we shall repeat the cyclic voltammetry to compound **C2**, in the same conditions applied by Kim *et al.* to methyl viologen and study its reduction and oxidation voltages variation due to the bromide and carboxymethyl in its chemical structure.

2.2.2. Experimental setup

PGSTAT100 from Autolab is used to apply cyclic voltammetry and Autolab RDE-2 for rotating disk experiments. The electrochemical cell is composed by:

- A Saturated Calomel Electrode (SCE) from Crison as the reference electrode.
- A Ring Pt electrode from Crison as the counter-electrode.
- As the working electrodes, both 3 mm Ø, hence 0.071 cm^2:
  - Gold / Au (Metrohm 6.1204.320)
  - Glassed Carbon Electrode / GCE (Metrohm 6.1204.300)

All experiments are performed in 12 mL PBS 7 pH 0.1 M solution under an inert Argon atmosphere (5' gurgling, 5' atmosphere application). Used WE is polished before every experiment. All experiments are performed without stirring.

2.3.3. Results

The results reproducing [333] for compound **C2** are shown in **Figure 97**. The dashed line is the voltagram for 0.5 mM of compound **C2** in solution, for which the current responses can't be distinguished. Increasing the concentration an order of magnitude made the anodic and cathodic peaks clear.

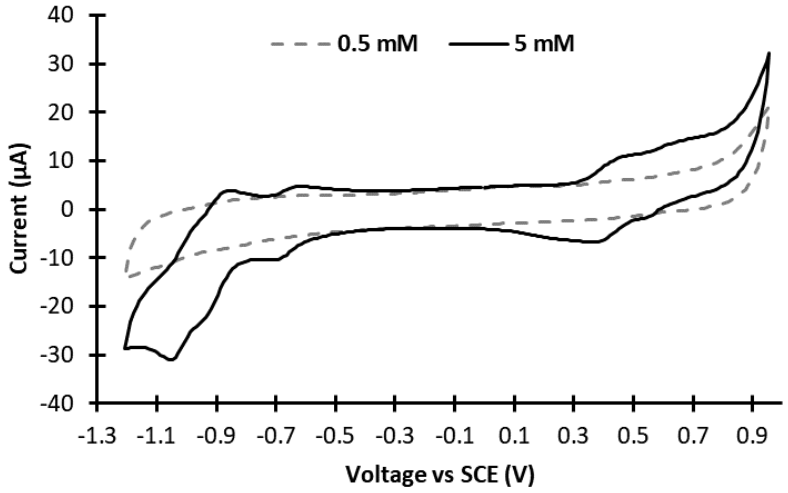

Figure 97. 20 mV/s cyclic voltammetry from -1.2 V to 0.95 V vs. SCE. WE: GCE. Dashed line: 0.5 mM of compound **C2**. Solid line: 5 mM of compound **C2**.

Using a gold WE instead modifies substantially the voltagram shape, as shown in **Figure 98**.

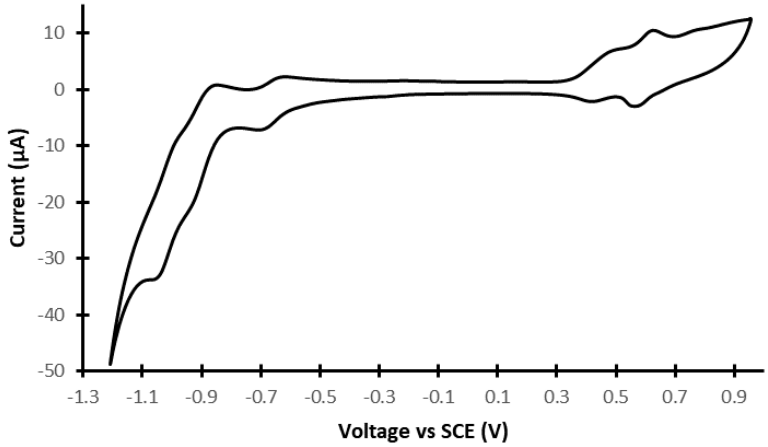

Figure 98. 20 mV/s cyclic voltammetry from -1.2 V to 0.95 V vs. SCE. WE: Gold. 5 mM of compound **C2**.

Compound **C2** presents worse solubility than compound **C3**, therefore its current response for the same concentration is smaller. Nevertheless, 5 mM response with GCE and

gold WEs show two main differences compared to the characterization voltagrams for compound **C3**:

- Three oxidation and two reduction processes are present in the positive voltage region, probably associated with iodide and bromide redox processes.
- A profound and irreversible reduction process is taking place with an approximate peak current potential of -900 mV vs. SCE, indicating a Kolbe electrolysis.

Figure 98 voltagram, the one corresponding to the use of the gold working electrode, presents more explicit current waves. Hence, it is the voltagram used to determine the threshold and peak current potentials. Processes (1) to (4) will be kept as shown in *2.1. Electrochemical characterization of compound C1*:

- $I_3^- + 2e^- \rightleftarrows 3I^-$ (**Equation 35**) as process (1).
- $3I_2 + 2e^- \rightleftarrows 2I_3^-$ (**Equation 36**) as process (2).
- $MV^{2+} + 1e^- \rightleftarrows MV^{\circ+}$ (**Equation 33**) as process (3).
- $MV^{\circ+} + 1e^- \rightleftarrows MV^0$ (**Equation 34**) as process (4).

Three additional processes, as commented below, shall be taken into consideration:

- $2 \cdot R - COOH + 4e^- \longrightarrow R - R + CO_2 + H_2$ (**Equation 39**) as process (5).
- $3Br_2 + 2e^- \leftrightarrows 2Br_3^-$ (**Equation 40**) as process (6).
- $2Br_3^- + 4e^- \leftrightarrows 6Br^-$ (**Equation 41**) as process (7).

Processes (3), (4) and (5) can be studied regarding the negative side of the cyclic voltagram. **Figure 99a** shows the graphical obtention of the current peak and threshold potentials for the oxidation processes, in red. **Figure 99b** shows the graphical obtention of the current peak and threshold potentials for the reduction processes, in blue.

The obtained threshold and current peak potentials are:

- $E_{th}^R(3) = -625$ mV
- $E_p^R(3) = -690$ mV
- $E_{th}^R(5) = -830$ mV
- $E_p^R(5) = -925$ mV
- $E_{th}^R(4) = -940$ mV
- $E_p^R(4) = -1060$ mV
- $E_{th}^O(4) = -940$ mV
- $E_p^O(4) = -860$ mV
- $E_{th}^O(3) = -710$ mV
- $E_p^O(3) = -640$ mV

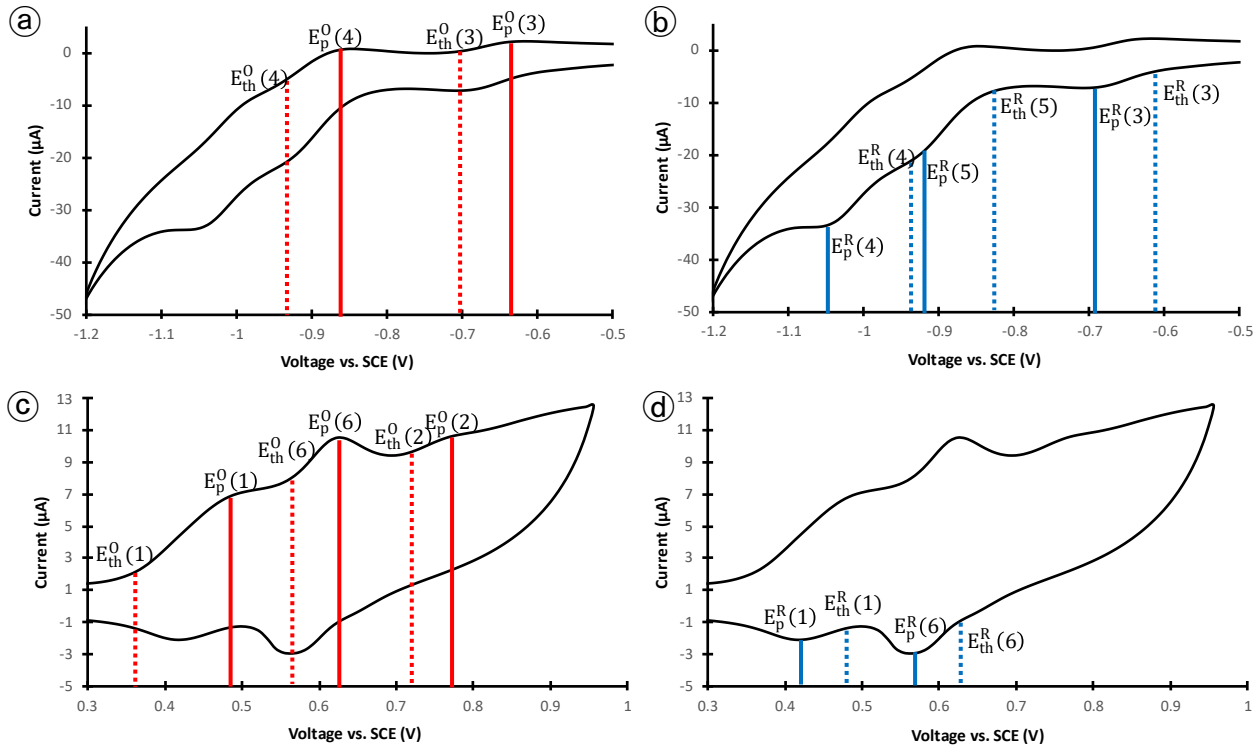

Figure 99. 20 mV/s cyclic voltammetry from -1.2 V to 0.95 V vs. SCE. WE: Gold. 5 mM of compound **C2**. ⓐ Detailed view on negative voltages vs. SCE: oxidation processes (3), (4) and (5). Current peak potential projection (solid red line) and threshold potential (dotted red line). ⓑ Detailed view on negative voltages vs. SCE: oxidation processes (3), (4) and (5). Current peak potential projection (solid blue line) and threshold potential (dotted blue line). ⓒ Detailed view on positive voltages vs. SCE: oxidation processes (1), (2) and (6). Current peak potential projection (solid red line) and threshold potential (dotted red line). ⓓ Detailed view on positive voltages vs. SCE: reduction processes (1) and (6). Current peak potential projection (solid blue line) and threshold potential (dotted blue line).

A Kolbe electrolysis is induced with a threshold potential of -830 mV vs. SCE and a current peak potential of -925 mV vs. SCE. This is an undesired effect in the controlled drug release application. Therefore, surpassing the mentioned threshold potential shall be avoided.

Figure 99c and **Figure 99d** show the graphical obtention of the respective iodide and bromide cations redox potentials, these are the processes (1), (2) and (6). We should keep in mind the conclusions regarding redox process (2) obtained in *2.1. Electrochemical characterization of compound C1*: whether it is irreversible in the present conditions or its reduction potential is in the far negative region < 1.2 V vs. SCE. It seems that process (7) is not reaching given the sweep range used in this cyclic voltammetry. Thus, no other reversible or irreversible processes are observed. It appears that bromide current waves present a larger area, meaning its reactivity is higher than the one present by the iodide cations.

The obtained threshold and current peak potentials are:

- $E_{th}^{O}(1) = 360$ mV
- $E_{p}^{O}(1) = 480$ mV
- $E_{th}^{O}(6) = 560$ mV
- $E_{p}^{O}(6) = 625$ mV
- $E_{th}^{O}(2) = 715$ mV
- $E_{p}^{O}(2) = 775$ mV
- $E_{th}^{R}(6) = 630$ mV
- $E_{p}^{R}(6) = 560$ mV
- $E_{th}^{R}(1) = 470$ mV
- $E_{p}^{R}(1) = 425$ mV

Nevertheless, given the poor solubility and the electrochemical complexity of the compound, the cyclic voltammetry experiments are repeated with both the gold electrode (see **Figure 100**, solid line) and GCE electrode (see **Figure 100**, dashed line) through a Rotating Disk Electrode (RDE) at 2500 rpm. The voltagram obtained with each of them is compared. The voltages for the anodic and cathodic currents suffer almost no difference.

The oxidation and reduction potentials, and the current associated with each process are almost identical, independent of the working electrode used.

Peak current potential in static conditions, *i.e.*, without rotating working electrode, will always be present before (in the direction of the sweep) the maximum transfer potential. In static conditions, the resultant species of the redox process at the vicinity of the WE may impede the arrival of new reagents, slowing down the reaction. Rotating conditions avoid this situation, impeding the formation of the mentioned barrier, and allowing the arrival of new reagents to the WE interface.

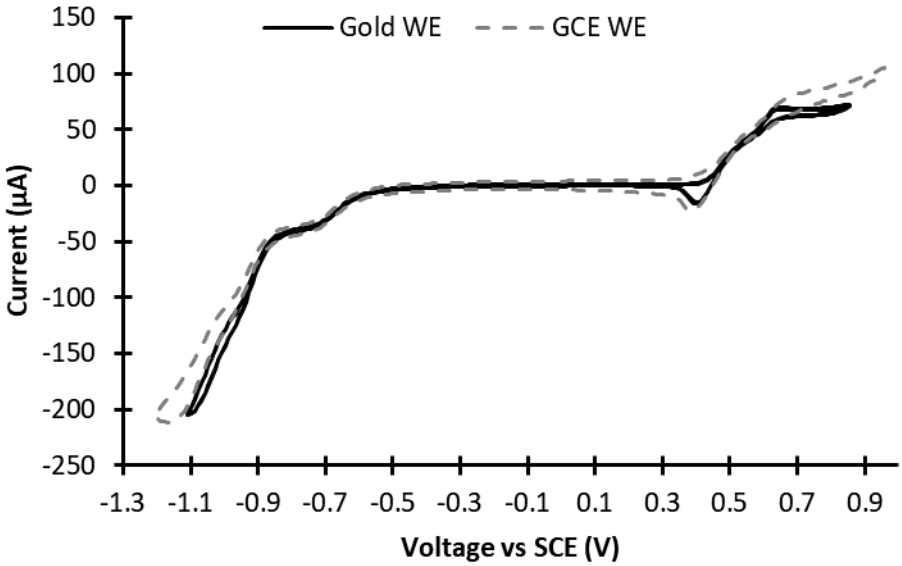

Figure 100. Cyclic voltagram comparison: GCE (dashed line) and gold (solid line) as WE.

Under RDE conditions, and given an arbitrary electrochemical process, namely (X), the threshold potential to start the reduction process (X), $E_{th}^{R}(X)$, can be identified by the increase of the current slope and shall correspond to the one obtained in static conditions. Once the process reaches its maximum transfer potential $E_{mt}^{R}(X)$, further voltages will not increment the reduction rate. Hence, the current slope will flatten. The same phenomenon can be applied to oxidation processes, hence obtaining $E_{th}^{O}(X)$ and $E_{mt}^{O}(X)$. Reversible processes will satisfy the following conditions (**Equation 42** and **Equation 43**):

$$E_{th}^{R}(X) = E_{mt}^{O}(X) \qquad \textbf{Equation 42}$$

$$E_{mt}^{O}(X) = E_{p}^{R}(X) \qquad \textbf{Equation 43}$$

The threshold potentials for the oxidation of processes (3) and (1) and the reduction of processes (6), (3), and (5) can be easily identified as the start of an increasing current slope (in absolute terms). Threshold potentials for processes that occur while the preceding process did not reach its maximum current are hidden. Maximum transfer potentials can be identified as a return to the background slope, mostly horizontal (with a slight slope in the extremes due to the current induced by higher absolute voltages and the solution inherent conductivity). Maximum transfer potentials for oxidation processes (4), (3), and (2), and for reduction processes (1), (3), and (4) can be obtained.

The study of redox processes (1), (2), and (6) is done regarding the positive voltages side of the voltagram, as shown in **Figure 101a**.

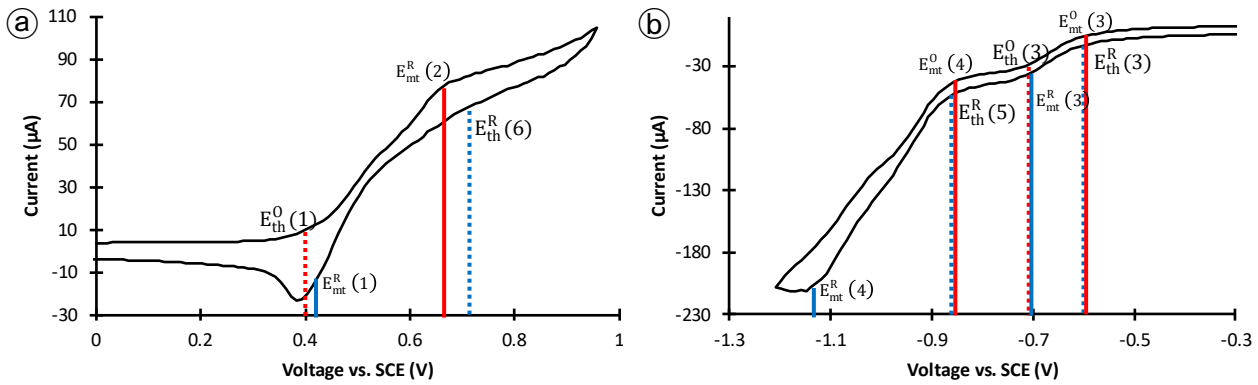

Figure 101. 20 mV/s cyclic voltammetry from -1.1 V to 0.85 V vs. SCE. WE: Gold RDE at 2500 rpm. 5 mM of compound **C2**. ⓐ Detailed view on positive voltages vs. SCE: processes (1), (2) and (6). Maximum transfer potential projection (solid line) and threshold potential (dotted line) for oxidation (in red) and reduction (in blue) processes. ⓑ Detailed view on negative voltages vs. SCE: processes (3), (4) and (5). Maximum transfer potential projection (solid line) and threshold potential (dotted line) for oxidation (in red) and reduction (in blue) processes.

From the former:

- $E_{th}^{O}(1) = 400$ mV
- $E_{mt}^{O}(2) = 660$ mV
- $E_{th}^{R}(6) = 710$ mV
- $E_{mt}^{R}(1) = 420$ mV

These values cannot be compared to those obtained by Sun *et al.* [335], given the difference in between both setups. It is relevant to point out that both redox processes occur in the >0 V vs. SCE region.

The study of redox processes (3), (4), and (5) is done regarding the negative voltages side of the voltagram, as shown in **Figure 101b**.

The threshold and peak potentials for processes (3), (4), and (5) are:

- $E_{th}^{R}(3) = -600$ mV
- $E_{mt}^{R}(3) = -710$ mV
- $E_{th}^{R}(5) = -870$ mV
- $E_{mt}^{R}(4) = -1130$ mV
- $E_{mt}^{O}(4) = -870$ mV
- $E_{th}^{O}(3) = E_{p}^{R}(3) = -710$ mV
- $E_{p}^{O}(3) = E_{th}^{R}(3) = -600$ mV

Comparing our results with the ones obtained by Kim *et al.* [333], in both static and RDE conditions and comparing the results in static conditions for compound **C2** with the results obtained for compound **C1**:

Kim *et al.* [333]:

- $E_{pc}^{1} = -736$ mV
- $E_{pc}^{2} = -1046$ mV
- $E_{pa}^{2} = -982$ mV
- $E_{pa}^{1} = -672$ mV

Static conditions (dif. w. C1):

- $E_{p}^{R}(3) = -690(+35)$ mV
- $E_{p}^{R}(4) = -1060(-10)$ mV
- $E_{p}^{O}(4) = -860(-20)$ mV
- $E_{p}^{O}(3) = -640(-15)$ mV

RDE conditions:

- $E_{mt}^{R}(3) = -710$ mV
- $E_{mt}^{R}(4) = -1130$ mV
- $E_{mt}^{O}(4) = -870$ mV
- $E_{mt}^{O}(3) = -600$ mV

The first reduction potential, the one of most interest, is 46 mV smaller than the results obtained by Kim *et al.* $E_{p}^{R}(3)$, -690 mV vs. SCE, indicating the voltage application that maximizes compound **C2** reduction to induce the cargo release taking into consideration mass limitation conditions. On RDE, the $E_{mt}^{R}(3)$ obtained is -710 mV vs. SCE, the difference between $E_{mt}^{R}(3)$ and $E_{p}^{R}(3)$ is an indicator of the mass transfer limitation effect for the present conditions. The reduction starts upon surpassing $E_{th}^{R}(3)$, -600 mV vs. SCE, therefore a voltage value between $E_{th}^{R}(3)$ and $E_{p}^{R}(3)$ can be applied to obtain the reduction at increasing rates. A Kolbe electrolysis is induced with a threshold potential of -830 mV vs. SCE. Hence, higher values than $E_{th}^{R}(5)$ shall be avoided.

Subsection summary: We characterized **C2**, the gate employed in the electro-responsive MSNs grafted onto the conductive polymer. **C2** is different from **C1**. Hence different thresholds and peak voltages for the electrochemical reaction of interest are expected. We identified the threshold voltage at -600 mV vs. SCE, 25 mV lower (in absolute terms) than for **C1**. Peak and maximum transfer voltages were identified at -690 mV and -710 mV vs. SCE, respectively (**C1** peak voltage was -725 mV vs. SCE). Therefore, **C2** presents even lower voltage levels needed to induce the cargo release. Additionally, undesired electrolysis would be induced upon surpassing the -830 mV vs. SCE. Hence -830 mV vs. SCE is an upper limit voltage to be avoided.

2.3. Electrochemical characterization of PEDOT:PSS-*co*-MA with gated MSNs

2.3.1. Literature review and analysis

PEDOT:PSS-*co*-MA exhibits oxidation and reduction potentials in the range of those of compound **C2**. Following the work of Collazos-Castro *et al.* with PEDOT:PSS over 1 cm^2 gold-coated glass slides (Sigma–Aldrich, 10 nm gold layer on a 2 nm Ti layer to bind the gold to an aluminasilicate glass) [326]. At 50 mV/s, the CV shows two waves corresponding to the reduction of PEDOT polarons and bipolarons (**Figure 102**):

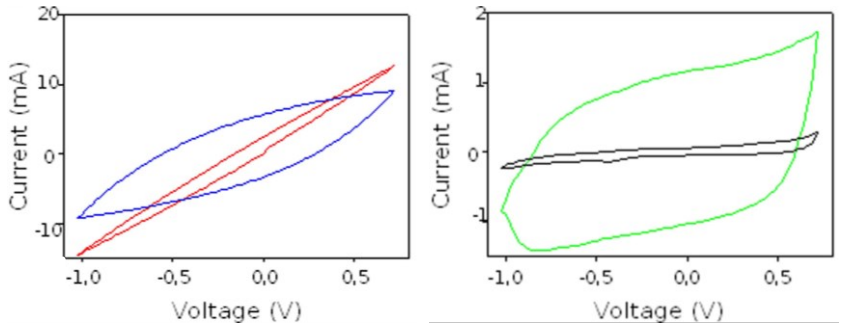

Figure 102. PEDOT:PSS decreases the impedance of gold electrodes and operates as an electrochemical pseudocapacitor. Data from experiments performed in pH 7.4, 0.05 M PBS. D) CV of 48 mC/cm^2-films at 0.05 V/s (black), 0.5 V/s (green); 5 V/s (blue) or 50 V/s (red). Reproduced with permission from [326]. Biomaterials © 2010 Elsevier.

PEDOT:PSS-*co*-MA (dash line) is compared with PEDOT:PSS (solid line) coating on a 0.92 mm long ⌀7 µm carbon microfiber electrodes by Collazos-Castro *et al.* at [328] as shown in **Figure 103**. The most suitable scan speed for the cyclic voltammetry over 1 cm^2 gold-coated glass slides is 0.05 V/s, *i.e.*, 50 mV/s. Higher scan speeds can be applied to the CV because a carbon micro-electrode is used instead.

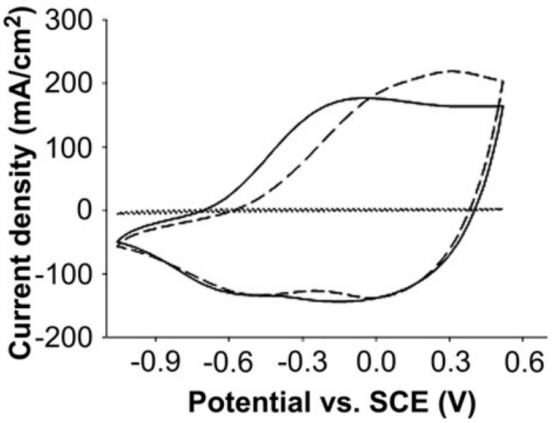

Figure 103. Cyclic voltammograms (50 V/s) (sic) of carbon microfiber electrodes uncoated (dotted line) or coated (96 mC/cm²) with PEDOT:PSS (solid line) or PEDOT:PSS-*co*-MA (dash line). Reproduced with permission from [328]. Biomaterials © 2013 Elsevier.

Therefore, from [328], we can conclude that PEDOT:PSS coated electrodes and PEDOT:PSS-*co*-MA coated electrodes will have almost identical reduction behavior. However, the latter presents higher oxidation voltages and ~20% higher anodic current for voltages higher than 0 V vs. SCE.

The redox reaction is described by Marzocchi *et al.* [87] and Tang *et al.* [338]. It is shown in **Equation 44**:

$$PEDOT^{+}:PSS^{-} + C^{+} + e^{-} \rightleftarrows PEDOT^{0} + C^{+}:PSS^{-} \qquad \textbf{Equation 44}$$

The fabrication process of the conductive polymer with gated MSNs will be explained in detail in *3.2.1. Design of conductive polymer bearing voltage-responsive MSN*. In summary, the PEDOT:PSS-*co*-MA is coated over 1 cm² gold-coated of glass slides, namely **P0**. Prof. Collazos-Castro's group themselves supplied these electrodes. Rh B loaded MSNs externally functionalized with (3-aminopropyl)trimethoxysilane, namely **S4**, were bonded to activated **P0** in the presence of the coupling agents EDC and sulfo-NHS in MES buffer, resulting in **P1**. 4,4'-bypiridinium-1-(carboxymethyl)-1'-methyl iodide bromide (**C2**) can be activated with the same procedure. The next step is forming an amide bond between the carboxylic group in **C2** and free amino moieties in MSNs. The overnight immersion of **P1** in activated **C2** yields **P2**, which presents a covalent attachment of **C2**. **P2** immersion in a heparin solution in PBS yields **P3**. For a visual representation, see **Figure 119**.

Given the electrochemical response of PEDOT:PSS-*co*-MA described by Collazos-Castro *et al.* [328], similar to the one of PEDOT:PSS, the cyclic voltammetry protocol over PEDOT:PSS described in [326] is used as reference, which uses the same 1 cm² gold-coated glass-slides as

we do. We will study its differences with **P3**, therefore visualizing compound **C2** redox processes in the presence of heparin and Rhodamine B under cyclic voltammetry.

We shall take into consideration the heparin and Rhodamine B redox response. Rhodamine B electrochemical behavior has been studied by Honeychurch [339]. Its chemical structure is shown in **Figure 104**.

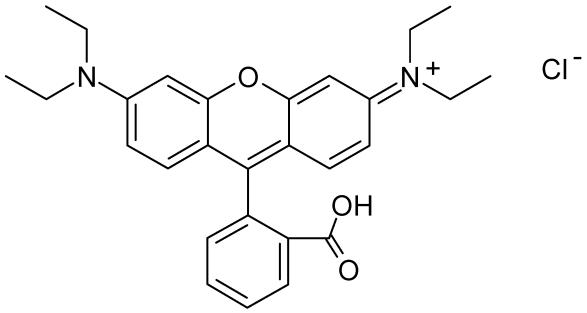

Figure 104. Structure of Rhodamine B. Reproduced from [339]. Sensors (CC BY 4.0) 2022 MDPI.

For neutral pH conditions and in the absence of a previously induced oxidation, the first reduction threshold potential is at -800 mV vs. SCE, and its peak potential is at -950 mV vs. SCE. Rh B reduction is far from compound **C2** reduction of interest with threshold and peak current potentials of -600 and -690 mV vs. SCE.

Guo *et al.* [340] and Guo & Amemiya [341] developed heparin detection voltammetric systems. With this purpose, these works clarify the heparin electrochemical behavior. Its chemical structure is shown in **Figure 105**.

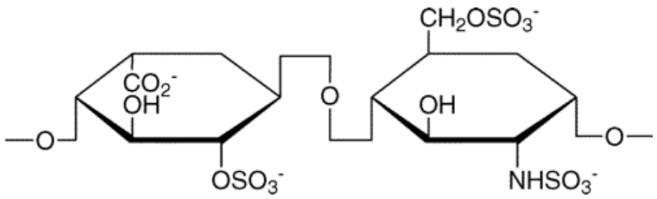

Figure 105. Major disaccharide repeating unit of heparin. Reproduced with permission from [340]. Analytical Chemistry © 2005 American Chemical Society.

The sensor response is in the reduction with a potential threshold of ~900 mV vs. SCE and with a peak potential of ~960 mV vs. SCE. This corresponds with the know oxidation peak potential for heparin of 900 mV vs. Ag/AgCl from former studies (see Chevion *et al.* [342]). Hence, no interference from heparin reduction is expected. However, compound **C2** reduction potential will be shifted to more negative potentials due to the electrostatic interaction with the heparin cap, as explored by Zhang *et al.* [343]. In their work, the threshold voltage is kept, and the peak potential is shifted 47 mV.

2.3.2. Experimental setup

PGSTAT100 from Autolab is used for the application of cyclic voltammetry. The electrochemical cell is composed by:

- A Saturated Calomel Electrode (SCE) from Crison as the reference electrode.
- A Ring Pt electrode from Crison as the counter-electrode.
- **P0** or **P3** as the working electrodes, respectively.

All experiments are performed in 12 mL PBS solution. All cyclic voltammetry experiments are performed without stirring. Potential pulse current response is applied under stirring conditions.

An image of the electrochemical cell is shown in **Figure 106**.

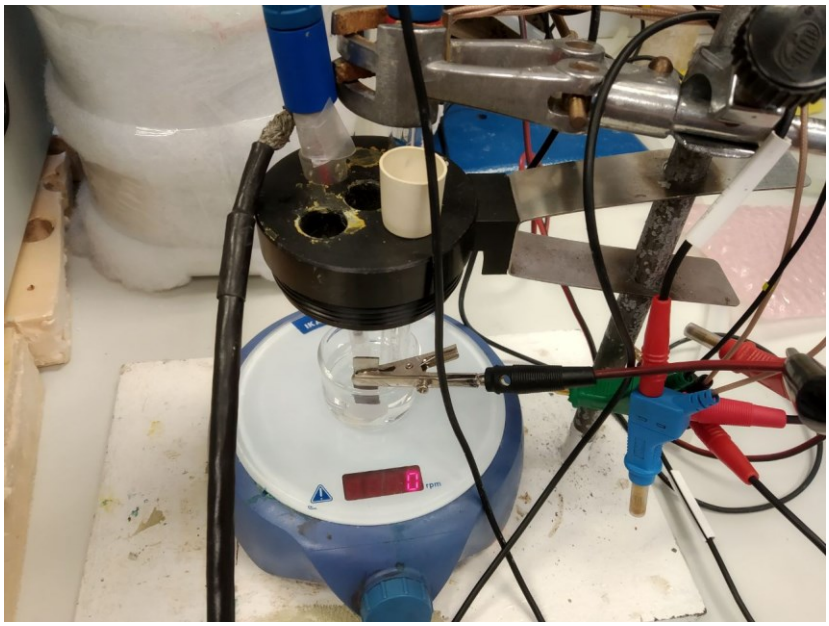

Figure 106. Electrochemical cell setup for the characterization of **C2** reduction under **P3** conditions.

2.3.3. PBS molarity influence on PEDOT:PSS-*co*-MA cyclic voltagram

A 100 mV/s cyclic voltammetry is performed under **P0** as the working electrode in two different PBS concentrations: 5 mM and 25 mM. The results are shown in **Figure 107**.

The results show that PEDOT:PSS-*co*-MA presents a reduction potential peak in -550 mV vs. SCE, starting at -400 mV, which is consistent with the results shown in **Figure 103**. The effect of the cathodic and anodic currents of the co-polymer is increased with the augment of PBS

concentration. Therefore, for the study of the compound **C2** redox processes under **P3** conditions, 5 mM PBS is used.

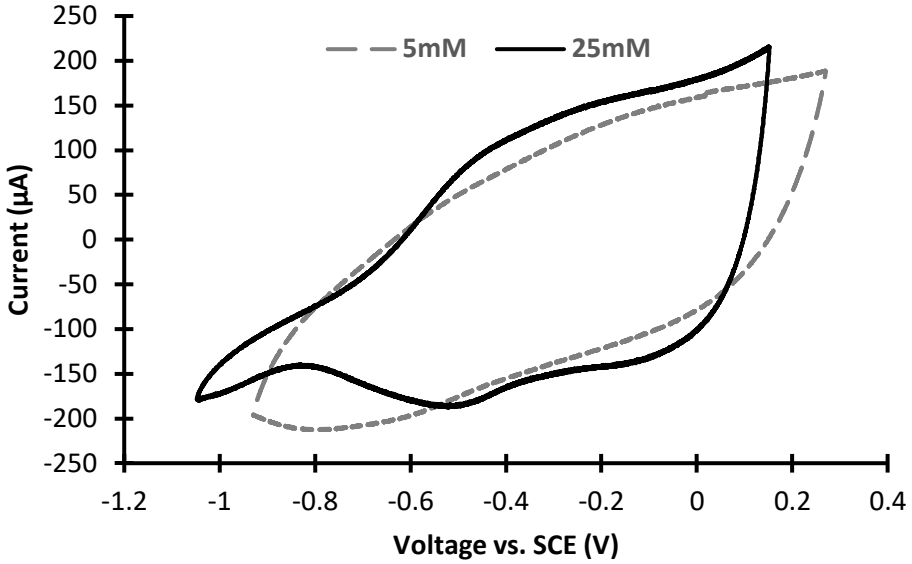

Figure 107. Cyclic voltagram (100 mV/s) on **P0** under two different PBS concentrations solution: 5 mM (dashed) and 25 mM (solid).

3.3.4. Compound C2 redox processes under P3 conditions

In the following **Figure 108**, **Figure 109**, and **Figure 110** are shown the cyclic voltammetry response of **P0** and **P3** in 5 mM PBS solution for 50 mV/s, 500 mV/s and 2 V/s respectively.

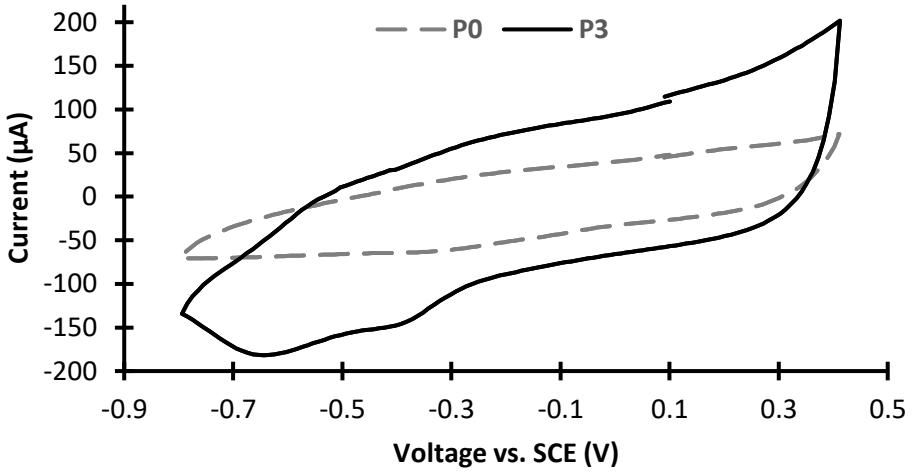

Figure 108. 50 mV/s comparative cyclic voltammetry of **P0** (dashed line) and **P3** (solid line) in 5 mM PBS.

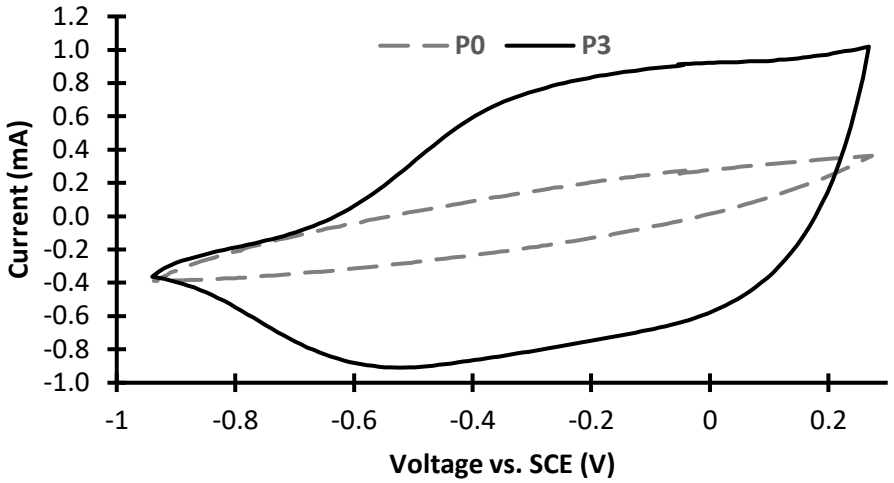

Figure 109. 500 mV/s comparative cyclic voltammetry of **P0** (dashed line) and **P3** (solid line) in 5 mM PBS.

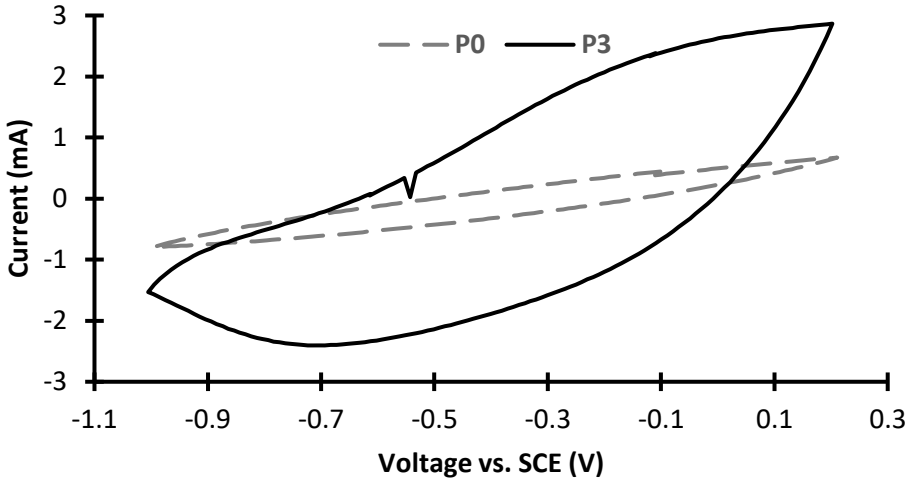

Figure 110. 2 V/s comparative cyclic voltammetry of **P0** (dashed line) and **P3** (solid line) in 5 mM PBS.

Voltagrams of **P0** can be interpreted as baselines for **P3** voltagrams, taking into account that **P3** is compound by **P0** with compound **C2**, mesoporous silica nanoparticles, heparin tape and Rh B cargo. Hence, **P3** response difference with respect to **P0** is due to these additional components. In all three cases **P0** currents are smaller in absolute terms than the ones in **P3**, and they can be attributed to the mentioned elements.

P0 small response can be explained to the PBS concentration selection: with 5 mM, PEDOT:PSS-*co*-MA redox curves are smoothed as shown in *2.3.3. PBS molarity influence on PEDOT:PSS-co-MA cyclic voltagram*. Higher scan speeds (500 mV/s and 2 V/s) make cathodic currents, corresponding to reducing voltages, difficult to observe.

50 mV/s voltagram, in **Figure 108**, shows reduction waves in a clearer way than other scan speeds. The analysis in the detail is performed in **Figure 111**.

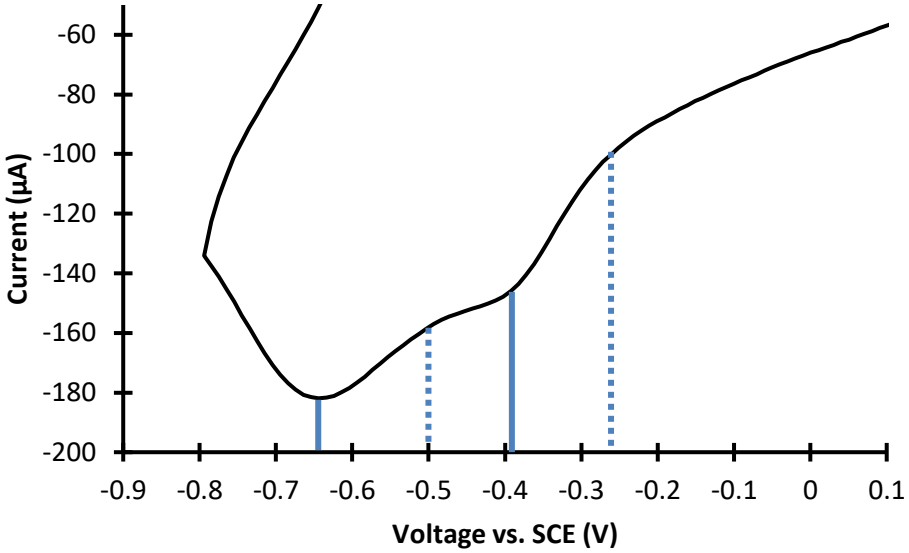

Figure 111. 50 mV/s cyclic voltammetry of **P3** in 5 mM PBS. Close view to negative voltages region. Threshold and peak current potentials indicated (dotted and solid blue lines respectively).

We may expect different reduction processes in this voltage range:

- -400 mV threshold, -550 mV peak vs. SCE from PEDOT:PSS-*co*-MA.
- -600 mV threshold, -690 mV peak vs. SCE from compound **C2**, in gold WE conditions.

The first current wave may be associated with the PEDOT:PSS-*co*-MA reduction, with a threshold voltage of -270 mV vs. SCE and peak voltage of -394 mV vs. SCE.

The compound **C2** reduction potential and is found in the second wave current with a threshold voltage of -500 mV vs. SCE and a peak potential of -650 mV vs. SCE.

3.3.5. Pulse response analysis

Subthreshold voltages (-420 mV vs. SCE) and trigger voltages (-640 mV vs. SCE, which is over the threshold and below reduction peak potential for compound **C2**) are applied to **P0** and **P3** in 5 mM PBS solution under stirring conditions for 10 minutes (900 s). Ring Pt electrode from Crison is used as the counter-electrode, and Saturated Calomel Electrode (SCE) from

Crison as the reference electrode as the previous experiments. 10 minutes response and first 100 seconds response zoom in are shown in **Figure 112** and **Figure 113**, respectively.

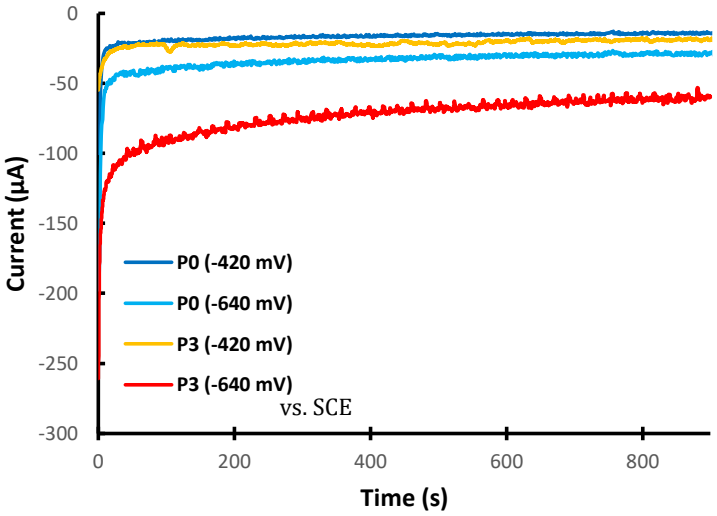

Figure 112. Potential pulse current response in 5 mM PBS for **P0** in subthreshold voltage (dark blue line), over-threshold voltage (cyan line), and **P3** in s subthreshold voltage (yellow line), over-threshold voltage (red line). 10 minutes experiment.

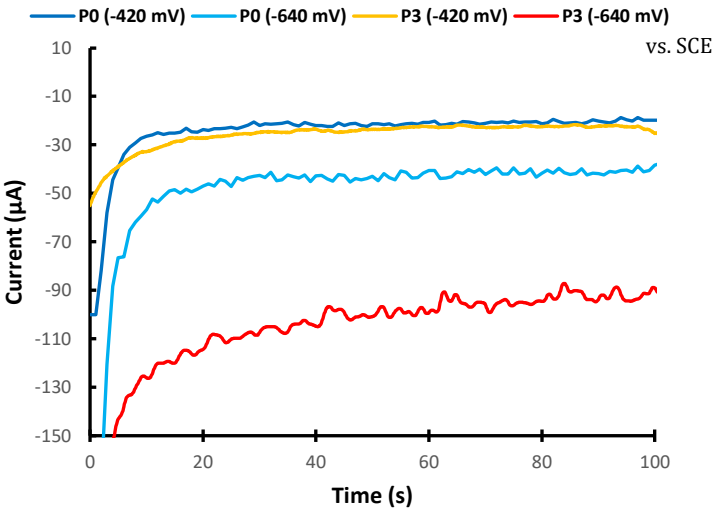

Figure 113. Potential pulse current response in 5 mM PBS for **P0** in subthreshold voltage (dark blue line), over-threshold voltage (cyan line), and **P3** in s subthreshold voltage (yellow line), over-threshold voltage (red line). First 100 seconds zoom in.

The current response for subthreshold voltage pulses is slightly different for **P0** and **P3**, as for **P3** a PEDOT:PSS-*co*-MA reduction (and an increase in its conductivity) is expected. The capacitance of **P0** presents smaller equivalent series resistance, as shown by the higher initial peak compared with the response of **P3**.

-640 mV vs. SCE voltage trigger current response in **P3** is significantly higher than in **P0** due to the compound **C2**reduction. **P3** current at second 5 is -140 μA, vs. -81 μA for **P0**. The difference is increased in the following time samples due to the rapid stabilization of **P0** response in -50 μA (second 15), which will slowly decrease to -40 μA (minute 10), whereas **P3** reaches -110 μA at second 30, and -100 μA at second 60. At second 900 (minute 10), the current is still -60 μA. Initial higher current should be related to the mentioned reductions. Once compound **C2** is reduced, heparin, the capping moiety, will no longer act as a diffusion barrier for Rh B, hence starting its release.

In a nutshell, three stages can be established:

1. First 5 s: non-faradaic current predominance, with a -250 μA peak.
2. Seconds 5 to 60: compound **C2** reduction make up 55% of the current.
3. From the second 60: ohmic current (33% of the current vs. the initial peak).

The fluorometry measurement of Rh B confirms the cargo's gradual release upon the trigger voltage's application, as shown in **Figure 114**.

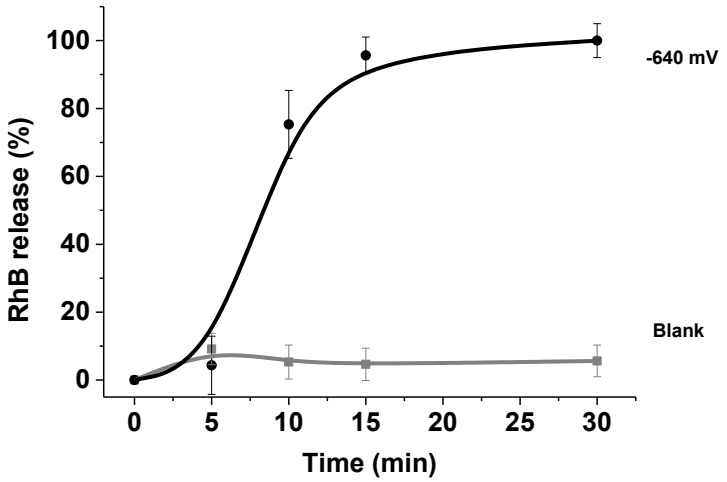

Figure 114. Release profiles of Rh B from **P3** films in PBS at pH 7.5 alone and upon the application of -640 mV vs. SCE. Reproduced with permission from [220]. Journal of Controlled Release © 2020 Elsevier.

Subsection summary: The conductive polymer PEDOT:PSS-*co*-MA bearing the electro-responsive MSNs is electroactive. It will suffer a reduction with -270 and -394 mV vs. SCE threshold and peak voltages, respectively. Nevertheless, this reduction has been reported positive for cell adhesion and proliferation. The **C2** threshold and peak voltages vary depending if it is in solution or as part of the molecular gates on the conductive polymer. The values vary from -600 to -500 mV vs. SCE for the threshold voltage, and from -690 to -650 mV vs. SCE for the peak voltage. The induced electrical current will be a function of the faradic and non-faradic effects of the conductive polymer and **C2** reductions upon applying the trigger potential.

3. Voltage-responsive MSN on PEDOT:PSS-*co*-MA design and validation

In this section we will reproduce our article, García-Fernández *et al.* [220], corresponding to the design, characterization and release using voltage-responsive mesoporous silica nanoparticles (MSNs), and the design, characterization and release of MSNs in the conductive polymer PEDOT:PSS-*co*-MA. Finally, we will show the validation in cell culture.

The chemicals *n*-cetyltrimethylammonium bromide (CTABr), sodium hydroxide (NaOH), tetraethylorthosilicate (TEOS), (3-iodopropyl)trimethoxysilane, (3-aminopropyl)trimethoxysilane (APTES), *N*-(3-dimethylaminopropyl)-*N'*-ethylcarbodiimide (EDC), *N*-hydroxysulfosuccinimide sodium salt (sulfo-NHS), 2-(*N*-morpholino)ethanesulfonic acid (MES), phosphate buffered saline (PBS), rhodamine B, acetaldehyde ACS reagent ≥99.5%, 4,4'-bipyridine, EDOT, poly[(4-styrenesulfonic acid)-*co*-(maleic acid)] (PSS-*co*-MA, 20,000 Mw), gold-coated glass slides, Dulbecco's Modified Eagle Medium (DMEM) and Fetal Bovine Serum (FBS) were purchased from Sigma Aldrich. The cell nuclei staining reagent Hoechst 33342 was purchased from Thermo Fisher Scientific and cell proliferation reagent WST-1 from Sigma Aldrich. All the other reagents were of a general laboratory grade and were purchased from Sigma, Fischer or Scharlab, unless otherwise stated.

3.1. Voltage-responsive MSN

3.1.1. Design of voltage-responsive MSN

The preparation process of the voltage-responsive MSN, namely **S3**, is shown in **Figure 115**. It involves using MSNs that were first loaded with Rh B (**S0**). Then, the external surface of the loaded nanoparticles was functionalized with (3-iodopropyl)trimethoxysilane (**S1**). Afterward, the iodopropyl moieties were reacted with *N*-methyl-4,4'-bipyridinium derivative **C1**, yielding **S2**. Finally, the pores were capped upon adding heparin (**S3**). **C1** was obtained by a simple reaction of 4,4'-bipyiridine with methyl iodide.

The surface of MSNs is functionalized with a positively charged N,N'-dimethyl-4,4'-bipyridinium (also known as paraquat or methyl viologen) derivative and capped with the negatively charged polysaccharide heparin via electrostatic interactions. The ionic electrostatic interaction between bipyridinium derivate and heparin on the external surface of the nanoparticles was expected to avoid the release of the entrapped cargo. In contrast, reducing the former by applying a voltage would result in the detachment of heparin from the surface

with subsequent pore opening and Rhodamine B (Rh B) release. Methyl viologen was selected because of its well-known redox properties and easy reduction at relatively low potentials, as shown by Bhatti *et al.* [344] and Orgill *et al.* [345]. Moreover, heparin (a sulfonated polysaccharide) is a biocompatible capping moiety that, for instance, has been used to improve neuronal growth, cell proliferation, and migration, as shown by Zhang [346] and Collazos-Castro *et al.* [347].

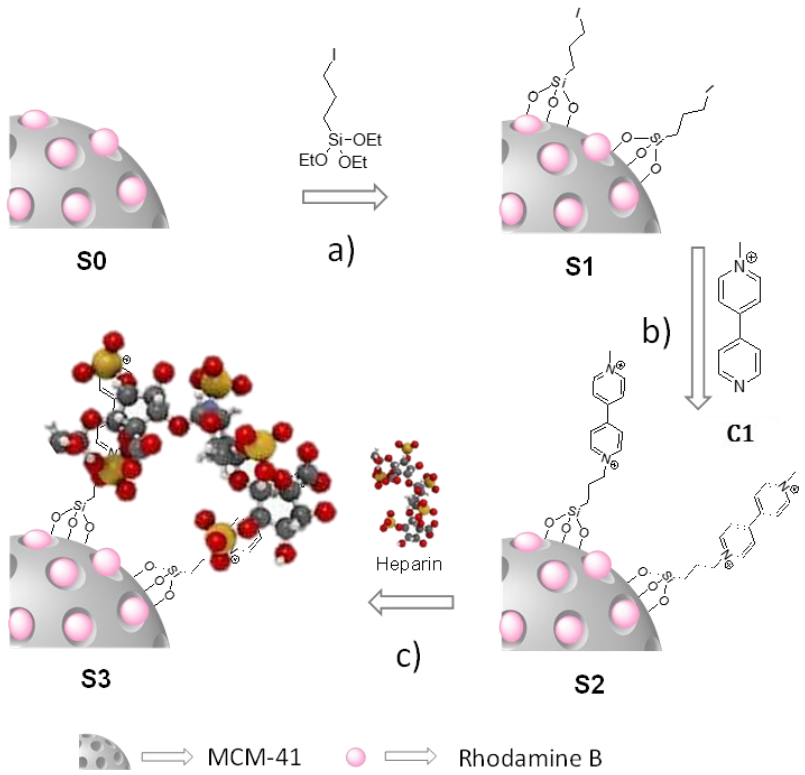

Figure 115. Schematic representation of the synthesis of voltage-responsive **S3** nanoparticles. MSNs are loaded with Rh B in CH_3CN for 24 h. Then, **S0** nanoparticles were functionalized with (3-iodopropyl)trimethoxysilane in CH_3CN at room temperature for 5.5 h (**S1**). The obtained nanoparticles are reacted with **C1** by nucleophilic substitution in refluxed CH_3CN for 72 h (**S2**). Finally, nanoparticles were suspended in heparin PBS solution for 3 h, yielding the final heparin-capped solid (**S3**). Reproduced with permission from [220]. Journal of Controlled Release © 2020 Elsevier.

Synthesis of MSNs loaded with Rhodamine B (S0): The starting MSNs were synthesized following well-established procedures as previously reported by García-Fernández *et al.* [348] and Lozano-Torres *et al.* [349]. Once obtained the starting material, nanoparticles (150 mg) and Rh B (45 mg, 0.8 mmol/g solid) were suspended in CH_3CN (6 mL). The suspension was stirred at room temperature for 24 h and, finally, the solid **S0** was obtained by centrifugation.

Synthesis of 3-iodopropyl-functionalized MSNs (S1): For the preparation of **S1**, 150 mg of **S0** was suspended in a saturated solution of Rh B in anhydrous CH_3CN (6 mL). An excess of (3-

iodopropyl)trimethoxysilane (58.8 µL, 4.25 mmol/gsolid) was added, and the final mixture was stirred at room temperature for 5.5 h. The resulting pink solid (**S1**) was isolated by centrifugation, washed twice with CH_3CN (5 mL), and dried at 37°C.

Synthesis of *N*-methyl-4,4'-bypiridinium (C1): 4,4´-bipyiridine (3.0 g, 19.3 mmol) was transferred to a two-necked round bottom flask equipped with a condenser. Anhydrous CH_3CN (120 mL) was added, and the system was purged with Argon. Once the solution was at reflux, methyl iodide (1200 µL, 19.3 mmol) was added dropwise, and the reaction was maintained at reflux for 12 h. Finally, the solvent was removed under reduced pressure. The product was purified by washing with cold methanol to precipitate the dimethylated compound. Methanol was removed under reduced pressure to obtain the product (**C1**) as an orange solid in 93.9% yield (5.39 g, 18.12 mmol).

Synthesis of heparin capped-MSNs (S3): Solid **S2** was obtained after an SN_2 bimolecular substitution between the iodopropyl moieties attached to the external surface of solid **S1** and product **C1**. For this synthesis, 75 mg of **S1** was suspended in a saturated solution of Rh B in anhydrous CH_3CN (6 mL), and compound **C1** was added (187.5 mg, 1.10 mmol). The suspension was refluxed for 72 h, and the final solid **S2** was isolated by centrifugation, washed twice with CH3CN, and dried at 37°C. Then, 20 mg of **S2** was suspended in PBS (5 mL), and 20 mg of heparin was added. The suspension was stirred for 3 h at room temperature. **S3** was isolated by centrifugation, washed with water, and dried at 37°C.

Synthesis of 3-aminopropyl functionalized MSNs (S4): For the preparation of **S4**, 150 mg of **S0** was suspended in a saturated solution of Rh B in anhydrous CH_3CN (6 mL). Then, an excess of (3-aminopropyl)trimethoxysilane (175.50 µL, 5 mmol/g solid) was added, and the final mixture was stirred at room temperature for 5.5 h. The resulting pink solid (**S4**) was isolated by centrifugation, washed twice with CH_3CN (5 mL), and dried at 37°C.

3.1.2. Characterization of voltage-responsive MSN

Contents of Rh B, 3-iodopropyl, bipyridinium dication, and heparin for the studied solids were determined by thermogravimetric analysis (TGA), elemental analysis (EA), and inductive coupled plasma mass spectrometry (ICP-MS).

Thermogravimetric analyses were carried out on a TGA/SDTA 851e Mettler Toledo balance, using an oxidant atmosphere (air, 80 mL/min) with a heating program consisting of a heating ramp of 10°C per min from 25°C to 100°C. The temperature was kept at 100°C for 60 min and, finally, a new heating ramp of 10°C per min from 100°C to 1000°C was applied and an

isothermal heating step at the final temperature for 30 min. Elemental analysis (EA) was performed in a CE Instrument CHNS1100. Inductively coupled plasma mass spectrometry (ICP-MS) was carried out in an ICP-MS Agilent 7900. Fourier-transform infrared (FTIR) spectra were recorded using a Nicolet 6700 instrument (Thermo Scientific, USA) in the 4000–400 cm^{-1} range.

Determination of organic matter in S3 material: Rh B amount in **S0** was obtained by TGA and EA. Nitrogen content indicated the presence of 0.023 mmol of dye per g of solid in **S0**. This data is in concordance with TGA results. For **S1** and **S2**, the dye was extracted via forced extraction in hot DMSO. 3-iodopropyltriethoxysilane amount in **S1** was obtained by ICP-MS (to determine the iodine content), and the same technique was used to determine the amount of bipyridinium derivate in **S2**, showing a complete Sn_2 reaction between 3-iodoproyltrimethoxysilane and bipyridinium derivate. Heparin content in **S3** was determined by EA of the sulfur amount in the final solid. Rh B content in **S4** was determined by forced extraction in hot DMSO. After extraction, the aminopropyltriethoxysilane content was determined by EA. The amounts obtained are in concordance with the TGA result.

MSNs characterization: MSNs as made (**S0**) and calcined MSNs together with solids, **S1**, **S2**, and **S3** were characterized using standard techniques. Powder X-ray diffraction (PXRD) measurements were performed on a Philips D8 Advance Diffractometer using CuKα radiation, and transmission electron microscopy (TEM) images were obtained with a 100 KV JEM-1010 microscope. The powder X-ray diffraction patterns of calcined MSNs are typical for mesoporous silica materials with four low-angle peaks characteristic of a hexagonal-ordered pore array indexed as (100), (110), (200), and (210) Bragg reflections. The porosity of the materials was determined by N_2 adsorption-desorption isotherms recorded with a Micromeritics ASAP2010 automated sorption analyzer. Besides, from N_2 adsorption-desorption measurements, values of specific surface, pore diameter and pore volume of 43.4, 2.36, and 0.07, respectively were determined for **S4**.

Nitrogen adsorption-desorption isotherms of MSNs, S1, and S4 materials: The curve for the calcined MSNs (**Figure 116a**) presents an adsorption step with intermediate P/P_0 values between 0.1 and 0.3, which correspond to a type IV isotherm. Applying the BET model, a specific area of 1298.3 m^2g^{-1} was obtained. From the BJH model on the adsorption curve of the isotherm ($P/P_0 < 0.8$), a pore diameter of 2.36 nm and pore volume of 0.82 cm^3g^{-1} were calculated. Also, a textural porosity was observed by the characteristic H1 hysteresis loop that appeared on the curve at high relative pressure ($P/P_0 > 0.8$). For solid **S1** and **S4**, the adsorption-desorption isotherms are typical of mesoporous systems with partially filled mesopores. The N_2 volume adsorbed, and the specific surface area significantly decreased compared with the starting material (**Figure 116, b-c**).

Values of specific surface areas of 409.8 $m^2 g^{-1}$and 43.4 and pore volumes of 0.11 $cm^3 g^{-1}$ and 0.07 were found for **S1** and **S4**, respectively. The characterizing values are summarized in **Table 4**.

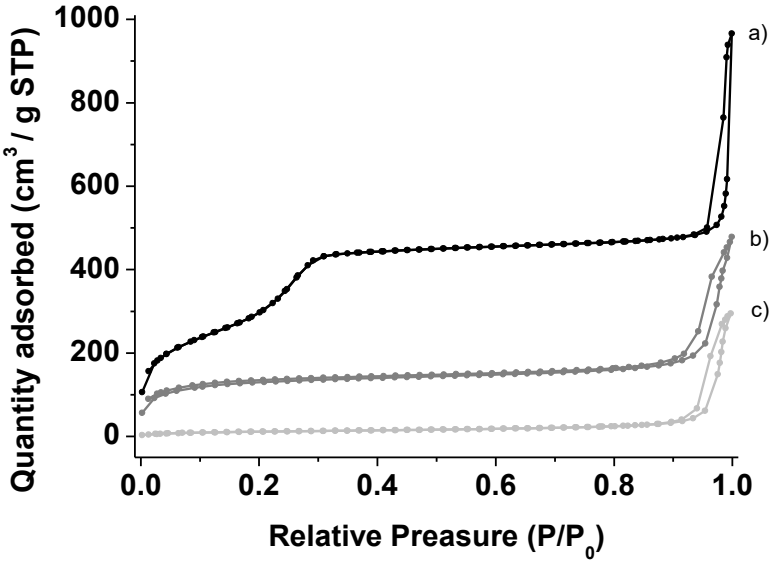

Figure 116. Nitrogen adsorption-desorption isotherms for (a) calcined MSNs; (b) **S1** solid; (c) **S4** solid. Reproduced with permission from [220]. Journal of Controlled Release © 2020 Elsevier.

Table 4. Specific surface, pore volume and pore size for starting MSNs and solids **S1** and **S4** from N_2 adsorption-desorption isotherm analysis. Reproduced with permission from [220]. Journal of Controlled Release © 2020 Elsevier.

Solid	S_{BET} ($m^2 g^{-1}$)	Pore volume[a] ($cm^3 g^{-1}$)	Pore size[a] (nm)
MSNs	1298.3	0.82	2.36
S1	409.8	0.11	-
S4	43.4	0.07	-

[a]Applying the BJH model.

Synthesis of (1,1'-dimethyl-4,4'-bipyridinium) dication (C3): 4,4´-bipyiridine (1.00 g, 6.43 mmol) was transferred to a two-necked round bottom flask equipped with a condenser. Then, anhydrous acetonitrile (40 mL) was added, and the system was purged with argon. Once the reaction was at reflux, methyl iodide (880 µl, 14.15 mmol) was added dropwise, and the reaction was maintained at reflux for 2 h. Finally, the solvent was removed in vacuum and washed three times with acetonitrile. Pure product **C3** was obtained as a red solid in 98.9% yield (2.79 g, 6.35 mmol).

Characterization of heparin-bipyridinium interactions: Moreover, in order to characterize the heparin-bipyridinium interactions responsible of the capping mechanism in **S3**, ^{1}H-NMR studies were carried out using heparin solutions in D_2O treated with increasing amounts of *N,N'*-dimethyl-4,4'-bipyridinium dication (**C3**) (0.1 M), and heparin (20 mg/mL). ^{1}H-NMR signals of heparin were monitored after the addition of increasing quantities of **C3** (from 0.2 to 1.1 eq.). ^{1}H NMR spectrum of heparin showed the typical signals of polysaccharide protons directly linked to hydroxyl moieties in the 3.6-4.4 ppm range and a broad doublet at ca. 3.31 ascribed to protons in the sugar backbone directly linked to a sulfonamide group. Addition of increasing quantities of **C3** induced moderate upfield shifts of the polysaccharide protons (3.5-4.2 ppm) and a remarkable upfield shift for the proton linked to the sulfonamide unit (from 3.31 to 3.03 ppm). The observed shifts are ascribed to electrostatic interactions between heparin and bipirydinium derivative **C3**. Based on ^{1}H-NMR titration results, the affinity constant of bipyridine derivative **C3** with heparin was calculated to be $(5.7 \pm 0.69) \times 10^{4}$. ^{1}H and ^{13}C NMR spectra were recorded on a Bruker FT-NMR Avance 400 (Ettlingen, Germany) spectrometer at 300 K, using TMS as an internal standard.

3.1.3. Release on voltage-responsive MSN

Cargo release studies with S3 in the presence of acetaldehyde. 1 mg of **S3** was suspended in 3.5 mL of water at pH 7.5 in the absence and presence of (0.5 mL) acetaldehyde. At certain fixed times, aliquots were separated, centrifuged, and the Rh B released was determined by monitoring the emission band at 576 nm ($\lambda_{ex} = 554$ nm). The release profiles obtained are shown in **Figure 117**. As could be seen, in the absence of acetaldehyde, a negligible Rh B release from **S3** was noted (ca. 10% after 120 min), indicating a tight pore closure due to the strong electrostatic interaction between the grafted bipyridinium dication and the negatively charged heparin. However, in the presence of acetaldehyde, a marked enhancement in the emission at 576 nm was observed, which is consistent with the release of Rh B from **S3**.

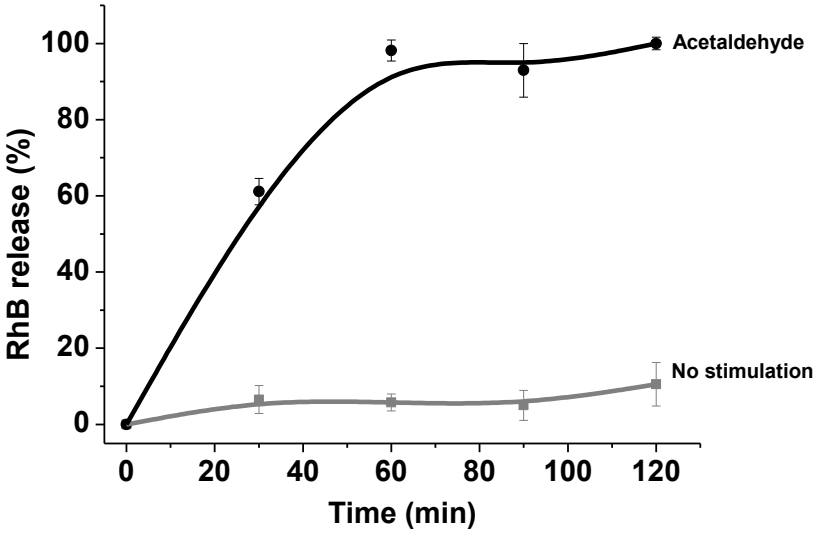

Figure 117. Release profiles of Rh B from **S3** nanoparticles in PBS at pH 7.5 in the absence and in the presence of acetaldehyde. Reproduced with permission from [220]. Journal of Controlled Release © 2020 Elsevier.

Cargo release studies with S3 in the application of the voltage trigger. For the voltage-triggered Rh B release experiments of heparin-capped MSNs **S3**, first, we studied the redox properties of methyl viologen (compound **C3**) and the carboxylic derivative **C2**. The experiments were carried out at room temperature with a potentiostat/galvanostat PGSTAT100 (Autolab) connected to a PC using an electrochemical cell with a stainless steel working electrode (diameter 30 mm, thickness 2 mm), a Pt ring electrode (Crison) as the counter electrode and a SCE (Crison) as the reference electrode. In an experiment, 4 mg of solid **S3** were suspended in 12 mL of PBS (10 mM, pH 7.5) in the electrochemical cell. Release of Rh B from **S3** was studied with and without the application of stimuli (-640 mV vs. SCE potential). At certain fixed times, aliquots were separated, centrifuged to eliminate the solid, and the Rh B released from **S3** was monitored following the emission band at 576 nm ($\lambda_{ex} = 554$ nm). The work of Ito & Kuwana [350], described that the methyl viologen dication displays a one-electron reduction at -615mV vs. SCE. We found reduction values of -600 mV for **C3** and -605 mV vs. SCE for **C2** in our conditions. Release experiments of Rh B in PBS suspensions of **S3** upon applying an electric potential (-640 mV vs. SCE) resulted in release profiles shown in **Figure 118** compared to non-stimulated **S3**. The potential of -640 mV vs. SCE was selected considering the electrochemical studies on molecule **C3** (*vide ante*). In the absence of electric potential, a low Rh B release was observed (ca. 7% of the maximum Rh B delivered after 60 min). However, when a continuous -640 mV vs. SCE potential was applied, a marked dye release was found that reached its maximum after only 30 min. Similar delivery profiles were observed when PBS suspensions of **S3** were treated with the reducing agent acetaldehyde (**Figure 117**), which strongly suggests that Rh B delivery was due to the reduction of the grafted bipyridinium. The reduction of bipyridinium induces a reduction in charge of this molecule, which weakens the

interaction with the negatively charged heparin, overall resulting in a detachment of the heparin from the surface of the nanoparticles and cargo release. This detachment of heparin from **S3** was assessed in additional experiments. Thus, sulfur content (by ICP-MS) in solution was determined when **S3** nanoparticles were suspended in water in the presence and in the absence of the electrochemical stimulus (both a voltage of -640 vs. SCE or the addition of acetaldehyde). Whereas sulfur content in the solution was negligible in the absence of stimuli, a significant increase of sulfur (due to heparin) was found upon application of the stimuli.

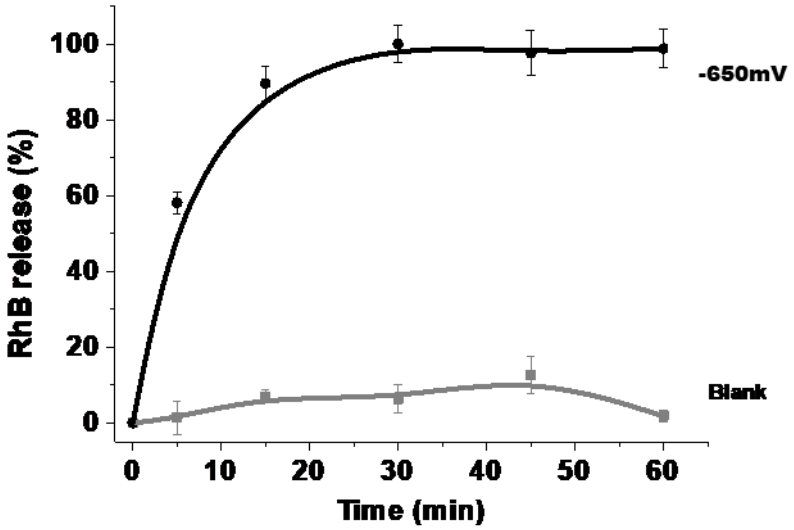

Figure 118. Release profiles of Rh B from **S3** nanoparticles in PBS at pH 7.5 alone and upon the application of a -640 mV vs. SCE potential. Reproduced with permission from [220]. Journal of Controlled Release © 2020 Elsevier.

3.2. Conductive polymer bearing voltage-responsive MSN

3.2.1. Design of conductive polymer bearing voltage-responsive MSN

Synthesis of PEDOT:PSS-co-MA (P0): An Autolab PGstat30 galvanostat/potentiostat was used for PEDOT:PSS-*co*-MA electro-polymerization at constant anodic current (100 μA/Cm^2, 96 mC/cm^2 polymerization charge) on gold-coated glass slides. A Pt foil served as the counter-electrode and a SCE as the reference electrode. The solution for electrodeposition contained 0.16 % (v/v) EDOT and 0.344 % (w/v) PSS-*co*-MA in aqueous potassium phosphate-buffered saline (Milli-Q water with 18.2 MΩ cm^2 containing 9 g NaCl, 0.8 g $Na_2HPO_4{\cdot}_2H_2O$ and 0.14 g KH_2PO_4 per liter) as reported by Collazos-Castro *et al.* [328].

Synthesis of PEDOT:PSS-co-MA films containing MSNs (P1): In the first step, carboxylic groups on the surface of PEDOT:PSS-*co*-MA were activated with a solution of 10 mg/mL of EDC (15 ml) and 10 mg/mL of sulfo-NHS (5 mL) in MES buffer (pH = 6) for 15 min at room temperature. Then 20 mg of **S4** nanoparticles were suspended in 5 ml of PBS buffer (pH = 7.4), and activated PEDOT:PSS-*co*-MA was immersed in the suspension. The reaction was stirred overnight in order to covalently attach MSNs to PEDOT:PSS-*co*-MA, giving **P1**. The final material was washed twice with PBS.

Synthesis of 4,4'-bypiridinium-1-(carboxymethyl)-1'-methyl iodide bromide (C2): Product **C2** was synthesized by a nucleophilic substitution reaction between **C1** and ethyl bromoacetate. Compound **C1** (1.6 g, 5.38 mmol) was transferred to a two-necked round bottom flask equipped with a condenser. Then, anhydrous acetonitrile (18 mL) was added, and the system was purged with Argon. Once the reaction was at reflux, ethyl bromoacetate (1500 µl, 12.15 mmol) was added dropwise, and the reaction was maintained at reflux for 5 h. Finally, the solid product obtained was filtered off and washed three times with acetonitrile. The intermediate ester was stirred in 200 mL of NaOH 1 M for 10 min, and then the solution was acidified until pH = 2 to hydrolyze the ester group. The final product was purified by washing with cold methanol. **C2** was obtained as an orange solid with a 90.2% yield. (1.12 g, 4.85 mmol).

Synthesis of PEDOT:PSS-*co*-MA films containing heparin capped-MSNs (P3): Covalent attachment of **2** was carried out by forming an amide bond between the carboxylic group in **C2** and free amino moieties in MSNs yielding **P2**. For this purpose, the carboxylic group in **C2** (73.5 mg, 0.2 mmol) was activated with a solution of 10 mg/mL of EDC (15 ml) and 10 mg/mL of sulfo-NHS (5 ml) in MES buffer (pH = 6) for 15 min at room temperature. Then pH was adjusted to 7.4 and **P1** was immersed into the solution, and the mixture was stirred overnight. The final material was washed twice with PBS. Finally, heparin (20 mg, 0.015 mmol) was dissolved in 5 ml of PBS (pH = 7.4), and **P2** was immersed in the solution. After 3 h at room temperature, the final electro-responsive material **P3** was obtained, washed with PBS (pH = 7.4), and dried at room temperature.

Figure 119 shows the synthesis procedure for the obtention of final material **P3**.

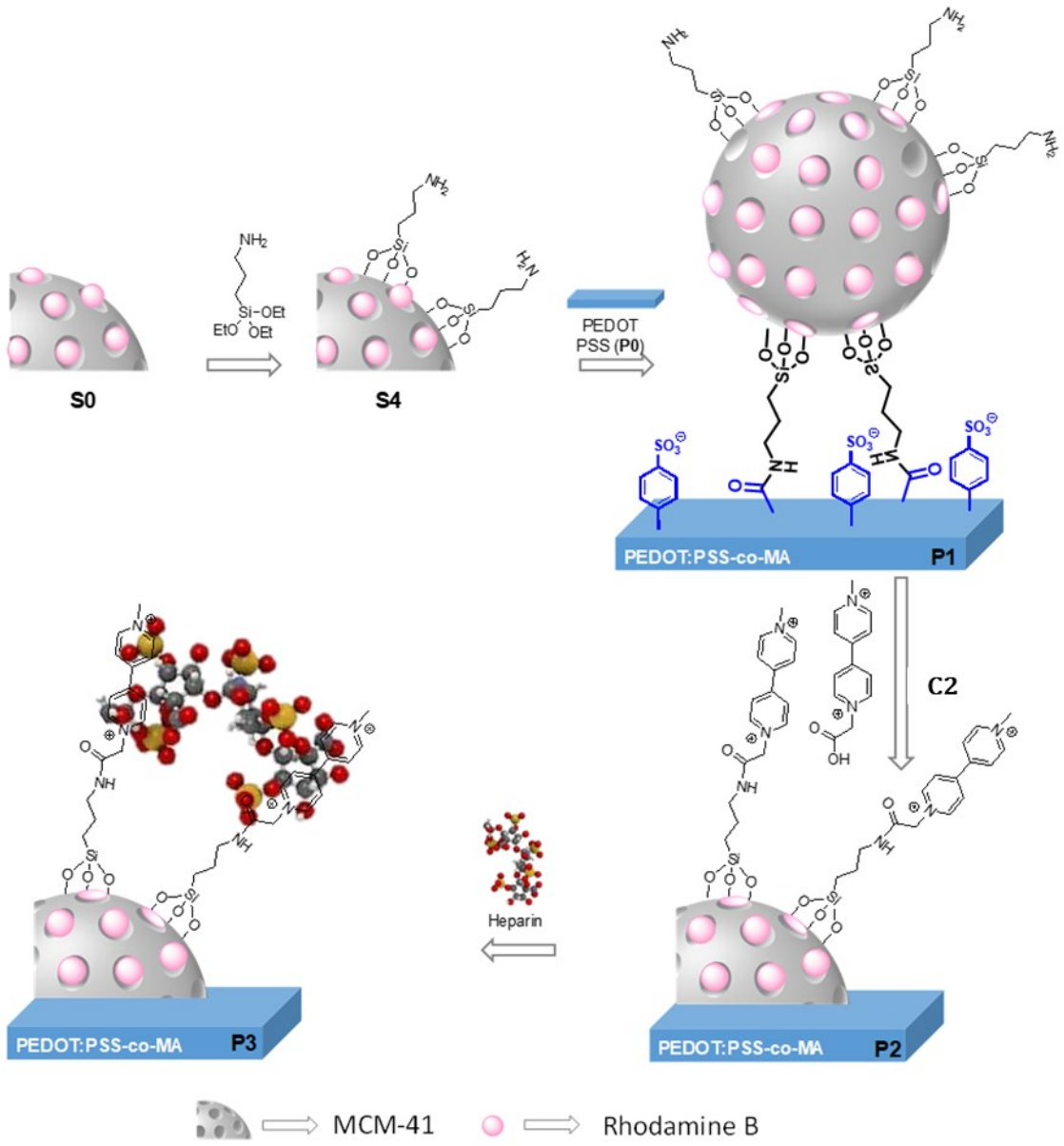

Figure 119. Synthesis of PEDOT:PSS-*co*-MA films containing heparin-capped MSNs (**P3**). MSNs are loaded with Rh B in CH_3CN for 24 h. Then, **S0** nanoparticles were functionalized with (3-aminopropyl)trimethoxysilane in CH_3CN at room temperature for 5.5 h (**S4**). PEDOT:PSS-*co*-MA material was immersed in an EDC/sulfo-NHS MES buffer solution (pH = 6) for 15 min at room temperature in order to activate carboxylic groups. Then, **S4** nanoparticles were added and the reaction was maintained overnight at room temperature to obtain **P1** material. After that, carboxylic acid of 4,4'-bypiridinium-1-(carboxymethyl)-1'-methyl bromide iodide was activated with EDC/sulfo-NHS in MES buffer (pH = 6) for 15 min at room temperature. Then, pH was adjusted to 7.4 and **P1** was immersed into the solution. The reaction was kept at room temperature overnight yielding **P2**. Finally, heparin was dissolved in PBS (pH 7.4) and **P2** was immersed in the solution for 24 h at room temperature. Reproduced with permission from [220]. Journal of Controlled Release © 2020 Elsevier.

To prepare the bipyridinium-heparin gated nanoparticles, we used **S0** MSNs and functionalized them with (3-aminopropyl)triethoxysilane to obtain **S4**. **S4** nanoparticles were

attached to the PEDOT:PSS-*co*-MA polymer forming amide bonds using NHS/EDC as coupling agents (**P1**). Once **S4** nanoparticles were assembled onto the polymer, the unbounded surface of the MSNs were functionalized with *N,N'*-bypiridinium-1-(carboxymethyl)-1'-methyl bromide iodide (**C2**) yielding **P2** films. The final material (**P3**) was obtained by capping the grafted nanoparticles containing positively-charged bipyridinium moieties with heparin by electrostatic interactions.

3.2.2. Characterization of conductive polymer bearing voltage-responsive MSN

Determination of organic matter in P3 material: In order to calculate the approximate contents of organic content in **P3**, the amount of nanoparticles anchored in **P3** was determined by the difference between the milligrams of nanoparticles suspended in the synthesis reaction (20mg of **S4**) and those obtained in the washing waters (7mg of **S4**). In **P3** films, Rh B content was determined by forced extraction in hot DMSO, while heparin content in **P3** was determined by subtraction of the sulfur content (by ICP-MS) in the starting heparin solution and the sulfur content in the solution after capping the nanoparticles in **P2** with heparin (to give **P3**).

Surface characterization of P0, P1, P2 and P3. To characterize the surface functionalization in the different materials, ATR studies were carried out. **P0** showed typical signals for PEDOT in 1600 to 800 cm^{-1} range, as reported by Sandoval *et al.* [351], whereas **P1** displayed a characteristic signal at 3000 cm^{-1} that corresponded to the symmetric and asymmetric -NH_2 stretching. Finally, **P3** material shows signals for OH groups as broad bands in the 3630 to 3044 cm^{-1} range and the presence of carboxylates (peak centered at 1614 cm^{-1}) and sulfonic groups (peaks at 1209 and 1016 cm^{-1} corresponding to symmetric and antisymmetric stretching vibrations of the –SO_3 group). A typical OH broad band in the 3630 to 3044 cm^{-1} range was found in **P3**. Moreover, peaks at 1614 cm^{-1} due to carboxylates and vibrations at 1209 and 1016 cm^{-1} attributed to symmetric and antisymmetric stretching vibrations of -SO_3 from heparin were also observed.

PEDOT:PSS-*co*-MA polymer and MSNs S4 attachment characterization: Attachment of the capped MSNs **S4** on the PEDOT:PSS-*co*-MA polymer was assessed by FESEM-FIB (**Figure 120**). FESEM-FIB images of **P0** (**Figure 120, a-b**) show a surface with no irregularities and a smooth morphology. In contrast, in images of **P3** (**Figure 120, d-e**), spherical MSNs homogeneously distributed over the entire surface were found, confirming the attachment of the nanoparticles on the PEDOT:PSS-*co*-MA films. Moreover, confocal microscopy images of **P3** displayed a homogeneously distributed red emission compared to **P0** due to the presence of the loaded Rh B in the attached nanoparticles (**Figure 120, c, f**).

High-resolution mass spectrometry (HRMS) data were obtained with a TRIPLETOF T5600 (ABSciex, USA) spectrometer. Field Emission Scanning Electron Microscope (FESEM) and Field Emission Scanning Electron Microscope with Focused Ion Beam (FESEM-FIB) images were recorded in an ULTRA 55 and AURIGA Compact systems, respectively.

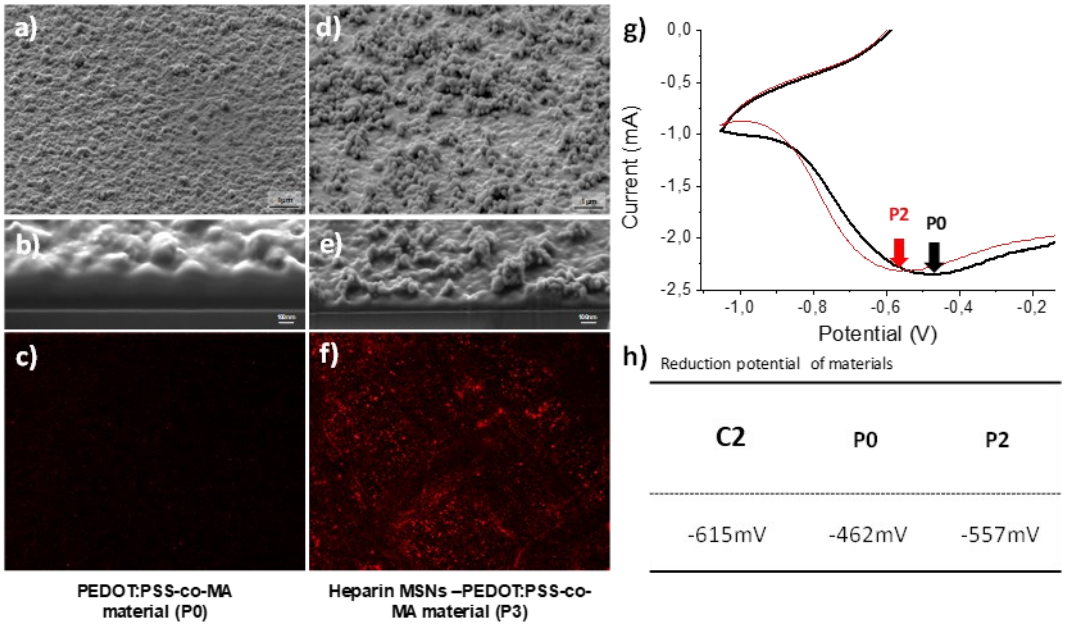

Figure 120. Characterization of PEDOT:PSS-*co*-MA containing heparin-capped MSNs. Left: (a) FESEM-FIB image of **P0** surface, (b) FESEM-FIB image of a cross-section of **P0**, (c) confocal image of **P0**. Right: (d) FESEM-FIB image of **P3** surface, (e) FESEM-FIB image of a cross-section of **P3**, (f) confocal image of **P3**. (g) Cyclic voltammogram of **P0** and **P2** showing the shift from -462 mV to -557 mV. (h) Reduction potential values for the bipyridinium derivative **C2** and the films **P0** and **P2** films. Reproduced with permission from [220]. Journal of Controlled Release © 2020 Elsevier.

PEDOT:PSS-*co*-MA polymer with and without MSNs characterization: P0 and **P2** were also characterized by cyclic voltammetry (**Figure 120, g-h**). When **P0** was used as the working electrode, a reduction peak at -462 mV vs. SCE was observed and attributed to the reduction of the PEDOT film. However, when **P2** (without Rh B) was used as the working electrode in the same conditions, a shift of the reduction peak from -462 to -557 mV was found, which is tentatively attributed to the presence of the electroactive methyl viologen derivative on the nanoparticles attached in **P2**.

3.2.3. Release on conductive polymer bearing voltage-responsive MSN

Cargo release studies with P3 in the presence of acetaldehyde: P3 film was introduced in 6.5 mL of PBS (10 mM, pH = 7.5), and the release of Rh B was monitored along time in the

absence and the presence of acetaldehyde (0.5 mL). At certain fixed times, aliquots were separated, and the Rh B released was determined by monitoring the emission band at 576 nm (λ_{ex} = 554 nm). The obtained release profiles are depicted in **Figure 121**. In the absence of acetaldehyde, a poor Rh B release from **P3** was observed (ca. 10% after 60 min). In contrast, a remarkable release of Rh B was obtained (reaching ca. 90% after 30 min) when acetaldehyde was added.

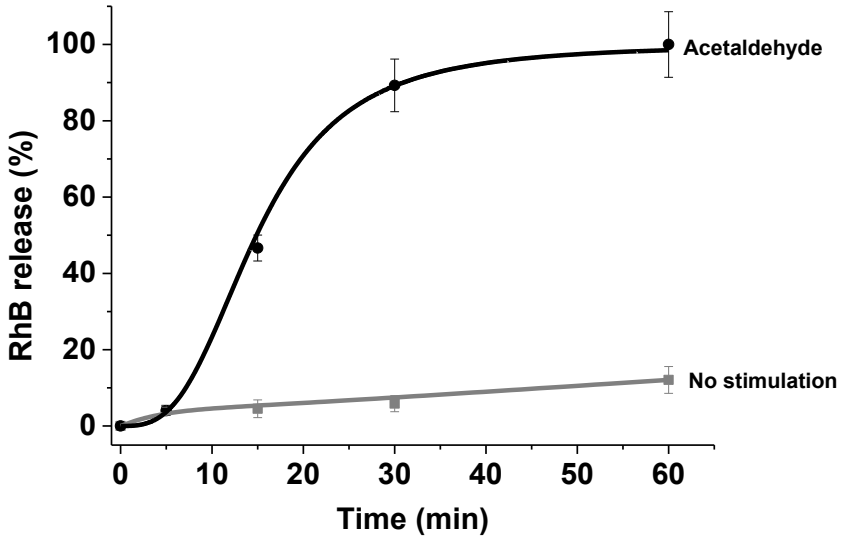

Figure 121. Release profiles of Rh B from **P3** films in PBS at pH 7.5 in the absence and in the presence of acetaldehyde. Reproduced with permission from [220]. Journal of Controlled Release © 2020 Elsevier.

Cargo release studies with P3 in the application of the voltage trigger: Once performed the delivery studies with **S3**, we move one step forward to monitor the release of Rh B from the heparin-capped nanoparticles grafted onto the PEDOT:PSS-co-MA film (**P3**). The experiments were performed with the potentiostat/galvanostat reference PGSTAT100 using an electrochemical cell with **P3** acting as the working electrode. The Pt ring electrode (Crison) was used as the counter electrode and a SCE (Crison) as the reference electrode. **P3** was immersed in 12 mL of PBS (10 mM, pH 7.5). The release of rhodamine B was registered at certain fixed times, in the absence and upon the application of a -640 mV vs. SCE potential. Rh B release was monitored over time without voltage application and when a -640 mV vs. SCE potential was applied (**Figure 122**). Without applied potential, a low delivery of Rh B was observed (less than 5% after 30 min).

In contrast, a significant release of Rh B was found from the **P3** film when a -640 mV vs. SCE potential was applied (ca. 90% of the total dye release after 15 min). Pore opening and Rh B release can be explained due to the reduction of the grafted bipyridinium derivative for **S3** nanoparticles *(vide ante)*. Moreover, in this case, the concomitant reduction of the conductive

polymer and its polarization to negative potentials may also help to induce the detachment of negatively charged heparin from the surface of the nanoparticles. Release studies also revealed that ca. 2 μg of cargo/cm^2 of the scaffold were delivered from **P3**, which is ca. 2- to 4-fold larger than typical amounts delivered in reported conductive polymers for drug release applications (Richardson *et al.* [249], Boehler *et al.* [250]). Similar delivery profiles were found when PBS suspensions of **P3** were treated with the reducing agent acetaldehyde (**Figure 121**), strongly suggesting that Rh B delivery is redox-controlled. These experiments demonstrate that the modified PEDOT:PSS-*co*-MA conductive polymer **P3** can show poor cargo release, yet deliver the payload at will upon application of an external voltage.

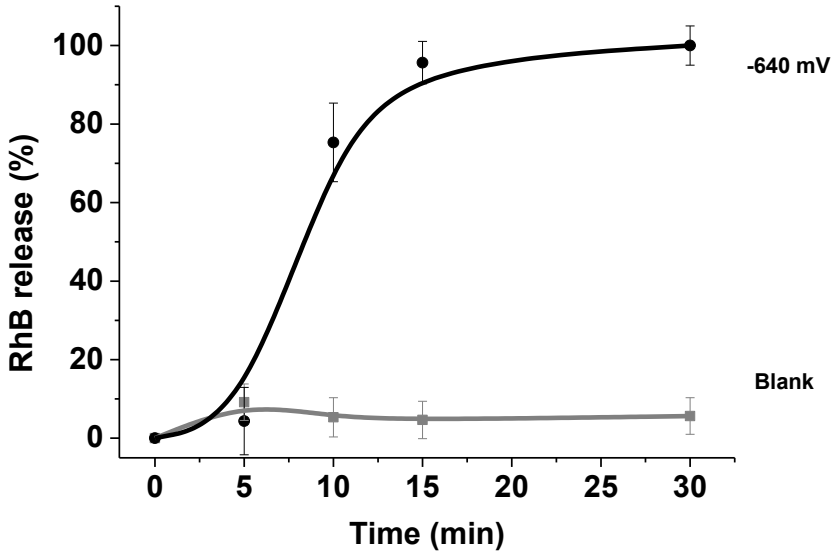

Figure 122. Release profiles of Rh B from **P3** films in PBS at pH 7.5 alone and upon the application of -640 mV vs. SCE. Reproduced with permission from [220]. Journal of Controlled Release © 2020 Elsevier.

3.3. Validation: ECDR on cell culture seeded on the CP-MSN assembly

In an attempt to further advance in the potential application of **P3** (the conductive polymer bearing voltage-responsive MSNs, namely *CP-MSN assembly*), we tested its biocompatibility and the possibility of using the film to deliver cargo (*i.e.*, Rh B) by simply applying an external electric voltage to cells in a realistic cell culture medium. To determine biocompatibility, **P0** and **P3** were compared in terms of their ability to support cell growth and proliferation. Moreover, as a positive control group, cells were also seeded onto the well-plate surface.

Cell culture conditions: HeLa human cervix adenocarcinoma cells were purchased from the German Resource Centre for Biological Materials (DSMZ) and were growing in DMEM supplemented with 10% FBS. Cells were incubated at 37°C in an atmosphere of 5% carbon dioxide and 95% air and underwent passage twice a week.

Cell proliferation studies: P0 and **P3** films were first sterilized by UV light for 30 min and placed in a 6-well plate. HeLa cells were seeded onto the films at 200,000 cells/mL in DMEM with 10% FBS. Cell viability before starting the experiment was determined by the Trypan Blue method, and the measured viability exceeded 95% in all cases. After 48 h, the cell growth was tested by adding the cell proliferation WST-1 reagent for 1 h. After 1 h, 100 µL of the medium containing the WST-1 reagent was placed in a 96-well plate, and the absorbance was measured at 595 nm in a Wallac 1420 workstation. Then, cells were washed with PBS, and a fresh medium was added. This process was repeated after 72 and 96 h.

Phase contrast microscopy images showed healthy-looking adherent cells on the surface of both **P0** and **P3** (**Figure 123 a, b**) films. These images concord with the viability result obtained after 96 h (**Figure 123 c**), where no significant cell death was observed in the PEDOT-based **P0** and **P3**.

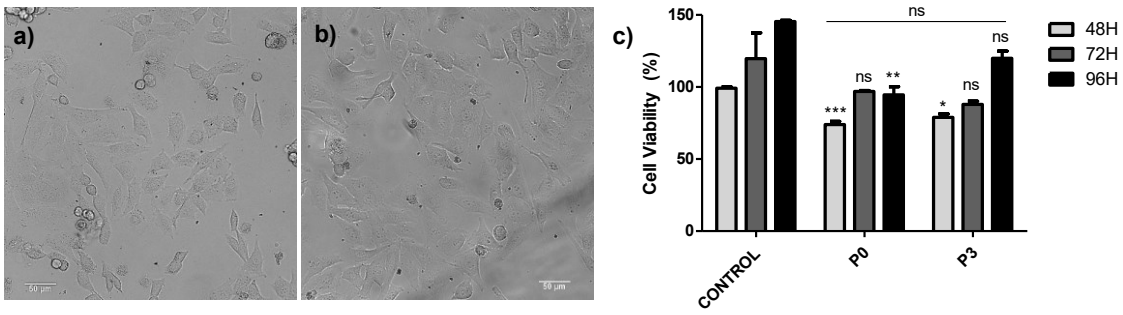

Figure 123. Phase contrast microscope image of HeLa cells on (a) **P0** and (b) **P3** films. (c) Cell viability of HeLa cells seeded onto well-plate surface (control), on **P0** and **P3** after 48, 72 and 96 h. The data represent the mean ± SEM and statistical significance was determined using a one-way ANOVA to compare the different sample groups at predetermined time (* $p < 0.05$, ** $p < 0.025$, *** $p < 0.001$). No significate change can be observe between the different material (**P0** and **P3**), the same result is obtained from **P3** vs. control at 96 h. Reproduced with permission from [220]. Journal of Controlled Release © 2020 Elsevier.

Controlled release of P3 in cell cultures of HeLa cells: P3 was placed over glass coverslip in a 6 well-plate and then cells were seeded and incubated at 37°C for 24 h in DMEM. After 24 h of incubation, cells were washed with PBS, and the DNA marker Hoechst 33342 (2 µg/mL) was added to visualize the cells seeded onto **P3** using a confocal microscope (Leica TCS SP8 AOBS). After the evaluation of the cells at 0 min, electrical triggering was performed using fully-validated electronic equipment, FAEVIS (Monreal-Trigo & Alcañiz [281]). The electrochemical

cell included **P3** as the working electrode, a Pt (1 mm Ø) electrode as the counter electrode and an Ag/AgCl (1 mm Ø) homemade electrode as the reference electrode. These electrodes overcame the spatial restriction of being introduced in the 6 well-plate. The applied potential was -600 mV vs. Ag/AgCl (-640 mV vs. SCE). After the application of the potential, Rh B released and internalized in cells was monitored by confocal microscopy. Release experiments were also carried out using acetaldehyde as a chemical reducing agent.

Controlled release from P3 in the presence of acetaldehyde in cell culture of HeLa cells: A confocal image of cells was taken (0 min). Immediately, acetaldehyde (0.5 μL) was added as the trigger, and confocal images after 15 min, 2 h, and 4 h were taken in order to assess the Rh B released from **P3**. The obtained results are shown in **Figure 124**. As could be seen, a negligible fluorescent signal of Rh B was observed before acetaldehyde addition (at 0 min). Addition of acetaldehyde induced rhodamine B release from the pores of MSNs attached to **P3**, which diffuses to the adhered cells. Confocal microscopy images (taken after 15 min, 2 h, and 4 h after acetaldehyde addition) demonstrated that Rh B concentration inside HeLa cells increased over time. Besides, Figure S10b shows the quantification of Rh B signal released inside HeLa cells. As could be seen, there was a ca. 9-fold emission enhancement at 4 h, which could be ascribed to the internalization of dye released from **P3** after acetaldehyde treatment. Fluorescence spectroscopy was carried out with a JASCO spectrofluorometer FP-8300.

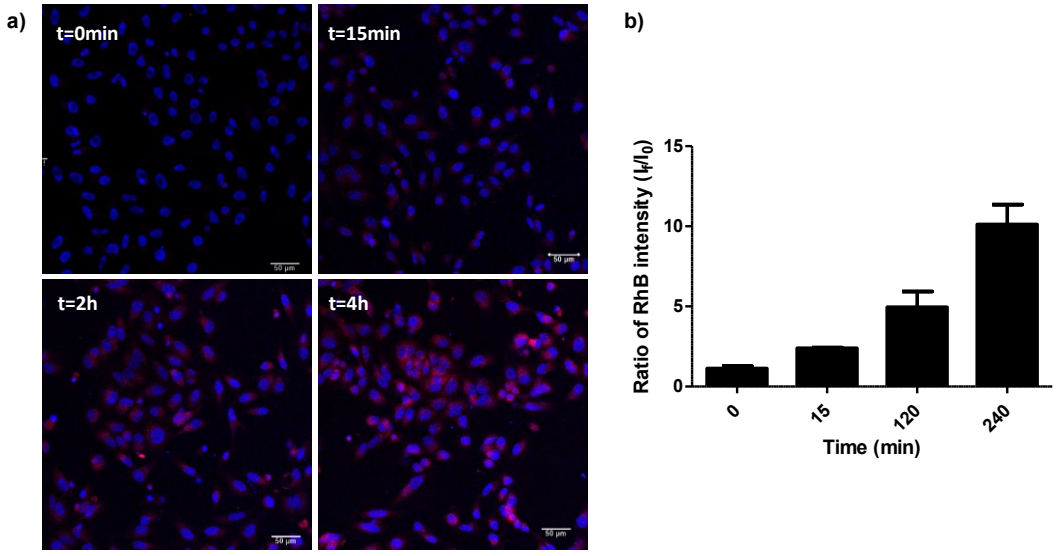

Figure 124. Confocal microscopy images of cellular controlled release studies with **P3** using acetaldehyde as stimulus. HeLa cells were examined after 24 h of seeding (t = 0) and after the addition of the acetaldehyde at t = 15 min, 2 h and 4 h. Rh B associated fluorescence is in red and the cellular nucleus marked with Hoechst 33342 in blue. (b) Ratio of mean fluorescence intensity (I_f/I_0) of Rh B in HeLa cells (Image J software analysis) over time after treatment with acetaldehyde. Reproduced with permission from [220]. Journal of Controlled Release © 2020 Elsevier.

Controlled release from P3 in the application of the voltage trigger in cell culture of HeLa cells: Rh B release studies from the voltage-responsive **P3** composite were tested in the presence of HeLa cells. HeLa cells were seeded over **P3** films that were used as the working electrode. A continuous voltage of -600 mV vs. Ag/AgCl was applied for 15 min and Rh B was followed by confocal microscopy. The Rh B delivered from **P3** and finally internalized by HeLa cells was monitored at t = 0, 2 h, and 4 h with the application or not of the -600 mV vs. Ag/AgCl potential (**Figure 125a**). In the absence of potential applied, the presence of Rh B inside HeLa cells was negligible after 24 h. However, after 15 min of voltage application, Rh B emission in HeLa cells was observed, with the fluorescence intensity inside cells clearly increasing with time (**Figure 125**b). Rh B controlled release from **P3** in cell culture was also checked after adding acetaldehyde as a chemical reducing agent (**Figure 124**) with similar results, strongly suggesting that the Rh B uptake by HeLa cells was ascribed to the voltage-induced Rh B release. These studies demonstrated that the cargo (*i.e.*, Rh B) remained inside the nanoparticles in the **P3** conducting even in a complex cell culture medium.

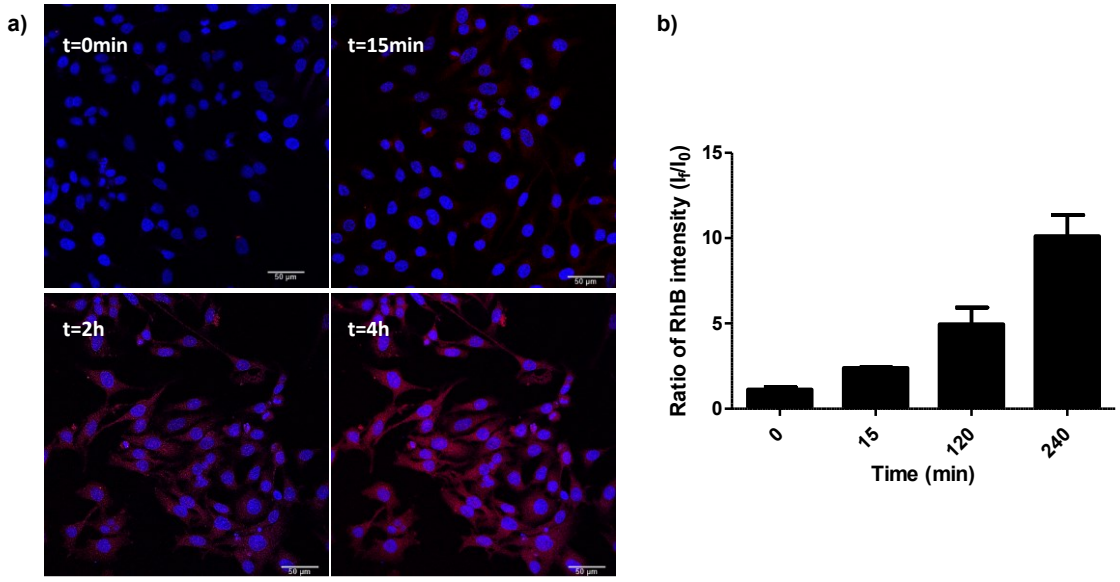

Figure 125. (a) Confocal microscopy images of cellular controlled release studies with **P3**. HeLa cells were examined after 24 h of seeding (t = 0) and upon the application of a continuous -600 mV vs. Ag/AgCl potential at t = 15 min, 2 h and 4 h. Rh B associated fluorescence is in red and the cellular nucleus marked with Hoechst 33342 in blue. b) Ratio of mean fluorescence intensity (I_f/I_0) of Rh B signal in HeLa cells (Image J software analysis) upon the application of a continuous -600 mV vs. Ag/AgCl potential at t = 15 min, 2 h and 4 h to film **P3**. Reproduced with permission from [220]. Journal of Controlled Release © 2020 Elsevier.

Besides, after the delivery experiment, FESEM-FIB images of the **P3** films (**Figure 126**) showed that MSNs remained attached to the polymeric backbone, indicating that it is the cargo but not the nanoparticles that are delivered from **P3**.

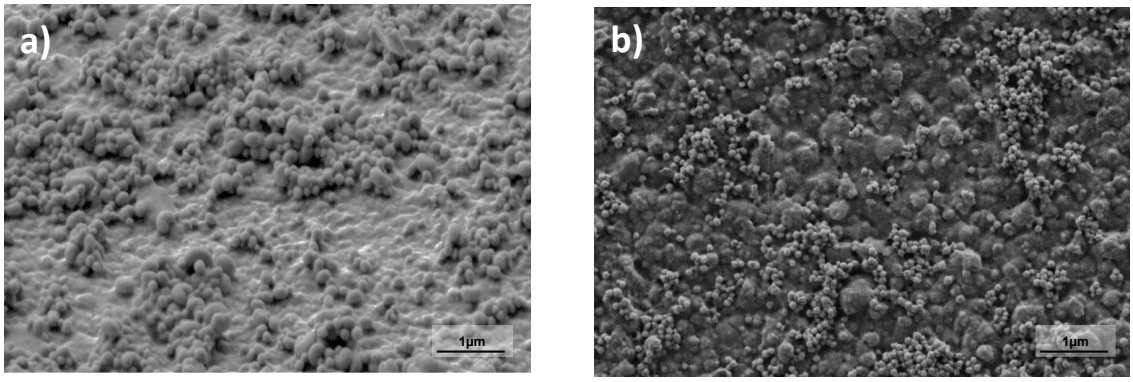

Figure 126. FESEM-FIB images of **P3** before a) and after b) the application of the electric stimulus. FESEM-FIB images showed that MSNs remained attached onto the polymeric backbone after the application of a -640 mV vs. SCE potential, pore opening and Rh B release. Reproduced with permission from [220]. Journal of Controlled Release © 2020 Elsevier.

4. Further research on ECDR

Additional ECDR research and development has been done within the framework of the present doctoral thesis. On the one hand, our main contribution to ECDR (García-Fernandez *et al.* [220]) is not feasible for the *in vivo* application. It is necessary to replace the ITO/glass slides used as support for the conductive polymer with a flexible, biocompatible, and biodegradable substrate. Hence, we have explored this transition to flexible substrates so that it can be implanted at the site of Spinal Cord Injury. On the other hand, we explored the ECDR from metallic and ceramic surfaces. However, these developments need further study, and their thorough explanation would make this dissertation surpass the maximum recommended length for a doctoral thesis. Hence, in this section, we will summarize these ongoing contributions.

4.1. Flexible substrate ECDR

The flexible substrate is Mitsubishi NB-TP-3GU100 PET, chosen according to the studies performed in section *3. Flexible substrate selection* of *Chapter 3. Electrostimulation for nervous tissue regeneration in vitro*.

Former conductive polymer on PEDOT:PSS-*co*-MA was electroplated using an ITO/glass slide as substrate. The ITO/glass features a metallic surface that allows the electroplating. To coat the new flexible PET substrate, commercially available PEDOT:PSS Heraeus V3 screen-printing ink is chosen, widely used for coating scaffolds for neural precursor cell grafting.

So far, the electrically controlled drug release (ECDR) has been designed from a substrate on which the initial cell culture is performed. The polymer layer to which the cells are attached is a temporary physical support. How to deal with this substrate in an *in vivo* situation is yet to be addressed: biodegradation, removal of the polymer at the end of the treatment, or even replacement of the polymer at different stages of the treatment are possible strategies.

Being aware of the question that remains to be solved, using a screen-printing method to prepare the substrates is an advantage because of the reduction of complexity and cost associated with manufacturing the substrates.

We used the PET-substrate Heraeus PEDOT:PSS scaffold to electrically release different cargos: Rhodamine B, serotonin, and curcumin. Unfortunately, they were unsuccessful. Hence, we assess a critical analysis of the protocol, identifying the mistake and proposing the following steps to accomplish this objective.

In all of them, the medium was 7.4 pH 0.1 M phosphate buffer saline (PBS), and the electrodes employed were:

- A PET substrate with 22 mm ⌀ Heraeus V3 PEDOT:PSS as the working electrode.
- 3 mm ⌀ Ag/AgCl (Ag wire polished and immersed in sodium hypochlorite 6% for 7 minutes) as the reference electrode.
- 3 mm ⌀ Platinum electrode as counter-electrode.

Chemical synthesis of loaded and gated MSNs bond to the conductive polymer is reproduced from *3.2.1. Design of conductive polymer bearing voltage-responsive MSN*, with Heraeus V3 screen-printed PEDOT:PSS over PET instead of electrodeposited PEDOT:PSS-*co*-MA over ITO/glass slides. Molecular gates are therefore composed of compound **C2** and heparin.

Fluorimetry measurements showed no significant increase in cargo concentration after every electrochemical stimulus. Acetaldehyde reduction neither produced cargo concentration to increase. Hence, presumably, the cargo is not present in the system. Electrical responses measured to cyclic voltammetry and pulse application may be the responses of PEDOT:PSS working electrode with compound **C2**.

No controlled drug release was achieved in any of the former experiments. After a thorough review, our collaborators from Martínez-Máñez's group raised a significant concern: the currently used screen-printed PEDOT:PSS was not co-polymerized with maleic acid. In the former PEDOT:PSS-*co*-MA, maleic acid doted the conductive polymer of carboxylic acid groups on its surface. These groups were activated using EDC and NHS, allowing the bonding of the

nanoparticles with (3-aminopropyl)trimethoxysilane. Without the maleic acid, no carboxylic acids are present on the surface of the conductive polymer, and the design shall be reconsidered.

4.2. ECDR from metallic and ceramic surfaces

So far, the electrically controlled release developed in this doctoral dissertation has focused on using a conductive polymeric surface as a working electrode. However, electrically controlled release from metallic or ceramic surfaces is a little explored subfield, although materials such as gold or alumina are widely used in inorganic-organic systems in biomedicine, such as prostheses and implantable devices (see Demann *et al.* [352] and Hannouche *et al*. [353]). The development of controlled drug release from metallic or ceramic surfaces is of great interest in bionics (see Srivastava *et al.* [354]) and in the emerging discipline of microbots (see Han *et al.* [355]), particularly in their biomedical applications (see Doutel *et al.* [356]). These robots could be enabled to communicate with biological systems using chemical signals in the same way that artificial chemical systems with communication capabilities are being designed (see Llopis-Lorente *et al.* [190]). We will not venture further applications here since history teaches us that basic research resembles the fable of the sorcerer's apprentice: the consequences of our small actions may end up beyond our current ability to imagine.

The attachment of thiol compounds can be used to bind the mesoporous silica nanoparticles (MSNs) to a gold surface (Luderer & Walschus [357]). Hence, we designed an electrically controlled drug release (ECDR) system from gold surfaces. With this aim, gold surface was functionalized with thioethanolamine by means of a thiol-Au bond, exposing the amine groups in the surface. On the other hand, MSNs were loaded with Rhodamine B and were externally functionalized with (3-iodopropyl)trimethoxysilane. Then, functionalized MSNs, which expose iodines, were attached to the surface via a nucleophilic substitution with the amine groups of the gold surface. After that, the pores of MSNs were gated using the bipyridine derivative by nucleophilic substitution and the heparin structure by electrostatic interactions, as shown in **Figure 127**.

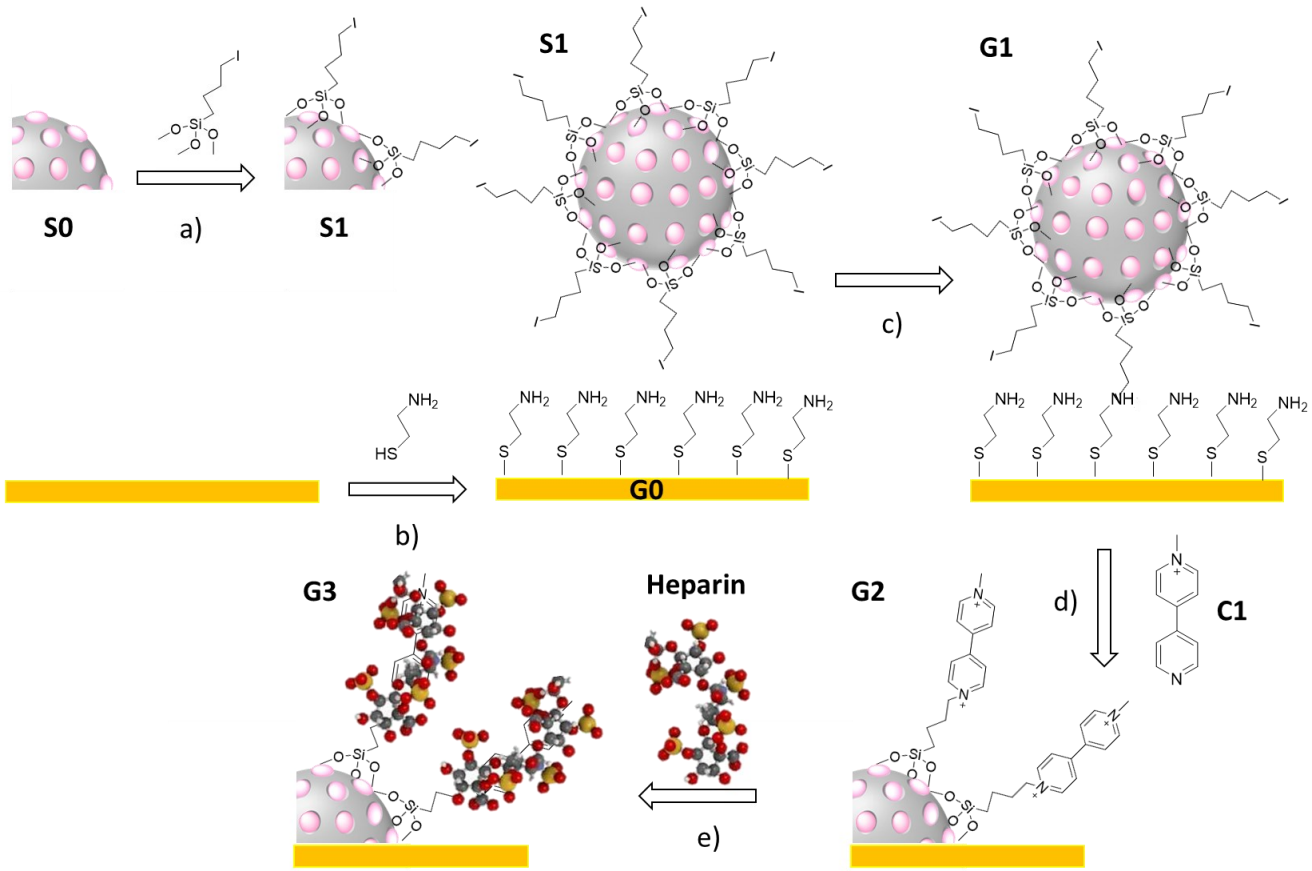

Figure 127. Synthesis of gold surfaces containing heparin-capped MSNs (**G3**). MSNs are loaded with Rh B in CH_3CN for 24 h. a) Then, **S0** nanoparticles were functionalized with (3-iodopropyl)trimethoxysilane in CH_3CN at room temperature for 5.5 h (**S1**). b) Gold material was functionalized with thioethanolamine, yielding **G0**. c) Then, **S1** nanoparticles were added, and the reaction was maintained overnight at room temperature to obtain **G1** material. d) The obtained bond nanoparticles are reacted with **C1** by nucleophilic substitution in refluxed CH_3CN for 72 h (**G2**). Finally, **G2** were immersed in heparin PBS solution for 3 h, yielding the final heparin-capped solid (**G3**).

A custom PCB with two squared gold electrodes of 1 mm^2 each, separated by 2 mm, was used to perform the ECDR experiments. We developed a custom potentiostat instrument with the capability of simultaneously measuring two reference electrodes, and we used it to assess the potential distribution in a 2-electrodes electrochemical cell when applying different voltages, surface ratios, and distances (Meersman *et al.* [358]). At the given situation (1:1 ratio between the counter-electrode and the working electrode, 2 mm distance), the application of -925 mV at the WE vs. the CE guaranteed that -650 mV vs. Ag/AgCl was at least applied in the WE-solution interface. Two situations were assessed: the functionalization of both WE and CE, and the functionalization of WE only. In both cases, the voltage trigger for 2 minutes induced the cargo release successfully, with a 500% increase in the Rh B concentration in solution vs. control (minor spontaneous release), a preliminary validation of the ECDR in gold surfaces, as

shown in **Figure 128**. Our institute is conducting further research to develop microbots through the EDISON[10] ERC project led by Prof. Martínez-Máñez based on this technology.

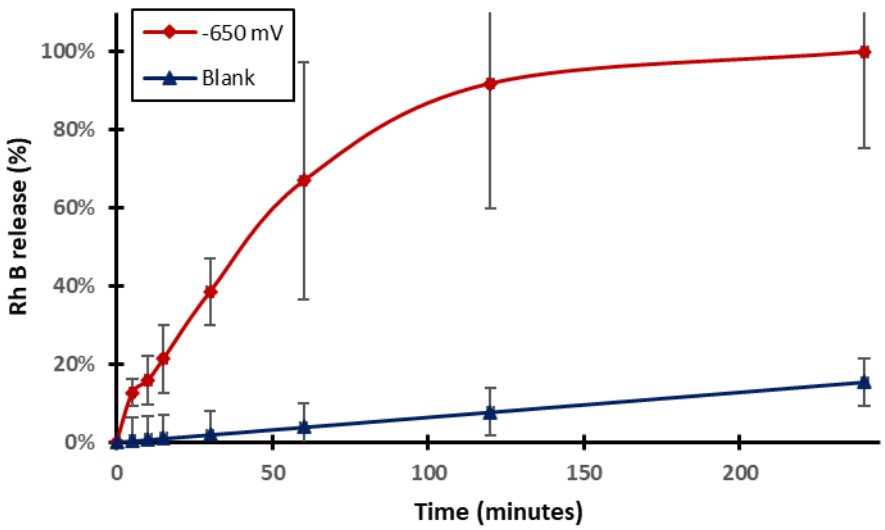

Figure 128. Release profiles of Rh B from **G3** material in PBS at pH 7.5 alone (blank, estimated based on the prior-to-potential application release measurements every 15 minutes for 4 h) and upon the application of -650 mV vs. SCE.

During the last triggerable release, we presumably induced the reduction of the bipyridinium dication, dissolving its electrostatic interaction with the heparin capping moiety. However, a reasonable question may arise: is it possible to apply such electric field that may induce enough repulsion force to detach the heparin capping moiety from the cation form of the viologen? In other terms: can we not only produce the ECDR electrochemically, but electrostatically?

As we hypothesized in the design of the voltage-responsive gates, we assumed they are based on bipyridinium dication and heparin electrostatic interaction. Nevertheless, the exact mechanism involved is yet to be discovered. Zhang *et al.* [343] indicated in the introduction to their chemosensor based on the same compounds: "viologens could serve as receptors to complex with heparin through the electrostatic binding, charge/electron transfer, and/or π-anion interactions, which was testified by the voltammetric perturbation on the redox potential of methyl viologen dications (MV^{2+}) by heparin".

Ceramic surfaces are also of great interest for the applications mentioned above. Nevertheless, they are non-conductive, making the electrochemical release unfeasible. Regarding biocompatibility, gold and alumina nanoporous membranes' cell viability were

[10] Project website: https://edison.webs.upv.es/

compared using an MTT assay by Adiga *et al.* [359]. Gold membranes showed 65% viability of the alumina membranes. Its superior viability makes alumina a ceramic material with great potential for ECDR.

With this aim, we bound electro-responsive Janus Au-MSNs loaded with Rhodamine B (Rh B) to alumina custom pair of electrodes of 1 mm^2 each. Janus nanoparticles are anisotropic colloidal particles which exhibit two surfaces of different chemical composition, in our case, gold and MSN, as described in Villalonga *et al.* [360]. The electrodes were immersed in a solution of 20 µL 3,6-dioxa-1,8-octanedithiol and 10 mL EtOH in agitation for 2 h. Then, they were stirred with EtOH. Janus MSNs were loaded and gated as described before and drop-casted on the electrodes. In the experiments, increasing voltages between the electrodes were applied for 2 minutes each, and measuring fluorescence afterward. The increasing voltage application (up to 40 V) only induced the final detachment of the alumina coating from the PCB electrodes without a significant increase in the Rh B release. We hypothesize that this may be related to the distance between the substrate and the heparin moieties due to the nanoparticles. *In silico* experiments proved the electric field distribution in the first nanometers of the solution. The generated electric field, decreasing with the squared of the distance, may not generate enough repealing force to the heparin molecules to induce their detachment.

The broad discipline of *gated materials* for controlled drug release is not restricted to nanoparticle gating. Gating porous surfaces is a well-known approach for storing and releasing cargo under different conditions. The use of porous alumina for extended release, given its porous nature, chemical inertness, and biocompatibility, is extensive, *e.g.*, Porta-i-Batalla *et al.* [361] built 3D nanoporous anodic alumina structures for this purpose, developing an extended-release platform. Porta-i-Batalla *et al.* [362] also developed pH-responsive gated-alumina surfaces, obtaining a pH-modulated extended-release platform between the extended-release and controlled drug release fields.

No electrostatically gated controlled drug release technology has been found using alumina as the container. Nevertheless, the work of Di Trani *et al.* [363], using a gated nanofluidic membrane with a Si-SiO_2-polySi-SiC interface, allowed the extended-release control of different cargos. Remarkably, the application of a negative voltage slowed the cargo release.

Li *et al.* reported the electrostatic control of negatively charged fluorescent molecules (fluorescein) with alumina-coated thin film electrodes [364]. Applying a negative potential vs. a reference electrode in the solution attracted the biomolecules in the solution to the alumina surface. In contrast, the application of a positive one repealed them, freeing them.

Inspired by these approaches, we aimed to gate the porous alumina surface without nanoparticles. We used commercial screen-printed electrode sets Metrohm AL10. The aluminum center (4 mm ⌀) is used as the working electrode and the carbon auxiliary concentric electrode as the counter-electrode. The atmosphere oxidation of the aluminum working electrode will produce a 1-2 nm thick alumina passivation (see the works of Ebinger & Yates [365], Nakamura *et al.* [366], Cai *et al.* [367,368], and Gorobez *et al.* [369]). Hence, no significant current will flow between both electrodes, not inducing any electrochemical reaction. The working electrode potential should not be referred to the solution potential, but to the counter-electrode's. Thus, no third reference electrode is employed in this experiment. The natural porous size is around 300 nm ⌀ (see Yang *et al.* [370]).

A silanization mixture of (3-aminopropyl)triethoxysilane (APTES), cetyltrimethy-lammonium bromide (CTAB), EtOH, and H_2SO_4 at 1:0.1:9:0.004 molar ratios was prepared and incubated at 60 °C for 90 min, following the protocol of Nayak *et al.* [371]. The electrodes were immersed in the solution for 90 min. Then, they were stirred with EtOH and dried at room temperature. The electrodes were immersed in a solution of 20 µL 3,6-dioxa-1,8-octanedithiol and 10 mL EtOH in agitation for 2 h. Then, the electrodes were stirred with EtOH, loaded with Rh B, and gated with the bipyridine derivative – heparin mechanism following the procedure described for the MSNs. Two different kinds of electrodes were prepared: fully gated and partially gated, as represented in **Figure 129**. In the latter, a spontaneous release is expected due to the presence of heparin without bipyridine dictation, thus acting as a positive control.

The principle of operation is shown in **Figure 130**. The percentage of the cargo released during the experiment will be used for the evaluation of the release, namely, total cargo. The results are shown in **Figure 131**.

In the fully gated electrodes, the initial spontaneous release after two water washes, each after an hour, represents 15-18% of the total cargo delivered. They released 66-73% of the total cargo after the electrical stimulus of -500 mV was applied to the working electrode vs. the counter-electrode for 100 s. After two additional water washes, they released 12-16% of the total cargo measured.

These values contrast with the positive control results. Following the same protocol, they released 47% of the cargo before the electrical trigger, 41% after the trigger, and the resting 12% after two additional washes.

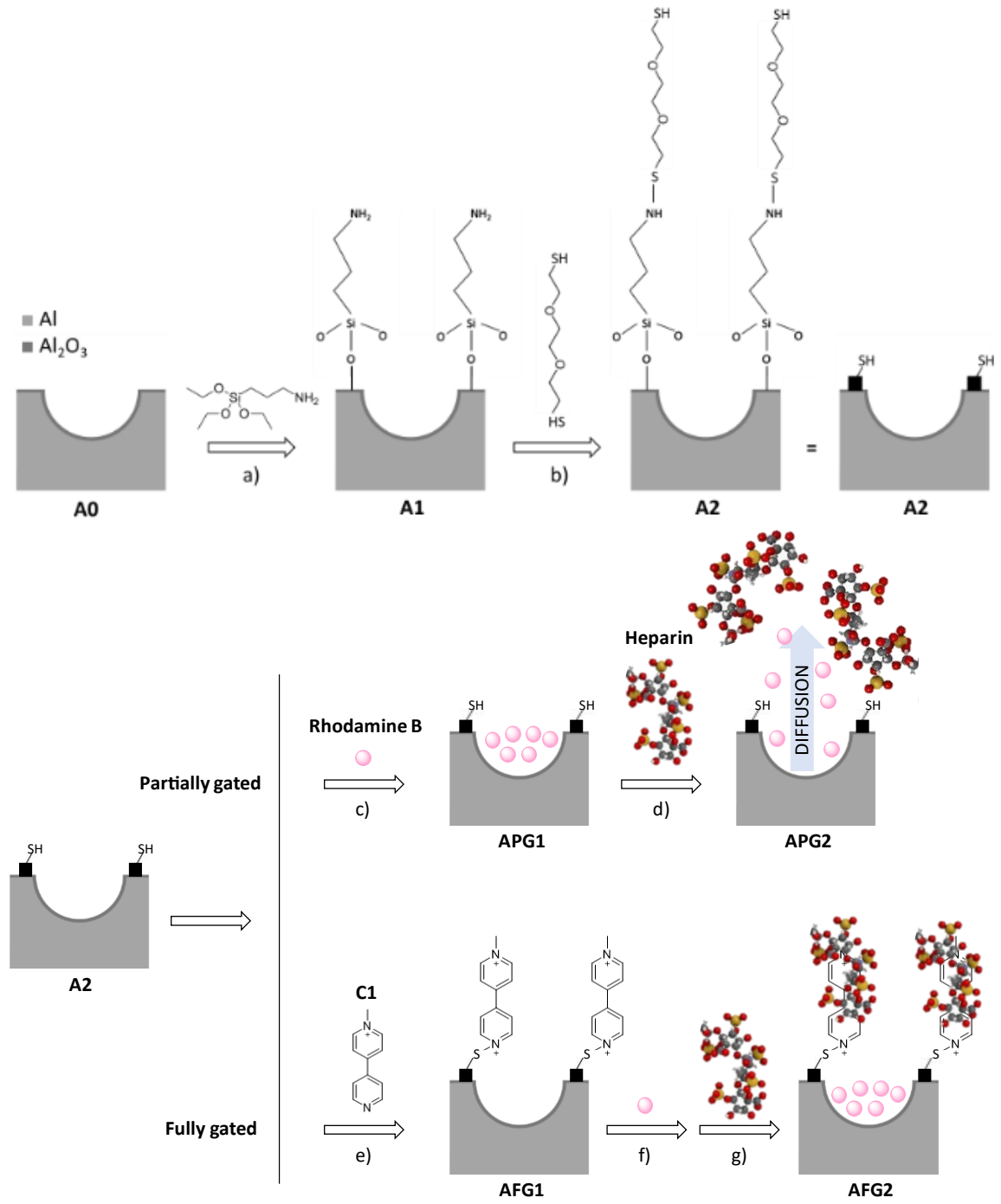

Figure 129. Synthesis of porous alumina surfaces gated with bipyridine derivative – heparin (fully gated: **AFG2**; and partially gated: **APG2**). a) **A0** alumina surface is functionalized with APTES, yielding **A1**. b) **A1** is functionalized with 3,6-dioxa-1,8-octanedithiol with EtOH at room temperature for 2 h, yielding **A2**. For the obtention of the **partially gated** electrodes (acting as positive control): c) The surface is loaded with Rh B in CH_3CN for 24 h (**APG1**). d) The electrodes were immersed in heparin PBS solution for 3 h (**APG2**). For the obtention of the **fully gated** electrodes: e) Functional groups are reacted with **C1** by nucleophilic substitution in refluxed CH_3CN for 72 h (**AFG1**). f) The surface is loaded with Rh B in CH_3CN for 24 h, and g) were immersed in heparin PBS solution for 3 h, yielding the final heparin-capped solid (**AFG2**).

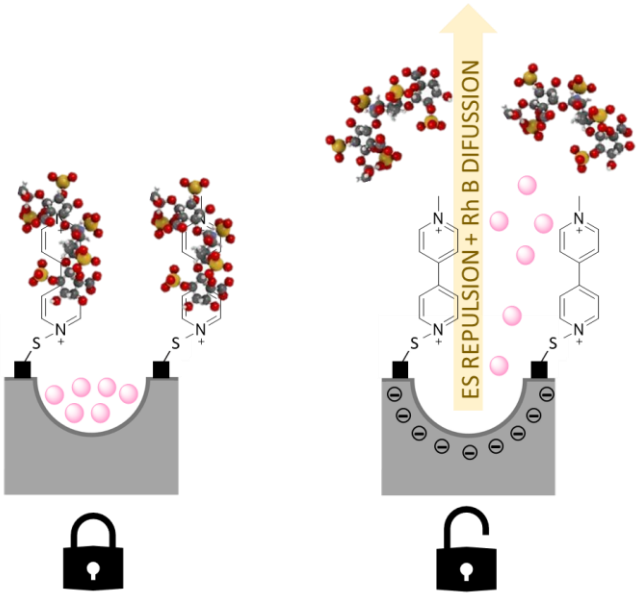

Figure 130. Principle of operation of the electrostatically controlled drug release from porous alumina (**AFG2**).

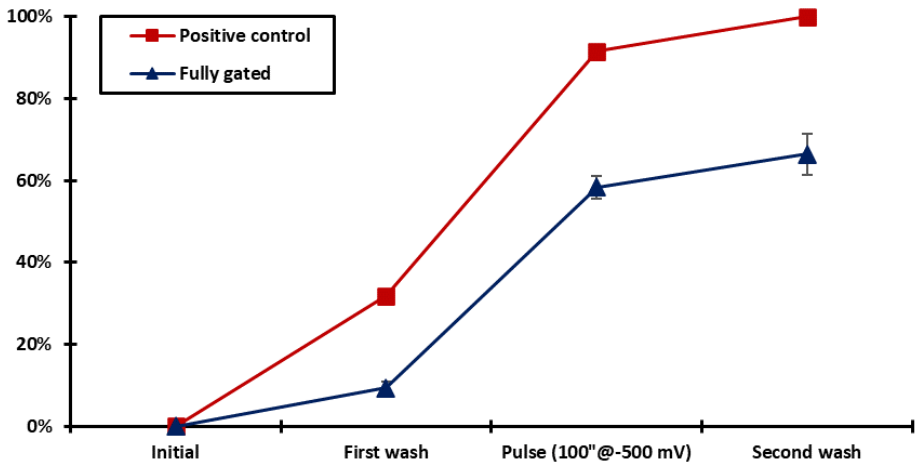

Figure 131. Release profiles of Rh B from **AFG2** material (fully gated) vs. **APG2** material (partially gated, positive control) in the application of TRIS washing (displaying spontaneous release), the application of a -500 mV pulse, and TRIS washing (displaying spontaneous release), sequentially.

The results of this proof-of-concept experiment validate the electrostatic controlled drug release technology. Nevertheless, further studies are needed to fully characterize the release rate depending on the potential applied, duration, and the geometrical configuration between the working electrode and the counter-electrode.

5. Conclusions

With an aging population and the afflictions of fatal diseases, the development of tools for tissue engineering and regenerative medicine is of interest. In this field, the design of conductive polymers with new functionalities is becoming a topic of growing interest. Notably, in the frame of this thesis, using a conductive polymer scaffold for relaying the lesion is a promising technique for Spinal Cord Injury.

Conductive polymers have been used in different biomedical applications; however, as delivery systems, conductive polymers have some drawbacks, such as low loading ability and a poor range of cargo that can be used. To overcome these limitations, we demonstrated herein that it is possible to combine conductive polymers with gated MSNs to deliver cargo upon applying a voltage. In particular, we prepared MSNs loaded with Rh B and capped by an electro-active shell formed by grafted bipyridinium cations and heparin.

Without an external voltage, heparin-coated MSNs (**S3**) cannot deliver the entrapped dye. However, a marked cargo release is observed upon applying a continuous -640 mV vs. SCE potential. This delivery is ascribed to the reduction of the bipyridinium dication that induced heparin detachment and subsequent pore opening. This mechanism is demonstrated by adding acetaldehyde as a chemical reducing agent.

We also prepared PEDOT:PSS-*co*-MA conductive polymers in which the capped nanoparticles are covalently attached (**P3** films). The prepared films can release the entrapped Rh B upon applying a -640 mV vs. SCE voltage. Cell proliferation studies with HeLa cells show that **P3** films are biocompatible. Besides, applying a -600mV vs. Ag/AgCl voltage induced Rh B release from the grafted MSNs, which are uptake by HeLa cells.

To the best of our knowledge, **P3** is the first example of a PEDOT-based conductive polymer equipped with gated MSNs. **P3** shows a remarkable cargo delivery triggered by applying an electric potential. Our studies also open the concept of developing conductive polymers combined with capped MSNs for the on-command delivery of selected cargos using different stimuli for several applications.

Furthermore, the translation of the PEDOT-based with gated MSNs to flexible substrates for its *in vivo* application has been explored. Unfortunately, with negative results that point out the need for further research.

Finally, the electrically controlled drug release (ECDR) from metallic and ceramic surfaces has been developed. A pair of gold electrodes with gated MSNs (**G3**) showed Rh B release after applying a -925 mV vs. its symmetrical electrode, inducing the electrochemical reaction that

produces the heparin detachment. It has been validated for two situations in which both are functionalized or only the working electrode. Furthermore, electrostatic ECDR has been explored. With this aim, we gated self-oxidized porous alumina electrodes loaded with Rh B with a bipyridine-heparin molecular gate. With the application of -500 mV vs. the adjacent GCE, a significant increase in the solution Rh B was measured, related to the controlled release. This release was performed without faradic processes, as shown in the measured null current. Both electrochemical ECDR in gold surfaces and electrostatic ECDR in alumina surfaces are novel contributions of this present doctoral thesis but need further study and validation before publication.

For the stimuli generation FAEVIS, described in *Chapter 1. Electronic instrumentation for in vitro electrostimulation and controlled drug release*, as an original design of this doctoral thesis, has been used. This electronic device can apply ECDR and electrostimulation stimuli in a cell culture environment in a flexible and sequenced way.

Chapter 3. Electrostimulation for nervous tissue regeneration *in vitro*

Electrostimulation of neural precursor cells (NPCs) is one of the most promising techniques for modulating their development. In this chapter, we will review the state of the art of direct-coupled electrostimulation of NPCs on a conductive substrate. Based on this review, we will conceptualize a set of tools for the developmental modulation of NPCs.

We will then describe the work on developing a substrate for *in vitro* research with potential portability to *in vivo* application. To this end, we indicate the general importance of using extracellular matrices. We select a flexible substrate on which a conductive coating will be applied. Different alternatives are evaluated, and once chosen, a study of the appropriate thickness and its resistance to degradation is carried out. Various options are explored to retain cell medium on the substrate. However, we only achieved adequate cell viability and adhesion in PEDOT:PSS after plasma activation. Finally, we show the results of electrostimulation experiments on different platforms.

Given the difficulties in the suitability of the biomaterials for the application, the scientific production of this chapter is limited to a participation in an international congress (Alamán-Escolano *et al.* [372]).

1. Electrostimulation on neural precursor cells (NPCs) with conductive substrates

In the *Introduction*, we addressed electrostimulation (ES) as a tool for modulating neural precursor cells (NPCs) development in subsection *3.2. Techniques based on electrostimulation* focusing on direct coupling electrostimulation with a conductive polymeric substrate. Its operating principle is still under study. The most recent hypothesis point out to the ionic perturbation of the electric double layer (Morgado *et al.* [373]). In the present section, we will discuss the different techniques and their effects and functional parameters.

According to Zhu *et al.* [107] and Cheng *et al.* [114], there are mainly four direct couplings ES techniques for NPC development modulation:

- **DCEF**: Direct Current (DC) Electric Field (EF), in which a constant voltage (10-500 mV/mm) is applied for minutes daily up to uninterruptedly for days.

- **ACEF**: Alternating Current EF, sinusoidal or square, 1-50 mV/mm, in a frequency of 0.1-10 Hz, from minutes daily up to uninterruptedly for days.
- **PCEF**: Pulsed Current EF, with 100-500 mV/mm or 4-32 mA/cm^2, with a pulse width of 0.1-200 ms, at 1-1000 Hz frequencies. It is usually applied for 30-60 minutes a day for several days.
- **BCEF**: Biphasic Current EF, the pulse is followed by a counter-pulse of the same amplitude and duration, with 20-90 mV/mm or 8-250 µA/cm^2, pulse width of 0.1-250 ms, at 2-100 Hz. Usually applied uninterruptedly, or 4-12 h/day, for one to four days.

It is compulsory to divide them according to the electrical setup employed as a crucial characteristic to review the effects of each of them. Nevertheless, comparing several studies involves a high degree of complexity due to the different scaffolds, coatings, growth factors, electrical parameters, protocol timings, and cell lineages used. No more than one of the mentioned main parameters is rarely shared between two studies. The three possible direct contact electrostimulation configurations are shown in **Figure 132**:

- **Direct gradient** electrical stimulation: in between the ends of a conductive scaffold
- **Solution gradient** electrical stimulation: in between two additional electrodes in solution.
- **Dual scaffold** electrical stimulation: using the seeded scaffold as a working electrode and a secondary scaffold as a counter-electrode.

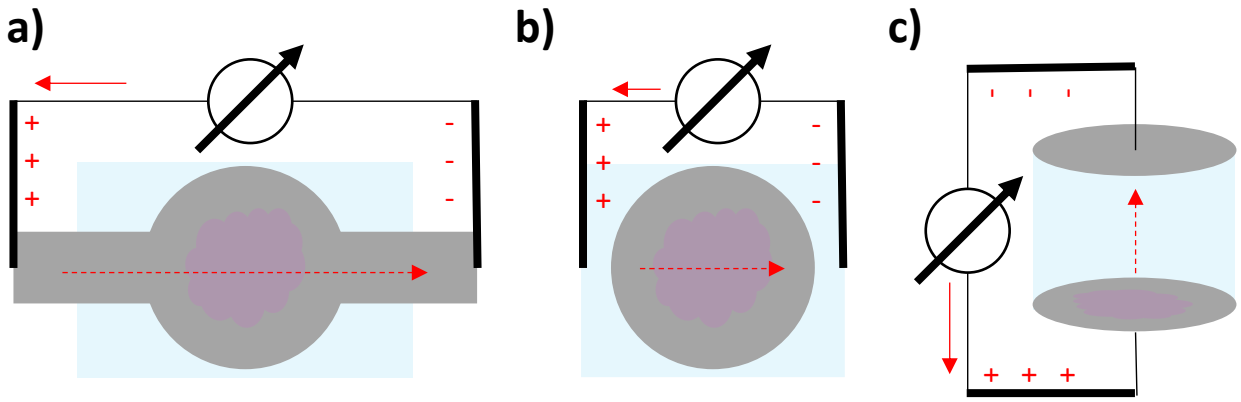

Figure 132. Three direct coupling electrostimulation options: **a)** electrical stimulation in between the ends of a conductive scaffold, **b)** electrostimulation between two additional electrodes in solution, or **c)** electrostimulation using the seeded scaffold as working electrode and using a secondary scaffold as counter-electrode.

We will now go into the effects of each electrostimulation technique (DCEF, ACEF, PCEF, BCEF) depending on the configuration used. Then, we will conceptualize electrostimulation tools based on this meta-analysis.

1.1. Direct gradient electrical stimulation

In the application of DCEF, Prabhakaran *et al.* [374] showed neural stem cell elongation by applying 100mV/mm for 1h a day for 10 days. Heo *et al.* [375] applied 2000 mV/mm for 24h a day for 10 days, obtaining positive results in neuronal differentiation. Thrivikraman *et al.* [105] applied 1, 10, and 50 mV/mm for 10 minutes a day for several days: 1 mV/mm did not have any effect, 10 mV/mm presented a positive influence in proliferation, differentiation, elongation, and maturation, but 50 mV/mm had a negative impact in cellular viability. Kobelt *et al.* [376] also applied 10 minutes/day for two days, 0.53 mV/mm and 1.83 mV/mm. Both had positive effects on alignment, differentiation, elongation, and maturation. Ghasemi-Mobarakeh *et al.* [377] applied 100 mV/mm for 15 to 60 minutes and evaluated the results after 24h, obtaining positive results in differentiation and elongation.

As observed, the absolute electric field values cannot be directly established to obtain a minimum effective threshold and a safety maximum. Whereas Thrivikraman *et al.* observed apoptosis with 50 mV/mm for 10 minutes, Heo *et al.* applied 2000 mV/mm 24 h a day for 10 days, obtaining positive results. Thrivikraman *et al.* reported no effect at 1 mV/mm, whereas Kobelt *et al.* had positive effects with just 0.53 mV/mm. Thrivikraman *et al.* study is particularly interesting because it addresses the substrate conductivity – electrical field intensity relation effect on elongation and viability, as shown in **Table 5**:

Table 5. Conductivity and electrical field (10 minutes/day) effect on elongation and viability. Data from Thrivikraman *et al.* [105].

	>3MΩ/m	(3000,200) kΩ/m	(200,0.02) kΩ/m	<0.02 Ω/m
10 mV/mm	Small extension	Extension	High extension	Less viability
50 mV/mm		Extension Less viability	No viability	No viability
100 mV/mm	Extension after 7 days	No viability	No viability	No viability

This electrical information is only sometimes present in publications. From the former, only Ghasemi-Mobarakeh *et al.* with 47 MΩ and Heo *et al.* with 300 MΩ show these values. Thrivikraman *et al.*, with 100 mV/mm for 10 minutes, observed certain elongation. Hence, we can assume that the prolongation of the electrical stimulation and the electric field intensity increase can produce positive effects in the elongation on highly resistive scaffolds. Nevertheless, the absolute optimal is between 200 kΩ/m and 20 Ω/m, given that the criteria to assess an extension as *small* for Thrivikram *et al.* is shorter than 200 μm, and observing *long* extensions of up to 0.85 mm.

Regarding the application of BCEF, Tang-Schomer [378] applied 90 mV/mm at 2 Hz for 4 days observing positive results in proliferation and elongation. Lee *et al.* [379] applied 100 μs width, 100 Hz 100 μA for four days, obtaining positive results in elongation and differentiation. None of them has information to obtain the conductivity of the scaffolds. Zhu *et al.* [380] reported increased proliferation, neuronal differentiation, and elongation by applying 100 μA current during 100 μs at 100 Hz for 24 h.

Sudwilai *et al.* [381] applied a mixed protocol consisting of 2h of 20 mV/mm DCEF followed by 4h of 20 mV/mm 50 Hz BCEF for three days, observing positive results in migration and elongation. The conductivity of the scaffold is 2-5 Ω/m, which is in the optimum range identified by Thrivikraman *et al.* The electrical field intensity and duration without viability degradation means there may be an exploration margin increasing those two parameters.

The most widely used electrostimulation in direct gradient configuration is PCEF: Pires *et al.* [382] applied 100 mV/mm asymmetric square 100 Hz signal for 12-24h/day for several days onto a seed 5.8 Ω/m PEDOT:PSS scaffold, observing increased neuronal differentiation and elongation. Yang *et al.* [383] applied a 3 μA intensity 1 Hz square signal for 30 minutes a day, every 12 h, for several days, observing increased neuronal differentiation and maturation. Huang *et al.* [384] applied a 20 Hz asymmetrical square stimulation for 15 minutes daily on a highly conductive scaffold for several days. Whereas 0.1 mV/mm had no effect, 1 mV/mm had a negative effect on cell viability. 0.5 mV/mm has a positive effect on maturation and elongation. These results are coherent with **Table 5**. Nguyen *et al.* [385] applied on a scaffold of 170 Ω/m 10 μA during 500 ms at 1 Hz for 30 minutes a day for three days, reporting increased proliferation, differentiation, elongation, and maturation. Fu *et al.* [386] applied 10 mV/mm at 100 Hz asymmetric square, 1h a day for also three days, reporting increased neuronal differentiation, elongation, proliferation, migration, and adhesion. It is the only study that mentions an *adhesion* effect of ES.

Hence, DCEF may be applied from 0.5 to 1000 mV/mm depending on the conductivity of the scaffold: the higher the resistance, the higher the voltage needed to produce effects. Moreover, because of Ohm's Law, it may mean that the effects are related to the *current* flowing through the scaffold. Overcurrents may induce apoptosis. A similar conclusion got Lee *et al.* [379]. The duration of the ES may go from minutes to non-stop for one or several days. 80% of the DCEF studies before reported positive elongation effects, also 80% reported neuronal differentiation, and 60% reported both simultaneously. 40% reported maturation, and one study each reported increased alignment and proliferation.

BCEF studies reported increased proliferation; out of the three, 66% reported increased neuronal differentiation, and the other 66% increased elongation. Combined DCEF and BCEF

reported elongation and migration effects. Frequencies vary from 2 Hz to 100 Hz, with symmetric application or width reduction up to 100 µs. It has been reported 90 mV/mm or 100 µA intensity, continuously for one to four days. Absolute values can increase given that this is a zero-DC ES, meaning it will not permanently and increasingly bias cells as DCEF and PCEF do.

Finally, PCEF reported positive neuronal differentiation in all the studies, elongation in 80% of them, proliferation in 60%, maturation in the other 60%, and migration and adhesion in 20%. Voltages may vary from 0.5 mV/mm up to 100 mV/mm, depending on the scaffold conductivity. In terms of current, 3 and 10 µA have been reported. Timing may go from 1 Hz up to 100 Hz, usually with pulse widths of half the duty cycle, from 15 minutes a day up to continuously applied for several days.

Keeping in mind that not every study measured all the parameters, we can obtain a summary picture of the effects of PCEF, BCEF, and DCEF in direct gradient electrical stimulation with the former percentages, as shown in **Figure 133**. PCEF, BCEF, and DCEF effects on neural stem cells / neural precursor cells in the literature, in direct gradient electrical stimulation configuration..

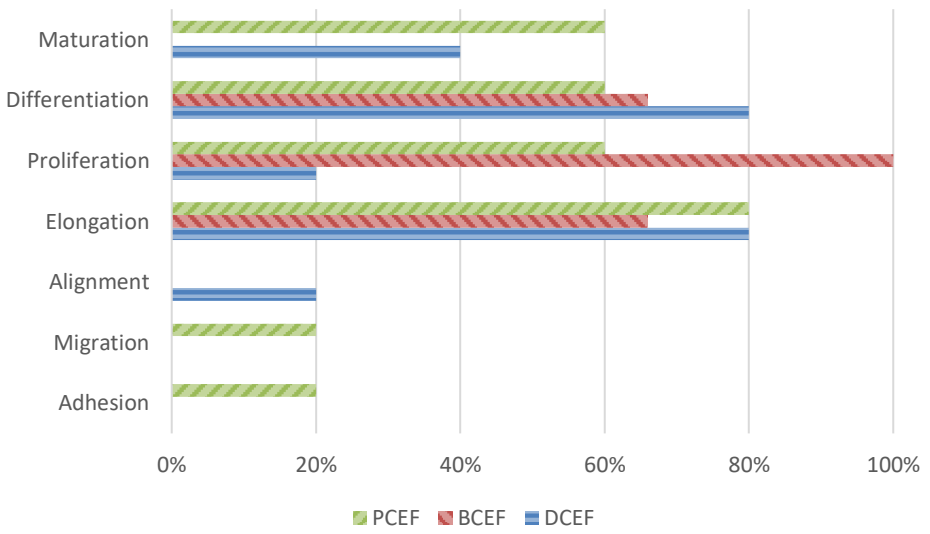

Figure 133. PCEF, BCEF, and DCEF effects on neural stem cells / neural precursor cells in the literature, in direct gradient electrical stimulation configuration.

PCEF, and short-duration DCEF (10'/day, Thrivikraman *et al.*), offer the most balanced response regarding maturation, differentiation, proliferation, and elongation. It seems that DCEF is the most effective in differentiation and presents the highest scores in elongation, but at the expense of proliferation and viability for long time stimulations. On the other hand, the BCEF proliferation effect is reported in all the studies and is reported as a dual tool for proliferation and differentiation in several studies.

1.2. Solution gradient electrical stimulation

When the electrical field is applied between two electrodes placed in the opposite sites of an *in vitro* environment, in which the cells are seeded on a scaffold (usually non-conductive), the induced current will flow mostly across the solution.

The application of DCEF stimulation in solution gradient configuration is the most common in the literature: Li *et al.* [387] applied 50-250 mV/mm for 3 h, Feng *et al.* [102] applied 16-300 mV/mm for different times, from 10 minutes up to 3 h, Li *et al.* [103] applied 50-100 mV/mm for 1 h. They all reported a migration effect during one to a few days of stimulation towards the cathode. Dong *et al.* [388] applied 50-250 mV/mm for 12 h every day for one and two weeks, and Naskar *et al.* [389] applied 8 mV/mm for 20h every day for 8 days. Both reported positive neuronal differentiation effects.

The application of ACEF in this configuration has been reported only by Matos & Cicerone [390], applying different electric field intensities and frequencies continuously for several days, reaching the three weeks duration. 1 Hz was the only frequency with a positive impact on proliferation and viability, being diminished by lower frequencies. 2 mV/mm field intensity induced neural differentiation, whereas 4-16 mV/mm induced a variety of differentiation in glia, oligodendrocytes, and neurons in the neural stem cell population.

Finally, Ariza *et al.* [391] explored the DCEF stimulation, with 437 mV/mm, 16 h every day, observing positive effects in migration, alignment, proliferation, neuronal differentiation, elongation, and maturation in neural precursor cells, at the expense of viability, and also explored the BCEF stimulation with a 46 mV/mm 0.5 Hz protocol for 30 minutes every day, reporting an increase in neuronal differentiation.

Hence, DCEF stimulation in solution gradient configuration has a migration effect towards the cathode and a relevant impact on neuronal differentiation. Nevertheless, other effects are reported just by one study, and viability can be diminished, probably when the current induced and stimulation time is too high. ACEF and BCEF have reported an increase in proliferation for 1 Hz and 0.5 Hz stimulation, and neuronal differentiation seems to be modulated by the electric field intensity.

1.3. Dual scaffold electrical stimulation

Finally, when the electrical stimulation is applied to the conductive substrate in which the cells are seeded, using a similar substrate as counter-electrode, BCEF and PCEF electrical stimulation are the only ones found in the literature.

Regarding BCEF, Chang *et al.* [392] applied a 200 µs width square signal every 10 ms, with an intensity of 8 µA/cm^2 constantly for several days, obtaining positive results in terms of proliferation and neuronal differentiation. Wang *et al.* [393] applied a 25-50 mV/mm square signal of 160 µs width every 8 ms for 12 h, positively impacting cellular viability. Stewart *et al.* [394] applied a square signal of 250 µA/cm^2 200 µs width every 4 ms for 8 h a day for three days, reporting enhanced elongation and neuronal differentiation.

On the other hand, applying PCEF, Jin *et al.* [395] with a triboelectric nanogenerator (electrical and timing parameters unknown) for 1h/day for several days reported an enhancement in maturation. Du *et al.* [104] applied 200 mV/mm 100 µs width pulse every 500 ms, 50 ms, and 10 ms for 1, 3, and 8 hours. All reported an increase in viability and neuronal differentiation.

Hence, this configuration reported viability and neuronal differentiation enhancement for 60% of the studies. Viability boosting is pointed out in a PCEF and a BCEF studies. In a study each, elongation, maturation, and proliferation increases have also been reported.

1.4. Conceptualization of electrostimulation tools

Having reviewed state of the art, evaluated the effects of electrostimulation on cells for the three types of configurations identified, and mentioned the electrical and temporal parameters applied in each publication, this subsection aims to conceptualize electrostimulation-based tools to obtain specific cellular response results. However, we must remember that these tools must be adjusted, like a calibration, before being really effective since, as we have observed, the conductivity of the substrate directly affects on the cellular response. These responses will be expected to differ depending on the cell line used or other factors.

- **TOOL 1: Elongation with differentiation and proliferation:** direct gradient configuration short DCEF (<10 minutes per day), BCEF, and PCEF reported elongation response, with a boost in neuronal differentiation and proliferation. Depending on the scaffold conductivity, the desired response is obtained for certain electric field intensity. Overstimulation induces cell viability diminution.
- **TOOL 2: Proliferation with differentiation modulation:** 1 Hz ACEF in solution gradient configuration showed proliferation and viability boost response. Differentiation into neurons is increased at low amplitudes (2 mV/mm), and the differentiation into other neural cells in a mixed output is obtained with higher amplitudes (4-16 mV/mm). Dual scaffold configuration PCEF and BCEF (100-200 µs width, 1-100 Hz, 1-250 µA/cm^2 or

200 mV/mm) also increase proliferation, viability, and neuronal differentiation, whereas 25-50 mV/mm 125 Hz stimulation increased viability without reporting a neuronal differentiation boost.

- **TOOL 3: Migration**: using a counter-electrode as a cathode, applying DCEF induces the migration towards the cathode of the cells. 50-250 mV/mm during several hours per day is reported to obtain this effect without viability diminution.

The maximum duration to be supported by the software is at least tens of days since protocols of up to 21 days exist in the literature. The maximum voltage observed is 1600 mV/mm, and the minimum pulse width 10 μs. Currents are in the order of tenths-hundreds of μA.

Therefore, we conceptualize the development of a platform that allows, from a graphical user interface, to program the electrical stimulus protocol that unleashes the specific electrically triggered controlled drug release at the selected time, as well as to apply the three ES techniques in at least the limits described by the literature in each of them. This rationale has been the basis for the *3. Equipment requirements* described in *Chapter 1. Electronic instrumentation for in vitro electrostimulation and controlled drug release*.

Section summary: We hypothesize then a good first approach to an effective three-step ES protocol would involve three ES tools:

- **TOOL 1:**
  - **Purpose:** would induce the neural precursor cells into long neurons, suitable for building the necessary relay mechanism.
  - **Configuration and electrostimulation:** direct gradient configuration short DCEF (<10 minutes per day), BCEF, and PCEF. Intensity and duration depending on substrate resistivity (see **Table 5**).
- **TOOL 2:**
  - **Purpose:** can be used to obtain an adequate environment for the former neurons, obtaining an appropriate mix of glia, oligodendrocytes, and neurons depending on the needs of the before-mentioned elongated cells.
  - **Configuration and electrostimulation:** (1) 1 Hz ACEF in solution gradient or (2) dual scaffold configuration PCEF and BCEF. Smaller intensities are associated with neuronal differentiation.
- **TOOL 3:**
  - **Purpose:** may be used to induce the *in vitro* built relay's detachment to be transferred *in vivo*.
  - **Configuration and electrostimulation:** solution gradient or dual-scaffold DCEF.

2. Extracellular matrix coating

The extracellular matrix (ECM) is a complex network of proteins and other macromolecules that provides structural and biochemical support to cells in their natural environment.

Matrigel[11] is a commonly used ECM protein mixture often used as a basis for *in vitro* cell culture, particularly for stem cells. Matrigel contains various ECM proteins, growth factors, and extracellular matrix components that mimic the native environment of cells, promoting cell attachment, survival, proliferation, and differentiation.

Stem cells, particularly neural precursor cells (NPCs), benefit from Matrigel *in vitro* as it provides a supportive environment that mimics the natural *in vivo* conditions. Overall, Matrigel can improve these cells' viability, proliferation, and differentiation, which can lead to more accurate *in vitro* models of cellular behavior.

As already mentioned, bioengineered scaffolds and substrates, such as conductive polymers and hydrogels, can support stem cell growth and differentiation. These materials can provide mechanical and electrical support, mimicking the physical and electrical cues that cells experience *in vivo*. Coating their surfaces with ECM, such as Matrigel, can enhance their viability, adhesion, proliferation, and differentiation, as Tonelli *et al.* [396] reported over carbon nanotube substrates. Similar results were reported by Zhou *et al.* [397] over PLLA-PPy. Particularly, Karagkiozaki *et al.* [86] , cell adhesion, viability, and proliferation were enhanced by the peptide-coating of the PEDOT:PSS substrate.

Section summary: The seeded neural precursor cells (NPCs) need adequate proteins, growth factors, and other components to present positive adherence, viability, proliferation, and differentiation over the bioengineered scaffold. These requirements can be met with an extracellular matrix coating such as Matrigel.

3. Flexible substrate selection

Transplanting neural precursor cells (NPCs) into sites of spinal cord injury (SCI), in combination with pharmacological therapy, showed promising results in improving forelimb

[11] It is the ECM employed in most of our experimental procedures. Corning's Matrigel additional information: https://www.corning.com/cala/es/products/life-sciences/products/surfaces/matrigel-matrix.html (accessed February 13th 2023).

function thanks to the axon regeneration and synapsis (Rosenzweig *et al.* [30], Kumamaru *et al.* [31]). Nevertheless, purely cell-based therapies seem not suited enough to restore the altered spinal architecture that underwent alterations leading to growth inhibition and loss of guidance through large distances. Neural tissue engineering approaches aim to produce adequate scaffolds with the needed mechanical and biological properties to recover function. These scaffolds can combine biomaterials, cells, and molecules to promote axonal regrowth and synapsis (see Rodríguez Doblado *et al.* [398]). This combination is also known as *biohybrid* in the literature (see Martínez-Ramos *et al.* [399]).

The biomaterial development or selection is fundamental to improving the transplantation outcomes given its influence on cell adhesion, survival, cell fate regulation, and long-term function (see Kharbikar *et al.* [44]).

PEDOT-based conductive polymers have demonstrated capabilities for the bioelectrochemical control of NPC development by electrostimulation (Collazos-Castro *et al.* [326]) and electrically controlled drug release (García-Fernández *et al.* [220]). Nevertheless, the latter used PEDOT:PSS-*co*-MA electrodeposited over ITO/glass slides with sputtered gold. This novel *in vitro* result presents two inconveniences:

1. The underlying gold impedes the electrostimulation as it short-circuits the electrical field applied between two substrate edges.
2. The electrodeposition needs metal to be coated during the process, namely gold. In the case of ITO/glass, it is a rigid substrate unsuitable for *in vivo* application.

Therefore, we will select a biocompatible flexible substrate that will be screen-printed with PEDOT:PSS.

First, we evaluated the cytotoxicity, cellular viability, adhesion, and cell fate properties of several substrates: PBA74, Inspire 2370, SEM EU50, SEM EU P405, VAF 445, and PDMS. All substrates were disinfected with 30' exposure to EtOH and 30' exposure to UV radiation.

Indirect cytotoxic analysis was performed according to ISO 10993-5. Briefly, NPCs were seeded at a density of 10^4 cells in 96-well plates for 24 hours. They were exposed to a liquid extract obtained after incubating 0.1 g of PBA74, Inspire 2370, SEM EU50, SEM EU P405, VAF 445, or PDMS in 1 ml of proliferative medium in order to study the possibly toxic substances leached from the biomaterial. The MTS assay was performed 24, 48, and 72 h after cell stimulation with the conditioned media or in control conditioned, non-exposed to the biomaterial. Cell viability was expressed as a percentage of change versus control (considered 100% viability). None of the substrates showed cytotoxicity for NPCs (**Figure 134**).

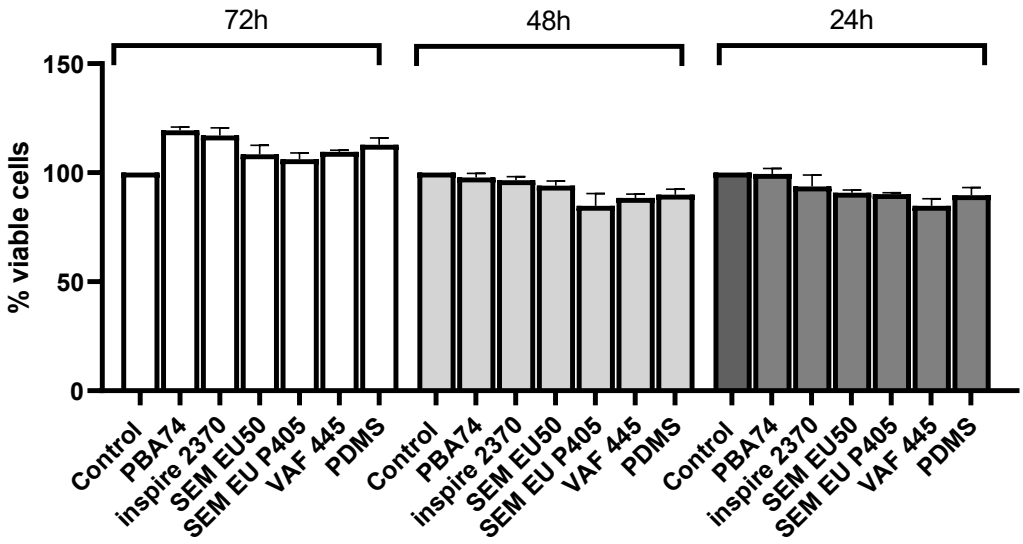

Figure 134. Evaluation of the cytotoxicity of 6 different substrates for neural progenitor cells (NPCs). Reproduced from [372].

Cell adhesion capacity of NPCs to the different substrates was determined by culturing 25 x 10^4 NPCs onto the different substrates in the absence or presence of Matrigel-coating and under proliferation conditions for three days. Cells were fixed with paraformaldehyde (PFA) and stained against Nestin (an intermediate filament protein expressed in NPCs). All evaluated substrates showed increased adhesion in Matrigel's presence (representative images shown in panel of **Figure 135**).

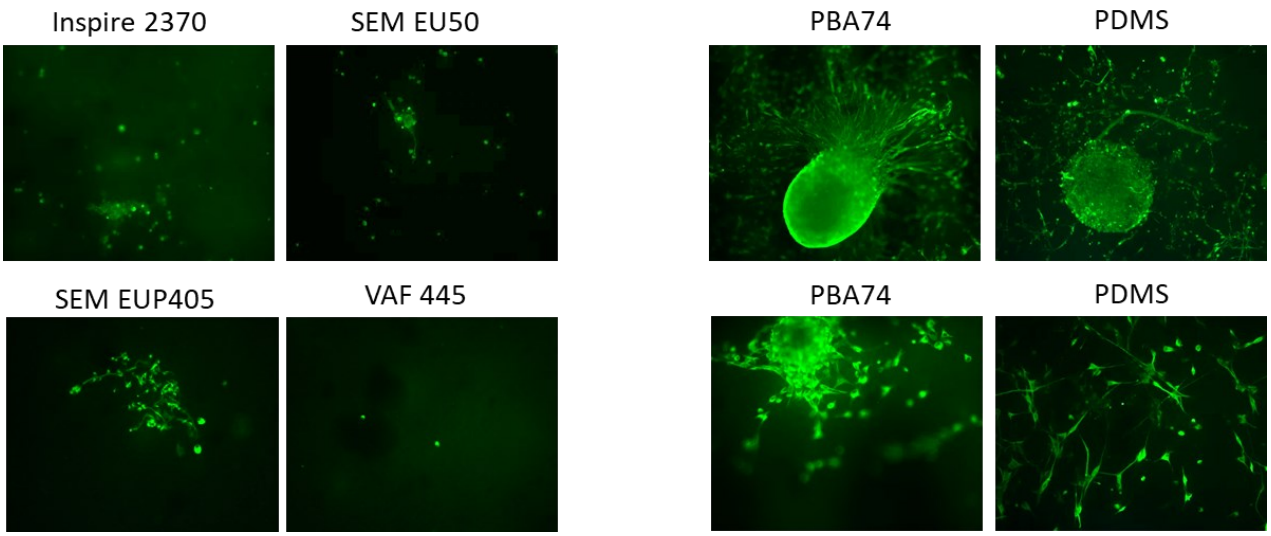

Figure 135. Evaluation of the adhesion capacity of 6 different substrates for neural progenitor cells (NPCs).

Overall, PBA74 and PDMS substrates showed improved qualities for NPCs cultures by showing increased number of NPCs and elongated morphology compared to the other substrates.

Nevertheless, none of the evaluated materials presented adequate screen-printability. Therefore, we selected the screen-printing PET NB-TP-3GU100, *a priori* similar to the evaluated PET Inspire 2370, but with better screen-printability. We evaluate the cellular adhesion and cytotoxicity following the same procedure with 10^5 NPCs cultures.

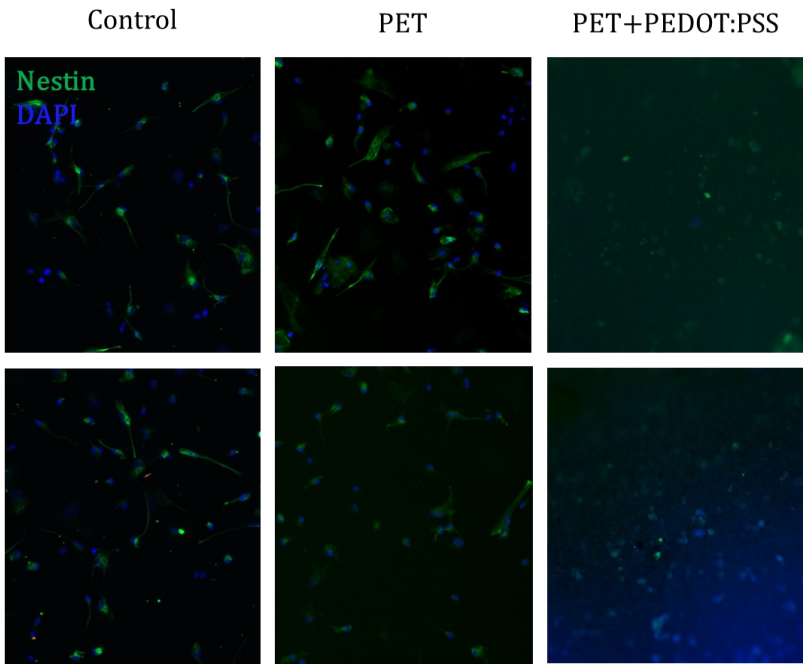

Figure 136. Immunofluorescence images of control (left), PET (center), and PET screen-printed with PEDOT:PSS (right).

Following the same MTS cell viability assay described for the previous six substrates, PET showed adequate but not significantly lower viability than the control. The PET immunofluorescence shows enhanced elongation in the cell morphology compared with the control. However, PEDOT:PSS screen-printed PET showed very low viability. The immunofluorescence evaluation with Nestin and DAPI (used to detect nuclei) markers is limited by the coating of PEDOT:PSS with a grayish-bluish color (**Figure 136**).

Section summary: Flexible substrates with suitable properties are fundamental to implementing the most promising spinal cord injury treatment strategy: the lesion relay. They need to be conductive and capable of carrying neural precursor cells. We evaluate several flexible substrates, finally choosing the PET NB-TP-3GU100, with good screen-printing capabilities. Nevertheless, its good cell attachment vanish when it is coated with PEDOT:PSS.

4. Conductive coating selection

Endowing the flexible substrate of conductive capabilities should not be with the cost of reducing its biocompatibility but enhancing its capabilities to attach the cell culture and promoting its viability, proliferation, and differentiation, among other parameters of interest. This section evaluates a hydrogel and several screen-printing PEDOT:PSS inks. The one displaying the best results is evaluated regarding the number of layers to increase cell attachment and in terms of degradation upon exposure to the cell culture environment. The section ends with a final comment on the discarded hydrogel approach, stressing its potentialities in combination with PEDOT composites according to the state of the art. All impedance measurements have been performed with two wires. The cable impedance is under 0.2 Ω and considered negligible in comparison of the smaller impedance measured in the order of 200 Ω.

4.1. Hydrogel-based conductive coating

Polychem's UV curable conductive hydrogel JN0917-A[12], based on polyacrylamide polymer, acrylic polymer, polyhydric alcohol, and metallic salts, was evaluated for endowing the flexible substrate of electrical conductivity. According to the manufacturer's technical information, it successfully passed the ISO 10993 tests with the best scores regarding *in vitro* cytotoxicity, skin irritation, and skin sensitization. The MTT assays from SGS Taiwan Ltd. reported no induced cytotoxicity to L929 cells (report no. PUB21B00275). Regarding its electrical characteristics. The typical resistivity is 1.6 kΩ/square, 0.4 S/cm. A typical layer of ⌀ 1 cm is 180-250 Ω from edge to edge.

150 µL of JN0917-A (from now on, hydrogel) was pipetted on the top of a coverslip, treated or not with Geltrex (basement membrane extract), into 24 well plates. Then, the hydrogel was curated by exposition to 362 nm light using a portable light source for 30 seconds. The hydrogel consistency was equivalent in coated or not coated coverslips. 50.000 cells (iNPCs) were seeded on the top of the hydrogel for 72 hours at 37 °C. The consistency of the hydrogel remained at adequate levels after 72 hours (**Figure 137**, left), but the cells did not expand. They kept a round morphology and died 72 hours after incubation (**Figure 137**, right). After fixation with PFA 4%, the hydrogel lost its previous consistency.

[12] We acknowledge Polychem's free sample delivery and technical information sent to evaluate the hydrogel for our application.

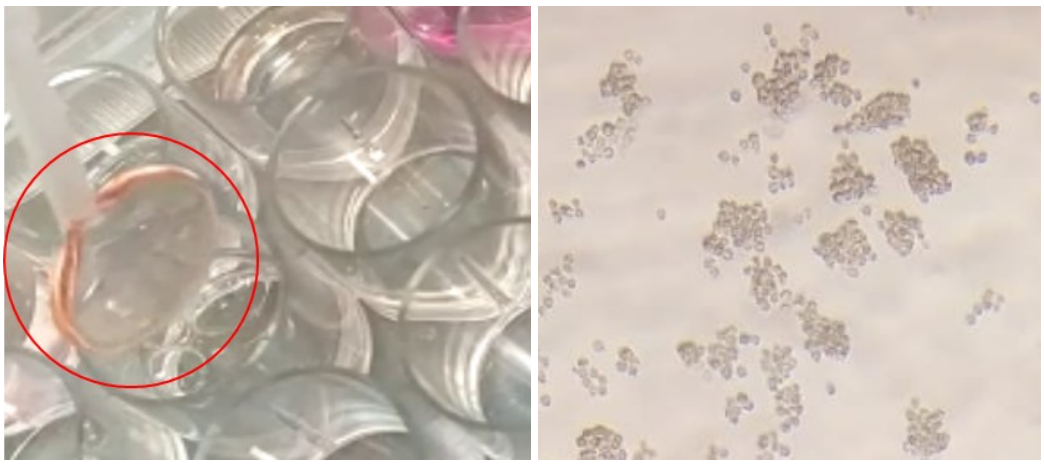

Figure 137. Hydrogel scaffold after 72 h of incubation (right) and microscope images of the seeded iNPCs with round morphology indicating poor attachment and viability (right). They were confirmed to be dead with immunofluorescence.

In a 24-well matrix we added 100 µL of hydrogel in four wells. We applied UV radiation for 60 seconds. We added cellular culture medium in two of them. The four wells were stored at 37 °C for 24 h. Then, we added medium in the last two. After 24h, we removed the excess medium, and the hydrogel scaffolds were moved to unused wells. Three of them had dissolved in the medium with thick gelatinous consistency. Only one of the four kept its post-UV curation consistency. This last scaffold was cut in two: (1) $33 \cdot 10^3$ iNSCs and (2) $25 \cdot 10^4$ NSCs were seeded, respectively.

Additionally, a mix of 50 µL hydrogel / 50 µL medium was UV-cured for 60 second and $33 \cdot 10^3$ iNSCs were seeded, namely substrate (3), to evaluate the lower consistencies adequacy.

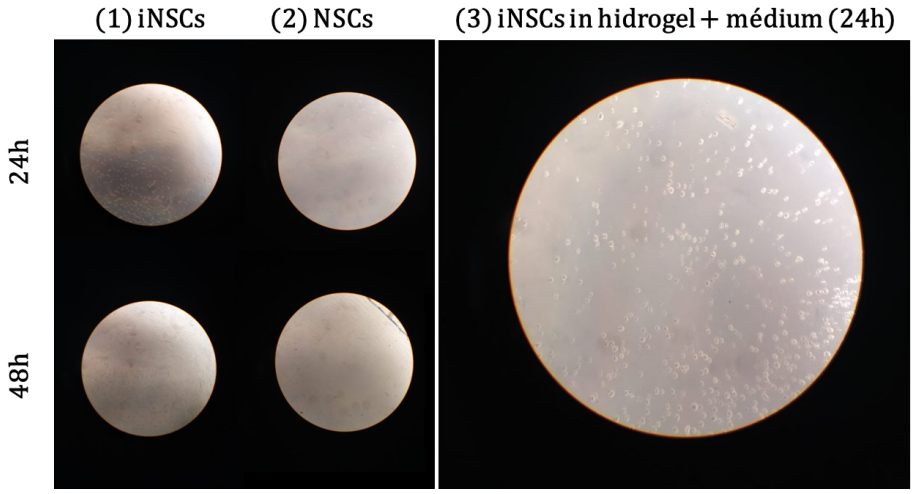

Figure 138. Confocal microscopy images of substrate (1) and (2) after 24h and 48h of incubation (left), and of substrate (3) after 24h of incubation (right).

All three substrates were incubated at 37 °C for 24 h. Microcopy showed promising adhesion in the substrate (1), poor adhesion in the substrate (2), and immersion inside the hydrogel for substrate (3) (**Figure 138**). After 48 h, we did immunofluorescence assays. The substrates did not lose their consistency in contact with PFA. Nevertheless, all cells were dead.

4.2. Screen-printed PEDOT:PSS conductive coating

We evaluated the PET NB-TP-3GU100 (from now on, just PET) screen-printed with four commercial PEDOT:PSS inks:

- Clevios SV4.
- Clevios SV3HV.
- SunChemical.
- Orgacon.

The screen-printed PETs cutouts, and a non-screen-printed PET cutout, were sterilized by ethanol immersion (70%) for 24 h. After drying out, Geltrex and Matrigel coating were applied (4 ˚C overnight, with DMEM/F12+Penicilin/Streptomycin, 24 h). A total of 10 substrates were evaluated. $50 \cdot 10^3$ mesenchymal cells were seeded for 3 days (incubation at 37 ˚C). Then, PFA fixing and DAPI immunofluorescence assays were performed (**Figure 139**).

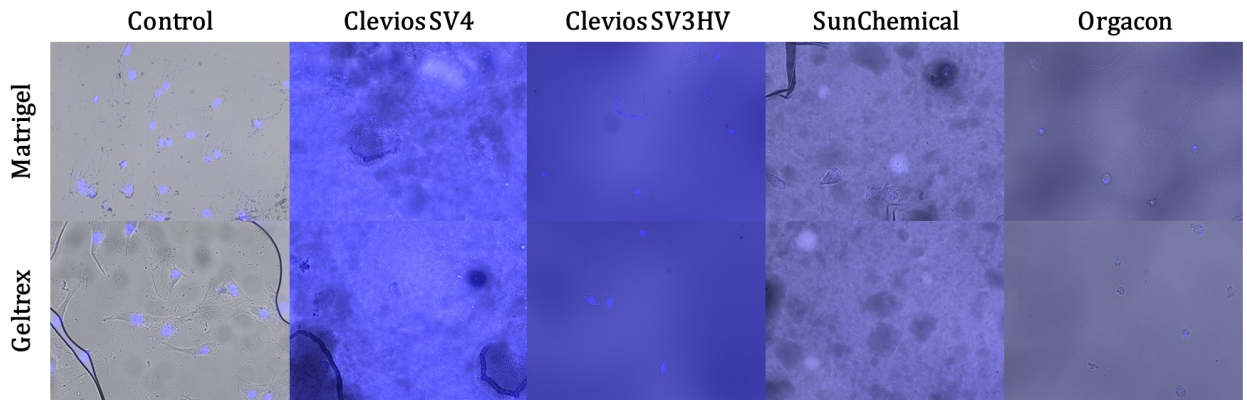

Figure 139. DAPI immunofluorescence on bare PET and screen-printed PET with different commercial PEDOT:PSS inks.

Among all the PEDOT:PSS inks evaluated, Clevios SV3 presents certain adhesion and viability with Matrigel and Geltrex. Nevertheless, the viability is extremely low.

4.3. Screen-printing layer amount optimization

To optimize the cell attachment, the most promising PEDOT:PSS screen-printing ink from the previous study, Clevios SV3, was applied over the PET on different amounts: 3, 6, 9, and 12 strokes. The PEDOT:PSS was mixed with ethylene glycol (4:1 by volume), and the mixture was re-dispersed for 1 h at 1000 rpm before printing. Printing was carried out by using AUREL 900 with a 75° shore squeegee hardness, 1 bar force, and 0.2 m/s, and cured in an air oven at 80 °C for 5 min. Cell attachment was compared versus the bare PET. Two replicates are evaluated for each condition.

The PET cutouts are sterilized with ethanol (70%) for 24 h and UV radiation (30"). Then, a PLL and laminin coating is applied for 24 h. Finally, we withdrew the coating, and 10^5 cells (Neuro-2A CCL-131 lineage, from now on referred as N2A) were seeded on each substrate. After 24 h, PFA fixing. Bright-field microscopy is used to assess cell attachment (**Figure 140**).

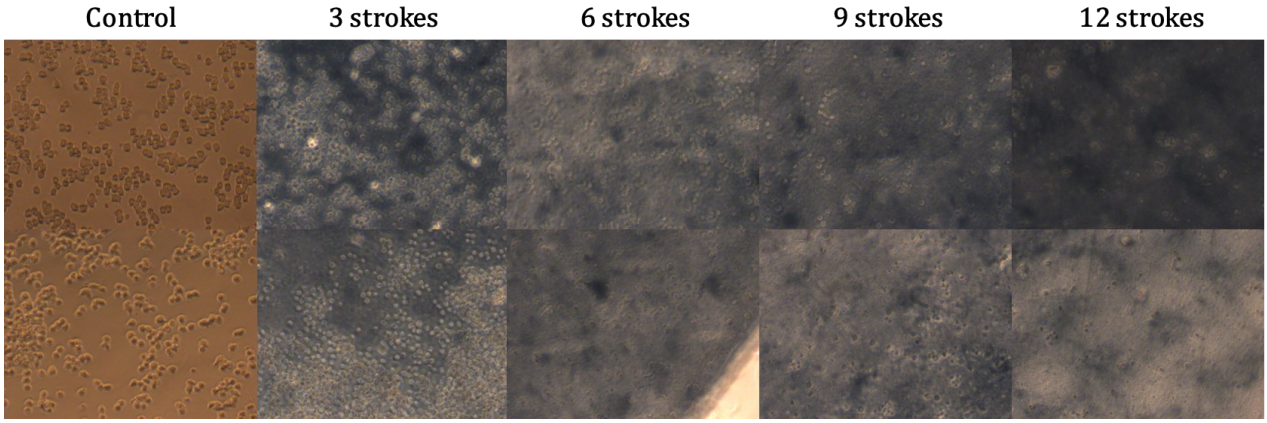

Figure 140. Microscopy images in bright field of different screen-printing PEDOT:PSS thickness cellular attachment.

There is a significant decrease in cellular attachment with the increase of PEDOT:PSS thickness. Less than 6 strokes showed cellular attachment similar to the control. Nevertheless, the increase in the PEDOT:PSS thickness diminishes the cell visibility in microscopy imaging.

4.4. PEDOT:PSS coating degradation in cell culture conditions

PEDOT:PSS conductive present certain degradation acceleration when is under higher humidity and temperature. We evaluated the resistance increase under constant 37 ˚C for 24 days. Furthermore, to assess the Matrigel coating influence in these variations, a control was used using tap water instead.

The initial (without coating) resistance on control and Matrigel samples was 300 and 337 Ω, respectively. The next impedance measurements will be normalized with these values.

The first day (Day 0), two measurements were performed: the initial, and after 1 h coating. The next 4 days, a measurement of the impedance every 24 h was performed. The medium evaporated in Day 4. Day 8 the impedance was measured again. Day 12 we refilled the medium and measured the impedance after 1 h. Evaporation and measurement, coating refill and measurement after 1 h, and evaporation and measurement were repeated on Day 16, 20 and 24, respectively. The process is shown in **Figure 141**.

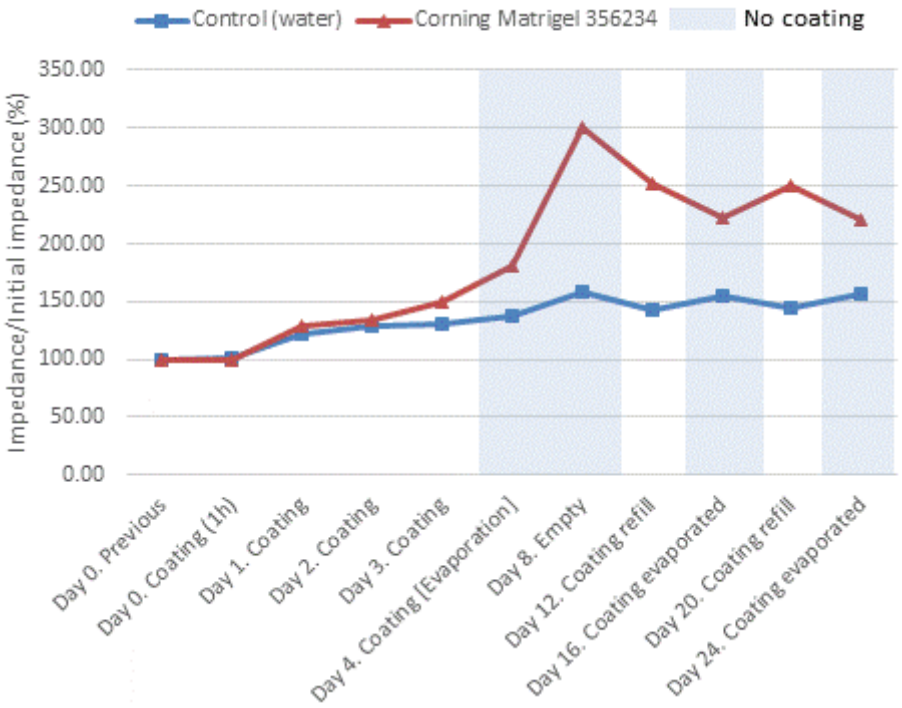

Figure 141. Impedance variation of screen-printed substrates with Matrigel presence and evaporation. Reproduced from [372].

Conductivity variations with Matrigel and water are comparable until Day 3, with a resistivity increase of 25% in both after 24 and 48 h. The Matrigel evaporation has a deeper impact on resistivity than the water evaporation (200% vs. 50% increases, respectively). Nevertheless, further refill-evaporation processes seem to don't have a relevant effect on the substrate resistivity, remaining around the 150% of the original impedance for water immersion, and 225% for Matrigel coating.

4.5. Comments on hydrogels

Even if, in our experiments, the conductive hydrogel tested presented poor cell viability after 72 h of incubation, promising results are being obtained in the state of the art. Remarkably, through their combination with PEDOT-based conductive polymers, obtaining conductive hydrogels. Abidian *et al.* reported positive results in peripheral nerve reconstruction through axonal regrowth through PEDOT-coated hydrogels [400]. The use of PEDOT nanoparticles to enhance the hydrogel with electrical conductivity is other approach that has reported positive results in peripheral nerve repair (Huang *et al.* [401]). Kayser & Lipomi endowed stretchable capabilities to PEDOT:PSS composites, a desirable feature for *in vivo* applications [402]. Shortly after, Luo *et al.* reported a stretchable self-healable conductive hydrogel [403]. Overall, hydrogel-PEDOT composites are a promising strategy to endow implantable scaffold stretchability and self-healing properties.

Section summary: Two approaches have been evaluated for endowing the selected PET substrate with electrical conductivity properties: the use of a conductive hydrogel and PEDOT:PSS screen-printable inks. Clevios SV3 PEDOT:PSS presented the best attachment but with poor results. They were improved by adjusting the PEDOT:PSS layer thickness to three screen-printing strokes. Degradation on cell culture conditions was evaluated for 24 days, reporting an initial increase in resistivity in the first week if there is no refill of the cellular medium, showing its suitability for long-duration experiments.

5. Physical structure for *in vitro* experimentation

This section will describe the different physical structures designed and evaluated to allow *in vitro* experimentation with screen-printed PETs. They must display biocompatibility and watertightness in the cell culture conditions for extended periods (up to 30 days).

The screen-printed PET presents a poor surface electrical connection with external alligator clips. Therefore, MPM's screen-printing silver ink NBSIJ[13] is employed to obtain a reliable connection between the alligator clips and the PEDOT:PSS conductive polymer.

[13] Reference: https://www.mpm.co.jp/electronic/eng/silver-nano/line-up.html (accessed February 14th 2023).

5.1. 3D-printed PLA 24-well matrix

The first approach to obtain isolated cell culture wells with screen-printed PET was designing a 3D-printable structure. It was designed by replicating the dimensions of a standard 24-well matrix and printed in PLA material. M4 holes were incorporated to allow the screwing of the matrix to a hard surface (PMMA), as shown in **Figure 142**. This way, the screen-printed PET would be under pressure, regulable with the M4 screws, between the PMMA hard surface and the PLA structure.

Figure 142. 3D-printed PLA 24-well matrix with M4 holes for screwing it to a PMMA lamina.

However, medium leakage was a constant problem. Solutions involving the addition of a 1 mm thick PDMS layer between the PMMA and the PET or using Sylgard 184 elastomer (PDMS) to glue the PLA structure to the PET substrate were insufficient.

The screen-printing masks are shown in **Figure 143**.

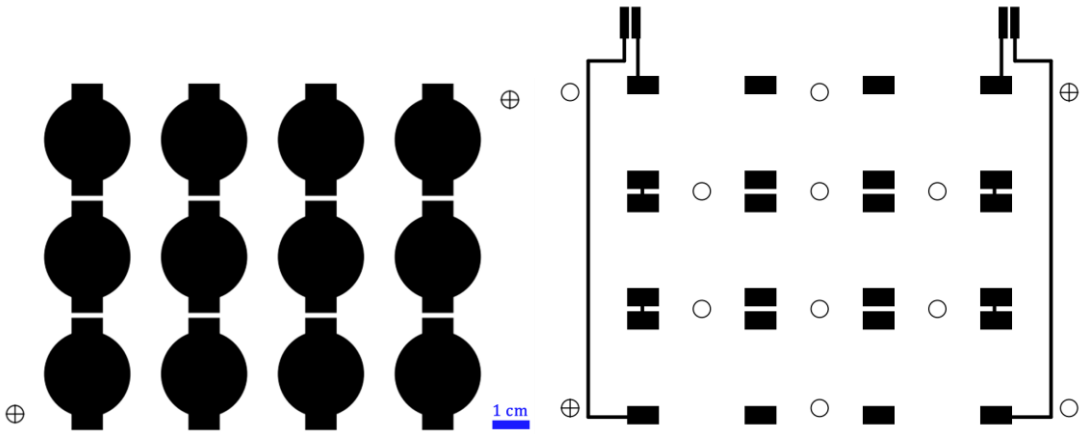

Figure 143. PEDOT:PSS (left) and silver (right) screen-printing masks.

5.2. PDMS 24-well matrix obtained with 3D-printed PLA negative

Because of the watertightness limitations, we tried to build a 3D-printed negative to obtain a PDMS well-matrix with the same dimensions (see **Figure 144**). Nevertheless, the PLA porosity made the PDMS pre-cured elastomer infiltrate, causing the impossibility of the obtention of the desired matrix. Fabricating the molds in steel, aluminum, or non-porous plastic would allow this design to obtain the PDMS matrix.

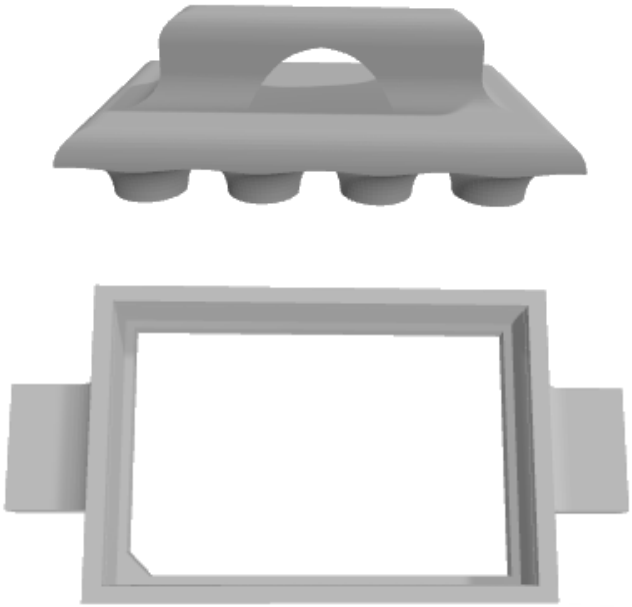

Figure 144. Negative molds for the 24-well PDMS matrix.

5.3. PDMS single well obtained with 3D-printed ABS negative

Following the philosophy of the precedent, we designed a simplified negative to obtain a single PDMS well (**Figure 145**). To avoid the porosity of the previous material that impeded this approach, we 3D-printed the design in ABS. We cleaned the inner surface with acetone to produce a watertight and smooth surface.

Nevertheless, cured PDMS adherence to the ABS inner surface was too high, impeding using this approach either.

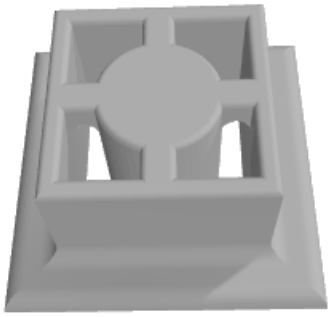

Figure 145. Simplified 3D-printable PDMS mold.

5.4. 3D-printed simplified well-duo

The fabrication of this *in vitro* setup is described in Alamán-Escolano *et al.* [372], and it is an original work of the present doctoral dissertation (**Figure 146**).

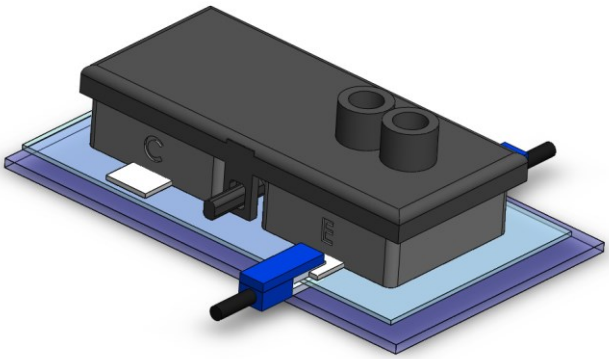

Figure 146. 3D representation of the electrostimulation and controlled drug release setup. Obtained with SolidWorks © 2018 Dassault Systèmes - SolidWorks Corporation.

The setup is shown in consists of:

- PMMA (Resinex Altuglas BS 100) surface offering bending resistance to the system.
- PET (Mitsubishi NB-TP-3GU100) substrate for PEDOT:PSS printing.
- PEDOT:PSS (Clevios V3, Heraeus), mixed with ethylene glycol (4:1 by volume)[a].
- PLA (RS Pro 125-4336) for the well-structure 3D-printing.
- The substrate external electrodes are screen-printed using ilver ink (C2020522D1).
- Silicone elastomer PDMS (Sylgard 184, 1673921 Dow Corning) for PMMA-PET and PET-PLA adhesion[b].

- Additive silicone (Dupliflex Protechno LB003677) as outer reinforcement in the PLA-PET adhesion to guarantee watertightness[c].

Fabrication methods:

[a] The mixture was re-dispersed for 1 h at 1000 rpm before printing. Printing was carried out by using AUREL 900 with a 75° shore squeegee hardness, 1 bar force, and 0.2 m/s, and cured in an air oven at 80 °C for 5 min.

[b] Applied at 1:10 by weight curing-elastomer, effusively stirred, applied to the surface and cured for 24 h at room temperature.

[c] Mixing the two silicone components, applying approximately 1 mL per well to its outer edges in contact with the PET. Drying time: 30' at room temperature.

The pad design, shown in **Figure 147**, is 10 mm width and 60 mm long from edge to edge, with 22 mm diameter screen-printed PEDOT:PSS.

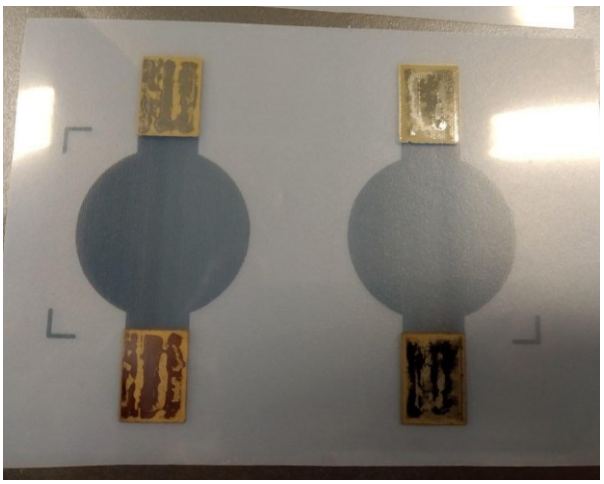

Figure 147. Screen-printed PET with PEDOT:PSS and silver for the well-duo setup.

The setup demonstrated watertighness for three days. Therefore, a Matrigel coating and 10^5 cell were seeded for three days. They were fixed with PFA and immunofluorescence markers DAPI, Nestin and Ki67 were used (see **Figure 148**). Ki67 protein is present during all active phases of the cell cycle but is absent from resting cells, makes it an excellent marker for determining the so-called growth fraction of a given cell population.

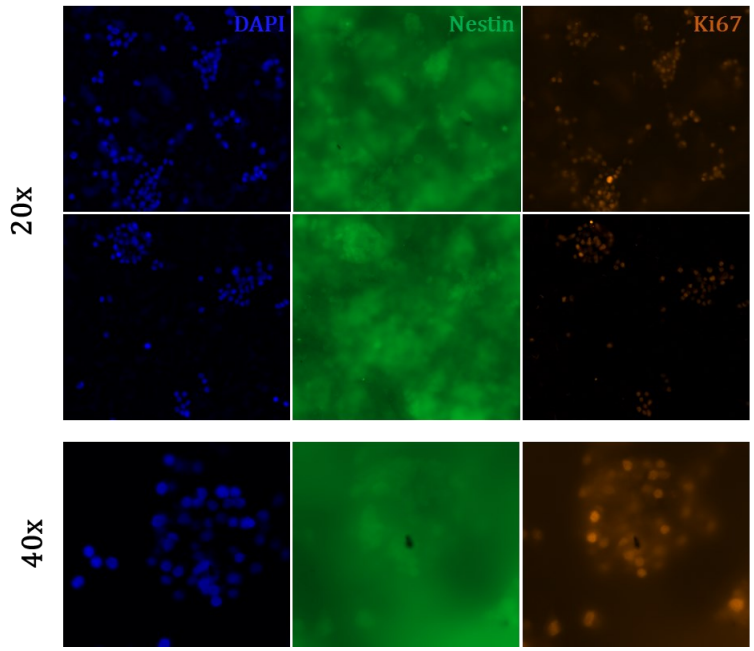

Figure 148. DAPI, Nestin, and Ki67 immunofluorescence at 20x and 40x amplification on the well-duo setup.

To increase the cell density $2 \cdot 10^5$ cells/well will be seeded in the following experiments. The well-due is the first setup to be used in electrostimulation experiments.

5.5. 3D-printed PLA well matrixes with additive silicone

By using additive silicon and modifying the well-matrix structure, we could reinforce the PET-PLA interfaces directly, ensuring watertightness even in complex structures. We designed a 3D structure with 7 columns (**Figure 149**) to use the multiplexing expansion module for IVESDRIS (*Chapter 1. Electronic instrumentation for in vitro electrostimulation and controlled drug release / 6.4. Extension module for stimulus multiplexing*).

A 3D representation of the structure is shown in **Figure 150**. Each well can be reinforced separately in the external PET-PLA interface with additive silicone.

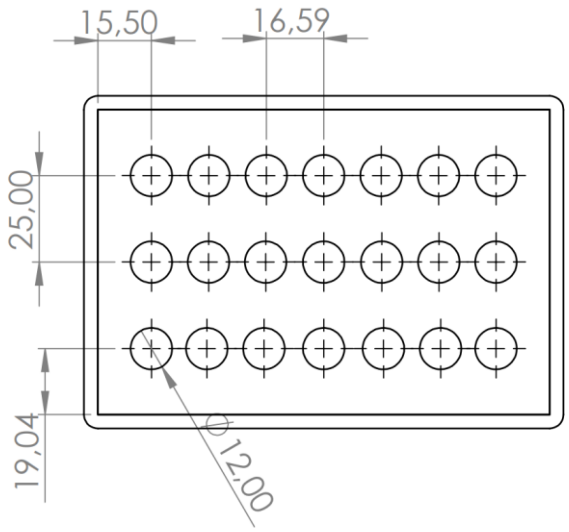

Figure 149. 3D-design for the 3x7 well-matrix.

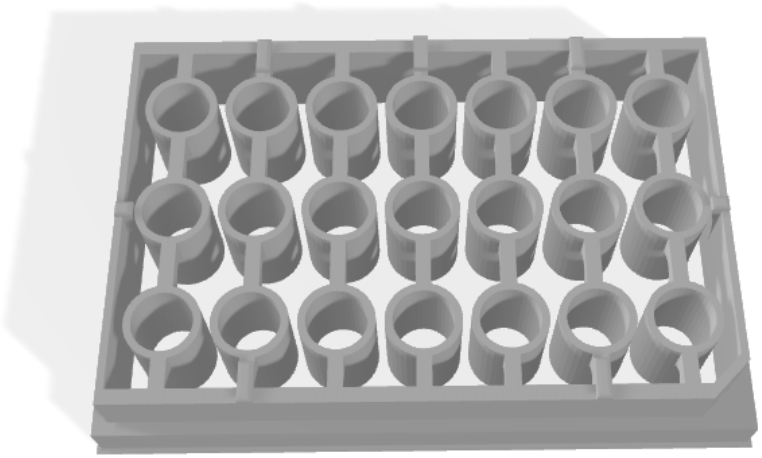

Figure 150. 3D representation of the 3x7 printable well-matrix.

However, the PLA porosity seemed to absorb part of the ethanol used in the sterilization, diffusing it in the *in vitro* cell culture and diminishing the cell viability. This is a problem shared with the well-duo setup. We assessed immersing the 3D pieces in PDMS to coat these pores, but it seemed ineffective in increasing the cell viability.

5.6. Commercial well matrix without bottom

Grainer Bio-One Sensoplate[14] is a 24-well cell culture matrix with removable crystal bottom. We could use the wall structure, fixed with additive silicone to the screen-printed PET, to avoid problems related to the PLA porosity. With this aim, we could use the screen-printing masks of *5.1. 3D-printed PLA 24-well matrix*. Nevertheless, the additive silicone had to be placed in the well's inner side, reducing the effective area for cell culture in the well. Therefore, we evaluated an alternative and more straightforward setup with which most electrostimulation experiments were carried out.

5.7. Screen-printed PET immersed in commercial cell culture well

The screen-printed PET mask was enlarged, so the edge-to-edge was 9.5 cm. The arm width was set to 0.5 cm, keeping the inner diameter at 2.2 cm where the cells are seeded. The last 0.75 cm of each side was covered with silver ink to ease the connection with the alligator clips. Due to the temporal shortage of silver ink, conductive epoxy (Chemtronics CircuitWorks[15]) was used to attach regular wires to establish a reliable connection. By attaching the arms to a commercial 6-well cell culture matrix, we could immerse the area of interest in a reliable manner, as shown in **Figure 151**. The commercial lid was drilled to allow putting out the arms of the setup and pipetting of the media.

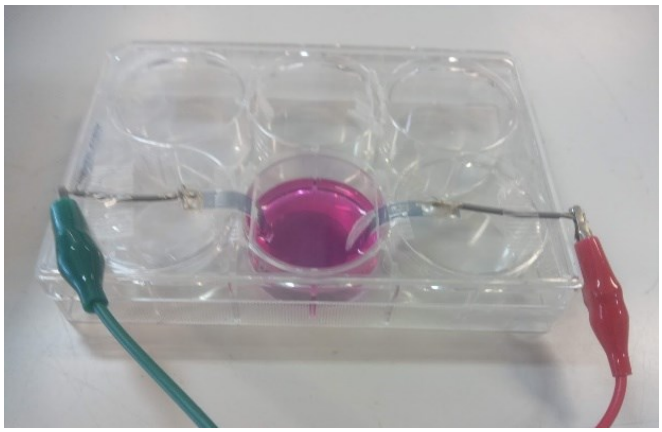

Figure 151. Immersed PET setup.

[14] More information at: https://shop.gbo.com/en/row/products/bioscience/microplates/sensoplate-glass-bottom-plates/24-well-sensoplate/662892.html (accessed February 15th, 2023).

[15] More information at: https://www.chemtronics.com/circuitworks-conductive-epoxy-2 (accessed February 15th, 2023).

It is relevant pointing out that the arms of the setup suppose two additional impedances in series. We statistically characterized that the center typically represents 22% of the edge-to-edge impedance, with a minimum value of 17% and a standard deviation of 33%. The typical center impedance (⌀ 2.2 cm) is 1.2 kΩ. Each substrate can be characterized if a potential gradient is applied before its use.

6. Plasma treatment to enhance cell attachment and viability

Plasma activation of PEDOT:PSS surfaces has reported increased cell attachment and viability (Ohahyion *et al.* [404], De Geyter & Morent [405]). The two effects in Ar plasma are due to the functionalization of carboxy and oxidized forms from atmospheric oxygen and due to better PEDOT and PSS crosslinking (James *et al.* [406]). The increased wettability effect is durable and can be measured with the contact angle formed with a fluid drop and, depending on the conditions, may last from hours to weeks (Izdebska-Podsiadły [407]).

Argon-Oxygen and Argon plasmas are the best options for increasing cell adhesion (Morent *et al.* [408]). Adequate coatings with extracellular nutrients and growth factors are still needed to enhance proliferation (Geyter & Morent [405]). There are reports in the literature where coatings are also activated with the PEDOT:PSS, enhancing their properties (López-Pérez *et al.* [409]).

Mainly, argon (Ar) corona discharge is available at *Centro de Investigación Príncipe Felipe* (València, Spain) through a BAL-TEC Multi Control System MCS 010. According to Ino *et al.* [410], overexposure can lead to PEDOT:PSS etching. We applied plasma activation at 6.7 mA, 0.2 bar, with a distance between the substrate and the corona ring of 4 cm. We seeded $5 \cdot 10^5$ N2A cells/substrate with different conditions.

We evaluated 6 different conditions on PEDOT:PSS screen-printed PET:

1. Control.
2. PLL[16] coating overnight.
3. 15” plasma activation.
4. 60” plasma activation.
5. 15” plasma activation and PLL coating for 2h.

[16] Poly-L-Lysine (PLL) is a synthetic, positively charged amino acid chain that enhances cell adhesion by altering surface charges on the culture substrate. Further studies from our collaborators from RTN revealed that the combination of Matrigel and PLL coatings displayed the best overall results.

6. PLL coating overnight before 15” plasma activation.

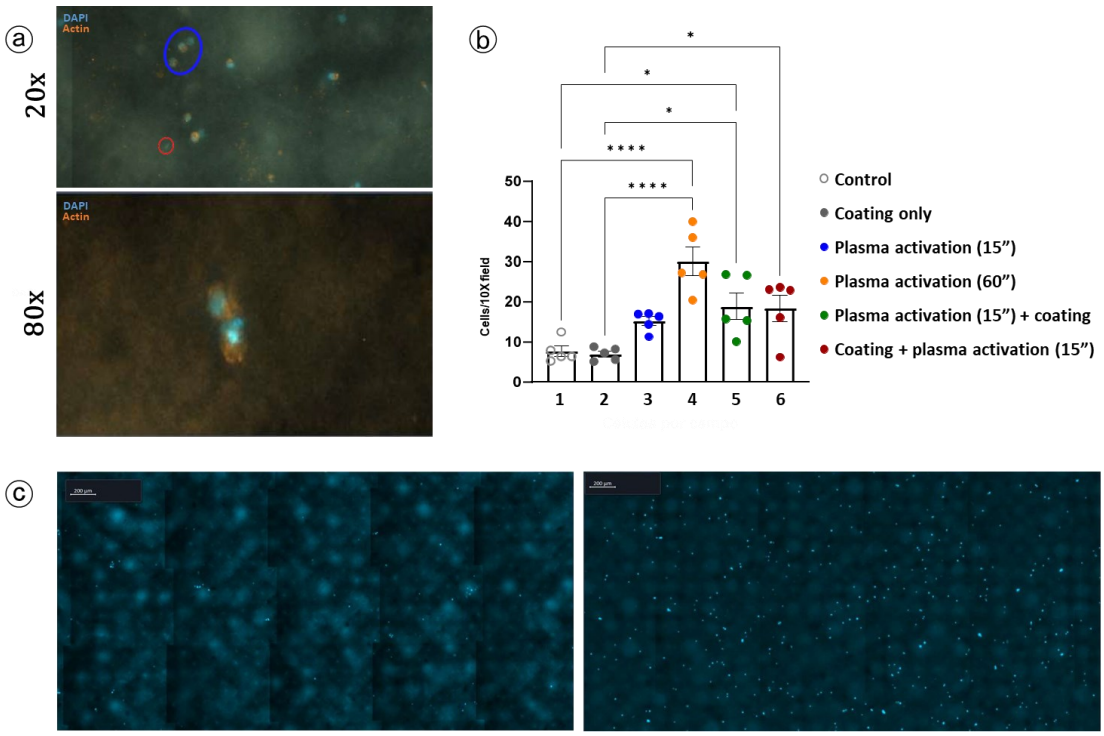

Figure 152. Cell attachment evaluation on screen-printed PEDOT:PSS on PET with Ar plasma activation and PLL coating. ⓐ A 20x and 80x DAPI and Actin immunofluorescence images are shown. Top image shows an Actin concentration with no DAPI circled in red (no cell), whereas in blue three cells can be distinguished. ⓑ Bar plot of the average cells per 10x field for the six conditions. ⓒ Comparison of control (left) and plasma activation for 60” (right) DAPI images.

The cells were incubated for 24 h and fixed with PFA. Immunofluorescence imaging with DAPI and Actin markers allows nuclei detection and morphology assessment, respectively. Using the two markers allows the distinction between Actin accumulations and actual cells (**Figure 152a** shows circled in red an Actin accumulation, and circled in blue three actual cells). The cell attachment show that the plasma activation for 60” displays 375% values versus control and coating only. Furthermore, no significant difference can be found between conditions 3, 5, and 6, *i.e.*, plasma activation for 15” with previous, posterior, or without PLL coating (**Figure 152b**). However, higher dispersion can be found in conditions 5 and 6 (with coating) than in 3 (without coating). We could expect that the coating addition would enhance cellular proliferation in more extended cell cultures. Thus, the plasma activation for 60” with a coating (previous or posterior to the activation) is the most promising methodology for cell seeding in electrostimulation experiments. Further optimization can be studied in parallel. Overall, the cellular density can be qualitatively compared in **Figure 152c**, showing control (left) vs. condition 4 (right).

Section summary: plasma activation of PEDOT:PSS has been reported to enhance cellular attachment. Our study shows that the Ar plasma activation for 60" displayed a 375% cellular attachment vs. control and control with PLL coating.

7. Electrostimulation assays

We have described the development of the conductive substrate in terms of flexible material selection, PEDOT:PSS screen-printing thickness, protein coating, plasma activation, and mechanical structure to allow the containment of cellular media. This section describes the methods and analyzes the results of applying different electrostimulation protocols in the well-duo and immersed setups. The capabilities of FAEVIS and IVESDRIS devices to apply electrostimulation flexibly are put into action. The limitations of the first are made clear in the first experiment, which is why IVESDRIS is designed and used from the second experiment onwards. Both devices are described in *Chapter 1. Electronic instrumentation for in vitro electrostimulation and controlled drug release*.

7.1. Electrostimulation on 3D-printed well-duo with FAEVIS

These firsts experiments were carried out with the well-duo setup (described in *5.4. 3D-printed simplified well-duo*), with a screen-printed PET with PEDOT:PSS Heraeus SV3. The PEDOT:PSS layer thickness optimization and Ar plasma activation studies are posterior to this experiment.

PET substrates were coated with Matrigel, and 100,000 neural precursor cells (NPCs) were seeded and cultured for 3 days. Basal cell adhesion was inferior to the positive control, such as glass coverslip. We applied two different electrostimulation (ES) patterns with the FAEVIS equipment in a direct gradient configuration:

1. **DCEF at 100 mV/cm for 2h, 3 days.**
2. **PCEF with 25 µA 100 µs pulses at 100 Hz for 24 h.**

We studied the effect of two different electrical stimulation (ES) patterns in NPCs proliferation by assessing the expression of Ki67 and the effect of ES in neurite outgrowth by direct morphology observation through Nestin staining (**Figure 153**).

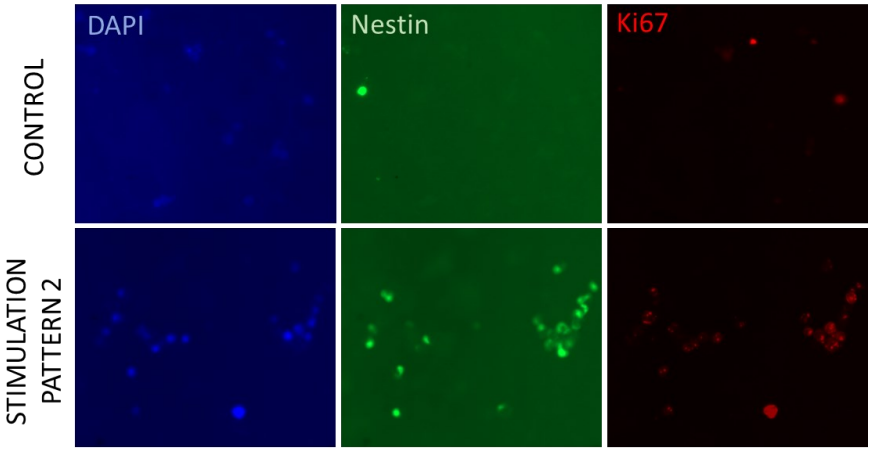

Figure 153. DAPI, Nestin, and Ki67 immunofluorescence assays on neural precursor cells seeded on the well-duo setup for three days. Comparison between control and PCEF (stimulation pattern 2).

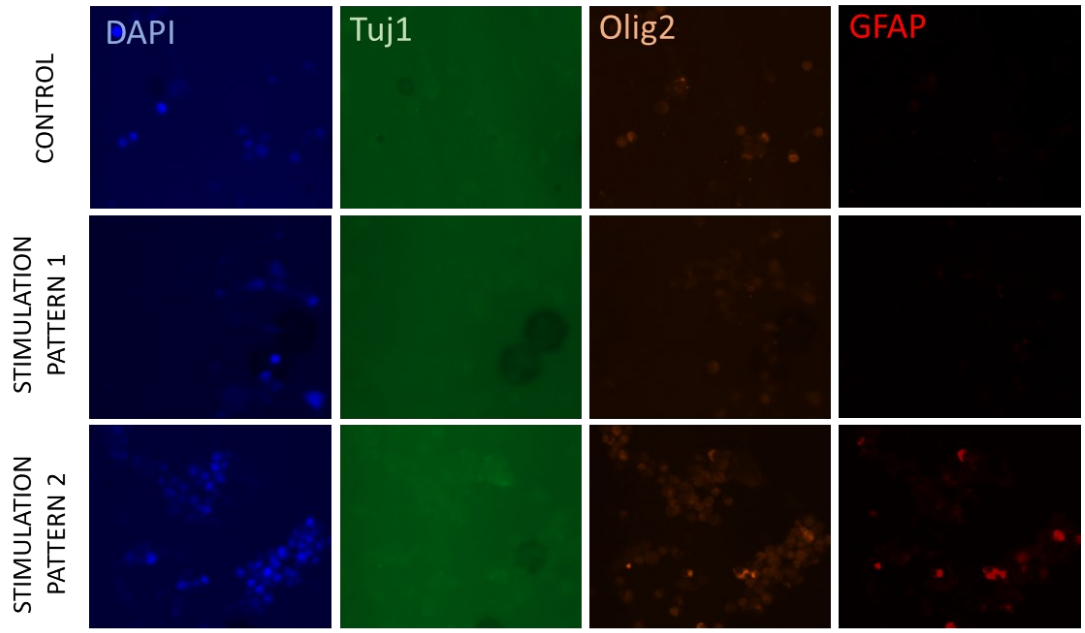

Figure 154. DAPI, Tuj1, Olig2, and GFAP immunofluorescence assays on neural precursor cells seeded on the well-duo setup for three days. Comparison between control, DCEF (stimulation pattern 1), and PCEF (stimulation pattern 2).

Following ES pattern 1 we could not detect viable cells after post-fixation and immunocytochemistry protocol. However, following ES pattern 2 we could observe enhanced proliferation capacity (increased Ki67 positive cells) compared to the control. We did not observe any effect on neurite outgrowth. These results fit with the expected response to TOOL 1, with overstimulation (ES pattern 1) and adequate levels of stimuli (ES pattern 2).

NPCs can differentiate in neurons, oligodendrocytes, or glial cells. We performed immunofluorescence studies using specific antibodies against Tuj1 (for neurons), GFAP (for astrocytes), and Olig2 (for oligodendrocytes) to study the influence of electrostimulation in neural stem cell fate. Results showed that ES did not promote NPCs differentiation to neurons under these conditions. However, to study the effect of ES on NPCs differentiation, NPCs should be cultured during a more extended protocol.

It is worth mentioning that FAEVIS presented significant problems in extending its autonomy for more than 24 h, and it needed to apply data triage to send the voltage measurements of the PCEF ES because of the short duration pulses. Furthermore, in this last ES, the application of zero current in the resting 9.9 ms was not guaranteed, with a typical error of <5 mV. Therefore, we designed IVESDRIS, the instrument with which the following experiments are performed. Both devices are described in *Chapter 1. Electronic instrumentation for in vitro electrostimulation and controlled drug release*.

7.2. Electrostimulation on PDMS varnished well-duo and immersed setups with IVESDRIS

We applied the stimuli using the new IVESDRIS device, capable of more adequately managing the multi-day duration of the experiments. **Figure 155** shows the cell culture hood with three IVESDRIS devices connected (left) and the zoom in to one of the well-duo setups connected to a IVESDRIS device (right). In these experiments the PEDOT:PSS strokes is set to 6 according to *4.3. Screen-printing layer amount optimization*.

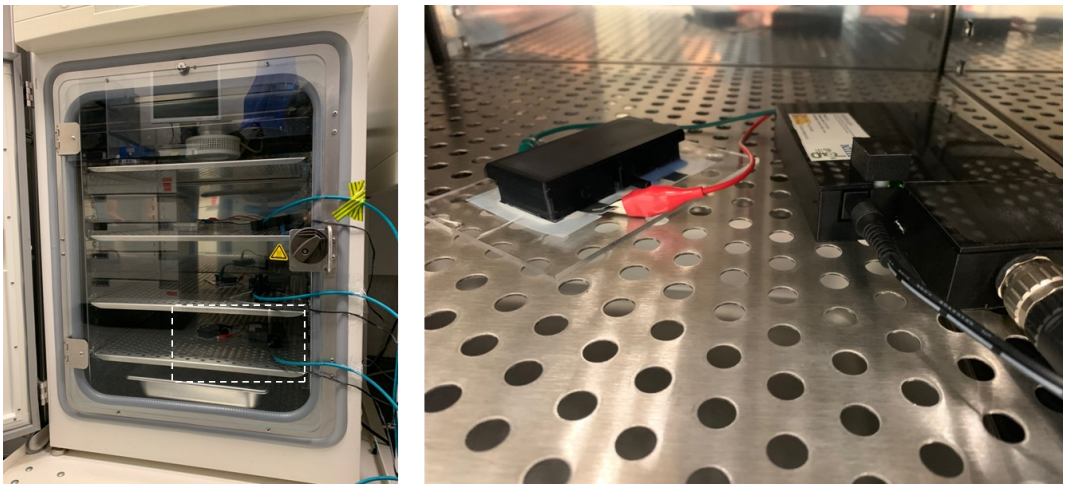

Figure 155. Cell culture hood with three IVESDRIS devices (left), and zoom in to one of them electrostimulating the NPCs seeded on a well-duo setup (right).

The setup consisted of two well-duo replicates varnished with PDMS so that in each duo, one of the wells is used as a control and the other electro-stimulated (**Figure 157b,d**), and a well of the immersed electro-stimulated setup (**Figure 157e**). Each substrate was sterilized through ethanol (70%) immersion overnight and UV exposure. They were washed with water afterward to remove ethanol residuals. PLL and Matrigel coating was applied for 2 h. After coating excess removal, 200,000 N2A cells were seeded per well.

In these electrostimulation experiments, we erroneously repeated the DCEF protocol (100 mV/cm, 2h/day, 3 days) in the direct gradient configuration. This protocol will be present in these and the subsequent experiment due to the misconception that such a duration increases viability, proliferation, elongation, and differentiation (TOOL 1 of *1.4. Conceptualization of electrostimulation tools*). For this, the duration should have been reduced to 10'/day, adjusting the voltage applied according to the conductivity of the substrate (see **Table 5** from *1.1. Direct gradient electrical stimulation*). The impedance variations are shown in **Figure 156** for the well-duo setups (top, blue and red) and for the immersed setup (bottom, purple). We can identify a connection problem in the immersed setup on the 2nd day. It was solved before the 3rd day of electrostimulation.

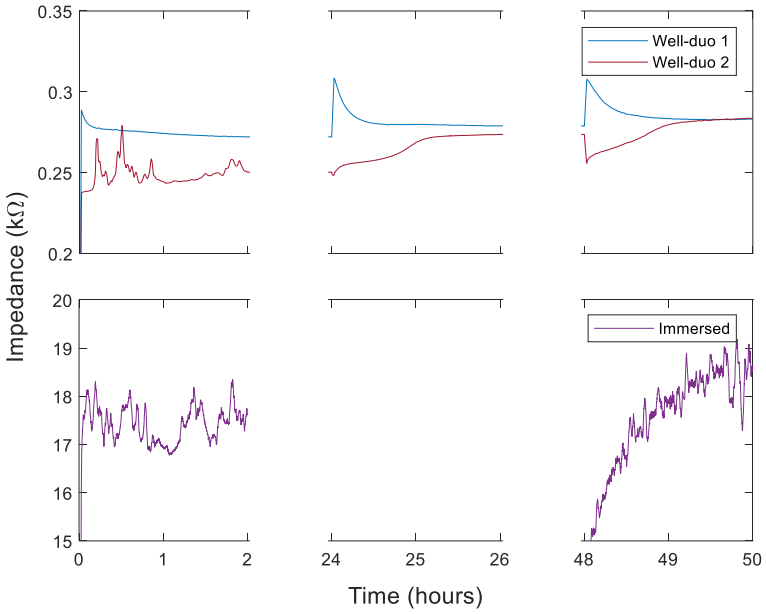

Figure 156. Impedance variations during electrostimulation assays for the two replicates of the well-duo setup and the immersed setup assessed. Obtained with MATLAB 2018 © Mathworks.

We performed CFDA immunofluorescence assays to assess cellular proliferation and morphology. In the well-duo setup, two regions were evaluated: center and border (see **Figure 157b** top left). **Figure 157a** and **b** show the results for the two regions in the stimulated and non-stimulated conditions for the two replicates. Proliferation is way higher in the border than

in the center, and stimulation enhances proliferation. **Figure 157f** shows the CFDA imaging for the immersed substrate setup. Cell proliferation is more uniform, and certain elongation in the cellular morphology can be identified.

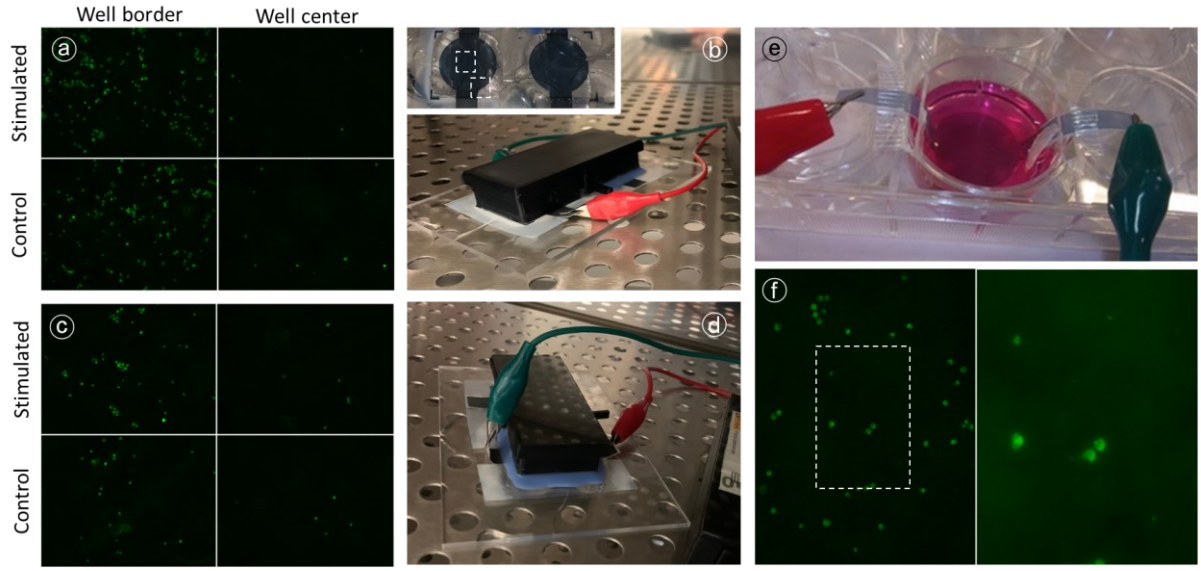

Figure 157. Panel with the setup images and CFDA immunofluorescence images for each well-duo setup (a-d) and the immersed setup (e, f).

We identified that the well-duo structure presented limitations for cell viability because the porosity of the PLA structure (3D printing material used) allowed the ethanol used in disinfection to permeate, diffusing during subsequent culture and electrostimulation, as exposed in *5.5. 3D-printed PLA well matrixes with additive silicone*. We used a PDMS coating to solve this issue. However, even with this solution we identified that cell adhesion was concentrated in the periphery of the well, with low density in the center. Due to the homogeneous cell attachment in the immersed setup vs. its absence in the well center in the well-duo setup, the immersed setup is further explored in the following experiments. Nevertheless, the extended length of the immersed setup (8.5 cm from edge to edge) increases the total resistance, and we have to consider that the inner 2.2 cm represent 17%-33% of the total impedance of the screen-printed PEDOT:PSS. In this setup, we applied 30 mV/cm (between 43 and 83 mV between the edges of the inner PEDOT:PSS circle of ⌀ 2.2 cm). Furthermore, the direct alligator clip in the PEDOT:PSS surface produced a non-reliable and high-impedance connection. Hence, to the edges of the setup screen-printed silver ink or regular wires attached with conductive epoxy were added for the following experiments, according to the final setup described in *5.7. Screen-printed PET immersed in commercial cell culture well*.

7.3. Electrostimulation on immersed setups with IVESDRIS

We repeated the experiment with the immersed setup. We employed five substrates:

- One unstimulated, working as *absolute control*, that was fixed at time 0.
- Two pairs of immersed setups were arranged in P-6 commercial cell culture matrixes.

One of the substrates was electrostimulated for each pair, and the other served as its paired control (**Figure 158**). They were fixed at T = 48 h.

We applied the electrostimulation in direct gradient configuration DCEF between the edges of the inner 2.2 cm ⌀ PEDOT:PSS circle (30 mV/cm, 2h/day) for 2 days. The impedance variations are shown in **Figure 159**. Compared with the *immersed* setup of the previous experiments in *7.2. Electrostimulation on PDMS varnished well-duo and immersed setups with IVESDRIS* the impedance has decreased from 17-18 kΩ to 3-4 kΩ, thanks to improved alligator connection through regular wires and conductive epoxy. We assess a significant difference between the two replicates: replicate 1 presents a decreasing transitory in both 2h electrostimulations.

Figure 158. Immersed setups in cell culture hood (left) and detail on the pair of immersed substrates 1 (right).

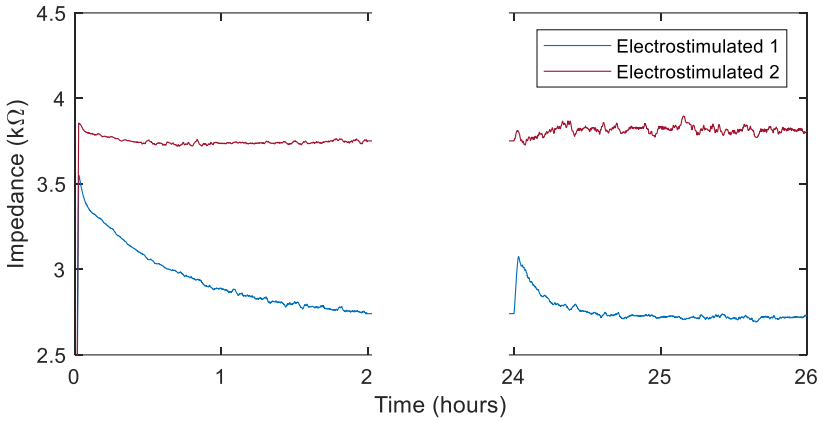

Figure 159. Impedance variations on electrostimulated immersed setups. Obtained with MATLAB 2018 © Mathworks.

The seeded N2A cells were fixed and marked with CFDA to assess the cellular viability and morphology by immunofluorescence imaging. The results are shown in **Figure 160**. The *Stimulated 1* well displays enhanced proliferation, while the unstimulated samples and the *Stimulated 2* sample show comparable results with the *absolute control* at T = 0 h. There are no significant differences between the center and the border of the wells.

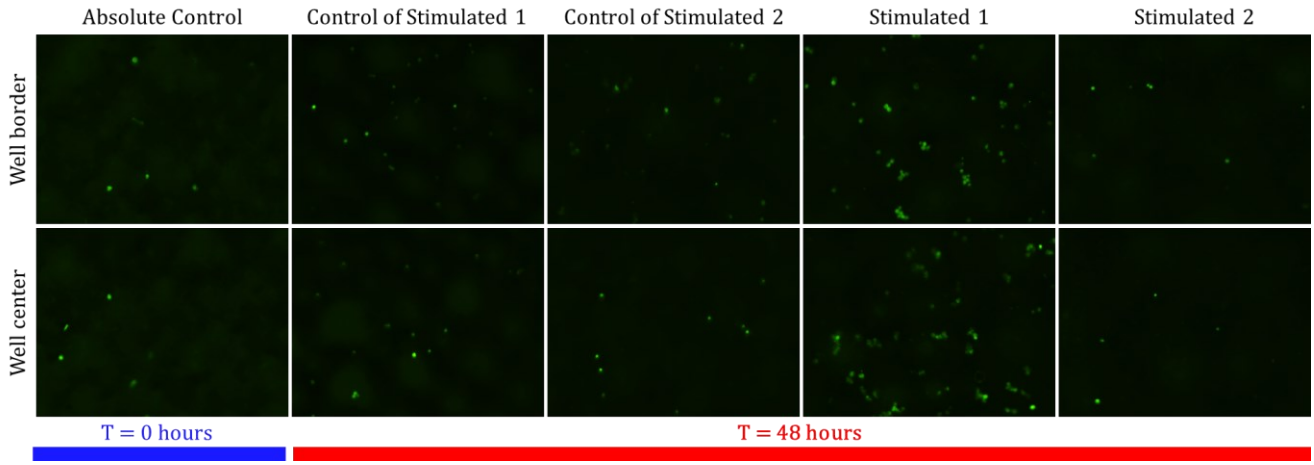

Figure 160. CFDA immunofluorescence imaging at initial time (left) and at T = 48 h (four right columns). The three left columns are unstimulated samples, the two right columns are stimulated samples.

Additionally, Tuj, Ki67, and DAPI antibodies were introduced. However, the first two were defective in labeling and are therefore excluded from the images. It appears that the cells cluster in the folds in the material. This is already known; cells prefer to *settle* in areas of topology change. From the **Figure 161** images, we can only conclude that there is cell adhesion but no morphology or differentiation. In one of the two electrostimulated samples, we assess a proliferation enhancement. The causality of this effect with the electrostimulation protocol needs further investigation.

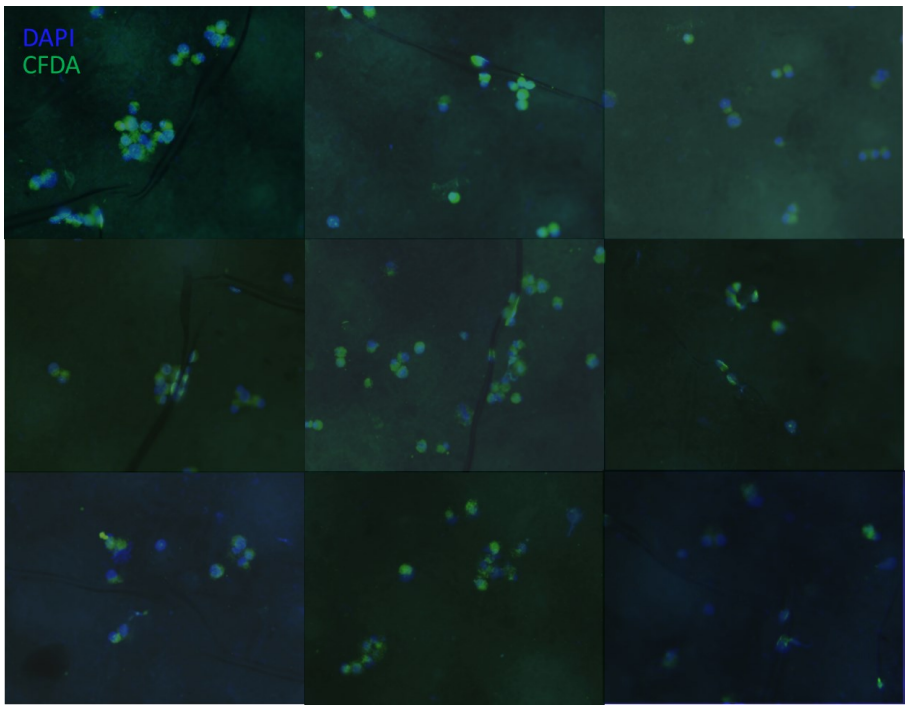

Figure 161. DAPI and CFDA immunofluorescence imaging of electrostimulated *Substrate 2*.

7.4. Electrostimulation on immersed setup with Ar plasma activated PEDOT:PSS

Immersed setup PEDOT:PSS screen-printed substrates were Ar plasma activated following the protocol described in *6. Plasma treatment to enhance cell attachment and viability*. 500,000 N2A cells were seeded in each of the five substrates employed in this experiment with no coating. One will be fixated at time 0 and the other at the end of the experiment without being electrically stimulated. The same protocol with different energy or duration will be applied to the other three before fixation.

The ES protocol is chosen for TOOL 1, following Zhu *et al.* [380], which reported increased proliferation, neuronal differentiation, and elongation by applying 100 µA current during 100 µs at 100 Hz for 24 h. Hence, we applied for 1 hour:

1. 10 µA, 100 µs, 100 Hz.
2. 100 µA, 100 µs, 100 Hz.
3. 100 µA, 1 ms, 100 Hz.

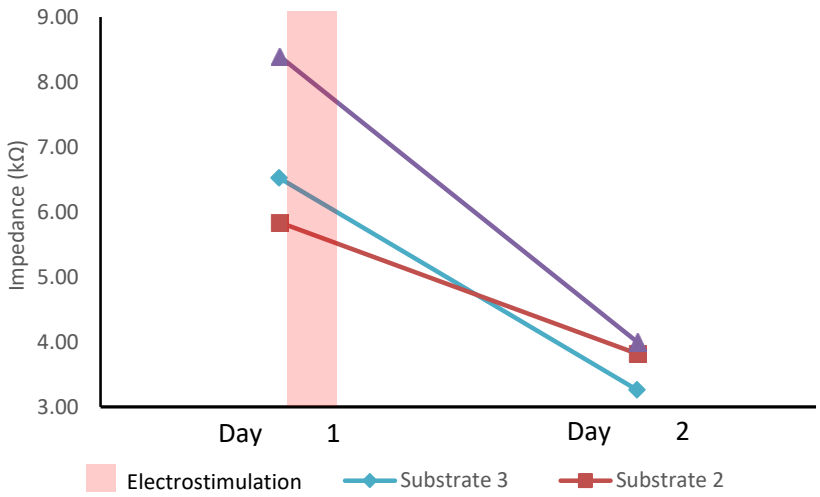

Figure 162. Impedance variations before electrostimulation, and after it with 17.5 h rest.

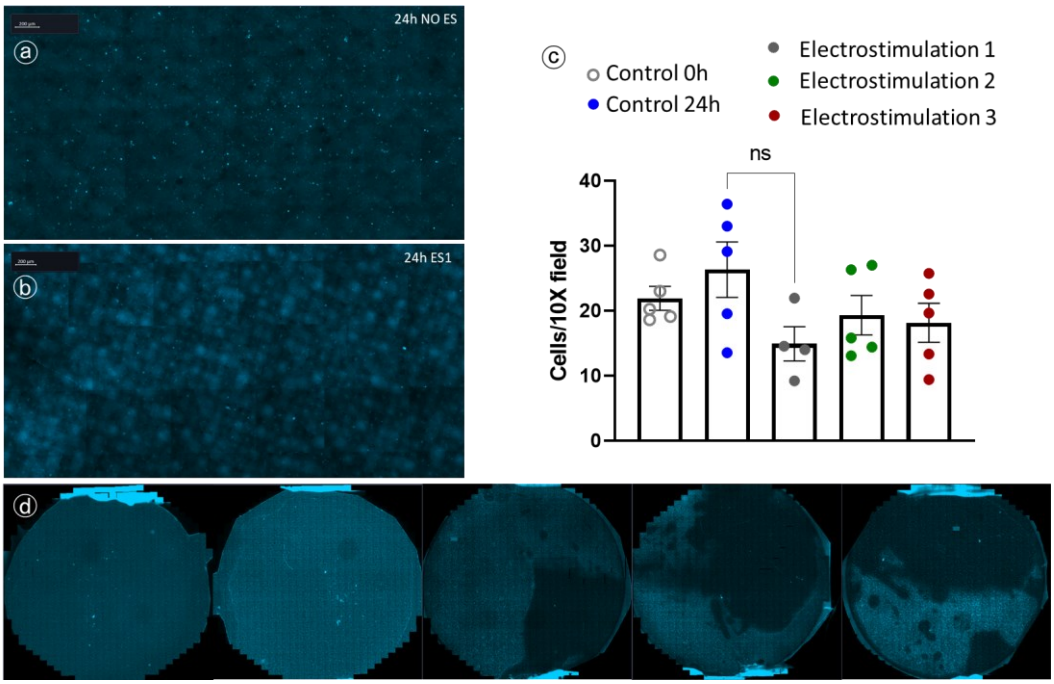

Figure 163. Immunofluorescence imaging of (a) 24h control and (b) electrostimulated substrate 1. (c) Cellular attachment is compared between the five substrates in the bar plot. (d) From left to right: control 0h, control 24h, ES1, ES2, and ES3 substrates on immunofluorescence imaging.

For 3 kΩ from edge to edge and 25% voltage drop in the 2.2 ⌀ cm center, it implies 0.3 mV/mm at 10 µA and 3.4 mV/mm at 100 µA, values close to the 0.54-1.84 mV/mm reported by Kobelt *et al.* [376] and the 10 mV/mm reported by Thrivikraman *et al.* [105] with positive results. The impedance variation of the immersed setup was 53% ±10% of its initial value, as shown in **Figure 162**. We measured the impedance before the electrostimulation and 17.5 h after its end. Nevertheless, in all electrostimulated substrates, cell attachment was reduced (**Figure 163a-c**). Furthermore, we can assess an evident deterioration of the PEDOT:PSS in the

immunofluorescence assay (**Figure 163d**). The cause of this phenomenon is yet to be investigated.

Section summary: The first electrostimulation trials, direct current (DCEF) for two hours for three days and pulsed current (PCEF) at 100 Hz for 24 h without rest, evidenced the limitations of the first device designed (FAEVIS) to perform long-duration experiments. Despite the limitations, an increase in cell proliferation was identified without an increase in differentiation into neurons. The new device to overcome the limitations mentioned above, IVESDRIS, was used for the following experiments. We identified that the well-duo structure presented limitations for cell viability because the porosity of the PLA structure (3D printing material used) allowed the ethanol used in disinfection to permeate, diffusing during subsequent culture and electrostimulation. We used a PDMS coating to solve this issue. However, even with this solution we identified that cell adhesion was concentrated in the periphery of the well, with low density in the center. The immersed setup offered a more homogeneous cell adhesion. After overcoming a connection problem with the immersed setup by adding a reliable interface between the alligator clips and the PEDOT:PSS, we performed two electrostimulation experiments with this setup. The first one, without activation of PEDOT:PSS with Ar plasma, showed an increase in cell proliferation without differentiation into neurons with the application of DCEF in one of the two electrostimulated replicates. In the second, with plasma activation, we applied biphasic pulsed electrostimulation (BCEF) for 24 h. This decreased cell viability and produced a visible change by immunofluorescence over a large part of the substrate area. In this area, cell viability was nil. This effect needs further investigation. Overall, we have satisfactorily electrostimulated the new platforms based on conductive polymers. However, their improvement and the exploration of the effects of electrostimulation protocols still have a long way to go in this line of research.

8. Conclusions and next steps

In this chapter, we have reviewed the state of the art in electrostimulation techniques for modulating the development of neural precursor cells seeded on conductive substrates. Having identified three possible configurations to perform this electrostimulation and having evaluated the results of the different studies, we have been able to conceptualize three tools to be able to promote different aspects of neural precursor cells selectively:

1. Neural differentiation, proliferation, and elongation.
2. Proliferation, modulating differentiation.
3. Migration.

After that, we described the whole development process of the setup to obtain a conductive substrate suitable for the application. We obtained a structure suitable for *in vitro* experimentation and evaluation, adequate for its future *in vivo* transference. This development has been composed of an iterative succession of design and evaluation, which has allowed the selection of the flexible substrate, the PEDOT:PSS ink for screen-printing, the number of strokes in the screen-printing process, the necessary coating of proteins and growth factors, the activation of the PEODT:PSS, and the structure for *in vitro* evaluation. We have performed electrostimulation experiments with our platforms and the devices designed in the framework of this PhD thesis, presumably inducing an increase in the proliferation of neuronal precursor cells, but not of the differentiation into neurons nor their elongation using a protocol corresponding to the type 1 tool with direct current. In the last experiment, with Ar plasma-activated PEDOT:PSS, electrostimulation (type 1, biphasic pulsed current) reduced cell viability and proliferation, creating large areas of the substrate without any viability. The reasons for this response are still unknown. Despite the inconclusive results in the time frame of the thesis, the present experiments have allowed the validation in a real environment of the devices designed and described in *Chapter 1. Electronic instrumentation for in vitro electrostimulation and controlled drug release*.

As for the next steps of the research line, promising advances in using PEDOT nanoparticles (see Serafin *et al.* [411]) would allow a more transferable approach to *in vivo* implantable. The PEDOT nanoparticles present very positive results in viability, proliferation, adhesion, differentiation, and elongation without electrostimulation. The application of modulation techniques could amplify these responses.

Chapter 4. Optogenetic stimulation for nervous tissue regeneration

Optogenetic stimulation is the third technique explored for neural precursor cell development modulation in this research work. After reviewing the state of the art in optogenetic stimulation instrumentation, a family of devices is developed. During the development of this Ph.D. thesis, the *Optogenetic Stimulation for In Vitro Experimentation* (OSIVE) family of devices academic production has been extensive.

The content of this chapter has been published partially in a Q1 publication (Monreal-Trigo *et al.* [412]), and three international congress participations (Monreal-Trigo *et al.* [413], Terrés-Haro *et al.* [414], and Beltran-Morte *et al.* [415]). Additionally, outside the framework of this doctoral thesis but within the research line, we co-authored another Q1 article (Terrés-Haro *et al.* [416]). Furthermore, two Bachelor's Degree Final Projects in Electronic Engineering have been also realized in this research line (Terrer Fos [417] and Coronel Montesinos [418]).

As commented in section *3.3. Techniques based on optogenetic stimulation* from the *Introduction*, neural precursor cells can be genetically modified with opsins. The opsins are receptors that can trigger biological processes, including calcium-dependent signaling between neurons, through specific light irradiation. Nevertheless, as will be further addressed, the available optogenetic stimulation instrumentation is voluminous. Hence, it is impeding their simultaneous use with commercial microscopy instrumentation. The combination of optogenetic stimulation and microscopy would allow for interrogating fast-transient responses, as Ca^{2+} influx is related to the synapsis processes. Tracking the rate of induction of these signals is of significant interest for spinal cord injury (SCI) repair. Furthermore, it would allow deepening our knowledge of these processes. This research line aims to develop an in-vitro platform for optogenetic stimulation with real-time microscopy feedback to interrogate fast-transient processes.

The review of the state of the art, the OSIVE Slim device [412] for in-vitro stimulation and the OSIVE IMS device [415] for irradiance measurement are described in the following sections. Then, OSIVE IMS is used to characterize OSIVE LI [414] and OSIVE Slim, and the experimental results of the optogenetic stimulation on artificially modified NPCs are exhibited as an experimental validation of the system.

1. Background

Optogenetics is a growing interest and is under active development, especially following the emergence of protein-coding opsin genes responsive to illumination at specific wavelengths of light. It has multiple applications in neuroscience, allowing to study of neuronal pathways or serving for therapeutic applications such as in the treatment of anxiety disorder, autism spectrum disorders (ASDs), or Parkinson's disease. More recently, optogenetics is opening its way also to stem cell-based therapeutic applications for neuronal regeneration after stroke or spinal cord injury.

Hand in hand with the development of the field, electronic equipment has been emerging to perform ex vivo experimentation, generally with highly specific characteristics in terms of temporal parameters and simultaneous experimentation (*i.e.*, the application of different protocols to different wells in the same well matrix). The use of laser (see Yu *et al.* [139]) and LED (see Weick *et al.* [419]) aimed over the culture dish through an optic fiber are the most straightforward setups.

In the early days of this discipline, an astable NE555-based optostimulation platform was developed for *in vitro* application (see Li *et al.* [420]), offering certain configuration capabilities through a hardware potentiometer and stating the future development of the next-generation optostimulation platforms based on microcontroller. In Abilez's work [421] a data acquisition card is used to control a LED source from a PC. The setup allows the monitoring of cardiac electrophysiology perturbation induced by optogenetic stimulation. This feedback is obtained through an optic microscope.

Nowadays, there are some devices available in the market and scientific repositories that offer great flexibility capabilities in terms of wavelength and configuration of the stimulus sequences:

- The Light Plate Apparatus (LPA) from Gerhardt *et al.* [422] is an open-hardware optogenetics and photobiology stimulation device, with instructions for its assembly and calibration, and offers a great deal of configuration flexibility through the LED selection from a calibrated list and a web-based configuration Graphic User Interface. The LPA is configurated for a standard 24-well plate, displaying up to 2 LEDs per well.
- The optoPlate-96 from Bugaj & Li [423] displays a geometrical conformation to insert in the standard 96-well and 384-well plates. Each cell is configured to be able to stimulate with far-red, red, and blue lights. A Graphic User Interface has been added to the system (see Thomas *et al.* [424]).

Nevertheless, both outstanding optogenetic stimulation platforms in state of the art are not intended to obtain real-time feedback. They are too voluminous to fit under commercial microscopes with high magnification. They are developed to fit over them the well plates for *in vitro* assays. Therefore, the results are assessed is performed afterward by harvesting the cells for flow cytometry or immunofluorescence analysis. With these instruments, real-time tracking becomes unfeasible.

The opsin-containing cells' response to optical stimulation consists of depolarizing and hyperpolarizing currents and transduction of signal-triggered events (see Mattis *et al.* [121]). The main properties concern the investigational equipment in optogenetic stimulation are stimulation time, irradiation, rest times (duty cycle), wavelength and light power density. The power density of optogenetics stimulation tools can vary from 0.04 mW/mm^2 peak (as in Bugaj & Li [423]), to 1 mW/mm^2 (as in Yu *et al.* [139] and Weick *et al.* [419]) or even higher (see Park [118]).

Calcium imaging has been extensively used to interrogate cellular activity determined by calcium dependent-signaling thanks to newly developed fluorescent calcium indicators such as Fluo-4 (see Paredes *et al.* [425]). Using confocal fluorescence sensors, real-time calcium imaging of NPCs or mature neuronal cells can be obtained. It allows evaluating their functional responses since intracellular calcium plays critical roles, for instance, in cell cycle control, cell death, or gene expression (see Berridge *et al.* [426]). Calcium imaging in mature neuronal cultures indicates synaptic plasticity in post-synaptic in a neuronal network (see Grienberger & Konnerth [427]).

2. Device specifications

Fast calcium waves imaging evaluation requires higher resolution instrumentation, such as confocal microscopy. Hence, we aim to develop an optogenetic stimulation platform that allows real-time high-resolution microscopy acquisition during stimulation.

This platform shall meet the following requirements:

- Configurable pulsed waveforms of a specific wavelength.
    - Up to millisecond resolution pulse.
    - Up to 10 mW/mm^2 irradiance.
- Allowing the multiple stimulations of different wells *in vitro*.
- Suitable for simultaneous surveillance through confocal microscopy during stimulation.

- Suitable for *ex vivo* stimulation.

The fulfillment of these specifications would represent a step forward to state of the art, offering sufficient flexibility to study in greater depth the intrinsic mechanisms of the discipline from the point of view that still needs to be addressed.

3. Conceptualization

Instead of developing a device with optical microscopy capabilities, making the design more expensive and complex, we developed an optogenetic stimulation platform that would fit inside a commercial microscope. Leica TSP-SP8[17] (**Figure 164**) is an inverted confocal microscope in service in the *Centro de Investigación Príncipe Felipe* (CIPF)'s Confocal Microscopy Service, and the model for which the stimulation devices will be designed to fit to.

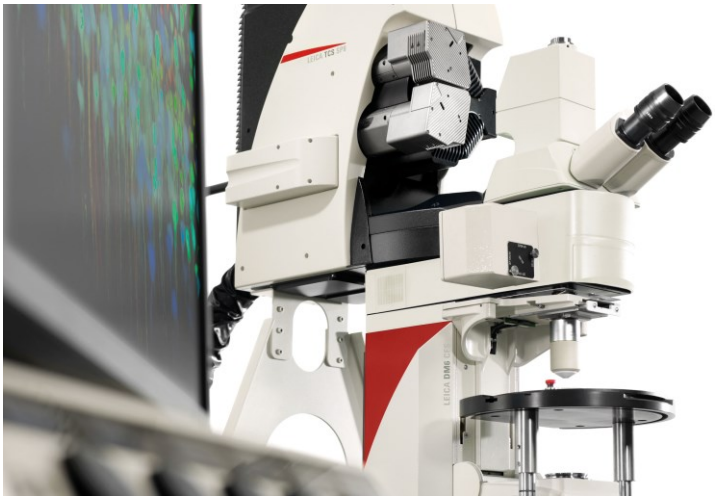

Figure 164. Leica TSP-SP8 © 2022 Leica Microsystems.

The increase in the irradiance scale implies an exponential increase in the complexity of the electronic design. Hence, electronic development was divided into: a low-irradiance device and a high-irradiance device. On the one hand, it allowed us to have as soon as possible a functional low-irradiance device and to study the opsins that respond with a lower irradiance threshold. On the other hand, it allowed obtaining experience for developing a high irradiance device.

[17] From: https://www.leica-microsystems.com/es/productos/microscopios-confocales/detalles/leica-tcs-sp8-mp/. Accessed: 2022-12-26

Nevertheless, the first low-irradiance optogenetic stimulation device did not comply with the height requirements to fit in the confocal microscope. It was also needed to develop a last device to characterize, calibrate and check the irradiance emitted by the stimulation devices.

Hence, the fulfillment of the specifications has been addressed by the development of a family of devices: the *Optogenetic Stimulation for In Vitro Experimentation* (OSIVE).

OSIVE family of devices:

- OSIVE low-irradiance (LI): up to 20 mW/cm^2.
- OSIVE *Slim*: slim version of OSIVE LI.
- OSIVE high-irradiance (HI): up to 10 mW/mm^2.
- OSIVE irradiance measurement system (IMS).

In the framework of the present doctoral thesis OSIVE *Slim* [412] (with OSIVE LI [414] as antecedent) and OSIVE IMS [415] are described.

4. OSIVE Slim: matrix for 24-well *in vitro* optogenetic stimulation

The problem addressed in this work is the development of a tool for in-vitro optogenetic stimulation while allowing the simultaneous monitoring of the induced fast transient responses.

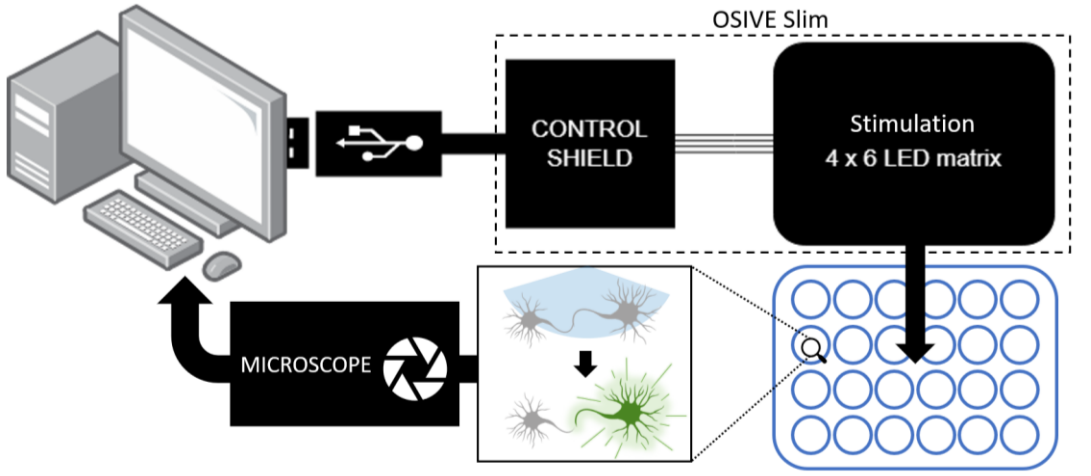

Figure 165. General system overview. The optogenetic stimulation matrix OSIVE Slim is commanded through a Graphic User Interface on a PC. The stimulated cells responses are tracked via confocal microscopy, observing the resulting response in the PC. Reproduced from [412]. IEEE Transactions in Biomedical Circuits and Systems (CC 4.0 BY) 2023 IEEE.

For this purpose, OSIVE Slim is designed to fit in a commercial confocal microscope, which will be used to obtain such real-time feedback. A 24-well plate is chosen to maximize the experimentation throughput: a total of eight different experimentation groups, with three replicates each, can be seeded, stimulated, and monitored simultaneously. The optogenetic stimulation array consists of 24 photoemitters matching the geometrical configuration of the wellplate. The photoemitters will be controlled through a USB interface from a PC. The general block diagram of the system is shown in **Figure 165.**

4.1. Antecedents

OSIVE LI (low-irradiance) [414] was the first OSIVE prototype to be developed. Its firmware and software are identical to the OSIVE Slim [412], which was improved in terms of hardware distribution to reduce its height to fit in the Leica TSP-SP8 confocal microscope.

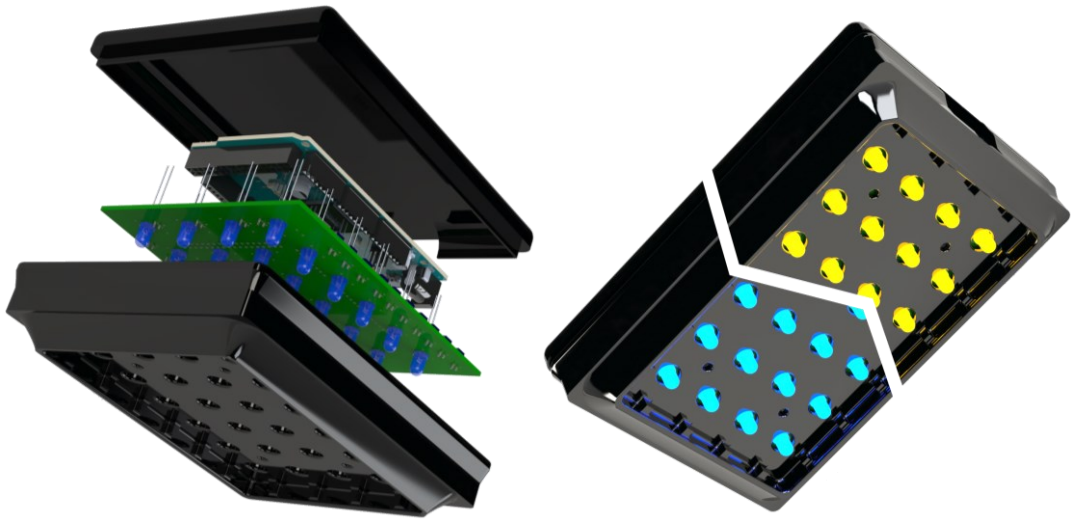

Figure 166. OSIVE LI. Left: exploded view. Right: representation of two models, with 470 and 590 nm LEDs. Reproduced from [414]. XIV IWOSMOR.

In **Figure 166**, a representation of the system is shown. Two models of OSIVE LI were developed to provide two different wavelengths using 24 LEDs at 470 and 590 nm for active and control stimulation, respectively. Both devices were calibrated with OSIVE IMS (described in section *5. OSIVE IMS: Irradiance measurement system*). They are employed to irradiate the monolayer cell culture at each well with an irradiance of 0 to 20 mW/cm^2, a pulse width modulation of 1 µHz to 1 kHz in frequency, and adding a resting period ranging from milliseconds to days. The variables were applied to groups of 3 LEDs.

4.2. Microscope considerations

The inverted confocal microscope Leica TSP-SP8 was employed for real-time acquisition and served for device configuration design. A block diagram of the system as a whole is shown in **Figure 167.** Hence, the optoelectronic system has to be placed over the plate, so the result of irradiation can be measured at the moment of application. Placing the device over the wellplate inside the microscope leads to a constraint in the size and form design of the system to fit the microscope chamber in the remaining 15 mm height. Satisfying this constraint will allow the closing of the microscope's lid. Not closing the lid will trigger the safety alarm related to possible laser reflections outside the confocal microscope. A limitation to bear in mind is the cables that need to be brought outside this chamber.

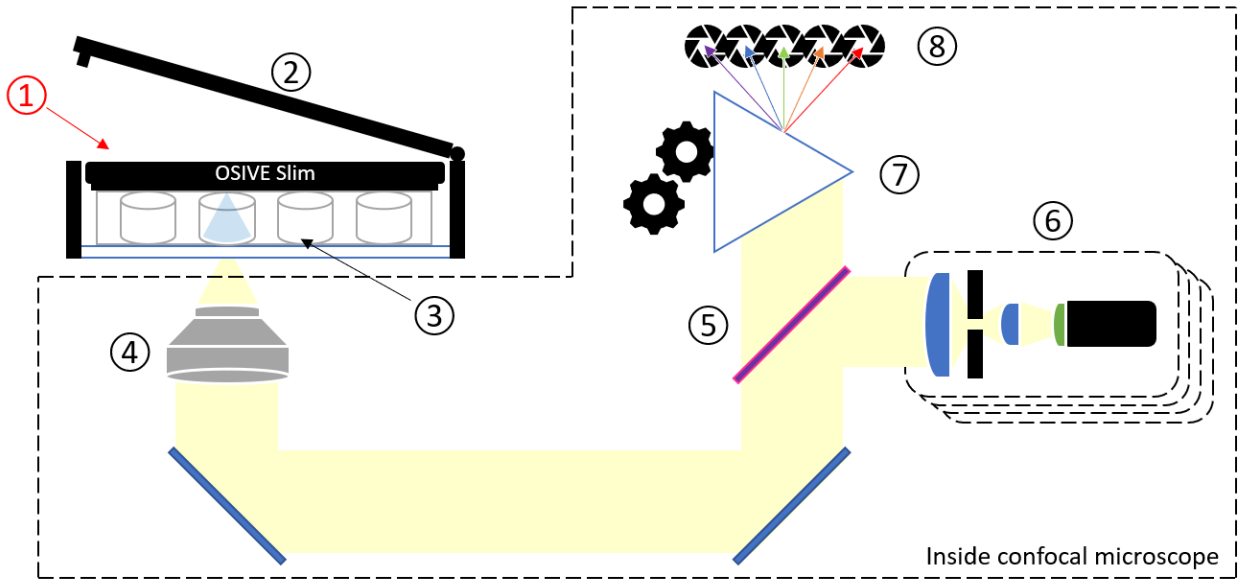

Figure 167. Optogenetic Stimulation for In-Vitro Experimentation (OSIVE), Slim version, over inverted confocal microscope setup. OSIVE Slim fits inside the space between the P-24 in-vitro well array and the microscope's enclosure, allowing the real-time measurement of the fast transients after a stimulation shot or burst. ① OSIVE Slim, ② laser safety lid, ③ P-24 well array, ④ objective lens, ⑤ color splitter, ⑥ laser array (collimated excitement pinhole), ⑦ adjustable prism, and ⑧ detectors. Reproduced from [412]. IEEE Transactions in Biomedical Circuits and Systems (CC 4.0 BY) 2023 IEEE.

4.3. Hardware design

In this section, the hardware design of OSIVE Slim is described following this structure: general system overview, irradiance control, microcontroller unit, supply, and dimensions.

- PCB design is performed using Autodesk's EAGLE 8.2.
- Transient simulation is performed using ADI's LTSpice XVII.

4.3.1. System general considerations

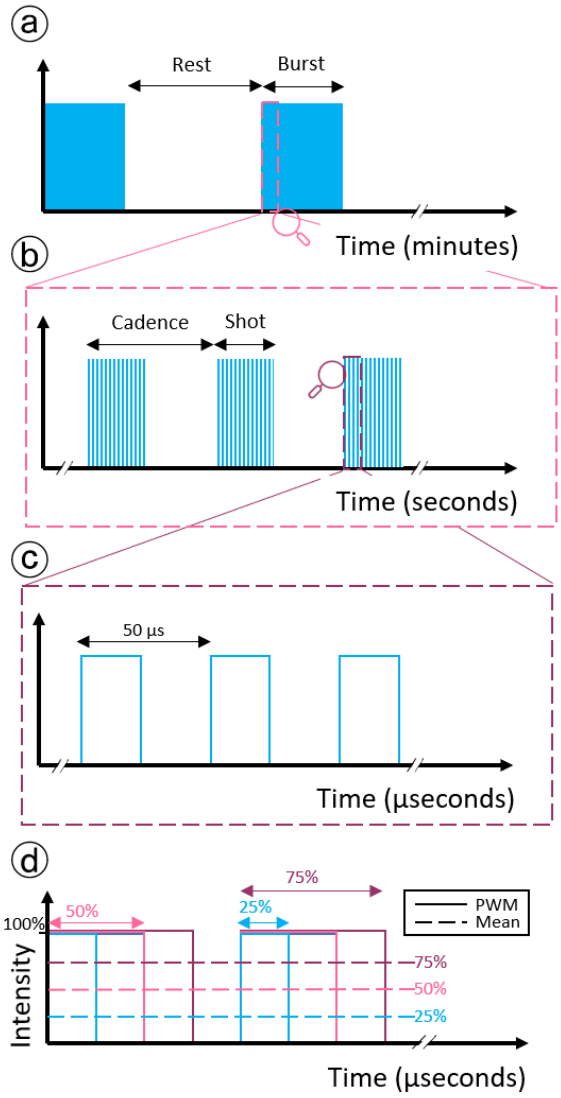

Figure 168. Configurable optogenetic stimulation pattern Pulse Width Modulation (PWM) controlled. ⓐ Each optogenetic stimulation is compounded by sequenced periods of burst stimulation and rest phases, which may last from seconds to hours. ⓑ A burst is composed of shots of stimulation, with certain width and cadence. ⓒ The shot intensity is regulated by a 20 kHz width modulated pulse, ⓓ obtaining the specified regulable average intensity. Reproduced from [412]. IEEE Transactions in Biomedical Circuits and Systems (CC 4.0 BY) 2023 IEEE.

The irradiance applied can be controlled with pulse-width modulation (PWM): a widely used technique to achieve a mean value with high resolution with the weighted switching between two states, high (*e.g.*, 3.3V) and low (0V). The stimulation protocol is pulsed: sequencing bursts of pulses (stimulation) with rest (no stimulation) phases. All, the number of bursts, the number of pulses or *shots* per burst, and the rest between bursts from seconds to hours, shall be configurable. Each shot has a certain cadence (period) and pulse width, configurable with millisecond resolution, allowing the fast switch between excitation and refractory phases within a burst. **Figure 168** shows a graphical representation of the configurable stimulation protocol. Consequently, the system shall be designed to drive each photoemitter at a selected power level, applying high-frequency pulses with different duty cycles and long-time on-off control. A Graphic User Interface (GUI) is implemented to configure all the beforementioned parameters. These parameters will be sent through USB to a microcontroller, handling all the necessary operations.

4.3.2. Irradiance control

Given the 470 nm optogenetic stimulation wavelength, the Broadcom's HLMP-CB2A-VW0DD LED is chosen for the OSIVE Slim optogenetic stimulation array. The procedure shown

below can be repeated for a different dominant wavelength LED according to the parameters indicated in its datasheet to assess whether it meets the irradiance requirements for the target application.

The LED's datasheet[18] states that at an angle of view α of 23°, its luminous intensity is between 4200 and 7200 mcd when 20 mA is applied. Knowing the bottom of the wells has a surface of 1.8 cm^2, and the lens outputs the light at a distance d of 15 mm height of it, we can apply a simple calculus to get the luminous flux in lumens (see representation in **Figure 169**).

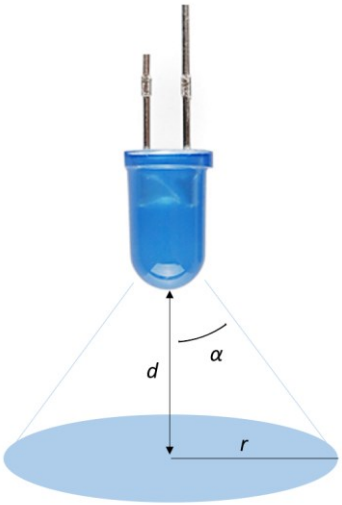

Figure 169. LED area irradiation representation, with main parameters: angle of view α, incident object distance d, and irradiated area radius r. Reproduced from [412]. IEEE Transactions in Biomedical Circuits and Systems (CC 4.0 BY) 2023 IEEE.

Compared with the area of the well, of 180 mm^2, this suggests that just the center part of the well will be irradiated A_{IR}: calculating r with simple trigonometry, the irradiated area ratio AR is obtained (**Equation 45**):

$$AR = \frac{A_{IR}}{A_{WELL}} = \frac{\pi r^2}{A_{WELL}} = \frac{\pi(d \cdot \tan\alpha)^2}{A_{WELL}} = 70.8\% \qquad \textbf{Equation 45}$$

The candela to lumen conversion is as follows (**Equation 46**):

$$1\ cd = 1\frac{lm}{sr} \qquad \textbf{Equation 46}$$

[18] Datasheet: https://docs.broadcom.com/doc/AV02-2228EN. Accessed: 2022-08-02.

Given that 1 candela is equivalent to 1 lumen per steradian (sr), we calculate the solid angle Ω produced by our LED given its angle of view α of 23° (**Equation 47**, relating the half-apex angle, in radians, with the solid angle, in steradians [428]).

$$\Omega = 2\pi \cdot (1 - \cos\alpha) = 0.5 \text{ sr} \qquad \textbf{Equation 47}$$

To the minimum and maximum margins of 4200 and 7200 mcd and applying **Equation 46**, we find that at 20 mA, the luminous flux (Φ) at the bottom of the wells will be between 2100 and 3600 mlm.

As the lumen is a subjective measurement of the luminosity, dependent on the wavelength and the human eye, we need to convert lumen to watt of irradiated power (radiant power, Φ_e), which is given by equivalence tables [429]: at 470 nm, 62.139 lm = 1 W (**Equation 48**).

$$\Phi_e(@\ 470 \text{ nm}) = \Phi \cdot \frac{1 \text{ W}}{62.139 \text{ lm}} \qquad \textbf{Equation 48}$$

Therefore, the minimum and maximum radiant fluxes are obtained: $\Phi_{e\,min} = 34$ mW, and $\Phi_{e\,max} = 58$ mW.

Irradiance flux density E_e is the radiant power per area, $A_{IR} = 127.4$ mm^2. Considering its minimum and maximum values obtained before, the minimum and maximum irradiance are obtained ($E_{e\,min}$ and $E_{e\,max}$) (**Equation 49**).

$$E_e = \frac{\Phi_e}{A_{IR}};\quad E_{e\,min} = 27\frac{\text{mW}}{\text{cm}^2};\quad E_{e\,max} = 45\frac{\text{mW}}{\text{cm}^2} \qquad \textbf{Equation 49}$$

To assess the adequacy of the former calculations, we prepared an experimental setup setting the nominal forward current I_F (20 mA) through an HLMP-CB2A-VW0DD LED. The voltage drop over the LED was V_D 2.9 V, equivalent to electrical power P_e of 58 mW. The LED's luminous efficiency, η_V, is the ratio to convert this electric power to radiant power.

In the LED's datasheet, the diode forward voltage V_D is 3.15 V at nominal I_F. In these conditions, the LED features $P_e = 63$ mW and $\Phi = 2.85$ lm. Applying **Equation 48**, the theoretical radiance flux is obtained, $\Phi_e = 46$ mW, and by **Equation 49**, the theoretical irradiance is obtained too, $E_e = 36$ mW/cm^2. The LED's luminous efficiency. η_V, at the nominal current, is 45 lm/W (**Equation 50**).

$$\eta_V = \frac{\Phi}{\Phi_e} \qquad \textbf{Equation 50}$$

After obtaining luminous efficiency at nominal conditions, η_V, luminous flux (Φ), and irradiance (E_e) are calculated with the experimental values: $\Phi = 2.61$ lm, and $E_e = 33$ mW/cm^2,

that fit with the typical values shown in the datasheet. We design the next control circuit to provide a wide range of irradiance values to the experiments, considering spatial and power supply restrictions (**Figure 170**).

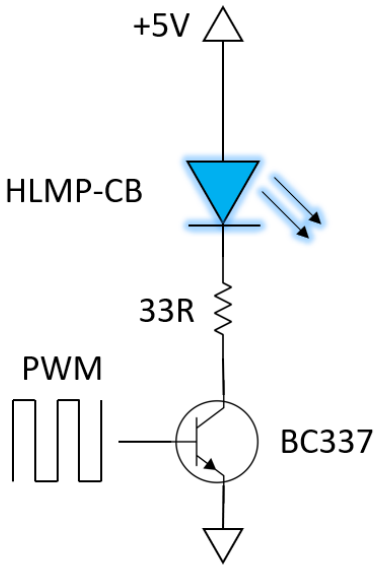

Figure 170. LED irradiation control simplified schematic. Reproduced from [412]. IEEE Transactions in Biomedical Circuits and Systems (CC 4.0 BY) 2023 IEEE.

Experimentally, we measured a current of 55 mA through the diode branch, a V_D of 3.14 V, and a V_{CEsat} of 24 mV (**Equation 51**).

$$I_{Csat} = \frac{5V - 3.14V - 0.024V}{33\Omega} = 55.6\ mA \qquad \textbf{Equation 51}$$

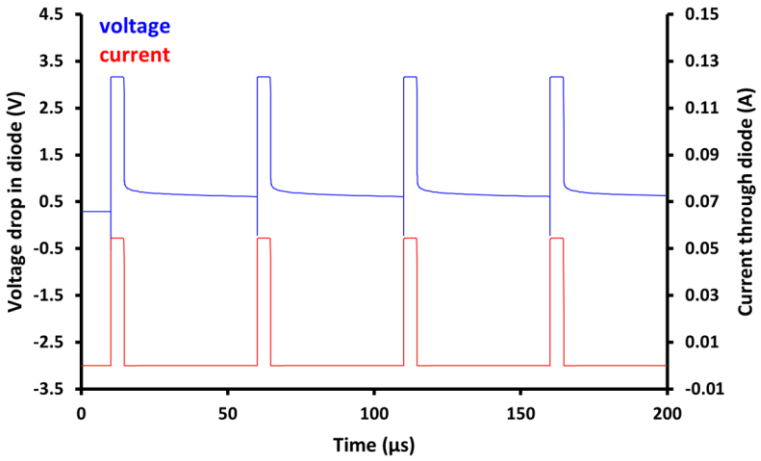

Figure 171. LED irradiation control simulation results, current and voltage through LED over PWM control. Reproduced from [412]. IEEE Transactions in Biomedical Circuits and Systems (CC 4.0 BY) 2023 IEEE.

Given these values, the theoretical calculations concur with the experimental values. The typical according to the transistor figures are: $V_{BE} = 0.7$ V, $h_{FE} = 100$ and $V_{CEsat} = 0.05$ V @ $I_C = 50$ mA. Moreover, the circuit is simulated in LTSpice. The results are shown in **Figure 171**, which concur with our prototype results and calculations.

Given these results and the LED forward current vs. relative luminous intensity curve (see Figure 3 in its datasheet, reproduced in **Figure 172**), we determine that at 55 mA current, the luminous intensity is 2.2 times the normalized intensity at 20 mA.

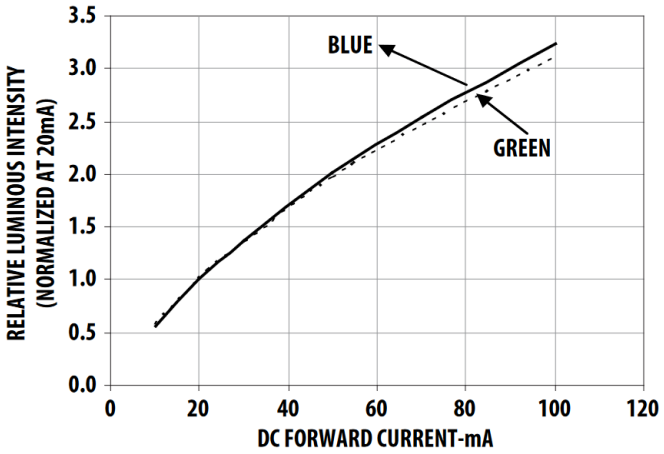

Figure 172. Relative Intensity vs. Forward Current in Broadcom's HLMP-CB2A-VW0DD LED. Source: HLMP-CB LED family datasheet.

Nominal irradiance has been calculated before, E_e(nominal) = 36 mW/cm^2, so this system's typical full-scale irradiance is 79 mW/cm^2. We should remember that the nominal irradiance by a given LED might be between its minimum and maximum values. The minimum, typical, and maximum irradiance values of irradiance for nominal and full-scale conditions are shown in **Table 6**.

Table 6. Nominal and full-scale photoemitter irradiance in their minimum, typical, and maximum efficiencies.

	Minimum	Typical	Maximum
Nominal (mW/mm^2)	27	36	45
Full-scale (mW/mm^2)	59	79	99

4.3.3. Microcontroller unit

OSIVE Slim is based on Arduino Due microcontroller board, with the Atmel SAM3X8E ARM Cortex-M3 CPU. It features:

- A microcontroller: Atmel SAM3X8E ARM Cortex-M3 CPU with 512KB of flash memory, 100MHz clock speed, and 96KB of SRAM.
- Digital I/O pins: 54 (of which 12 can be used as PWM outputs)
- Analog input pins: 12 (3.3V max input)
- Analog output pins: 2 (DAC)
- USB connector: Type B
- Power jack: Barrel connector, 7-12V
- On-board DC-DC converter: 3V and 1.8V output
- Operating voltage: 3.3V
- Input voltage (recommended): 7-12V
- Input voltage (limits): 6-20V
- Digital I/O current: 130mA
- DC current per I/O pin: 7mA
- DC current for 3.3V pin: 50mA
- Flash memory: 512KB
- SRAM: 96KB
- EEPROM: None
- Clock speed: 84MHz

Source: Arduino Due documentation, available at the official site [430].

The Arduino Due is a powerful microcontroller board that is well-suited for projects that require a lot of processing power, such as real-time image processing, 3D rendering, and other demanding tasks. It is also a good choice for projects that require a lot of I/O pins, as it has many digital and analog I/O pins, as is the case of OSIVE Slim.

The complete Arduino Due pinout is shown in **Figure 173**. PWM configurable GPIO in the microcontroller board are pins 2 to 13. To independently control eight groups of 3 LEDs and irradiate 24-wells, each group is controlled via a PWM output. Pins 13 to 10, and 5 to 2, respectively, are employed to control LED groups 1 to 8.

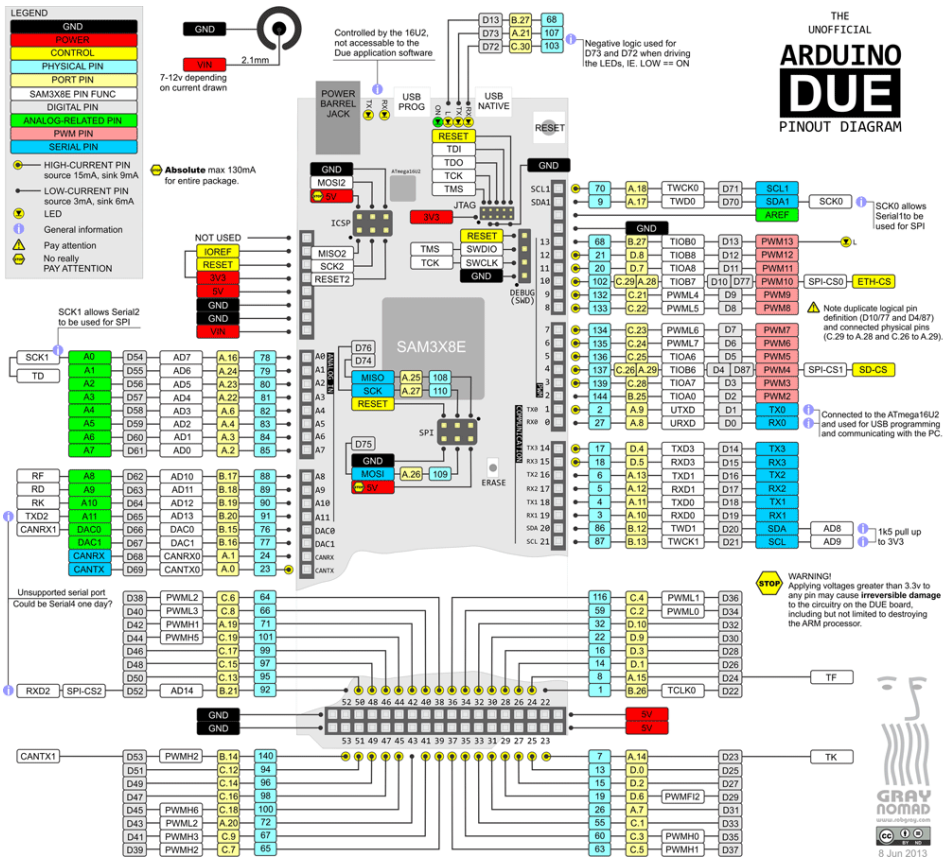

Figure 173. Full Arduino DUE pinout. Source: Gray Nomad.

4.3.4. Supply considerations

Regarding the power consumption and supply considerations, OSIVE Slim can be powered directly from a USB port from the computer hosting the Graphic User Interface. USB 2.0 ports supply up to 500 mA, and 24 LEDs at maximum power will draw 400 mA (**Equation 52**), adding up to the maximum of 130 mA of the Arduino DUE consumption.

$$I_{LED\ max} = E_{FS} \cdot \frac{20\ mA}{E_e} = 30\ mW/cm^2 \frac{20\ mA}{36\ mW/cm^2} \qquad \textbf{Equation 52}$$

Otherwise, the 5V USB micro-B power connector or the ⌀2.1 mm 7-12 V power jack connector supply the necessary power to OSIVE Slim from any commercial power supply.

4.3.5. Dimensions considerations

To satisfy the control and height constraints, OSIVE Slim is designed within two subsystems:

- A Control Shield, based on Arduino DUE board (with an Atmel SAM3X8E microcontroller as core), is used as system's controller and interface with the PC.

- A Stimulation Matrix of 4x6 LEDs in groups of 3, geometrically matching the 24-well plate and 1.45 mm height, with the necessary NPN transistors and current limiting resistors.

4.3.6. PCB design

Two PCBs are designed, one to match the 24-well dimensions, with a LED irradiating each well, and a secondary shield PCB for the Arduino Due microcontroller board. Both PCBs incorporate 1.25 mm pitch 10-position Molex PicoBlade™ connectors to supply and send the PWM control signals from the Arduino Due to the 24-LED PCB.

The schematics can be found in the *Annexes*:

- OSIVE Slim 24-LED PCB at *Annex 10. OSIVE Slim Schematic 1/2* and *Annex 11. OSIVE Slim Schematic 2/2*.
- OSIVE Slim Due-Shield at *Annex 12. OSIVE Slim DUE-Shield Schematic*.

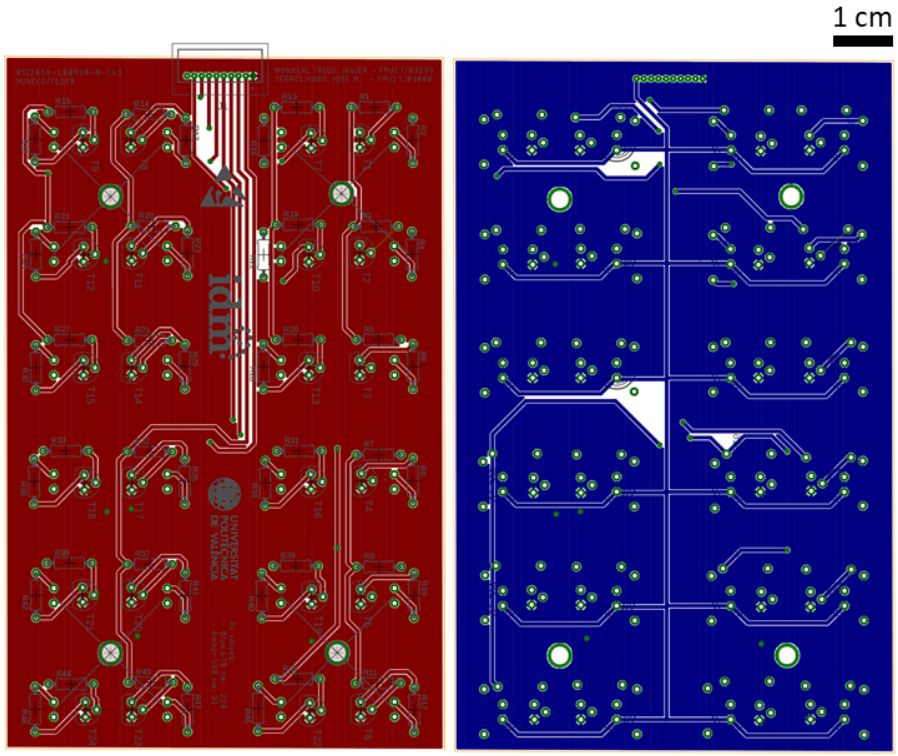

Figure 174. OSIVE Slim 24-LED PCB top layer (left) and bottom layer (right). Obtained with EAGLE © 2022 Autodesk.

They have been fabricated as two-layer PCB (Eurocircuits © 6C class), and they are shown in **Figure 174** and **Figure 175**.

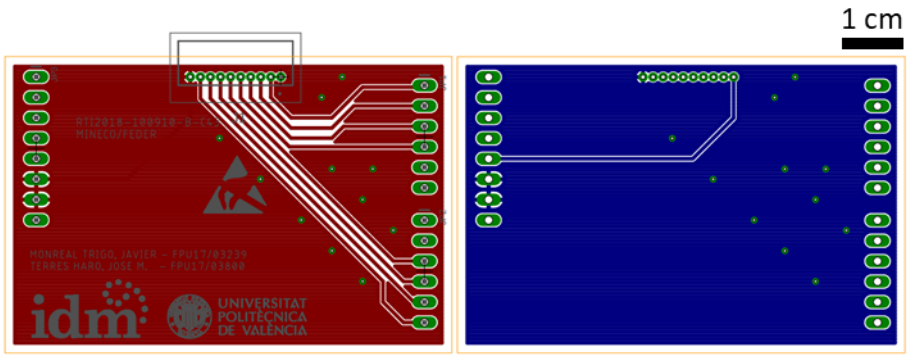

Figure 175. OSIVE Slim DUE-Shield PCB top layer (left) and bottom layer (right). Obtained with EAGLE © 2022 Autodesk.

4.4. Firmware description

This subsection will first address the microcontroller code attending to the hardware control. Then, the specific behavior is shown through a flowchart.

The Atmel SAM3X8E firmware, in C, is programmed with Atmel Studio (currently renamed as Microchip Studio).

C is the most widely used programming language for microcontroller applications. It is a compiled language, offering fast execution and more efficient use of memory compared to interpreted languages. It also provides a good balance between high-level functionality and low-level control. This makes it possible to write code that is easy to understand and maintain while still having access to the hardware features of the microcontroller.

4.4.1. General description of the microcontroller code

The average power output of each LED is diminished through PWM to avoid functioning over the absolute maximum ratings, limiting the irradiance to 30 mW/cm^2, the full-scale irradiance E_{FS}. This is done with the PWM modules of the Atmel SAM3X8E 32-bit ARM Cortex-M3 core, configured to output a 20 kHz PWM with a varying duty cycle between 0 and 20%. This PWM has also been modulated to output configurable shots of light up to 20 Hz (50 ms period), so a time for excitation/refractory period can be estimated and set. A rest time of up

to 72 hours between trains of pulses is also added. The general block diagram for the LED control is shown in **Figure 176**.

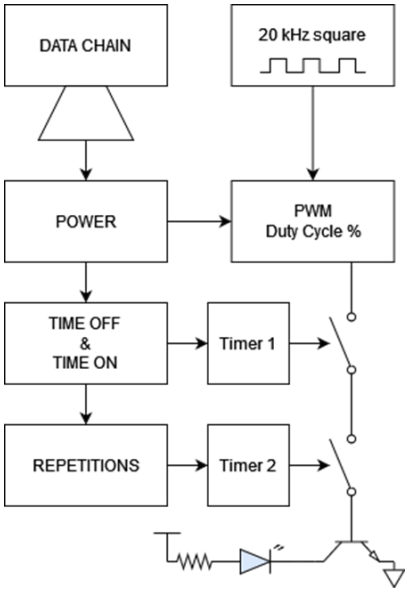

Figure 176. General block diagram of the photo emitter control. The data chain sent to the device shall carry the information regarding timing and power. Intensity is regulated through the PWM's duty cycle. Timing requirements for each channel need two hardware timers. The PWM signal will be applied to the pre-actuator (an NPN transistor) when both timers are in burst and shot states, respectively. Reproduced from [412]. IEEE Transactions in Biomedical Circuits and Systems (CC 4.0 BY) 2023 IEEE.

The user sets the exact output values for the power, excitation, and refractory period times, the number of pulses, and repetitions in the Graphical User Interface connected to the microcontroller by USB to serial conversion.

4.4.2. Flowchart of firmware

The microcontroller's firmware is always running a thread that checks for new messages upon arrival, verifies the data chain integrity, and executes one of two options:

- Over stop command:
  - Turns off every photoemitter.
  - Restarts and holds the timers.
- Over start command:
  - Stores the received information.
  - Sets up the timers.
  - Sets the "experiment on" flag (EOF).

In both cases, it sends the corresponding acknowledgement message. Once the message has been processed, or there is no message, it will check the EOF to assess, and if it proceeds, setup every timer with the corresponding action (turn on or off, at the specified power, the group of LEDs). Once timers have been set, each PWM module will automatically generate the control signals. After this, it will start from the beginning. The simplified flowchart is shown in **Figure 177**.

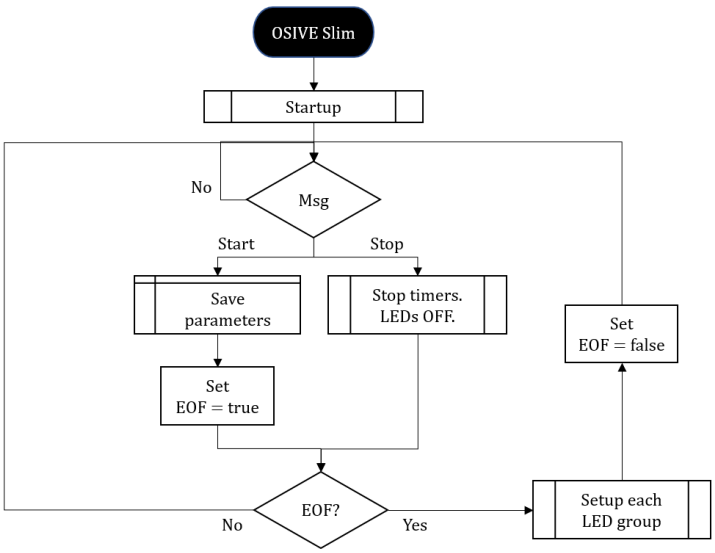

Figure 177. Simplified flowchart for the firmware in the Arduino Due microcontroller. Adapted from [412]. IEEE Transactions in Biomedical Circuits and Systems (CC 4.0 BY) 2023 IEEE.

The *LED groups* process refer to the setup process for each PWM line. Each PWM line attacks the control of a group of three LEDs. The microcontroller checks whether each group needs to be turned off or pulsed. If a group is pulsing, the pattern will be set up according to the parameters established by the GUI before the start.

4.5. PC Graphic User Interface description

The Graphic User Interface is implemented in Processing[19], allowing the global configuration of OSIVE Slim and its real-time control.

Processing is a programming language and development environment designed for creating interactive visual projects, such as graphical user interfaces (GUIs), animations, and

[19] More information at: https://processing.org/

data visualizations. It is based on the Java programming language and includes a built-in graphics library that makes drawing and manipulating graphics easy.

In this subsection, the user interface design and the general behavior of the GUI are addressed.

4.5.1. User interface design

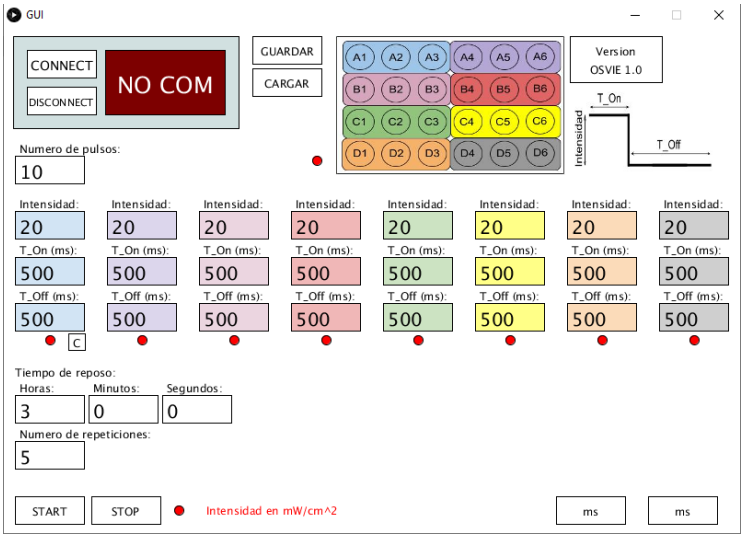

Figure 178. Graphic User Interface. It allows the P-24 configuration in eight groups, each of them with independent intensity, shot duration (time on), and cadence (time off). The number of shots or pulses per burst, the number of bursts, and the rest time between bursts is common. Reproduced from [412]. IEEE Transactions in Biomedical Circuits and Systems (CC 4.0 BY) 2023 IEEE.

The design GUI is shown in **Figure 178**. It enables the user to select the power, time off and time on of the pulse, the number of pulses, the number of bursts, and the resting time between bursts.

4.5.2. Flowchart of the graphic user interface

The GUI, after startup, handles the events coming from the user manual input. That is to say:

- The connection and disconnection to the USB interface (to the COM virtual port).
- The setup of all the parameters for an upcoming experiment.
- The start and stop commands.

With this purpose, it will send the necessary data to the Control Shield to run an experiment, or sending the high priority stop message.

All messages implement checksum to ensure transmission integrity of the message received, sending an acknowledge message from OSIVE Slim which triggers the corresponding GUI indicator. A simplified flowchart is shown in **Figure 179**.

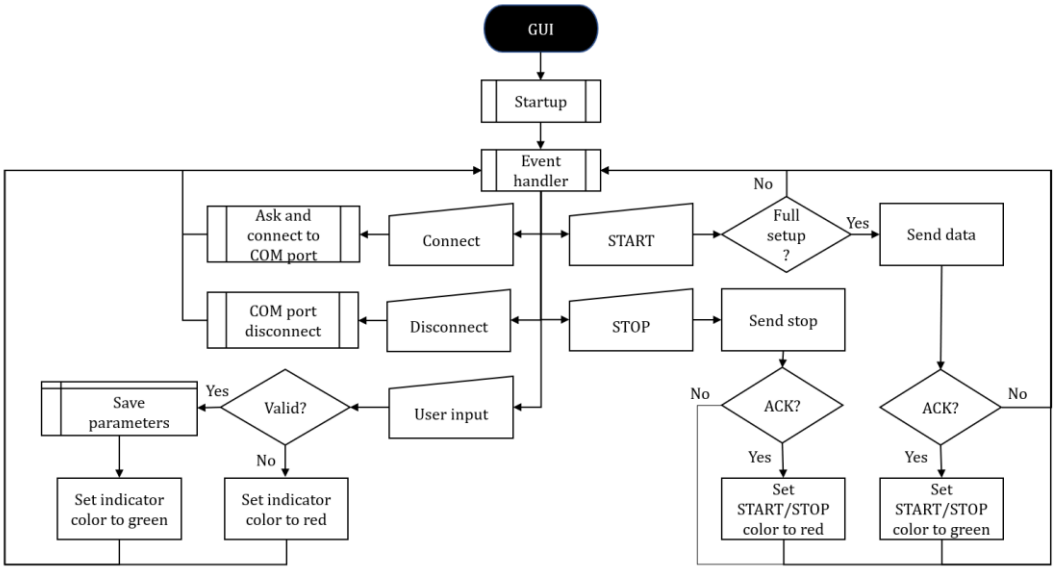

Figure 179. Simplified flowchart for the Graphic User Interface. Adapted from [412]. IEEE Transactions in Biomedical Circuits and Systems (CC BY 4.0) 2023 IEEE.

4.6. Final appearance

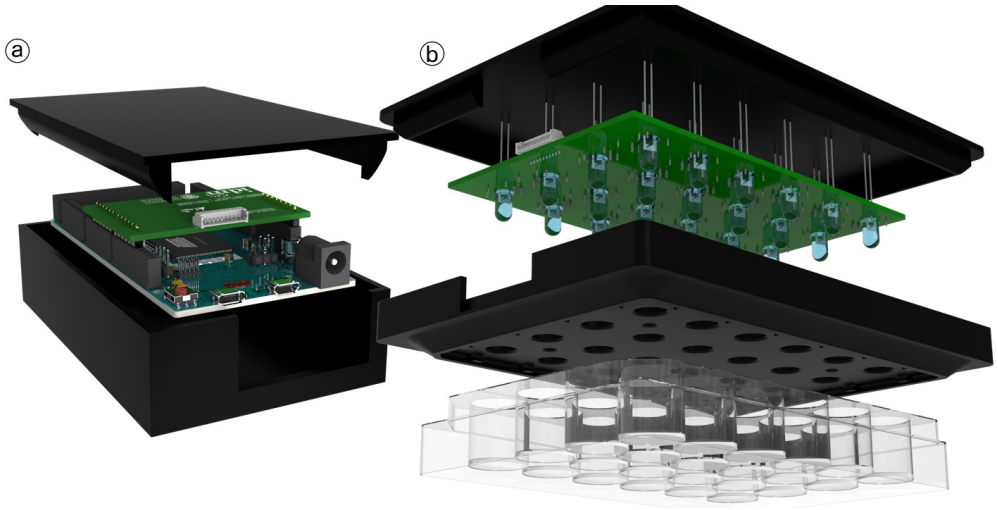

Figure 180. 3D models of the two subsystems of OSIVE Slim: ⓐ Control Shield, based on Arduino DUE microcontroller, interfacing through USB with the PC. ⓑ Stimulation Matrix, with current limiter resistors and

NPN transistors. Reproduced from [412]. IEEE Transactions in Biomedical Circuits and Systems (CC 4.0 BY) 2023 IEEE.

OSIVE Slim with a standard 24-well matrix for in-vitro culture exploded view is shown in **Figure 180**.

4.7. Reproduction guide

In the following virtual space can be found:

- Gerber files and bill of materials for ordering the OSIVE Slim PCBs.
- Firmware files for flashing the Arduino Due microcontroller board.
- STL parts to 3-D print the boxes.
- Processing executable file for the Graphic User Interface deployment.

Link to virtual space: https://github.com/JMonrealT/OSIVE-Slim. Share, build, and modify OSIVE Slim, registered under BY-NC-SA Creative Commons 4.0 License.

5. OSIVE IMS: Irradiance measurement system

With the purpose of calibrating the other OSIVE devices, a real-time monochromatic irradiance measurement system commanded by a graphical user interface has been developed, OSIVE IMS (Irradiance Measurement System). It features:

- Seven simultaneous measurement scales.
- The largest scale having a full scale of 27 mW/mm^2.
- The one with highest resolution with a full scale of 0.04 mW/mm^2.
- 1024 points resolution per scale.
- Monochromatic wavelength selection for sensitivity adjustment of the sensor.

OSIVE IMS is commanded by means of a graphical user interface through a personal computer. The instrument has been designed to meet the broadest needs for measuring monochromatic irradiance in optogenetics applications. It features 7 ADCs with different amplification gains chained together. A real-time selection algorithm is executed On the computer side to select the most suitable scale at each instant. The device has been successfully used to calibrate low and high-intensity optogenetics stimulation units, and a structure has been implemented for a real-time feedback sensor.

5.1. Hardware design

Regarding the hardware design, the conceptualization of the system is described, then justifying the microcontroller selection and finally addressing the analog circuits designed.

About the development tools used, the PCB is designed using Autodesk's EAGLE 8.2.

5.1.1. System general design

The system is based on Vishay's BPW24R photoreceptor: its relative sensitivity curve is shown in **Figure 176**. As relative sensitivity, it is taking the most sensitive wavelength as reference: 870 nm. The system will allow the user to choose the wavelength of the source and apply the spectral sensitivity corresponding to this wavelength.

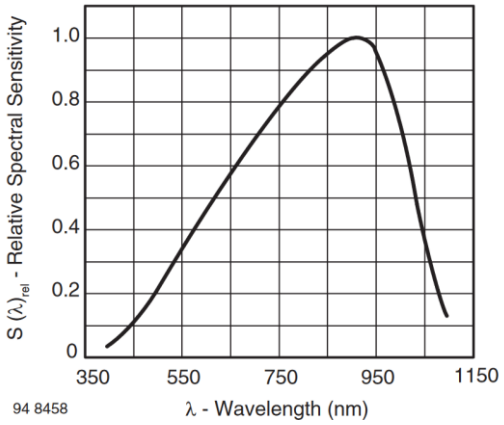

Figure 181. Relative Spectral Sensitivity vs. Wavelength in Vishay's BPW24R photoreceptor. Source: BPW24R datasheet[20].

The BPW24R's output current is proportional to the irradiance received. Its absolute spectral sensitivity, $s(\lambda,V_R)$, is a function of the incident wavelength λ and reverse voltage V_R. For the most sensitive wavelength and the standard V_R, the absolute spectral sensitivity is shown in **Equation 53**.

$$s(\lambda = 870\ \text{nm}, V_R = 5\text{V}) = 0.6\ \text{A/W} \qquad \textbf{Equation 53}$$

An I-V converter, a low-pass filter, and seven cascaded non-inverter amplifiers adequate the signal for the different 7 ADC inputs of the microcontroller Arduino Nano. Those non-

[20] BPW24R datasheet: https://www.vishay.com/docs/81520/bpw24r.pdf

inverter amplifiers have an absolute gain of 3 and are implemented with ultralow offset voltage operational amplifiers OPAx376. A general view of the system is shown in **Figure 182**.

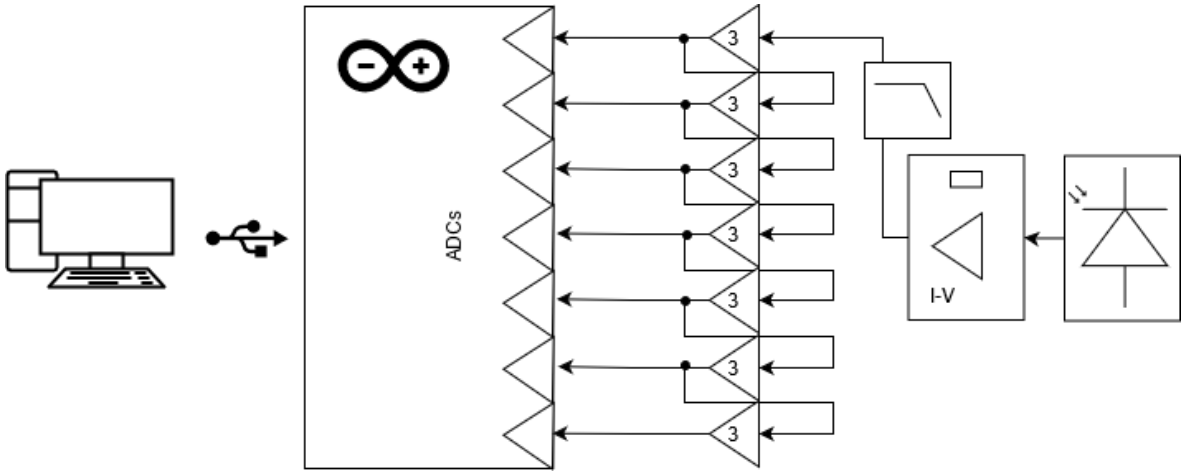

Figure 182. General diagram of OSIVE IMS.

Each operational amplifier IC is decoupled with 1 nF and 100 nF capacitors next to the power supply pin to reduce digital noise.

5.1.2. Microcontroller unit

OSIVE IMS is based on Arduino Nano: a small, breadboard-friendly microcontroller board based on the ATmega328 microcontroller, which is in turn based on the AVR architecture and can run at clock speeds up to 20 MHz. It featuresas 14 digital I/O pins, 6 of which can be used as pulse width modulation (PWM) outputs and 8 analog input pins with 10-bit resolution. It also features:

- Memory: the ATmega328 has 32 KB of flash memory for storing code (of which 2 KB is used for the bootloader), 1 KB of SRAM, and 1 KB of EEPROM.
- Power: it can be powered through the mini-USB connection or by an external power supply. It can operate at voltages between 5 and 12 volts.
- Size: only 18.5 mm x 43 mm.

Arduino Nano USB micro-B is used to power and control OSIVE IMS from the PC. 5V's pin (12) is used to power the rest of the system, which is the output of the board regulator with a 200-500 mA current source capability (depending on the model). ADC input pins A0 to A6 (4 to 10) are used as inputs for the different cascaded outputs `SCALE0` to `SCALE6`, as shown in **Figure 183**.

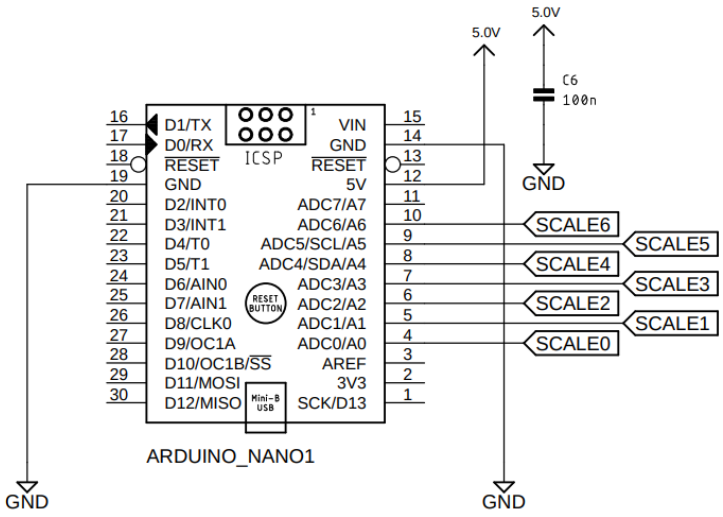

Figure 183. Arduino Nano microcontroller connection to OSIVE IMS.

5.1.3. Current-to-voltage converter and low-pass filter

The BPW24R, for reverse voltages smaller than 5V, I_{RL} vs. V_R is constant for each irradiance (see **Figure 184**), *i.e.*, s(λ=870 nm) = 0.6 A/W as shown in **Equation 53**.

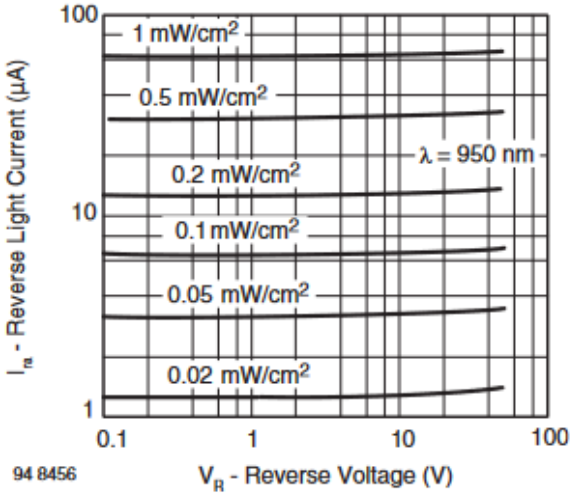

Figure 184. Reverse light current vs. reverse voltage of BPW24R. Source: BPW24R datasheet.

The current-to-voltage converter (IVC) and low-pass filter (LPF) of OSIVE IMS are shown in **Figure 185**. The IVC is composed of U1OA1, R1, and C7. The negative feedback, *i.e.*, the OA's output (pin 1) connection to its inverting input (pin 3), in non-saturation conditions, will

produce a *virtual short-circuit*: it will reach the stability condition by setting such an output voltage that non-inverting and inverting inputs are virtually to the same voltage.

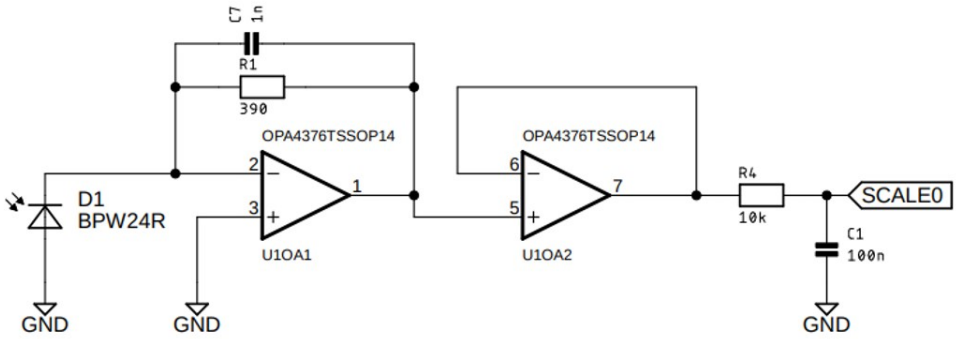

Figure 185. Current-to-voltage converter and low-pass filter of OSIVE IMS.

The photoreceptor will generate a current proportional to the irradiance from its cathode to the anode at 0.6 A/W (at 870 nm, otherwise apply s(λ) from **Figure 181**). Given the input high-impedance condition of the OA, the current will flow through R1 and C7 from OA's output, producing a positive voltage drop (regarding OA's output from the virtual short-circuit point). The current full-scale $I_{D1}(\text{max})$ with R1 = 390 Ω, usually called R_{SHUNT}, is calculated, converted to irradiated power, P(max), and to irradiance, E(max), in **Equation 54**, **Equation 55**, and **Equation 56**, regarding that the effective area (A) of the BPW24R is 0.78 mm².

$$I_{D1}(\text{max}) = \frac{5\ \text{V}}{390\ \Omega} = 12.82\ \text{mA} \qquad \textbf{Equation 54}$$

$$P(\text{max}) = \frac{I_{D1}(\text{max})}{s(\lambda = 870\ \text{nm})} = 21.4\ \text{mW} \qquad \textbf{Equation 55}$$

$$E(\text{max}) = \frac{P(\text{max})}{A} = 27.4\ \text{mW/mm}^2 \qquad \textbf{Equation 56}$$

Capacitor C7 is placed for compensating the zero introduced by the diode capacitance (11 pF[21]) and the series of differential and common-mode input capacitances of the OA (6.5 and 13 pF, respectively[22]). However, its design was unnecessary, and no stability issues were found.

The low-pass filter, preceded by U1OA2 in buffer configuration, offers a single-order filter at cutoff frequency f_c shown in **Equation 57**. Nevertheless, the sampling frequency of the system is set to 1 Hz, so that f_c could be further reduced to 2 Hz and meet Nyquist's condition.

[21] BPW24R datasheet: https://www.vishay.com/docs/81520/bpw24r.pdf
[22] OPAx376 datasheet: https://www.ti.com/lit/ds/symlink/opa376.pdf

$$f_c = \frac{1}{2\pi \cdot R4 \cdot C1} = 159\ \text{Hz}$$ **Equation 57**

The U10A2 follower is unnecessary. It is a vestige from the first version of the design in which the operating voltage range of the analog circuit had to be adapted to the operating voltage range of the MCU ADC. However, given the ultra-low offset of the chosen operational amplifiers, its impact on the instrument's overall performance is probably negligible.

5.1.4. Cascaded amplification

From `SCALE0` LPF output, the signal is amplified through OAs in a non-inverting amplifier configuration, as shown in **Figure 186**. The gain, G, is set following **Equation 58**. For all the gain stages, $G = 3$.

$$G = \frac{R2}{R3} + 1$$ **Equation 58**

This way, the device features seven simultaneous measurement scales, the largest having a full scale of 27 mW/mm² and the one with highest resolution with a full scale of 0.04 mW/mm² (3^6 times less). Regarding the cascaded amplification of the offset of the first stages, the 5 µV typical, 25 µV maximum offset of the OPAx376 makes that this error can be amplified up to 3 mV (typical) and 18 mV (maximum) in `SCALE6`. This makes 0.007% and 0.36% of the full-scale value. Nevertheless, the effect is minimized through the background value subtraction, where the effect of the offset errors will be the predominant cause of the non-zero output voltage.

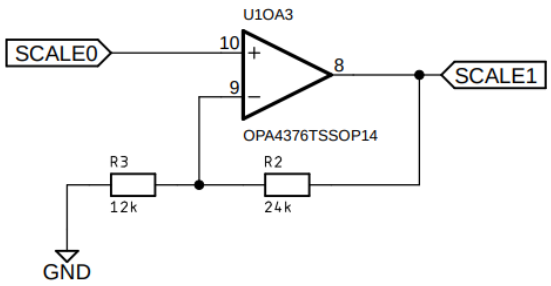

Figure 186. OSIVE IMS x3 gain stage through operational amplifier in non-inverting amplifier configuration.

5.1.5. PCB design

The PCB is designed to fit the Arduino Nano board and leave space enough to fit the photoemitter below any well in a standard 24-well culture dish. The system needs 8 operational amplifiers, for which OPA4376 ICs are chosen, each with 4 OAs.

The schematic for OSIVE IMS *Annexes*, in *Annex 13. OSIVE IMS Schematic* and it has been fabricated as a two-layer PCB (Eurocircuits © 6C class), as shown in **Figure 187**.

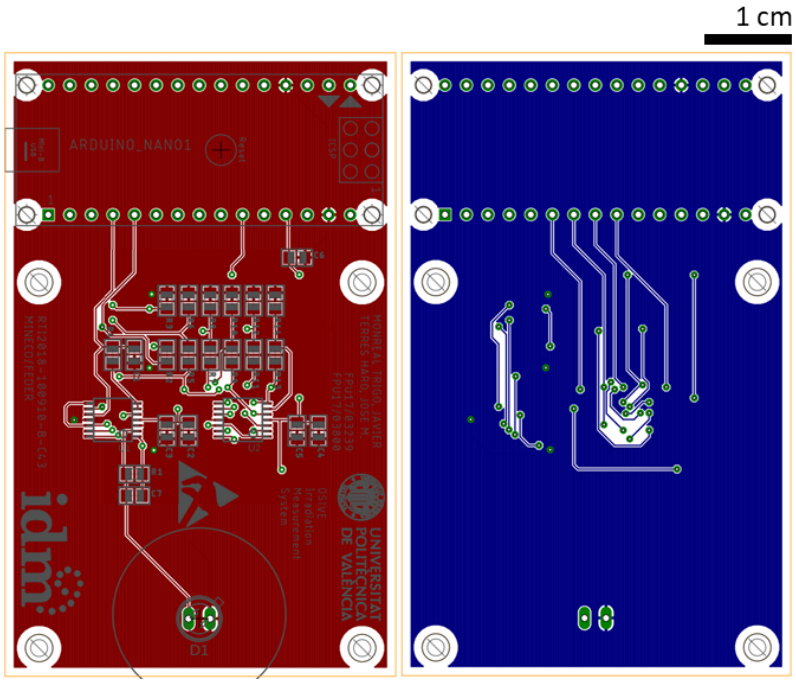

Figure 187. OSIVE IMS PCB top layer (left) and bottom layer (right).

5.2. Firmware description

The Arduino IDE[23] is used for firmware development. It is a free software application that allows users to write, upload, and debug code for Arduino boards. It includes a text editor, compiler, debugger, and library of pre-written code called "sketches". Arduino language, a high-level programming language based on C++, is employed.

The output of each stage is routed to an ADC input of the microcontroller, providing a variable resolution depending on the amplification employed. The minimum resolution of 0.004 mW/cm² is available at `SCALE6` (3.8 mW/mm² full-scale), whereas the resolution will

[23] Source: https://www.arduino.cc/en/software

increase to 0.0268 mW/mm² at the SCALE0 full-scale of 27.39 mW/mm²; both at the photoreceptor's highest sensitivity wavelength. The resolution for each scale is shown in **Table 7**. A dynamic gain selection is executed and displayed in real-time on a graphical user interface.

As shown in **Figure 188**, the system waits for the start command to start measuring. It measures the 7 ADCs, averages 64 samples for each of them, and sends the resulting values throughout UART-USB communications to the PC. It stops its 1 Sps measurement when it receives the corresponding command from the PC.

Table 7. Resolution for each stage of OSIVE IMS, namely SCALE.

Signal	Full-scale (mW/mm²)	Resolution (mW/cm²)[a]
SCALE0	27.39	2.68
SCALE1	9.13	0.89
SCALE2	3.04	0.297
SCALE3	1.01	0.099
SCALE4	0.338	0.033
SCALE5	0.113	0.011
SCALE6	0.038	0.004

[a] Note: 1 mW/mm² = 100 mW/cm²

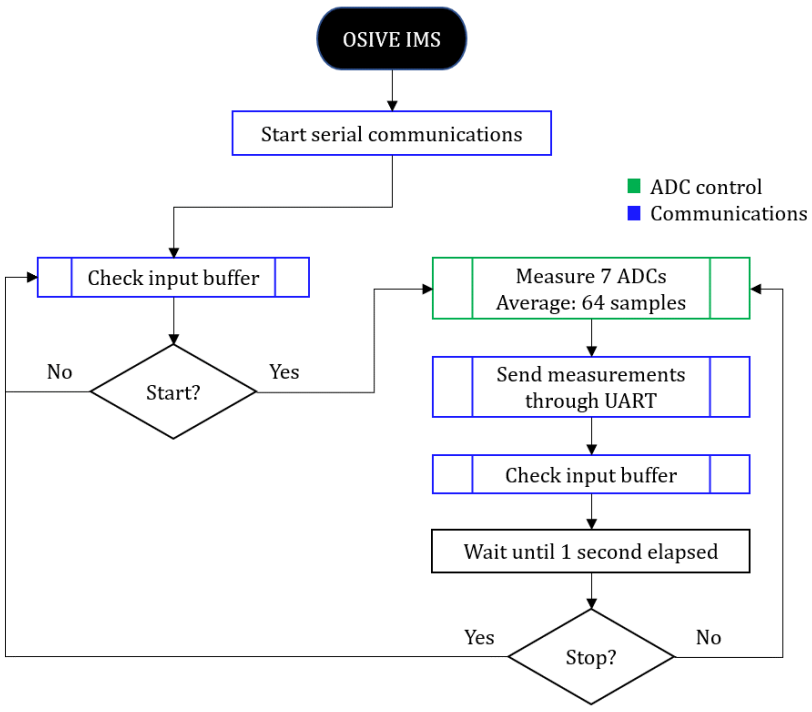

Figure 188. OSIVE IMS' firmware flowchart.

5.3. PC Graphic User Interface description

MATLAB AppDesigner tool is used for the implementation of the GUI. It provides a drag-and-drop interface for adding and arranging GUI components such as plots, buttons, and tables. AppDesigner also includes a set of built-in functions for interacting with the GUI, such as handling user input and updating the display. It is programmed in MATLAB language.

The graphic user interface (GUI) is composed of three functional areas, as shown in **Figure 189**:

- COM port scan, selection, and connection/disconnection.
- Wavelength selection.
- Real-time results display.

The communications setup comprises a `Rescan` button, a `Connect` button, and a drop-down list for the COM Port selection. The wavelength selection is performed through the slide bar located on the GUI's right side. The BPW24R sensibility curve is plotted, and an indicator circle will mark the point of the curve chosen by the user. The wavelength is displayed as well in the cyan textbox below.

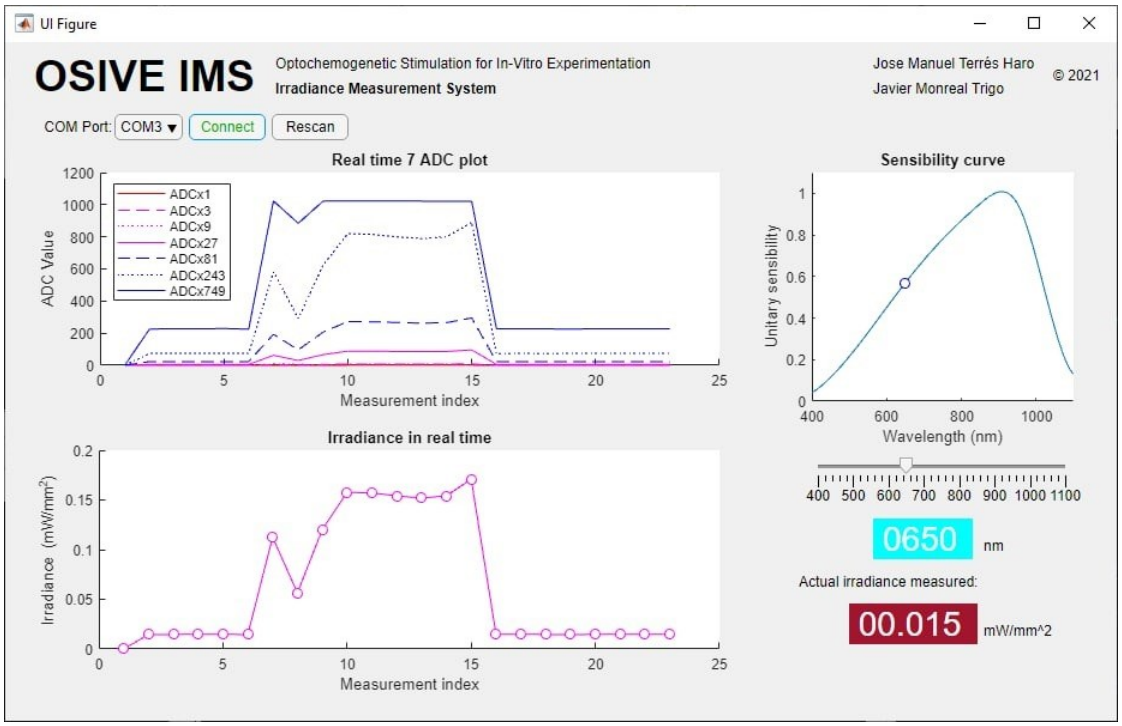

Figure 189. OSIVE IMS Graphic User Interface. Obtained with MATLAB 2018 © Mathworks.

The photoreceptor sensitivity is 0.6 A/W for $\lambda = 870$ nm. This wavelength offers the maximum sensitivity. The wavelength chosen by the user will set the unitary variable relative sensitivity, $s_r(\lambda)$. $s(\lambda)$ is obtained as the product of 0.6 A/W and $s_r(\lambda)$. The former **Equation 56** relates incident power, P, and photoreceptor area, A, to obtain irradiance, E. The conversion from the generated current I_{D1} and the power is given by the sensitivity $s(\lambda)$ (**Equation 55**). Finally, **Equation 54** relates the current-voltage converter (IVC) output with its input current. This output, after filtered, is connected to the `SCALE0` analog input. Hence, the irradiance, E, can be obtained from V_{SCALE0} (**Equation 59**).

$$E = \frac{P}{A} = \frac{I_{D1}/s(\lambda)}{A} = \frac{\frac{V_{SCALE0}}{R_{SHUNT}}/s(\lambda)}{A} \qquad \textbf{Equation 59}$$

The digitalized value of V_{SCALE0}, D_{SCALE0}, is received in the GUI. The digitalization is performed according to **Equation 60**. Each consecutive SCALE is the result of applying a gain-3 to its predecessor. The digitalization function applies to all of them.

$$D_{SCALE0} = \min\left(\frac{V_{SCALE0}}{5\ V} \cdot 2^{n_{BITS}}, 2^{n_{BITS}} - 1\right) \qquad \textbf{Equation 60}$$

The real-time measurement is displayed in two different graphs: on the top side, the 7 ADC digital values are plotted. For each value, upon reception, the ADC closest but under the 90% of the digital full-scale (1023) is chosen and converted to irradiance. The plot below shows the real-time evolution of the irradiance. The last value is shown in the red box textbox, in the south-east corner of the GUI. Both plots will display only the last two minutes.

As shown in **Figure 190**, after all the widgets initialization the GUI waits for the command to establish a COM connection. Once achieved, every input data frame is processed. All ADC digital values are plotted, and the highest not saturating is normalized, multiplied times its gain and the wavelength sensitivity, and plotted in the irradiance in real-time plot. A label is updated in real-time with the current value too.

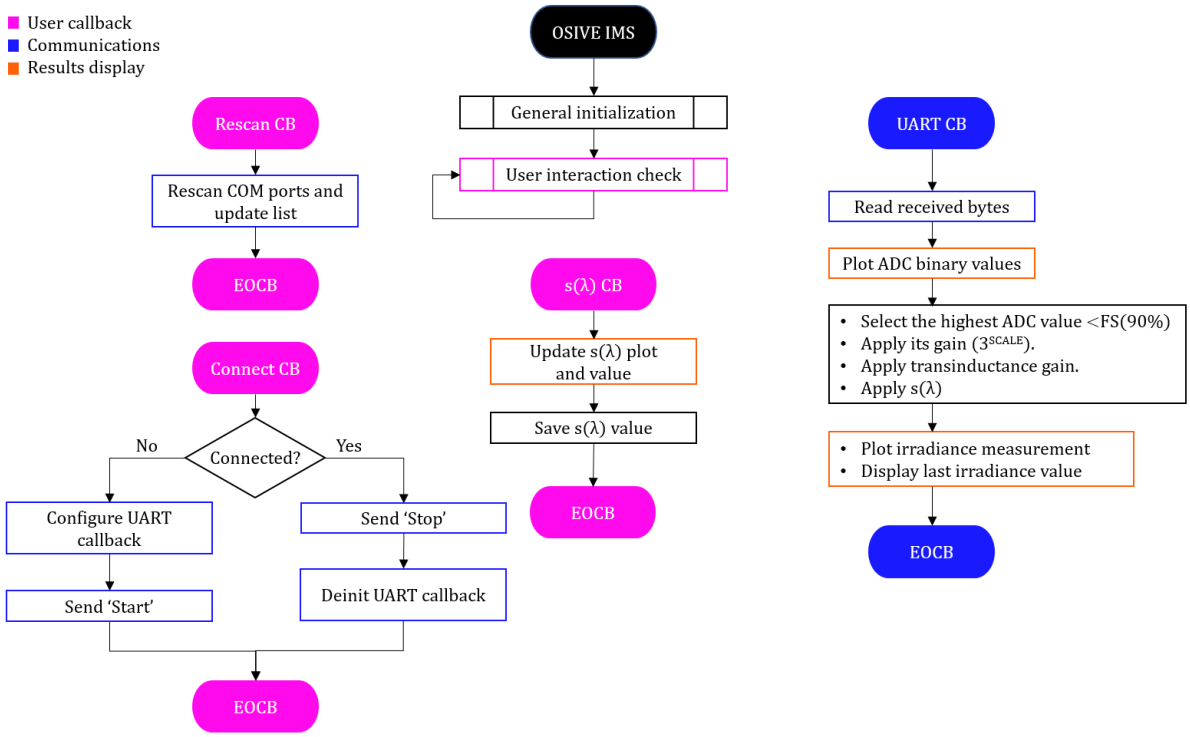

Figure 190. OSIVE IMS GUI simplified flowchart.

5.4. Final appearance

OSIVE IMS PCB is shown in **Figure 191**, with 73 mm x 46 mm dimensions.

The system has been designed to be placed either at the distance of a standard cell multi-well plate for stimulation equipment calibration or under the transparent multi-well plate matrix to give real-time feedback of the applied irradiance after the absorption measurement.

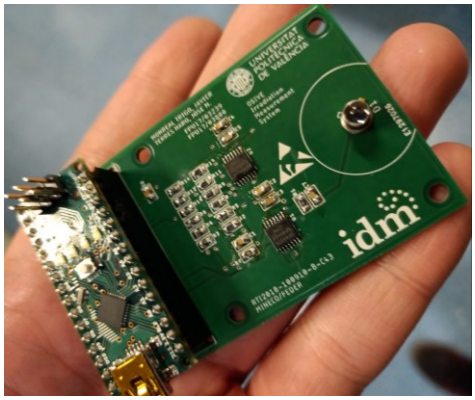

Figure 191. OSIVE Irradiation Measurement System device with no-enclosure.

OSIVE IMS has been designed for photoemitter calibration and real-time feedback. For these purposes two different structures have been developed (**Figure 192** and **Figure 193**).

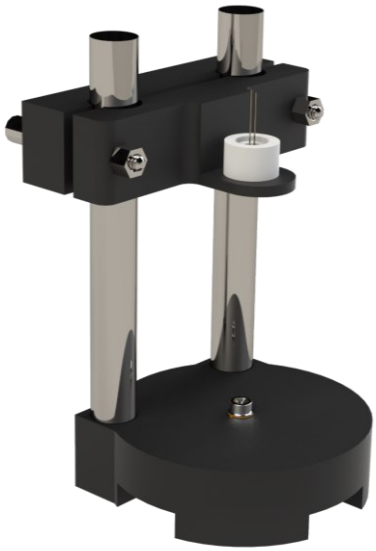

Figure 192. OSIVE IMS application structure for photoemitter calibration. Reproduced from [417].

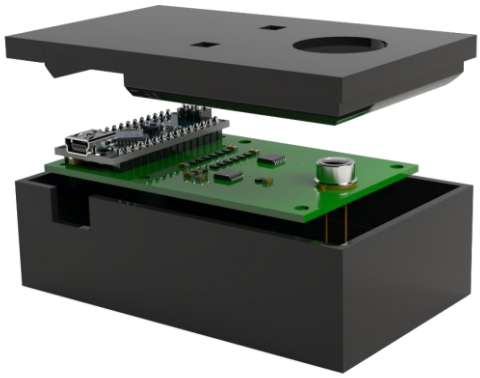

Figure 193. OSIVE IMS application structure for real-time feedback.

5.5. Reproduction guide

In the following virtual space can be found:

- Gerber files and bill of materials for ordering a OSIVE IMS PCB.
- Firmware files for flashing the Arduino Nano microcontroller board.
- STL parts to 3-D print the boxes.
- MATLAB software for the Graphic User Interface deployment.

Link to virtual space: https://github.com/JMonrealT/OSIVE-IMS. Share, build, and modify OSIVE IMS, registered under BY-NC-SA Creative Commons 4.0 License.

6. OSIVE Slim characterization

OSIVE IMS has been used for the OSIVE Slim full-scale calibration, as shown in **Figure 194**. A second-order polynomial fit reaches an R^2 of 0.9971.

Nevertheless, the PWM duty cycle range of 0-20% is used to trace a 0-30 mW/cm^2 operating range for the experimental application in which the bPAC opsin is targeted. This opsin has reported sensibility in the 0.2-2 mW/cm^2.

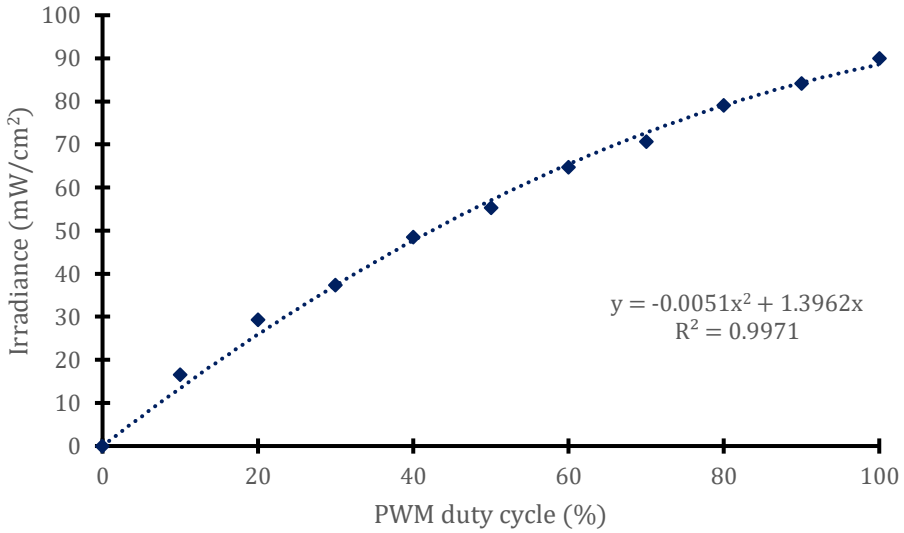

Figure 194. OSIVE Slim full-scale calibration plot.

7. OSIVE Slim experimental validation

The results of optogenetic stimulation are usually evaluated by immunofluorescence or flow cytometry. And the observation of transient responses after stimulation, as in cardiac electrophysiology studies, by optical microscopy. However, certain phenomena, such as the ultra-fast calcium waves acquisition upon simultaneous optogenetics, were beyond the scope of current instrumentation since they require higher image resolution in real-time, employing, for instance, time-lapse confocal microscopy.

Therefore, in this work, we developed OSIVE Slim: an optogenetic stimulation tool specifically designed to fit in a high-resolution fast-sampling-rate microscope. OSIVE Slim features 24 photoemitters, fitting a standard 24-well plate for *in vitro* cell culture. The instrument has been validated applying 100 ms pulsed blue light stimulation on engineered

neurons, measuring through an inverted confocal microscope the propagation of the induced calcium waves. This experimental validation is intended to serve as a proof of concept, opening the way to use the tool in the *in vitro* study of other opsins.

For the mentioned validation, a synthetic excitable cell model was generated by a genetic modification of primary rat cortical neurons to induce artificial expression of a bPAC able to respond to brief pulses of blue light. Previous reports using hippocampal neurons *in vitro* have shown that in response to saturating light pulses, bPACs induce large photocurrents sufficient to induce action potential firing neurons. bPAC-induced currents peaked in the order of hundreds of milliseconds (bPAC, one-half peak after 723 $\pm$ 101ms) (see Stierl *et al.* [431]). Then, bPAC increases intracellular cyclic adenosine monophosphate (cAMP) (see Oldani *et al.* [432]). In turn, the cAMP opens a cAMP-gated ion channel, whole-cell Ca^{2+} transients, and voltage changes [431]. This system then serves as a platform for calcium sensors evaluation upon optogenetics stimulation, monitoring the monolayer and adherent cortical neuronal cultures.

Primary cultures of cortical neurons were obtained from fetuses at 14.5 days of gestation (E14.5). Briefly, the brain cortex was mechanically triturated and, once homogeneous, filtered through a nylon net with 90 µm pores and centrifuged at 500 rcf for 5 min. Cell pellets were first seeded into DMEM high glucose supplemented with 10% fetal bovine serum (FBS) and 1% Penicilin/Streptomycin (P/S) (plating medium) into poly-L-lysine (PLL)-coated bottom-glass 24 well plates (Cellvis; Mountain View, CA; #P24-0-N). After 2 h of incubation at 37 °C, 5% CO2, the plating medium was replaced by Neurobasal medium supplemented with 1X B27 supplement (Gibco), 50 mM Glutamax (Gibco), and 1X P/S. Expression of bPAC protein in cortical neurons was achieved by viral infection using an AAV9 vector (pAAV-CamkII-bPac(WT)-mCherry-minWPRE) three days after plating at 10^5 transducing units/cell (Addgene #118278). The DNA construct delivered to the cells carries a codon-optimized gene encoding the blue-light-activated photo-stimulated adenylated cyclase (bPAC) to generate intracellular cAMP (see Bernal Sierra *et al.* [433]) fused to a red reporter (mCherry) under a neuronal promoter (CamkII). One week after the infection, the successful expression of bPAC was verified by observation of red fluorescence conferred by mCherry. Before the time-lapse recording, the cells were incubated with 3 µM Fluo-4 AM (Thermo Fisher) following the manufacturer's recommendations. For the calcium recordings, we have used a confocal microscope (Leica TSP-SP8) equipped with resonant scanning mirrors to allow the adequate imaging speed required for real-time recordings of calcium in living cells[24]. Moreover, our

[24] Link: https://www.microscopyu.com/techniques/confocal/resonant-scanning-in-laser-confocal-microscopy. Accessed: 2022-10-14

confocal system allows us to maintain adequate temperature and CO_2 levels for live imaging. During the recording, we acquired 1 image every 25 ms (40 frames/s) for 120 s. Forty seconds after the beginning of the recording, photostimulation was applied using the OSIVE Slim device with blue light (100 ms pulses at 470 nm every 10 s), which efficiently induced Ca^{2+} influx assayed using a Fluor4 probe. Next, we measured the timing of cAMP activity *in vitro*. After a light flash of 4 s, cAMP continued to rise in the dark with a time constant of 23 s.

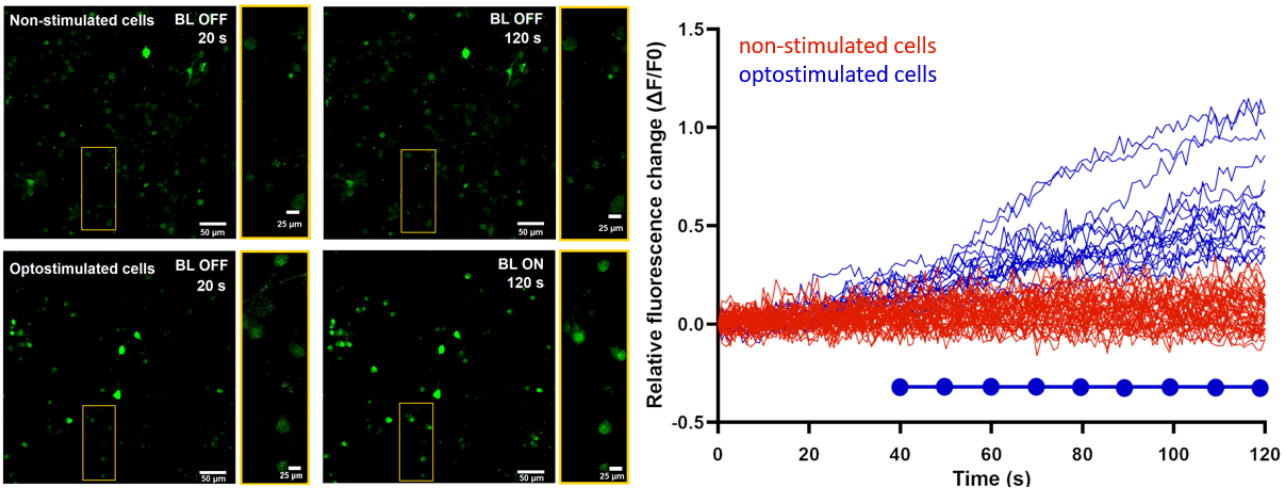

Figure 195. *Left panel:* Microscope time-lapse frames of primary rat fetal cortical neurons wild type (upper panel) or artificially modified to express the photostimulable protein bPAC (lower panel). The latter cells have been stimulated with 100 ms blue light (BL) pulses every 10 s starting after 40s of the beginning of the recording. Fluo-4 for calcium detection (green signal) was added to both conditions. Snapshot at 20 s (blue light off) and 120 s (blue light on) of the recording and higher magnification images of selected areas (yellow rectangles) are shown. Blue light stimulation in bPAC expressing cells resulted in increased calcium contain identify by the increased green fluorescence signal as highlighted in the yellow rectangle. *Right panel:* Graphical representation of the relative fluorescence signal quantified in individual cells from non-stimulated condition on wild type neurons (red) and stimulated condition on artificially modified neurons (blue) over the time of BL stimulation indicated with the blue dotted line. Reproduced from [412]. IEEE Transactions in Biomedical Circuits and Systems (CC 4.0 BY) 2023 IEEE.

Calcium dynamics are studied based on the increment of fluorescent given by Fluo-4 (green fluorescent probe for calcium). They are produced upon optogenetic stimulation. Simultaneously, image acquisition is performed, as shown in **Fig. 11**. Optostimulated cells consist of transduced cortical neurons expressing the optoactivable adenylate cyclase protein (bPAC) under the control of a neuronal promoter (CAMKKII). They were stimulated with 100 ms blue light on - 10 s blue light off pulses, at 0.2 mW/cm^2, starting after 40 s of the beginning of the recording (as indicated within the blue dotted line, **Fig. 11**). The non-stimulated group corresponds with not exposed wild cells. The increment in fluorescent can be appreciated in stimulated cells but not in non-stimulated indicating that the blue light stimulation induces calcium accumulation in the transfected cells.

8. Conclusions

We developed and validated the active optogenetic stimulation device OSIVE Slim. It has made optogenetic stimulation with real-time fluorescence measurement possible. The device, fully configurable regarding irradiance and temporal parameters, opens the door to studying optogenetically-induced transient phenomena flexibly and economically using a commercial inverted confocal microscope. In turn, optostimulation with other wavelengths is within reach by changing the photoemitter, following the comprehensive step-by-step procedure described.

An irradiance measurement device, OSIVE IMS, has been developed for application in the discipline of optogenetics. Its measurement ranges are extensive. The solution has been implemented using a dynamic gain selection. Therefore, this approach takes advantage of the need for a constant relative resolution to the full scale. The device has been successfully validated in calibrating low and high-irradiance optogenetic stimulation devices.

Chapter 5. Biosensors for multiple real-time measurement

The application of the different techniques for the modulation of nerve tissue regeneration has severe limitations without feedback to determine whether it is necessary to reduce, maintain, or increase the stimulus at each moment. For providing such feedback, the biosensors need to feature: high selectivity to operate in complex media, ultra-high sensitivity due to the ultra-low concentration of the analytes of interest, such as serotonin, and high temporal and spatial resolution. Such biosensors would offer effective sensing capabilities for pharmacological stimulation, electrostimulation, and optogenetic stimulation.

Our group has been developing the instrumentation for different biosensor technologies, such as electronic tongues, OECTs, impedimetric, and aptamer-FET biosensors. Among the previous, the development of biosensors based on aptamer-FET technology is the most promising and advanced approach to reach our purpose, for which we collaborate with Prof. Anne Andrews' group at the University of California, Los Angeles (UCLA).

In this last chapter, we will address the development of aptamer-FET biosensors instrumentation framed in the duration of the doctoral thesis. The content has been submitted to a Q1 journal (Monreal-Trigo *et al.*, Sensors & Actuators B: Chemical, Elsevier), and it has been published in four international congress participations (Monreal-Trigo *et al.* [434], Heidenreich *et al.* [435], Beltran-Morte *et al.* [436], and Benedicto Centeno *et al.* [437]). Furthermore, two Bachelor's Degree Final Projects in Electronic Engineering have also been developed in the research line (Beltrán Morte [438] and Benedicto Centeno [439]). Although finally outside the framework of this thesis dissertation, an international congress participation (Pacherres *et al.* [440]) and a Bachelor's Degree Final Project in Electronic Engineering (Pacherres Ancajima [441]) have been published in aptamer-impedimetric biosensors.

Aptamers coupled with field effect transistors (FETs) biosensors allow for sensitive, selective, label-free sensing of small molecules. Target molecules include neurotransmitters such as serotonin and dopamine. Measuring multiple targets (including neutral molecules, *e.g.*, peptide neuromodulators and non-electroactive species) will lead to a powerful biomedical tool. The goal is to measure biochemical flux in real-time in response to stimuli and behavioral responses.

The chapter starts with a review of the state of the art of electronic instrumentation, identifying the need to develop the specific instrumentation for the multiplexed measurement of aptamer-FET biosensors. The present work is the third iteration of this electronic design. The two previous versions are shown as the research line background. With the limitations and

learnings from the previous versions, the device specifications are set. A topology modification in the biosensor array is proposed. Then, the bioFET array and the new device MBMS designs are described. Finally, the experiments with pH variations and the preliminary neurotransmitter measurements are exposed as validation.

1. Instrumentation state of the art

Commercial galvanostats and silicon characterizers are high-quality professional instruments with high resolution and accuracy. They also display multiple scaling/gain options, making them the gold star for aptamer-FET biosensors research. Still, their disadvantages are their high cost and lack of portability, which hinder or impede their use in specific applications, including in-vivo measurements and the development of wearables. They present limitations in the sensor array measurement due to the small number of channels that can operate simultaneously, and they do not display any fast-switched multiplexing options. These platforms are highly flexible, which in turn leads to high complexity.

Furthermore, these instruments prioritize measurement resolution vs. sampling rate by software, which is also a limiting factor for advancing the development of biosensors at the forefront of science. By developing specific instrumentation, biosensor capabilities can be optimized. Movassaghi *et al.* [442] show a clear example of these capabilities: we developed a custom measurement platform for the application of fast-scan cyclic voltammetry (FSCV) and rapid pulse voltammetry (RPV). Using a 5 μm diameter PEDOT:Nafion carbon fiber working electrode, a detection limit of 6 pM was obtained for dopamine and serotonin analytes by the machine-learning combination of the outputs of these two techniques.

Advanced platforms, such as *MEDIC*, standout for their capabilities in measuring different target molecules by exchanging probes modularly for several hours with high sensitivity and specificity at the sub-minute temporal resolution (see Ferguson *et al.* [443]). MEDIC is based on cyclic voltammetry over gold electrodes with aptamers on circulating fluids. However, such an instrumentation approach is not feasible when non-invasive, spatial resolution, or sub-second temporal resolution is required. For non-invasive measurement, an aptamer-FET cortisol monitoring watch has been developed with a LOD of 1 pM (see Wang *et al.* [444]). Also, cortisol, as an electrochemically inactive biomolecule, is not detectable with FSCV-RPV, which is another advantage of aptamer-FET technologies. The possibilities of effective area reduction, selectivity, and signal readout from miniaturized electronics make aptamer-FET biosensors the leading solution for versatility in in-vivo measurement, given the advances in bioFETs miniaturization (see Suryaganesh *et al.* [445]). In state of the art, from Andrews' group, the 50

μm width *Neuroprobe* stands out: an aptamer-FET biosensor with two channels detecting from fM to μM serotonin concentrations, with a 10-second temporal resolution with the instrumentation platform used (see Zhao *et al.* [446]). The biomolecule quantitative analysis based on bioFETs presents high sensitivity and fast response. Still, portability, simple operation, commercial availability, and reliability are challenges faced by bioFETs development (see Wadhera *et al.* [269]).

The multiplexed measurement of multiple sensors is useful to interrogate different analytes simultaneously or increase the measurement system reliability by the presence of replicates. Physically, it is usually performed by placing multiple transistors as multiple channels of the same biosensor, such as in the *Neuroprobe* beforementioned, displaying two channels. Multiplexing, understood as the term used in the medical field to obtain different information from the same sensor can read the different channels sequentially or simultaneously. Increasing the switch-and-sample rate over the biochemical dynamics makes a third option available. The pseudo-simultaneity of the measurement is obtained by the sequential reading of the channels at a sampling rate considerably higher (2-10 times) than the sensor response. Nevertheless, liquid-insulated gate transistors, such as these bioFET technologies, present high capacitances. This is an approach with a complex implementation because of these capacitances' low-pass-filter effect and capacitive coupling crosstalk between channels.

Liu *et al.* [447] show the multiplexed monitoring of dopamine and serotonin using aptamer-FET technology using a Keysight B1500A semiconductor parameter analyzer. The outstanding results of 10 fM LOD are only limited by the <1 Hz temporal resolution and the application of the same voltage sweep to all the bioFETs to minimize the influence of the electrical crosstalk. Overcoming this limitation in a miniaturized instrument would allow the availability of high-performance biosensor technology, allowing the use of a wide range of highly selective aptamers available in state of the art. Another example of a multiplexed system can be found in the monitoring of catecholamine neurotransmitters (CA-NTs) dopamine, noradrenaline, and adrenalin, performed using an OECT array with 30 nM LOD and 50 ms sample rate on a biosensor of 1 mm x 200 μm x 15 mm (see Xie *et al.* [448]). Nevertheless, the biosensor response takes $\sim$1 minute. No crosstalk is reported, given that they apply a constant voltage to every channel, avoiding capacitive coupling. As we will address in the following section, we hypothesize that applying sweeping voltages to the biosensor may enhance its temporal capabilities.

Devices with a high spatial and temporal resolution and high channel density have been recently developed for the *in vivo* recording of neuronal electrophysiological signals through potentiometry (see Shobe *et al.* [449]) and neurophotonics (see Moreaux *et al.* [450] and Choi

et al. [451]). These outstanding works set the benchmarks for the final integration of the new generation of biosensors that aim not only to interrogate the electrical dimension of the biological circuits, but its biochemical spheres, as the aptamer-FET biosensors.

Therefore, **we aim to develop a multiplexed measurement device** capable of **independently applying voltage sweeps** to several aptamer-FETs biosensors. Given the temporal dynamics of the neuronal biochemical responses, applying these sweeps at **10 Hz frequency** is required. As we will further address, V_{GS} sweeps may **enhance the biosensor resolution** and **accelerate the aptamer-biomolecule dissociation**, increasing the temporal response vs. decreases in the target molecule concentration. However, in this research line, we face the challenge of the electrolyte-gated FET **high capacitances**. This electrical characteristic **menace signal integrity with instability, low-pass filter effects, and crosstalk**. The custom hardware to be developed aims to be portable, down scalable, and cost-effective.

2. Research line background

Professor Anne Andrews' group at UCLA has been identifying with Milan Stojanović's group at Columbia University several new aptamers for biomolecules, specifically neurochemicals. Aptamers for serotonin and dopamine (monoamines), glucose (sugar), S-1P (lipid) (see Nakatsuka *et al.* [278]), phenylalanine (amino acid) (see Cheung *et al.* [452]), and cortisol (steroid) (see Wang *et al.* [444]), show the binding capabilities to different kind of biomolecules that the aptamer technology displays. The Columbia partners further isolated aptamers for norepinephrine, epinephrine, acetylcholine, glutamate, GABA, and dynorphin. This summarized list glows the enormous potential of this technology.

The aptamers with the highest affinity (*i.e.,* selectivity and sensitivity) also present a high *dissociation constant*, K_D. We addressed this concept in subsection *6.3. Aptamers and aptamer-FET biosensors* of the *Introduction*: the dissociation constant is the ratio between the dissociation rate (the time it takes to reach a 63% solution of the aptamer-molecule complex after a concentration decrease) and the association rate (the time it takes to reach a 63% aptamer-molecule complex formation for a concentration increase). K_D units are M^{-1}.

Andrews' research group measures the aptamer-FET K_D values via fluorescence-based displacement assays. For dopamine and serotonin, K_D is on the order of nM, whereas for aptamers of phenylalanine, K_D is on the order of µM. As commented, K_D is an indicator of relative target dissociation vs. association speeds, and these aptamer-FET featured LODs as low as fM. A higher K_D aptamer-FET presents poorer temporal resolution using standard IT measurements, *i.e.,* the biosensor control by constant voltages and measuring I_{DS} over time, as

seen in *6.4. Calibrated response of aptamer-FET biosensors* of the *Introduction*. High-affinity (low K_D) aptamers dissociate slower, resulting in a trade-off between selectivity-sensibility and temporal resolution for the aptamer-FET biosensors.

The objective is to create techniques for electrically enhance the temporal resolution of aptamer-FET sensors. Our collaborators in UCLA speculate that the direct application of an electric field will assist in inducing the dissociation state of an aptamer-target complex based on prior research on DNA assembled on surfaces. Briefly, the application of positive voltages vs. its potential of zero charge (pzc) has demonstrated to compensate the negative charge density of ssDNA molecules, facilitating hybridization with complementary strands, as shown by Wong & Melosh [279,453], Ho *et al.* [454], and Tymoczko *et al.* [455]. Negative voltages were used to cause dissociation or melting, thus displaying the opposite effect. The increment in the application of negative potentials can also induce the desorption of ssDNA or dsDNA from the surface, as shown by Cabeca *et al.* [456], Rant *et al.* [457], and Kelley *et al.* [458]. Further electrical stimuli have shown a relevant impact on the association constant and the target-aptamer bond formation and rupture processes, as shown by Fixe *et al.* [459,460], Cabeca *et al.* [456], Vernick *et al.* [461]. The use of fluorescence techniques has enabled to monitor the reaction progression and the hybridization and melting efficiencies, as shown by Fixe *et al.* [459], Cabeca *et al.* [456], Wong & Melosh [453], and Ho *et al.* [454]. The same mechanisms have also been reported using field-effect sensors, as displayed by Vernick *et al.* [461], Souteyrand *et al.* [462], Fritz *et al.* [463], and Kim *et al.* [464].

This suggests that gate voltage can control target dissociation to surface-bound single-stranded DNA, so aptamer-FET gate voltage modulation would improve target detection and increase temporal resolution when using high-affinity aptamers. Following this approach, the aptamer-FET sensor response is monitored in terms of the source-drain current (I_{DS}) as the result of applying a drain-source bias voltage (V_{DS}) and sweeping the gate voltage (V_{GS}) relative to the source. In principle, target binding induces a conformational change of the aptamer on the semiconductor, which also reorients the negatively charged backbone. Hence, the aptamer-FET sensor response is the result of changes in transconductance caused by the movement of negative charges closer or further away to the semiconductor surface.

The purpose of developing custom hardware and software is to investigate gate voltage sweeps systematically to determine the effects of gate-voltage parameters (*e.g.*, sweep rates, voltage ranges, step sizes, hold times) on aptamer-FET signals associated with target recognition and with respect to time.

In 2016, the first perfboard prototype of this custom hardware was developed by Prof. Miguel Alcañiz during his research stay at Anne Andrews' group. Nevertheless, the main efforts

were focused on developing the RPV-FSCV platform, results recently published by Movassaghi *et al.* [442].

In 2018, when Javier Monreal was starting his thesis, UCLA student Rahul Iyer joined Andrew's lab and led the efforts to design and develop a PCB prototype, taking up the baton of the work started by Prof. Alcañiz. For this purpose, Prof. Alcañiz and Mr. Monreal assisted and supervised the hardware design. The first prototype was based on an Arduino UNO microcontroller board, using its onboard ADCs and external SPI DACs, aiming for the multiplexed measurement of up to three bioFETs simultaneously. This first PCB prototype displayed poor noise performance. In the absence of means to identify the problem, it was blamed on possible capacitive couplings in the analog signals coming from the SPI digital communications. A second version, based on an Arduino Due microcontroller board, was developed then. It replaced the external SPI DACs with the Arduino Due ones. Nevertheless, the noise performance was insufficient.

In 2020, students Flor Boydens, Vicent Beltran, and Jakob Sabbe, mentored by Prof. Alcañiz and Mr. Monreal, developed in the Universitat Politècnica de València an 8-switched drain, common-gate, independent-source multiplexed system for the measurement of functionalized OECTs and FETs. This work is shown in V. Beltran's BEng Final Project [438]. The first successful results are shown in the XIV IWOSMOR International Congress [436].

The measurement system is based on Atmel's ATSAMD11D14A microcontroller, commanding 12-bit Maxim Integrated's MAX5725BAUP+ DAC through SPI and analog multiplexers through its GPIO. Texas Instruments' TMUX111PWR was employed for current-scale selection, and Analog Devices' ADG708CRUZ for FET drains multiplexing. A general diagram is shown in **Figure 196**.

A basic GUI was implemented in MATLAB's AppDesigner, and an initial electrical validation was performed using through-hole resistors in between source and drain terminals for each FET, with values adequate to test the different current scales ($\pm$200 nA, $\pm$500 nA, $\pm$1 µA, $\pm$10 µA). The GUI and its noise performance for each current scale is shown in **Figure 197**.

Regarding the PCB design, it is isolated from the grid through a battery supply (727.0388 6V1.2Ah RS Pro) and the USB communications with the PC are isolated through Mikroe-2674[25]. A PCB photography with each component labeled is shown in **Figure 198**.

[25] More information at: https://www.mikroe.com/usb-uart-2-click

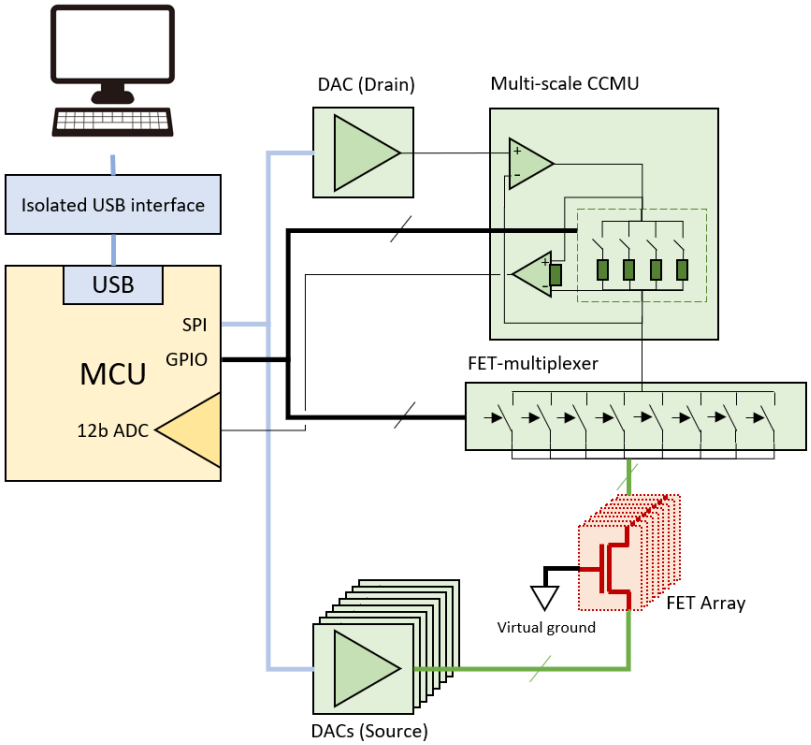

Figure 196. Block diagram of the 8-switched-channels measuring system, based on a multi-scale compensated current measurement unit (CCMU), a FET multiplexer, and SPI digital-to-analog converters (DAC), controlled via a microcontroller unit (MCU) with an embedded analog-to-digital converter (ADC). Data is sent over USB through an isolated interface to a PC in real-time.

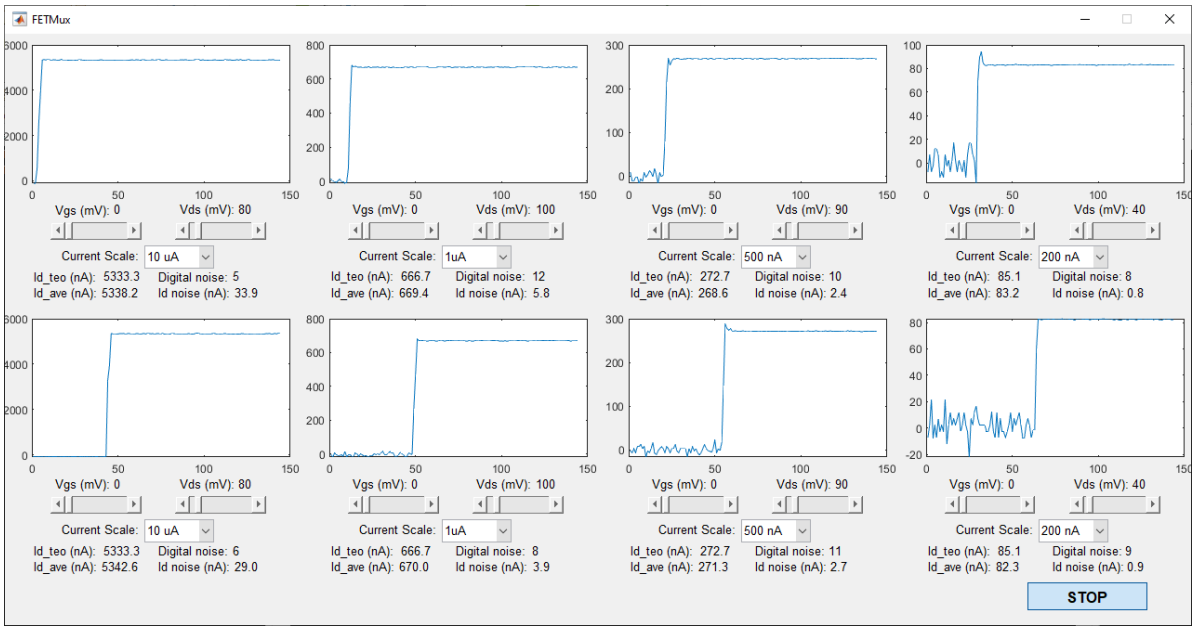

Figure 197. 8-switched channels measurement system basic GUI showing first electrical validation with 1% tolerance resistors. Noise performance is measured for the last 100 samples in samples (12 bit ADC) and I (nA). The theoretically expected and average measured values are also displayed.

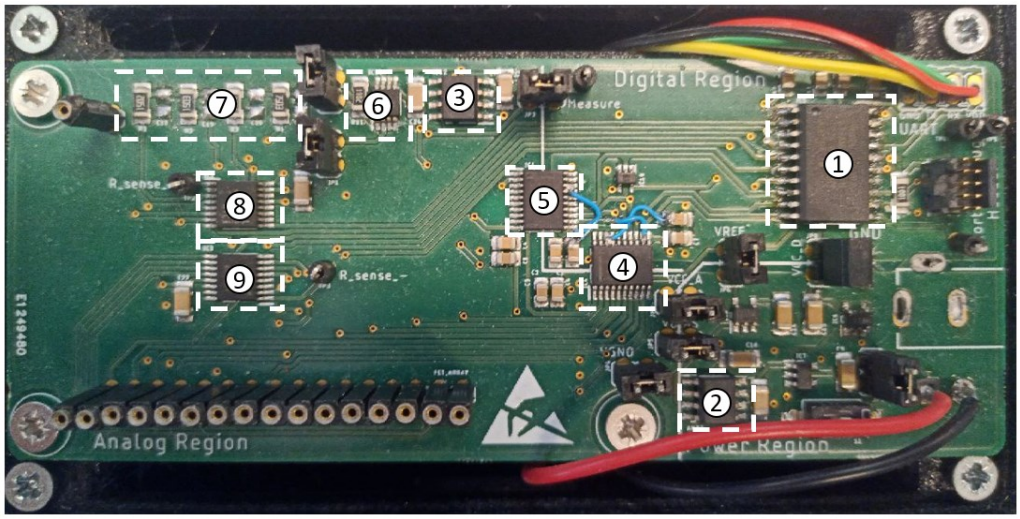

Figure 198. Photograph of the PCB of the 8-switched-channels measuring system. The components are (1) MCU, (2) virtual-ground generator, (3) drain-bias controller, (4) sources digital-to-analog converters, (5) drain digital-to-analog converter, (6) instrumentation amplifier, (7) shunt resistors, (8) current-scale multiplexer, and (9) transistor multiplexer.

Our first successful results in the measurement with this technology and custom hardware correspond to the measurement of serotonin with this platform. Both, in IT (**Figure 199**) and IV (**Figure 200**) modes.

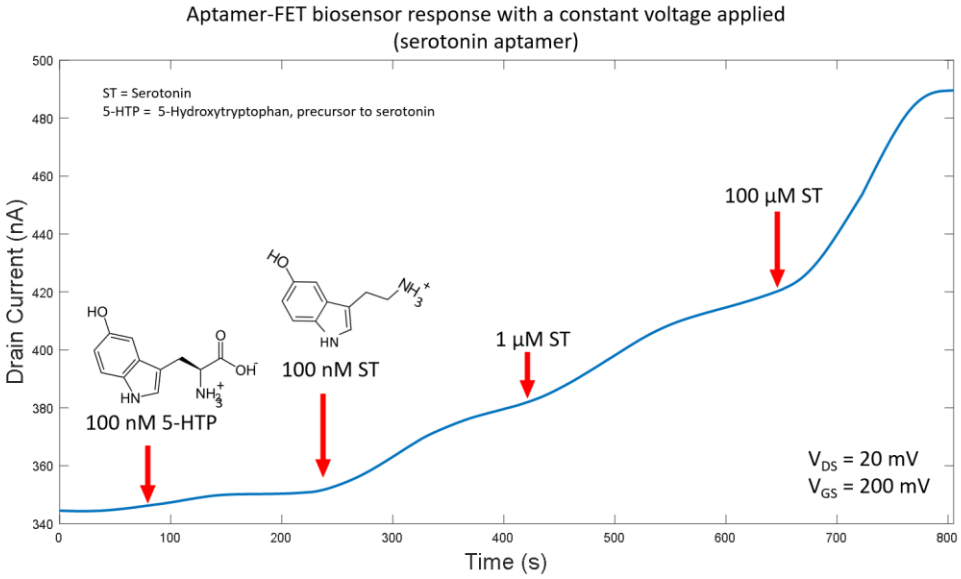

Figure 199. IT measurements with 5-HTP and serotonin injections. Reproduced from [436].

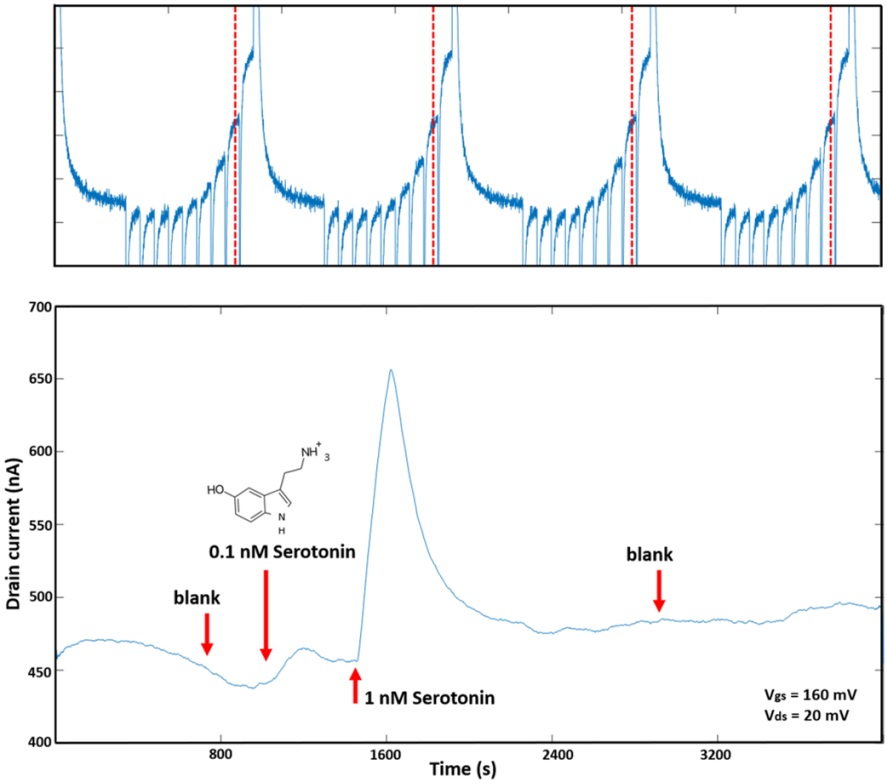

Figure 200. IV mode serotonin concentration biosensor response. **Top:** Current response to gate-voltage sweep, the vertical red dashed line indicates the point taken each period. **Bottom:** One-point per IV-cycle drain current plot over time, with the aCSF and serotonin injections indicated. Reproduced from [436].

For both validations, artificial cerebrospinal fluid (aCSF) (1x) is used as buffer/blank, and different concentrations of 5-Hydroxytryptophan (5-HTP), and serotonin (ST) are used as interferent and target molecules, respectively.

The IT experiment was performed keeping constant values for V_{DS} and V_{GS} of 20 and 200 mV. A point is acquired every 2 ms. For the IV experiment, a V_{GS} sweep was performed from 0 to 180 mV in 20 mV steps every 250 ms. At each cycle's end, V_{GS} was held at 0 mV for 1 s. The total period time is 3.25 s. The evolution of the signal is shown for $V_{GS} = 160$mV, showing one point per sweep cycle. In both cases, a 100-sample moving average digital filter is applied.

Both experiments show the specificity of the system, designed to react primarily in front of serotonin, whereas the similar molecule 5-HTP induces an almost negligible current response. Comparing the sensitivity obtained with each mode, a few tens of nA are obtained due to 100 nM ST in IT mode, whereas the same magnitude order is obtained for 0.1 nM ST in IV mode. Also, while in IT mode, there is no decrease in current over time, in IV mode, the sensor response is a wave with a higher offset than the initial one. We hypothesize it is an indication that it is possible to induce dissociation of the target molecule with the aptamer by applying

electric fields, allowing to decrease the effective k_{off} time constant and potentially improving the temporal resolution of this sensor technology.

Nevertheless, these results correspond to the measurement of one single bioFET. The multiplexed measurement increased the counter-peaks shown in the IV results (**Figure 200**, **Top**) and crosstalk that completely masked the signal of interest.

In order to isolate and study the counter-peaks found in the multiplexed mode, we propose developing a new system without switching for the application of the voltage on the drain of the bioFETs, so that they are constantly and simultaneously polarized. Two features must also be improved in this new version: the V_{DS} application and the I_{DS} measurement resolution.

3. Device specifications

The new Multiplexed BioFET Measurement System (MBMS) emanates from the shortcomings of its predecessor:

- The high I_{DS} offset due to the V_{DS} biasing even at V_{GS}=0 mV makes the system to operate in the $\pm$1 or $\pm$10 μA scales, which current resolution is 0.5 and 5 nA, respectively. The increase in the ADC resolution can address the needed increase in the I_{DS} resolution.
- V_{DS} was generated through two DACs, applying V_D and V_S to each bioFET. Both needed to change simultaneously during a voltage sweep to keep V_{DS} constant. This produced two problems that need to be solved:
    - V_D and V_S could apply values in discrete steps of 0.73 mV, calculated according to the settings. The 1-bit change in the V_D-V_S produced artifacts as significant I_{DS} variations.
    - While V_{GS} typical range is [0, 1] V, the V_{DS} one is [0, 30] mV. This voltage generation forces both to have the same resolution, while V_{DS} could be better tunned with an increase in its resolution.
- The crosstalk and counter-peak effects should be studied without the drain-switching multiplexing. MBMS shall be capable of applying V_D and V_S to all bioFETs simultaneously and disconnecting V_D in real time to simulate the behavior of its predecessor.

With the first experiences of measuring in IV mode, and in order to be able to measure biological processes occurring within one second, the IV sweep frequency must be at least 10

Hz. This would allow capturing phenomena with transitory times of ~200 ms. Therefore, in 100 ms all voltage steps must be applied, acquiring the respective I_{DS} current points.

Hence, MBMS technical requirements are listed as follows:

- 16-bit ADCs, for x16 resolution in I_{DS} measurement (0.3 nA @ ±10 µA scale).
- V_{DS} x10 resolution, from 0.73 mV to ~7 µV in the ±150 mV range.
- Simultaneously apply V_{DS} and V_{GS} independently, and acquire I_{DS} in all channels.
- Capabilities to behave like its predecessor switching V_D.
- Increase in the temporal resolution for measuring 4-channels to 200 µs, leading to 500 acquired points in IV-sweep mode at 10 Hz.

A general diagram of the system is shown in **Figure 201**, from the biosensor to its real-time response representation.

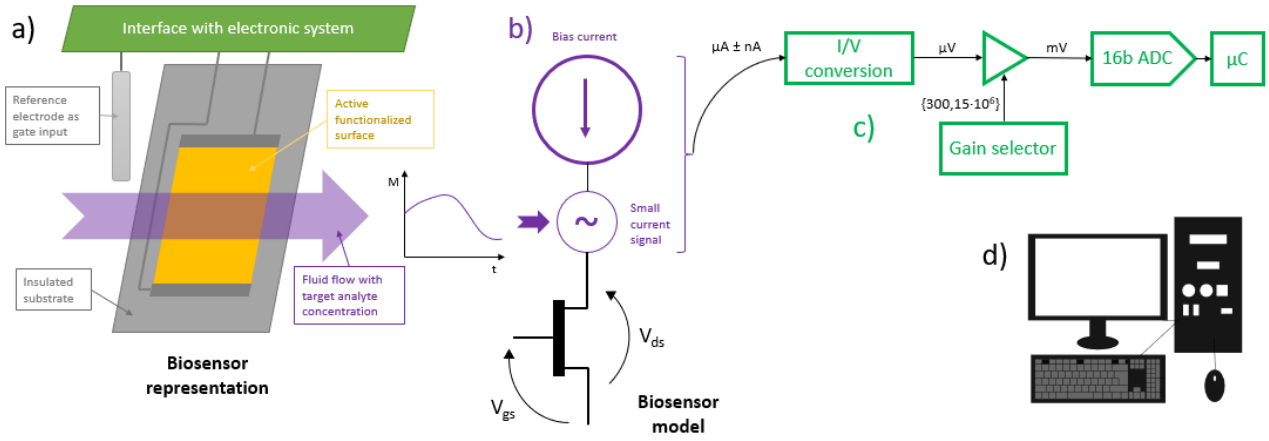

Figure 201. General diagram: from the biosensor (a) to the PC data acquisition (d) in two stages: signal generation (b) and electronic instrumentation (c). In the PC side, a necessary data analysis is performed. Reproduced from [434].

As usability requirements, developing a real-time instrumentation control GUI with all the necessary features required in the research praxis is necessary. Additionally, the obtention of the calibrated response (CR) through post-processing should be incorporated into the system's software tools. Finally, these CR post-processed results should lead to a model building employed in real scenarios.

Therefore, the MBMS instrumentation concept, including its software tools, is represented in **Figure 202**. It would consist of three differentiated parts:

- The measurement system, including the biosensor array and the instrumentation.

- The model exploitation software allowing for the real-time control of the instrumentation with the concentration measurement display.
- The model exploitation software allowing for the real-time control of the instrumentation with the concentration measurement display.

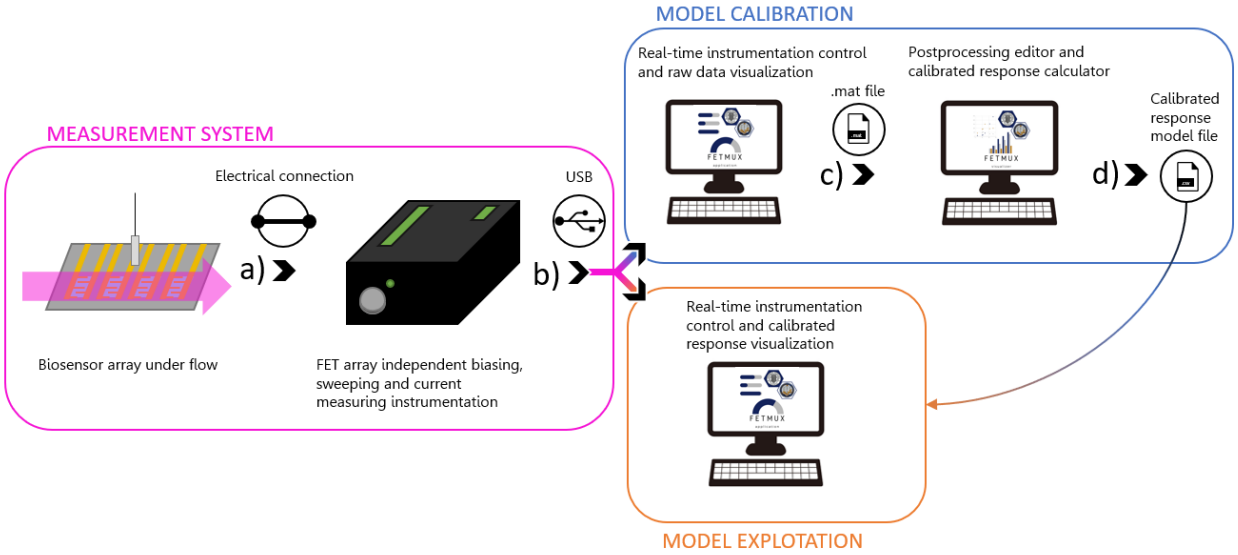

Figure 202. General system diagram, representing from left to right: a) The biosensor is electrically connected to the instrumentation. b) The latter is controlled in real-time by a custom application running on a PC. c) Data is stored in a file; a specific application is used to obtain the calibrated response model that d) can be used for the following measurements.

4. Simultaneous measurement with spatial proximity

In applications where miniaturization of the biosensor or spatial resolution is required, inter-channel interference is the main threat to signal integrity over a simultaneous or pseudo-simultaneous multiplexed measurement. Apart from the multiple biomolecules quantization in real-time, these limitations are also well-represented in the pH measurement technologies, in which bioFETs compete with optical and electrochemical biosensors (see Vivaldi *et al.* [465]). BioFETs presented a significant development in their sensitivity, linearity, and miniaturization for pH measurement. However, the current standard topology allows having only one sensor measuring simultaneously per solution, as shows the advances in state of the art (*e.g.*, Parizi *et al.* [466], Das *et al.* [467], Cho *et al.* [468], Kang *et al.* [469]). The common biasing of the transistors of the different channels is a solution to this problem. Still, it severely limits the flexibility needed to optimize the transconductance response of each channel with its required voltages. Another possible solution is the sequenced measurement of each channel at the

expense of temporal resolution. Our solution, based on common-gate virtual-ground topology, overcomes these limitations, allowing the simultaneous multiplexed measurement of several channels in a miniaturized bioFET array.

4.1. Common-source topology limitations

The In_2O_3 bioFETs used in this work are N-type (NFET) transistors: trans-impedance decreases with the increase of the gate voltage versus the source (V_{GS}) over a specific drain voltage versus the source (V_{DS}). The FET's gate is accessible through a reference electrode (RE) in the solution, *i.e.*, it is an electrolyte gated FET, as shown in **Figure 203**; therefore, over an array of this kind of biosensors, there is just one single electrical point for gating all the NFETs, as shown in **Figure 204**.

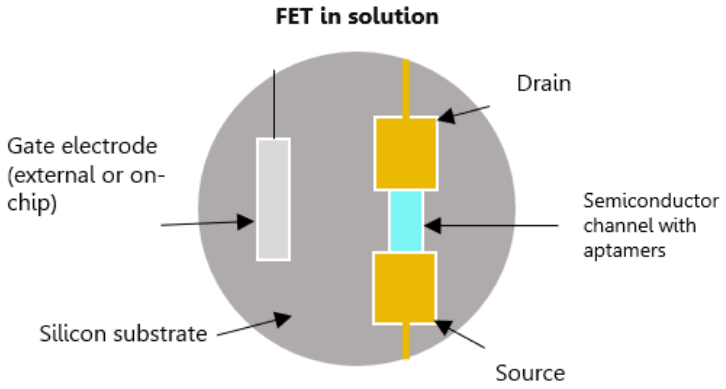

Figure 203. Representation of single aptamer-FET biosensor over the substrate in solution.

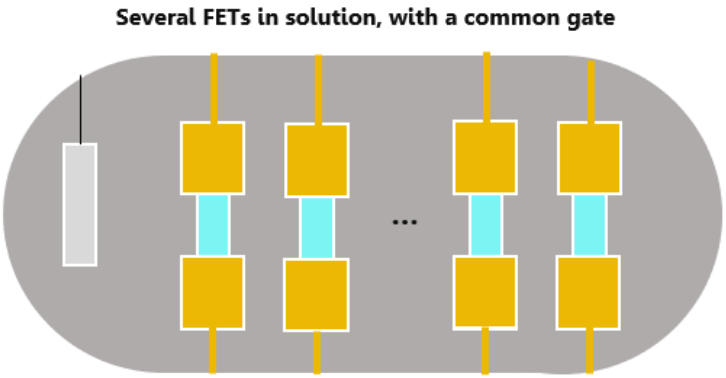

Figure 204. Representation of an array of bioFETs using a common gate electrode in the solution.

To command the NFET array multiplexing simultaneously, this situation makes unfeasible the usual topology for controlling an NFET array: the common-source to ground configuration,

as shown in **Figure 205**. Hence, it is impossible to simultaneously apply different V_{GS} to each of the NFETs in this topology. This topology limits the read-out to a sequenced operation of each FET, which is a significant constraint in terms of temporal performance.

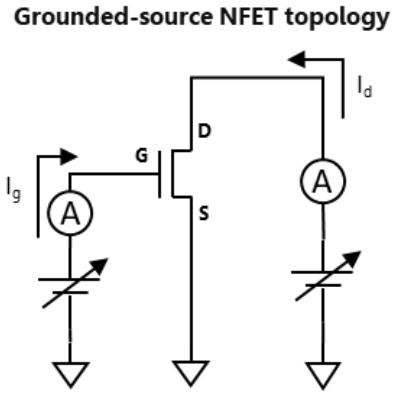

Figure 205. Typical grounded-source transistor topology, only suitable for single channel or sequential applications.

4.2. Common-gate topology proposal

In this design, a common-gate topology is proposed, shown in **Figure 206**. The RE voltage (gate voltage) is connected to a virtual ground (VGND) with a constant tension of half the unipolar supply voltage of the system. As in the former topology, two variable voltage sources are needed for each FET, and a current measurement unit. V_{GS} and V_{DS} are obtained straightforwardly as $V_{GS} = V_{VGND} - V_S$ and $V_{DS} = V_D - V_S$, being V_D and V_S voltage sources. Still, it is important to note that V_{DS} is no longer independent of V_{GS} as in the common-source topology. A change in the latter shall be followed by an immediate change in the former by a dynamic modification of the V_D voltage generator to keep V_{DS} constant. The shorter this response, the smaller the transient time until a steady response.

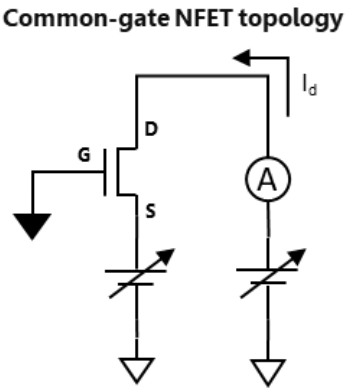

Figure 206. Proposed topology for the independent gate-voltage applicate in bioFET arrays

5. BioFET array design

The semiconducting material utilized at the sensing interface of field-effect transistors (FETs) is crucial for device sensitivity, stability, and reproducibility. High field-effect mobilities and large current on-off ratios of thin films of metal oxides, such as In_2O_3 (see Kim *et al.* [470]), InGaZnO (see Kim *et al.* [471] and Park *et al.* [472]), or ZnO, make of them suitable for biological applications while being inexpensive to fabricate. Andrews' group at UCLA chose thin-film indium oxide for bioFETs: thin-films of indium oxide are fabricated using sol-gel techniques, which are more easily transferable to other labs than high-pressure and temperature chemical-vapor deposition. Because of the improved electron transport, thin-film sensitivity (3–4 nm) of indium oxide is increased. It also exhibits less parasitic capacitance and is stable under physiological conditions (see Chen *et al.* [473]). These films can be applied to numerous rigid or flexible surfaces (as shown by Kim *et al.* [470], see Liu *et al.* [474], and Nakatsuka *et al.* [278]). In_2O_3 can therefore be utilized for wearable and implanted sensor platforms (see Liu *et al.* [474] and Rim *et al.* [475]). In this thesis dissertation, we employ thin-film indium oxide as the signal transduction component in field-effect transistors to quantify pH changes and small molecule targets, such as neurotransmitters (as already shown in the works of Cheung *et al.* [452], and Nakatsuka *et al.* [278], and Wang *et al.* [476]).

Regarding its electrical characteristics, channel capacitance C_{CH} is proportional to the width of the channel W (*i.e.*, the drain and source overlapping distance on the channel) and inversely proportional to its length L (*i.e.*, the distance between drain and source), as reported by Schöning & Poghossian [477]. The electrolyte gated FETs have a third dimension over the distance between the reference electrode (RE) and the channel. Hence, the considered capacitance is volumetric and depends on the RE-channel distance, as reported by Friedlein *et al.* [478]. The gate capacitance C_G is proportional to the area ratio A_G/A_{CH}, where A_G is the area of the gate electrode and A_{CH} is the channel area. The impedance between the gate electrode and the channel is a series connection of C_G, $C_{CH,}$ and the resistance between the reference electrode and channel through the electrolyte (see Nissa *et al.* [479]). Therefore, $A_G \geq A_{CH}$ allows a $C_G \approx C_{CH}$, maximizing the resulting capacitance C_R. A high capacitive load is a big concern for the stability of the electronic design (see Lundberg [480]). Consequently, C_R is maximized according to $C_R \alpha (A_G, W, L^{-1}, A_{CH}^{-1})$ to test the stability of the proposed topology.

To fabricate FET biosensors without needing photolithography, we employed a dual shadow mask approach on heavily doped silicon wafers (University Wafer, Boston, MA). First, In_2O_3 rectangles (3.3 mm x 2.1 mm) were deposited via RF sputtering (Denton Discovery 550 sputtering system) to serve as the semiconducting channel material. The thickness was set at 16 nm by controlling the sputtering time. This thickness was determined to be the minimum thickness at which devices yielded consistent performance while maintaining high sensitivity

to ionic (pH) changes (see Aroonyadet *et al.* [481]). The In_2O_3 rectangles were spaced 6.6 mm apart. Our previous experiments showed that a physical discontinuity in the In_2O_3 layer is necessary to prevent crosstalk in simultaneous monitoring. Then, source and drain electrodes were patterned using a second shadow mask and depositing a 10 nm Ti adhesion layer followed by 50 nm Au via electron-beam evaporation (CHA Solution electron beam). The result is shown in **Figure 207**, with L = 45 µm, W = 6.5 mm, A_{CH} = 0.3 mm². An Ag/AgCl reference electrode ⌀ 2 mm with 1 mm immersion (A_G≈9.5 mm²) was used as the gate for all FET measurements by inserting it into the flow channel.

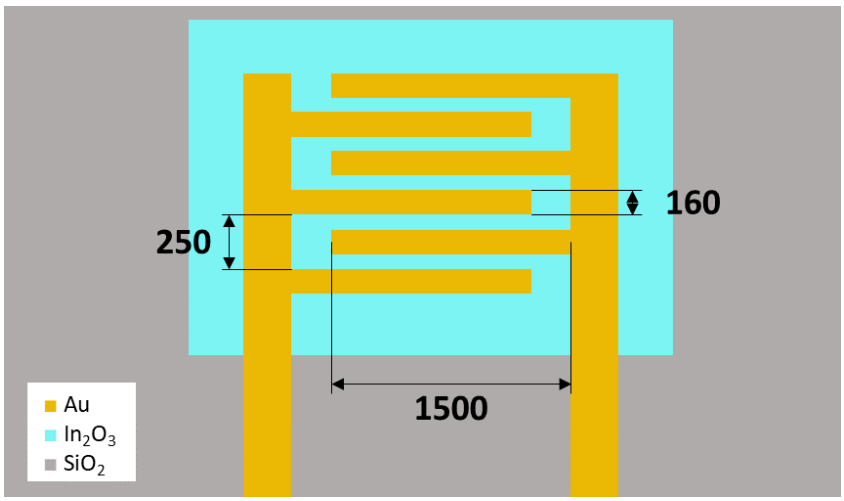

Figure 207. Source and drain geometry over In_2O_3 channel geometry. Units in µm. Channel effective length L = 45 µm. Channel effective width W = 6.5 mm. Channel effective area A_{CH} = 0.3 mm².

6. MBMS: multiple bio-FET measurement system

In the Multiplexed Bio-FET Measurement System (MBMS) presented in this work, the instrumentation has been designed to allow the simultaneous multiplexing of four channels in a common-gate topology. A general block diagram is shown in **Figure 208**. the MBMS displays four multi-scale compensated current measurement units (CCMU), one for each channel.

For each multi-scale CCMU, the current measurement resolution is increased by 4 bits using an external 16-bit ADC controlled through an SPI interface. Additionally, the switched multiplexing operation can be mimicked through the null option in the current scale selector, opening all channels of the analog multiplexer.

As known, the V_{DS} voltage has a direct influence on the I_{DS}. In the common-source topology, it is considered to remain steady during a V_{GS} sweep. In the common-gate topology

proposed in this work, the V_{DS} value, a difference between the V_D and V_S voltage sources, has been implemented through the CCMU negative-feedback subcircuit beforementioned.

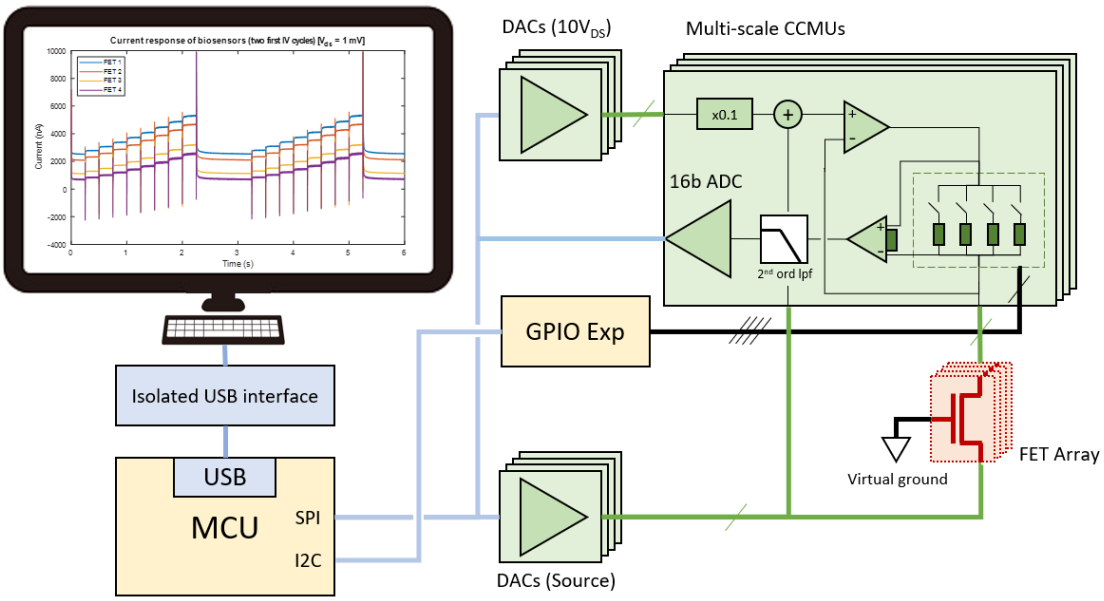

Figure 208. Block diagram of the FET-based multiplexed biosensor measuring system (MBMS), based on 4 multi-scale compensated current measurement units (CCMUs), with SPI digital-to-analog converters (DACs) and analog-to-digital converters (ADCs), controlled via a microcontroller unit (MCU). Data is sent over USB through an integrated isolated interface to a PC in real-time.

The CCMU obtains the V_D to be applied as an analog function of the applied V_S and the setpoint V_{DS} (two DAC outputs). This way I_{DS} recovery transitory time is minimized. The V_{DS} typical values are 1-10 mV, and the V_{GS} typical values range from 0 to 300 mV. Therefore, the V_{DS} setpoint from its DAC is set with 10 times gain and amplified with a 0.1 gain before the adder. This results in an increased V_{DS} resolution and thus reduces V_{DS} variations between V_{GS} steps.

This section will address MBMS hardware design, firmware implementation, and the application code for real-time control and data analysis. Then, an electrical validation comparing its measurement capabilities with a commercial silicon characterizer is displayed. Finally, the appearance of the device is shown.

6.1. Hardware design

Regarding the hardware design, we will first address the instrument's main ICs: MCU, GPIO expander, DACs, and ADCs. Then, we will describe the design of the multi-scale CCMU.

Other general concerns about supply and communications will be mentioned. Finally, we will comment the PCB design.

The complete schematics of MBMS can be found in the *Annexes:*

- *Annex 14. MBMS Schematic (1/8)*
- *Annex 15. MBMS Schematic (2/8)*
- *Annex 16. MBMS Schematic (3/8)*
- *Annex 17. MBMS Schematic (4/8)*
- *Annex 18. MBMS Schematic (5/8)*
- *Annex 19. MBMS Schematic (6/8)*
- *Annex 20. MBMS Schematic (7/8)*
- *Annex 21. MBMS Schematic (8/8)*

About the development tools used, the PCB is designed using Autodesk's EAGLE 8.2. Analog circuitry simulations have been performed using LabCenter's Proteus 8.1, and analog filter design has been performed with the assistance of Texas Instrument's Filter Design Tool[26].

6.1.1. Microcontroller unit

MBMS microcontroller unit (MCU) is inherited from its predecessor: Atmel's (now Microchip's) ATSAMD11D14A microcontroller. It is based on the 32-bit ARM Cortex-M0+ processor and has 256KB of flash memory, 32KB of SRAM. It operates at a maximum frequency of 48 MHz and has a low power sleep mode, making it suitable for low-power applications.

It incorporates embedded DAC and ADC modules, but they are not of interest to our application. It is worth it mentioning its USB 2.0 full-speed device and embedded host and serial communication interfaces, including I2C, SPI, and USART, that will be deployed in this project.

Another criterion why this microcontroller was chosen is the extensive, accessible, and comprehensive documentation for which the manufacturer is well-known.

The MCU programmer and pinout are shown in **Figure 209**. SWD clock is pulled up to the supply, and two decoupling capacitors (100 nF, 4.7 µF) are placed close to the supply pin VDD following the manufacturer's layout recommendations. Programming testpoints (TP) for

[26] TI's Filter Design Tool: https://www.ti.com/design-resources/design-tools-simulation/filter-designer.html (Accessed: 15th January 2023).

SWCLK, SWDIO, and $\overline{\text{RST}}$ of the programming and debugging digital protocol SWD are set, and a general testpoint (TP18) for development purposes.

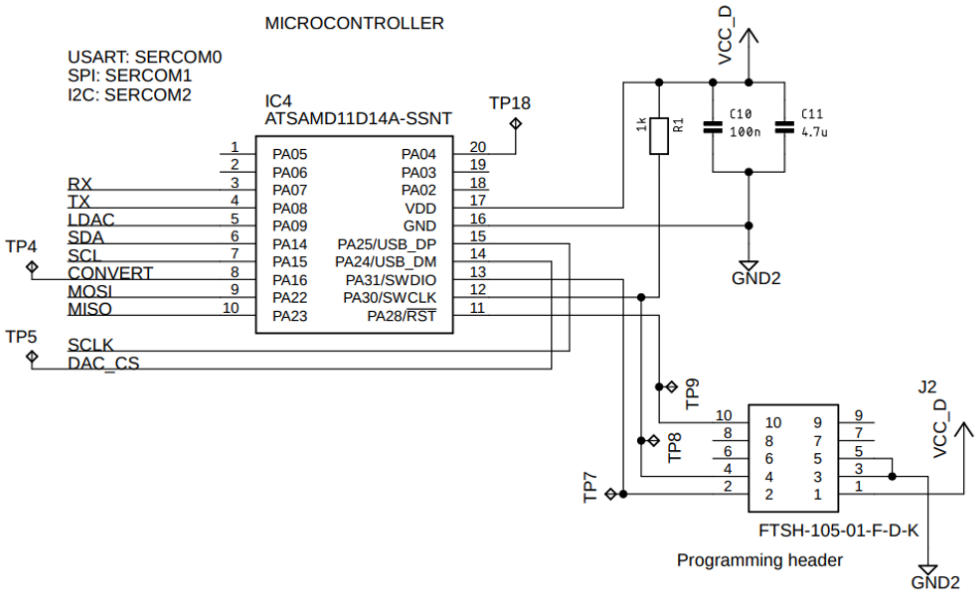

Figure 209. MCU pinout and programmer at MBMS.

The functionality assigned to each MCU pin is as follows:

- PA07 and PA08 (IC pins 3 and 4) are employed as RX and TX pins of the UART communication with the PC, which will be further addressed in *6.1.7. Serial communications with PC*.
- PA14 and PA15 (IC pins 6 and 7) are used as SDA and SCL for the I2C communications with the GPIO Expander.
- PA22, PA23, and PA25 (IC pins 9, 10, and 15) are used as MOSI, MISO, and SCLK for the SPI communications with the ADCs and DACs.
- SPI needs additional lines to select the chip to which the master is addressing. These lines are called *chip select* (CS). PA24 (IC pin 14) is used for DAC CS, with the signal `DAC_CS`. Additionally, PA09 (IC pin 5) is used for the DAC control line `LDAC`. PA16 (IC pin 8) is used for ADC CS, with the signal `CONVERT`. Both will be further addressed in their subsections *6.1.3. SPI-controlled DACs* and *6.1.4. SPI-controlled ADCs*. Both `DAC_CS` and `CONVERT` signals have testpoints, TP5 and TP4, respectively.
- Finally, PA28, PA30, and PA31 (IC pins 11, 12, and 13) are used for $\overline{\text{RST}}$, SWCLK, and SWDIO, of the SWD protocol for programming the internal flash memory of the microcontroller (flashing) and enabling debugging the code execution.

6.1.2. GPIO expander

I2C-controlled 16-pin Microchip's MCP23017 was chosen to control the scale selection on the multi-scale CCMUs. The communication order's payload from the MCU consists of two commands: the 8-bit address to modify MCP23017 register A or B and the 8-bit data values for such register. Every address and values data package is ended with STOP and NACK bits. This makes a total communication transfer of 36 bits.

MCP20317 can work in Standard Mode (Sm, 100 kbps), Fast Mode (Fm, 400 kbps), or Fast Mode Plus (Fm+, 1.7 Mbps). The general digital supply is established at 3.3 V, allowing the operation at Sm and Fm. All scales in every multi-scale CCMU can be modified with Fm in less than 100 µs. It could be reduced to less than 25 µs with the GPIO expander supply to 5 V.

MCP23017 pins address CCMU analog multiplexers for current scale selection, as shown in **Figure 210**:

- SCL and SDA I2C control signals to IC pins 12 and 13, with 4k7 pull-up resistors.
- CCMU 1 control signals `M1_1` to `M1_4` connected to GPB0-3, IC pins 1-4.
- CCMU 2 control signals `M2_1` to `M2_4` connected to GPB4-7, IC pins 5-8.
- CCMU 3 control signals `M3_1` to `M3_4` connected to GPA0-3, IC pins 21-24.
- CCMU 4 control signals `M4_1` to `M4_4` connected to GPA4-7, IC pins 25-28.

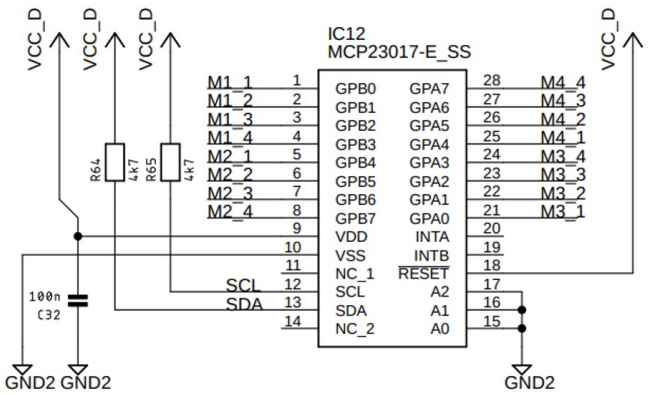

Figure 210. GPIO expander pinout.

6.1.3. SPI-controlled DACs

Maxim Integrated's (now Analog Devices Integrated's) MAX5725BAUP+ SPI-controlled 8-channels 12-bit DACs IC is used for the application. Its pinout and functional components are shown in **Figure 211**.

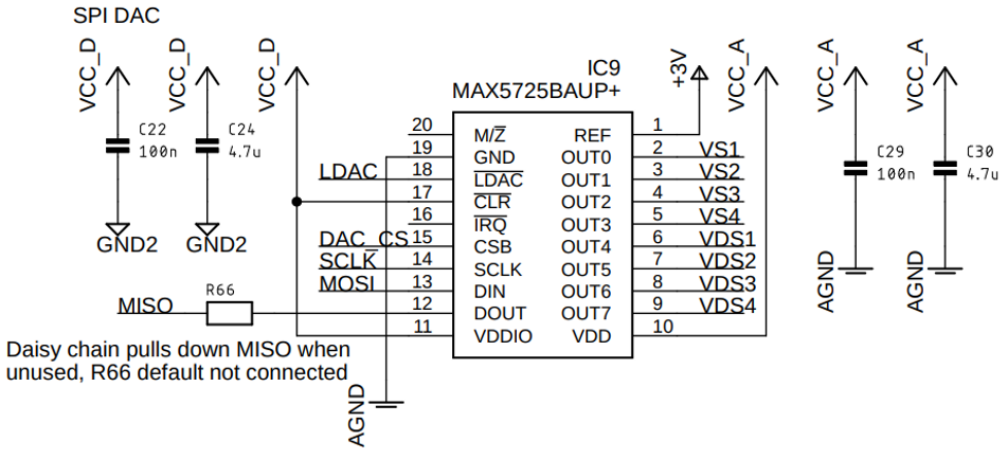

Figure 211. 8-channel DAC IC SPI-controlled pinout.

As a digital/analog interface, the IC uses 3.3 V digital and analog voltage supplies (VCC_D and VCC_A) and a +3V analog reference. They are addressed in *6.1.6. Supply considerations*.

100 nF and 4.7 µF capacitors are used in analog and digital supplies for decoupling purposes. Given the condition of the MISO occupation by the ADC daisy chain, R66 will be left unconnected in the final application. However, it is placed to enable the MAX5725 register checkout by the MCU during the firmware development.

- IC pins 12 to 14 are connected to MISO, MOSI, and SCLK SPI signals.
- IC pin 15, chip select (CSB) is connected to signal DAC_CS.
- IC pin 18 is connected to signal LDAC.
    - Its HIGH value latches the last value of all DAC channels.
    - Its LOW value enables the transfer of the CODE register to the OUT.
- IC pins 2 to 9, corresponding to the DAC OUT 0 to 7, are connected:
    - OUT 0 to 3 to VS of CCMUs 1 to 4.
    - OUT 4 to 7 to the setpoint 10·VDS of CCMUs 1 to 4.

To configure a DAC channel, it is needed to send a LOADn command composed of 3 bytes. The configuration of a total of 8 channels adds up to 192 bits at 2 Mbps SPI communications, performed in 96 µs.

6.1.4. SPI-controlled ADCs

A 16-bit digital-to-analog converter (ADC) with an SPI interface is used to digitalize the IDS current readout of each channel. The IC employed is the AD7988-5 from Analog Devices Integrated.

It offers up to 500 kSps, and for the present application, it will be set up to work at 125 kSps, close to the 100 kSps at which, according to the datasheet, offers a SINAD of 97 dB, and a THD of 100 dB. Increasing the sampling frequency diminishes the quality parameters of the acquisition at an accelerated pace.

Each ADC will digitalize the instrumentation amplifier (IA) output of each CCMU, which will be addressed in the following subsection *6.1.5. Multi-scale compensated current measurement units (CCMU)*. All four ADCs are connected in a daisy-chain configuration. Instead of following the typical SPI configuration for each ADC, its digital input (SDI) is connected to the general MOSI shared line, and its digital output (SDO) is connected to the MISO shared line. In the daisy chain, the SDO of the 1st slave device (SD) is connected to the SDI of the 2nd SD, which in turn will have connected its SDO to the SDI of the 3rd SD, and so on. The last SD's SDO is connected to the MISO line. This is shown in **Figure 212** for our ADCs.

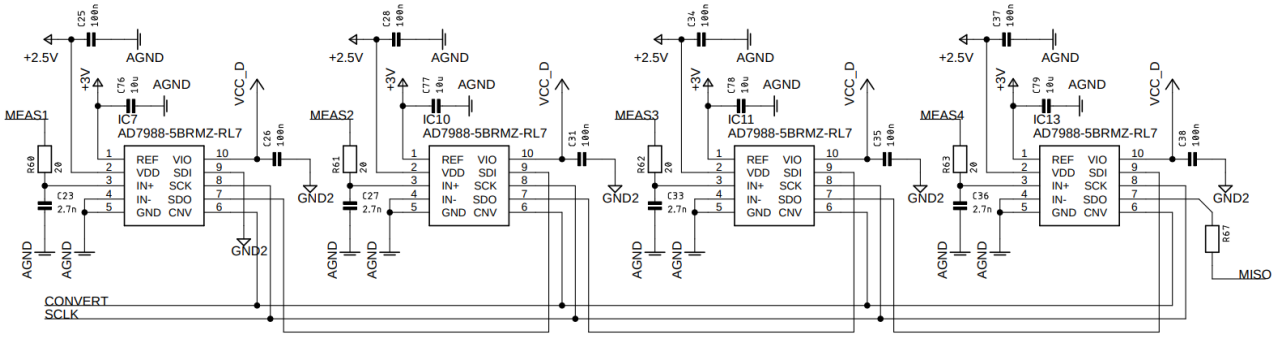

Figure 212. Four SPI-controlled ADCs AD7988-5 connected in daisy-chain configuration.

Being the 1st, 2nd, 3rd, and 4th SD ADCs IC7, IC10, IC11 and IC13, they follow the SDI-SDO-MISO connection scheme mentioned before. To work in a daisy-chain configuration, the SDI of the 1st SD must be connected to the ground. The `CONVERT` signal, with positive logic, triggers the start of the conversion. Then, 16 SCLK pulses are needed to perform the conversion, and 64 additional ones to shift register the acquired 16-bit values to the MISO line and the MCU. At a 2 MHz SPI clock, it takes 40 µs. During acquisition and while the ADC is not sending a result, it pulls its SDO to the ground. This makes the MISO line to be permanently occupied by the daisy-chain. R67 is normally short-circuited, but it has been introduced to be able to read the DAC outputs by opening this connection and short-circuiting temporally R66.

Each ADC is supplied with a +2.5 V required for the digitalization, a +3 V analog reference, and the general-purpose digital voltage VCC_D at +3.3 V. Each supply input has the decoupling capacitor recommended by the manufacturer close by. Additionally, the recommended RC input filter, with $f_c \approx 3$ MHz, is deployed at the IN+ pin of each ADC.

6.1.5. Multi-scale compensated current measurement units (CCMU)

The multi-scale compensated current measurement unit (CCMU) without the V_D obtention subcircuit for channel 1 is shown in **Figure 213**. This circuit is replicated for every channel.

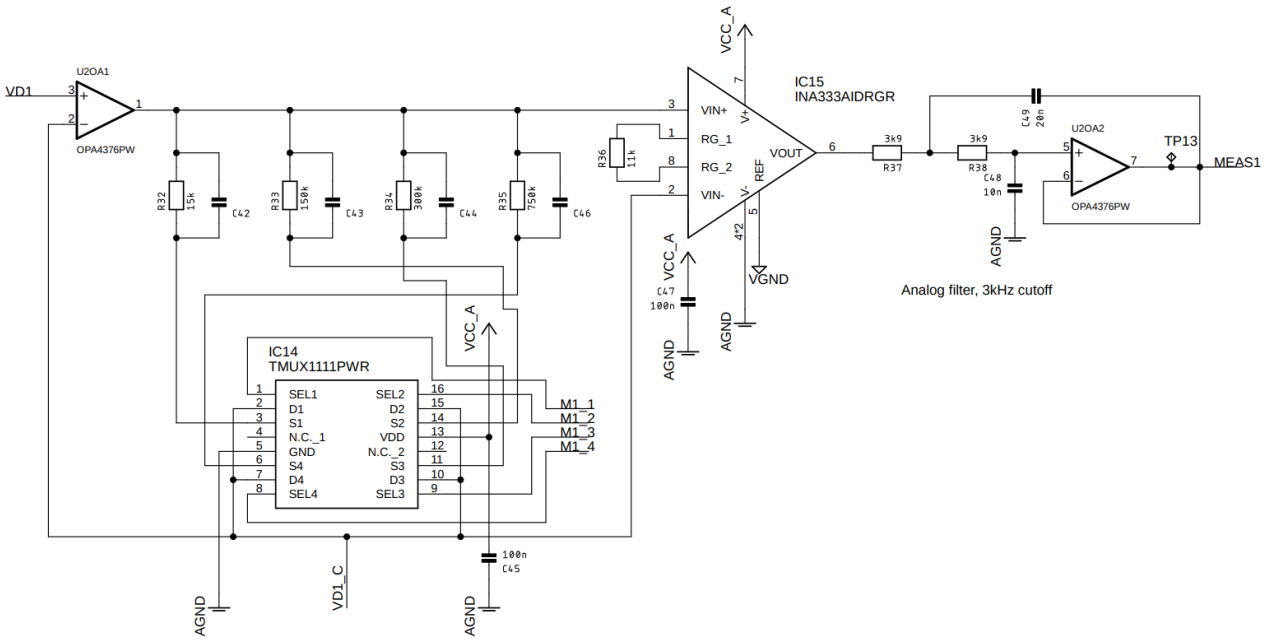

Figure 213. Multi-scale CCMU schematic without V_D obtention circuit for channel 1.

For channel 1, VD1_C point is connected to the drain of bioFET 1. Current measurement is performed using a shunt resistor (R32 to R35 in **Figure 213**) as negative feedback (the electrical connection of its output to its inverting input, V-) on an operational amplifier, the U2OA1 in **Figure 213**. The setpoint for V_D for the bioFET 1 is applied to its non-inverting input (V+). In non-saturation conditions, the output of U2OA1 will be such to meet the condition V+ = V-. The shunt resistors are designed to produce, in steady conditions, a maximum over-voltage (V_{out} from the U2OA1 vs. VD1_C) of 150 mV, governed by **Equation 61**. The operating range of the analog system will be [0.2, 2.8] V, avoiding close-to-rail situations with poorer linearity.

$$V_{out} = I_{DS} \cdot R_{SHUNT} + V_{DS} + V_S = I_{DS} \cdot R_{SHUNT} + V_D$$ **Equation 61**

The overvoltage produced by the I_D over the shunt resistor ($I_{DS} \cdot R_{SHUNT} = V_{out} - V_D$) is measured by an instrumentation amplifier (IA) INA333 (Texas Instruments) with 10 gain (G). It is a micro-power (50 µA), low-offset voltage (25 µV), low drift, low noise, and low input bias current (200 pA) IA. It offers 35 kHz BW and 100 dB CMRR at G=10. The gain is set through R36, namely R_G, following **Equation 62**.

$$G = 1 + \left(\frac{100\ k\Omega}{R_G}\right)$$ **Equation 62**

Shunt resistor selection is made in real-time by the microcontroller through a GPIO expander, commanding a TMUX1111 (Texas Instruments) analog multiplexer per channel. The scales available are ±200 nA, ±500 nA, ±1 µA, ±10 µA. This makes a resolution (R) for each scale of 6 pA, 15 pA, 30 pA, and 300 pA, following **Equation 63**, where r_{FS} is the full-scale range (*e.g.,* 20 µA for the ±10 µA scale), and n the number of bits of the ADC.

$$R = \frac{r_{FS}}{2^n}$$ **Equation 63**

Finally, IA's output is filtered with a 2nd order Butterworth response analog filter, with a 3 kHz cut-off, before the ADC.

Figure 214 shows the subcircuit for the obtention of the before-mentioned VD setpoint from two voltage sources from the DAC outputs: VDS, a $10 \cdot V_{DS}$ setpoint, and VS, the voltage applied to the source of the bioFET.

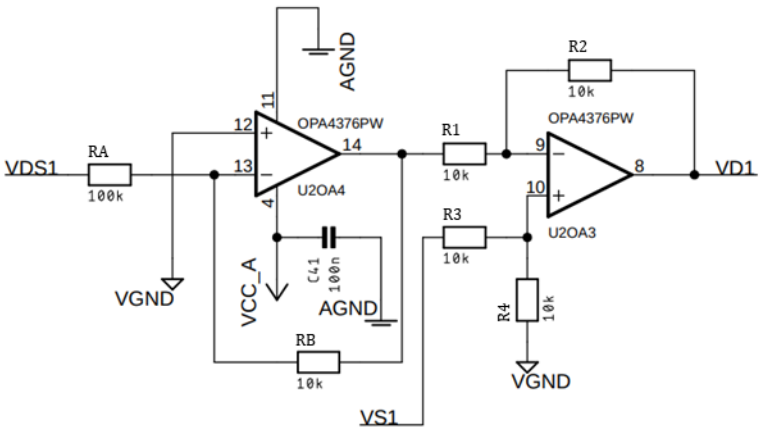

Figure 214. VD setpoint obtention subcircuit from VDS setpoint ($10 \cdot V_{DS}$) and the voltage applied to the source of the bio-FET (VS) for channel 1.

The first stage of the circuit, composed of OA U2OA4 is an inverting amplifier. The gain at the output of this stage follows **Equation 64**.

$$G_{STAGE\ 1} = -\frac{RB}{RA} \qquad \textbf{Equation 64}$$

This produced due to the negative-feedback condition, in which the output of the OA will reach stability when V+ = V-. Given the high-impedance condition of the OA inputs, $I_{RB} = I_{RA}$, which in turn, renaming VDS1 as V_{in}, can be expressed applying Ohm's law as:

$$\frac{V_{out} - V_{VGND}}{RB} = \frac{V_{VGND} - V_{in}}{RA} \longrightarrow \frac{V_{out}}{-V_{in}} = -G_{STAGE\ 1} = \frac{RB}{RA} \qquad \textbf{Equation 65}$$

The 2nd stage is in subtractor configuration. Its transfer function is shown in **Equation 66**. When all the resistors share the same value and given that V_{OUT} of STAGE 1 is $-V_{DS}$, V_D is obtained by adding V_{DS} to V_S.

$$V_D = \left(\frac{R1 + R2}{R3 + R4}\right)\frac{R4}{R1}V_S - \frac{R2}{R1}V_{OUT_{STAGE\ 1}} = V_S + V_{DS} \qquad \textbf{Equation 66}$$

The negative-feedback condition through R2, and in non-saturation conditions, V+ is $R4/(R3+R4)\cdot V_S$ The stability condition will be reached when V+ = V-, then $I_{R2} = I_{R1}$, and can be expressed as:

$$\frac{V_D - V_+}{R2} = \frac{V_+ - V_1}{R1} \longrightarrow V_D = \frac{R2}{R1}(V_+ - V_1) + V_+ = \\ = \left(1 + \frac{R2}{R1}\right)\left(\frac{R4}{R3 + R4}\right)V_S - \frac{R2}{R1}V_1 \qquad \textbf{Equation 67}$$

Where V_{OUT} of STAGE 1 is named V_1, and the output of the STAGE 2 OA, V_D.

6.1.6. Supply considerations

The noise performance of the system is critical since trans-impedance variations of the biosensors can reflect variations in the drain current (I_D) in the order of <1nA.

Therefore, the MBMS is supplied by a 6.2V battery, obtaining the 5V for the isolated communications with the PC through NCP730 LDO (OnSemi) and 3.6V for the general supply of the system from an LDO MIC5219 (Microchip). The former and the charger connector, battery connector, and panel button placers are shown in **Figure 215**.

PJ-102A will connect the input supply to the battery, disconnecting the system when the charger is plugged in. This way, the user is not allowed to use the MBMS permanently connected

to the grid, which would lead to decreased performance. Only when the charger is unplugged, there is enough battery charge, and the panel button is switched on, will the LDOs generate adequate voltages for the system's operation. For each of them, the manufacturer-recommended bypass capacitors are set.

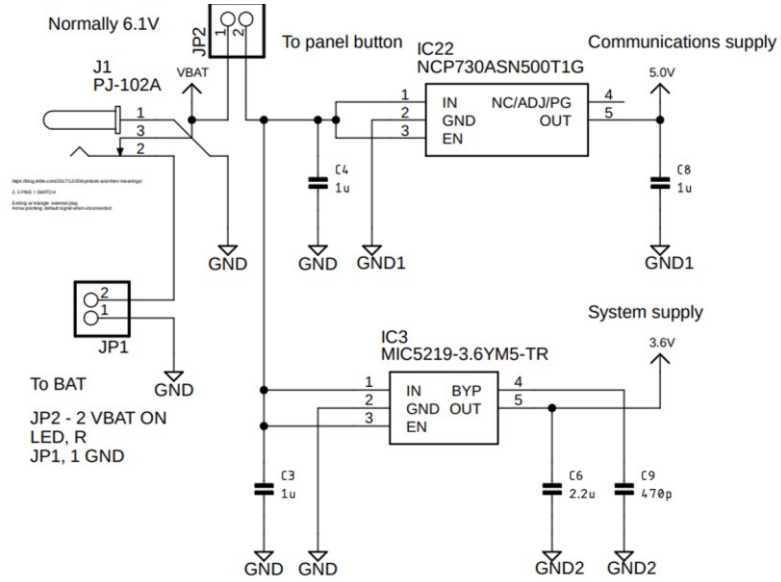

Figure 215. Charger connector PJ-102A, panel on/off button and battery connector circuit, with the first stage LDOs.

Digital and analog 3.3V supplies are obtained from LD39015M LDOs (ST) from the former 3.6V supply, as shown in **Figure 216**. From now on, the relevant signals will include testpoints (TP) to ease the measurement of such variables through external instrumentation during development.

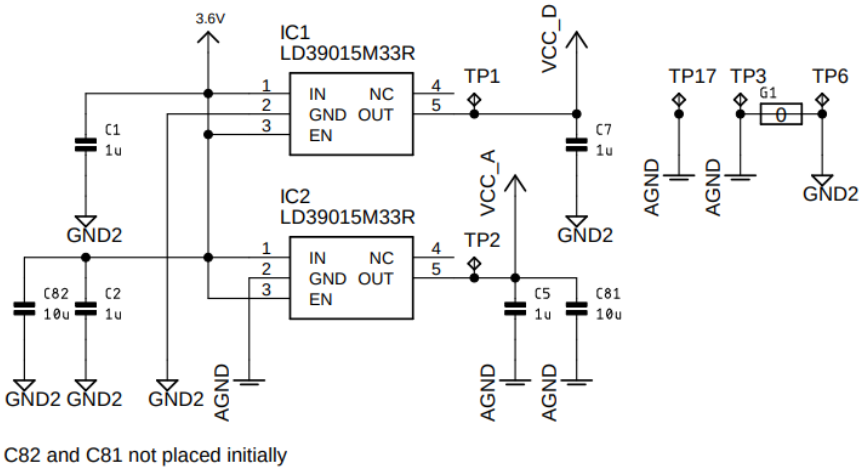

Figure 216. Digital and analog 3.3 V supplies (VCC_D and VCC_A), bypass capacitors and testpoints.

Five different ground symbols can be found in the design. Two of them can be found in **Figure 216**:

- AGND, corresponding to the analog ground plane.
- GND2, corresponding to the *clean* digital plane.

A further separation of the digital ground plane in communications (GND1) and measurement or clean (GND2) is performed in order to try to minimize the influence of serial communications on the measurements.

Finally, isolated GND3 for the communications with the PC, and simple GND, referred to as the negative terminal of the battery, complete the five symbols before-mentioned. They are connected through 0 Ω SMD components with the prefix G. These connections between GND, GND1, and GND2 are shown in **Figure 217** and will be further addressed in *6.1.8. PCB design*.

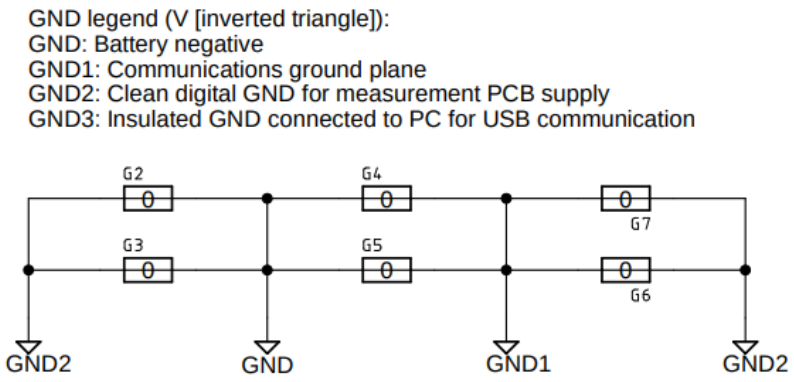

Figure 217. Interconnection between battery ground (GND), clean digital ground (GND1) and communications ground (GND2).

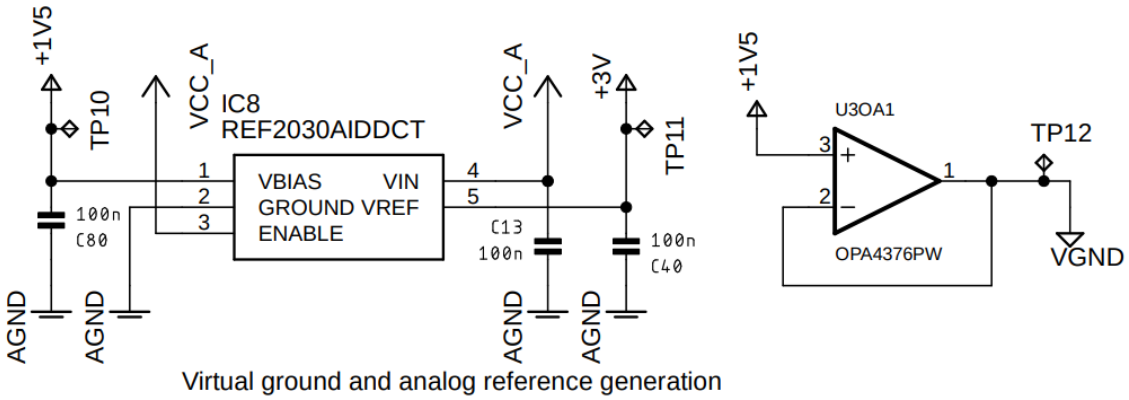

Figure 218. Virtual ground (+1.5 V) and +3 V (analog reference) obtention from REF2030.

On analog signal processing, low-noise operational amplifiers OPAx376 have been used. The DAC and the ADCs use the REF2030 (Texas Instruments) reference IC to obtain their 3V

reference. From the same IC +1.5 V (half of the +3 V analog reference) is obtained, which is buffered through an OA to offer VGND with certain sink and source capabilities, as shown in **Figure 218**. The manufacturer recommends the decoupling capacitors C13, C40, and C80.

Finally, +2.5 V needed for the ADC operation is obtained through an OA in follower configuration, obtaining the input voltage from a close-to-100 kΩ resistor-based voltage divider, with a reasonable tradeoff between thermal noise and power consumption, as shown in **Figure 219**.

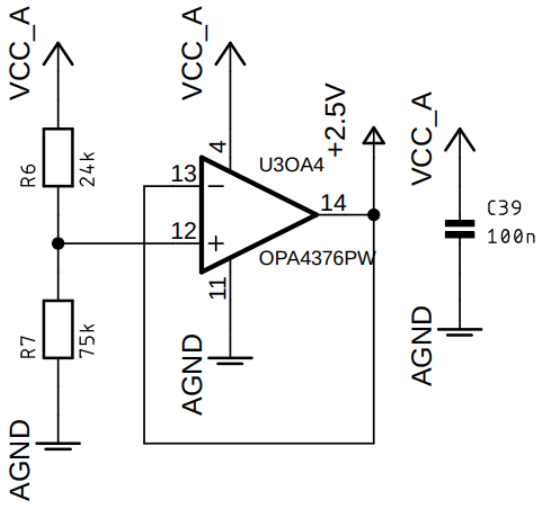

Figure 219. +2.5 V obtention circuit through a resistive divider and an OA in follower configuration.

6.1.7. Serial communications with PC

USB communication isolation is implemented using the ADUM4160 digital isolator from Analog Devices Integrated. It uses *iCoupler* technology to provide galvanic isolation of up to 4 kV_{RMS} for a period of one minute. It has a data rate of up to 100 Mbps and is capable of transmitting digital signals across the isolation barrier with low jitter and skew. The device has a low power consumption of just 50 mW.

The USB to UART conversion is performed through the popular FTDI FT232RL. The device integrates a USB transceiver, a voltage-level converter, and a clock generator, and it supports data rates of up to 3 Mbps.

As shown in **Figure 220**, both ICs are connected to the digital communications ground plane (GND1), except for the USB communications with the PC, using its specific ground plane (GND3).

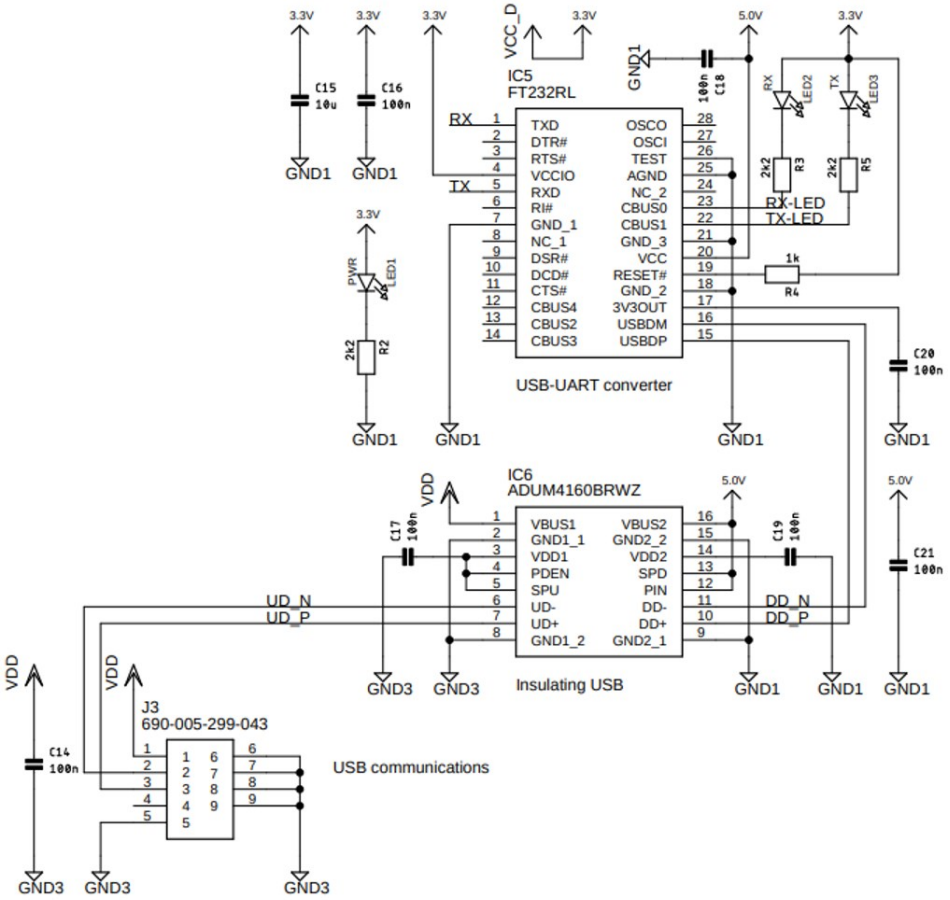

Figure 220. USB-UART conversion, RX&TX&Power indicators, and USB communications isolation circuits.

Decoupling capacitors are placed following the manufacturer's instructions. FT232RL lines CBUS0 and CBU1 indicate the reception and transmission events, respectively. Their connections to the indicator LEDs RX (red) and TX (orange) allow the user to easily identify if the communications are occurring. A green power indicator LED is also added (LED1).

6.1.8. PCB design

Given that noise reduction in analog signals is critical in this application, the serial communications with the PC have been galvanically isolated, as stated in *6.1.7. Serial communications with PC*. Critical component selection has been made with low-noise criteria. In each of them, decoupling capacitors have been placed following manufacturer recommendations. As commented in *6.1.6. Supply considerations*, a total of five ground planes are deployed in the MBMS. As is common in mixed-signal designs, the PCB is divided into two physically isolated ground planes electrically connected by a single point: the digital and the analog ground plane. This digital ground is split in two to reduce the impact of the USB communications: the communications digital ground plane and the clean digital ground plane.

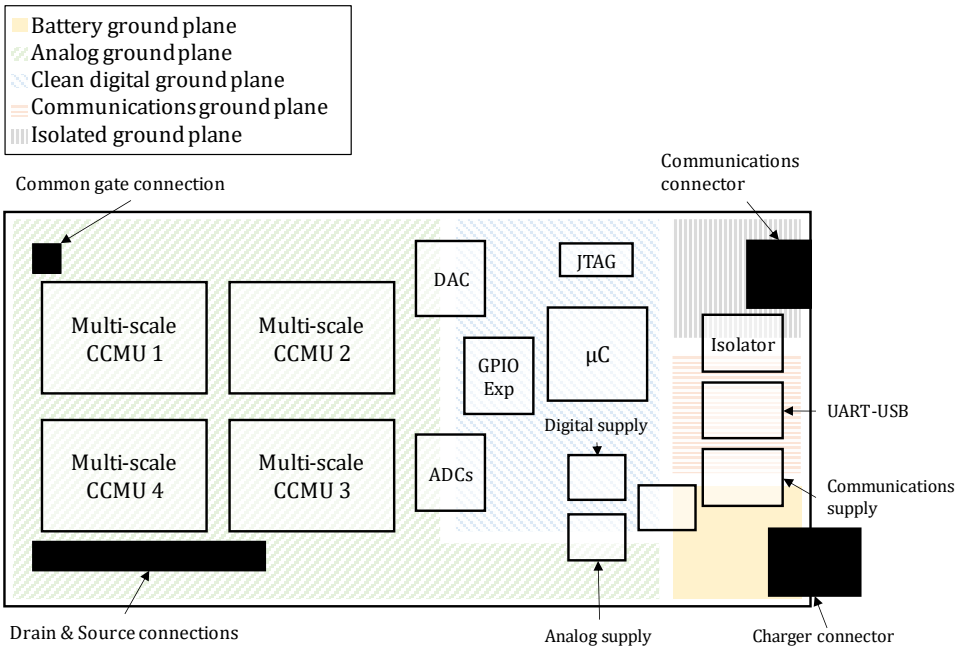

Figure 221. General layout diagram for MBMS.

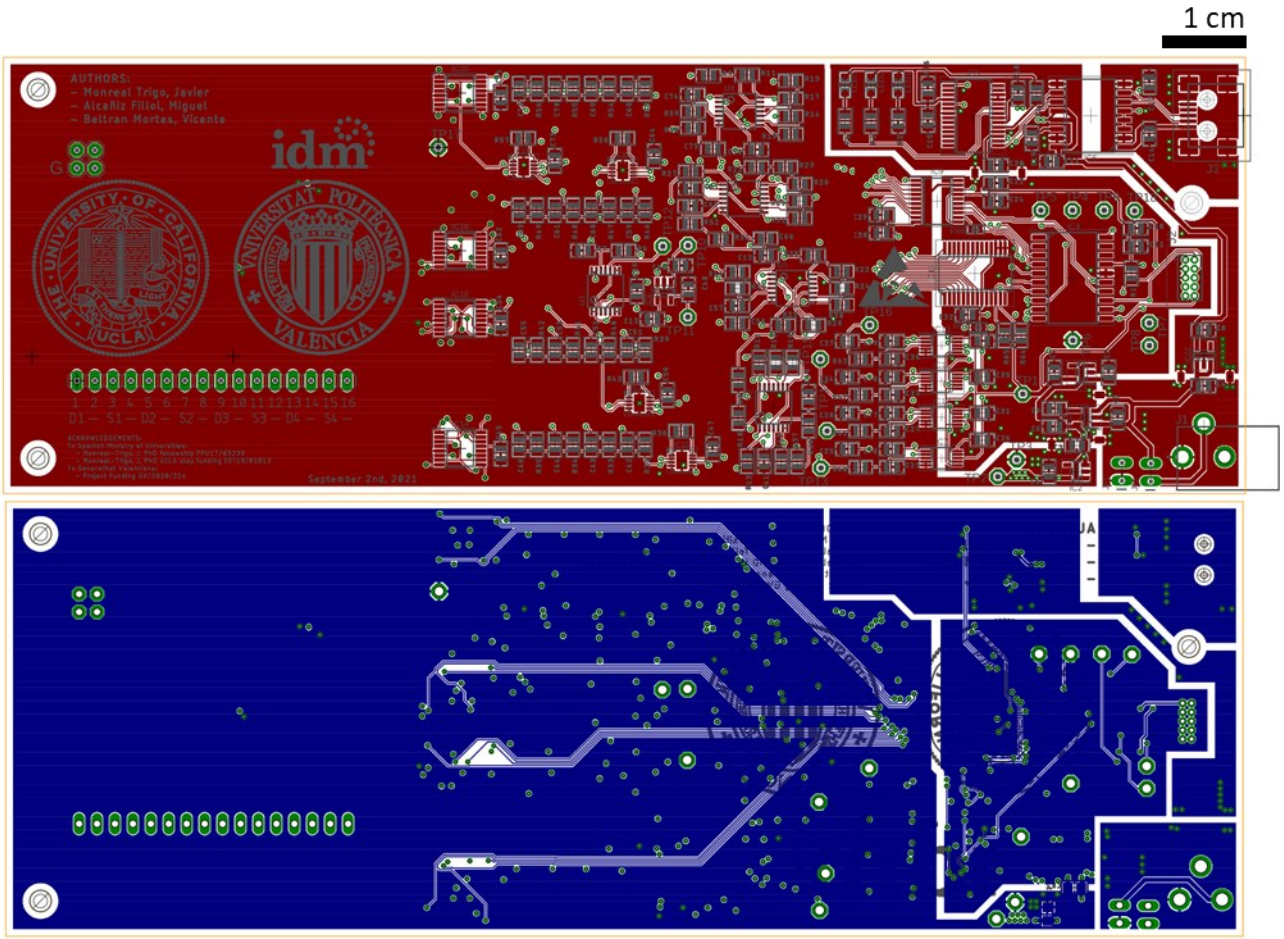

Figure 222. MBMS top and bottom layers. Obtained with EAGLE © 2022 Autodesk.

This latter is connected to the analog ground plane through one SMD connection. On the other hand, both digital ground planes are connected through two points to allow the UART data to be transmitted. The fourth ground plane is the battery one, connected to both digital ground planes at one point, where their respective supplies are generated. Finally, the fifth ground plane corresponds to the isolated ground plane for serial communications with the PC. The general layout scheme of the MBMS is shown in **Figure 221**.

External layers are set as ground planes and internal as voltage planes, obtaining an additional in-built capacitance for decoupling purposes.

With these criteria, the layout of the four-layer PCB (standard fabrication technologies, Eurocircuits © 6C class) is shown in **Figure 222**.

6.2. Firmware description

In this application, the ATSAMD11D14A microcontroller, which has a variety of communication capabilities, including SPI, I2C, and UART serial communication, is employed. The Microchip Studio IDE and the ATMEL-ICE debugging and programming tool are used for firmware development.

The ATSAMD11D14A microcontroller will be programmed in C++. This high-level programming language is easy to read and write but powerful enough to handle the low-level tasks required for interacting with hardware peripherals. C++ is often used for microcontroller programming because of its versatility and performance, and various tools and frameworks widely support it.

The Microchip Studio IDE is a comprehensive development platform that includes a text editor, compiler, debugger, and a variety of libraries and frameworks for interacting with different peripherals and devices. The ATMEL-ICE tool is a reliable and easy-to-use debugging and programming tool specifically designed for use with Microchip microcontrollers, including the ATSAMD11D14A. Together, these tools provide a powerful and comprehensive development platform for programming and debugging microcontroller-based projects.

This section will describe the firmware used to control the ATSAMD11D14A microcontroller, along with its memory requirements and serial communication protocols for PC communication. The firmware's configuration for the specific application, real-time voltage and current acquisition and transmission capabilities, and real-time parameter changes will also be covered.

6.2.1. General description of the microcontroller firmware

In the microcontroller firmware, the I2C and SPI communications are controlled by the CPU, while the UART communications are set up to be handled by DMA. This allows for simultaneous communication between the SPI ICs (ADCs and DAC) and the PC through UART-USB. Upon start, the general clocks, pinout, SPI, I2C, UART, DMA, and a 200 μs timer are all configured.

Each serial communication is set to the maximum speed according to the most limiting element. For UART, the maximum speed is 1 Mbps. For SPI it is 2 Mbps, and for I2C, it is 600 kHz. This ensures that communication is as fast as possible.

The DAC ICs are configured through SPI commands, and hardware control (CLEAR, LDAC) is disabled. All DACs are set to output a virtual ground (2048 digital value), and the current scales are set to disconnect the CCMUs. This ensures that the MBMS is in a known and stable state, without applying any electrical stimulus to the bioFETs, when it begins operation.

Once all these configurations have been set, the DMA reception callback is enabled. This allows the microcontroller to receive data packages from the PC. After the first DMA callback enable, the CPU in the main thread enters an infinite loop. The operation is different depending on a flag indicating whether or not the experiment is on. In either case, the message reception flag is evaluated, and the input message is processed if raised.

When a correct configuration is established, and the experience has been initiated, the following steps are executed every 200 μs:

- Current scales are changed if necessary.
- Each MBMS channel will apply the corresponding V_S and V_{DS} voltages.
- The data reception flag from PC is queried, and if so, the input message is processed.
- Otherwise, partial data reception is evaluated to flush the input buffer.
- It will wait for 10 μs until the ADCs conversion is triggered.
- The ADC measurements are set to be sent through the UART DMA.

The general flowchart of the MBMS is shown in **Figure 223**:

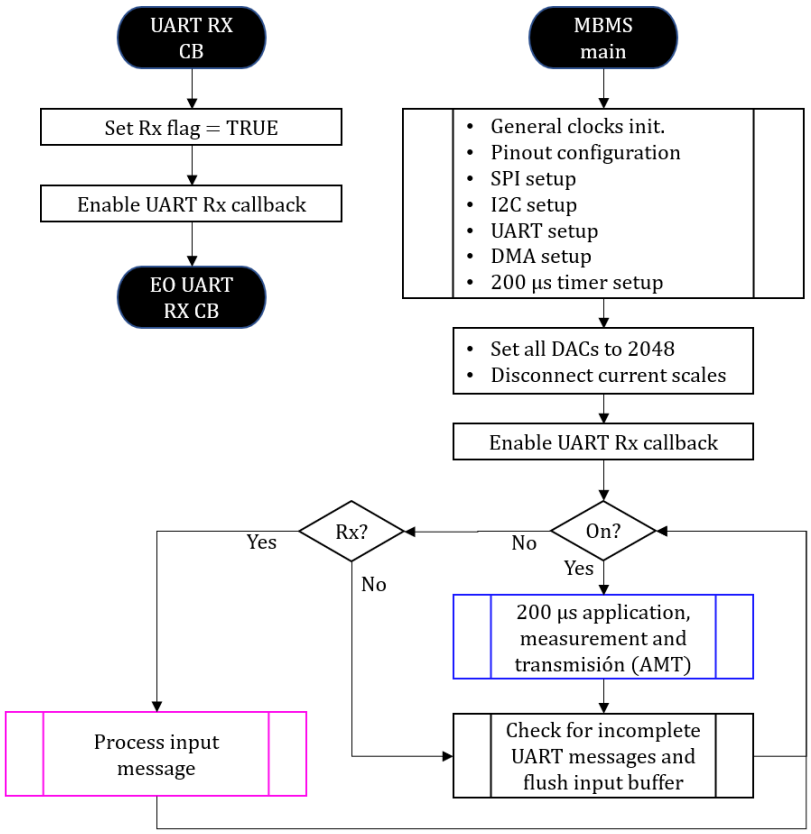

Figure 223. General flowchart of the MBMS MCU firmware.

6.2.2. Memory considerations

The DAC resolution of 12 bits and the ADC effective resolution of 16 bits imposes the use of long unsigned integer variables (`uint16_t`) to store such values. Nevertheless, given the configuration philosophy that will be further addressed in *6.2.4. Experience setup*, vector arrays have only one element per channel. Additionally, unsigned integer vectors (`uint8_t`) are used for:

- UART data reception, with 16 elements.
- UART data transmission, with 9 elements.
- I2C transmission buffer, with 2 elements.

From the total 256KB of FLASH memory and 32KB of SRAM, 4.6% and 5.2% are used, respectively.

6.2.3. Serial communications with the PC

Receiving a data package will raise a flag and reenable the callback, allowing it to end its operation (for instance, the real-time voltage application and current acquisition) before addressing the input message.

The input buffer is restarted if any bytes have been received but not a full 16-byte message for more than 1 ms. This ensures that the microcontroller can process and handle incoming messages properly, even if they are incomplete or have errors.

The first byte of the message, namely the header, indicates the kind of message that is being received:

- `0xCC` is used to check the communications. The PC will receive a 9-byte reply with `0xCC` as the first and final bytes.
- `0x5A` is used to start an experiment, setting the `ON` flag high.
- `0x50` is used to stop an experiment, setting the `ON` flag low.
- `0xDD` allows the simultaneous modification of all DAC outputs and current scales. V_S are only modifiable in IT mode. It will be further addressed in *6.2.6. Real-time change of parameters*.
- `0xAA` is the configuration header. Due to its complexity, it will be detailed next subsection.

After the correct reception of a message, the input buffer is reset to all zeros.

6.2.4. Experience setup

The setup of an experience is performed through the reception of five messages, the first of them starting with the configuration header, indicating in byte 2 the mode of operation for each channel in its 4 lower bits. Bit 0 corresponds to channel 1, and bit 3 corresponds to channel 4, indicating 0 the IT operation and 1 the IV operation of that channel. The following 4 messages of 16 bytes carry the necessary information for each channel's configuration, as shows **Figure 224**. All voltage values transferred are directely the DAC digital values to be applied.

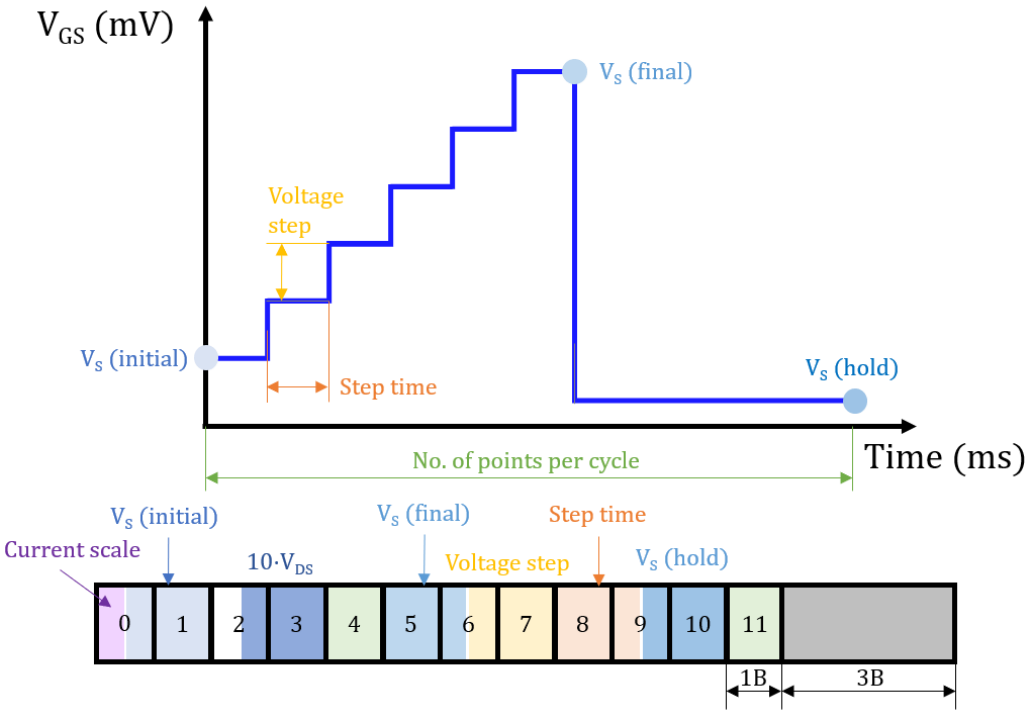

Figure 224. Data package for the configuration of one channel.

If the channel is set to work in IV mode, according to the voltage step, step time (no. of points, T_{NOP}), and initial and final V_S values, the number of points for the sweep (S_{NOP}) is calculated following **Equation 68**. The hold time number of points, H_{NOP}, is obtained by subtracting the S_{NOP} from the total number of points per cycle. If the channel is set up to work in IT mode, initial V_S will be applied upon start, with no posterior change, and values carried by the bytes 4 to 11 will be ignored.

$$S_{NOP} = \frac{V_S(final) - V_S(initial)}{V_S(step)} \cdot T_{NOP} \qquad \textbf{Equation 68}$$

6.2.5. Real-time voltage application, current acquisition, and transmission

The application, measurement, and transmission are performed every 200 µs when the experience is on. If new current scale values or new V_{DS} values have been received, they are updated through their respective I2C and SPI commands.

Then, each IV-mode channel situation is checked through the `FETIndex[channel]` pointer. It is compared with the `SweepPts`, `CyclePoints`, and `StepPeriod` variables for each `channel` to assess if it is in the actual sweep or the hold parts of the whole sweep, or

restart the sweep once it has reached its end, updating the V_S value through SPI if necessary. Each channel in IT mode will apply the last received V_S value.

The data reception flag from the PC is queried; if so, the input message is processed. Otherwise, partial data reception is evaluated to flush the input buffer after 1 ms (5 cycles). A wait of a minimum of 10 µs is performed until the ADCs conversion is triggered. The ADC measurements are set to be sent through the UART DMA.

Given that this is a periodic execution every 200 µs, the system will wait until the 200 µs timer overflows its count, restart the timer and start from the beginning. A general flowchart is shown in **Figure 225**.

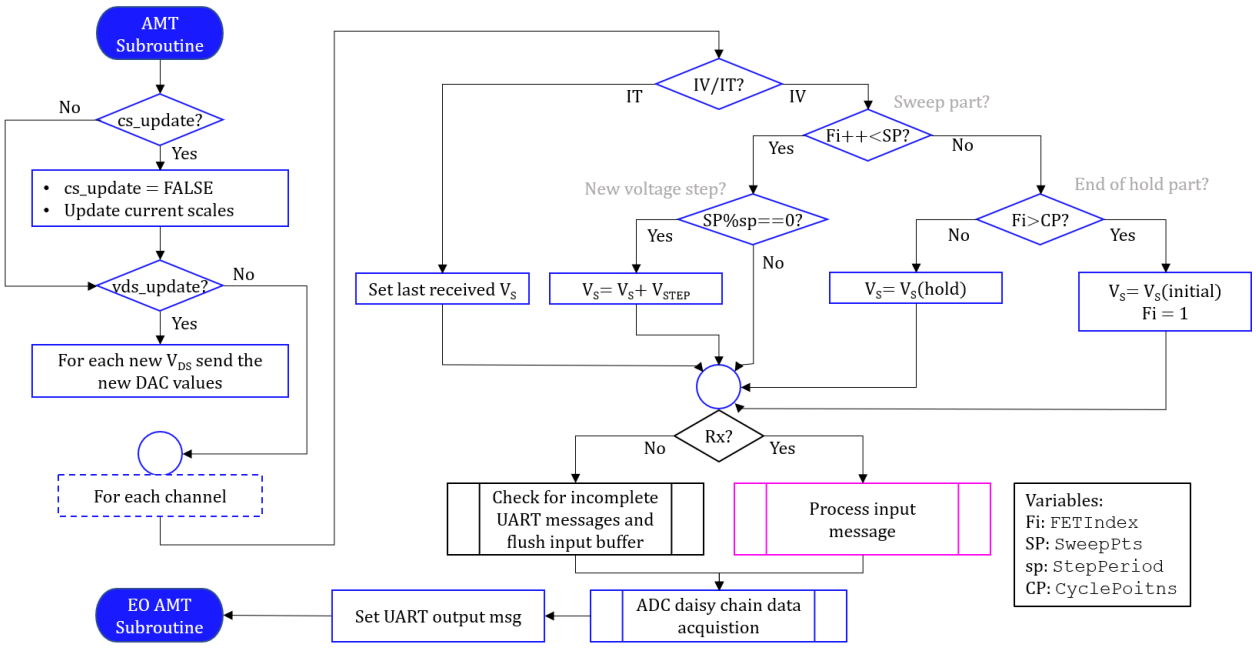

Figure 225. AMT (application, measurement, transmission) subroutine simplified flowchart,

The timing diagram is shown in **Figure 226a**. As observed, the on-execution change of a current scale will induce a delay in such period due to I2C operation in Fm instead of Fm+, exceeding the 200 µs. This excess will be 50 µs if no V_{DS} values are updated or 100 µs if both need to be changed. Given that this situation will only occur during the cycle in which the current scales are changed, the influence on the instrument output signal is negligible. **Figure 226b** shows how the MBMS can mimic the switched operation of its predecessor with a 250 µs sequential operation. The V_{DS} will increase the cycle duration by 50 µs, but again, this duration increase influence will be negligible in the whole operation of the system.

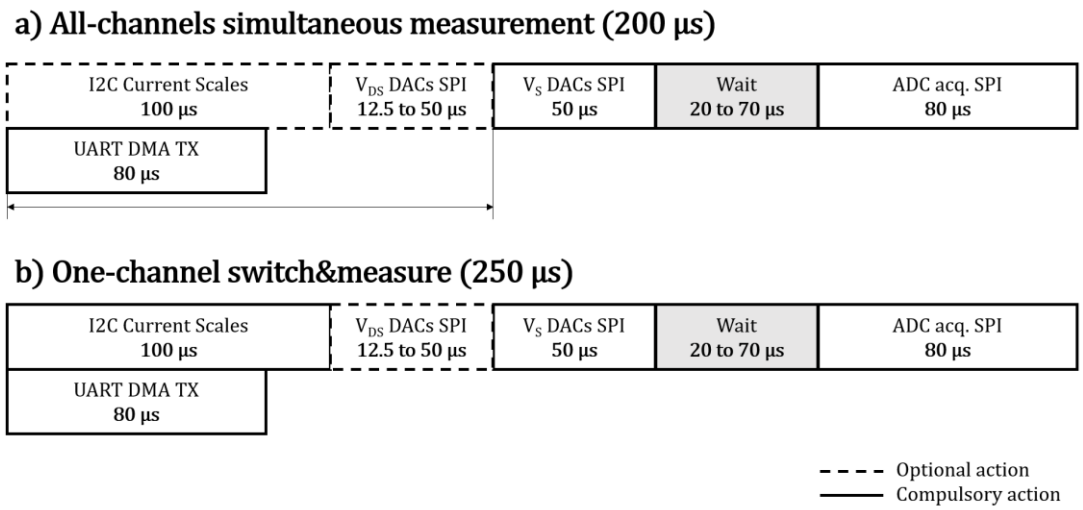

Figure 226. Periodic actions decomposition for simultaneous and switch&measure modes.

6.2.6. Real-time change of parameters

`0xDD` allows the simultaneous modification of all DAC outputs and current scales. V_S are only changed in IT mode. The data frame of this message is shown in **Figure 227**. If the new current scales are different from the ones already applied, the `cs_update` flag will be raised. The same will happen with the V_{DS} values and the `vds_update` flag.

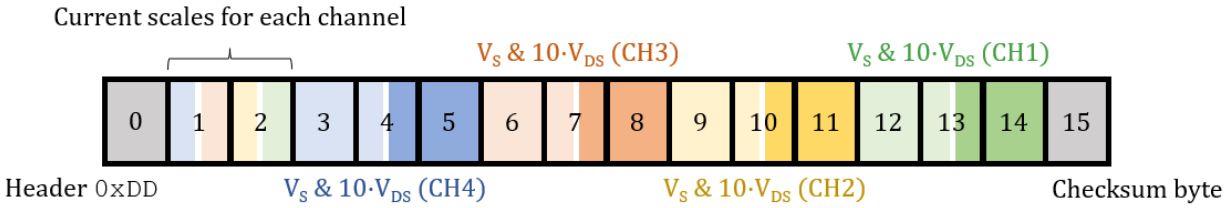

Figure 227. All-voltages and current scales real-time modification data frame.

6.3. Application code for the PC Graphic User Interface

This subsection will delve into the graphical user interface (GUI) hosted on a personal computer (PC) for controlling the MBMS instrument. The GUI is implemented using MATLAB App Designer, a powerful tool for designing and building graphical user interfaces in MATLAB that has been described in previous chapters. This GUI serves as the primary interface for real-time control of the MBMS instrument, and in the following subsection, we will also discuss the GUI for data analysis.

Designed to be versatile, the GUI can control both the MBMS instrument and its predecessor. We will take a closer look at the various features of the GUI, including the *Settings* tab, the FET configuration, the single view tab, the *Overview* tab, and the ability to introduce event stamps in real time. Additionally, we will examine the output data file obtained once an experiment is completed. Overall, this subsection aims to provide a comprehensive understanding of the capabilities and functionality of the GUI, allowing effective control and manipulation of the MBMS instrument.

6.3.1. Settings tab

The settings tab in the GUI is where various parameters can be configured to control the instrument's behavior. The main features of this tab include the following:

- **Device selection**: This feature allows the user to choose between the MBMS (4FET-Sim) and its predecessor (8FET-Mux).
- **Path to save results**: This textbox allows the user to specify the folder in which to save the experiment results.
- **Read cycles per plot**: This parameter controls how many UART receptions must occur before updating the plot. This is useful in slow computers to ensure the correct real-time execution.
- **Selected FETs**: This feature specifies the number of channels working in a multiplexed way. This option is only available for the predecessor of the MBMS. Otherwise, it is locked to 4 channels.
- **Plot time range**: This parameter allows the user to set the time range of the plot in seconds for IT mode, IV-mode multiple cycles plot, or IV-mode one point per cycle plot.
- **Display only One Cycle in IV mode**: This checkbox allows the user to toggle between multiple cycle plot or last cycle plot for the channels working in IV mode.

The settings tab is intuitive and easy to use, providing a simple interface to configure the instrument as needed. The GUI in this tab is shown in **Figure 228**.

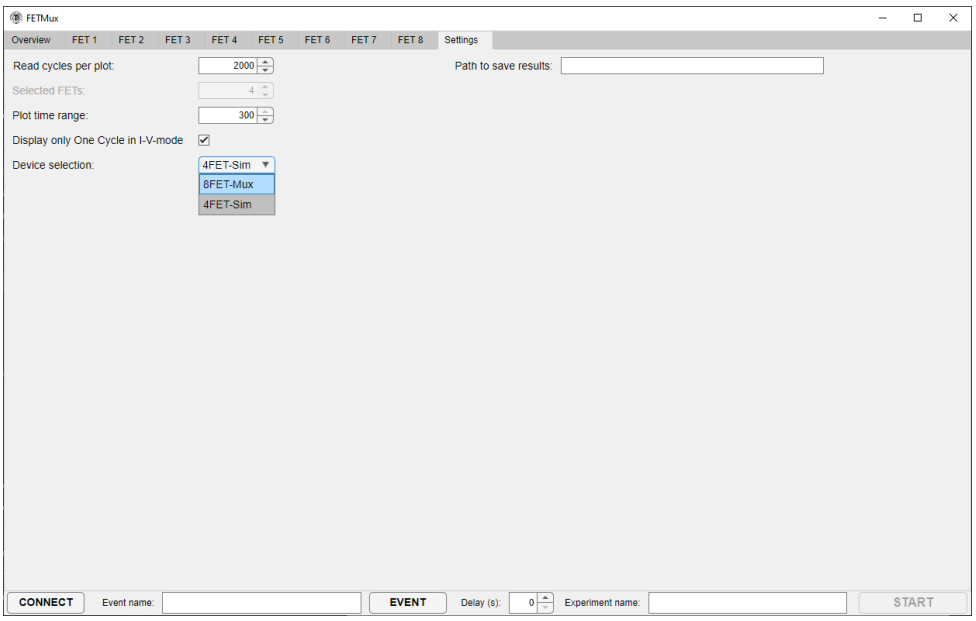

Figure 228. Settings tab of the MBMS GUI. Obtained with MATLAB 2018 © Mathworks.

The general control of the MBMS instrument is achieved through the controls located in the bottom part of the GUI. These controls are shared across all the different tabs, providing users with a consistent and intuitive interface.

The CONNECT button is an essential control that allows users to easily establish a connection with the instrument. When pressed, the GUI will automatically search for MBMS through all available COM ports and wait for a response from the MBMS in each of them. If the instrument is successfully detected, the GUI will establish a connection the START button will become enabled. A warning message will pop up if the instrument is not found, informing the user that no connection can be established.

Another important control is the Experiment name, which sets the file name in which the output data will be saved. This feature is important to ensure that the data is properly labeled and easily located. The details of this feature will be discussed in a later subsection *6.3.5. Output datafile*.

Finally, the START/STOP button is only enabled when the MBMS is connected. This button is the main switch to start and stop the experiment. Once pressed, the experiment will begin, and the instrument will start acquiring data. Pressing the button again will stop the experiment, and the acquired data will be saved for further analysis.

6.3.2. FET configuration tab

The FET configuration tab in the GUI, shown in **Figure 228**, allows users to independently set up each channel before the experiment launch, visualize each channel in real time, and modify the current scale or applied voltages during the experiment. Depending on the mode chosen and if the experience is started, specific controls are disabled, and their color is changed to gray to indicate it to the user.

The parameters configured on this tab include mode, current scale, VDS, VGS, and in the case of IV mode, the rest of the necessary parameters. Those later are used to calculate and display the cycle time. Users can set each channel to work on IV mode to display the results in either sweep or value mode. In sweep mode, the whole sweep or sweeps are displayed, whereas, in value mode, only one current point of each sweep over time is displayed. A small IV cycle plot is also shown to make it easier for users to select a point using a slider.

In addition to these features, the FET configuration tab displays the average and typical deviation of the last 20 samples of each cycle. These metrics provide an approximation of the transimpedance and noise in hold conditions. This feature allows the user to monitor their experiments' performance in real-time and make adjustments as necessary.

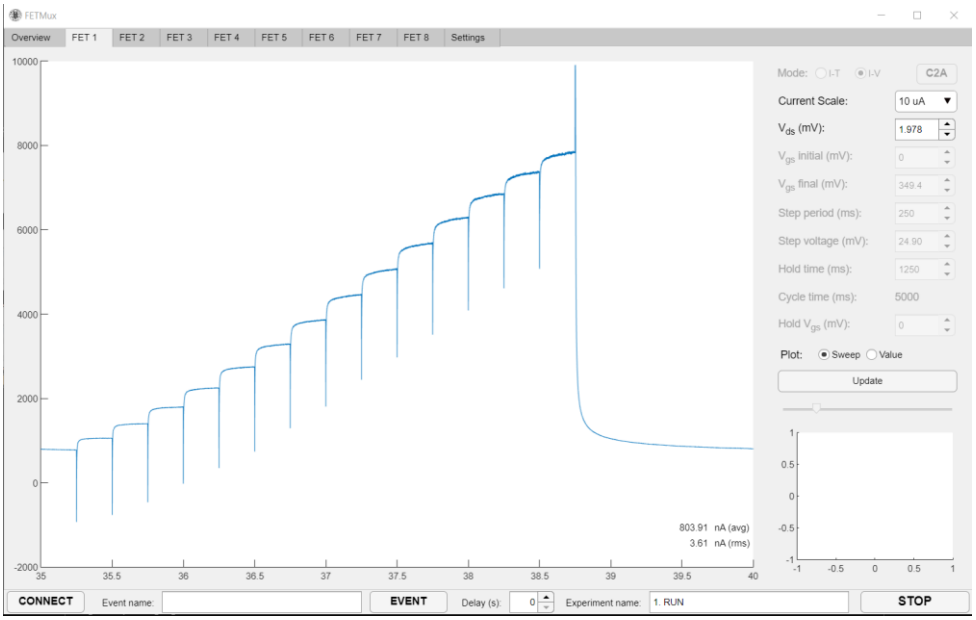

Figure 229. FET 1 tab during an experiment, displaying an IV-sweep. Real-time values and metrics are displayed in the main plot, whereas the available control items can be distinguished in the right-side control menu. Obtained with MATLAB 2018 © Mathworks.

6.3.3. Overview tab

The Overview tab in the GUI provides users with a comprehensive view of the instrument's performance. This tab allows the simultaneous display of up to 8 channels, showing the last updated results. The tab displays the last IV cycle or cycles plot, or the IT plot, of each channel so that users can visualize the measurement.

Additionally, the Overview tab displays the last 20 samples' average and typical deviation. These metrics are displayed beneath each channel plot, as shown in **Figure 230**. This feature allows users to monitor multiple channels' performance quickly and easily simultaneously.

The Overview tab provides a convenient and efficient way to monitor multiple channels of the instrument. This tab is a great tool to make a fast comparison between the different channels and quickly identify any problems or discrepancies in the measurement. The simultaneous display of the channels makes it much easier to understand how the device is performing and make any necessary adjustments.

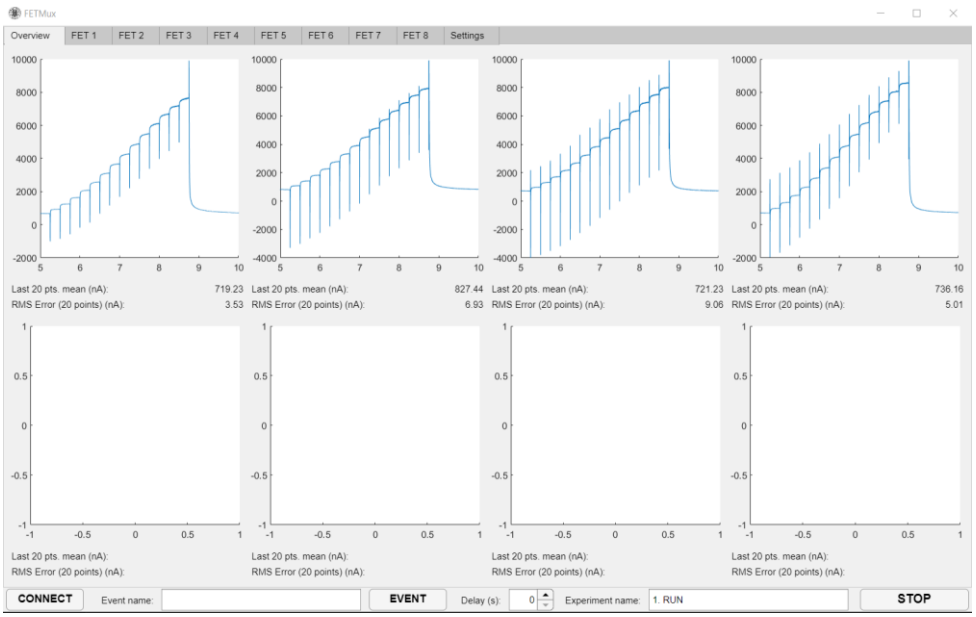

Figure 230. Multi-FET simultaneous measurement Overview tab of the MBMS GUI. Obtained with MATLAB 2018 © Mathworks.

In both the single-view tabs and the Overview tab, every plot can be handled to zoom in, select, and pan, among others.

6.3.4. Event stamps

One of the most useful features of the GUI is the ability to add customized event stamps. This feature allows the user to add annotations to the data, providing additional context and making it easier to understand the experiment results.

The event stamps are controlled through the bottom controls of the GUI. The user simply types the event's name in the textbox to add an event stamp and presses the EVENT button. Once an event stamp has been added, it will be displayed in the real-time plots, as shown in **Figure 231**.

The event stamps are shared across all channels, which allows the user to check for cross-sensitivity across the different channels. With the custom text, the user could identify if the event executed is only applied to one channel, which can be helpful when analyzing the results.

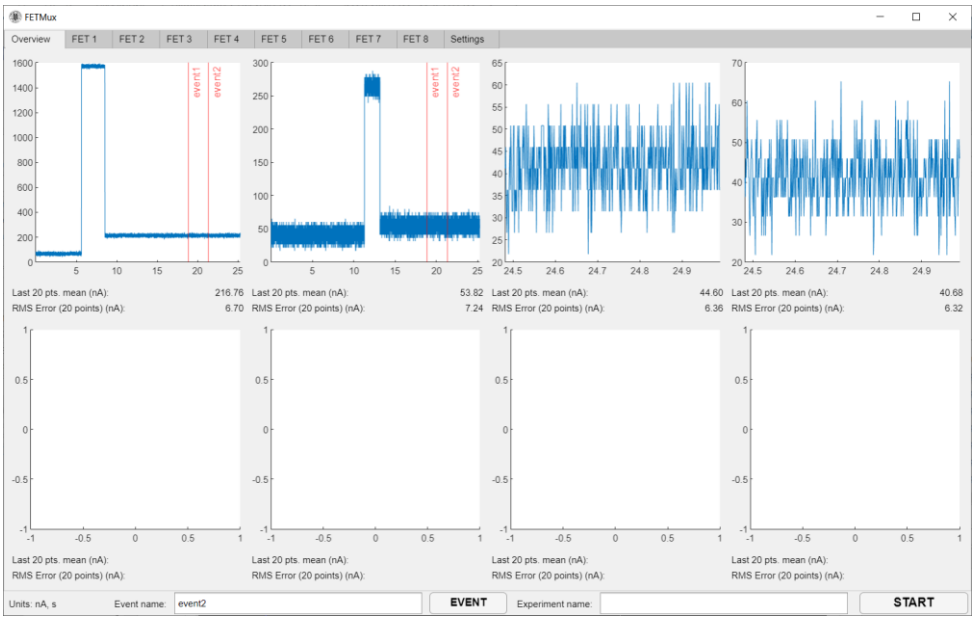

Figure 231. Example of the use of event stamps in the MBMS GUI. Obtained with MATLAB 2018 © Mathworks.

6.3.5. Output datafile

The output data file obtained after an experiment is in the .mat extension. It can be converted into .csv with the data analysis GUI described in the following section *6.4. Application code for the PC Data Analysis Tool*.

The structure of the datafile is shown in **Figure 232**. The first row describes the experiment name, its start timestamp, and the device employed: MBMS (4FET) or its precedent (8FET).

Next, the setup of each channel is addressed in the 8 following rows, displaying it is in IV or IT mode, or it is OFF. If in IV mode, the additional parameters needed to describe the whole sweep are indicated in mV and ms units.

Then, a semicolon-separated table shows all the values of the experiments, with a common *Time* (in seconds) first column and a total of 32 columns in which the current scale, current measurement I_{DS} (in nA), V_{DS} (in mV), and V_{GS} (in mV) is indicated for each channel.

Finally, the last rows are reserved to indicate the end of the experiment timestamp and the events registered during its execution, displaying in the first column the event timestamp in seconds and in the second column its associated label.

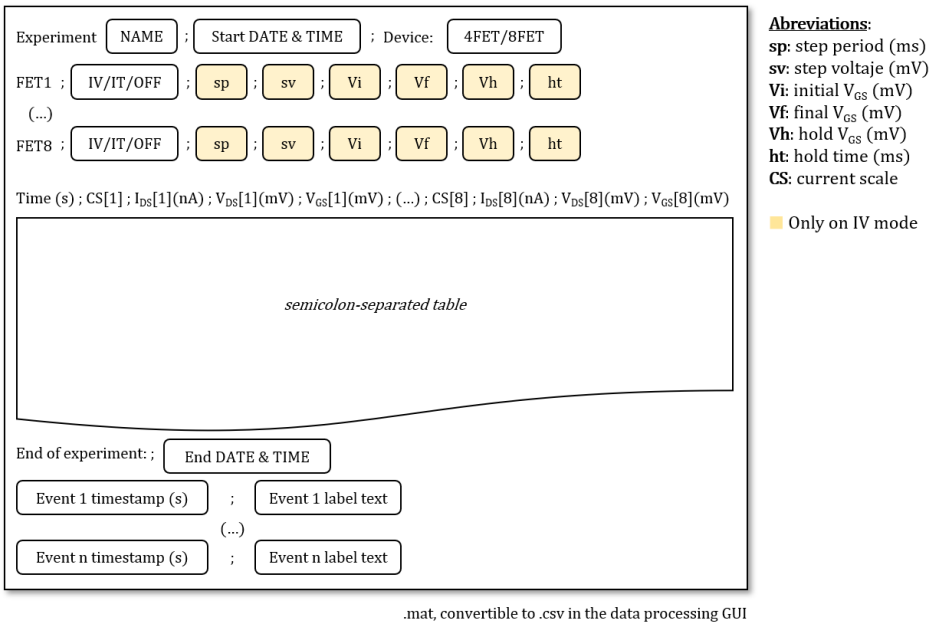

Figure 232. MBMS output datafile structure.

6.4. Application code for the PC Data Analysis Tool

In addition to the GUI for real-time control of the MBMS instrument, a second GUI for analyzing the obtained data has been designed. This allows the conversion of the .mat file to .csv for processing by specific scripts in other development environments. The GUI consists of a main interface with three tabs containing:

1. The controls necessary to load, select and display the raw data.
2. Display in embedded spreadsheet format.
3. Tab for the overlay display of the cycles in IV mode, with sample selection and filtering tools in preparation for obtaining the calibrated response (CR).

From this last tab, it is possible to enter the CR mode, which executes a pop-up window.

Every plot can be saved in .fig extension for its aesthetic modification for the obtention of a standalone figure by right-clicking the plot of the GUI.

6.4.1. Load data and raw visualization

The first tab, namely *Control*, allows the data upload to the GUI through the LOAD DATA button. Upon completion, all the associated information will be displayed in the datafile. The user can select which channels wants to be displayed and whether the applied voltages or legend should be shown in the plot. Additionally, they can zoom in through the *Visualization control* panel or export the .mat file to .csv through the *CSV export* panel. An example of the use of this tab is shown in **Figure 233**.

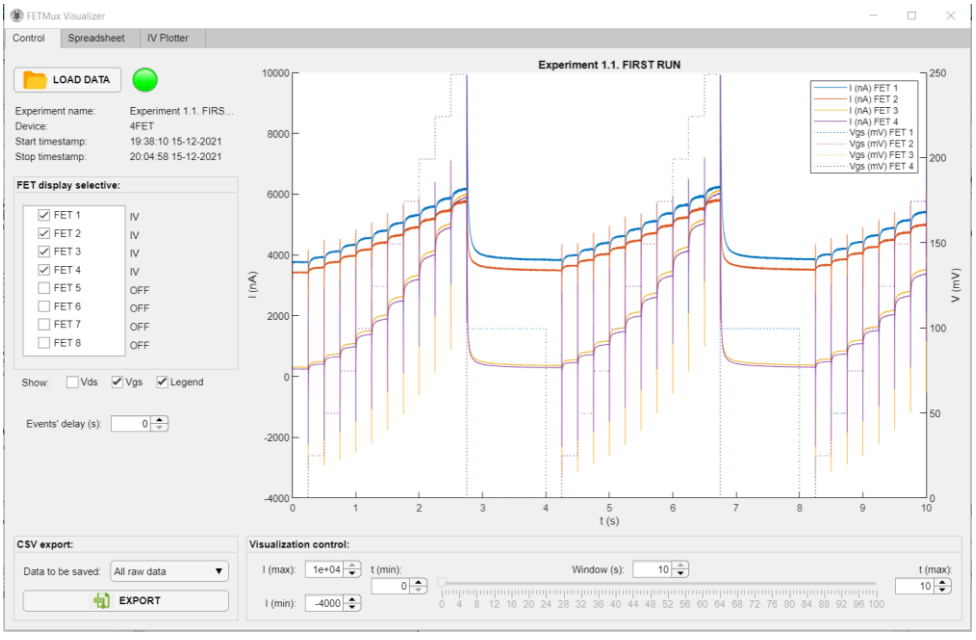

Figure 233. Data Analysis MBMS GUI, Control tab. Obtained with MATLAB 2018 © Mathworks.

6.4.2. Spreadsheet view tab

The *Spreadsheet* tab allows the value-by-value display of the recorded data, as shown in **Figure 234**.

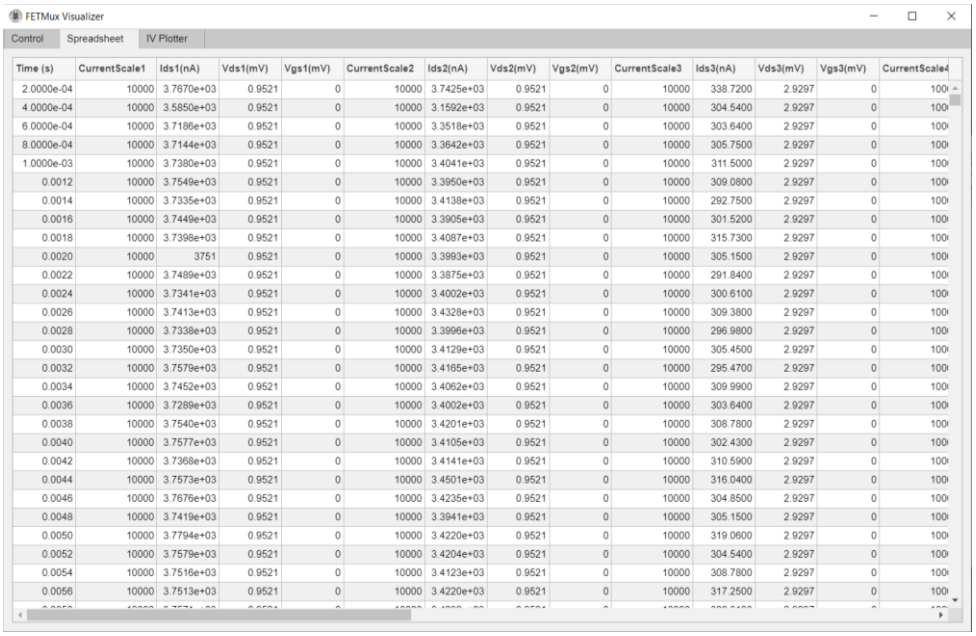

Time (s)	CurrentScale1	Ids1(nA)	Vds1(mV)	Vgs1(mV)	CurrentScale2	Ids2(nA)	Vds2(mV)	Vgs2(mV)	CurrentScale3	Ids3(nA)	Vds3(mV)	Vgs3(mV)	CurrentScale4
2.0000e-04	10000	3.7670e+03	0.9521	0	10000	3.7425e+03	0.9521	0	10000	338.7200	2.9297	0	100
4.0000e-04	10000	3.5850e+03	0.9521	0	10000	3.1592e+03	0.9521	0	10000	304.5400	2.9297	0	100
6.0000e-04	10000	3.7186e+03	0.9521	0	10000	3.3518e+03	0.9521	0	10000	303.6400	2.9297	0	100
8.0000e-04	10000	3.7144e+03	0.9521	0	10000	3.3642e+03	0.9521	0	10000	305.7500	2.9297	0	100
1.0000e-03	10000	3.7380e+03	0.9521	0	10000	3.4041e+03	0.9521	0	10000	311.5000	2.9297	0	100
0.0012	10000	3.7549e+03	0.9521	0	10000	3.3950e+03	0.9521	0	10000	309.0800	2.9297	0	100
0.0014	10000	3.7335e+03	0.9521	0	10000	3.4138e+03	0.9521	0	10000	292.7500	2.9297	0	100
0.0016	10000	3.7449e+03	0.9521	0	10000	3.3905e+03	0.9521	0	10000	301.5200	2.9297	0	100
0.0018	10000	3.7398e+03	0.9521	0	10000	3.4087e+03	0.9521	0	10000	315.7300	2.9297	0	100
0.0020	10000	3751	0.9521	0	10000	3.3993e+03	0.9521	0	10000	305.1500	2.9297	0	100
0.0022	10000	3.7489e+03	0.9521	0	10000	3.3875e+03	0.9521	0	10000	291.8400	2.9297	0	100
0.0024	10000	3.7341e+03	0.9521	0	10000	3.4002e+03	0.9521	0	10000	300.6100	2.9297	0	100
0.0026	10000	3.7413e+03	0.9521	0	10000	3.4328e+03	0.9521	0	10000	309.3800	2.9297	0	100
0.0028	10000	3.7338e+03	0.9521	0	10000	3.3996e+03	0.9521	0	10000	296.9800	2.9297	0	100
0.0030	10000	3.7350e+03	0.9521	0	10000	3.4129e+03	0.9521	0	10000	305.4500	2.9297	0	100
0.0032	10000	3.7579e+03	0.9521	0	10000	3.4165e+03	0.9521	0	10000	295.4700	2.9297	0	100
0.0034	10000	3.7452e+03	0.9521	0	10000	3.4062e+03	0.9521	0	10000	309.9900	2.9297	0	100
0.0036	10000	3.7289e+03	0.9521	0	10000	3.4002e+03	0.9521	0	10000	303.6400	2.9297	0	100
0.0038	10000	3.7540e+03	0.9521	0	10000	3.4201e+03	0.9521	0	10000	308.7800	2.9297	0	100
0.0040	10000	3.7577e+03	0.9521	0	10000	3.4105e+03	0.9521	0	10000	302.4300	2.9297	0	100
0.0042	10000	3.7368e+03	0.9521	0	10000	3.4141e+03	0.9521	0	10000	310.5900	2.9297	0	100
0.0044	10000	3.7573e+03	0.9521	0	10000	3.4501e+03	0.9521	0	10000	316.0400	2.9297	0	100
0.0046	10000	3.7676e+03	0.9521	0	10000	3.4235e+03	0.9521	0	10000	304.8500	2.9297	0	100
0.0048	10000	3.7419e+03	0.9521	0	10000	3.3941e+03	0.9521	0	10000	305.1500	2.9297	0	100
0.0050	10000	3.7794e+03	0.9521	0	10000	3.4220e+03	0.9521	0	10000	319.0600	2.9297	0	100
0.0052	10000	3.7579e+03	0.9521	0	10000	3.4204e+03	0.9521	0	10000	304.5400	2.9297	0	100
0.0054	10000	3.7516e+03	0.9521	0	10000	3.4123e+03	0.9521	0	10000	308.7800	2.9297	0	100
0.0056	10000	3.7513e+03	0.9521	0	10000	3.4220e+03	0.9521	0	10000	317.2500	2.9297	0	100

Figure 234. *Spreadsheet* tab view in MBMS Data Analysis GUI. Obtained with MATLAB 2018 © Mathworks.

6.4.3. IV Plotter tab

The IV Plotter tab in the GUI of the MBMS instrument is designed to provide a comprehensive data analysis experience for users. The main plot in the center of the tab displays the data obtained in a one-cycle view, with one cycle plotted over the other. The left, right, and bottom panels contain various controls and information to aid the analysis, as shown in **Figure 235**.

The left panel, called *Plotting parameters*, allows the user to set a Master channel, which will be used as the reference for plotting all the other channels. The user can also choose the first and last cycle to be plotted. The user can also choose to plot the V_{DS} and V_{GS} values, display a legend, or apply fading to each cycle. *Fading* is a feature that makes the transparency of the first cycles higher than the last ones, making it easier to detect linear trends or sudden changes in the data.

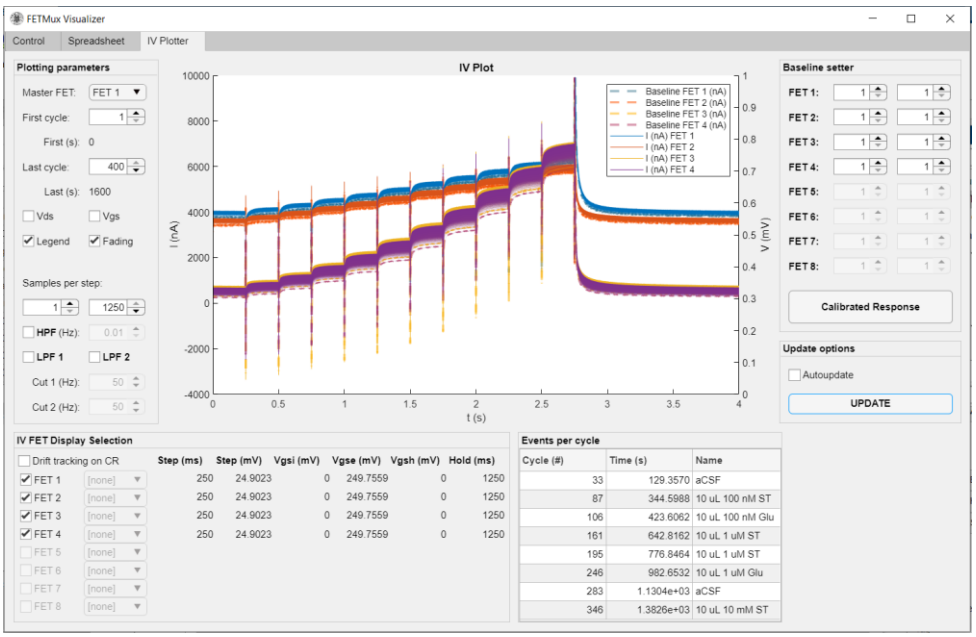

Figure 235. *IV Plotter* tab view in MBMS Data Analysis GUI before using smart features. Obtained with MATLAB 2018 © Mathworks.

The bottom part of the left control panel contains smart functions. Each VGS step has a transient spike at its beginning and a stabilization time. The user can choose the samples to use for data analysis. The first and last samples are set by default, selecting the whole step. A high-pass filter and two low-pass filters can be activated, and the cut-off frequency of each filter can be set once the corresponding checkbox is clicked.

The bottom control panel, *IV FET Display Selection*, allows the user to select which channels to plot and shows the settings of each channel. A table displaying events (time, cycle in which it occurred, and label inserted by the user) is also shown.

Finally, the right control panel allows the user to set a calibrated response baseline as the average of a set of cycles for each channel. This feature offers users the ability to create an independent baseline for each channel by averaging multiple cycles, resulting in a reduction of noise in the data.

Comparatively, the results of using such smart functions can be observed in **Figure 236**, in which the data is ready to be submitted to the *Calibrated Response* submodule.

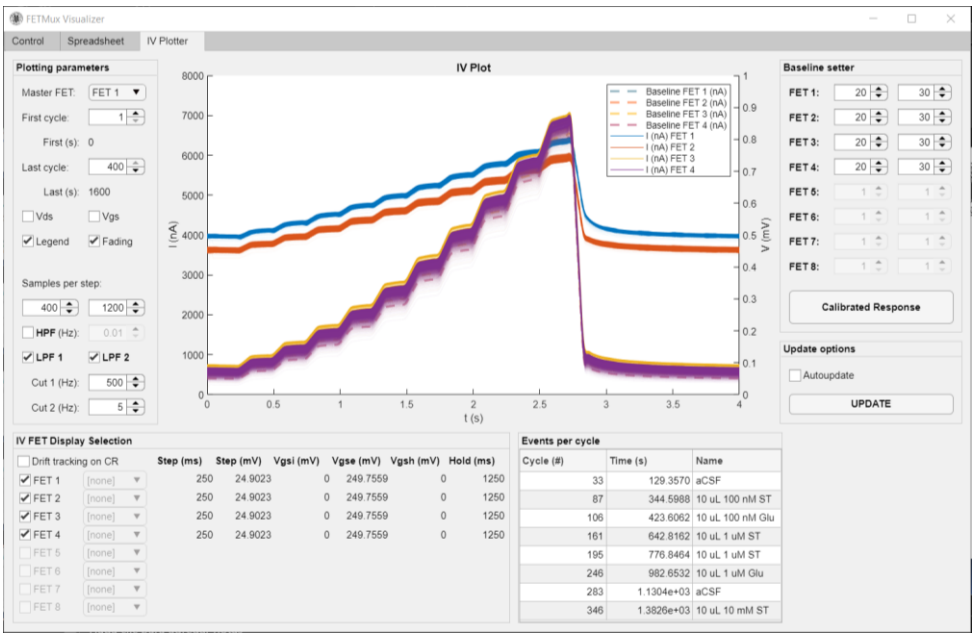

Figure 236. *IV Plotter* tab view in MBMS Data Analysis GUI before using smart features. Obtained with MATLAB 2018 © Mathworks.

6.4.4. Calibrated response

The calibrated response (CR) has been addressed in *Introduction / 6.4. Calibrated response of aptamer-FET biosensors*. It eliminates the device-to-device variations intrinsic to the aptamer-FET technologies with the current production capabilities. Its characteristic equation (shown in **Equation 7**) is reproduced and represented in **Figure 237**.

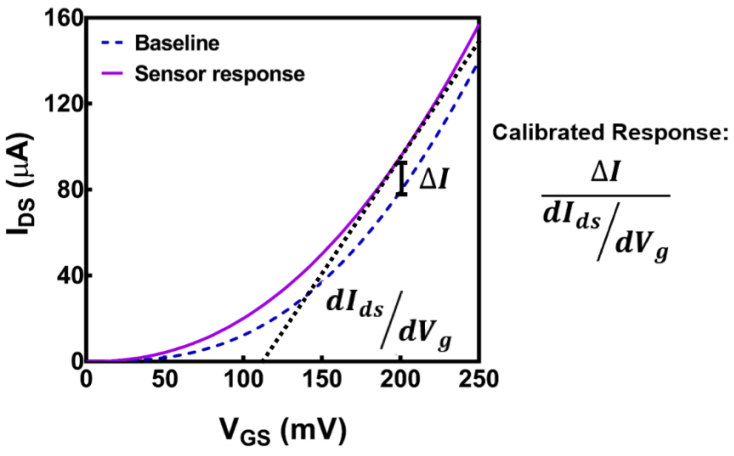

Figure 237. Calibrated response graphical representation. Reproduced with permission from [278]. Science © 2018.

The baseline curve is a sweep stored in the absence of the target molecule. The absolute response, ΔI, can be obtained for any V_{GS} for each sweep. The calibrated response (CR, in mV) is obtained as its division vs. dI_{DS}/dV_{GS} at that V_{GS} value.

This method relies on correlations between absolute sensor responses and gate dependence in liquid-gate sensing setups: the transconductance (g_m) at a given V_{GS} will differ between several FETs in the absence of the target analyte. For each FET, the initial g_m is proportional to ΔI. The same occurs with the dI_{DS}/dV_{GS} term; it is proportional to the initial g_m. Nevertheless, at a V_{GS} setting the FET operation in a linear regime, the influence in the g_m of the aptamer conformational change has a higher impact on ΔI than on the dI_{DS}/dV_{GS} term.

To increase our temporal resolution, we will perform discrete and uniform voltage steps in the IV sweep, each with a specific duration. The calibrated response (CR) can be obtained for each step, corresponding to V_{GS} value. With this aim, **Equation 7** is discretized: an initial set of cycles is used to establish the baseline I_{DS} current for every step, namely $I_{baseline}$. Averaging a set of cycles contributes to reducing noise influence. For the step of interest, ς, the current measurement is systematically subtracted with $I_{baseline}[\varsigma]$, obtaining the absolute variation $\Delta I_{DS}[\varsigma]$. For discretizing the dI_{DS}/dV_{GS} term, it is obtained as the ratio between $I_{DS}[\varsigma]$-$I_{DS}[\varsigma$-$1]$ and V_{GS} step. The CR for a sweep is shown in **Equation 69**:

$$CR[\varsigma] = \frac{\Delta I_{DS}[\varsigma]}{I_{DS}[\varsigma] - I_{DS}[\varsigma - 1] \Big/ V_{GS\ step}}, \text{where } \Delta I_{DS}[\varsigma] = I_{DS}[\varsigma] - I_{baseline}[\varsigma] \qquad \textbf{Equation 69}$$

The former discretization considers that only one sample is acquired per step. However, each step presents a transitory time before I_{DS} reaches its final value. Hence, the implementation will be performed with a constant sampling period T_S significantly smaller than the step time, with n samples acquired per voltage step. The number of samples of the transitory, d_t, will be discarded. The N used samples, with initial and final indexes K_i and K_f, respectively, can be obtained as a function of ς, n, and d_t. Obtaining I_{DS} as an N-samples average improves noise performance. In the same way, $I_{baseline}$ values are obtained with the same procedure, and as the average of a set of C cycles from cycles c_i to c_f. CR for cycle j and step ς can be obtained as shown in **Equation 70**:

$$CR[j, \varsigma] = \frac{\sum_{i=K_i}^{K_f} I_{DS}[j, i] \ - \frac{1}{C} \sum_{c=c_i}^{c_f} \sum_{i=K_i}^{K_f} I_{baseline}[c, i]}{\left(\sum_{i=K_i}^{K_f} I_{DS}[j, i] - \sum_{i=K_i}^{K_f} I_{DS}[j, i - n]\right) \Big/ V_{GS\ step}}, \qquad \textbf{Equation 70}$$

$$K_i = (\varsigma - 1)n + d_t, K_f = (\varsigma - 1)(n + 1), N = n - d_t, \forall n: 0 \leq d_t < n$$

It should be noted that it is a division of N-sample averages. Hence, $\frac{1}{N}$ terms cancel each other and are not shown. Depending on the current signal transient time, K_i should be modified with $d_t>0$. For further optimization:

1. $\frac{1}{C}\sum_{c=c_i}^{c_f}\sum_{i=K_i}^{K_f} I_{baseline}[c,i]$ shall be calculated once and stored for reutilization.
2. $\sum_{i=K_i}^{K_f} I_{DS}[j,i]$ should be calculated once to be used in two subsequent operations:
   a. $\sum_{i=K_i}^{K_f} I_{DS}[j,i] - \frac{1}{C}\sum_{c=c_i}^{c_f}\sum_{i=K_i}^{K_f} I_{baseline}[c,i]$
   b. $\sum_{i=K_i}^{K_f} I_{DS}[j,i] - \sum_{i=K_i}^{K_f} I_{DS}[j,i-n]$

The *Calibrated Response* submodule will use as input the processed data in the *IV Plot* tab of the main window. Loading the experiment results, we can obtain a CR plot for every V_{GS} step and every selected channel, as shown in **Figure 238**. In the case of multiple step-selection, each step is plotted with a different line thickness.

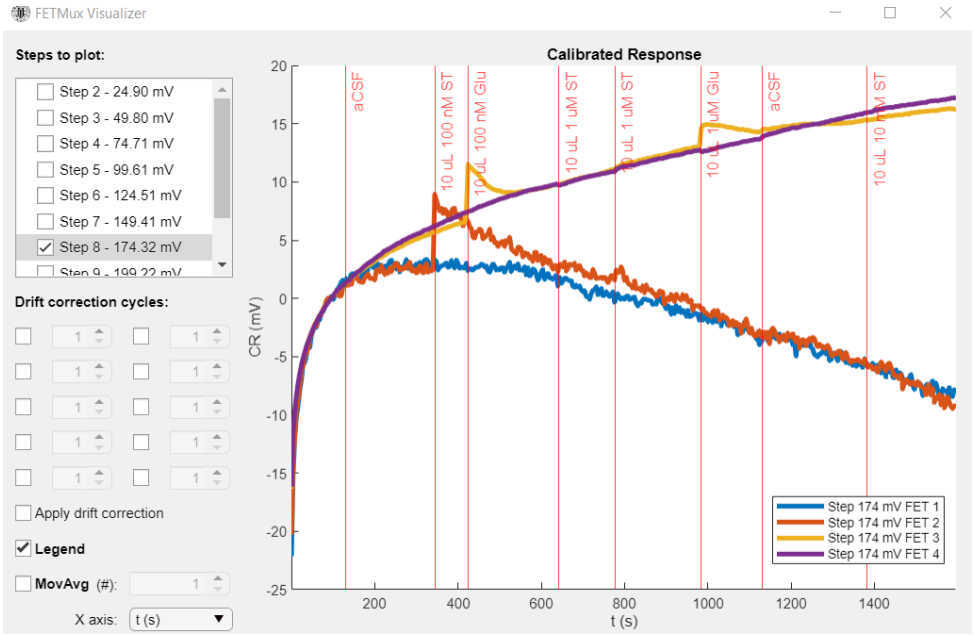

Figure 238. Calibrated Response window on MBMS Data Analysis GUI. Obtained with MATLAB 2018 © Mathworks.

The main plot of the Calibrated Response window is designed to display events and their corresponding labels clearly. As depicted in **Figure 238**, events are represented by vertical lines on the time axis, corresponding to their timestamp.

To address the inherent drift in the CR, the GUI includes a drift correction feature, a measurement technique based on paired biosensors. One is active, with high sensitivity to the target molecule, and the other is passive, with a slight modification to lose its binding capacity.

This allows tracking the drift with the passive bioFET and subtracting it from the active bioFET response. The drift correction cycles table provides a convenient way for users to reproduce the drift by choosing points in which the scrambled and sensitive biosensors' response match, allowing for accurate differential results. Additionally, a moving average function is implemented in the bottom left corner of the window to enhance the noise performance of the measurement. This allows users to easily obtain the CR of the biosensors upon events, as shown in **Figure 239**.

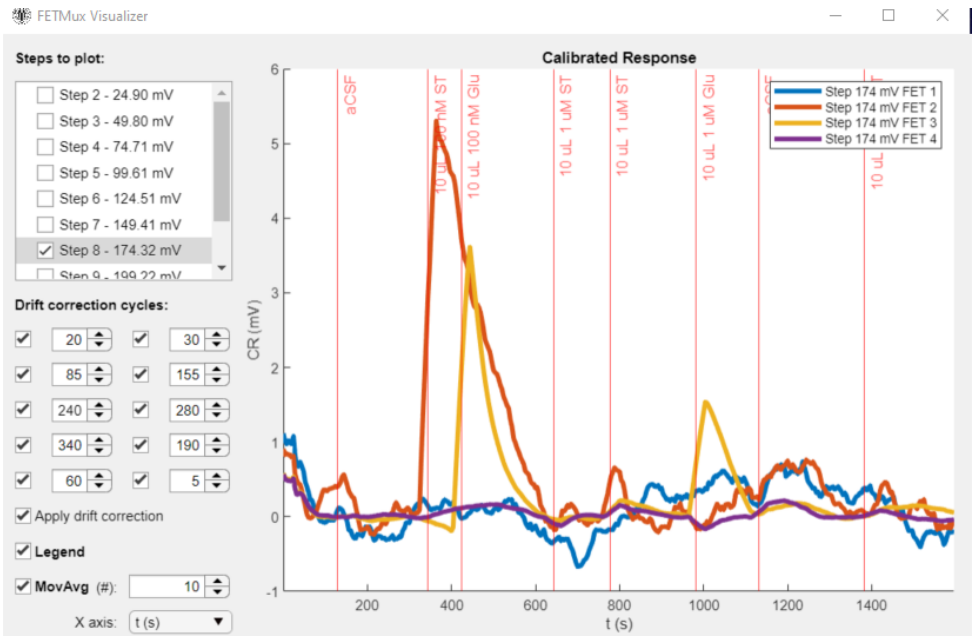

Figure 239. Calibrated Response window on MBMS Data Analysis GUI, results with drift correction and averaging. Obtained with MATLAB 2018 © Mathworks.

6.5. Electrical validation of MBMS vs. Keithley 4200A-SCS Semiconductor Characterizer

As an electrical validation of our equipment, a comparison of the response of the MBMS vs. the commercial silicon characterizer Keithley 4200A-SCS was performed. The stimulus consisted of a sweep of the voltage between gate and source (V_{GS}) applied over an unfunctionalized FET passivated with dodecane thiol, measuring every 10 mV the current through the drain (I_D). Keithley 4200A-SCS current measurement is over source current I_S, being $I_S = I_D + I_G$. Gate current $I_G <<< I_S$, $\therefore I_S \approx I_D$. The notation for the current that flows from the drain to the source is I_{DS}. The sweep was performed from 0 to 200 mV, with 10 mV steps, at 2 mV V_{DS}, with three replicates for each device.

The results obtained (see **Figure 240**) show that our device (MBMS) presents a response with slightly greater linearity (99.74% mean R^2 on MBMS vs. 98.76% mean R^2 on Keithley 4200A-SCS). It should be noted that the decrease in the linearity of the Keithley response is aggravated by the automatic scale change of the current measurement in 5 µA. Regarding the repeatability of each measurement, there is a slightly reduced repeatability for each I_D sample on the MBMS (71 nA on Keithley 4200A-SCS vs. 221 nA MBMS mean standard deviation).

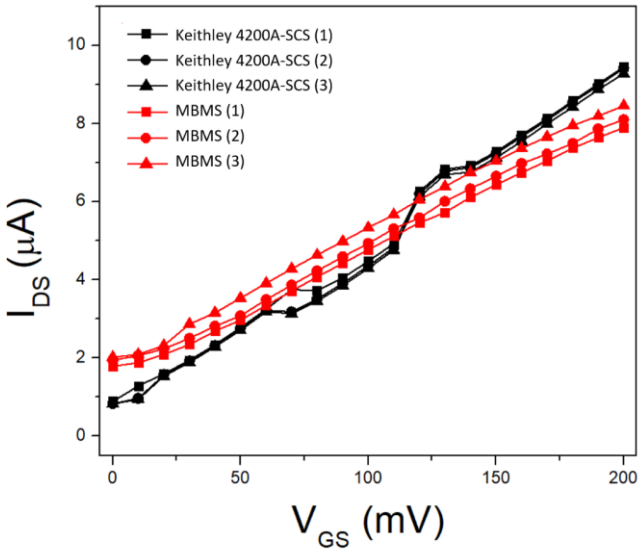

Figure 240. Comparative validation of the multiplexed biosensor measurement system (MBMS) versus silicon characterizer Keithley 4200A-SCS. V_{GS} sweep – I_{DS} measurement comparison.

The offset between the sweeps increase in the I_{DS} during the first measurement cycles is an observed effect with minimal but not negligible influence on the measurement. It ceases after several cycles of operation, with the constant application of V_{DS}. We hypothesize it is related to the gate-drain Miller charge, an effect widely studied in signal amplifiers and power circuits. However, we have not found any literature on electrolyte-gated FETs, which will require further study from our side.

This effect in the Keithley 4200A-SCS measurement is not found, given that it does not perform a periodical measurement but waits for the stability conditions established in the software settings to be met before acquisition.

6.6. Final appearance

The photograph in **Figure 241** shows the printed circuit board (PCB) of the 4-simultaneous-channels measuring system, MBMS. It includes labeled: MCU, insulated serial

communications, digital-to-analog converters, analog-to-digital converters, analog signal adaptation systems, virtual-ground generator, instrumentation amplifiers, shunt resistors, and current-scale multiplexers. All these components are integrated into a compact PCB layout, allowing for a highly portable and versatile measurement tool for aptamer-FET and OECT biosensors. The left side of the PCB has been expanded and freed from any IC close by to ease the measurement of signals of interest during development, keeping apart the cables for the biosensor connection.

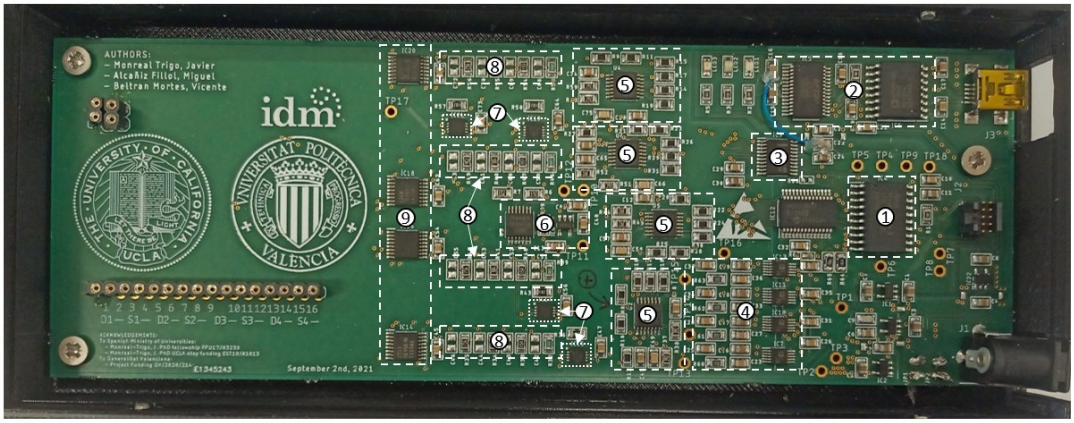

Figure 241. Photograph of the PCB of the 4-simultaneous-channels measuring system MBMS. The components are (1) MCU, (2) insulated serial communications, (3) digital-to-analog converters, (4) analog-to-digital converters, (5) [x4] analog signal adaptation, (6) virtual-ground generator, (7) [x4] instrumentation amplifier, (8) [x4] shunt resistors, and (9) [x4] current-scale multiplexers.

Figure 242. Left: Keithley 4200A-SCS from Tektronix official webpage[27]. Right: MBMS (right) and its predecessor (left) to scale, with the Parameter Analyzer, and with x2 amplification.

[27] Source: https://www.tek.com/en/products/keithley/4200a-scs-parameter-analyzer#. Accessed March 28th, 2023.

Our custom hardware aims to measure small currents with low noise while being portable and lightweight, as shown in **Figure 242**, with dimension scales.

6.7. Reproduction guide

In the following virtual space can be found:

- Gerber files and bill of materials for ordering a MBMS PCB.
- Firmware files for flashing the ATSAMD11D14A microcontroller.
- STL parts to 3-D print the box.
- Bill of materials for the MBMS assembly.
- MATLAB software for the real-time control Graphic User Interface deployment.
- MATLAB software for the data analysis tool.

Link to virtual space: https://github.com/JMonrealT/MBMS. Share, build, and modify MBMS, registered under BY-NC-SA Creative Commons 4.0 License.

7. Validation

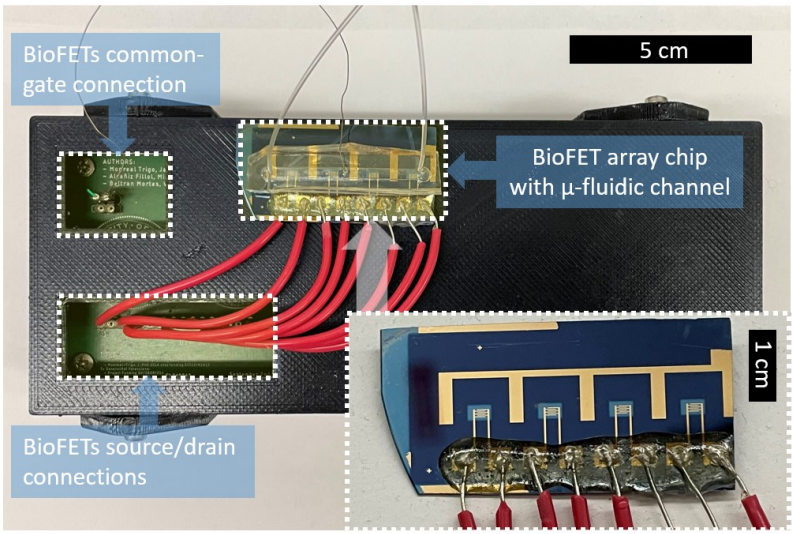

Figure 243. Experiments setup: MBMS platform connected to the bioFET array chip with the µ-fluidic channel. Detail on the bioFET array chip without the µ-fluidic channel.

The validation of the MBMS device is essential to demonstrate its performance and capabilities. To achieve this, two experiments were carried out. The first experiment involved the simultaneous pH measurement using all four channels of the device, resulting in the

generation of a calibration curve. The second experiment involved the preliminary measurement of two different neurotransmitters, glutamate and serotonin, using aptamer-functionalized biosensors paired with scramble-sequence aptamer biosensors for drift correction. These experiments provide a real evaluation of the device's capabilities and serve as a foundation for further research and applications.

In both of them a PDMS μ-fluidic channel for the solution flow through the aptamer-FET biosensor array is employed. The connection of the Ag/AgCl gate electrode, drain, and source connections to MBMS are shown in **Figure 243**.

The chemical materials employed for the validation experiments are:

- Purchased from Sigma-Aldrich:
  - 3-aminopropyl)trimethoxysilane (APTES)
  - Trimethoxy(propyl)silane (PTMS)
  - 1-dodecanethiol
- From DOW chemical:
  - Polydimethylsiloxane (PDMS)
- From MG chemical:
  - Silver epoxy.

7.1. Simultaneous pH measurement in microfluidic system

To functionalize the FETs for pH sensing, (3-aminopropyl)trimethoxysilane and trimethoxy(propyl)silane 1:9 (v/v) were thermally evaporated via vapor-phase deposition onto In_2O_3 surfaces at 40 °C for 1 h followed by 10 min curing on a hot plate at 80 °C. Then, the entire device was incubated in 1 mM ethanolic 1-dodecanethiol for 1 h to passivate Au electrodes.

The fluidic system employed in the experiment included a pressure generator (Elveflow AF1 Mk2), flow rate sensor (Elveflow MFS4), and multiplex pneumatic valve switch (Elveflow Distributor MUX) capable of delivering up to seven different solutions. The system was controlled using the Elveflow smart interface GUI.

Figure 244 represents the fluidic system is shown, in which all six channels are filled with a buffer of different pH values. In the representation, the drain current response of each biosensor will vary according to the instant presence of the target analyte in the flow.

The different pH solutions sequentially flowed onto the bioFET array (200 µL/min) to validate the real-time response of the multiplexed sensing system. The calibrated response (CR) is shown as the final output response.

To measure simultaneously the transimpedance response over multiple biosensors, pH variations from 7.4 to 5.5 and back to 7.4, with steps at pH 7, 6.5, and 6, were applied to a four-channel bioFET array. Each biosensor was biased at 1 mV V_{DS}, performing an IV-sweep. The applied V_{GS} of 0 to 200 mV, with a step of 250 ms, 25 mV was oversampled with a 5 kHz I_D sampling rate (every 200 µs). Between sweeps, a hold time of 750 ms was applied at 0 mV V_{GS}. Therefore, the total period to complete a sweep is 3 s, and the output sample rate is 333 mHz.

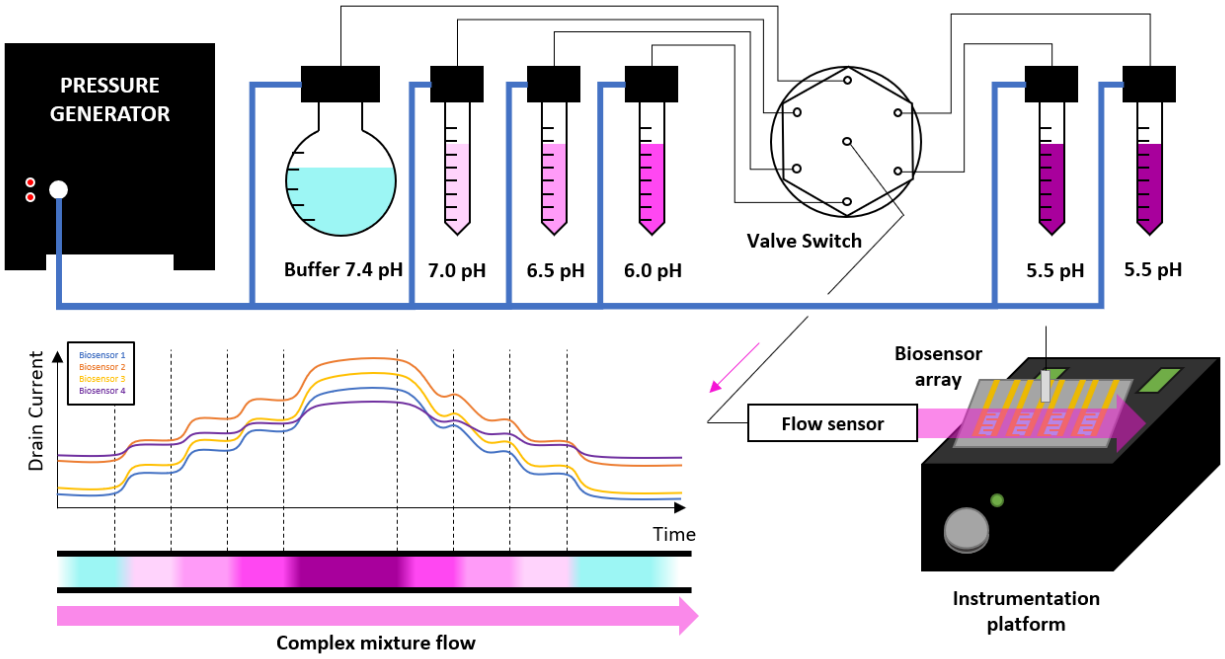

Figure 244. Set-up representation, a controlled flow goes through the biosensor array. Drain current variations are related with flow's pH. pH in flow is controlled, providing six different solutions, arranged with different pH levels. Each channel responds by varying its drain current according to the pH in the solution.

The pH biosensor development based on In_2O_3 channel FET technology has already been characterized (see Wang *et al.* [476]). The self-assembly of the (3-aminopropyl)triethoxysilane (APTES) diluted with trimethoxy(propyl)silane (PTMS) creates a pH-sensitive interface over the channel of the FET. Increasing pH values will provoke the deprotonation of the APTES amine tail groups while decreasing values will cause its protonation. For our specific situation, given N-type FET-based biosensors, the channel surface charge will be augmented by the decreasing pH values, *i.e.,* increasing I_D and, therefore, the calibrated response.

The calibrated response of each biosensor for the step with $V_{GS} = 100$ mV is shown in **Figure 245a**, with a progressive increase as the medium moves away from 7.4 pH. There is a

time delay in the response of all the FETs taking FET 4 as a reference, with the most extended delay being FET 1. This phenomenon is explained by the arrangement of the biosensor array, in which the first FET in the succession of the fluidic system was FET 4, and the last was FET 1. In **Figure 245b**, the calibrated response vs. pH variations is shown in both directions, decrease and increase, showing the reversibility of the biosensor.

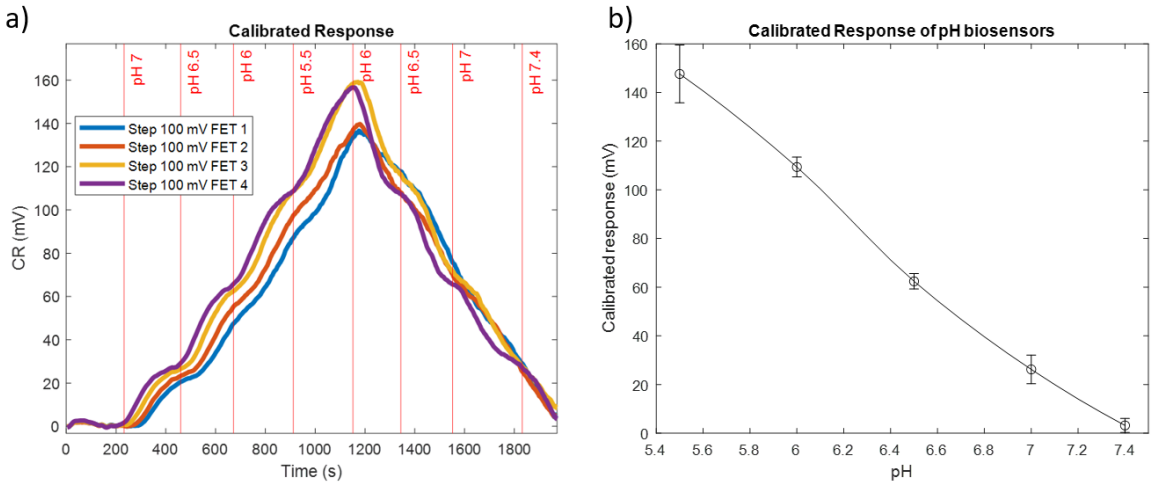

Figure 245. Calibrated response for a multiplexed measurement of 4 bioFETs: (a) Calibrated response measurement over biosensor array. (b) Calibrated response versus pH calibration curve.

7.2. Preliminary measurement of neurotransmitters

The preliminary measurement of neurotransmitters, serotonin and glutamate, is performed using all four channels of MBMS. Instead of using a flow system, different target molecule concentrations in aCSF are pipetted into the channel, with already 200 µL aCSF.

For the measurement of each target molecule, a pair of biosensors is employed, obtaining a differential signal. Both bioFETs of the pair are manufactured simultaneously in close positions in the resulting array. This allows they will match their drift responses associated with their parasitic capacitances. Each pair consist of a sensitive aptamer-FET biosensor (active), and a scrambled-sequence-aptamer functionalized FET biosensor (control). Scrambling the sequence offers the aptamer-FET almost the same electrical behavior as its full-sequence aptamer but losing its conformational change capabilities upon the presence of the target molecule.

The chemical methods for the reproduction of the aptamers ST18T2 (targeting serotonin) and Glutamate (targeting glutamate) will be available upon publication from our collaborators from Andrews' group (UCLA).

Each biosensor was biased at 1 mV V_{DS}, performing an IV-sweep. The applied V_{GS} of 0 to 250 mV, with a step of 250 ms, 25 mV was oversampled with a 5 kHz I_D sampling rate (sampling every 200 µs). Between sweeps, a hold time of 1250 ms was applied at 0 mV V_{GS}. Therefore, the total period to complete a sweep is 4 s, and the output sample rate is 250 mHz. **Figure 246** shows the results of the average I_{DS} current variations for one single step (175 mV) of the IV stimulation. The events are colored in blue for aCSF addition, purple for glutamate, and red for serotonin, each adding 10 µL.

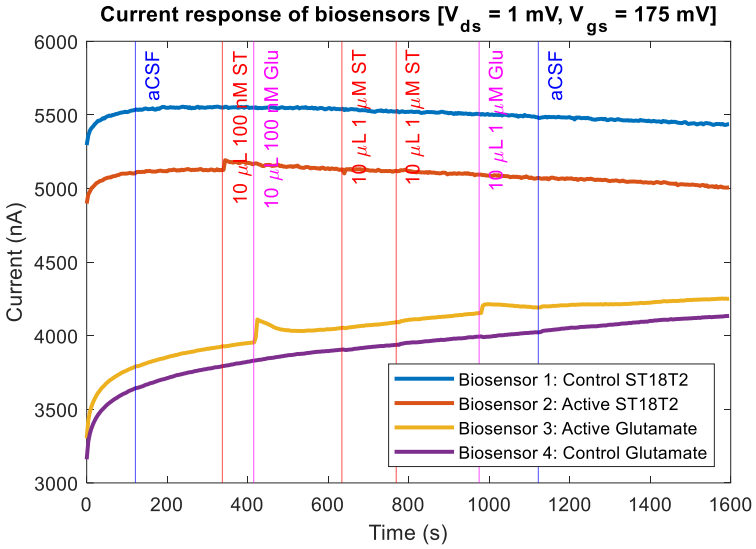

Figure 246. Plotting mean of the last 750 samples of the step V_{GS} = 175 mV vs. time. Reproduced from [434].

Following the example we described in *6.4. Application code for the PC Data Analysis Tool*, the calibrated response for each channel is obtained, as shown in **Figure 247**.

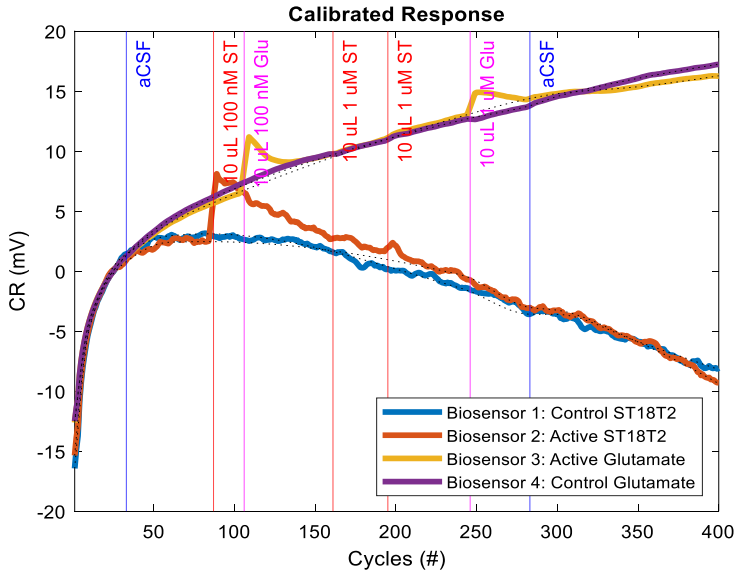

Figure 247. Calibrated response (CR) for every channel, was obtained with the cycles 20 to 30 as the baseline. Values are shown with a moving average of 5 samples. The dotted lines show the estimated drift of the CR. Each active channel's estimated drift is obtained regarding the control channel. Reproduced from [434].

By correcting the drift, the interpretability of the signal becomes crystal clear, as shown in **Figure 248**. The signal-to-noise ratio depends on the root-mean-squared variation of the noise on both control and active channels. The peak signal for serotonin quantization is 6 mV vs. a peak-to-peak noise of 1 mV for the detection of 100 nM 10 µL in 220 µL, *i.e.*, 4.6 nM. The peak signal for glutamate is 5 mV vs. 0.5 peak-to-peak noise for 4.4 nM. With these preliminary results, we can estimate that the limit of detection would be around 1 nM for both analytes.

It is important to note the saturation effect that seems to appear. The higher concentration injections (up to 84 nM of serotonin and 42 nM of glutamate) offer a smaller response than their predecessors. This phenomenon and the temporal response and dissociation are two issues to be addressed and improved to make the aptamer-FET biosensors the gold standard for biochemical measurement.

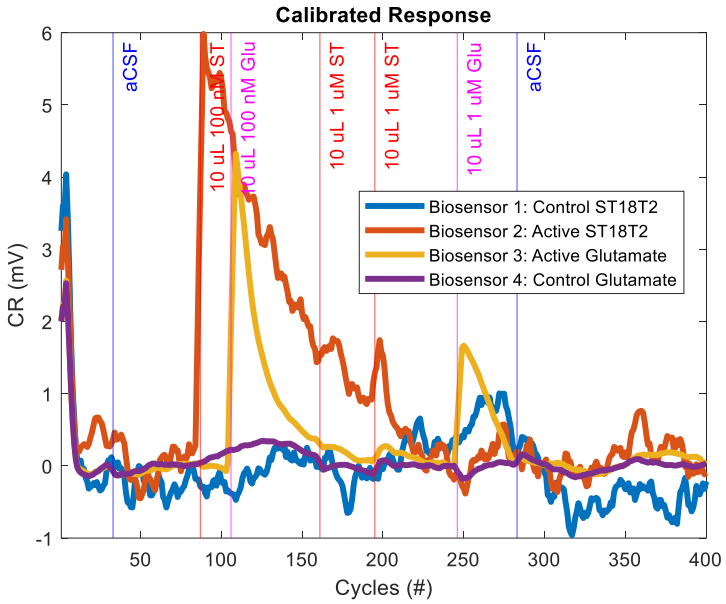

Figure 248. Drift corrected calibrated response of channels 2 and 3 vs. 1 and 4 respectively. Reproduced from [434].

8. Miniaturized FET array electrical response

From Andrews' group, the *Neuroprobe* is the state-of-the-art miniaturization of this sensor technology, with two aptamer-FET biosensors in a 50 µm width tip to be inserted *in vivo*. With this device, they have been able to detect from fM to µM serotonin concentrations, with a 10-second temporal resolution with the instrumentation platform used (see Zhao *et al.* [446]).

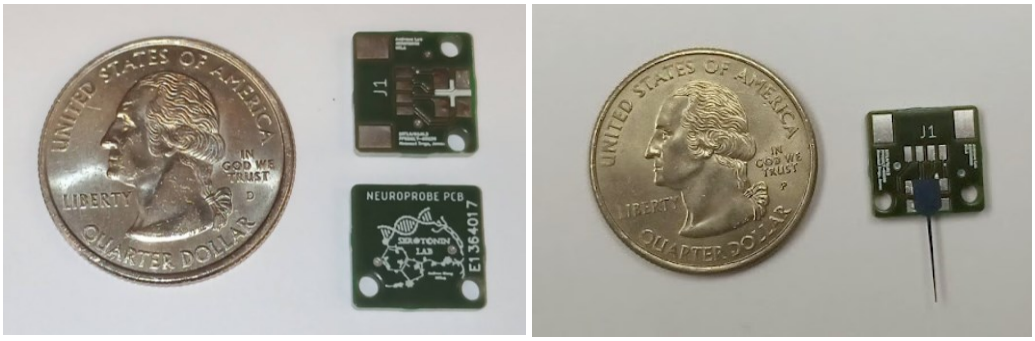

Figure 249. Neuroprobe PCB without (left) and with (right) the Neuroprobe itself, with a quarter dolar for size reference.

Using PCB (standard fabrication technologies, Eurocircuits © 6C class), we designed a reliable interface to connect the Neuroprobe to MBMS. The Neuroprobe is connected to the PCB through conductive epoxy (MG chemical). The PCB has a right-angle 4-header 1.25 mm pitch Molex connector, to which a Picoblade connector can be connected. With 12 mm x 12 mm dimensions, the Neuroprobe PCB is shown in **Figure 249**.

The stabilization time for I_{DS} after a V_{GS} step is compared for the Neuroprobe µ-FETs and the cm-scale FETs employed in the validation of MBMS. 2 mV V_{GS} steps at 20 ms were applied for both of them. The V_{GS} range of the IV sweep and V_{DS} were chosen to maximize each bioFET response.

- The µ-FETs were swept from 0 to 400 mV V_{GS} with 30 mV V_{DS} biasing.
- The cm-FETs were swept from 0 to 180 mV V_{GS} with 5 mV V_{DS} biasing.

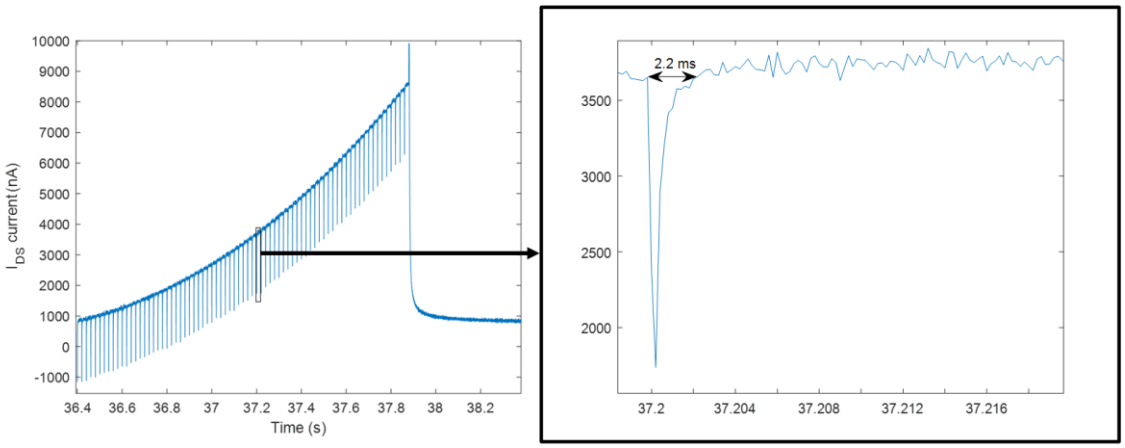

Figure 250. cm-FETs sweep response (left) and V_{GS} = 84 mV step zoom in (right). The stabilization time for I_{DS} = 2.2 ms.

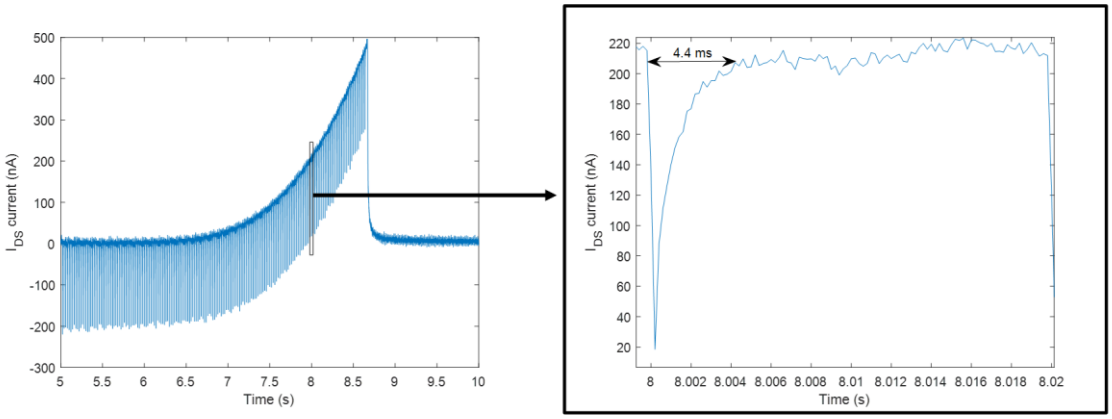

Figure 251. μ-FETs sweep response (left) and $V_{GS} = 324$ mV step zoom in (right). The stabilization time for $I_{DS} = 4.4$ ms.

The step chosen to zoom in was at $V_{GS} = 324$ mV for the μ-FETs, and $V_{GS} = 84$ mV for the cm-FETs, corresponding to steps in the mid-range of their ohmic-region response. The responses are shown in **Figure 250** and **Figure 251**.

The needed stabilization time for the I_{DS} current after a V_{GS} step, for the needed V_{DS} biasing conditions, makes the electrical response of the Neuroprobe twice the test FET array.

9. Conclusions and next steps

The developed platform has a temporal resolution per sample of 200 μs, with the capability to bias and sweep all four channels simultaneously. This allows nominally sweeping all channels at 5 Hz with 1000 points per sweep or 50 Hz at 100 points per sweep. This sampling rate would enable the monitoring of fast chemical processes, such as the ones present at the synapse between nerve endings, by selectively capturing their neurotransmitters. The linearity and resolution are comparable for the application domain to that obtained with the Keithley 4200A-SCS silicon characterizer.

The temporal response of the bioFETs is conditioned by two factors: surface chemistry and current stabilization upon bias and gate voltage change. Regarding the former, the two phenomena in the validation experiments are the APTES amine tail groups protonation-deprotonation with the pH variations and the aptamer association-dissociation times with the target molecules. On the other hand, the electrical current stabilization is inversely proportional to the bioFET capacitance, which in turn exhibits a direct relationship with the gate width/length and the gate-channel area ratio of the bioFET. In both our validations, the geometrical relationships of the design induced a temporal response in the order of few

milliseconds to the current response of the bioFET I_D vs. a voltage change in V_{DS} or V_{GS}. This situation is particularly unfavorable for the stability of the measured current signal in the face of a transient bias in voltage, demonstrating the stability of the proposed common-gate virtual-ground topology. The temporal response of the biosensor to pH changes is in the order of tens of seconds ($\tau \approx 75$ seconds), thus being the surface chemistry the limiting factor for the temporal resolution of the biosensor. The same happens with the second validation. Even if the association time for both serotonin and glutamate is extremely short, the dissociation time was $\tau \approx 25$ seconds for the glutamate aptamer and $\tau \approx 200$ seconds for the serotonin aptamer.

The main novelty of the electronic design is that it allows the simultaneous multiplexed measurement of several channels in a miniaturized bioFET array. Newly using the gate as the system reference, it is possible to perform the V_{GS} and V_{DS} voltage application with a single gate avoiding contest situations that would occur when trying to maintain the classical common-source topology. There are short-time current transitions in the order of a few milliseconds because, in the new topology, V_{DS} is a function of V_{GS}. A V_{GS} change is made by a change in the V_S, being V_G constantly connected to a virtual ground. Hence, to keep V_{DS} steady, each V_S change shall be followed by a change in V_D. The delay between V_S and V_D changes induces transitory currents, enhanced by the intrinsic capacitance in electrolyte gated bioFETs. This effect needs further study. Nevertheless, in the worst-case scenario of 5 ms stabilization time per step, up to 10 steps can be applied at 10 Hz IV-sweep, making the MBMS a versatile and flexible tool for the research and development of new aptamer-FET biosensors *in vitro* and *in vivo*.

A new optimized GUI and firmware have already been developed, which allows the application of totally customizable V_{GS} for each channel independently. For the IT mode, it allows the configuration of the sample period. All channels can be setvup from the first tab of the new GUI, as shown in **Figure 252**. From both the *Single-FET View* tab and the *Multi-FET View* tab, all parameters (current scales, V_{DS}, and, if available, V_{GS}, can be changed), as shown in **Figure 253** and **Figure 254**. Pressing any UPDATE button sends the new configuration for all channels. The Settings controls placed in the last tab in the former version of the GUI are now available on the bottom side of the new GUI, shared across all tabs.

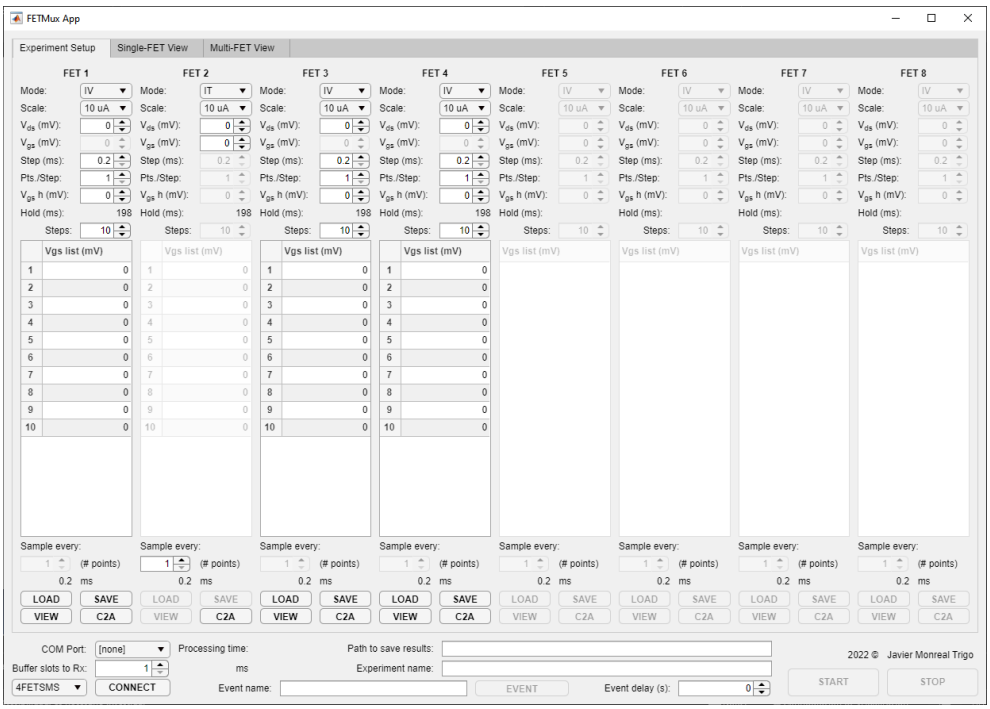

Figure 252. Experiment Setup tab on the new MBMS real-time control GUI. Obtained with MATLAB 2018 © Mathworks.

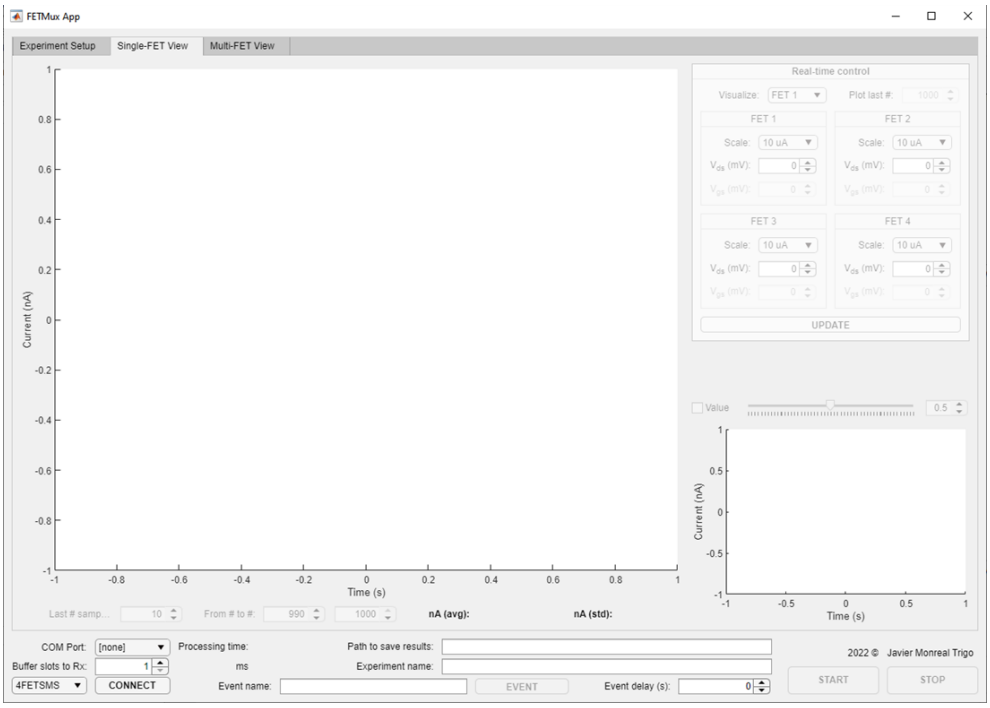

Figure 253. Single-FET View tab on the new MBMS real-time control GUI. Obtained with MATLAB 2018 © Mathworks.

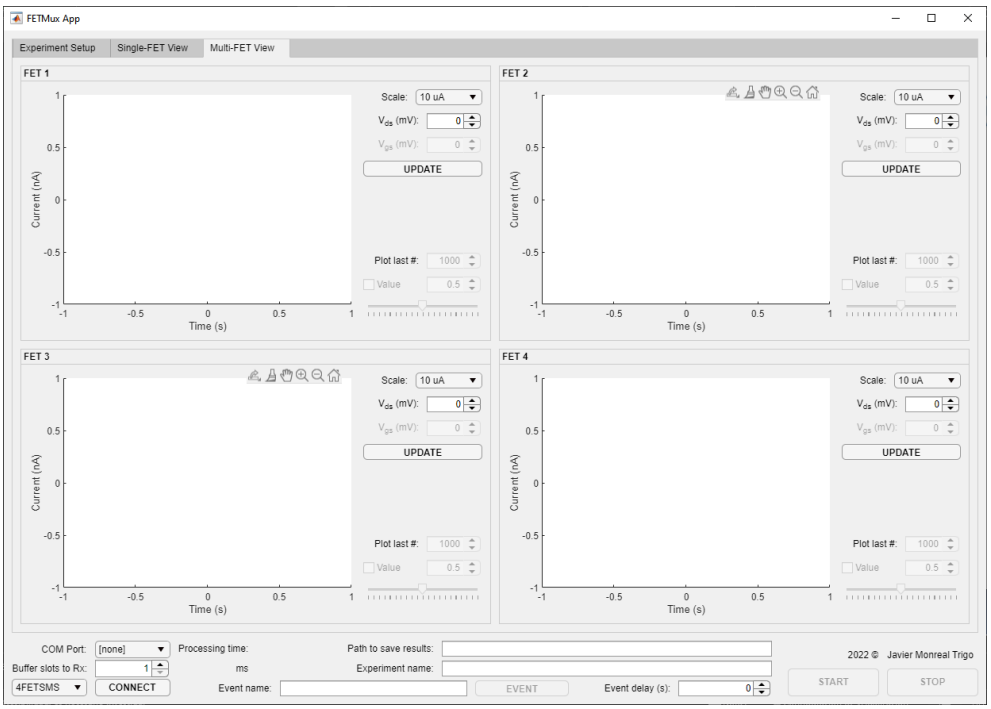

Figure 254. Multi-FET View tab on the new MBMS real-time control GUI. Obtained with MATLAB 2018 © Mathworks.

In the next phase of our research, we aim to thoroughly study of the equations that govern the I_{DS} current spikes upon V_{GS} change. This will enable us to optimize the design of the FET array and instrumentation electronics to reduce the stabilization time. By gaining a deeper understanding of the underlying physics, we hope to improve the performance and efficiency of the device.

Additionally, we will investigate the impact of switched multiplexing on current stabilization. Switched multiplexing offers a trade-off between temporal response and electronics area and consumption reduction. This approach utilizes just one circuit unit for biasing, sweeping, and acquiring the sample for a set of FETs, whereas simultaneous multiplexing requires a circuit for each channel. This reduction in electronics' size is crucial for *in vivo* applications that require high-density probes, one for each analyte to be interrogated in real-time. By carefully balancing the benefits and limitations of different multiplexing approaches, we hope to improve the device's overall performance and make it more suitable for *in vivo* applications.

Conclusions

The most promising approach for treating spinal cord injury is to bridge the lesion by means of stem cells, particularly **neural precursor cells**. These cells must be provided with a **support structure** and **adequate stimuli** to proliferate and generate **functional tissue** connecting both ends of the damaged spinal cord. Designing suitable structures and the necessary stimuli are a core part of tissue and neural engineering. For the generation of these stimuli, we identified three types of techniques as the most promising for the modulation of this cell development, which gives name to the title of this thesis: **pharmacological stimulation, electrostimulation, and optogenetic stimulation**. It is important to note that, in the literature, these techniques are mostly explored separately. The efforts made in this thesis have been directed toward developing platforms for *in vitro* experimentation that would allow their **combination**.

In the framework of this doctoral thesis, we have designed several electronic devices capable of applying these stimuli. In turn, we have developed the necessary instrumentation for real-time measurement of the biochemical responses, thus potentially allowing us to adjust the intensity of the stimulation in real time. The **main contribution** of this thesis is the **design and development of biosensors and bioactuators to advance the exploration of these modulation techniques**. However, in a **transdisciplinary** line of research, the challenges of electronic instrumentation are intimately linked to other challenges. As contributions of this doctoral thesis work beyond the electronic design, it is worth mentioning: the design, characterization, and validation of **a new technology for controlled drug release by electrical stimulation**; and the study, design, and evaluation of different combinations to obtain a **scaffold based on conductive polymer potentially implantable** in the spinal cord injury, adapted for the *in vitro* study of electrostimulation.

Going into the details of these latter contributions, the design and evaluation of the new scaffold have been carried out in collaboration with the RTN group of the Centro de Investigación Príncipe Felipe. **We have developed a biocompatible platform for evaluating different electrostimulation protocols**, intending to explore it **all together with the pharmacological stimulation by electrically controlled release**, and also bearing in mind its implantable transfer for *in vivo* research. The scaffold is based on a flexible PET substrate screen-printed with PEDOT:PSS activated with Ar plasma and coated with Matrigel and PLL. However, the effects of electrostimulation have been primarily adverse for cell viability, and new approaches using nanoparticles have promising results that are worth evaluating before proceeding with our approach based on screen-printed PEDOT:PSS.

On the other hand, regarding pharmacological stimulation, in this work, we have developed, characterized, and validated, in collaboration with the NanoSens group of our institute, **a technology for controlled drug release by low-voltage electrical stimulation**. The bipyridine-heparin molecular gates are electrochemically sensitive to voltages below 700 mV, allowing the release of a pharmacological load using **an external electrical pulse that is harmless to the cells present**. This technology **has been incorporated into a conductive substrate**, providing enhanced pharmacological stimulation capabilities. In particular, the enhanced substrate is a PEDOT derivative. Furthermore, we have also explored the capabilities of these technology to endow **ceramic and metallic surface**, such alumina and gold, with electrically control drug release, with satisfactory preliminary results.

For the combined application of electrostimulation and the electrical stimuli needed to induce controlled drug release, we have designed two electronic devices, FAEVIS and IVESDRIS. These have been characterized and validated in real applications, the latter being an improved version of the former. However, there have been no opportunities to combine both techniques in the duration of this PhD thesis.

The advances made in stimulation by controlled light radiation in cells genetically modified to be sensitive to light through the incorporation of proteins called *opsins* have also been made in collaboration with the RTN group. **Regarding optogenetic stimulation devices, we have designed a device for multiple controlled irradiations in commercial 24-well cell culture arrays, OSIVE Slim**. The main innovation of this device is its reduced dimensions, allowing it to fit inside an inverted confocal microscope. **Imaging simultaneously with stimulation allows the evaluation of transient responses, such as calcium waves**, which are otherwise invisible. A complementary electronic measurement device has also been designed to characterize the optogenetic stimulation equipment in terms of irradiance, OSIVE IMS. The optogenetic stimulation device, OSIVE Slim, can be used simultaneously with the electrostimulation and release device, FAEVIS or IVESDRIS. However, the separate validation of the different stimulation possibilities has consumed the entire duration of the thesis, and the actual exploration of the combinations between the techniques is one of the promising next steps to be undertaken.

Finally, the state of the art refers to the need for measurement of the responses induced by modulation techniques in order to be able to adjust their intensity. **Every stimulus has a threshold intensity at which it produces the desired effect and a limit value at which it produces an adverse effect**. These threshold and limit values are dynamic, depending on multiple factors such as the cellular stage of development, the presence of other stimuli, and environmental nutrients. **The cellular response**, which is **biochemical in nature**, is produced by the secretion and uptake of various analytes. Among them, for neural precursor cells, neurotransmitters are

of particular interest. Serotonin secretion is one of the most studied biomarkers. Likewise, feedback on the growth factors and other drugs released or introduced as modulation stimuli to neural development is also of particular interest. In this thesis's framework, we collaborated with the Serotonin Group at the University of California, Los Angeles (UCLA), to develop ultra-selective biosensors for real-time measurement of analytes. The biosensors are based on field effect transistors (FET) with modified channels, grafting aptamers, molecular chains that change their conformation when they anchor a target molecule. This doctoral thesis contributes to the **design of the necessary instrumentation to measure the variations in transimpedance** that these biosensors offer as transduction of the amount of target analyte in the measured solution. **The novelty of this instrumentation is the ability to simultaneously measure several spatially proximate biosensors with a temporal resolution far superior to that offered by commercial silicon characterizers**. The instrumentation, MBMS, has been validated by simultaneous measurement of pH variations and preliminary measurement of the first functionalized biosensors for serotonin and glutamate measurement. However, significant challenges remain before obtaining closed-loop feedback from techniques for modulating neural precursor cell development.

Future lines of research

Continuing with the work described in the first three chapters of the thesis, we are currently working on obtaining an **electrostimulation protocol** favorable for the viability, proliferation, differentiation, and elongation of **neural precursor cells** *in vitro*, together with our collaborators from the RTN group at the CIPF. We are also evaluating alternatives with the Polymer Materials group of the Universitat de València's Materials Science Institute (ICMUV) for several purposes. We aim to provide the conductive polymer substrate PEDOT:PSS with carboxy groups to **incorporate electro-responsive nanoparticles**. We are also assessing structuring the conductive polymer as nanoparticles, which would allow building 3D scaffolds more suitable for the *in vivo* stage. Having a conductive polymer-based platform with the capacity to host voltage-responsive nanoparticles and good properties for cell culture would allow **exploring the combination of electrostimulation and pharmacological stimulation** for modulating the development of neuronal precursor cells as never before.

The possibilities opened up by the new technology of electrically controlled drug release are hardly predictable. Preliminary results of release from nanoparticles anchored to metallic surfaces are auspicious. Likewise, we had some satisfactory first experiences of electrostatic release from gated porous ceramic surfaces. In this case, entrapping the charge directly in the surface's pores using the same molecular gates. One of the tasks ahead is the **precise electrodynamic characterization of the release**, *i.e.*, as a function of voltage and time, for each of the described circumstances: with nanoparticles in suspension, anchored to a conductive polymer, anchored to a metallic surface, or with the molecular gates directly trapping the charge in the pores of a ceramic surface; which we aspire to perform continuing with the collaboration of the NanoSens group of our institute IDM.

In the ongoing ERC Advanced Grant EDISON (101052997), we propose, based on these advances, to develop **engineered particles for chemical communications**: that can communicate with each other, with cellular organisms, and even respond chemically to complex orders encoded in an electromagnetic transmission. Developing **microbots, micrometric-dimension devices integrating electronics,** is the major challenge for the latest objective. We aim to design microdevices capable of operating with external radiation as a supply source. Also, this radiation would carry the trigger command, so the microdevice must feature decoding capabilities. Finally, upon the reception of the command, it shall be capable of **applying a local electrical** pulse to induce the release in voltage-responsive **nanoparticles anchored to their metal microelectrodes**. We have designed and tested a proof-of-concept based on a PCB with satisfactory results. We have also developed a new hardware platform with enhanced current

measurement resolution to measure the release-related electrical currents in micrometric surface areas bearing voltage-responsive nanoparticles. Its firmware and software are yet to be implemented.

In the application of **nerve tissue regeneration, developing an interactive software environment** for the programming and monitoring of *in vitro* assays, as well as for the post-processing of the results, is one of the following steps to be carried out. On the other hand, we have designed a **first prototype PCB to apply these electrical stimuli *in vivo***. The prototype, on a rigid PCB for its first evaluation, is designed for future transfer to flexible PCB. It is **ultra-low power and is powered and commanded by infrared radiation**. Penetration and dissipation experiments at 890 nm wavelength allow estimating that the **implantable device** could operate at 1-1.5 cm depth, adequate for its implant on the lesion site of the spinal cord injury. On the other hand, instead of inducing release across all the scaffold, this prototype has an array of electrodes and counter electrodes distributed on the surface of the scaffold, with which **we aim to evaluate the concept of the partial release** in a continuous conductive polymer carrying electro-responsive nanoparticles. Developing other electrochemically sensitive molecular gates at other potentials would allow the selective release of different drugs trapped in nanoparticles with different molecular gates.

As can be appreciated, the application of electrostimulation and controlled release techniques have significant challenges ahead. However, they contrast with our vision for optogenetic stimulation techniques. We are focusing our efforts on enabling the combination of electrostimulation and controlled release. We hope that in the future, we will be able to incorporate this third technique of modulating neural precursor cell development into our studies.

Regarding the **development of biosensors**, we have multiple lines of research underway with really promising expectations. They range from **aptamer-FETs**, whose advances have been described in depth in this PhD thesis, to **electronic tongues**, along with **electrochemical transistors** (OECTs) and **impedance spectroscopy** (IES) as aptamer-functionalized biosensors. Electrolyte-gated biosensors, such as aptamer-functionalized FETs and OECTs, exhibit high Miller capacitances that limit transistor response time to changes in bias and gate voltages. An **in-depth study of their physicochemical characteristics** is one of the main tasks we must address **to sharpen the design of electronic instrumentation** and improve the performance of these biosensors. Likewise, because aptamers are designed to have an ultraselective response in a very short time upon an increase in the concentration of the target analyte, their response time to a decrease in this concentration is protracted by default. There are indications that **the dissociation times can be reduced by appropriate electrical stimulation**, so we intend to continue collaborating with the Serotonin Group at UCLA to investigate further and overcome

these limitations. We have already designed a new device that will allow greater flexibility in the choice of connection topology in a biosensor array and measuring the circulating currents in each terminal. However, we must develop the firmware and software necessary for its control.

Serotonin monitoring is the most important biomolecule to establish a closed control loop in applying techniques to modulate neural precursor cell development. The Serotonin group has recently published *in vivo* real-time monitoring of serotonin study using electrochemical techniques inspired by the operation of voltammetric electronic tongues (e-tongues) (Movassaghi *et al.* [442]). We are assessing to **integrate *in vitro* serotonin e-tongues** or other non-selective electrochemical biosensors **to explore stimulation control based on this biochemical variable**.

Finally, during this thesis, we published a paper in which we could **detect bladder cancer in urine samples using an e-tongue** (Monreal-Trigo *et al.* [482]). E-tongues have been used in a wide range of applications in agrifood and biomedicine. In this sense, we are evaluating different applications based on the last publication. We are assessing the use of disposable electrodes to detect bladder cancer, which may ease its wide use in the clinical routine. Moreover, we are analyzing the detection of prostate cancer from urine samples, distinguishing between hyperplasia, cancer, or none of them, by advanced multivariate algorithms. **We hope to be able to transfer the developments in biosensors for a specific application to other applications, which in turn will allow us to deepen our knowledge of how biosensors work and improve their performance**.

References

[1] D. Van Der Kooy, S. Weiss, Why stem cells?, Science (1979). 287 (2000) 1439–1441. https://doi.org/10.1126/science.287.5457.1439.

[2] P. Gao, M.P. Postiglione, T.G. Krieger, L. Hernandez, C. Wang, Z. Han, C. Streicher, E. Papusheva, R. Insolera, K. Chugh, O. Kodish, K. Huang, B.D. Simons, L. Luo, S. Hippenmeyer, S.H. Shi, Deterministic Progenitor Behavior and Unitary Production of Neurons in the Neocortex, Cell. 159 (2014) 775–788. https://doi.org/10.1016/J.CELL.2014.10.027.

[3] M. Götz, Revising concepts about adult stem cells: Imaging adult neurogenesis reveals surprising behavior of progenitor cells, Science (1979). 359 (2018) 639–640. https://doi.org/10.1126/science.aar7732.

[4] M. Götz, S. Sirko, J. Beckers, M. Irmler, Reactive astrocytes as neural stem or progenitor cells: In vivo lineage, In vitro potential, and Genome-wide expression analysis, Glia. 63 (2015) 1452–1468. https://doi.org/10.1002/GLIA.22850.

[5] F.M. Watt, B.L.M. Hogan, Out of eden: Stem cells and their niches, Science (1979). 287 (2000) 1427–1430. https://doi.org/DOI: 10.1126/science.287.5457.1427.

[6] G. Kolios, Y. Moodley, Introduction to Stem Cells and Regenerative Medicine, Respiration. 85 (2013) 3–10. https://doi.org/10.1159/000345615.

[7] J.K. Biehl, B. Russell, Introduction to Stem Cell Therapy, J Cardiovasc Nurs. 24 (2009) 98. https://doi.org/10.1097/JCN.0B013E318197A6A5.

[8] V. Martínez-Cerdeño, S.C. Noctor, Neural progenitor cell terminology, Front Neuroanat. 12 (2018) 104. https://doi.org/10.3389/fnana.2018.00104.

[9] J.C. Furlan, V. Noonan, A. Singh, M.G. Fehlings, Assessment of Impairment in Patients with Acute Traumatic Spinal Cord Injury: A Systematic Review of the Literature, J Neurotrauma. 28 (2011) 1445. https://doi.org/10.1089/NEU.2009.1152.

[10] L.A. Simpson, J.J. Eng, J.T.C. Hsieh, D.L. Wolfe, The health and life priorities of individuals with spinal cord injury: A systematic review, J Neurotrauma. 29 (2012) 1548. https://doi.org/10.1089/NEU.2011.2226.

[11] S.L. James, M.S. Bannick, W.C. Montjoy-Venning, L.R. Lucchesi, L. Dandona, R. Dandona, C. Hawley, S.I. Hay, M. Jakovljevic, I. Khalil, K.J. Krohn, A.H. Mokdad, M. Naghavi, E. Nichols, R.C. Reiner, M. Smith, V.L. Feigin, T. Vos, C.J.L. Murray, J.E. Sunshine, M.G. Yost, R.G. Ellenbogen, R. Kalani, S.D. Morrison, C.S. Crowe, B.B. Massenburg, A. Theadom, B.J. Te Ao, S. Balalla, K.M. Jones, R. Ofori-Asenso, S. Li, S. Sobhani, S.M. Hosseini, M.A. Mansournia, M. Yaseri, M. Anjomshoa, S.M. Mousavi, A. Haj-Mirzaian, A. Haj-Mirzaian, R. Malekzadeh, H. Poustchi, G. Roshandel, S.G. Sepanlou, M. Afarideh, A. Esteghamati, S. Esteghamati, M. Ganji, A. Kasaeian, A. Rahimi-Movaghar, S. Eskandarieh, M.A. Sahraian, M. Shams-Beyranvand, N. Abbasi, F. Farzadfar, S.N. Irvani, V. Rahimi-Movaghar, P. Salamati, M. Sharif-Alhoseini, S.M. Fereshtehnejad, K.K.V. Mate, R.

Abdulkader, H.N. Abraha, T.D. Kassa, Y.L. Nirayo, K.G. Weldegwergs, K.E. Gezae, Z.M. Zenebe, M.G. Degefa, A. Kahsay, S.W. Asgedom, A.K. Gebre, E.M. Yimer, A.B. Belachew, H. Meles, J.C. Adsuar, S. Zodpey, S. Agrawal, A. Awasthi, G.A. Kumar, A. Ahmadi, F. Najafi, F. Rajati, H. Khazaie, M.H. Farzaei, M. Moradi, S. Rezaei, M. Soofi, S. Siabani, S. Rezaeian, M.B. Ahmed, T.T. Gebrehiwot, G.T. Feyissa, M.A. Hussen, A. Aichour, I. Aichour, M.T.E. Aichour, R.O. Akinyemi, M.O. Owolabi, N. Akseer, Z.A. Bhutta, A. Badawi, F. Alahdab, G.M. Kassa, A. Alebel, F.W.S. Wagnew, Y.A. Belay, C.T. Leshargie, S.A. Alghnam, B.A. Ali, U. Alsharif, M.H. Temsah, K. Altirkawi, D. V. Davitoiu, S. Hostiuc, M. Beuran, I. Negoi, C.L. Andrei, H. Ansari, M.G. Ansha, C.A.T. Antonio, S.C.Y. Appiah, M. Levi, F. Ariani, M. Biffino, N.G. Asefa, S. Atique, M.A. Rahman, T. Wijeratne, B.P. Ayala Quintanilla, T.B. Ayuk, P.S. Azzopardi, A. Rafiei, H. Badali, M. Mohammadi, M. Moosazadeh, A. Daryani, A. Banstola, K.B. Tran, S.L. Barker-Collo, T.W. Bärnighausen, N. Bedi, A. Tehrani-Banihashemi, H. Shabaninejad, M. Behzadifar, A. Kabir, M. Yousefifard, M. Moradi-Lakeh, M. Behzadifar, B. Bekele, H.Y. Hassen, A. Henok, B. Biadgo, D.A. Bennett, A.C. Goulart, I.M. Bensenor, P.A. Lotufo, Y.P. Wang, E. Yisma, A. Berhane, K. Deribe, Y.J. Yasin, G.T. Demoz, A. Bhalla, S. Bhaumik, A. Bijani, M. Zamani, N. Bililign, M. Kumar, C. Birungi, S. Boufous, A. Brazinova, A.W. Brown, M. Car, A. Majeed, S. Rawaf, D.L. Rawaf, H. Shoman, R. Cárdenas, J.J. Carrero, Z. El-Khatib, N. Roy, F. Carvalho, J. V. Santos, E. Fernandes, J.P. Silva, C.A. Castañeda-Orjuela, H.J. Hoffman, F. Catalá-López, Y. Chaiah, O. Temsah, A.P. Champs, J.C. Chang, J.Y.J. Choi, D.J. Christopher, C. Cooper, S. Djalalinia, H.P. Do, T.H. Nguyen, D.T. Doku, T.M. Drake, A. Sheikh, I.N. Soyiri, M. Dubey, M.M.M. Santric Milicevic, E. Dubljanin, A. Faro, I. Filip, A. Radfar, F. Fischer, T. Fukumoto, F.G. Gankpe, G. Gopalkrishna, J.A. Haagsma, S. Polinder, A.T. Khoja, G.D. Pinilla-Monsalve, R.R. Hamadeh, S. Hamidi, J.M. Haro, H. Hassankhani, R. Havmoeller, M.I. Hegazy, D. Hendrie, T.R. Miller, D.T. Hibstu, Z.Y. Kassa, M.K. Hole, E. Homaie Rad, G. Hu, O.S. Ilesanmi, S. Jayaraman, R.P. Jha, J.B. Jonas, B. Moazen, Z. Jorjoran Shushtari, J.J. Jozwiak, M. Jürisson, M. Kahssay, M.L. Liben, A. Karch, A.P. Kengne, Y.S. Khader, H. Safari, M.A. Khafaie, N. Khalid, E.A. Khan, M.S. Khan, M.S. Usman, T.J. Siddiqi, Y.H. Khang, J. Khubchandani, A.A. Kiadaliri, D. Kim, Y.E. Kim, S.J. Yoon, A. Kisa, A.S. Winkler, A. Koyanagi, B. Kuate Defo, B. Kucuk Bicer, R. Lalloo, M. Moradinazar, F.H. Lami, V.C. Lansingh, D.O. Laryea, A. Latifi, S. Safiri, R. Lunevicius, N.B. Mahotra, M. Majdan, A.L. Manda, M.M. Mehndiratta, V. Mehta, A. Melese, P.T.N. Memiah, W. Mendoza, G. Mengistu, M.S. Shiferaw, M.G. Tekle, T.J. Meretoja, A. Meretoja, C.E.I. Szoeke, T. Mestrovich, T. Miazgowski, G.K. Mini, A. Mirica, E.M. Mirrakhimov, M. Molokhia, L. Monast, L. Ronfani, S. Mondello, G. Moradi, M.M. Moschos, S. Murthy, K.I. Musa, G. Mustafa, G. Naik, D.C. Schwebel, V. Nangia, B.R. Nascimento, D.N.A. Ningrum, P.S. Nyasulu, A.M.N. Renzaho, F.A. Ogbo, I.H. Oh, A. Okoro, A.T. Olagunju, T.O. Olagunju, P.R. Olivares, S.S. Otstavnov, M.P.A. Dnb, S. Pakhale, A.R. Pandey, K. Pesudovs, S. Prakash, M. Qorbani, A. Rafay, M. Rahman, M.A. Stokes, S.M. Shariful Islam, R.K. Rai, U. Ram, C. Reis, S. Resnikoff, L. Roever, B.F. Sunguy, G.M. Ruhago, B. Saddik, R.D.F. Saldanha, A.M. Samy, J. Sanabria, B. Sartorius, M. Satpathy, I.J.C. Schneider, M.A.A. Shaikh, M. Sharif, J. She, J. Shen, K.N. Sheth, K. Shibuya, M. Shigematsu, R. Shiri, I. Shiue, D.A. Silveira, A.M. Soares Filho, D.N. Sinha, J.B. Soriano, D.J. Stein, M.B. Sufiyan, B.L. Sykes, R. Tabarés-Seisdedos, M. Tortajada-Girbés, R. Topor-Madry, B.X. Tran, L. Tudor Car, K.N. Ukwaja, I. Ullah, O.A. Uthman, P.R. Valdez, T.J. Vasankari, N. Venketasubramanian, F.S. Violante, Y. Waheed, A. Werdecker, G.M.A. Wyper, Y. Yano, P. Ye, P. Yip, N. Yonemoto, M.Z. Younis, C. Yu, Z. Zaidi, S.B. Zaman, Global, regional, and national burden of traumatic brain injury and spinal cord injury, 1990–2016: a systematic analysis for the Global Burden of Disease Study 2016, Lancet Neurol. 18 (2019) 56–87. https://doi.org/10.1016/S1474-4422(18)30415-0.

[12] A. Ahmad, S. Ashraf, S. Komai, Optogenetics Applications for Treating Spinal Cord Injury, Asian Spine J. 9 (2015) 299. https://doi.org/10.4184/ASJ.2015.9.2.299.

[13] M. Shinozaki, N. Nagoshi, M. Nakamura, H. Okano, Mechanisms of Stem Cell Therapy in Spinal Cord Injuries, Cells 2021, Vol. 10, Page 2676. 10 (2021) 2676. https://doi.org/10.3390/CELLS10102676.

[14] A. Blesch, M.H. Tuszynski, Transient growth factor delivery sustains regenerated axons after spinal cord injury, J Neurosci. 27 (2007) 10535–10545. https://doi.org/10.1523/JNEUROSCI.1903-07.2007.

[15] M.A. Anderson, J.E. Burda, Y. Ren, Y. Ao, T.M. O'Shea, R. Kawaguchi, G. Coppola, B.S. Khakh, T.J. Deming, M. V. Sofroniew, Astrocyte scar formation aids central nervous system axon regeneration, Nature. 532 (2016) 195–200. https://doi.org/10.1038/NATURE17623.

[16] A. Kaplan, M. Bueno, L. Hua, A.E. Fournier, Maximizing functional axon repair in the injured central nervous system: Lessons from neuronal development, Dev Dyn. 247 (2018) 18–23. https://doi.org/10.1002/DVDY.24536.

[17] M. V. Sofroniew, Dissecting spinal cord regeneration, Nature 2018 557:7705. 557 (2018) 343–350. https://doi.org/10.1038/s41586-018-0068-4.

[18] N. Klapka, H.W. Müller, Collagen matrix in spinal cord injury, J Neurotrauma. 23 (2006) 422–435. https://doi.org/10.1089/NEU.2006.23.422.

[19] C. Schachtrup, J.K. Ryu, M.J. Helmrick, E. Vagena, D.K. Galanakis, J.L. Degen, R.U. Margolis, K. Akassoglou, Fibrinogen triggers astrocyte scar formation by promoting the availability of active TGF-β after vascular damage, Journal of Neuroscience. 30 (2010) 5843–5854. https://doi.org/10.1523/JNEUROSCI.0137-10.2010.

[20] B.T. Lang, J.M. Cregg, M.A. Depaul, A.P. Tran, K. Xu, S.M. Dyck, K.M. Madalena, B.P. Brown, Y.L. Weng, S. Li, S. Karimi-Abdolrezaee, S.A. Busch, Y. Shen, J. Silver, Modulation of the proteoglycan receptor PTPσ promotes recovery after spinal cord injury, Nature. 518 (2015) 404–408. https://doi.org/10.1038/NATURE13974.

[21] A.R. Filous, J. Silver, "Targeting astrocytes in CNS injury and disease: A translational research approach," Prog Neurobiol. 144 (2016) 173–187. https://doi.org/10.1016/J.PNEUROBIO.2016.03.009.

[22] C. Göritz, D.O. Dias, N. Tomilin, M. Barbacid, O. Shupliakov, J. Frisén, A pericyte origin of spinal cord scar tissue, Science (1979). 333 (2011) 238–242. https://doi.org/10.1126/SCIENCE.1203165.

[23] K.L. Adams, V. Gallo, The diversity and disparity of the glial scar, Nat Neurosci. 21 (2018) 9–15. https://doi.org/10.1038/S41593-017-0033-9.

[24] Y. Zhu, C. Soderblom, V. Krishnan, J. Ashbaugh, J.R. Bethea, J.K. Lee, Hematogenous macrophage depletion reduces the fibrotic scar and increases axonal growth after spinal cord injury, Neurobiol Dis. 74 (2015) 114–125. https://doi.org/10.1016/J.NBD.2014.10.024.

[25] Y.A. Mironova, R.J. Giger, Where no synapses go: gatekeepers of circuit remodeling and synaptic strength, Trends Neurosci. 36 (2013) 363–373. https://doi.org/10.1016/J.TINS.2013.04.003.

[26] P. Lu, H. Yang, L.L. Jones, M.T. Filbin, M.H. Tuszynski, Combinatorial Therapy with Neurotrophins and cAMP Promotes Axonal Regeneration beyond Sites of Spinal Cord Injury, Journal of Neuroscience. 24 (2004) 6402–6409. https://doi.org/10.1523/JNEUROSCI.1492-04.2004.

[27] M.E. Schwab, S.M. Strittmatter, Nogo limits neural plasticity and recovery from injury, Curr Opin Neurobiol. 27 (2014) 53–60. https://doi.org/10.1016/J.CONB.2014.02.011.

[28] J.E. Burda, M. V. Sofroniew, Reactive Gliosis and the Multicellular Response to CNS Damage and Disease, Neuron. 81 (2014) 229–248. https://doi.org/10.1016/J.NEURON.2013.12.034.

[29] K. Kadoya, P. Lu, K. Nguyen, C. Lee-Kubli, H. Kumamaru, L. Yao, J. Knackert, G. Poplawski, J.N. Dulin, H. Strobl, Y. Takashima, J. Biane, J. Conner, S.C. Zhang, M.H. Tuszynski, Spinal cord reconstitution with homologous neural grafts enables robust corticospinal regeneration, Nature Medicine 2016 22:5. 22 (2016) 479–487. https://doi.org/10.1038/nm.4066.

[30] E.S. Rosenzweig, J.H. Brock, P. Lu, H. Kumamaru, E.A. Salegio, K. Kadoya, J.L. Weber, J.J. Liang, R. Moseanko, S. Hawbecker, J.R. Huie, L.A. Havton, Y.S. Nout-Lomas, A.R. Ferguson, M.S. Beattie, J.C. Bresnahan, M.H. Tuszynski, Restorative effects of human neural stem cell grafts on the primate spinal cord, Nature Medicine 2018 24:4. 24 (2018) 484–490. https://doi.org/10.1038/nm.4502.

[31] H. Kumamaru, P. Lu, E.S. Rosenzweig, K. Kadoya, M.H. Tuszynski, Regenerating Corticospinal Axons Innervate Phenotypically Appropriate Neurons within Neural Stem Cell Grafts, Cell Rep. 26 (2019) 2329-2339.e4. https://doi.org/10.1016/J.CELREP.2019.01.099.

[32] B.J. Hilton, E. Anenberg, T.C. Harrison, J.D. Boyd, T.H. Murphy, W. Tetzlaff, Re-Establishment of Cortical Motor Output Maps and Spontaneous Functional Recovery via Spared Dorsolaterally Projecting Corticospinal Neurons after Dorsal Column Spinal Cord Injury in Adult Mice, Journal of Neuroscience. 36 (2016) 4080–4092. https://doi.org/10.1523/JNEUROSCI.3386-15.2016.

[33] A.S. Wahl, W. Omlor, J.C. Rubio, J.L. Chen, H. Zheng, A. Schröter, M. Gullo, O. Weinmann, K. Kobayashi, F. Helmchen, B. Ommer, M.E. Schwab, Asynchronous therapy restores motor control by rewiring of the rat corticospinal tract after stroke, Science (1979). 344 (2014) 1250–1255. https://doi.org/10.1126/science.1253050.

[34] T.M. O'Shea, J.E. Burda, M. V. Sofroniew, Cell biology of spinal cord injury and repair, J Clin Invest. 127 (2017) 3259–3270. https://doi.org/10.1172/JCI90608.

[35] M. Cusimano, D. Biziato, E. Brambilla, M. Doneg, C. Alfaro-Cervello, S. Snider, G. Salani, F. Pucci, G. Comi, J.M. Garcia-Verdugo, M. De Palma, G. Martino, S. Pluchino, Transplanted neural stem/precursor cells instruct phagocytes and reduce secondary tissue damage in the injured spinal cord, Brain. 135 (2012) 447–460. https://doi.org/10.1093/BRAIN/AWR339.

[36] B. Martínez-Rojas, · Esther Giraldo, R. Grillo-Risco, M.R. Hidalgo, E. López-Mocholi, A. Alastrue-Agudo, F. García-García, V. Moreno-Manzano, NPC transplantation rescues sci-driven cAMP/EPAC2 alterations, leading to neuroprotection and microglial modulation, Cellular and Molecular Life Sciences 2022 79:8. 79 (2022) 1–21. https://doi.org/10.1007/S00018-022-04494-W.

[37] A. Kumar, H.K. Mishra, P. Dwivedi, J.R. Subramaniam, Secreted trophic factors of Human umbilical cord stromal cells induce differentiation and neurite extension through PI3K and independent of cAMP pathway, Ann Neurosci. 22 (2015) 97. https://doi.org/10.5214/ANS.0972.7531.220208.

[38] W. Gu, F. Zhang, Q. Xue, Z. Ma, P. Lu, B. Yu, Transplantation of bone marrow mesenchymal stem cells reduces lesion volume and induces axonal regrowth of injured spinal cord, Neuropathology. 30 (2010) 205–217. https://doi.org/10.1111/J.1440-1789.2009.01063.X.

[39] J. Sharp, J. Frame, M. Siegenthaler, G. Nistor, H.S. Keirstead, Human Embryonic Stem Cell-Derived Oligodendrocyte Progenitor Cell Transplants Improve Recovery after Cervical Spinal Cord Injury, Stem Cells. 28 (2010) 152–163. https://doi.org/10.1002/STEM.245.

[40] Y. Mukhamedshina, O. Gracheva, D. Mukhutdinova, Y. Chelyshev, A. Rizvanov, Mesenchymal stem cells and the neuronal microenvironment in the area of spinal cord injury, Neural Regen Res. 14 (2019) 227. https://doi.org/10.4103/1673-5374.244778.

[41] Y. Kamata, M. Isoda, T. Sanosaka, R. Shibata, S. Ito, T. Okubo, M. Shinozaki, M. Inoue, I. Koya, S. Shibata, T. Shindo, M. Matsumoto, M. Nakamura, H. Okano, N. Nagoshi, J. Kohyama, A robust culture system to generate neural progenitors with gliogenic competence from clinically relevant induced pluripotent stem cells for treatment of spinal cord injury, Stem Cells Transl Med. 10 (2021) 398–413. https://doi.org/10.1002/SCTM.20-0269.

[42] M. Hunt, P. Lu, M.H. Tuszynski, Myelination of axons emerging from neural progenitor grafts after spinal cord injury, Exp Neurol. 296 (2017) 69–73. https://doi.org/10.1016/J.EXPNEUROL.2017.07.005.

[43] G.J. Duncan, S.B. Manesh, B.J. Hilton, P. Assinck, J. Liu, A. Moulson, J.R. Plemel, W. Tetzlaff, Locomotor recovery following contusive spinal cord injury does not require oligodendrocyte remyelination, Nat Commun. 9 (2018). https://doi.org/10.1038/S41467-018-05473-1.

[44] B.N. Kharbikar, P. Mohindra, T.A. Desai, Biomaterials to enhance stem cell transplantation, Cell Stem Cell. 29 (2022) 692–721. https://doi.org/10.1016/J.STEM.2022.04.002.

[45] N. Bhardwaj, D. Devi, B.B. Mandal, Tissue-Engineered Cartilage: The Crossroads of Biomaterials, Cells and Stimulating Factors, Macromol Biosci. 15 (2015) 153–182. https://doi.org/10.1002/MABI.201400335.

[46] H. Janovjak, S. Kleinlogel, Optogenetic neuroregeneration, Neural Regen Res. 17 (2022) 1468. https://doi.org/10.4103/1673-5374.330596.

[47] M. Tessier-Lavigne, C.S. Goodman, The Molecular Biology of Axon Guidance, Science (1979). 274 (1996) 1123–1133. https://doi.org/10.1126/SCIENCE.274.5290.1123.

[48] J. Dodd, T.M. Jessell, Axon Guidance and the Patterning of Neuronal Projections in Vertebrates, Science (1979). 242 (1988) 692–699. https://doi.org/10.1126/SCIENCE.3055291.

[49] J.L. Goldberg, M.P. Klassen, Y. Hua, B.A. Barres, Amacrine-Signaled Loss of Intrinsic Axon Growth Ability by Retinal Ganglion Cells, Science (1979). 296 (2002) 1860–1864. https://doi.org/10.1126/SCIENCE.1068428.

[50] Z. He, Y. Jin, Intrinsic Control of Axon Regeneration, Neuron. 90 (2016) 437–451. https://doi.org/10.1016/J.NEURON.2016.04.022.

[51] L.X. Deng, P. Deng, Y. Ruan, Z.C. Xu, N.K. Liu, X. Wen, G.M. Smith, X.M. Xu, A Novel Growth-Promoting Pathway Formed by GDNF-Overexpressing Schwann Cells Promotes Propriospinal Axonal Regeneration, Synapse Formation, and Partial Recovery of Function after Spinal Cord Injury, Journal of Neuroscience. 33 (2013) 5655–5667. https://doi.org/10.1523/JNEUROSCI.2973-12.2013.

[52] L.T. Alto, L.A. Havton, J.M. Conner, E.R. Hollis, A. Blesch, M.H. Tuszynski, Chemotropic guidance facilitates axonal regeneration and synapse formation after spinal cord injury, Nature Neuroscience 2009 12:9. 12 (2009) 1106–1113. https://doi.org/10.1038/nn.2365.

[53] F. Sun, K.K. Park, S. Belin, D. Wang, T. Lu, G. Chen, K. Zhang, C. Yeung, G. Feng, B.A. Yankner, Z. He, Sustained axon regeneration induced by co-deletion of PTEN and SOCS3, Nature 2011 480:7377. 480 (2011) 372–375. https://doi.org/10.1038/nature10594.

[54] L.I. Benowitz, Z. He, J.L. Goldberg, Reaching the brain: Advances in optic nerve regeneration, Exp Neurol. 287 (2017) 365–373. https://doi.org/10.1016/J.EXPNEUROL.2015.12.015.

[55] F. Bei, H.H.C. Lee, X. Liu, G. Gunner, H. Jin, L. Ma, C. Wang, L. Hou, T.K. Hensch, E. Frank, J.R. Sanes, C. Chen, M. Fagiolini, Z. He, Restoration of Visual Function by Enhancing Conduction in Regenerated Axons, Cell. 164 (2016) 219–232. https://doi.org/10.1016/j.cell.2015.11.036.

[56] Y. Liu, X. Wang, W. Li, Q. Zhang, Y. Li, Z. Zhang, J. Zhu, B. Chen, P.R. Williams, Y. Zhang, B. Yu, X. Gu, Z. He, A Sensitized IGF1 Treatment Restores Corticospinal Axon-Dependent Functions, Neuron. 95 (2017) 817-833.e4. https://doi.org/10.1016/j.neuron.2017.07.037.

[57] K. Zukor, S. Belin, C. Wang, N. Keelan, X. Wang, Z. He, Short Hairpin RNA against PTEN Enhances Regenerative Growth of Corticospinal Tract Axons after Spinal Cord Injury, Journal of Neuroscience. 33 (2013) 15350–15361. https://doi.org/10.1523/JNEUROSCI.2510-13.2013.

[58] V.S. Boyce, L.M. Mendell, Neurotrophins and spinal circuit function, Front Neural Circuits. 8 (2014) 59. https://doi.org/10.3389/FNCIR.2014.00059.

[59] M.A. Anderson, T.M. O'Shea, J.E. Burda, Y. Ao, S.L. Barlatey, A.M. Bernstein, J.H. Kim, N.D. James, A. Rogers, B. Kato, A.L. Wollenberg, R. Kawaguchi, G. Coppola, C. Wang, T.J. Deming, Z. He, G. Courtine, M. V. Sofroniew, Required growth facilitators propel axon regeneration across complete spinal cord injury, Nature. 561 (2018) 396–400. https://doi.org/10.1038/S41586-018-0467-6.

[60] L.T. Alto, L.A. Havton, J.M. Conner, E.R. Hollis, A. Blesch, M.H. Tuszynski, Chemotropic guidance facilitates axonal regeneration and synapse formation after spinal cord injury, Nat Neurosci. 12 (2009) 1106–1113. https://doi.org/10.1038/NN.2365.

[61] L.X. Deng, P. Deng, Y. Ruan, Z.C. Xu, N.K. Liu, X. Wen, G.M. Smith, X.M. Xu, A novel growth-promoting pathway formed by GDNF-overexpressing Schwann cells promotes propriospinal axonal regeneration, synapse formation, and partial recovery of function after spinal cord injury, J Neurosci. 33 (2013) 5655–5667. https://doi.org/10.1523/JNEUROSCI.2973-12.2013.

[62] P.H. Özdinler, J.D. Macklis, IGF-I specifically enhances axon outgrowth of corticospinal motor neurons, Nat Neurosci. 9 (2006) 1371–1381. https://doi.org/10.1038/NN1789.

[63] R.E. White, F.Q. Yin, L.B. Jakeman, TGF-alpha increases astrocyte invasion and promotes axonal growth into the lesion following spinal cord injury in mice, Exp Neurol. 214 (2008) 10–24. https://doi.org/10.1016/J.EXPNEUROL.2008.06.012.

[64] A.G. Rabchevsky, I. Fugaccia, A. Fletcher-Turner, D.A. Blades, M.P. Mattson, S.W. Scheff, Basic fibroblast growth factor (bFGF) enhances tissue sparing and functional recovery following moderate spinal cord injury, J Neurotrauma. 16 (1999) 817–830. https://doi.org/10.1089/NEU.1999.16.817.

[65] J. Janowska, J. Gargas, M. Ziemka-Nalecz, T. Zalewska, L. Buzanska, J. Sypecka, Directed glial differentiation and transdifferentiation for neural tissue regeneration, Exp Neurol. 319 (2019) 112813. https://doi.org/10.1016/J.EXPNEUROL.2018.08.010.

[66] C.L. Lin, P. Heron, S.R. Hamann, G.M. Smith, Functional distinction between NGF-mediated plasticity and regeneration of nociceptive axons within the spinal cord, Neuroscience. 272 (2014) 76–87. https://doi.org/10.1016/J.NEUROSCIENCE.2014.04.053.

[67] I. Elliott Donaghue, R. Tam, M. V. Sefton, M.S. Shoichet, Cell and biomolecule delivery for tissue repair and regeneration in the central nervous system, J Control Release. 190 (2014) 219–227. https://doi.org/10.1016/J.JCONREL.2014.05.040.

[68] E. Aznar, M. Oroval, L. Pascual, J.R. Murguía, R. Martínez-Máñez, F. Sancenón, Gated Materials for On-Command Release of Guest Molecules, Chem Rev. 116 (2016) 561–718. https://doi.org/10.1021/ACS.CHEMREV.5B00456.

[69] P. Kumar, P. Tambe, K.M. Paknikar, V. Gajbhiye, Mesoporous silica nanoparticles as cutting-edge theranostics: Advancement from merely a carrier to tailor-made smart delivery platform, Journal of Controlled Release. 287 (2018) 35–57. https://doi.org/10.1016/J.JCONREL.2018.08.024.

[70] M. Wang, X. Yang, P. Zhang, L. Cai, X. Yang, Y. Chen, Y. Jing, J. Kong, X. Yang, F.-L. Sun, M.Y. Wang, X.M. Yang, X.B. Yang, Y.W. Chen, Y.Y.F. Jing, P. Zhang, L. Cai, L. Kong, X.W. Yang, Sustained Delivery Growth Factors with Polyethyleneimine-Modified Nanoparticles Promote Embryonic Stem Cells Differentiation and Liver Regeneration, Advanced Science. 3 (2016) 1500393. https://doi.org/10.1002/ADVS.201500393.

[71] E. Cheah, Z. Wu, S.S. Thakur, S.J. O'Carroll, D. Svirskis, Externally triggered release of growth factors - A tissue regeneration approach, Journal of Controlled Release. 332 (2021) 74–95. https://doi.org/10.1016/J.JCONREL.2021.02.015.

[72] H. Wu, F. Li, S. Wang, J. Lu, J. Li, Y. Du, X. Sun, X. Chen, J. Gao, D. Ling, Ceria nanocrystals decorated mesoporous silica nanoparticle based ROS-scavenging tissue adhesive for highly efficient regenerative wound healing, Biomaterials. 151 (2018) 66–77. https://doi.org/10.1016/J.BIOMATERIALS.2017.10.018.

[73] M.A. Tria, M. Fusco, G. Vantini, R. Mariot, Pharmacokinetics of Nerve Growth Factor (NGF) Following Different Routes of Administration to Adult Rats, Exp Neurol. 127 (1994) 178–183. https://doi.org/10.1006/EXNR.1994.1093.

[74] M.J. Roberts, M.D. Bentley, J.M. Harris, Chemistry for peptide and protein PEGylation, Adv Drug Deliv Rev. 54 (2002) 459–476. https://doi.org/10.1016/S0169-409X(02)00022-4.

[75] S. Kontos, J.A. Hubbell, Drug development: longer-lived proteins, Chem Soc Rev. 41 (2012) 2686–2695. https://doi.org/10.1039/C2CS15289D.

[76] T.N. Vo, F.K. Kasper, A.G. Mikos, Strategies for controlled delivery of growth factors and cells for bone regeneration, Adv Drug Deliv Rev. 64 (2012) 1292–1309. https://doi.org/10.1016/J.ADDR.2012.01.016.

[77] P. Tayalia, D.J. Mooney, Controlled Growth Factor Delivery for Tissue Engineering, Advanced Materials. 21 (2009) 3269–3285. https://doi.org/10.1002/ADMA.200900241.

[78] L.M. Caballero Aguilar, S.M. Silva, S.E. Moulton, Growth factor delivery: Defining the next generation platforms for tissue engineering, Journal of Controlled Release. 306 (2019) 40–58. https://doi.org/10.1016/J.JCONREL.2019.05.028.

[79] K. Ladewig, Drug delivery in soft tissue engineering, Expert Opinion on Drug Delivery. 8 (2011) 1175–1188. https://doi.org/10.1517/17425247.2011.588698.

[80] Y. Tabata, Tissue Regeneration Based on Growth Factor Release, Tissue Engineering. 9, 5-15 (2004). https://doi.org/10.1089/10763270360696941.

[81] R.A. Siegel, C.G. Pitt, A strategy for oscillatory drug release general scheme and simplified theory, Journal of Controlled Release. 33 (1995) 173–188. https://doi.org/10.1016/0168-3659(94)00082-6.

[82] A. Kikuchi, T. Okano, Pulsatile drug release control using hydrogels, Adv Drug Deliv Rev. 54 (2002) 53–77. https://doi.org/10.1016/S0169-409X(01)00243-5.

[83] B.B.C. Youan, Chronopharmaceutics: gimmick or clinically relevant approach to drug delivery?, Journal of Controlled Release. 98 (2004) 337–353. https://doi.org/10.1016/J.JCONREL.2004.05.015.

[84] M. Wei, Y. Gao, X. Li, M.J. Serpe, Stimuli-responsive polymers and their applications, Polym Chem. 8 (2016) 127–143. https://doi.org/10.1039/C6PY01585A.

[85] A. Raza, T. Rasheed, F. Nabeel, U. Hayat, M. Bilal, H.M.N. Iqbal, Endogenous and Exogenous Stimuli-Responsive Drug Delivery Systems for Programmed Site-Specific Release, Molecules 2019, Vol. 24, Page 1117. 24 (2019) 1117. https://doi.org/10.3390/MOLECULES24061117.

[86] V. Karagkiozaki, P.G. Karagiannidis, M. Gioti, P. Kavatzikidou, D. Georgiou, E. Georgaraki, S. Logothetidis, Bioelectronics meets nanomedicine for cardiovascular implants: PEDOT-based nanocoatings for tissue regeneration, Biochimica et Biophysica Acta (BBA) - General Subjects. 1830 (2013) 4294–4304. https://doi.org/10.1016/J.BBAGEN.2012.12.019.

[87] M. Marzocchi, I. Gualandi, M. Calienni, I. Zironi, E. Scavetta, G. Castellani, B. Fraboni, Physical and Electrochemical Properties of PEDOT:PSS as a Tool for Controlling Cell Growth, ACS Appl Mater Interfaces. 7 (2015) 17993–18003. https://doi.org/10.1021/acsami.5b04768.

[88] A. de Mel, G. Jell, M.M. Stevens, A.M. Seifalian, Biofunctionalization of biomaterials for accelerated in situ endothelialization: A review, Biomacromolecules. 9 (2008) 2969–2979. https://doi.org/10.1021/bm800681k.

[89] R. Balint, N.J. Cassidy, S.H. Cartmell, Electrical Stimulation: A Novel Tool for Tissue Engineering, Tissue Engineering Part B: Reviews (2012) 48–57. https://doi.org/10.1089/TEN.TEB.2012.0183.

[90] C. Chen, X. Bai, Y. Ding, I.S. Lee, Electrical stimulation as a novel tool for regulating cell behavior in tissue engineering, Biomaterials Research 23:1. 23 (2019) 1–12. https://doi.org/10.1186/S40824-019-0176-8.

[91] A.F. Kanaan, A.P. Piedade, Electro-responsive polymer-based platforms for electrostimulation of cells, Mater Adv. 3 (2022) 2337–2353. https://doi.org/10.1039/D1MA01012C.

[92] C.A. Angeli, M. Boakye, R.A. Morton, J. Vogt, K. Benton, Y. Chen, C.K. Ferreira, S.J. Harkema, Recovery of Over-Ground Walking after Chronic Motor Complete Spinal Cord Injury, N Engl J Med. 379 (2018) 1244–1250. https://doi.org/10.1056/NEJMOA1803588.

[93] F.B. Wagner, J.B. Mignardot, C.G. Le Goff-Mignardot, R. Demesmaeker, S. Komi, M. Capogrosso, A. Rowald, I. Seáñez, M. Caban, E. Pirondini, M. Vat, L.A. McCracken, R. Heimgartner, I. Fodor, A. Watrin, P. Seguin, E. Paoles, K. Van Den Keybus, G. Eberle, B. Schurch, E. Pralong, F. Becce, J. Prior, N. Buse, R. Buschman, E. Neufeld, N. Kuster, S. Carda, J. von Zitzewitz, V. Delattre, T. Denison, H. Lambert, K. Minassian, J. Bloch, G. Courtine, Targeted neurotechnology restores walking in humans with spinal cord injury, Nature. 563 (2018) 65–93. https://doi.org/10.1038/S41586-018-0649-2.

[94] J.S. Jara, S. Agger, E.R. Hollis, Functional Electrical Stimulation and the Modulation of the Axon Regeneration Program, Front Cell Dev Biol. 8 (2020) 736. https://doi.org/10.3389/FCELL.2020.00736.

[95] Z. Liu, X. Wan, Z. Lin Wang, L. Li, Z. Liu, X. Wan, Z.L. Wang, L. Li, Electroactive Biomaterials and Systems for Cell Fate Determination and Tissue Regeneration: Design and Applications, Advanced Materials. 33 (2021) 2007429. https://doi.org/10.1002/ADMA.202007429.

[96] L. Leppik, K.M.C. Oliveira, M.B. Bhavsar, J.H. Barker, Electrical stimulation in bone tissue engineering treatments, European Journal of Trauma and Emergency Surgery 2020 46:2. 46 (2020) 231–244. https://doi.org/10.1007/S00068-020-01324-1.

[97] B. Guo, P.X. Ma, Conducting Polymers for Tissue Engineering, Biomacromolecules. 19 (2018) 1764–1782. https://doi.org/10.1021/ACS.BIOMAC.8B00276.

[98] G. Kaur, R. Adhikari, P. Cass, M. Bown, P. Gunatillake, Electrically conductive polymers and composites for biomedical applications, RSC Adv. 5 (2015) 37553–37567. https://doi.org/10.1039/C5RA01851J.

[99] S.H. Park, Y.J. Kang, S. Majd, A Review of Patterned Organic Bioelectronic Materials and their Biomedical Applications, Advanced Materials. 27 (2015) 7583–7619. https://doi.org/10.1002/ADMA.201501809.

[100] E. Šafaříková, J. Ehlich, S. Stříteský, M. Vala, M. Weiter, J. Pacherník, L. Kubala, J. Víteček, Conductive Polymer PEDOT:PSS-Based Platform for Embryonic Stem-Cell Differentiation, International Journal of Molecular Sciences 2022, Vol. 23, Page 1107. 23 (2022) 1107. https://doi.org/10.3390/IJMS23031107.

[101] M. Talikowska, X. Fu, G. Lisak, Application of conducting polymers to wound care and skin tissue engineering: A review, Biosens Bioelectron. 135 (2019) 50–63. https://doi.org/10.1016/J.BIOS.2019.04.001.

[102] J.F. Feng, J. Liu, X.Z. Zhang, L. Zhang, J.Y. Jiang, J. Nolta, M. Zhao, Guided Migration of Neural Stem Cells Derived from Human Embryonic Stem Cells by an Electric Field, Stem Cells. 30 (2012) 349–355. https://doi.org/10.1002/STEM.779.

[103] Y. Li, M. Weiss, L. Yao, Directed Migration of Embryonic Stem Cell-derived Neural Cells In An Applied Electric Field, Stem Cell Rev Rep. 10 (2014) 653–662. https://doi.org/doi.org/10.1007/s12015-014-9518-z.

[104] J. Du, G. Zhen, H. Chen, S. Zhang, L. Qing, X. Yang, G. Lee, H.Q. Mao, X. Jia, Optimal electrical stimulation boosts stem cell therapy in nerve regeneration, Biomaterials. 181 (2018) 347–359. https://doi.org/10.1016/J.BIOMATERIALS.2018.07.015.

[105] G. Thrivikraman, G. Madras, B. Basu, Intermittent electrical stimuli for guidance of human mesenchymal stem cell lineage commitment towards neural-like cells on electroconductive substrates, Biomaterials. 35 (2014) 6219–6235. https://doi.org/10.1016/J.BIOMATERIALS.2014.04.018.

[106] L. Sordini, F.F.F. Garrudo, C.A.V. Rodrigues, R.J. Linhardt, J.M.S. Cabral, F.C. Ferreira, J. Morgado, Effect of Electrical Stimulation Conditions on Neural Stem Cells Differentiation on Cross-Linked PEDOT:PSS Films, Front Bioeng Biotechnol. 9 (2021) 73. https://doi.org/10.3389/FBIOE.2021.591838.

[107] R. Zhu, Z. Sun, C. Li, S. Ramakrishna, K. Chiu, L. He, Electrical stimulation affects neural stem cell fate and function in vitro, Exp Neurol. 319 (2019) 112963. https://doi.org/10.1016/J.EXPNEUROL.2019.112963.

[108] M.A. De Menorval, F.M. Andre, A. Silve, C. Dalmay, O. Français, B. Le Pioufle, L.M. Mir, Electric pulses: a flexible tool to manipulate cytosolic calcium concentrations and generate spontaneous-like calcium oscillations in mesenchymal stem cells, Scientific Reports 6:1. 6 (2016) 1–9. https://doi.org/10.1038/srep32331.

[109] F.M.P. Tonelli, A.K. Santos, K.N. Gomes, L.O. Ladeira, R.R. Resende, D.A. Gomes, S.L. Da Silva, Stem cells and calcium signaling, Adv Exp Med Biol. 740 (2012) 891–916. https://doi.org/10.1007/978-94-007-2888-2_40.

[110] M.W.G.D.M. de Groot, M.M.L. Dingemans, K.H. Rus, A. de Groot, R.H.S. Westerink, Characterization of Calcium Responses and Electrical Activity in Differentiating Mouse Neural Progenitor Cells In Vitro, Toxicological Sciences. 137 (2014) 428–435. https://doi.org/10.1093/TOXSCI/KFT261.

[111] M. Mahar, V. Cavalli, Intrinsic mechanisms of neuronal axon regeneration, Nature Reviews Neuroscience 2018 19:6. 19 (2018) 323–337. https://doi.org/10.1038/s41583-018-0001-8.

[112] M.O. Krucoff, S. Rahimpour, M.W. Slutzky, V.R. Edgerton, D.A. Turner, Enhancing nervous system recovery through neurobiologics, neural interface training, and neurorehabilitation, Front Neurosci. 10 (2016) 584. https://doi.org/10.3389/FNINS.2016.00584.

[113] J. Kolosnjaj-Tabi, L. Gibot, I. Fourquaux, M. Golzio, M.P. Rols, Electric field-responsive nanoparticles and electric fields: physical, chemical, biological mechanisms and therapeutic prospects, Adv Drug Deliv Rev. 138 (2019) 56–67. https://doi.org/10.1016/J.ADDR.2018.10.017.

[114] H. Cheng, Y. Huang, H. Yue, Y. Fan, Electrical Stimulation Promotes Stem Cell Neural Differentiation in Tissue Engineering, Stem Cells Int. (2021). https://doi.org/10.1155/2021/6697574.

[115] Q. Li, B. Kang, L. Wang, T. Chen, Y. Zhao, S. Feng, R. Li, H. Zhang, Microfluidics embedded with microelectrodes for electrostimulation of neural stem cells proliferation, Chinese Chemical Letters. 33 (2022) 1308–1312. https://doi.org/10.1016/J.CCLET.2021.08.006.

[116] W. Hu, Q. Li, B. Li, K. Ma, C. Zhang, X. Fu, Optogenetics sheds new light on tissue engineering and regenerative medicine, Biomaterials. 227 (2020) 119546. https://doi.org/10.1016/J.BIOMATERIALS.2019.119546.

[117] G. Spagnuolo, F. Genovese, L. Fortunato, M. Simeone, C. Rengo, M. Tatullo, The Impact of Optogenetics on Regenerative Medicine, Applied Sciences 2020, Vol. 10, Page 173. 10 (2019) 173. https://doi.org/10.3390/APP10010173.

[118] S. Park, R.A. Koppes, U.P. Froriep, X. Jia, A.K.H. Achyuta, B.L. McLaughlin, P. Anikeeva, Optogenetic control of nerve growth, Scientific Reports 2015 5:1. 5 (2015) 1–9. https://doi.org/10.1038/srep09669.

[119] J. Joshi, M. Rubart, W. Zhu, Optogenetics: Background, Methodological Advances and Potential Applications for Cardiovascular Research and Medicine, Front Bioeng Biotechnol. 7 (2020) 466. https://doi.org/10.3389/FBIOE.2019.00466.

[120] M.L. Rein, J.M. Deussing, The optogenetic (r)evolution, Molecular Genetics and Genomics. 287 (2012) 95–109. https://doi.org/10.1007/S00438-011-0663-7.

[121] J. Mattis, K.M. Tye, E.A. Ferenczi, C. Ramakrishnan, D.J. O'Shea, R. Prakash, L.A. Gunaydin, M. Hyun, L.E. Fenno, V. Gradinaru, O. Yizhar, K. Deisseroth, Principles for applying optogenetic tools derived from direct comparative analysis of microbial opsins, Nature Methods 9:2. 9 (2011) 159–172. https://doi.org/10.1038/nmeth.1808.

[122] N. Jayaprakash, Z. Wang, B. Hoeynck, N. Krueger, A. Kramer, E. Balle, D.S. Wheeler, R.A. Wheeler, M.G. Blackmore, Optogenetic Interrogation of Functional Synapse Formation by Corticospinal Tract Axons in the Injured Spinal Cord, Journal of Neuroscience. 36 (2016) 5877–5890. https://doi.org/10.1523/JNEUROSCI.4203-15.2016.

[123] J. Deubner, P. Coulon, I. Diester, Optogenetic approaches to study the mammalian brain, Curr Opin Struct Biol. 57 (2019) 157–163. https://doi.org/10.1016/J.SBI.2019.04.003.

[124] D.B.L. Teh, A. Prasad, W. Jiang, N. Zhang, Y. Wu, H. Yang, S. Han, Z. Yi, Y. Yeo, T. Ishizuka, L. Wong, N. Thakor, H. Yawo, X. Liu, A. All, Driving Neurogenesis in Neural Stem Cells with High Sensitivity Optogenetics, Neuromolecular Med. 22 (2020) 139–149. https://doi.org/10.1007/s12017-019-08573-3.

[125] S.D. Klapper, E.J. Sauter, A. Swiersy, M.A.E. Hyman, C. Bamann, E. Bamberg, V. Busskamp, On-demand optogenetic activation of human stem-cell-derived neurons, Scientific Reports 2017 7:1. 7 (2017) 1–9. https://doi.org/10.1038/s41598-017-14827-6.

[126] A.J. Weitz, J.H. Lee, Probing Neural Transplant Networks in Vivo with Optogenetics and Optogenetic fMRI, Stem Cells Int. (2016). https://doi.org/10.1155/2016/8612751.

[127] R. Habibey, K. Sharma, A. Swiersy, V. Busskamp, Optogenetics for neural transplant manipulation and functional analysis, Biochem Biophys Res Commun. 527 (2020) 343–349. https://doi.org/10.1016/J.BBRC.2020.01.141.

[128] M.M. Daadi, J.Q. Klausner, B. Bajar, I. Goshen, C. Lee-Messer, S.Y. Lee, M.C.G. Winge, C. Ramakrishnan, M. Lo, G. Sun, K. Deisseroth, G.K. Steinberg, Optogenetic stimulation of neural grafts enhances neurotransmission and downregulates the inflammatory response in experimental stroke model, Cell Transplant. 25 (2016) 1371–1380. https://doi.org/10.3727/096368915X688533.

[129] J.A. Steinbeck, S.J. Choi, A. Mrejeru, Y. Ganat, K. Deisseroth, D. Sulzer, E. V. Mosharov, L. Studer, Optogenetics enables functional analysis of human embryonic stem cell–derived grafts in a Parkinson's disease model, Nature Biotechnology 2015 33:2. 33 (2015) 204–209. https://doi.org/10.1038/nbt.3124.

[130] M. Cunningham, J.H. Cho, A. Leung, G. Savvidis, S. Ahn, M. Moon, P.K.J. Lee, J.J. Han, N. Azimi, K.S. Kim, V.Y. Bolshakov, S. Chung, hPSC-derived maturing GABAergic interneurons ameliorate seizures and abnormal behavior in epileptic mice, Cell Stem Cell. 15 (2014) 559–573. https://doi.org/10.1016/j.stem.2014.10.006.

[131] N. Avaliani, A.T. Sørensen, M. Ledri, J. Bengzon, P. Koch, O. Brüstle, K. Deisseroth, M. Andersson, M. Kokaia, Optogenetics Reveal Delayed Afferent Synaptogenesis on Grafted Human-Induced Pluripotent Stem Cell-Derived Neural Progenitors, Stem Cells. 32 (2014) 3088–3098. https://doi.org/10.1002/STEM.1823.

[132] J. Ryu, P.F.Y. Vincent, N.K. Ziogas, L. Xu, S. Sadeghpour, J. Curtin, A.S. Alexandris, N. Stewart, R. Sima, S. du Lac, E. Glowatzki, V.E. Koliatsos, Optogenetically transduced human ES cell-derived neural progenitors and their neuronal progenies: Phenotypic characterization and responses to optical stimulation, PLoS One. 14 (2019) e0224846. https://doi.org/10.1371/JOURNAL.PONE.0224846.

[133] M.J. Sharpe, N.J. Marchant, L.R. Whitaker, C.T. Richie, Y.J. Zhang, E.J. Campbell, P.P. Koivula, J.C. Necarsulmer, C. Mejias-Aponte, M. Morales, J. Pickel, J.C. Smith, Y. Niv, Y. Shaham, B.K. Harvey, G. Schoenbaum, Lateral Hypothalamic GABAergic Neurons Encode Reward Predictions that Are Relayed to the Ventral Tegmental Area to Regulate Learning, Current Biology. 27 (2017) 2089-2100.e5. https://doi.org/10.1016/j.cub.2017.06.024.

[134] J.B. Bryson, C.B. Machado, M. Crossley, D. Stevenson, V. Bros-Facer, J. Burrone, L. Greensmith, I. Lieberam, Optical control of muscle function by transplantation of stem cell-derived motor neurons in mice, Science. 344 (2014) 94–97. https://doi.org/10.1126/science.1248523.

[135] M. Garita-Hernandez, M. Lampič, A. Chaffiol, L. Guibbal, F. Routet, T. Santos-Ferreira, S. Gasparini, O. Borsch, G. Gagliardi, S. Reichman, S. Picaud, J.A. Sahel, O. Goureau, M. Ader, D. Dalkara, J. Duebel,

Restoration of visual function by transplantation of optogenetically engineered photoreceptors, Nature Communications 2019 10:1. 10 (2019) 1–13. https://doi.org/10.1038/s41467-019-12330-2.

[136] S.J. Wang, C.H. Weng, H.W. Xu, C.J. Zhao, Z.Q. Yin, Effect of optogenetic stimulus on the proliferation and cell cycle progression of neural stem cells, Journal of Membrane Biology. 247 (2014) 493–500. https://doi.org/10.1007/s00232-014-9659-7.

[137] V. Paschon, F.F. Correia, B.C. Morena, V.A. da Silva, G.B. dos Santos, M.C.C. da Silva, A.F. Cristante, S.M. Willerth, F.E. Perrin, A.H. Kihara, CRISPR, Prime Editing, Optogenetics, and DREADDs: New Therapeutic Approaches Provided by Emerging Technologies in the Treatment of Spinal Cord Injury, Molecular Neurobiology 2020 57:4. 57 (2020) 2085–2100. https://doi.org/10.1007/S12035-019-01861-W.

[138] W.W. Deng, G.Y. Wu, L.X. Min, Z. Feng, H. Chen, M.L. Tan, J.F. Sui, H.L. Liu, J.M. Hou, Optogenetic Neuronal Stimulation Promotes Functional Recovery After Spinal Cord Injury, Front Neurosci. 15 (2021) 371. https://doi.org/10.3389/FNINS.2021.640255.

[139] S.P. Yu, J.K. Tung, Z.Z. Wei, D. Chen, K. Berglund, W. Zhong, J.Y. Zhang, X. Gu, M. Song, R.E. Gross, S.Z. Lin, L. Wei, Optochemogenetic Stimulation of Transplanted iPS-NPCs Enhances Neuronal Repair and Functional Recovery after Ischemic Stroke, Journal of Neuroscience. 39 (2019) 6571–6594. https://doi.org/10.1523/JNEUROSCI.2010-18.2019.

[140] S.L. Delaney, J.L. Gendreau, M. D'Souza, A.Y. Feng, A.L. Ho, Optogenetic Modulation for the Treatment of Traumatic Brain Injury, Stem Cells and Development. 29 (2020) 187–197. https://doi.org/10.1089/SCD.2019.0187.

[141] S. Ceto, K.J. Sekiguchi, Y. Takashima, A. Nimmerjahn, M.H. Tuszynski, Neural Stem Cell Grafts Form Extensive Synaptic Networks that Integrate with Host Circuits after Spinal Cord Injury, Cell Stem Cell. 27 (2020) 430-440.e5. https://doi.org/10.1016/J.STEM.2020.07.007.

[142] E. Giraldo, D. Palmero-Canton, B. Martinez-Rojas, M.D.M. Sanchez-Martin, V. Moreno-Manzano, Optogenetic Modulation of Neural Progenitor Cells Improves Neuroregenerative Potential, International Journal of Molecular Sciences 2021, Vol. 22, Page 365. 22 (2020) 365. https://doi.org/10.3390/IJMS22010365.

[143] X. Xu, T. Mee, X. Jia, New era of optogenetics: from the central to peripheral nervous system, Crit Rev Biochem Mol Biol. 55 (2020) 1–16. https://doi.org/10.1080/10409238.2020.1726279.

[144] J.B. Bryson, C.B. Machado, I. Lieberam, L. Greensmith, Restoring motor function using optogenetics and neural engraftment, Curr Opin Biotechnol. 40 (2016) 75–81. https://doi.org/10.1016/J.COPBIO.2016.02.016.

[145] S.E. Mondello, M.D. Sunshine, A.E. Fischedick, S.J. Dreyer, G.D. Horwitz, P. Anikeeva, P.J. Horner, C.T. Moritz, Optogenetic surface stimulation of the rat cervical spinal cord, J Neurophysiol. 120 (2018) 795–811. https://doi.org/10.1152/jn.00461.2017.

[146] E.J.F. Dickinson, A.J. Wain, The Butler-Volmer equation in electrochemical theory: Origins, value, and practical application, Journal of Electroanalytical Chemistry. 872 (2020) 114145. https://doi.org/10.1016/J.JELECHEM.2020.114145.

[147] R. Guidelli, R.G. Compton, J.M. Feliu, E. Gileadi, J. Lipkowski, W. Schmickler, S. Trasatti, Defining the transfer coefficient in electrochemistry: An assessment (IUPAC Technical Report), Pure and Applied Chemistry. 86 (2014) 245–258. https://doi.org/10.1515/pac-2014-5026.

[148] R.G. Compton, E. Laborda, K.R. Ward, Understanding Voltammetry, Imperial College Press, 2013. https://doi.org/10.1142/Q0155.

[149] I.C. Emeji, O.M. Ama, U.O. Aigbe, K. Khoele, P.O. Osifo, S.S. Ray, Electrochemical Cells, Engineering Materials. (2020) 65–84. https://doi.org/10.1007/978-3-030-43346-8_4.

[150] C. Batchelor-Mcauley, E. Kätelhön, E.O. Barnes, R.G. Compton, E. Laborda, A. Molina, Recent Advances in Voltammetry, ChemistryOpen. 4 (2015) 224–260. https://doi.org/10.1002/OPEN.201500042.

[151] P.S. Singh, S.G. Lemay, Stochastic Processes in Electrochemistry, Anal Chem. 88 (2016) 5017–5027. https://doi.org/10.1021/ACS.ANALCHEM.6B00683.

[152] P.T. Kissinger, W.R. Heinemann, Laboratory Techniques in Electroanalytical Chemistry, Marcel Dekker Inc., New York, 1996.

[153] A.J. Bard, L.R. Faulkner, H.S. White, Electrochemical methods: fundamentals and applications, John Wiley & Sons, Inc., 2006.

[154] M. Alcañiz Fillol, Diseño de un sistema de lengua electrónica basado en técnicas electroquímicas voltamétricas y su aplicación en el ámbito agroalimentario, Universitat Politècnica de València, 2011. https://doi.org/10.4995/THESIS/10251/11303.

[155] C.G. Zoski, Handbook of Electrochemistry, Elsevier, 2004.

[156] C. Jin Mei, S. Ainliah Alang Ahmad, A review on the determination heavy metals ions using calixarene-based electrochemical sensors, Arabian Journal of Chemistry. 14 (2021) 103303. https://doi.org/10.1016/J.ARABJC.2021.103303.

[157] D. Harvey, Analytical Chemistry 2.0-an open-access digital textbook, Anal Bioanal Chem. 399 (2011) 149–152. https://doi.org/10.1007/S00216-010-4316-1.

[158] J.R. Macdonald, E. Barsoukov, Impedance Spectroscopy: Theory, Experiment, and Applications, 3rd ed., John Wiley & Sons, Inc, 2005.

[159] R. Masot Peris, Desarrollo de un sistema de medida basado en espectroscopía de impedancia para la determinación de parámetros fisicoquímicos en alimentos, 2010. https://riunet.upv.es/handle/10251/8502.

[160] Y.G. Vlasov, A. V. Legin, A.M. Rudnitskaya, Electronic tongue: Chemical sensor systems for analysis of aquatic media, Russian Journal of General Chemistry 2008 78:12. 78 (2009) 2532–2544. https://doi.org/10.1134/S1070363208120335.

[161] L. Gil Sánchez, Diseño de lenguas electrónicas potenciométricas construidas conelectrodos metálicos y con tecnología de capa gruesa para análisis de medios complejos, Universitat Politècnica de València, 2007. https://doi.org/https://doi.org/10.4995/Thesis/10251/135954.

[162] A. Martínez-Ibernón, J.E. Ramón, J.M. Gandía-Romero, I. Gasch, M. Valcuende, M. Alcañiz, J. Soto, Characterization of electrochemical systems using potential step voltammetry. Part II: Modeling of reversible systems, Electrochim Acta. 328 (2019) 135111. https://doi.org/10.1016/J.ELECTACTA.2019.135111.

[163] D. Harvey, Modern Analytical Chemistry, The McGraw-Hill Companies. Inc, 2000.

[164] F. Winquist, Voltammetric electronic tongues – basic principles and applications, Microchimica Acta 2008 163:1. 163 (2008) 3–10. https://doi.org/10.1007/S00604-007-0929-2.

[165] E. Dalcanale, R. Pinalli, Controlled Release, Encyclopedia of Polymeric Nanomaterials. (2015) 439–449. https://doi.org/10.1007/978-3-642-29648-2_314.

[166] P.I. Lee, J.X. Li, Evolution of Oral Controlled Release Dosage Forms, John Wiley & Sons, Ltd, 2010. https://doi.org/10.1002/9780470640487.CH2.

[167] B.B.C. Youan, Chronopharmaceutical drug delivery systems: Hurdles, hype or hope?, Adv Drug Deliv Rev. 62 (2010) 898–903. https://doi.org/10.1016/J.ADDR.2010.04.010.

[168] D. Choudhary, H. Goykar, K. Rajpoot, R.K. Tekade, Chronopharmacokinetics, Biopharmaceutics and Pharmacokinetics Considerations: Volume 1 in Advances in Pharmaceutical Product Development and Research. (2021) 163–194. https://doi.org/10.1016/B978-0-12-814425-1.00008-5.

[169] B. Gowthami, S.V.G. Krishna, D.S. Rao, Application of coating technology to chronotherapeutic drug delivery systems: Recent publications and patents, Current Research in Pharmacology and Drug Discovery. 2 (2021) 100015. https://doi.org/10.1016/J.CRPHAR.2021.100015.

[170] S.Y. Lin, Thermoresponsive gating membranes embedded with liquid crystal(s) for pulsatile transdermal drug delivery: An overview and perspectives, Journal of Controlled Release. 319 (2020) 450–474. https://doi.org/10.1016/J.JCONREL.2019.12.046.

[171] P. Davoodi, L.Y. Lee, Q. Xu, V. Sunil, Y. Sun, S. Soh, C.H. Wang, Drug delivery systems for programmed and on-demand release, Adv Drug Deliv Rev. 132 (2018) 104–138. https://doi.org/10.1016/J.ADDR.2018.07.002.

[172] L.A. Villarruel Mendoza, N.A. Scilletta, M.G. Bellino, M.F. Desimone, P.N. Catalano, Recent Advances in Micro-Electro-Mechanical Devices for Controlled Drug Release Applications, Front Bioeng Biotechnol. 8 (2020) 827. https://doi.org/10.3389/FBIOE.2020.00827.

[173] R. Jamaledin, P. Makvandi, C.K.Y. Yiu, T. Agarwal, R. Vecchione, W. Sun, T.K. Maiti, F.R. Tay, P.A. Netti, Engineered Microneedle Patches for Controlled Release of Active Compounds: Recent Advances in Release Profile Tuning, Adv Ther (Weinh). 3 (2020) 2000171. https://doi.org/10.1002/ADTP.202000171.

[174] A. Zur Mühlen, C. Schwarz, W. Mehnert, Solid lipid nanoparticles (SLN) for controlled drug delivery – Drug release and release mechanism, European Journal of Pharmaceutics and Biopharmaceutics. 45 (1998) 149–155. https://doi.org/10.1016/S0939-6411(97)00150-1.

[175] S. Freiberg, X.X. Zhu, Polymer microspheres for controlled drug release, Int J Pharm. 282 (2004) 1–18. https://doi.org/10.1016/J.IJPHARM.2004.04.013.

[176] A. Hernández Montoto, R. Montes, A. Samadi, M. Gorbe, J.M. Terrés, R. Cao-Milán, E. Aznar, J. Ibañez, R. Masot, M.D. Marcos, M. Orzáez, F. Sancenón, L.B. Oddershede, R. Martínez-Máñez, Gold Nanostars Coated with Mesoporous Silica Are Effective and Nontoxic Photothermal Agents Capable of Gate Keeping and Laser-Induced Drug Release, ACS Appl Mater Interfaces. 10 (2018) 27644–27656. https://doi.org/10.1021/ACSAMI.8B08395.

[177] G. Huang, J. Gao, Z. Hu, J. V. St. John, B.C. Ponder, D. Moro, Controlled drug release from hydrogel nanoparticle networks, Journal of Controlled Release. 94 (2004) 303–311. https://doi.org/10.1016/J.JCONREL.2003.10.007.

[178] A. Alves-Sampaio, C. García-Rama, J.E. Collazos-Castro, Biofunctionalized PEDOT-coated microfibers for the treatment of spinal cord injury, Biomaterials. 89 (2016) 98–113. https://doi.org/10.1016/J.BIOMATERIALS.2016.02.037.

[179] A. García-Fernández, E. Aznar, R. Martínez-Máñez, F.A. Sancenón García-Fernández, E. Aznar, R. Martínez-Máñez, F. Sancenón, A. García-Fernández, F. Sancenón CIBER de Bioingeniería Biomateriales Nanomedicina CIBER-BBN, S.A. García-Fernández, New Advances in In Vivo Applications of Gated Mesoporous Silica as Drug Delivery Nanocarriers, Small. 16 (2020) 1902242. https://doi.org/10.1002/SMLL.201902242.

[180] J.H. Lee, Y. Yeo, Controlled drug release from pharmaceutical nanocarriers, Chem Eng Sci. 125 (2015) 75–84. https://doi.org/10.1016/J.CES.2014.08.046.

[181] F. Sancenõn, L. Pascual, M. Oroval, E. Aznar, R. Martínez-Máñez, Gated Silica Mesoporous Materials in Sensing Applications, ChemistryOpen. 4 (2015) 418–437. https://doi.org/10.1002/OPEN.201500053.

[182] D. Tarn, C.E. Ashley, M. Xue, E.C. Carnes, J.I. Zink, C. Jeffrey Brinker, Mesoporous silica nanoparticle nanocarriers: biofunctionality and biocompatibility, ACS Publications. 46 (2012) 792–801. https://doi.org/10.1021/ar3000986.

[183] Y. Zhou, G. Quan, Q. Wu, X. Zhang, B. Niu, B. Wu, Y. Huang, X. Pan, C. Wu, Mesoporous silica nanoparticles for drug and gene delivery, Acta Pharm Sin B. 8 (2018) 165–177. https://doi.org/10.1016/J.APSB.2018.01.007.

[184] Z. Li, J. C. Barnes, A. Bosoy, J. F. Stoddart, J. I. Zink, Mesoporous silica nanoparticles in biomedical applications, Chem. Soc. Rev. 41 (2012) 2590–2605. https://doi.org/10.1039/C1CS15246G.

[185] C. Argyo, V. Weiss, C. Bräuchle, T. Bein, Multifunctional mesoporous silica nanoparticles as a universal platform for drug delivery, Chemistry of Materials. 26 (2014) 435–451. https://doi.org/10.1021/CM402592T.

[186] V. Candela Noguera, Study, development and improvement of MCM-41-type MSN synthesis oriented to biomedical applications, Universitat Politècnica de València, 2022. https://doi.org/10.4995/THESIS/10251/182386.

[187] A. Llopis Lorente, Enzyme-functionalized hybrid mesoporous nanodevices for sensing, controlled release and molecular communication, Universitat Politècnica de València, 2019. https://doi.org/10.4995/THESIS/10251/117612.

[188] E. Yamamoto, K. Kuroda, Colloidal Mesoporous Silica Nanoparticles, Bulletin of the Chemical Society of Japan. 89 (2016) 501–539. https://doi.org/10.1246/BCSJ.20150420.

[189] A. Llopis-Lorente, B. De Luis, A. García-Fernández, S. Jimenez-Falcao, M. Orzáez, F. Sancenón, R. Villalonga, R. Martínez-Máñez, Hybrid Mesoporous Nanocarriers Act by Processing Logic Tasks: Toward the Design of Nanobots Capable of Reading Information from the Environment, ACS Appl Mater Interfaces. 10 (2018) 26494–26500. https://doi.org/10.1021/ACSAMI.8B05920.

[190] A. Llopis-Lorente, P. DÍez, A. Sánchez, M.D. Marcos, F. Sancenón, P. Martínez-Ruiz, R. Villalonga, R. Martínez-Máñez, Interactive models of communication at the nanoscale using nanoparticles that talk to one another, Nature Communications 8:1. 8 (2017) 1–7. https://doi.org/10.1038/ncomms15511.

[191] C.Y. Lai, B.G. Trewyn, D.M. Jeftinija, K. Jeftinija, S. Xu, S. Jeftinija, V.S.Y. Lin, A mesoporous silica nanosphere-based carrier system with chemically removable CdS nanoparticle caps for stimuli-responsive controlled release of neurotransmitters and drug molecules, J Am Chem Soc. 125 (2003) 4451–4459. https://doi.org/10.1021/JA028650L.

[192] R. Liu, X. Zhao, T. Wu, P. Feng, Tunable redox-responsive hybrid nanogated ensembles, J Am Chem Soc. 130 (2008) 14418–14419. https://doi.org/10.1021/JA8060886.

[193] H. Qu, L. Yang, J. Yu, T. Dong, M. Rong, J. Zhang, H. Xing, L. Wang, F. Pan, H. Liu, A redox responsive controlled release system using mesoporous silica nanoparticles capped with Au nanoparticles, RSC Adv. 7 (2017) 35704–35710. https://doi.org/10.1039/C7RA04444E.

[194] E.R. Edelman, J. Kost, H. Bobeck, R. Langer, Regulation of drug release from polymer matrices by oscillating magnetic fields, J Biomed Mater Res. 19 (1985) 67–83. https://doi.org/10.1002/JBM.820190107.

[195] Y.H. Bae, T. Okano, R. Hsu, S.W. Kim, Thermo-sensitive polymers as on-off switches for drug release, Die Makromolekulare Chemie, Rapid Communications. 8 (1987) 481–485. https://doi.org/10.1002/MARC.1987.030081002.

[196] S. Miyazaki, C. Yokouchi, M. Takada, External control of drug release: controlled release of insulin from a hydrophilic polymer implant by ultrasound irradiation in diabetic rats, J Pharm Pharmacol. 40 (1988) 716–717. https://doi.org/10.1111/J.2042-7158.1988.TB07001.X.

[197] J. Kost, K. Leong, R. Langer, Ultrasound-enhanced polymer degradation and release of incorporated substances, Proc Natl Acad Sci U S A. 86 (1989) 7663–7666. https://doi.org/10.1073/PNAS.86.20.7663.

[198] S. Mura, J. Nicolas, P. Couvreur, Stimuli-responsive nanocarriers for drug delivery, Nature Materials 12:11. 12 (2013) 991–1003. https://doi.org/10.1038/nmat3776.

[199] B.P. Timko, T. Dvir, D.S. Kohane, Remotely Triggerable Drug Delivery Systems, Advanced Materials. 22 (2010) 4925–4943. https://doi.org/10.1002/ADMA.201002072.

[200] S.S. Said, S. Campbell, T. Hoare, Externally Addressable Smart Drug Delivery Vehicles: Current Technologies and Future Directions, Chemistry of Materials. 31 (2019) 4971–4989. https://doi.org/10.1021/acs.chemmater.9b01798.

[201] J. Liu, C. Detrembleur, S. Mornet, C. Jérôme, E. Duguet, Design of hybrid nanovehicles for remotely triggered drug release: an overview, J Mater Chem B. 3 (2015) 6117–6147. https://doi.org/10.1039/C5TB00664C.

[202] S. Alberti, G.J.A.A. Soler-Illia, O. Azzaroni, Gated supramolecular chemistry in hybrid mesoporous silica nanoarchitectures: controlled delivery and molecular transport in response to chemical, physical and biological stimuli, Chemical Communications. 51 (2015) 6050–6075. https://doi.org/10.1039/C4CC10414E.

[203] Q. Yang, S. Wang, P. Fan, L. Wang, Y. Di, K. Lin, F.S. Xiao, pH-responsive carrier system based on carboxylic acid modified mesoporous silica and polyelectrolyte for drug delivery, Chemistry of Materials. 17 (2005) 5999–6003. https://doi.org/10.1021/cm051198v.

[204] Y.J. Yang, X. Tao, Q. Hou, Y. Ma, X.L. Chen, J.F. Chen, Mesoporous silica nanotubes coated with multilayered polyelectrolytes for pH-controlled drug release, Acta Biomater. 6 (2010) 3092–3100. https://doi.org/10.1016/J.ACTBIO.2010.02.042.

[205] S. Giri, B.G. Trewyn, M.P. Stellmaker, V.S.Y. Lin, Stimuli-responsive controlled-release delivery system based on mesoporous silica nanorods capped with magnetic nanoparticles, Angew Chem Int Ed Engl. 44 (2005) 5038–5044. https://doi.org/10.1002/ANIE.200501819.

[206] R. Liu, X. Zhao, T. Wu, P. Feng, Tunable redox-responsive hybrid nanogated ensembles, J Am Chem Soc. 130 (2008) 14418–14419. https://doi.org/10.1021/JA8060886.

[207] Y. Zhao, B.G. Trewyn, I.I. Slowing, V.S.Y. Lin, Mesoporous silica nanoparticle-based double drug delivery system for glucose-responsive controlled release of insulin and cyclic AMP, J Am Chem Soc. 131 (2009) 8398–8400. https://doi.org/10.1021/JA901831U.

[208] Y. Salinas, M. V. Solano, R.E. Sørensen, K.R. Larsen, J. Lycoops, J.O. Jeppesen, R. Martínez-Máñez, F. Sancenõn, M.D. Marcos, P. Amorõs, C. Guillem, Chromo-Fluorogenic Detection of Nitroaromatic Explosives by Using Silica Mesoporous Supports Gated with Tetrathiafulvalene Derivatives, Chemistry – A European Journal. 20 (2014) 855–866. https://doi.org/10.1002/CHEM.201302461.

[209] E. Climent, R. Martínez-Máñez, F. Sancenón, M.D. Marcos, J. Soto, A. Maquieira, P. Amorós, Controlled Delivery Using Oligonucleotide-Capped Mesoporous Silica Nanoparticles, Angewandte Chemie. 122 (2010) 7439–7441. https://doi.org/10.1002/ANGE.201001847.

[210] A. Llopis-Lorente, B. Lozano-Torres, A. Bernardos, R. Martínez-Máñez, F. Sancenón, Mesoporous silica materials for controlled delivery based on enzymes, Pubs.Rsc.Org. 5 (2013) 1–3. https://doi.org/10.1039/C7TB00348J.

[211] T. Tagami, W.D. Foltz, M.J. Ernsting, C.M. Lee, I.F. Tannock, J.P. May, S.D. Li, MRI monitoring of intratumoral drug delivery and prediction of the therapeutic effect with a multifunctional thermosensitive liposome, Biomaterials. 32 (2011) 6570–6578. https://doi.org/10.1016/J.BIOMATERIALS.2011.05.029.

[212] H.W. Yang, M.Y. Hua, H.L. Liu, C.Y. Huang, R.Y. Tsai, Y.J. Lu, J.Y. Chen, H.J. Tang, H.Y. Hsien, Y.S. Chang, T.C. Yen, P.Y. Chen, K.C. Wei, Self-protecting core-shell magnetic nanoparticles for targeted, traceable, long half-life delivery of BCNU to gliomas, Biomaterials. 32 (2011) 6523–6532. https://doi.org/10.1016/J.BIOMATERIALS.2011.05.047.

[213] N.Y. Rapoport, A.M. Kennedy, J.E. Shea, C.L. Scaife, K.H. Nam, Controlled and targeted tumor chemotherapy by ultrasound-activated nanoemulsions/microbubbles, Journal of Controlled Release. 138 (2009) 268–276. https://doi.org/10.1016/J.JCONREL.2009.05.026.

[214] N.K. Mal, M. Fujiwara, Y. Tanaka, Photocontrolled reversible release of guest molecules from coumarin-modified mesoporous silica, Nature 2003 421:6921. 421 (2003) 350–353. https://doi.org/10.1038/nature01362.

[215] C. Mauriello Jimenez, D. Aggad, J.G. Croissant, K. Tresfield, D. Laurencin, D. Berthomieu, N. Cubedo, M. Rossel, S. Alsaiari, D.H. Anjum, R. Sougrat, M.A. Roldan-Gutierrez, S. Richeter, E. Oliviero, L. Raehm, C. Charnay, X. Cattoën, S. Clément, M. Wong Chi Man, M. Maynadier, V. Chaleix, V. Sol, M. Garcia, M. Gary-Bobo, N.M. Khashab, N. Bettache, J.O. Durand, Porous Porphyrin-Based Organosilica Nanoparticles for NIR Two-Photon Photodynamic Therapy and Gene Delivery in Zebrafish, Adv Funct Mater. 28 (2018) 1800235. https://doi.org/10.1002/ADFM.201800235.

[216] A. Hernández Montoto, A. Llopis-Lorente, M. Gorbe, J. M. Terrés, R. Cao-Milán, B. Díaz de Greñu, M. Alfonso, J. Ibañez, M.D. Marcos, M. Orzáez, R. Villalonga, R. Martínez-Máñez, F. Sancenón, Janus Gold Nanostars–Mesoporous Silica Nanoparticles for NIR-Light-Triggered Drug Delivery, Chemistry – A European Journal. 25 (2019) 8471–8478. https://doi.org/10.1002/CHEM.201900750.

[217] A. Hernández-Montoto, M. Gorbe, A. Llopis-Lorente, J.M. Terrés, R. Montes, R. Cao-Milán, B. DÍaz De Greñu, M. Alfonso, M. Orzaez, M.D. Marcos, R. Martínez-Máñez, F. Sancenón, A NIR light-triggered drug delivery system using core–shell gold nanostars–mesoporous silica nanoparticles based on multiphoton absorption photo-dissociation of 2-nitrobenzyl PEG, Chemical Communications. 55 (2019) 9039–9042. https://doi.org/10.1039/C9CC04260A.

[218] J. Ge, E. Neofytou, T.J. Cahill, R.E. Beygui, R.N. Zare, Drug release from electric-field-responsive nanoparticles, ACS Nano. 6 (2012) 227–233. https://doi.org/10.1021/NN203430M.

[219] J.S. Im, B.C. Bai, Y.S. Lee, The effect of carbon nanotubes on drug delivery in an electro-sensitive transdermal drug delivery system, Biomaterials. 31 (2010) 1414–1419. https://doi.org/10.1016/J.BIOMATERIALS.2009.11.004.

[220] A. García-Fernández, B. Lozano-Torres, J.F. Blandez, J. Monreal-Trigo, J. Soto, J.E. Collazos-Castro, M. Alcañiz, M.D. Marcos, F. Sancenón, R. Martínez-Máñez, Electro-responsive films containing voltage responsive gated mesoporous silica nanoparticles grafted onto PEDOT-based conducting polymer, Journal of Controlled Release. 323 (2020) 421–430. https://doi.org/10.1016/J.JCONREL.2020.04.048.

[221] N. Paradee, J. Thanokiang, A. Sirivat, Conductive poly(2-ethylaniline) dextran-based hydrogels for electrically controlled diclofenac release, Materials Science and Engineering: C. 118 (2021) 111346. https://doi.org/10.1016/J.MSEC.2020.111346.

[222] A. Mohapatra, C. Wells, A. Jennings, M. Ghimire, S.R. Mishra, B.I. Morshed, Electric Stimulus-Responsive Chitosan/MNP Composite Microbeads for a Drug Delivery System, IEEE Trans Biomed Eng. 67 (2020) 226–233. https://doi.org/10.1109/TBME.2019.2911579.

[223] Y. Yun, H. Wu, J. Gao, W. Dai, L. Deng, O. Lv, Y. Kong, Facile synthesis of Ca2+-crosslinked sodium alginate/graphene oxide hybrids as electro- and pH-responsive drug carrier, Materials Science and Engineering: C. 108 (2020) 110380. https://doi.org/10.1016/J.MSEC.2019.110380.

[224] C.M. Wells, M. Harris, L. Choi, V.P. Murali, F.D. Guerra, J.A. Jennings, Stimuli-Responsive Drug Release from Smart Polymers, Journal of Functional Biomaterials 2019, Vol. 10, Page 34. 10 (2019) 34. https://doi.org/10.3390/JFB10030034.

[225] N.K. Guimard, N. Gomez, C.E. Schmidt, Conducting polymers in biomedical engineering, Prog Polym Sci. 32 (2007) 876–921. https://doi.org/10.1016/J.PROGPOLYMSCI.2007.05.012.

[226] S. Tajik, H. Beitollahi, F.G. Nejad, I.S. Shoaie, M.A. Khalilzadeh, M.S. Asl, Q. Van Le, K. Zhang, H.W. Jang, M. Shokouhimehr, Recent developments in conducting polymers: applications for electrochemistry, RSC Adv. 10 (2020) 37834–37856. https://doi.org/10.1039/D0RA06160C.

[227] X. Wang, L. Zhi, K. Müllen, Transparent, conductive graphene electrodes for dye-sensitized solar cells, Nano Lett. 8 (2008) 323–327. https://doi.org/10.1021/NL072838R.

[228] S.J. Leigh, R.J. Bradley, C.P. Purssell, D.R. Billson, D.A. Hutchins, A Simple, Low-Cost Conductive Composite Material for 3D Printing of Electronic Sensors, PLoS One. 7 (2012). https://doi.org/10.1371/JOURNAL.PONE.0049365.

[229] D. Zhang, K. Ryu, X. Liu, E. Polikarpov, J. Ly, M.E. Tompson, C. Zhou, Transparent, conductive, and flexible carbon nanotube films and their application in organic light-emitting diodes, Nano Lett. 6 (2006) 1880–1886. https://doi.org/10.1021/NL0608543.

[230] C. Boehler, Z. Aqrawe, M.A.-B. in Medicine, undefined 2019, Applications of PEDOT in bioelectronic medicine, Future Medicine. 2 (2019) 89–99. https://doi.org/10.2217/bem-2019-0014.

[231] H. Palza, P.A. Zapata, C. Angulo-Pineda, Electroactive Smart Polymers for Biomedical Applications, Materials 2019, Vol. 12, Page 277. 12 (2019) 277. https://doi.org/10.3390/MA12020277.

[232] D. Svirskis, J. Travas-Sejdic, A. Rodgers, S. Garg, Electrochemically controlled drug delivery based on intrinsically conducting polymers, Journal of Controlled Release. 146 (2010) 6–15. https://doi.org/10.1016/J.JCONREL.2010.03.023.

[233] D. Uppalapati, B.J. Boyd, S. Garg, J. Travas-Sejdic, D. Svirskis, Conducting polymers with defined micro- or nanostructures for drug delivery, Biomaterials. 111 (2016) 149–162. https://doi.org/10.1016/J.BIOMATERIALS.2016.09.021.

[234] S. Inal, J. Rivnay, A.O. Suiu, G.G. Malliaras, I. McCulloch, Conjugated Polymers in Bioelectronics, Acc Chem Res. 51 (2018) 1368–1376. https://doi.org/10.1021/ACS.ACCOUNTS.7B00624.

[235] M. Naseri, L. Fotouhi, A.E.-T.C. Record, undefined 2018, Recent Progress in the development of conducting polymer-based nanocomposites for electrochemical biosensors applications: a mini-review, The Chemical Record. 18 (2018) 599–618. https://doi.org/10.1002/tcr.201700101.

[236] Z. Aqrawe, J. Montgomery, J. Travas-Sejdic, D. Svirskis, Conducting Polymers as Electrode Coatings for Neuronal Multi-electrode Arrays, Trends Biotechnol. 35 (2017) 93–95. https://doi.org/10.1016/J.TIBTECH.2016.06.007.

[237] H. Vara, J.C.-C.-A.A.M.& Interfaces, undefined 2015, Biofunctionalized conducting polymer/carbon microfiber electrodes for ultrasensitive neural recordings, ACS Publications. 7 (2015) 27016–27026. https://doi.org/10.1021/acsami.5b09594.

[238] R. Green, M.R. Abidian, R. Green, M.R. Abidian, Conducting polymers for neural prosthetic and neural interface applications, Wiley Online Library. 27 (2015) 7620–7637. https://doi.org/10.1002/adma.201501810.

[239] K. Kenry, B. Liu, Recent Advances in Biodegradable Conducting Polymers and Their Biomedical Applications, Biomacromolecules. 19 (2018) 1783–1803. https://doi.org/10.1021/ACS.BIOMAC.8B00275.

[240] A. Zhang, K. Jung, A. Li, J. Liu, C. Boyer, Recent advances in stimuli-responsive polymer systems for remotely controlled drug release, Prog Polym Sci. 99 (2019) 101164. https://doi.org/10.1016/J.PROGPOLYMSCI.2019.101164.

[241] Y. Brudno, D.J. Mooney, On-demand drug delivery from local depots, Journal of Controlled Release. 219 (2015) 8–17. https://doi.org/10.1016/J.JCONREL.2015.09.011.

[242] S.B. Campbell, T. Hoare, Externally addressable hydrogel nanocomposites for biomedical applications, Curr Opin Chem Eng. 4 (2014) 1–10. https://doi.org/10.1016/J.COCHE.2013.12.003.

[243] Q.V. Nguyen, D.P. Huynh, J.H. Park, D.S. Lee, Injectable polymeric hydrogels for the delivery of therapeutic agents: A review, Eur Polym J. 72 (2015) 602–619. https://doi.org/10.1016/J.EURPOLYMJ.2015.03.016.

[244] J. Zhang, Q. Huang, J. Du, Recent advances in magnetic hydrogels, Polym Int. 65 (2016) 1365–1372. https://doi.org/10.1002/PI.5170.

[245] S. Merino, C. Martín, K. Kostarelos, M. Prato, E. Vázquez, Nanocomposite hydrogels: 3D polymer-nanoparticle synergies for on-demand drug delivery, ACS Nano. 9 (2015) 4686–4697. https://doi.org/10.1021/ACSNANO.5B01433.

[246] R. Wadhwa, C.F. Lagenaur, X.T. Cui, Electrochemically controlled release of dexamethasone from conducting polymer polypyrrole coated electrode, Journal of Controlled Release. 110 (2006) 531–541. https://doi.org/10.1016/J.JCONREL.2005.10.027.

[247] E. Shamaeli, N. Alizadeh, Nanostructured biocompatible thermal/electrical stimuli-responsive biopolymer-doped polypyrrole for controlled release of chlorpromazine: Kinetics studies, Int J Pharm. 472 (2014) 327–338. https://doi.org/10.1016/J.IJPHARM.2014.06.036.

[248] D. Esrafilzadeh, J.M. Razal, S.E. Moulton, E.M. Stewart, G.G. Wallace, Multifunctional conducting fibres with electrically controlled release of ciprofloxacin, Journal of Controlled Release. 169 (2013) 313–320. https://doi.org/10.1016/J.JCONREL.2013.01.022.

[249] R.T. Richardson, A.K. Wise, B.C. Thompson, B.O. Flynn, P.J. Atkinson, N.J. Fretwell, J.B. Fallon, G.G. Wallace, R.K. Shepherd, G.M. Clark, S.J. O'Leary, Polypyrrole-coated electrodes for the delivery of charge and neurotrophins to cochlear neurons, Biomaterials. 30 (2009) 2614–2624. https://doi.org/10.1016/J.BIOMATERIALS.2009.01.015.

[250] C. Boehler, C. Kleber, N. Martini, Y. Xie, I. Dryg, T. Stieglitz, U.G. Hofmann, M. Asplund, Actively controlled release of Dexamethasone from neural microelectrodes in a chronic in vivo study, Biomaterials. 129 (2017) 176–187. https://doi.org/10.1016/J.BIOMATERIALS.2017.03.019.

[251] L. Qiu, Y. Zhao, B. Li, Z. Wang, L. Cao, L. Sun, Triple-stimuli (protease/redox/pH) sensitive porous silica nanocarriers for drug delivery, Sens Actuators B Chem. 240 (2017) 1066–1074. https://doi.org/10.1016/J.SNB.2016.09.083.

[252] X. Chen, H. Sun, J. Hu, X. Han, H. Liu, Y. Hu, Transferrin gated mesoporous silica nanoparticles for redox-responsive and targeted drug delivery, Colloids Surf B Biointerfaces. 152 (2017) 77–84. https://doi.org/10.1016/J.COLSURFB.2017.01.010.

[253] Y. Zhang, L. Han, Y. Zhang, Y.Q. Chang, X.W. Chen, R.H. He, Y. Shu, J.H. Wang, Glutathione-mediated mesoporous carbon as a drug delivery nanocarrier with carbon dots as a cap and fluorescent tracer, Nanotechnology. 27 (2016) 355102. https://doi.org/10.1088/0957-4484/27/35/355102.

[254] Z. Luo, Y. Hu, K. Cai, X. Ding, Q. Zhang, M. Li, X. Ma, B. Zhang, Y. Zeng, P. Li, J. Li, J. Liu, Y. Zhao, Intracellular redox-activated anticancer drug delivery by functionalized hollow mesoporous silica nanoreservoirs with tumor specificity, Biomaterials. 35 (2014) 7951–7962. https://doi.org/10.1016/J.BIOMATERIALS.2014.05.058.

[255] X. Du, L. Xiong, S. Dai, F. Kleitz, S. Zhang Qiao, Intracellular Microenvironment-Responsive Dendrimer-Like Mesoporous Nanohybrids for Traceable, Effective, and Safe Gene Delivery, Adv Funct Mater. 24 (2014) 7627–7637. https://doi.org/10.1002/ADFM.201402408.

[256] A. Raza, U. Hayat, T. Rasheed, M. Bilal, H.M.N. Iqbal, Redox-responsive nano-carriers as tumor-targeted drug delivery systems, Eur J Med Chem. 157 (2018) 705–715. https://doi.org/10.1016/J.EJMECH.2018.08.034.

[257] I.U. Shah, S.A. Jadhav, V.M. Belekar, P.S. Patil, Smart polymer grafted silica based drug delivery systems, Polym Adv Technol. (2022). https://doi.org/10.1002/PAT.5890.

[258] Y. Xiao, T. Wang, Y. Cao, X. Wang, Y. Zhang, Y. Liu, Q. Huo, Enzyme and voltage stimuli-responsive controlled release system based on β-cyclodextrin-capped mesoporous silica nanoparticles, Dalton Transactions. 44 (2015) 4355–4361. https://doi.org/10.1039/C4DT03758H.

[259] T. Wang, G.P. Sun, M.D. Wang, B.J. Zhou, J.J. Fu, Voltage/pH-Driven Mechanized Silica Nanoparticles for the Multimodal Controlled Release of Drugs, ACS Appl Mater Interfaces. 7 (2015) 21295–21304. https://doi.org/10.1021/ACSAMI.5B05619.

[260] X. Jiao, R. Sun, Y. Cheng, F. Li, X. Du, Y. Wen, Y. Song, X. Zhang, A Voltage-Responsive Free-Blockage Controlled-Release System Based on Hydrophobicity Switching, ChemPhysChem. 18 (2017) 1317–1323. https://doi.org/10.1002/cphc.201700117.

[261] F.E. Perrin, H.N. Noristani, Serotonergic mechanisms in spinal cord injury, Exp Neurol. 318 (2019) 174–191. https://doi.org/10.1016/J.EXPNEUROL.2019.05.007.

[262] M. Ghosh, D.D. Pearse, The role of the serotonergic system in locomotor recovery after spinal cord injury, Front Neural Circuits. 8 (2015) 151. https://doi.org/10.3389/FNCIR.2014.00151.

[263] Z. Oueghlani, L. Juvin, F.M. Lambert, L. Cardoit, G. Courtand, F. Masmejean, J.R. Cazalets, G. Barrière, Serotonergic modulation of sacral dorsal root stimulation-induced locomotor output in newborn rat, Neuropharmacology. 170 (2020) 107815. https://doi.org/10.1016/J.NEUROPHARM.2019.107815.

[264] D.J. Fickbohm, P.S. Katz, Paradoxical Actions of the Serotonin Precursor 5-hydroxytryptophan on the Activity of Identified Serotonergic Neurons in a Simple Motor Circuit, Journal of Neuroscience. 20 (2000) 1622–1634. https://doi.org/10.1523/JNEUROSCI.20-04-01622.2000.

[265] Z. Li, O. Polat, E. Seker, Z. Li, O. Polat, E. Seker, Voltage-Gated Closed-Loop Control of Small-Molecule Release from Alumina-Coated Nanoporous Gold Thin Film Electrodes, Adv Funct Mater. 28 (2018) 1801292. https://doi.org/10.1002/ADFM.201801292.

[266] A. Haleem, M. Javaid, R.P. Singh, R. Suman, S. Rab, Biosensors applications in medical field: A brief review, Sensors International. 2 (2021) 100100. https://doi.org/10.1016/J.SINTL.2021.100100.

[267] E. Cesewski, B.N. Johnson, Electrochemical biosensors for pathogen detection, Biosens Bioelectron. 159 (2020) 112214. https://doi.org/10.1016/J.BIOS.2020.112214.

[268] D.G. Rackus, M.H. Shamsi, A.R. Wheeler, Electrochemistry, biosensors and microfluidics: a convergence of fields, Chem Soc Rev. 44 (2015) 5320–5340. https://doi.org/10.1039/C4CS00369A.

[269] T. Wadhera, D. Kakkar, G. Wadhwa, B. Raj, Recent Advances and Progress in Development of the Field Effect Transistor Biosensor: A Review, Journal of Electronic Materials 2019 48:12. 48 (2019) 7635–7646. https://doi.org/10.1007/S11664-019-07705-6.

[270] C. Peruzzi, S. Battistoni, D. Montesarchio, M. Cocuzza, S.L. Marasso, A. Verna, L. Pasquardini, R. Verucchi, L. Aversa, V. Erokhin, P. D'Angelo, S. Iannotta, Interfacing aptamers, nanoparticles and graphene in a hierarchical structure for highly selective detection of biomolecules in OECT devices, Scientific Reports 2021 11:1. 11 (2021) 1–11. https://doi.org/10.1038/s41598-021-88546-4.

[271] W. Zhou, P.J. Jimmy Huang, J. Ding, J. Liu, Aptamer-based biosensors for biomedical diagnostics, Analyst. 139 (2014) 2627–2640. https://doi.org/10.1039/C4AN00132J.

[272] N.I. Khan, E. Song, Lab-on-a-Chip Systems for Aptamer-Based Biosensing, Micromachines 2020, Vol. 11, Page 220. 11 (2020) 220. https://doi.org/10.3390/MI11020220.

[273] M. Liu, J. Song, S. Shuang, C. Dong, J.D. Brennan, Y. Li, A graphene-based biosensing platform based on the release of DNA probes and rolling circle amplification, ACS Nano. 8 (2014) 5564–5573. https://doi.org/10.1021/NN5007418.

[274] Y.M. Wang, Z. Wu, S.J. Liu, X. Chu, Structure-Switching Aptamer Triggering Hybridization Chain Reaction on the Cell Surface for Activatable Theranostics, Anal Chem. 87 (2015) 6470–6474. https://doi.org/10.1021/ACS.ANALCHEM.5B01634.

[275] X. Zuo, F. Xia, Y. Xiao, K.W. Plaxco, Sensitive and selective amplified fluorescence DNA detection based on exonuclease III-aided target recycling, J Am Chem Soc. 132 (2010) 1816–1818. https://doi.org/10.1021/JA909551B/SUPPL_FILE/JA909551B_SI_001.PDF.

[276] L. Zhao, X. Qi, X. Yan, Y. Huang, X. Liang, L. Zhang, S. Wang, W. Tan, Engineering Aptamer with Enhanced Affinity by Triple Helix-Based Terminal Fixation, (2019). https://doi.org/10.1021/jacs.9b09292.

[277] Y. Zhao, F. Chen, Q. Li, L. Wang, C. Fan, Isothermal Amplification of Nucleic Acids, (2015). https://doi.org/10.1021/acs.chemrev.5b00428.

[278] N. Nakatsuka, K.-A. Yang, J.M. Abendroth, K.M. Cheung, X. Xu, H. Yang, C. Zhao, B. Zhu, Y.S. Rim, Y. Yang, P.S. Weiss, M.N. Stojanović, A.M. Andrews, Aptamer-field-effect transistors overcome Debye length limitations for small-molecule sensing, Science. 362 (2018) 319–324. https://doi.org/10.1126/SCIENCE.AAO6750.

[279] I.Y. Wong, N.A. Melosh, An Electrostatic Model for DNA Surface Hybridization, Biophys J. 98 (2010) 2954. https://doi.org/10.1016/J.BPJ.2010.03.017.

[280] F.N. Ishikawa, M. Curreli, H.K. Chang, P.C. Chen, R. Zhang, R.J. Cote, M.E. Thompson, C. Zhou, A Calibration Method for Nanowire Biosensors to Suppress Device-to-device Variation, ACS Nano. 3 (2009) 3969. https://doi.org/10.1021/NN9011384.

[281] J. Monreal-Trigo, M. Alcañiz, Electronic system for combined techniques: electrostimulation and controlled electrochemical drug release, in: XIII International Workshop on Sensors and Molecular Recognition (IWOSMOR 2019), València, 2019: pp. 76–79.

[282] J. Monreal-Trigo, C. Bastida-Molina, R. Vengut-Tro, M. Alcañiz Fillol, Remote electronic system for long-duration in-vitro combination of electrostimulation and electrically controlled drug release, in: XIV International Workshop on Sensors and Molecular Recognition (IWOSMOR 2021), 2021: pp. 198–201.

[283] L. Alamán Escolano, Diseño, desarrollo y validación de un sistema biocompatible para la estimulación eléctrica multiplexada de tejido nervioso in-vitro, 2021. https://riunet.upv.es/handle/10251/171740.

[284] M. Łabańska, P. Ciosek-Skibińska, W. Wróblewski, Critical Evaluation of Laboratory Potentiometric Electronic Tongues for Pharmaceutical Analysis—An Overview, Sensors, Vol. 19, Page 5376. 19 (2019) 5376. https://doi.org/10.3390/S19245376.

[285] L. Lvova, I. Jahatspanian, L.H.C. Mattoso, D.S. Correa, E. Oleneva, A. Legin, C. Di Natale, R. Paolesse, Potentiometric E-Tongue System for Geosmin/Isoborneol Presence Monitoring in Drinkable Water, Sensors 2020, Vol. 20, Page 821. 20 (2020) 821. https://doi.org/10.3390/S20030821.

[286] H. Ghrissi, A.C.A. Veloso, Í.M.G. Marx, T. Dias, A.M. Peres, A Potentiometric Electronic Tongue as a Discrimination Tool of Water-Food Indicator/Contamination Bacteria, Chemosensors 2021, Vol. 9, Page 143. 9 (2021) 143. https://doi.org/10.3390/CHEMOSENSORS9060143.

[287] R.B. Belugina, Y.B. Monakhova, E. Rubtsova, A. Becht, C. Schollmayer, U. Holzgrabe, A. V. Legin, D.O. Kirsanov, Distinguishing paracetamol formulations: Comparison of potentiometric "Electronic Tongue" with established analytical techniques, J Pharm Biomed Anal. 188 (2020) 113457. https://doi.org/10.1016/J.JPBA.2020.113457.

[288] V. Semenov, S. Volkov, M. Khaydukova, A. Fedorov, I. Lisitsyna, D. Kirsanov, A. Legin, Determination of three quality parameters in vegetable oils using potentiometric e-tongue, Journal of Food Composition and Analysis. 75 (2019) 75–80. https://doi.org/10.1016/J.JFCA.2018.09.015.

[289] V. da C. Arca, A.M. Peres, A.A.S.C. Machado, E. Bona, L.G. Dias, Sugars' Quantifications Using a Potentiometric Electronic Tongue with Cross-Selective Sensors: Influence of an Ionic Background, Chemosensors, Vol. 7, Page 43. 7 (2019) 43. https://doi.org/10.3390/CHEMOSENSORS7030043.

[290] J. Do Kim, H.G. Byun, D.J. Kim, Y.K. Ham, W.S. Jung, C.O. Yoon, A simple taste analyzing system design for visual and quantitative analysis of different tastes using multi-array chemical sensors and pattern recognition techniques, Talanta. 70 (2006) 546–555. https://doi.org/10.1016/J.TALANTA.2006.01.020.

[291] P.W. Ruch, R. Hu, L. Capua, Y. Temiz, S. Paredes, A. Lopez, J. Barroso, A. Cox, E. Nakamura, K. Matsumoto, A portable potentiometric electronic tongue leveraging smartphone and cloud platforms, ISOEN 2019 - 18th International Symposium on Olfaction and Electronic Nose, Proceedings. (2019). https://doi.org/10.1109/ISOEN.2019.8823244.

[292] Z. Jarolímová, J. Bosson, G.M. Labrador, J. Lacour, E. Bakker, Ion Transfer Voltammetry in Polyurethane Thin Films Based on Functionalised Cationic [6]Helicenes for Carbonate Detection, Electroanalysis. 30 (2018) 1378–1385. https://doi.org/10.1002/ELAN.201800080.

[293] Z. Jarolímová, J. Bosson, G.M. Labrador, J. Lacour, E. Bakker, Ion Transfer Voltammetry at Thin Films Based on Functionalized Cationic [6]Helicenes, Electroanalysis. 30 (2018) 650–657. https://doi.org/10.1002/ELAN.201700669.

[294] F.A. Alatraktchi, S.B. Andersen, H.K. Johansen, S. Molin, W.E. Svendsen, Fast Selective Detection of Pyocyanin Using Cyclic Voltammetry, Sensors 2016, Vol. 16, Page 408. 16 (2016) 408. https://doi.org/10.3390/S16030408.

[295] P. Pattananuwat, D. Aht-ong, Controllable morphology of polypyrrole wrapped graphene hydrogel framework composites via cyclic voltammetry with aiding of poly (sodium 4-styrene sulfonate) for the

flexible supercapacitor electrode, Electrochim Acta. 224 (2017) 149–160. https://doi.org/10.1016/J.ELECTACTA.2016.12.036.

[296] L.A.J. Silva, W.P. da Silva, J.G. Giuliani, S.C. Canobre, C.D. Garcia, R.A.A. Munoz, E.M. Richter, Use of pyrolyzed paper as disposable substrates for voltammetric determination of trace metals, Talanta. 165 (2017) 33–38. https://doi.org/10.1016/J.TALANTA.2016.12.009.

[297] K.Y. Lee, A. Ambrosi, M. Pumera, 3D-printed Metal Electrodes for Heavy Metals Detection by Anodic Stripping Voltammetry, Electroanalysis. 29 (2017) 2444–2453. https://doi.org/10.1002/ELAN.201700388.

[298] M. Ashjari, H. Karimi-Maleh, F. Ahmadpour, M. Shabani-Nooshabadi, A. Sadrnia, M.A. Khalilzadeh, Voltammetric analysis of mycophenolate mofetil in pharmaceutical samples via electrochemical nanostructure based sensor modified with ionic liquid and MgO/SWCNTs, J Taiwan Inst Chem Eng. 80 (2017) 989–996. https://doi.org/10.1016/J.JTICE.2017.08.046.

[299] M. Khaydukova, C. Medina-Plaza, M.L. Rodriguez-Mendez, V. Panchuk, D. Kirsanov, A. Legin, Multivariate calibration transfer between two different types of multisensor systems, Sens Actuators B Chem. 246 (2017) 994–1000. https://doi.org/10.1016/J.SNB.2017.02.099.

[300] A. Bagheri, M. Hassani Marand, Voltammetric and Potentiometric Determination of Cu2+ Using an Overoxidized Polypyrrole Based Electrochemical Sensor, Russian Journal of Electrochemistry. 56 (2020) 453–461. https://doi.org/10.1134/S1023193520060026/TABLES/1.

[301] A.S. Shatla, A.A. Abd-El-Latif, S. Ayata, D. Demir, H. Baltruschat, Iodide adsorption at Au(111) electrode in non-aqueous electrolyte: AC-voltammetry and EIS studies, Electrochim Acta. 334 (2020) 135556. https://doi.org/10.1016/J.ELECTACTA.2019.135556.

[302] H.-W. Jee, K.-J. Paeng, Y. Son, Y. Jang, K. Rho, N. Myung, Electrosynthesis of Cobalt Telluride Thin Films by Voltammetry Combined with Electrochemical Quartz Crystal Microgravimetry, J Electrochem Soc. 166 (2019) H3035–H3039. https://doi.org/10.1149/2.0101905JES/XML.

[303] N. Myung, H.-Y. Park, H.-W. Jee, E.B. Sohn, S.J. Lee, K.-J. Paeng, I. Rhee, A. Vali, K. Rajeshwar, Electrosynthesis of MoTe2 Thin Films: A Combined Voltammetry-Electrochemical Quartz Crystal Microgravimetry Study of Mechanistic Aspects, J Electrochem Soc. 167 (2020) 116510. https://doi.org/10.1149/1945-7111/ABA15E.

[304] E.O. Baldeón, M. Alcañiz, R. Masot, E.M. Fuentes, J.M. Barat, R. Grau, Voltammetry pulse array developed to determine the antioxidant activity of camu–camu (Myrciaria dubia (H.B.K.) McVaug) and tumbo (Passiflora mollisima (Kunth) L.H. Bailey) juices employing voltammetric electronic tongues, Food Control. 54 (2015) 181–187. https://doi.org/10.1016/J.FOODCONT.2015.01.044.

[305] C.C. Segura, J.F. Osma, Miniaturization of Cyclic Voltammetry Electronic Systems for Remote Biosensing , Int J Biosens Bioelectron. 3 (2017) 68. https://doi.org/10.15406/ijbsbe.2017.03.00068.

[306] G. Pennazza, M. Santonico, L. Vollero, A. Zompanti, A. Sabatini, N. Kumar, I. Pini, W.F.Q. Solano, L. Sarro, A. D'Amico, Advances in the electronics for cyclic voltammetry: The case of gas detection by using microfabricated electrodes, Front Chem. 6 (2018) 327. https://doi.org/10.3389/FCHEM.2018.00327.

[307] S. Lin, W. Yu, B. Wang, Y. Zhao, K. En, J. Zhu, X. Cheng, C. Zhou, H. Lin, Z. Wang, H. Hojaiji, C. Yeung, C. Milla, R.W. Davis, Noninvasive wearable electroactive pharmaceutical monitoring for personalized therapeutics, Proc Natl Acad Sci U S A. 117 (2020) 19017–19025. https://doi.org/10.1073/PNAS.2009979117.

[308] J. Dieffenderfer, M. Wilkins, C. Hood, E. Beppler, M.A. Daniele, A. Bozkurt, Towards a sweat-based wireless and wearable electrochemical sensor, Proceedings of IEEE Sensors (2017). https://doi.org/10.1109/ICSENS.2016.7808470.

[309] G. Poulladofonou, C. Freris, A. Economou, C. Kokkinos, Wearable Electronic Finger for Date Rape Drugs Screening: From "do-It-Yourself" Fabrication to Self-Testing, Anal Chem. 94 (2022) 4087–4094. https://doi.org/10.1021/ACS.ANALCHEM.2C00015.

[310] S.D. Adams, E.H. Doeven, K. Quayle, A.Z. Kouzani, MiniStat: Development and Evaluation of a Mini-Potentiostat for Electrochemical Measurements, IEEE Access. 7 (2019) 31903–31912. https://doi.org/10.1109/ACCESS.2019.2902575.

[311] P. Lopin, K. V. Lopin, PSoC-Stat: A single chip open source potentiostat based on a Programmable System on a Chip, PLoS One. 13 (2018) e0201353. https://doi.org/10.1371/JOURNAL.PONE.0201353.

[312] Y.C. Li, E.L. Melenbrink, G.J. Cordonier, C. Boggs, A. Khan, M.K. Isaac, L.K. Nkhonjera, D. Bahati, S.J. Billinge, S.M. Haile, R.A. Kreuter, R.M. Crable, T.E. Mallouk, An Easily Fabricated Low-Cost Potentiostat Coupled with User-Friendly Software for Introducing Students to Electrochemical Reactions and Electroanalytical Techniques, J Chem Educ. 95 (2018) 1658–1661. https://doi.org/10.1021/ACS.JCHEMED.8B00340.

[313] D.M. Jenkins, B.E. Lee, S. Jun, J. Reyes-De-Corcuera, E.S. McLamore, ABE-Stat, a Fully Open-Source and Versatile Wireless Potentiostat Project Including Electrochemical Impedance Spectroscopy, J Electrochem Soc. 166 (2019) B3056–B3065. https://doi.org/10.1149/2.0061909JES/XML.

[314] A. Ainla, M.P.S. Mousavi, M.N. Tsaloglou, J. Redston, J.G. Bell, M.T. Fernández-Abedul, G.M. Whitesides, Open-Source Potentiostat for Wireless Electrochemical Detection with Smartphones, Anal Chem. 90 (2018) 6240–6246. https://doi.org/10.1021/ACS.ANALCHEM.8B00850.

[315] O.S. Hoilett, J.F. Walker, B.M. Balash, N.J. Jaras, S. Boppana, J.C. Linnes, KickStat: A Coin-Sized Potentiostat for High-Resolution Electrochemical Analysis, Sensors 2020, Vol. 20, Page 2407. 20 (2020) 2407. https://doi.org/10.3390/S20082407.

[316] J.E. Davis, E.C. Toren, On the Instability of Current Followers in Potentiostat Circuits, Anal Chem. 46 (1974) 647–650. https://doi.org/10.1021/AC60342A006.

[317] Potentiostat stability mystery explained. Application Note #4. Bio-Logic Science Instruments, 2005. https://www.biologic.net/documents/potentiostat-stability-electrochemistry-battery-application-note-4/ (accessed October 17, 2022).

[318] R. Doelling, Potentiostats: An introduction to the principle of potentiostatic control, including basic potentiostatic circuits, electrochemical applications, and some notes on electrode and cell design, 2000.

[319] Reference Electrode Effects on Potentiostat Performance Background, Gamry Instruments, 2009.

[320] Getting to Know Your Potentiostat: Potentiostat Stability Considerations. Technical Note 200.

[321] Potentiostat instability. SpectroInlets. EC-MS Technical Note #3, 2022. https://spectroinlets.com/wp-content/uploads/2022/01/Technical_note__3.pdf (accessed October 18, 2022).

[322] Potential Error Correction (iR Compensation). Technical Note 101.

[323] J.G. Hardy, H. Li, J.K. Chow, S.A. Geissler, A.B. McElroy, L. Nguy, D.S. Hernandez, C.E. Schmidt, Conducting polymer-based multilayer films for instructive biomaterial coatings, Future Sci OA. 1 (2015) 79. https://doi.org/10.4155/FSO.15.79.

[324] M. Yousefifard, A. Sarveazad, A. Babahajian, S.N. Rafiei Alavi, A. Madani Neishaboori, A.R. Vaccaro, M. Hosseini, V. Rahimi-Movaghar, Growth Factor Gene-Modified Cells in Spinal Cord Injury Recovery: A Systematic Review, World Neurosurg. 162 (2022) 150-162.e1. https://doi.org/10.1016/J.WNEU.2022.03.012.

[325] J. Monreal Trigo, Diseño, desarrollo y validación de un sistema electrónico de electroestimulación y liberación electroquímica controlada de fármacos para la mejora de la capacidad de regeneración de células nerviosas, Universitat Politècnica de València, 2018. https://riunet.upv.es/handle/10251/110996.

[326] J.E. Collazos-Castro, J.L. Polo, G.R. Hernández-Labrado, V. Padial-Cañete, C. García-Rama, Bioelectrochemical control of neural cell development on conducting polymers, Biomaterials. 31 (2010) 9244–9255. https://doi.org/10.1016/J.BIOMATERIALS.2010.08.057.

[327] Y. Cho, R. Shi, A. Ivanisevic, R. Ben Borgens, A mesoporous silica nanosphere-based drug delivery system using an electrically conducting polymer, Nanotechnology. 20 (2009) 275102. https://doi.org/10.1088/0957-4484/20/27/275102.

[328] J.E. Collazos-Castro, G.R. Hernández-Labrado, J.L. Polo, C. García-Rama, N-Cadherin- and L1-functionalised conducting polymers for synergistic stimulation and guidance of neural cell growth, Biomaterials. 34 (2013) 3603–3617. https://doi.org/10.1016/J.BIOMATERIALS.2013.01.097.

[329] N. Wang, A. Kähkönen, P. Damlin, T. Ääritalo, J. Kankare, C. Kvarnström, Electrochemical synthesis and characterization of branched viologen derivatives, Electrochim Acta. 154 (2015) 361–369. https://doi.org/10.1016/J.ELECTACTA.2014.12.075.

[330] C.L. Bird, A.T. Kuhn, Electrochemistry of the viologens, Chem Soc Rev. 10 (1981) 49–82. https://doi.org/10.1039/CS9811000049.

[331] M. Ito, T. Kuwana, Spectroelectrochemical study of indirect reduction of triphosphopyridine nucleotide: I. Methyl viologen, ferredoxin-TPN-reductase and TPN, J Electroanal Chem Interfacial Electrochem. 32 (1971) 415–425. https://doi.org/10.1016/S0022-0728(71)80144-4.

[332] Potenciales estándar de Electrodos de Referencia • Jenck,. https://www.jenck.com/utilidades/potenciales-estandar-de-electrodos (accessed October 27, 2022).

[333] H.J. Kim, W.S. Jeon, Y.H. Ko, K. Kim, Inclusion of methylviologen in cucurbit[7]uril, Proc Natl Acad Sci U S A. 99 (2002) 5007–5011. https://doi.org/10.1073/pnas.062656699.

[334] A.I. Popov, D.H. Geske, V. 80, D.H. Geske1, Studies on the Chemistry of Halogen and of Polyhalides. XVI. Voltammetry of Bromine and Interhalogen Species in Acetonitrile, Journal of American Chemical Society 80, 20 (1958) 5346-5349. https://doi.org/10.1021/ja01553a007.

[335] H. Sun, L. Zhang, Z.S. Wang, Single-crystal CoSe2 nanorods as an efficient electrocatalyst for dye-sensitized solar cells, J Mater Chem A Mater. 2 (2014) 16023–16029. https://doi.org/10.1039/C4TA02238F.

[336] N. Sbei, S. Aslam, N. Ahmed, Organic synthesis via Kolbe and related non-Kolbe electrolysis: an enabling electro-strategy, React Chem Eng. 6 (2021) 1342–1366. https://doi.org/10.1039/D1RE00047K.

[337] M. Tariq, Electrochemistry of Br-/Br2 Redox Couple in Acetonitrile, Methanol and Mix Media of Acetonitrile-Methanol: An Insight into Redox Behavior of Bromide on Platinum (Pt) and Gold (Au) Electrode, Zeitschrift Fur Physikalische Chemie. 234 (2020) 295–312. https://doi.org/10.1515/ZPCH-2018-1321.

[338] C.W. Tang, S.A. Vanslyke, C.H. Chen, J. Appl Phys, M.A. Baldo, Y. You, A. Shoustikov, S. Sib-ley, M.E. Thompson, S.R. Forrest, Y.G. Ma, H.Y. Zhang, J.C. Shen, C.M. Che, S. Met, X.Z. Jiang, A.K. Y Jen, B. Carlson, L.R. Dalton, S. Lamansky, P. Djurovich, D. Murphy, F. Abdel-Razzaq, H. Lee, C. Adachi, P.E. Burrows, H.Z. Xie, M.W. Liu, O.Y. Wang, X.H. Zhang, C.S. Lee, L.S. Hung, S.T. Lee, P.F. Teng, H.L. Kwong, H. Zheng, T.D. Anthopoulos, J.P. J Markham, E.B. Namdas, I.D. W Samuel, M.J. S Paulose, D.K. Rayabarapu, J. Duan, C. Cheng, -w Huang, M. Shanmugasundaram, H. Chang, B. David Nilsson, N. Robinson, M. Berggren, R. Forchheimer, M. Berggren, D. Nilsson, N. Robinson, R. Forchheimer, Electrochemical Logic Circuits, Advanced Materials. 17 (2005) 353–358. https://doi.org/10.1002/ADMA.200401273.

[339] K.C. Honeychurch, Voltammetric Behaviour of Rhodamine B at a Screen-Printed Carbon Electrode and Its Trace Determination in Environmental Water Samples, Sensors, Vol. 22, Page 4631. 22 (2022) 4631. https://doi.org/10.3390/S22124631.

[340] J. Guo, Y. Yuan, S. Amemiya, Voltammetric detection of heparin at polarized blood plasma/1,2-dichloroethane interfaces, Anal Chem. 77 (2005) 5711–5719. https://doi.org/10.1021/AC050833D.

[341] J. Guo, S. Amemiya, Voltammetric heparin-selective electrode based on thin liquid membrane with conducting polymer-modified solid support, Anal Chem. 78 (2006) 6893–6902. https://doi.org/10.1021/AC061003I/SUPPL_FILE/AC061003ISI20060721_035401.PDF.

[342] S. Chevion, M. Hofmann, R. Ziegler, M. Chevion, P.P. Nawroth, The antioxidant properties of thioctic acid: characterization by cyclic voltammetry, Biochem Mol Biol Int. 41 (1997) 317–327. https://doi.org/10.1080/15216549700201331.

[343] Z. Zhang, R. Zhou, Y. Dong, M. Song, L. Tian, Z. Zhao, An indicator displacement assay-based optical chemosensor for heparin with a dual-readout and a reversible molecular logic gate operation based on the pyranine/methyl viologen, Biosens Bioelectron. 194 (2021) 113612. https://doi.org/10.1016/J.BIOS.2021.113612.

[344] N. K. Bhatti, M. S. Subhani, A. Y. Khan, R. Qureshi, A. Rahman, Heterogeneous electron transfer rate constants of viologen monocations at a platinum disk electrode, Turkish Journal of Chemistry. 30(2) (2006) 165-180. https://journals.tubitak.gov.tr/chem/vol30/iss2/5/ (accessed September 23, 2022).

[345] J.J. Orgill, C. Chen, C.R. Schirmer, J.L. Anderson, R.S. Lewis, Prediction of methyl viologen redox states for biological applications, Biochem Eng J. 94 (2015) 15–21. https://doi.org/10.1016/J.BEJ.2014.11.005.

[346] L. Zhang, Glycosaminoglycan (GAG) Biosynthesis and GAG-Binding Proteins, Prog Mol Biol Transl Sci. 93 (2010) 1–17. https://doi.org/10.1016/S1877-1173(10)93001-9.

[347] J.E. Collazos-Castro, C. García-Rama, A. Alves-Sampaio, Glial progenitor cell migration promotes CNS axon growth on functionalized electroconducting microfibers, Acta Biomater. 35 (2016) 42–56. https://doi.org/10.1016/J.ACTBIO.2016.02.023.

[348] A. García-Fernández, G. García-Laínez, M.L. Ferrándiz, E. Aznar, F. Sancenón, M.J. Alcaraz, J.R. Murguía, M.D. Marcos, R. Martínez-Máñez, A.M. Costero, M. Orzáez, Targeting inflammasome by the inhibition of caspase-1 activity using capped mesoporous silica nanoparticles, Journal of Controlled Release. 248 (2017) 60–70. https://doi.org/10.1016/J.JCONREL.2017.01.002.

[349] B. Lozano-Torres, L. Pascual, A. Bernardos, M.D. Marcos, J.O. Jeppesen, Y. Salinas, R. Martínez-Máñez, F. Sancenón, Pseudorotaxane capped mesoporous silica nanoparticles for 3,4-methylenedioxymethamphetamine (MDMA) detection in water, Chemical Communications. 53 (2017) 3559–3562. https://doi.org/10.1039/C7CC00186J.

[350] M. Ito, T. Kuwana, Spectroelectrochemical study of indirect reduction of triphosphopyridine nucleotide: I. Methyl viologen, ferredoxin-TPN-reductase and TPN, J Electroanal Chem Interfacial Electrochem. 32 (1971) 415–425. https://doi.org/10.1016/S0022-0728(71)80144-4.

[351] A.P. Sandoval, M.F. Suárez-Herrera, J.M. Feliu, IR and electrochemical synthesis and characterization of thin films of PEDOT grown on platinum single crystal electrodes in [EMMIM]Tf 2 N ionic liquid, Beilstein J. Org. Chem. 11 (2015) 348–357. https://doi.org/10.3762/bjoc.11.40.

[352] E.T.K. Demann, P.S. Stein, J.E. Haubenreich, Gold as an Implant in Medicine and Dentistry, J Long Term Eff Med Implants. 15 (2005) 687–698. https://doi.org/10.1615/JLONGTERMEFFMEDIMPLANTS.V15.I6.100.

[353] D. Hannouche, M. Hamadouche, R. Nizard, P. Bizot, A. Meunier, L. Sedel, Ceramics in total hip replacement, Clin Orthop Relat Res. 430 (2005) 62–71. https://doi.org/10.1097/01.BLO.0000149996.91974.83.

[354] S.K. Srivastava, V.G. Yadav, Bionic Manufacturing: Towards Cyborg Cells and Sentient Microbots, Trends Biotechnol. 36 (2018) 483–487. https://doi.org/10.1016/J.TIBTECH.2017.11.002.

[355] K. Han, C. Wyatt, O.D. Velev, K. Han, C.W. Shields, I.O.D. Velev, Engineering of Self-Propelling Microbots and Microdevices Powered by Magnetic and Electric Fields, Adv Funct Mater. 28 (2018) 1705953. https://doi.org/10.1002/ADFM.201705953.

[356] E. Doutel, F.J. Galindo-Rosales, L. Campo-Deaño, Hemodynamics Challenges for the Navigation of Medical Microbots for the Treatment of CVDs, Materials 2021, Vol. 14, Page 7402. 14 (2021) 7402. https://doi.org/10.3390/MA14237402.

[357] F. Luderer, U. Walschus, Immobilization of oligonucleotides for biochemical sensing by self-assembled monolayers: Thiol-organic bonding on gold and silanization on silica surfaces, Top Curr Chem. 260 (2005) 37–56. https://doi.org/10.1007/128_003/COVER.

[358] K. Meersman, B. Pyck, A. López-Rodríguez, J. Monreal-Trigo, M. Alcañiz Fillol, Evaluation of the potential distribution in a two-electrode electrochemical cell, in: XV International Workshop on Sensors and Molecular Recognition (IWOSMOR 2022), València, 2022: pp. 80–82.

[359] S.P. Adiga, C. Jin, L.A. Curtiss, N.A. Monteiro-Riviere, R.J. Narayan, Nanoporous membranes for medical and biological applications, Wiley Interdiscip Rev Nanomed Nanobiotechnol. 1 (2009) 568–581. https://doi.org/10.1002/WNAN.50.

[360] R. Villalonga, P. Díez, A. Sánchez, E. Aznar, R. Martínez-Máñez, J.M. Pingarrõn, Enzyme-Controlled Sensing–Actuating Nanomachine Based on Janus Au–Mesoporous Silica Nanoparticles, Chemistry – A European Journal. 19 (2013) 7889–7894. https://doi.org/10.1002/CHEM.201300723.

[361] M. Porta-i-Batalla, E. Xifré-Pérez, C. Eckstein, J. Ferré-Borrull, L.F. Marsal, 3D Nanoporous Anodic Alumina Structures for Sustained Drug Release, Nanomaterials 2017, Vol. 7, Page 227. 7 (2017) 227. https://doi.org/10.3390/NANO7080227.

[362] M. Porta-i-Batalla, C. Eckstein, E. Xifré-Pérez, P. Formentín, J. Ferré-Borrull, L.F. Marsal, Sustained, Controlled and Stimuli-Responsive Drug Release Systems Based on Nanoporous Anodic Alumina with Layer-by-Layer Polyelectrolyte, Nanoscale Res Lett. 11 (2016) 1–9. https://doi.org/10.1186/S11671-016-1585-4.

[363] N. Di Trani, A. Silvestri, A. Sizovs, Y. Wang, D.R. Erm, D. Demarchi, X. Liu, A. Grattoni, Electrostatically gated nanofluidic membrane for ultra-low power controlled drug delivery, Lab Chip. 20 (2020) 1562–1576. https://doi.org/10.1039/D0LC00121J.

[364] Z. Li, O. Polat, E. Seker, Voltage-Gated Closed-Loop Control of Small-Molecule Release from Alumina-Coated Nanoporous Gold Thin Film Electrodes, Adv Funct Mater. 28 (2018) 1801292. https://doi.org/10.1002/ADFM.201801292.

[365] H. Ebinger, J. Yates, Electron-impact-induced oxidation of Al(111) in water vapor: Relation to the Cabrera-Mott mechanism, Phys Rev B. 57 (1998) 1976. https://doi.org/10.1103/PhysRevB.57.1976.

[366] R. Nakamura, D. Tokozakura, H. Nakajima, J.G. Lee, H. Mori, Hollow oxide formation by oxidation of Al and Cu nanoparticles, J Appl Phys. 101 (2007) 074303. https://doi.org/10.1063/1.2711383.

[367] N. Cai, G. Zhou, K. Müller, D.E. Starr, Comparative study of the passivation of Al(111) by molecular oxygen and water vapor, Journal of Physical Chemistry C. 117 (2013) 172–178. https://doi.org/10.1021/JP305740S.

[368] N. Cai, G. Zhou, K. Müller, D.E. Starr, Temperature and pressure dependent Mott potentials and their influence on self-limiting oxide film growth, Appl Phys Lett. 101 (2012) 171605. https://doi.org/10.1063/1.4764552.

[369] J. Gorobez, B. Maack, N. Nilius, Growth of Self-Passivating Oxide Layers on Aluminum—Pressure and Temperature Dependence, Physica Status Solidi (b). 258 (2021) 2000559. https://doi.org/10.1002/PSSB.202000559.

[370] Z. Yang, N. Chen, X. Qin, Fabrication of Porous Al2O3 Ceramics with Submicron-Sized Pores Using a Water-Based Gelcasting Method, Materials 2018, Vol. 11, Page 1784. 11 (2018) 1784. https://doi.org/10.3390/MA11091784.

[371] N. Nayak, R. Huertas, J.G. Crespo, C.A.M. Portugal, Surface modification of alumina monolithic columns with 3-aminopropyltetraethoxysilane (APTES) for protein attachment, Sep Purif Technol. 229 (2019) 115674. https://doi.org/10.1016/J.SEPPUR.2019.115674.

[372] L. Alamán-Escolano, J. Monreal-Trigo, J.F. Blandez, E. Garcia-Breijo, E. Giraldo-Reboloso, M. del M. Sanchez-Martin, V. Moreno-Manzano, In-vitro culture well for the combined application of electrostimulation and electrically-controlled drug release, in: XIV International Workshop on Sensors and Molecular Recognition (XV IWOSMOR), Instituto Interuniversitario de Investigación de Reconocimiento Molecular y Desarrollo Tecnológico, Valencia, 2021: pp. 152–155.

[373] J. Morgado, L. Sordini, F. Castelo Ferreira, Electronic to ionic transduction of the electric field applied to PEDOT:PSS substrates to the cell cultures on top, Bioelectrochemistry. 145 (2022) 108099. https://doi.org/10.1016/J.BIOELECHEM.2022.108099.

[374] M.P. Prabhakaran, L. Ghasemi-Mobarakeh, G. Jin, S. Ramakrishna, Electrospun conducting polymer nanofibers and electrical stimulation of nerve stem cells, J Biosci Bioeng. 112 (2011) 501–507. https://doi.org/10.1016/J.JBIOSC.2011.07.010.

[375] D.N. Heo, N. Acquah, J. Kim, S.J. Lee, N.J. Castro, L.G. Zhang, Directly Induced Neural Differentiation of Human Adipose-Derived Stem Cells Using Three-Dimensional Culture System of Conductive Microwell with Electrical Stimulation, Tissue Engineering Part A. 24 (2018) 537–545. https://doi.org/10.1089/TEN.TEA.2017.0150.

[376] L.J. Kobelt, A.E. Wilkinson, A.M. McCormick, R.K. Willits, N.D. Leipzig, Short Duration Electrical Stimulation to Enhance Neurite Outgrowth and Maturation of Adult Neural Stem Progenitor Cells, Ann Biomed Eng. 42 (2014) 2164–2176. https://doi.org/10.1007/S10439-014-1058-9.

[377] L. Ghasemi-Mobarakeh, M.P. Prabhakaran, M. Morshed, M.H. Nasr-Esfahani, S. Ramakrishna, Electrical Stimulation of Nerve Cells Using Conductive Nanofibrous Scaffolds for Nerve Tissue Engineering, Https://Home.Liebertpub.Com/Tea. 15 (2009) 3605–3619. https://doi.org/10.1089/TEN.TEA.2008.0689.

[378] M.D. Tang-Schomer, 3D axon growth by exogenous electrical stimulus and soluble factors, Brain Res. 1678 (2018) 288–296. https://doi.org/10.1016/J.BRAINRES.2017.10.032.

[379] S.J. Lee, W. Zhu, M. Nowicki, G. Lee, D.N. Heo, J. Kim, Y.Y. Zuo, L.G. Zhang, 3D printing nano conductive multi-walled carbon nanotube scaffolds for nerve regeneration, J Neural Eng. 15 (2018) 016018. https://doi.org/10.1088/1741-2552/AA95A5.

[380] W. Zhu, T. Ye, S.J. Lee, H. Cui, S. Miao, X. Zhou, D. Shuai, L.G. Zhang, Enhanced neural stem cell functions in conductive annealed carbon nanofibrous scaffolds with electrical stimulation, Nanomedicine. 14 (2018) 2485–2494. https://doi.org/10.1016/J.NANO.2017.03.018.

[381] T. Sudwilai, J.J. Ng, C. Boonkrai, N. Israsena, S. Chuangchote, P. Supaphol, Polypyrrole-coated electrospun poly(lactic acid) fibrous scaffold: effects of coating on electrical conductivity and neural cell growth, Journal of Biomaterials Science, Polymer Edition. 25 (2014) 1240–1252. https://doi.org/10.1080/09205063.2014.926578.

[382] F. Pires, Q. Ferreira, C.A.V. Rodrigues, J. Morgado, F.C. Ferreira, Neural stem cell differentiation by electrical stimulation using a cross-linked PEDOT substrate: Expanding the use of biocompatible conjugated conductive polymers for neural tissue engineering, Biochimica et Biophysica Acta (BBA) - General Subjects. 1850 (2015) 1158–1168. https://doi.org/10.1016/J.BBAGEN.2015.01.020.

[383] K. Yang, S.J. Yu, J.S. Lee, H.R. Lee, G.E. Chang, J. Seo, T. Lee, E. Cheong, S.G. Im, S.W. Cho, Electroconductive nanoscale topography for enhanced neuronal differentiation and electrophysiological maturation of human neural stem cells, Nanoscale. 9 (2017) 18737–18752. https://doi.org/10.1039/C7NR05446G.

[384] Y.J. Huang, H.C. Wu, N.H. Tai, T.W. Wang, Carbon Nanotube Rope with Electrical Stimulation Promotes the Differentiation and Maturity of Neural Stem Cells, Small. 8 (2012) 2869–2877. https://doi.org/10.1002/SMLL.201200715.

[385] A.T. Nguyen, S. Mattiassi, M. Loeblein, E. Chin, D. Ma, P. Coquet, V. Viasnoff, E.H.T. Teo, E.L. Goh, E.K.F. Yim, Human Rett-derived neuronal progenitor cells in 3D graphene scaffold as an in vitro platform to study the effect of electrical stimulation on neuronal differentiation, Biomedical Materials. 13 (2018) 034111. https://doi.org/10.1088/1748-605X/AAAF2B.

[386] C. Fu, S. Pan, Y. Ma, W. Kong, Z. Qi, X. Yang, Effect of electrical stimulation combined with graphene-oxide-based membranes on neural stem cell proliferation and differentiation, Artif Cells Nanomed Biotechnol. 47 (2019) 1867–1876. https://doi.org/10.1080/21691401.2019.1613422.

[387] L. Li, Y.H. El-Hayek, B. Liu, Y. Chen, E. Gomez, X. Wu, K. Ning, L. Li, N. Chang, L. Zhang, Z. Wang, X. Hu, Q. Wan, K.E. Ning, Q.I. Wan, Direct-Current Electrical Field Guides Neuronal Stem/Progenitor Cell Migration, Stem Cells. 26 (2008) 2193–2200. https://doi.org/10.1634/STEMCELLS.2007-1022.

[388] Z. yong Dong, Z. Pei, Z. Li, Y. ling Wang, A. Khan, X. ting Meng, Electric field stimulation induced neuronal differentiation of filum terminale derived neural progenitor cells, Neurosci Lett. 651 (2017) 109–115. https://doi.org/10.1016/J.NEULET.2017.05.001.

[389] S. Naskar, V. Kumaran, Y.S. Markandeya, B. Mehta, B. Basu, Neurogenesis-on-Chip: Electric field modulated transdifferentiation of human mesenchymal stem cell and mouse muscle precursor cell coculture, Biomaterials. 226 (2020) 119522. https://doi.org/10.1016/J.BIOMATERIALS.2019.119522.

[390] M.A. Matos, M.T. Cicerone, Alternating current electric field effects on neural stem cell viability and differentiation, Biotechnol Prog. 26 (2010) 664–670. https://doi.org/10.1002/BTPR.389.

[391] C.A. Ariza, A.T. Fleury, C.J. Tormos, V. Petruk, S. Chawla, J. Oh, D.S. Sakaguchi, S.K. Mallapragada, The Influence of Electric Fields on Hippocampal Neural Progenitor Cells, Stem Cell Reviews and Reports 6:4. 6 (2010) 585–600. https://doi.org/10.1007/S12015-010-9171-0.

[392] K.A. Chang, J.W. Kim, J. a. Kim, S. Lee, S. Kim, W.H. Suh, H.S. Kim, S. Kwon, S.J. Kim, Y.H. Suh, Biphasic Electrical Currents Stimulation Promotes both Proliferation and Differentiation of Fetal Neural Stem Cells, PLoS One. 6 (2011) e18738. https://doi.org/10.1371/JOURNAL.PONE.0018738.

[393] M. Wang, P. Li, M. Liu, W. Song, Q. Wu, Y. Fan, Potential protective effect of biphasic electrical stimulation against growth factor-deprived apoptosis on olfactory bulb neural progenitor cells through the brain-derived neurotrophic factor–phosphatidylinositol 3′-kinase/Akt pathway, Experimental Biology and Medicine. 238 (2013) 951–959. https://doi.org/10.1177/1535370213494635.

[394] E. Stewart, N.R. Kobayashi, M.J. Higgins, A.F. Quigley, S. Jamali, S.E. Moulton, R.M.I. Kapsa, G.G. Wallace, J.M. Crook, Electrical Stimulation Using Conductive Polymer Polypyrrole Promotes Differentiation of Human Neural Stem Cells: A Biocompatible Platform for Translational Neural Tissue Engineering, Tissue Engineering Part C: Methods. 21 (2014) 385–393. https://doi.org/10.1089/TEN.TEC.2014.0338.

[395] Y. Jin, J. Seo, J.S. Lee, S. Shin, H.J. Park, S. Min, E. Cheong, T. Lee, S.W. Cho, Triboelectric Nanogenerator Accelerates Highly Efficient Nonviral Direct Conversion and In Vivo Reprogramming of Fibroblasts to Functional Neuronal Cells, Advanced Materials. 28 (2016) 7365–7374. https://doi.org/10.1002/ADMA.201601900.

[396] F.M.P. Tonelli, A.K. Santos, K.N. Gomes, E. Lorençon, S. Guatimosim, L.O. Ladeira, R.R. Resende, Carbon nanotube interaction with extracellular matrix proteins producing scaffolds for tissue engineering, Int J Nanomedicine. 7 (2012) 4511. https://doi.org/10.2147/IJN.S33612.

[397] X. Zhou, A. Yang, Z. Huang, G. Yin, X. Pu, J. Jin, Enhancement of neurite adhesion, alignment and elongation on conductive polypyrrole-poly(lactide acid) fibers with cell-derived extracellular matrix, Colloids Surf B Biointerfaces. 149 (2017) 217–225. https://doi.org/10.1016/J.COLSURFB.2016.10.014.

[398] L.R. Doblado, C. Martínez-Ramos, M.M. Pradas, Biomaterials for Neural Tissue Engineering, Frontiers in Nanotechnology. 3 (2021) 21. https://doi.org/10.3389/FNANO.2021.643507.

[399] C. Martínez-Ramos, L.R. Doblado, E.L. Mocholi, A. Alastrue-Agudo, M.S. Petidier, E. Giraldo, M.M. Pradas, V. Moreno-Manzano, Biohybrids for spinal cord injury repair, J Tissue Eng Regen Med. 13 (2019) 509–521. https://doi.org/10.1002/TERM.2816.

[400] M.R. Abidian, E.D. Daneshvar, B.M. Egeland, D.R. Kipke, P.S. Cederna, M.G. Urbanchek, Hybrid Conducting Polymer–Hydrogel Conduits for Axonal Growth and Neural Tissue Engineering, Adv Healthc Mater. 1 (2012) 762–767. https://doi.org/10.1002/ADHM.201200182.

[401] L. Huang, X. Yang, L. Deng, D. Ying, A. Lu, L. Zhang, A. Yu, B. Duan, Biocompatible Chitin Hydrogel Incorporated with PEDOT Nanoparticles for Peripheral Nerve Repair, ACS Appl Mater Interfaces. 13 (2021) 16106–16117. https://doi.org/10.1021/ACSAMI.1C01904.

[402] L. V. Kayser, D.J. Lipomi, Stretchable Conductive Polymers and Composites Based on PEDOT and PEDOT:PSS, Advanced Materials. 31 (2019) 1806133. https://doi.org/10.1002/ADMA.201806133.

[403] J. Luo, J. Yang, X. Zheng, X. Ke, Y. Chen, H. Tan, J. Li, J. Luo, X. Zheng, X. Ke, H. Tan, J. Li, J. Yang, Y. Chen, A Highly Stretchable, Real-Time Self-Healable Hydrogel Adhesive Matrix for Tissue Patches and Flexible Electronics, Adv Healthc Mater. 9 (2020) 1901423. https://doi.org/10.1002/ADHM.201901423.

[404] D. Ohayon, C. Pitsalidis, A.M. Pappa, A. Hama, Y. Zhang, L. Gallais, R.M. Owens, Laser Patterning of Self-Assembled Monolayers on PEDOT:PSS Films for Controlled Cell Adhesion, Adv Mater Interfaces. 4 (2017) 1700191. https://doi.org/10.1002/ADMI.201700191.

[405] N. De Geyter, R. Morent, Cold plasma surface modification of biodegradable polymer biomaterials, Biomaterials for Bone Regeneration: Novel Techniques and Applications. (2014) 202–224. https://doi.org/10.1533/9780857098104.2.202.

[406] J. James, B. Joseph, A. Shaji, P. Nancy, N. Kalarikkal, S. Thomas, Y. Grohens, G. Vignaud, Microscopic Analysis of Plasma-Activated Polymeric Materials, Non-Thermal Plasma Technology for Polymeric Materials: Applications in Composites, Nanostructured Materials, and Biomedical Fields. (2019) 287–317. https://doi.org/10.1016/B978-0-12-813152-7.00011-1.

[407] J. Izdebska-Podsiadły, Application of Plasma in Printed Surfaces and Print Quality, Non-Thermal Plasma Technology for Polymeric Materials: Applications in Composites, Nanostructured Materials, and Biomedical Fields. (2019) 159–191. https://doi.org/10.1016/B978-0-12-813152-7.00006-8.

[408] R. Morent, N. De Geyter, T. Desmet, P. Dubruel, C. Leys, Plasma Surface Modification of Biodegradable Polymers: A Review, Plasma Processes and Polymers. 8 (2011) 171–190. https://doi.org/10.1002/PPAP.201000153.

[409] P.M. López-Pérez, A.P. Marques, R.M.P.D. Silva, I. Pashkuleva, R.L. Reis, Effect of chitosan membrane surface modification via plasma induced polymerization on the adhesion of osteoblast-like cells, J Mater Chem. 17 (2007) 4064–4071. https://doi.org/10.1039/B707326G.

[410] T. Ino, T. Hayashi, K. Ueno, H. Shirai, Atmospheric-pressure argon plasma etching of spin-coated 3,4-polyethylenedioxythiophene:polystyrenesulfonic acid (PEDOT:PSS) films for cupper phtalocyanine (CuPc)/C60 heterojunction thin-film solar cells, Thin Solid Films. 519 (2011) 6834–6839. https://doi.org/10.1016/J.TSF.2011.04.042.

[411] A. Serafin, M.C. Rubio, M. Carsi, P. Ortiz-Serna, M.J. Sanchis, A.K. Garg, J.M. Oliveira, J. Koffler, M.N. Collins, Electroconductive PEDOT nanoparticle integrated scaffolds for spinal cord tissue repair, Biomater Res. 26 (2022) 63. https://doi.org/10.1186/S40824-022-00310-5.

[412] J. Monreal-Trigo, J.M. Terres-Haro, B. Martinez-Rojas, M. del M. Sanchez-Martin, E. Giraldo, V. Moreno Manzano, M. Alcaniz Fillol, Optogenetic Stimulation Array for Confocal Microscopy Fast Transient Monitoring, IEEE Trans Biomed Circuits Syst. (2022) 1–10. https://doi.org/10.1109/TBCAS.2022.3226558.

[413] J. Monreal-Trigo, J.M. Terrés-Haro, E. Giraldo-Reboloso, V. Moreno-Manzano, Development and perspectives of optochemogenetic devices at IDM, XIV IWOSMOR. (2021) 24–27.

[414] J.M. Terrés-Haro, J. Monreal-Trigo, B. Martinez-Rojas, E. Giraldo-Reboloso, V. Moreno-Manzano, OSIVE prototype for optochemogenetic stimulation, XIV IWOSMOR. (2021) 140–143.

[415] V. Beltrán-Morte, J. Monreal-Trigo, J.M. Terrés-Haro, E. Giraldo, B. Martínez-Rojas, V. Moreno-Manzano, High irradiance real-time measurement system for in-vitro optogenetic stimulation, XIV IWOSMOR. (2021) 206–209.

[416] J.M. Terrés-Haro, J. Monreal-Trigo, M. del M. Sánchez-Martín, B. Martínez-Rojas, E. Giraldo, V. Moreno-Manzano, M. Alcañiz Fillol, High-irradiance optogenetic stimulation device for in-vitro real-time rapid transitory response observation, ACS Photonics. (2023).

[417] G.A. Terrer Fos, Diseño e implementación de ópticas y de un equipo de medición de irradiancia para su aplicación en el desarrollo de nuevas terapias de reconstrucción de tejido nervioso, Universitat Politècnica de València, 2021. http://hdl.handle.net/10251/171801.

[418] J.D. Coronel Montesinos, Diseño, desarrollo y validación de la etapa de potencia de un sistema de estimulación optoquimiogenética de alta intensidad., Universitat Politècnica de València, 2021. http://hdl.handle.net/10251/175010.

[419] J.P. Weick, M.A. Johnson, S.P. Skroch, J.C. Williams, K. Deisseroth, S.C. Zhang, Functional Control of Transplantable Human ESC-Derived Neurons Via Optogenetic Targeting, Stem Cells. 28 (2010) 2008–2016. https://doi.org/10.1002/STEM.514.

[420] Q. Li, P. Wei, H. Hu, X. Ma, L. Wang, Design of in vitro light stimulation device; Design of in vitro light stimulation device, 2009. https://doi.org/10.1109/FBIE.2009.5405838.

[421] O.J. Abilez, Optogenetic LED array for perturbing cardiac electrophysiology, Annu Int Conf IEEE Eng Med Biol Soc. 2013 (2013) 1619–1622. https://doi.org/10.1109/EMBC.2013.6609826.

[422] K.P. Gerhardt, E.J. Olson, S.M. Castillo-Hair, L.A. Hartsough, B.P. Landry, F. Ekness, R. Yokoo, E.J. Gomez, P. Ramakrishnan, J. Suh, D.F. Savage, J.J. Tabor, An open-hardware platform for optogenetics and photobiology, Scientific Reports 2016 6:1. 6 (2016) 1–13. https://doi.org/10.1038/srep35363.

[423] L.J. Bugaj, W.A. Lim, High-throughput multicolor optogenetics in microwell plates, Nature Protocols 2019 14:7. 14 (2019) 2205–2228. https://doi.org/10.1038/s41596-019-0178-y.

[424] O.S. Thomas, M. Hörner, W. Weber, A graphical user interface to design high-throughput optogenetic experiments with the optoPlate-96, Nature Protocols 2020 15:9. 15 (2020) 2785–2787. https://doi.org/10.1038/s41596-020-0349-x.

[425] R.M. Paredes, J.C. Etzler, L.T. Watts, W. Zheng, J.D. Lechleiter, Chemical calcium indicators, Methods. 46 (2008) 143–151. https://doi.org/10.1016/J.YMETH.2008.09.025.

[426] M.J. Berridge, P. Lipp, M.D. Bootman, The versatility and universality of calcium signalling, Nature Reviews Molecular Cell Biology 2000 1:1. 1 (2000) 11–21. https://doi.org/10.1038/35036035.

[427] C. Grienberger, A. Konnerth, Imaging Calcium in Neurons, Neuron. 73 (2012) 862–885. https://doi.org/10.1016/J.NEURON.2012.02.011.

[428] S.P. Parker, ed., Steradian, McGraw-Hill Dictionary of Scientific and Technical Terms. (1997) 306.

[429] S. Williamson, H. Cummins, Light and color in nature and art, John Wiley & Sons, 1983.

[430] Due | Arduino Documentation | Arduino Documentation, (n.d.). https://docs.arduino.cc/hardware/due (accessed December 26, 2022).

[431] M. Stierl, P. Stumpf, D. Udwari, R. Gueta, R. Hagedorn, A. Losi, W. Gärtner, L. Petereit, M. Efetova, M. Schwarzel, T.G. Oertner, G. Nagel, P. Hegemann, Light modulation of cellular cAMP by a small bacterial photoactivated adenylyl cyclase, bPAC, of the soil bacterium Beggiatoa, J Biol Chem. 286 (2011) 1181–1188. https://doi.org/10.1074/JBC.M110.185496.

[432] S. Oldani, L. Moreno-Velasquez, L. Faiss, A. Stumpf, C. Rosenmund, D. Schmitz, B.R. Rost, SynaptoPAC, an optogenetic tool for induction of presynaptic plasticity, J Neurochem. 156 (2021) 324–336. https://doi.org/10.1111/JNC.15210.

[433] Y.A. Bernal Sierra, B.R. Rost, M. Pofahl, A.M. Fernandes, R.A. Kopton, S. Moser, D. Holtkamp, N. Masala, P. Beed, J.J. Tukker, S. Oldani, W. Bönigk, P. Kohl, H. Baier, F. Schneider-Warme, P. Hegemann, H. Beck, R. Seifert, D. Schmitz, Potassium channel-based optogenetic silencing, Nature Communications 2018 9:1. 9 (2018) 1–13. https://doi.org/10.1038/s41467-018-07038-8.

[434] J. Monreal-Trigo, L.K. Heidenreich, M. Hartel, J.M. Terrés-Haro, O. Lukayonova, M. Alcañiz Fillol, Data analysis graphic user interface for transistor-based biosensors, in: XV International Workshop on Sensors and Molecular Recognition (IWOSMOR 2022), València, 2022: pp. 83–86.

[435] L.K. Heidenreich, J. Monreal-Trigo, M.C. Hartel, O. Lukoyanova, M. Alcañiz Fillol, A.M. Andrews, Custom measurement platform for aptamer Field Effect Transistor arrays, in: Brain Research Institute 31st Annual Neuroscience Poster Session, Los Angeles, 2021.

[436] V. Beltrán Morte, J. Monreal-Trigo, J. Sabbe, F. Boydens, M. Alcañiz Fillol, L.K. Heidenreich, Low cost measurement system for biosensors based on Organic Electrochemical Transistors (OECTs) and Field Effect Transistors (FETs), in: XIV International Workshop on Sensors and Molecular Recognition (IWOSMOR 2021), Valencia, Spain, 2021: pp. 28–31.

[437] J. Benedicto Centeno, K. Meersman, J. Monreal-Trigo, A. López-Rodríguez, M. Alcañiz Fillol, Design and implementation of an electronic measurement system based on electrochemical organic transistors (OECTs) functionalized with aptamers, in: XV International Workshop on Sensors and Molecular Recognition (IWOSMOR 2022), València, 2022: pp. 73–75.

[438] V. Beltrán Morte, Sistema de medida para biosensores de serotonina basados en Transistores de Efecto de Campo (FET) funcionalizados con aptámeros, Universitat Politècnica de València, 2021. https://riunet.upv.es/handle/10251/171799.

[439] J. Benedicto Centeno, Sistema de medida multicanal basado en Transistores Orgánicos Electroquímicos (OECTs) funcionalizados con aptámeros, Universitat Politècnica de València, 2022.

[440] V. Pacherres, B. Pyck, A. López-Rodríguez, J. Monreal-Trigo, M. Alcañiz Fillol, Design and implementation of an electronic system for the measurement of impedimetric sensors functionalised with aptamers, in:

XV International Workshop on Sensors and Molecular Recognition (IWOSMOR 2022), València, 2022: pp. 91–94.

[441] V.T. Pacherres Ancajima, Diseño e implementación de un sistema electrónico para la medida de sensores impedimétricos funcionalizados con aptámeros, Universitat Politècnica de València, 2022.

[442] C.S. Movassaghi, K.A. Perrotta, H. Yang, R. Iyer, X. Cheng, M. Dagher, M.A. Fillol, A.M. Andrews, Simultaneous serotonin and dopamine monitoring across timescales by rapid pulse voltammetry with partial least squares regression, Anal Bioanal Chem. 413 (2021) 6747. https://doi.org/10.1007/S00216-021-03665-1.

[443] B.S. Ferguson, D.A. Hoggarth, D. Maliniak, K. Ploense, R.J. White, N. Woodward, K. Hsieh, A.J. Bonham, M. Eisenstein, T.E. Kippin, K.W. Plaxco, H.T. Soh, Real-time, aptamer-based tracking of circulating therapeutic agents in living animals, Sci Transl Med. 5 (2013) 213ra165. https://doi.org/10.1126/SCITRANSLMED.3007095.

[444] B. Wang, C. Zhao, Z. Wang, K.A. Yang, X. Cheng, W. Liu, W. Yu, S. Lin, Y. Zhao, K.M. Cheung, H. Lin, H. Hojaiji, P.S. Weiss, M.N. Stojanović, A.J. Tomiyama, A.M. Andrews, S. Emaminejad, Wearable aptamer-field-effect transistor sensing system for noninvasive cortisol monitoring, Sci Adv. 8 (2022) 967. https://doi.org/10.1126/SCIADV.ABK0967.

[445] M. Suryaganesh, T.S. Arun Samuel, T. Ananth Kumar, M. Navaneetha Velammal, Advanced FET-Based Biosensors—A Detailed Review, Lecture Notes in Networks and Systems. 281 (2022) 273–284. https://doi.org/10.1007/978-981-16-4244-9_22.

[446] C. Zhao, K.M. Cheung, I.W. Huang, H. Yang, N. Nakatsuka, W. Liu, Y. Cao, T. Man, P.S. Weiss, H.G. Monbouquette, A.M. Andrews, Implantable aptamer-field-effect transistor neuroprobes for in vivo neurotransmitter monitoring, Sci Adv. 7 (2021) 7422. https://doi.org/10.1126/SCIADV.ABJ7422.

[447] Q. Liu, C. Zhao, M. Chen, Y. Liu, Z. Zhao, F. Wu, Z. Li, P.S. Weiss, A.M. Andrews, C. Zhou, Flexible Multiplexed In2O3 Nanoribbon Aptamer-Field-Effect Transistors for Biosensing, IScience. 23 (2020) 101469. https://doi.org/10.1016/J.ISCI.2020.101469.

[448] K. Xie, N. Wang, X. Lin, Z. Wang, X. Zhao, P. Fang, H. Yue, J. Kim, J. Luo, S. Cui, F. Yan, P. Shi, Organic electrochemical transistor arrays for real-time mapping of evoked neurotransmitter release in vivo, Elife. 9 (2020). https://doi.org/10.7554/ELIFE.50345.

[449] J.L. Shobe, L.D. Claar, S. Parhami, K.I. Bakhurin, S.C. Masmanidis, Brain activity mapping at multiple scales with silicon microprobes containing 1,024 electrodes, J Neurophysiol. 114 (2015) 2043. https://doi.org/10.1152/JN.00464.2015.

[450] L.C. Moreaux, D. Yatsenko, W.D. Sacher, J. Choi, C. Lee, N.J. Kubat, R.J. Cotton, E.S. Boyden, M.Z. Lin, L. Tian, A.S. Tolias, J.K.S. Poon, K.L. Shepard, M.L. Roukes, Integrated Neurophotonics: Toward Dense Volumetric Interrogation of Brain Circuit Activity—at Depth and in Real Time, Neuron. 108 (2020) 66–92. https://doi.org/10.1016/J.NEURON.2020.09.043.

[451] J. Choi, A.J. Taal, E.H. Pollmann, C. Lee, K. Kim, L.C. Moreaux, M.L. Roukes, K.L. Shepard, A 512-Pixel, 51-kHz-Frame-Rate, Dual-Shank, Lens-less, Filter-less Single Photon Avalanche Diode CMOS Neural Imaging Probe, IEEE J Solid-State Circuits. 54 (2019) 2957. https://doi.org/10.1109/JSSC.2019.2941529.

[452] K.M. Cheung, K.A. Yang, N. Nakatsuka, C. Zhao, M. Ye, M.E. Jung, H. Yang, P.S. Weiss, M.N. Stojanović, A.M. Andrews, Phenylalanine Monitoring via Aptamer-Field-Effect Transistor Sensors, ACS Sens. 4 (2019) 3308–3317. https://doi.org/10.1021/ACSSENSORS.9B01963.

[453] I.Y. Wong, N.A. Melosh, Directed hybridization and melting of DNA linkers using counterion-screened electric fields, Nano Lett. 9 (2009) 3521–3526. https://doi.org/10.1021/NL901710N.

[454] D. Ho, W. Hetrick, N. Le, A. Chin, R.M. West, Editors' Choice—Electric Field-Induced DNA Melting with Detection by Square Wave Voltammetry, J Electrochem Soc. 166 (2019) B236. https://doi.org/10.1149/2.0671904JES.

[455] J. Tymoczko, W. Schuhmann, M. Gebala, Electrical potential-assisted DNA hybridization. How to mitigate electrostatics for surface DNA hybridization, ACS Appl Mater Interfaces. 6 (2014) 21851–21858. https://doi.org/10.1021/AM5027902.

[456] R. Cabeça, M. Rodrigues, D.M.F. Prazeres, V. Chu, J.P. Conde, The effect of the shape of single, sub-ms voltage pulses on the rates of surface immobilization and hybridization of DNA, Nanotechnology. 20 (2009). https://doi.org/10.1088/0957-4484/20/1/015503.

[457] U. Rant, K. Arinaga, S. Fujita, N. Yokoyama, G. Abstreiter, M. Tornow, Electrical manipulation of oligonucleotides grafted to charged surfaces, Org Biomol Chem. 4 (2006) 3448–3455. https://doi.org/10.1039/B605712H.

[458] S.O. Kelley, J.K. Barton, N.M. Jackson, L.D. McPherson, A.B. Potter, E.M. Spain, M.J. Allen, M.G. Hill, Orienting DNA helices on gold using applied electric fields, Langmuir. 14 (1998) 6781–6784. https://doi.org/10.1021/LA980874N.

[459] F. Fixe, H.M. Branz, N. Louro, V. Chu, D.M.F. Prazeres, J.P. Conde, Electric-field assisted immobilization and hybridization of DNA oligomers on thin-film microchips, Nanotechnology. 16 (2005) 2061–2071. https://doi.org/10.1088/0957-4484/16/10/014.

[460] F. Fixe, H.M. Branz, N. Louro, V. Chu, D.M.F. Prazeres, J.P. Conde, Immobilization and hybridization by single sub-millisecond electric field pulses, for pixel-addressed DNA microarrays, Biosens Bioelectron. 19 (2004) 1591–1597. https://doi.org/10.1016/J.BIOS.2003.12.012.

[461] S. Vernick, S.M. Trocchia, S.B. Warren, E.F. Young, D. Bouilly, R.L. Gonzalez, C. Nuckolls, K.L. Shepard, Electrostatic melting in a single-molecule field-effect transistor with applications in genomic identification, Nat Commun. 8 (2017). https://doi.org/10.1038/NCOMMS15450.

[462] E. Souteyrand, J.P. Cloarec, J.R. Martin, C. Wilson, I. Lawrence, S. Mikkelsen, M.F. Lawrence, Direct detection of the hybridization of synthetic homo-oligomer DNA sequences by field effect, Journal of Physical Chemistry B. 101 (1997) 2980–2985. https://doi.org/10.1021/JP963056H.

[463] J. Fritz, E.B. Cooper, S. Gaudet, P.K. Sorger, S.R. Manalis, Electronic detection of DNA by its intrinsic molecular charge, Proc Natl Acad Sci U S A. 99 (2002) 14142. https://doi.org/10.1073/PNAS.232276699.

[464] D.S. Kim, Y.T. Jeong, H.J. Park, J.K. Shin, P. Choi, J.H. Lee, G. Lim, An FET-type charge sensor for highly sensitive detection of DNA sequence, Biosens Bioelectron. 20 (2004) 69–74. https://doi.org/10.1016/J.BIOS.2004.01.025.

[465] F. Vivaldi, P. Salvo, N. Poma, A. Bonini, D. Biagini, L. Del Noce, B. Melai, F. Lisi, F. Di Francesco, Recent Advances in Optical, Electrochemical and Field Effect pH Sensors, Chemosensors 2021, Vol. 9, Page 33. 9 (2021) 33. https://doi.org/10.3390/CHEMOSENSORS9020033.

[466] K.B. Parizi, A.J. Yeh, A.S.Y. Poon, H.S.P. Wong, Exceeding Nernst limit (59mV/pH): CMOS-based pH sensor for autonomous applications, Technical Digest - International Electron Devices Meeting, IEDM. (2012). https://doi.org/10.1109/IEDM.2012.6479098.

[467] A. Das, D.H. Ko, C.H. Chen, L.B. Chang, C.S. Lai, F.C. Chu, L. Chow, R.M. Lin, Highly sensitive palladium oxide thin film extended gate FETs as pH sensor, Sens Actuators B Chem. 205 (2014) 199–205. https://doi.org/10.1016/J.SNB.2014.08.057.

[468] W.J. Cho, C.M. Lim, Sensing properties of separative paper-based extended-gate ion-sensitive field-effect transistor for cost effective pH sensor applications, Solid State Electron. 140 (2018) 96–99. https://doi.org/10.1016/J.SSE.2017.10.025.

[469] H.L. Kang, S. Yoon, D. ki Hong, S. Song, Y.J. Kim, W.H. Kim, W.K. Seong, K.N. Lee, Verification of Operating Principle of Nano Field-effect Transistor Biosensor with an Extended Gate Electrode, Biochip J. 14 (2020) 381–389. https://doi.org/10.1007/S13206-020-4410-1.

[470] J. Kim, Y.S. Rim, H. Chen, H.H. Cao, N. Nakatsuka, H.L. Hinton, C. Zhao, A.M. Andrews, Y. Yang, P.S. Weiss, Fabrication of high-performance ultrathin In2O3 film field-effect transistors and biosensors using chemical lift-off lithography, ACS Nano. 9 (2015) 4572–4582. https://doi.org/10.1021/ACSNANO.5B01211.

[471] H. Kim, Y.S. Rim, J.Y. Kwon, Evaluation of Metal Oxide Thin-Film Electrolyte-Gated Field Effect Transistors for Glucose Monitoring in Small Volume of Body Analytes, IEEE Sens J. 20 (2020) 9004–9010. https://doi.org/10.1109/JSEN.2020.2988269.

[472] S. Park, S. Lee, C.H. Kim, I. Lee, W.J. Lee, S. Kim, B.G. Lee, J.H. Jang, M.H. Yoon, Sub-0.5 V Highly Stable Aqueous Salt Gated Metal Oxide Electronics, Scientific Reports 2015 5:1. 5 (2015) 1–9. https://doi.org/10.1038/srep13088.

[473] H. Chen, Y.S. Rim, I.C. Wang, C. Li, B. Zhu, M. Sun, M.S. Goorsky, X. He, Y. Yang, Quasi-Two-Dimensional Metal Oxide Semiconductors Based Ultrasensitive Potentiometric Biosensors, ACS Nano. 11 (2017) 4710–4718. https://doi.org/10.1021/ACSNANO.7B00628.

[474] Q. Liu, C. Zhao, M. Chen, Y. Liu, Z. Zhao, F. Wu, Z. Li, P.S. Weiss, A.M. Andrews, C. Zhou, Flexible Multiplexed In2O3 Nanoribbon Aptamer-Field-Effect Transistors for Biosensing, IScience. 23 (2020) 101469. https://doi.org/10.1016/J.ISCI.2020.101469.

[475] Y.S. Rim, S.H. Bae, H. Chen, J.L. Yang, J. Kim, A.M. Andrews, P.S. Weiss, Y. Yang, H.R. Tseng, Printable Ultrathin Metal Oxide Semiconductor-Based Conformal Biosensors, ACS Nano. 9 (2015) 12174–12181. https://doi.org/10.1021/ACSNANO.5B05325.

[476] B. Wang, C. Zhao, Z. Wang, K.A. Yang, X. Cheng, W. Liu, W. Yu, S. Lin, Y. Zhao, K.M. Cheung, H. Lin, H. Hojaiji, P.S. Weiss, M.N. Stojanović, A.J. Tomiyama, A.M. Andrews, S. Emaminejad, Wearable aptamer-field-effect transistor sensing system for noninvasive cortisol monitoring, Sci Adv. 8 (2022) 967. https://doi.org/10.1126/SCIADV.ABK0967.

[477] M.J. Schöning, A. Poghossian, Recent advances in biologically sensitive field-effect transistors (BioFETs), (2002). https://doi.org/10.1039/b204444g.

[478] J.T. Friedlein, R.R. McLeod, J. Rivnay, Device physics of organic electrochemical transistors, Org Electron. 63 (2018) 398–414. https://doi.org/10.1016/J.ORGEL.2018.09.010.

[479] J. Nissa, P. Janson, M. Berggren, D.T. Simon, J. Nissa, P. Janson, M. Berggren, D.T. Simon, The Role of Relative Capacitances in Impedance Sensing with Organic Electrochemical Transistors, Adv Electron Mater. 7 (2021) 2001173. https://doi.org/10.1002/AELM.202001173.

[480] K.H. Lundberg, Internal and external op-amp compensation: A control-centric tutorial, Proceedings of the American Control Conference. 6 (2004) 5197–5211. https://doi.org/10.23919/ACC.2004.1384678.

[481] N. Aroonyadet, X. Wang, Y. Song, H. Chen, R.J. Cote, M.E. Thompson, R.H. Datar, C. Zhou, Highly scalable, uniform, and sensitive biosensors based on top-down indium oxide nanoribbons and electronic enzyme-linked immunosorbent assay, Nano Lett. 15 (2015) 1943–1951. https://doi.org/10.1021/NL5047889.

[482] J. Monreal-Trigo, M. Alcañiz, M.C. Martínez-Bisbal, A. Loras, L. Pascual, J.L. Ruiz-Cerdá, A. Ferrer, R. Martínez-Máñez, New bladder cancer non-invasive surveillance method based on voltammetric electronic tongue measurement of urine, IScience. 25 (2022). https://doi.org/10.1016/J.ISCI.2022.104829.

Annexes

Annex 01. FAEVIS Schematic 1/2

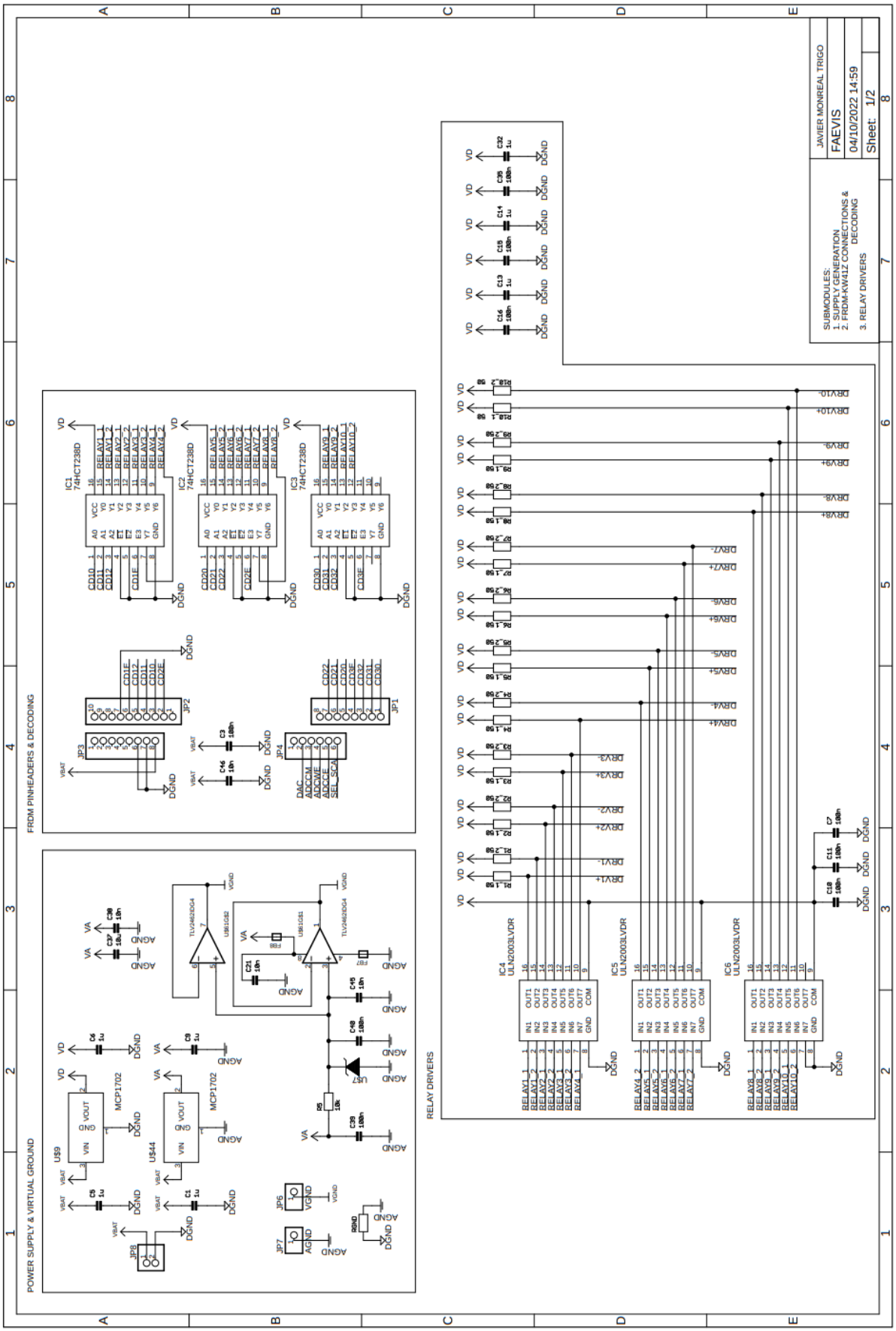

Annex 02. FAEVIS Schematic 2/2

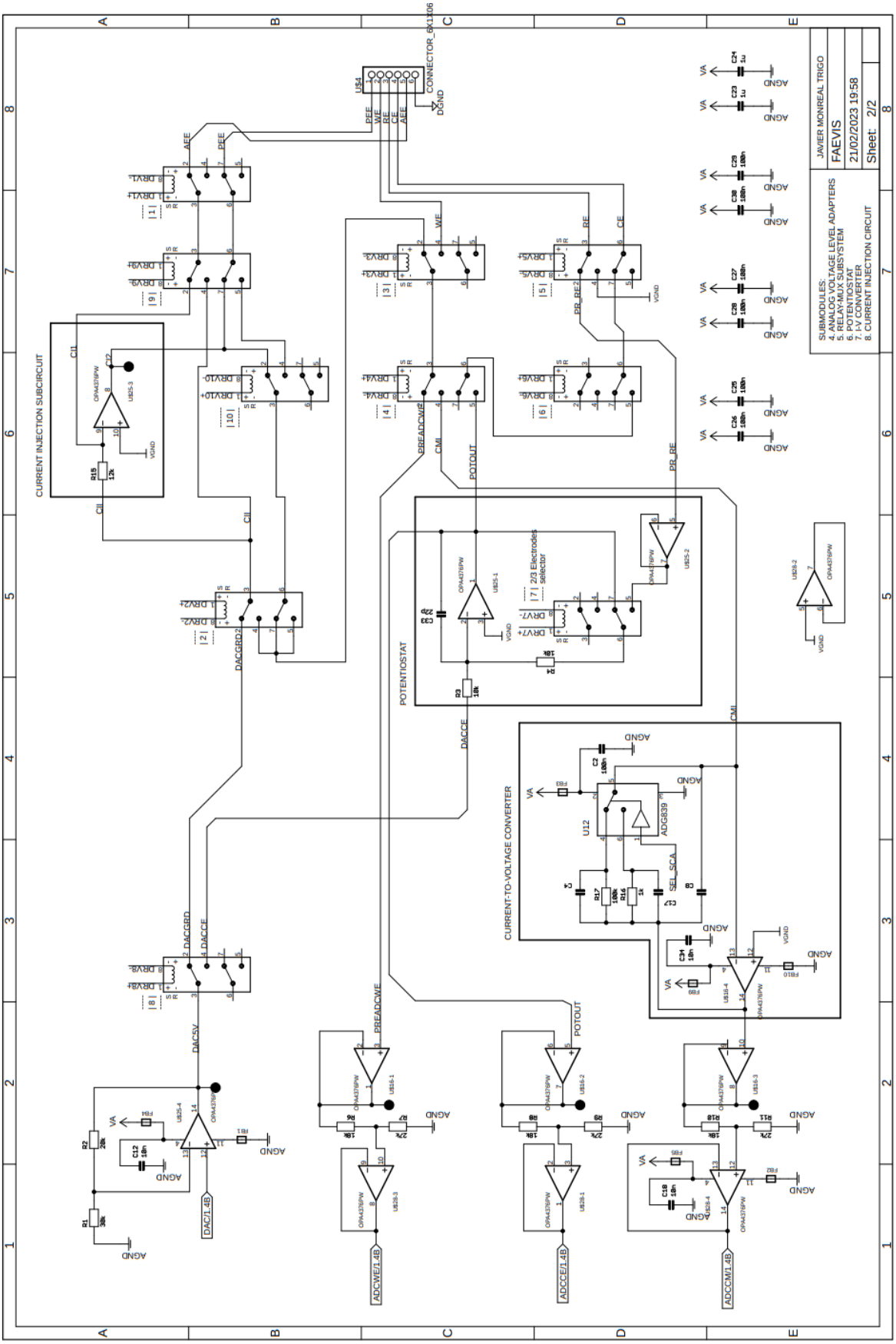

Annex 03. FAEVIS' Bluetooth Low Energy communications

As commented in *5.1.2. Wireless communications*, a USB BLE dongle with the same MKW41Z microcontroller as the one in FAEVIS, is used as a BLE-UART interface to the PC where the GUI is hosted. The USB dongle and FAEVIS share the same BLE control and application functions but with different input message processing codes.

All the BLE protocol is managed by an Operational System Abstraction Layer (OSAL). In our implementation, *FreeRTOS* real-time operating system is used. *FreeRTOS* is a high-performance and low-resource consumption freeware. It simplifies the coordination between BLE layers and frees some hardware interrupts in the MCU, which will be used for the application. In fact, in NXP's documentation and resources, there are far fewer options and content developed for BLE in *bare metal* (without an operating system) than with RTOS.

Now that the operation of the BLE protocol is contextualized, we can address the adopted solution: BLE contains a multitude of official attribute profiles for different applications, but since its target are low-power devices, no attribute profile allows establishing a continuous serial communication, which is of interest in this project. That is why we implement, based on the BLE protocol, a custom protocol for this application, with automatic connection capability between FAEVIS and its dongle, implementing a serial communication with stop & wait transmission. The protocol is designed to be completely reversible, overriding the hierarchy present in BLE to establish a classic OTA serial communication between two peers.

A customized profile is implemented for GATT with only one service, characteristic, and attribute: a 20-bytes value (its maximum size). In this way, for the Host layers of each of the peers, the communication is simple:

- It becomes independent of which will be set as Central (master), and the other as Peripheral (slave).
- Each peer will act as the Server for Hermes, available for the other as a Client.
- A message is sent from the Client to the Server as an attribute write, raising a notification in the Server side.

This way, a simple full-duplex serial communication based on modified Bluetooth Low Energy has been implemented. Given the operating logic of traditional messengers and mailboxes, the protocol is named Hermes, after the Greek messenger god. See the profile representation in **Annex Figure 1** The attribute protocol (ATT) layer is modified so that only the two peers can connect, improving the system's security.

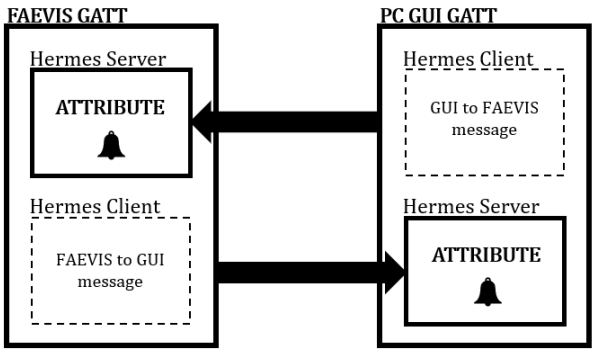

Annex Figure 1. General representation of the Hermes BLE profile.

Message handling by the dongle's microcontroller is simple: it sends what is received by BLE through UART and by UART through BLE. The processing of receptions and sends via UART are handled by a hardware timer interrupt programmed with 1 ms period.

However, message processing in FAEVIS is more complex since it must also implement the Hermes application protocol. The Hermes ISR will check if the flags indicate new input messages or messages to send, actuating accordingly.

Data messages are always composed of the following structure (**Annex Figure 2**):

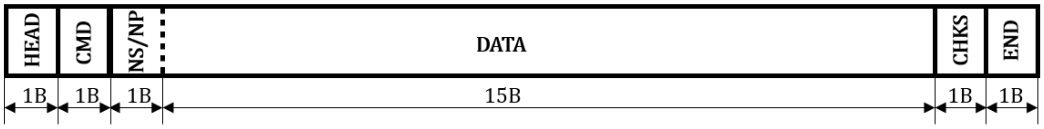

Annex Figure 2.. Data frame of Hermes communication. Every message has a header [0] and an end [19] byte. Bytes [1] and [18] are reserved for the command information and checksum, respectively. Bytes [2] and bytes [3-17] carries the data content. In long communications (waveform transmission or electrical signals acquisition feedback), byte [2] is used as container of the number of points (NP) and Nseq (NS) byte in the go-back-N protocol.

When FAEVIS has received a new message, an application-level integrity check is performed (checksum). If there is an integrity error, the error reply (`0xEE` CMD) will be sent from FAEVIS to the GUI. Otherwise, the message CMD is analyzed.

Different communication actions from the GUI to FAEVIS can be established:

- Simple commands involve a single answer from FAEVIS acknowledging or with information.
- Configuration data transmission involves several data packages from the GUI to FAEVIS, with ACK after each message from FAEVIS to the GUI.

- Experience data transmission, which involves several data packages from FAEVIS to the GUI, with ACK after each message from the GUI.

Next, we are going to list all the available commands according to the CMD byte of the frame, classified into the three groups above:

Simple commands (GUI to FAEVIS, FAEVIS just ACK):

- `0x11`: *are you alive?*, expects an echo reply.
- `0x55`: start experience.
- `0xBB`: stop experience.
- `0x77`: stop transmission.
- `0xDD`: set DAC value.
- `0xA1`: WE ADC autocalibration.
- `0xA2`: CE and CM large scale ADC autocalibration.
- `0xA3`: CE and CM precision scale ADC autocalibration.
- `0xB2`: Send `0xA2` or `0xA3` data to GUI.
- `0xC1`: set potentiometry configuration. It shall be coherent, otherwise it will reply error.
- `0xC2`: set voltammetry or electrostimulation configuration. It shall be coherent, otherwise it will reply error.
- `0xEE`: error, expecting FAEVIS to resend the last message.

Configuration data transmission:

- `0x58`: set waveform to be applied in voltammetry or electrostimulation (it is needed to apply `0xC2` first).

Experience data transmission:

- `0x1D`: start sending potentiometry data, order from GUI to FAEVIS.
  - Will be acknowledged with `0x17`, starting experience data transmission.
- `0x17`: keep sending potentiometry data. Can be replied with:
  - `0x17`: new experience data transmission.
  - `0x1E`: end of potentiometry data transmission header from FAEVIS.
- `0x2D`: start sending CM data, order from GUI to FAEVIS.
  - Will be acknowledged with `0x27`, starting experience data transmission.
- `0x27`: keep sending CM data. Can be replied with:

    - 0x27: new experience data transmission.
    - 0x2E: end of CM data transmission header from FAEVIS.
- 0x3D: start sending CE voltage data, order from GUI to FAEVIS.
    - Will be acknowledged with 0x37, starting experience data transmission.
- 0x37: keep sending CE voltage data. Can be replied with:
    - 0x37: new experience data transmission.
    - 0x3E: end of CE voltage data transmission header from FAEVIS.
- 0x8D: restart measurement, once received 10,000 samples, from GUI to FAEVIS.
    - It shall be followed by 0x2D or 0x3D from GUI after FAEVIS' ACK.

Annex 04. IVESDRIS's MBSI Schematic 1/5

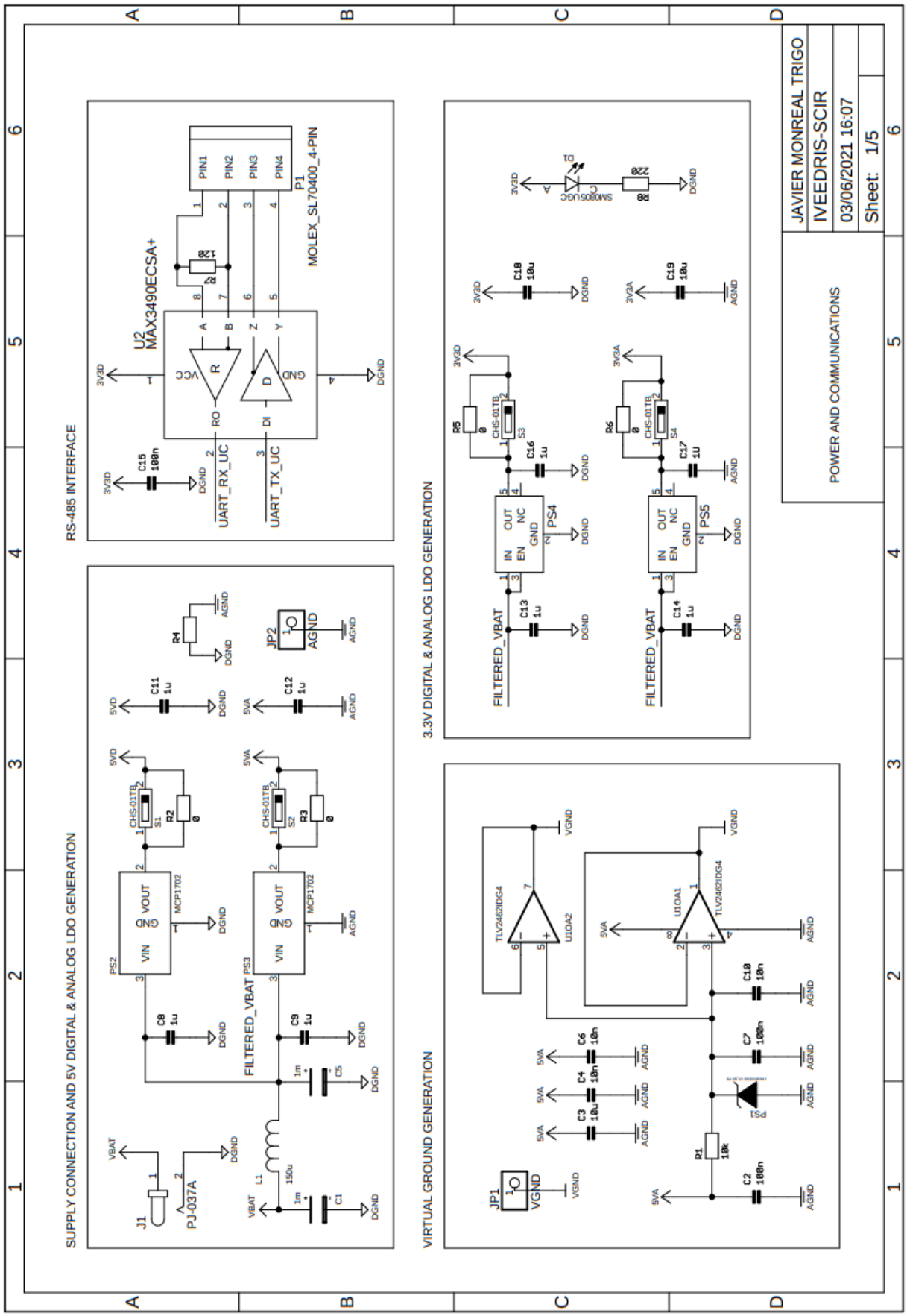

Annex 05. IVESDRIS's MBSI Schematic 2/5

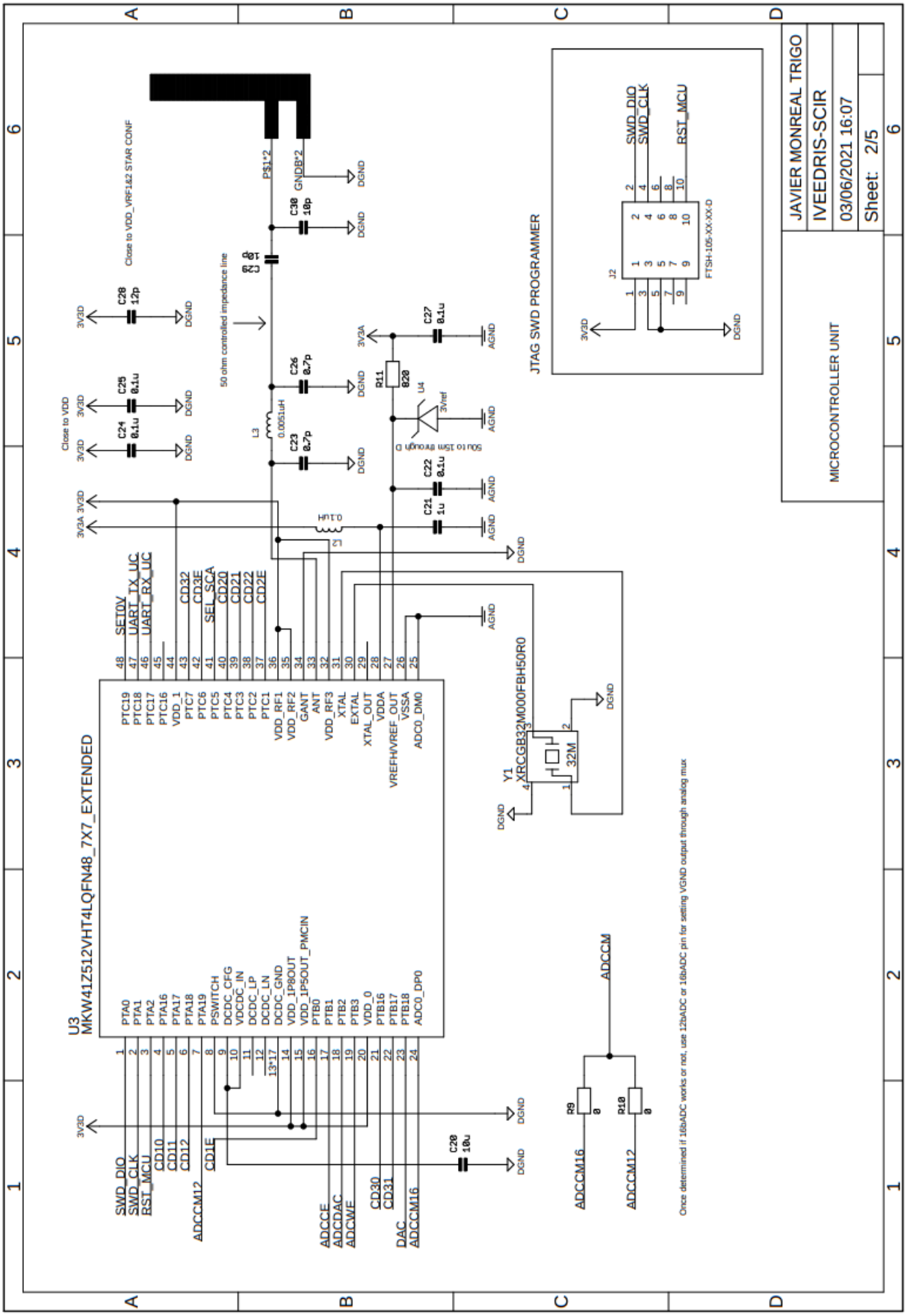

Annex 06. IVESDRIS's MBSI Schematic 3/5

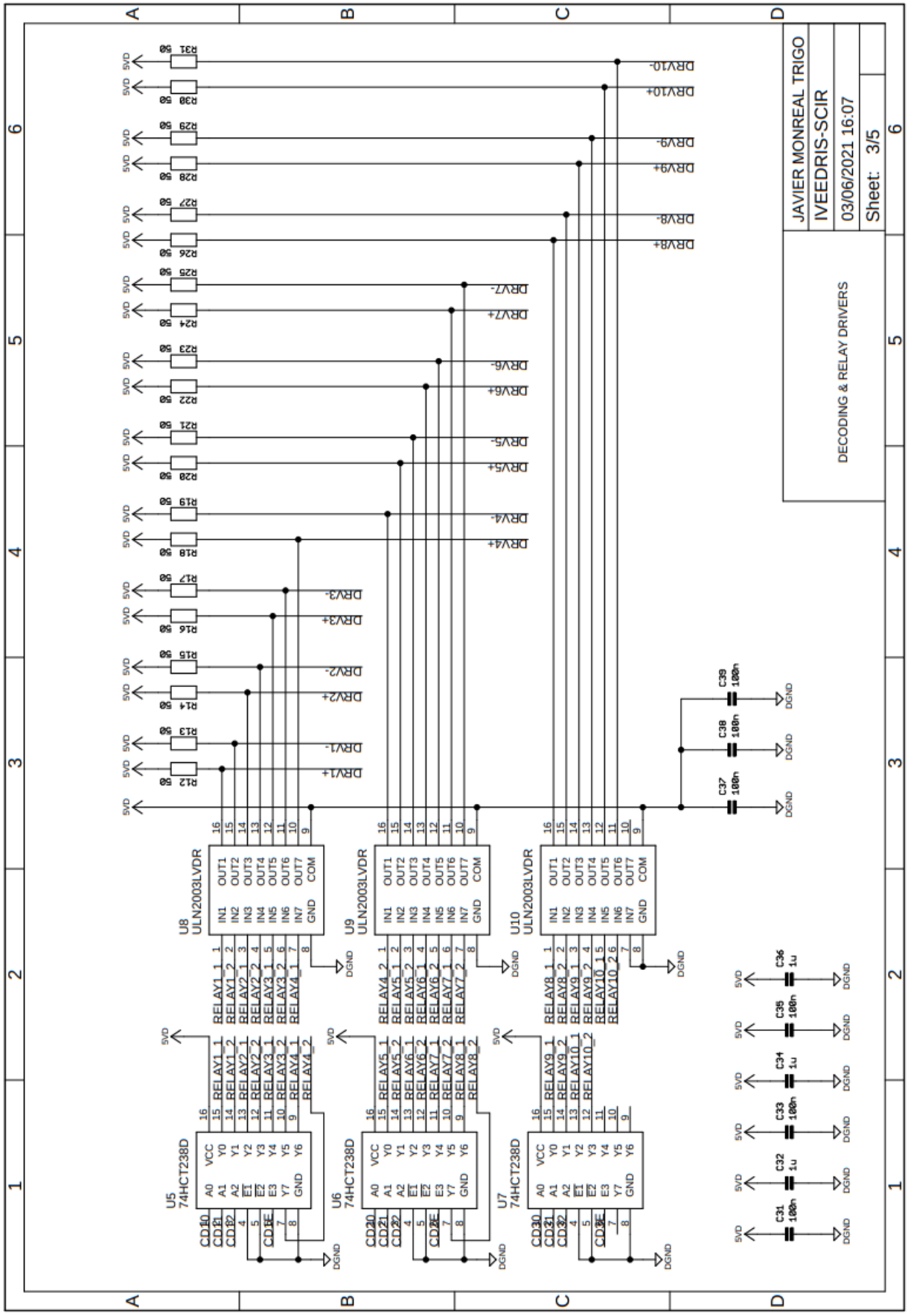

Annex 07. IVESDRIS's MBSI Schematic 4/5

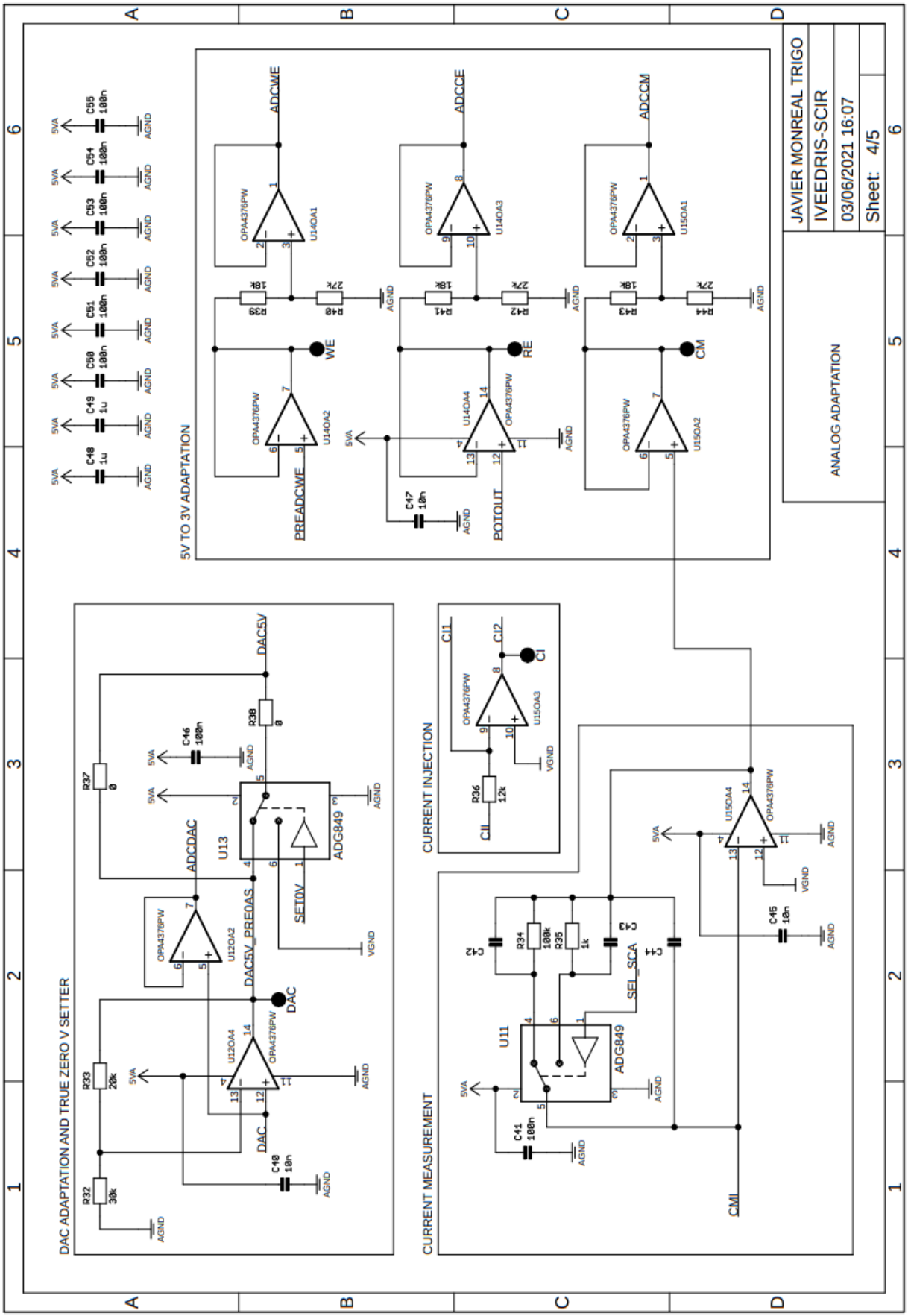

Annex 08. IVESDRIS's MBSI Schematic 5/5

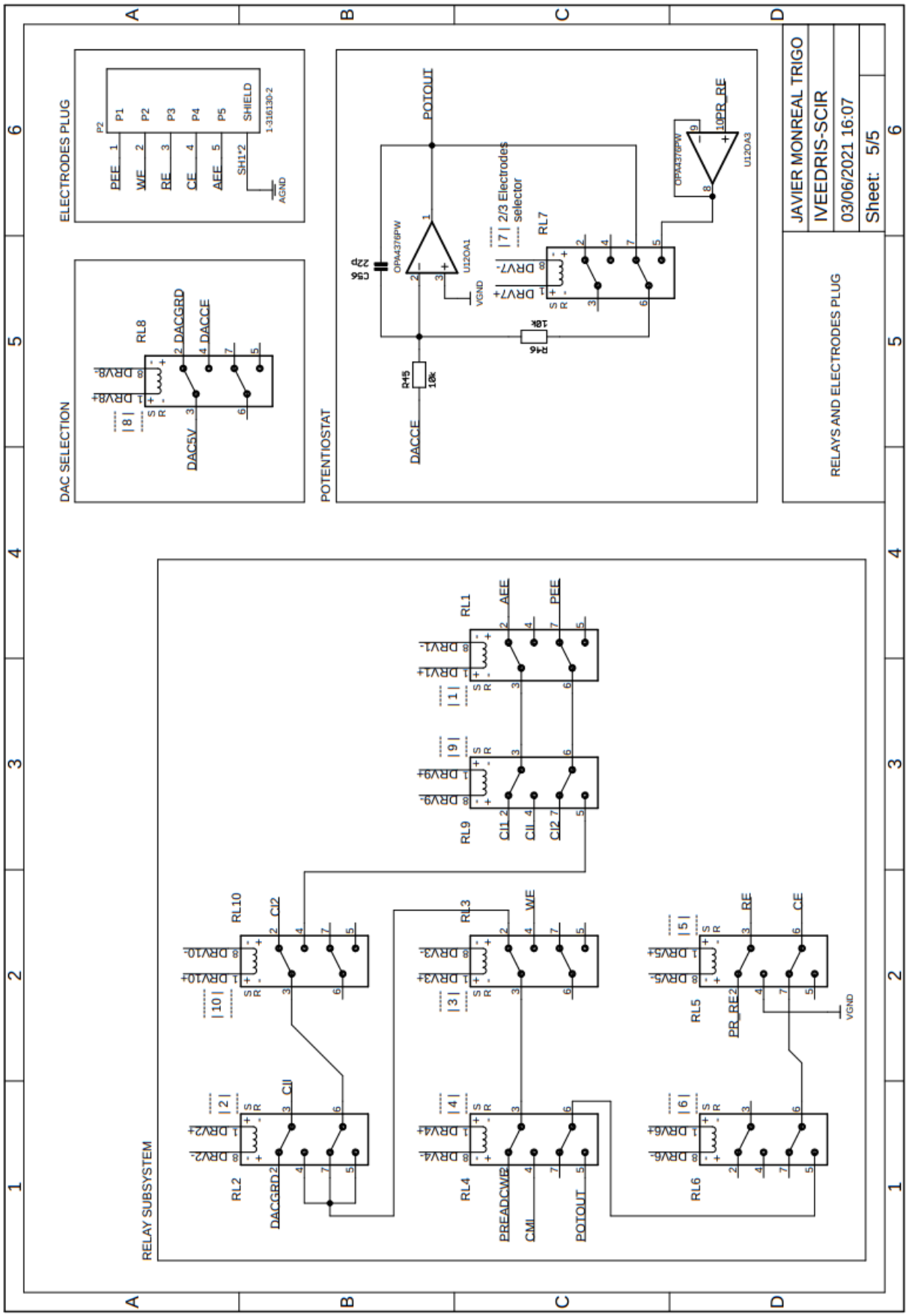

Annex 09. IVESDRIS' SCB Shield Schematic

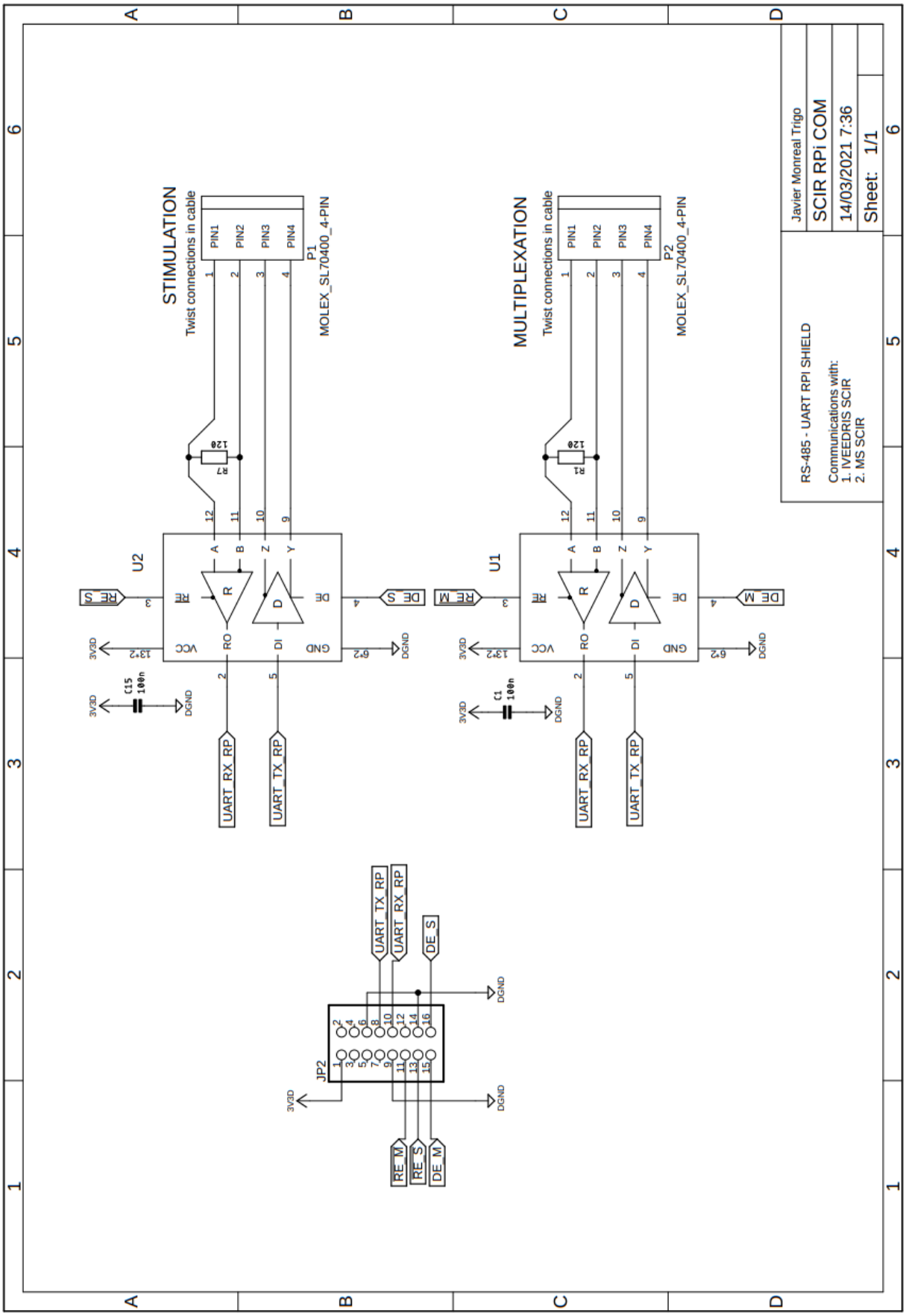

Annex 10. OSIVE Slim Schematic 1/2

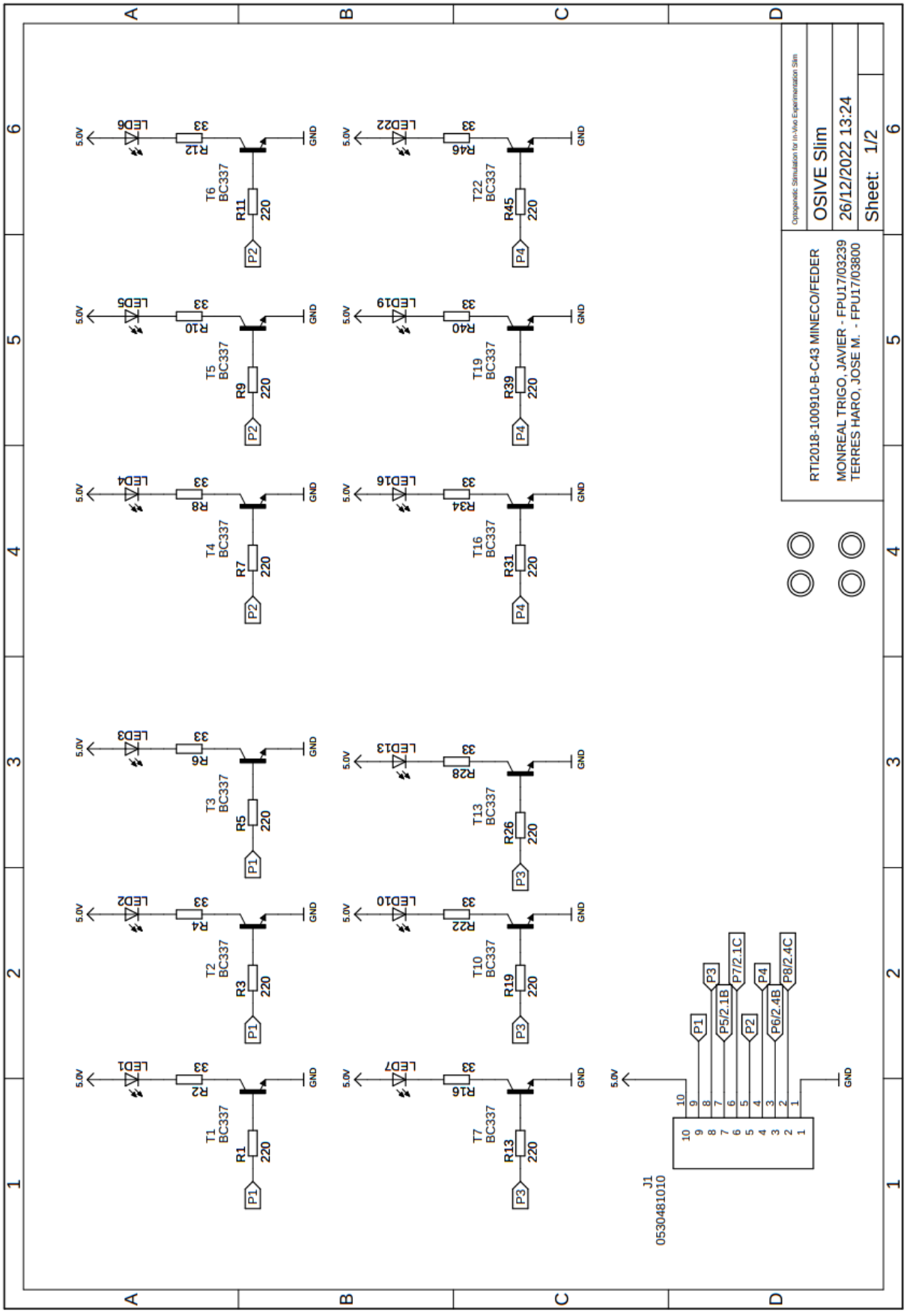

Annex 11. OSIVE Slim Schematic 2/2

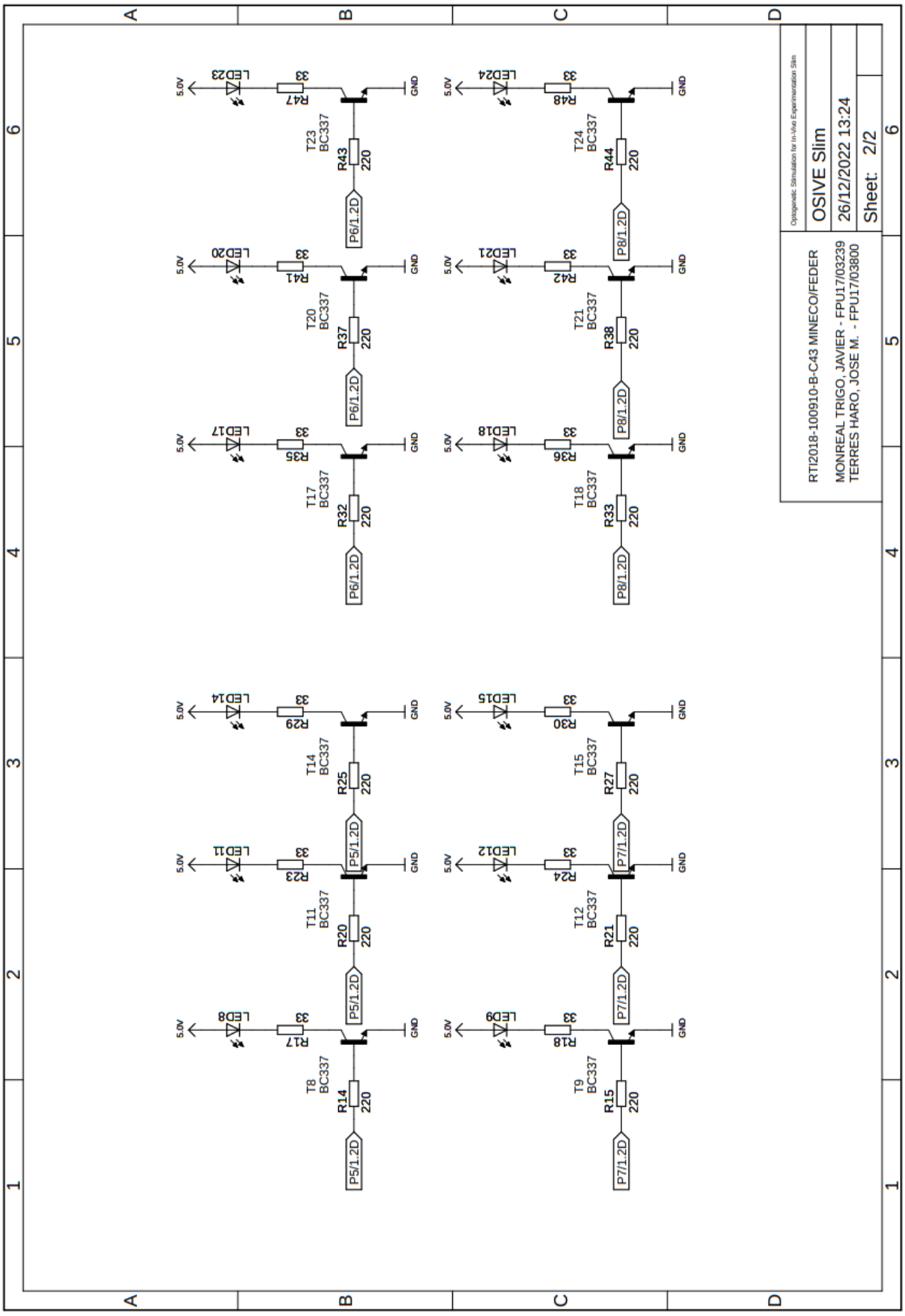

Annex 12. OSIVE Slim DUE-Shield Schematic

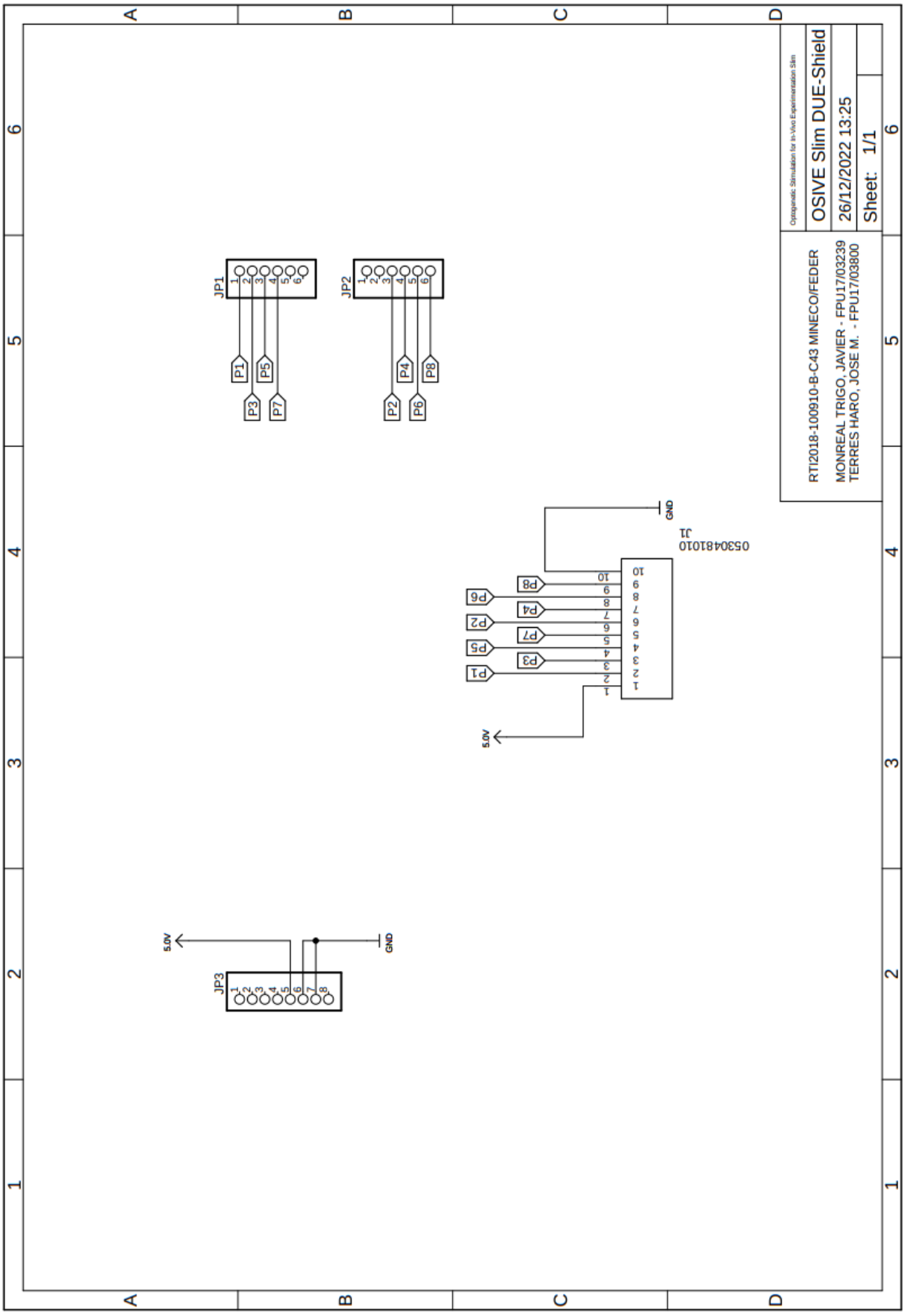

Annex 13. OSIVE IMS Schematic

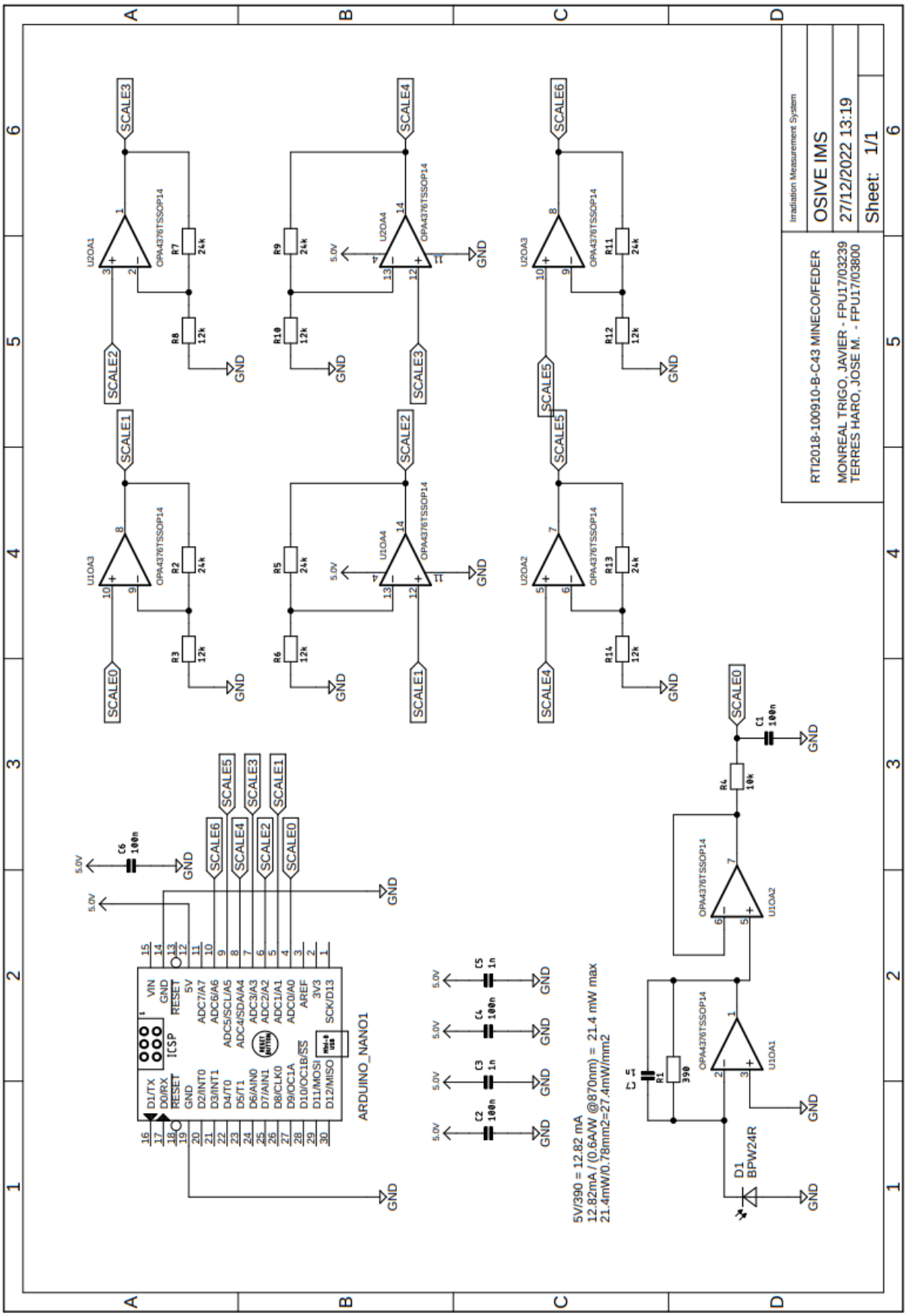

Annex 14. MBMS Schematic (1/8)

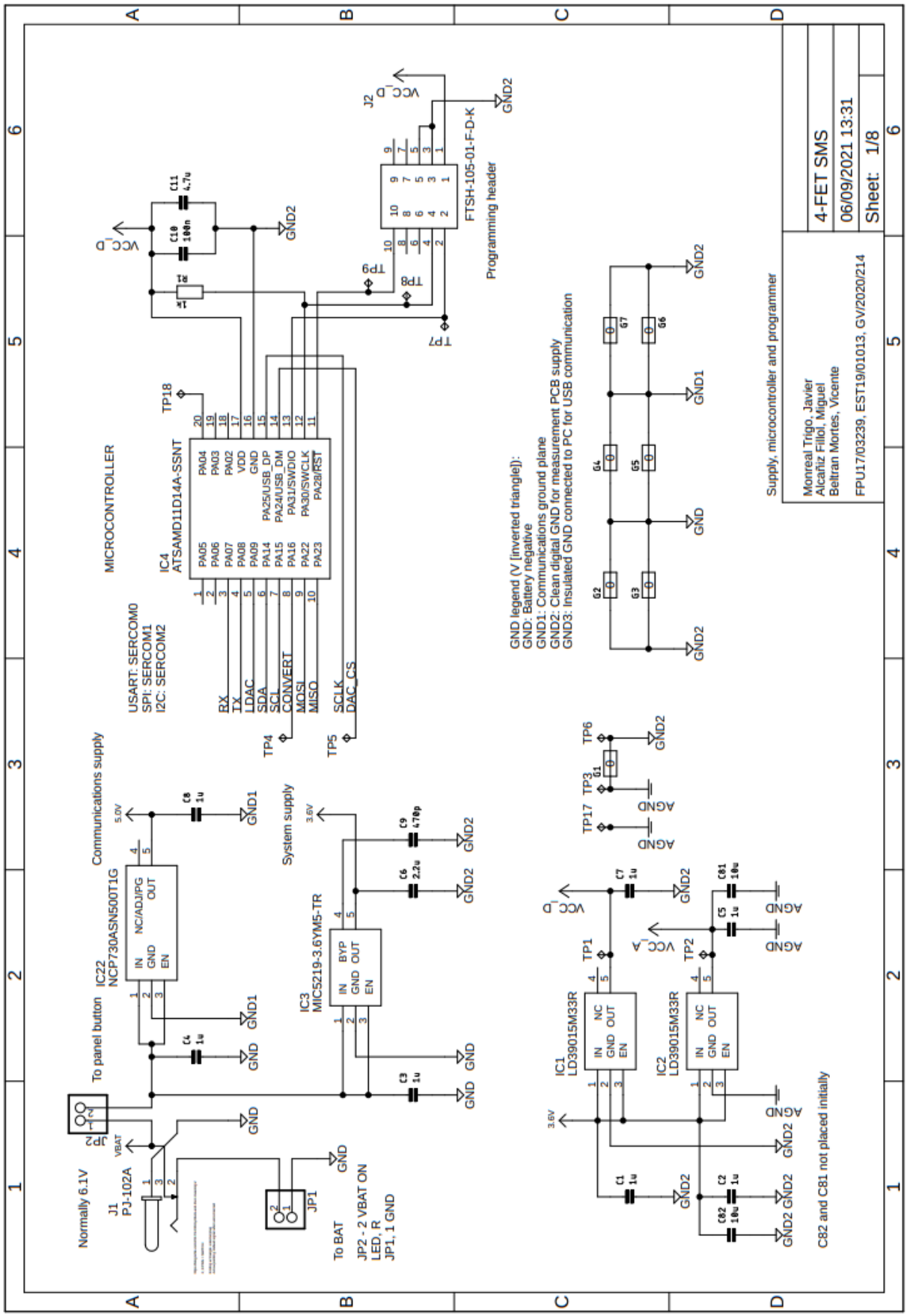

Annex 15. MBMS Schematic (2/8)

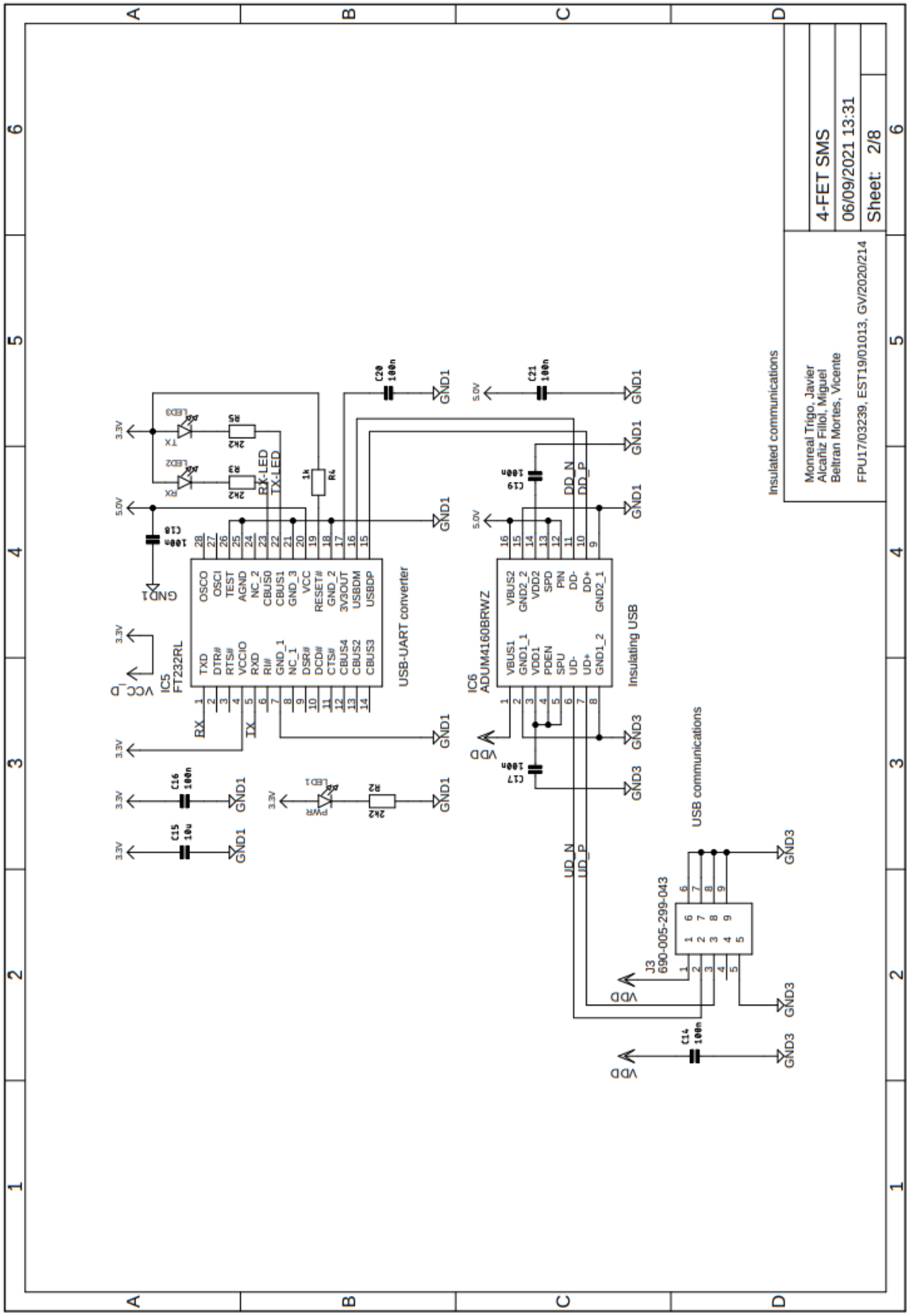

Annex 16. MBMS Schematic (3/8)

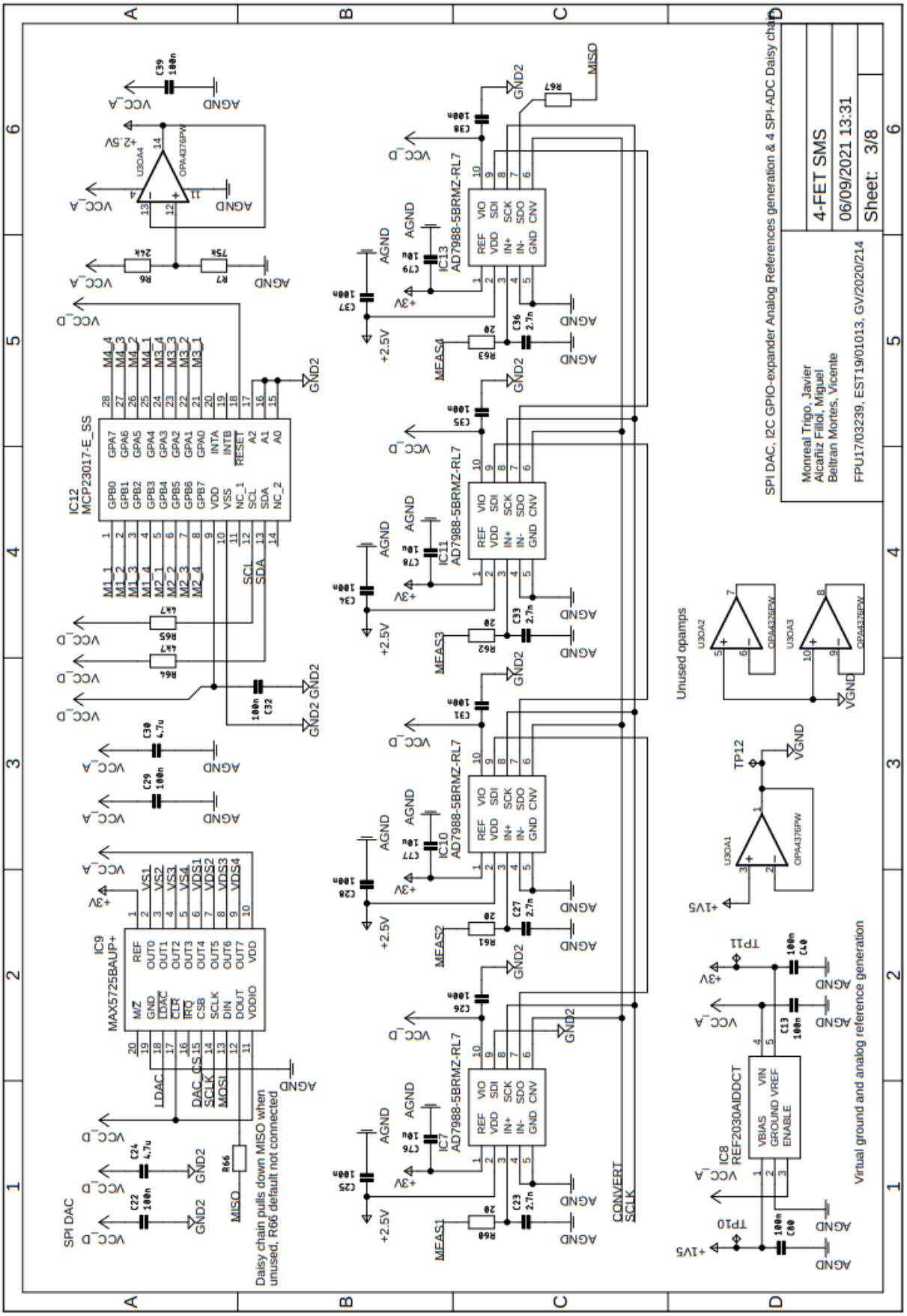

Annex 17. MBMS Schematic (4/8)

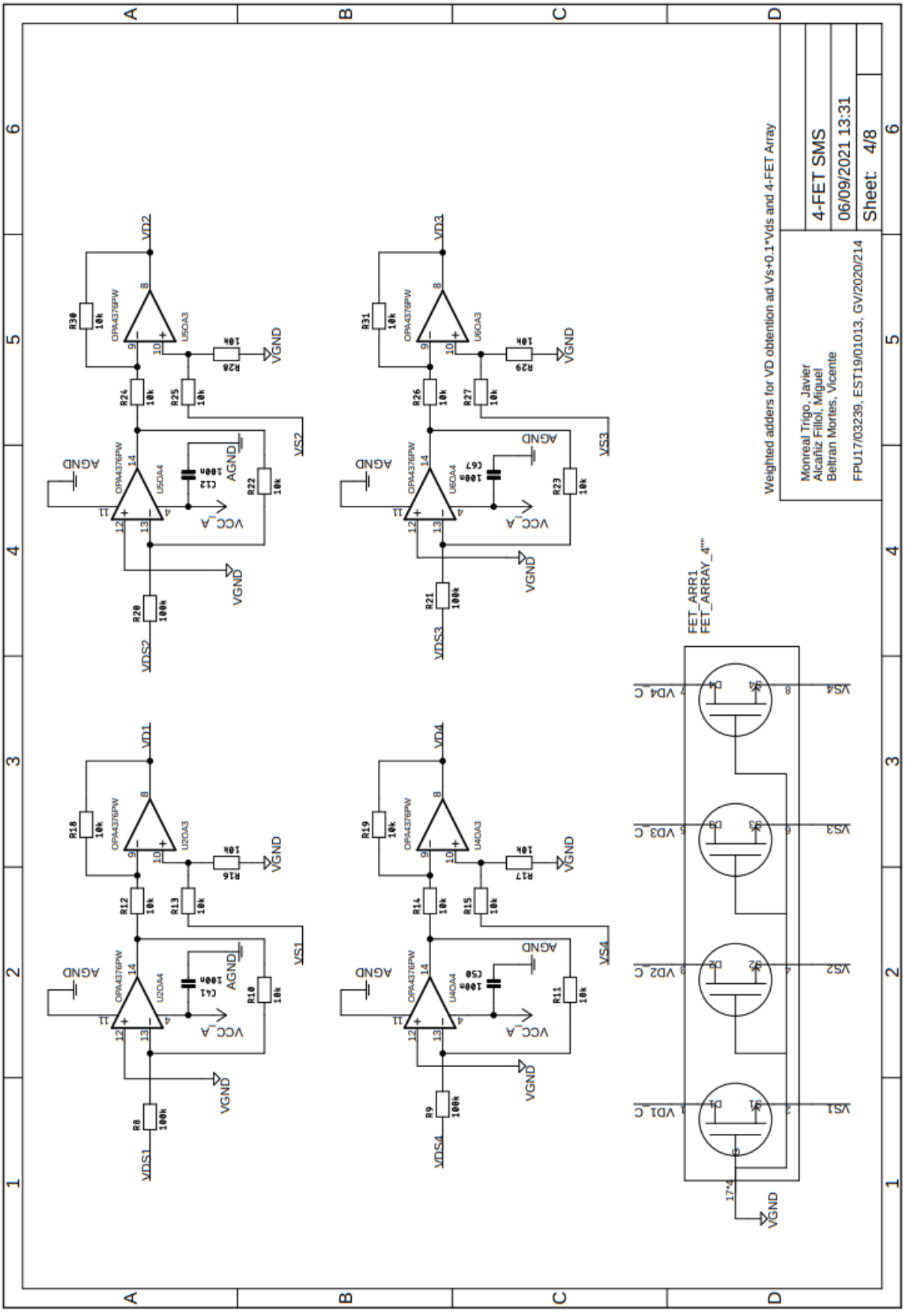

Annex 18. MBMS Schematic (5/8)

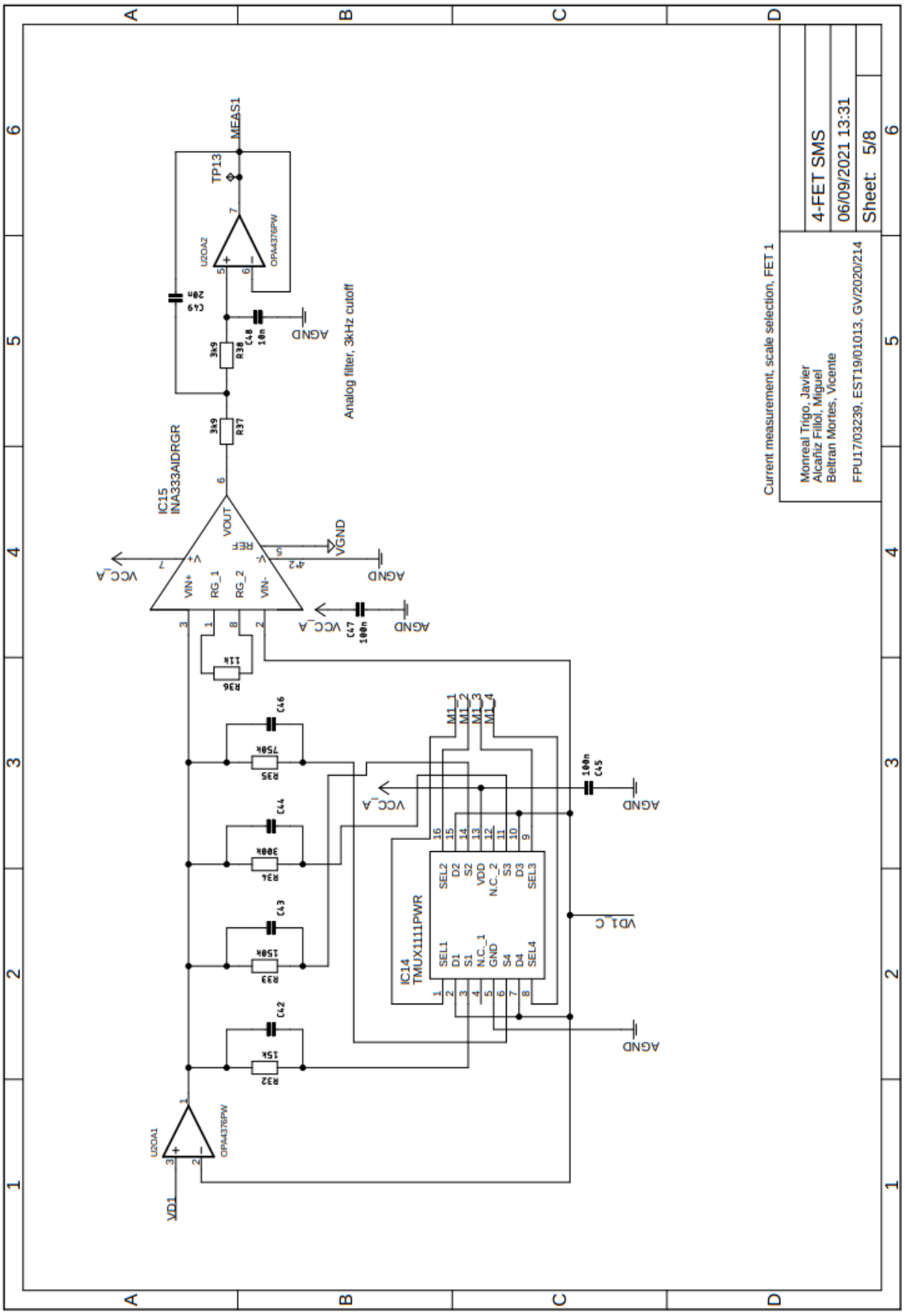

Annex 19. MBMS Schematic (6/8)

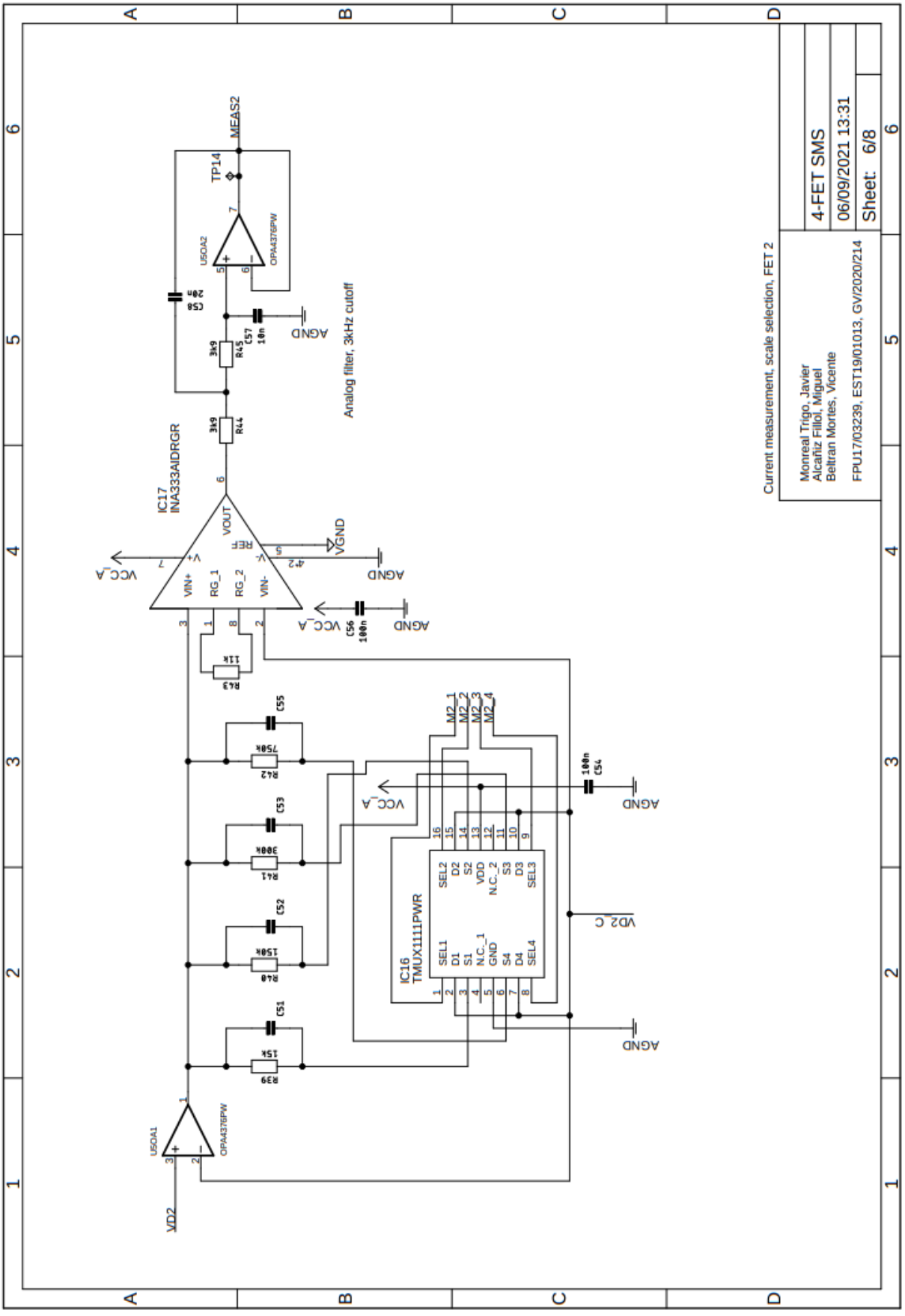

Annex 20. MBMS Schematic (7/8)

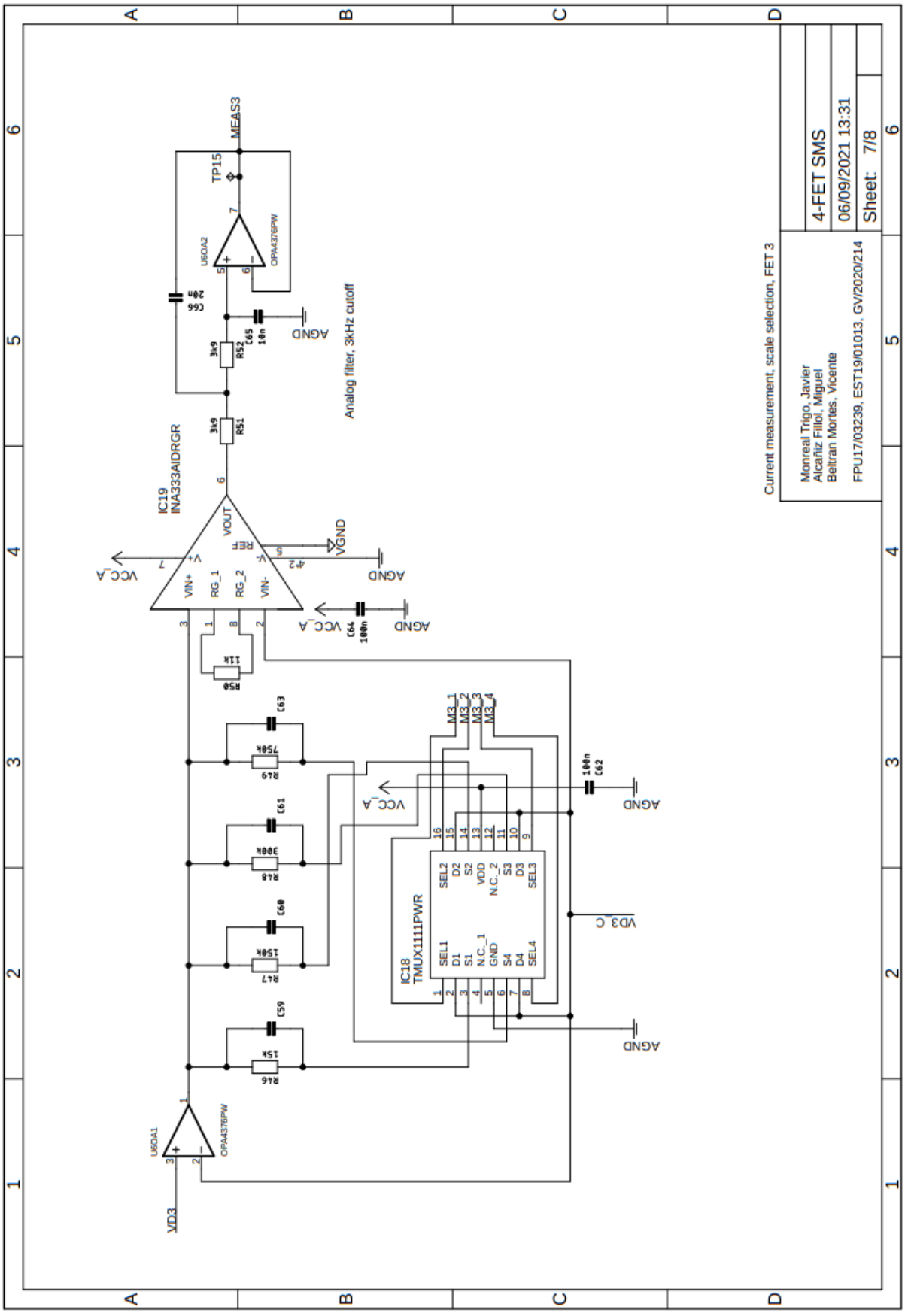

Annex 21. MBMS Schematic (8/8)